Reductive Binding of C–O and Nitro Substrates at a Pyrazolate-Bridged Preorganized Dinickel Scaffold

Dissertation

zur Erlangung des mathematisch-naturwissenschaftlichen Doktorgrades „Doctor rerum naturalium“

der Georg-August-Universität Göttingen im Promotionsprogramm Catalyisis for Sustainable Synthesis (CaSuS) der Georg August University School of Science (GAUSS)

vorgelegt von

Thomas Kothe

aus Gelnhausen

Göttingen, 2020

Betreuungsausschuss

Prof. Franc Meyer

Institut für Anorganische Chemie, Georg-August-Universität Göttingen

Prof. Sven Schneider

Institut für Anorganische Chemie, Georg-August-Universität Göttingen

Prof. Marc Walter

Institut für Anorganische und Analytische Chemie, Technische Universität Braunschweig

Prüfungskomitee

Referent: **Prof. Franc Meyer**

Institut für Anorganische Chemie, Georg-August-Universität Göttingen

Korreferent: **Prof. Sven Schneider**

Institut für Anorganische Chemie, Georg-August-Universität Göttingen

2. Korreferent: **Prof. Marc Walter**

Institut für Anorganische und Analytische Chemie, Technische Universität Braunschweig

Prof. Konrad Koszinowski

Institut für Organische und Biomolikulare Chemie, Georg-August-Universität Göttingen

Prof. Dietmar Stalke

Institut für Anorganische Chemie, Georg-August-Universität Göttingen

Dr. Christian Sindlinger

Institut für Anorganische Chemie, Georg-August-Universität Göttingen

Datum der mündlichen Prüfung: 05.11.2020

List of Abbreviations

Å	Ångström
ACS	Acetyl CoA synthase
Ar	Aryl
BDE	Bond dissociation energy
Bn	Benzyl
Bu	Butyl
CODS	CO dehydrogenase
COSY	Correlated spectroscopy
Cp	Cyclopentadienyl anion
Cp*	Pentamethylcyclopentadienyl anion
CV	Cyclic voltammetry
3,5-DCTB	3,5-di-*tert*-butylcatechol
DDQ	2,3-Dichloro-5,6-dicyano-1,4-benzoquinone
DFT	Density Functional Theory
dipp	Diisopropylphenyl
DME	Dimethoxy ethane
DMSI	Dimethyl sulfoxide
e^-	Electron
EA	Elemental analysis
EPR	Electron Paramagnetic Resonance
ESI	Electrospray ionization
et al.	*Et alia*
FeCp2/Fc	bis(η^5-cyclopentadienyl)iron(II); ferrocene
$FeCp^*_2$/Fc*	bis(η^5-pentamethylcyclopentadienyl)iron(II); decamethylferrocene
HMBC	Heteronuclear multiple-bond
HSQC	Heteronuclear single quantum correlation

IR	Infrared
L	Ligand
Lut	Lutidine
M	Metal
Me	Methyl
MCR	Methyl-coM reductase
MO	Molecular orbital
MS	Mass spectrometry
m/z	Mass per charge
$\tilde{v}$	Wavenumber
NMR	Nuclear magnetic resonance
SOD	Nickel superoxide dismutase
Ts	Tosyl
Ph	Phenyl
Ppm	Parts per million
Pz	Pyrazole
RT	Room temperature, 25 °C
SOMO	Single occupied molecular orbital
TEMPO	(2,2,6,6-tetramethylpiperidine-1-oxyl)
Tf	Trifluoromethyl
THF	Tetrahydrofuran
THF-d_8	Deuterated tertahydrofuran
UV/vis	Ultraviolet/visible
Vs.	*Versus*
VT	Variable temperature

Table of Content

1 General Introduction **1**

1.1 Nickel in Enzyme Systems 1

1.2 β-Diketiminate Ligand Scaffolds 2

1.3 The Pyrazolate-Bridged Bis(β-diketiminate) Ligand System 4

2 Thesis Outline **7**

3 Reproduction and Improvement of the Synthesis of Dinickel Dihydride and Dinitrogen Complexes **8**

3.1 Biological Inspiration behind the Hydrogen Release Coupled Substrate Reductions 8

3.2 Synthesis of the Dinickel Dihydrido Complex **2-K** 9

3.3 Abstraction of One Hydrido Ligand for the Single Reduction of Dinitrogen 13

4 Alkylation of a Bimetallic Dinickel Site and its Application as an Acetyl CoA Synthase Model **16**

4.1 Introduction 16

4.1.1 Nickel alkyl complexes 16

4.1.2 Acetyl CoA Synthase 16

4.1.3 Model Complexes for the Acetyl CoA Synthase 18

4.1.4 Objective 19

4.2 Results and Discussion 20

4.2.1 Methylation of the Dinickel Moiety 20

4.2.2 Mechanism of the Generation of the Dinickel Methylate Complex **6** 26

4.2.3 Synthesis of bridging Dinickel Alkylidene Complexes 28

4.2.4 Reactivity of the Dinickel Methyl Complex towards CO 34

4.3 Conclusion 39

5 Activation of CO on a Dinickel Site and Proton Coupled Interconversion to a Reduced Formaldehyde Moiety **40**

5.1 Introduction 40

5.1.1 CO as a Ligand in Metal Complexes 40

5.1.2 Activation of CO in Nickel(I) Carbonyl Complexes 41

5.1.3 Metal Mediated Reduction of CO 42

5.1.4 Nickel-based Aldehyde Reduction 43

5.1.3 Objective 46

5.2. Results and Discussion 47

5.2.1 CO activation *via* a single electron reduced dinickel complex 47

5.2.2 Mechanistic Studies of the CO Activation 51

5.2.3 Hydride Addition to the Dinickel Formyl Complex **10^{H}** 54

5.2.4 Reductive Binding of Formaldehyde to the Dinickel Moiety 55

5.2.5 Hydride Transfer Reactivity of **2-K** towards Formaldehyde in Benzene 59

5.2.6 Oxidation of the oxymethylene unit in **11-K** 63

5.2.7 Reductive Binding of Benzaldehyde 66

5.2.8 Reactivity of the Dinickel Benzaldehyde Complex Towards Dihydrogen 70

5.2.9 The Cation Influence on the Structure of Dinickel Benzaldehyde Complex **13-K** 72

5.2.10 Effects of the *para* Substituents in Dinickel Arylaldehydes 74

5.3 Conclusion 78

6 Reductive Binding of Nitro Substrates on a Bimetallic Dinickel Site 79

6.1 Introduction 79

6.1.1 Reduction of Nitro Compounds to Amines 79

6.1.2 Derivatives of Dihydroxylamines 80

6.1.3 Nickel Complexes of Nitro Group Reduction Intermediates 80

6.1.4 Objective 82

6.2 Results and Discussion 83

6.2.1 Chemoselective Reduction of a Nitro Function in Presence of a Carbonyl function 83

6.2.2 Reductive Binding of Nitrobenzene 89

6.2.3 Formal Deoxygenation of the Dinickel Nitrobenzene Complex **14^{Ph}-K** 95

6.2.4. Reductive Binding of Nitromethane 102

6.2.5 Alkali Metal Cation Dependent Thermal Stability of the Dinickel Nitromethane complexes 107

6.3 Conclusion 113

7 Experimental Part 114

7.1 Materials and Methods 114

7.2 Instrumentation 114

7.3 Synthetic Procedures 116

8 Literature 140

9 Appendix 148

9.1 NMR Data 148

9.2 IR Data 200

9.3 UV-vis Data 210

9.4 Mass Spectrometry Data 214

9.5 Experimental X-ray Data 218
9.6 DFT Calculation 224
Acknowledgements 230

1 General Introduction

1.1 Nickel in Enzyme Systems

Nickel is a relatively abundant element and is usually acquired by organisms in form of Ni^{II}.[1] In this oxidation state, nickel ions are usually found with coordination numbers of 4, 5 or 6 around the metallic center. Four coordinate nickel ions are mainly associated with diamagnetic square planar or paramagnetic tetrahedral coordination geometries around the metallic center. The valence shell electron configuration of $3d^8 4s^2$ enables nickel to stabilize the uncharged Ni^0 state in a molecular complex relatively easy by achieving the configuration $3d^{10}$. Unlike the common oxidation states 0 and +II, the states +I and +III are rather scarce due to the thermal instability and high reactivity of such complexes. However, this makes them interesting as possible intermediate states in enzymatic catalytic cycles.

Although the majority of metalloenzymes contain iron, copper and zinc or main group metals such as magnesium and calcium, the importance of enzymes where nickel serves as an essential cofactor is well documented.[2] While they exclusively occur in microbial organisms,[3] out of the eight known nickel enzymes, seven involve the utilization and production of small molecules that play a key role in the global carbon, nitrogen and oxygen cycles. Important examples are Ni-Fe hydrogenase (H_2ase), nickel superoxide dismutase (SOD), urease, CO dehydrogenase (CODH), acetyl CoA synthase (ACS) and methyl-coM reductase (MCR). Their active centers are presented in Figure 1. Nickel appears to be especially suited for these substrate conversions, due to its plasticity and ability to adapt a potential span of 1.5 V between the different oxidation states.[4] Inspired by this versatility, employing nickel as a central unit in synthetic systems for the activation of small molecules in catalysis has recently become object to intensive research.[5]

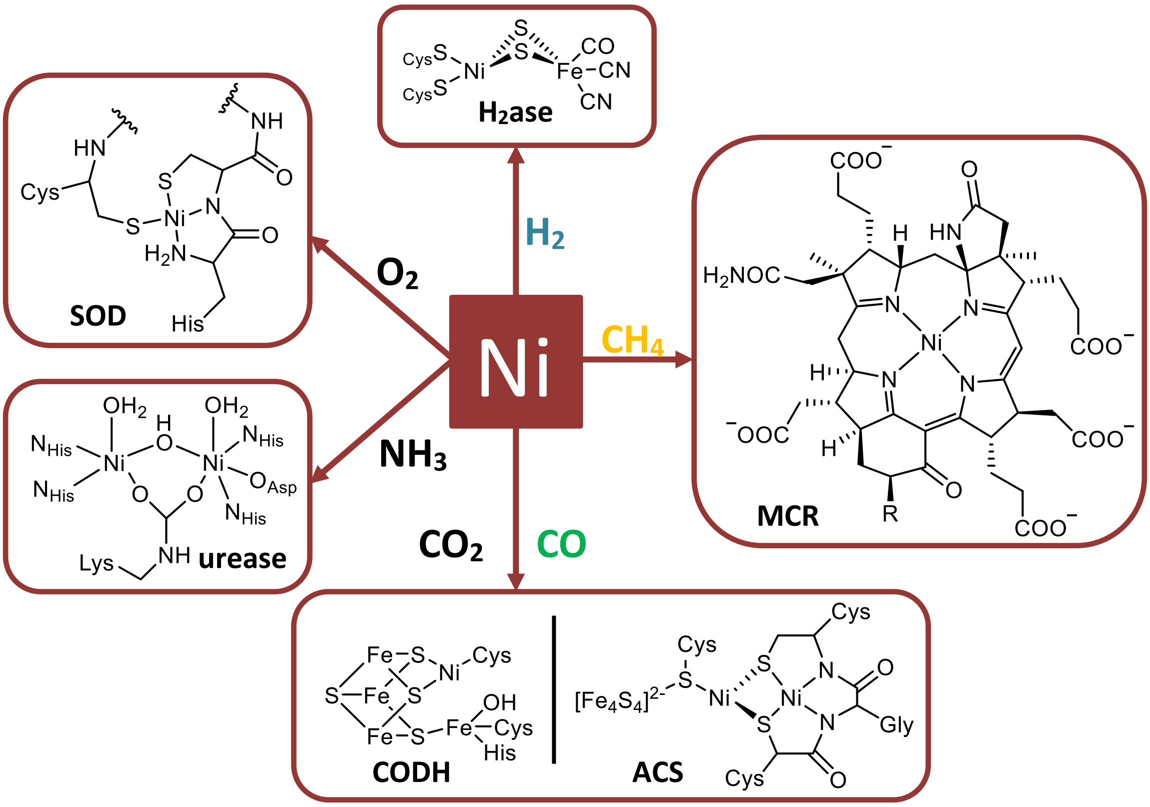

Figure 1: Selection of active sites of nickel containing enzymes involved in small molecule transformations. Reactions of colored formulas are partially object of this work.

1.2 β-Diketiminate Ligand Scaffolds

Due to their easy accessibility and strong binding properties, β-diketiminate ligands present a popular platform in many fields of coordination chemistry. The commonly used notation “nacnac” is a modification of the abbreviation acac, used for acetylacetone, which is the simplest proxy for β-diketonato ligands. However, β-diketiminates are preferably used, since they offer the possibility of changing the substituents at the nitrogen donors. This not only offers the potential for a fine tuning of the steric protection around the coordinated metal center, but also for a manipulation of the electronic properties of the ligand.

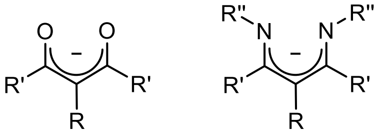

Figure 2: General structure of β-diketonato- (left) and β-diketiminate (right) chelate ligands.

The first β-diketiminate systems were developed in the late 1960s and studied in regard to their classical coordination chemistry with metals like Co, Ni, and Cu. These studies provided the first descriptions of the influence of different R substituents at the chelate moiety on the complex geometry.[6] However, it was during the 1990s that their steric tunability and therefore utility as a spectator ligand in catalytic applications were recognized. As the tendency to form stable complexes is provoked by the remarkable electron donating ability, β-diketiminates have featured in complexes with many elements of the periodic table in addition to transition metals including main group elements[7],[8] and lanthanides.[9]

Their monoanionic chelating nature makes them a unique class of supporting ligand. A diagram of the calculated energy levels of the molecular orbitals (MO) of β-diketiminate chelates is displayed in Figure 3. Within a β-diketiminato complex, the metal d-orbitals mainly overlap with the in-plane orbitals, $5b_2$ and $6a_2$, leading to two σ-bond interactions between the ligand and the metal center implying that the β-diketiminate chelate can be seen as a $4e^-$ donor. Only in the case the metal-ligand chelate ring deviates from the planar geometry to an envelope or boat shape, an overlap with the $2b_1$ MO results in an additional π-donation of two electrons.[10]

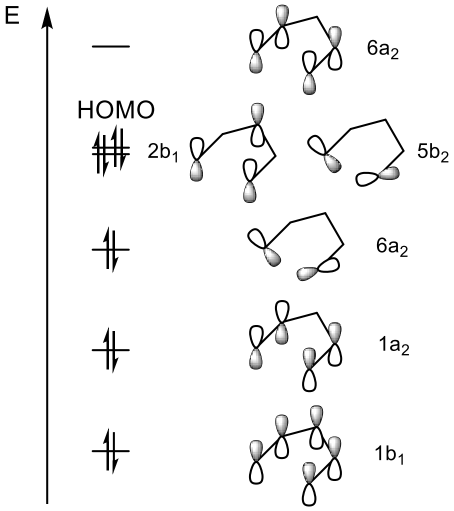

Figure 3: Proposed electronic structure of the planar, conjugated ligand core of a β-diketiminate ligand.[10]

The versatility of the nacnac ligand scaffold has been utilized to obtain remarkable results in the field of small molecule activation. Scheme 1 presents an example of a N_2 reduction based on the work of Limberg *et al.*. The initial reduction with potassium graphite (KC_8) results in the formation of the binuclear Ni^I complex **II**. The compound is stable in hexane and incorporates either H_2 or N_2 accompanied by the elimination of LiBr upon coming in contact with the respective gases.**[11]** In the case of H_2 the metal centers in the resulting bimetallic high-spin nickel(II) hydride complex **III** show a tetrahedral geometry and are found to be antiferromagnetically coupled.[12]

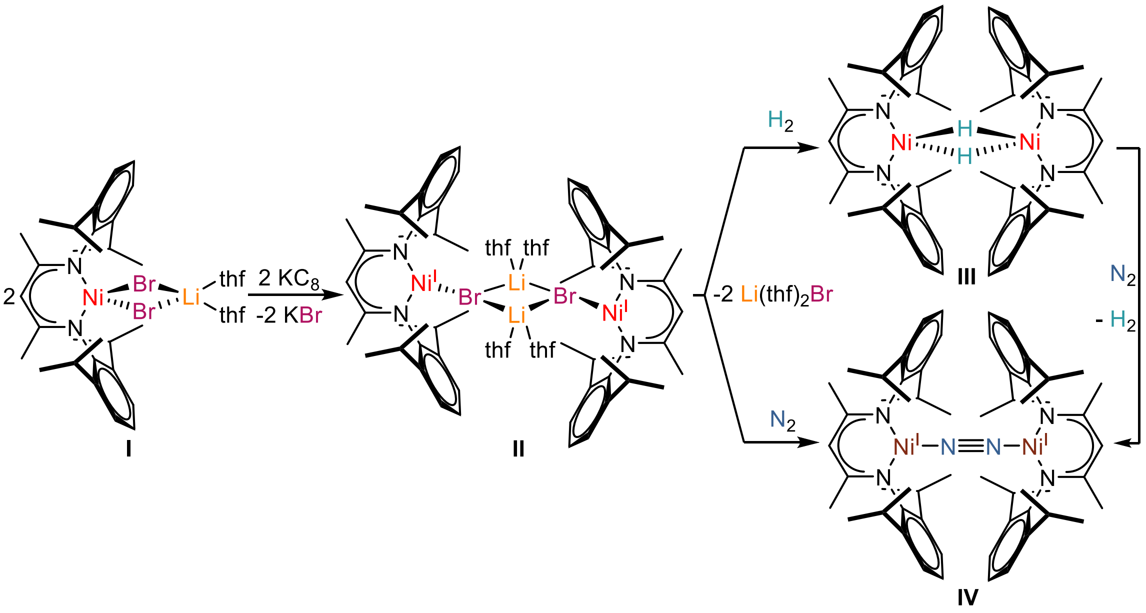

Scheme 1: Synthesis and reaction of β-diketiminate Ni(I) complex **B** with H_2 and N_2.[11]

Additionally, in the synthesis of the dinickel(I) dinitrogen complex **IV** *via* the **II**, the **III** binds dinitrogen under concomitant hydrogen evolution. The coordinating N_2 bond shows only a slight elongation [d_{N-N}(**IV**) = 1.120(4) Å vs. $d_{N-N}(N_2)$ = 1.08 Å] which indicates that there is little transfer of electron density from the Ni atoms to the N_2 molecule. However, it is possible to further reduce **IV** with one or two equivalents of KC_8, decreasing the bond order in the N_2 moiety significantly and therefore reaching a higher degree of activation (Scheme 1).[13]

As shown in the example above, the formation of bimetallic species is a common theme among low-valent β-diketiminate transition metal complexes and their substrate activation products. To exploit this, a strategy for a ligand scaffold providing two separate β-diketiminate binding sites in close proximity seems intriguing because the resulting preorganized bimetallic complexes hold potential for superior substrate binding properties. Early works used phenyl- or pyridyl linkers to connect two β-diketiminate chelates. These systems were used to establish homo bimetallic calcium and zinc complexes for CO_2/epoxide copolymerization.[14] Later, the pyridyl linked scaffold **V** was used to obtain a dinuclear pyridyl bridged bis(β-diketiminato) nickel(II) complex. The initial μ-bromido complex **VI** yields a dinuclear nickel μ-hydrido complex upon treatment with $KHBEt_3$. This mixed valent Ni^INi^{II} complex **VII** was the object of spectroscopic and reactivity studies (Figure 4).[15]

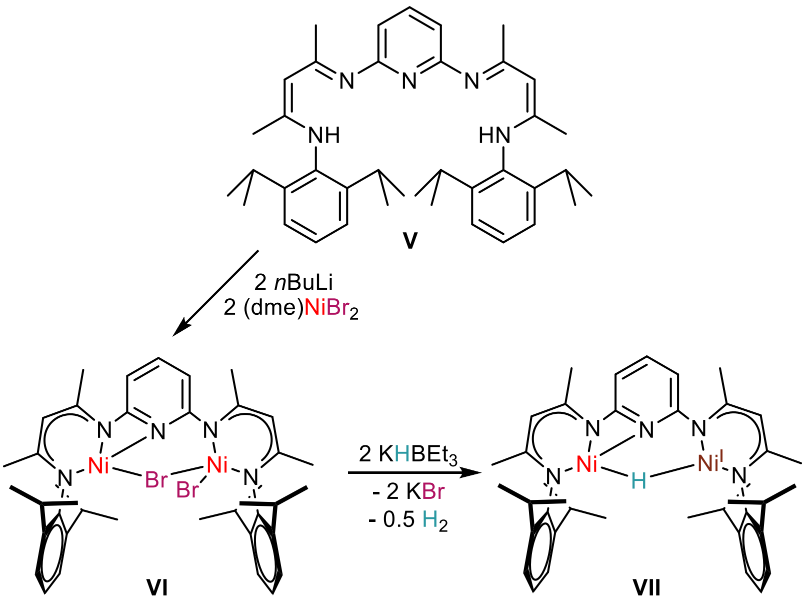

Figure 4: Synthesis and reaction of the dinuclear pyridyl bridged bis(β-diketiminate) nickel(II) complex **VI** to the mixed valent dinickel hydrido complex **VII**.

1.3 The Pyrazolate-Bridged Bis(β-diketiminate) Ligand System

To further exploit the strategy of assembling two β-diketiminate units in one ligand scaffold, a bridging pyrazole moiety can be a suitable alternative to the pyridyl linker. Pyrazole provides additional N-donors directing the two coordinated metal ions within metal-metal distances of 2.6-4.5 Å.[16] This enables the resulting preorganized bimetallic complexes to perform a wide range of metal-metal cooperativity induced substrate activations. The negative charge of the pyrazolate causes a stronger chelating affect compared to the pyridyl unit in ligand **V**, leading to higher affinity to bind two metals.

The pyrazolate bridged bis(β-diketiminate) ligand was first established by Manz with bulky diisopropylphenyl substituents at the nitrogen donors.[17] Triple deprotonation of **H_3L** and subsequent addition of $NiBr_2$(dme) yields the dinickel μ-bromido complex **1**$^{\mathbf{Br}}$. In contrast to the dinuclear complex **VI**, the pyrazolate bridged analogue **1**$^{\mathbf{Br}}$ features only one bromido ligand which bridges between the nickel(II) ions resulting in a similar coordination environment for both metals. They adapt a roughly square planar coordination and consequently are found in a diamagnetic low-spin state.[18] Treatment of **1**$^{\mathbf{Br}}$ with $KHBEt_3$ affords complex **2-K**. Instead of a bridging hydrido ligand as found in the mixed valent complex **VII**, the dinickel(II) complex **2-K** has two terminal hydrides in close proximity to each other. These Ni–H units interact with a K^+ which is found to be encapsulated in between the flanking aryl groups of the β-diketiminate units of the ligand (Figure 5).

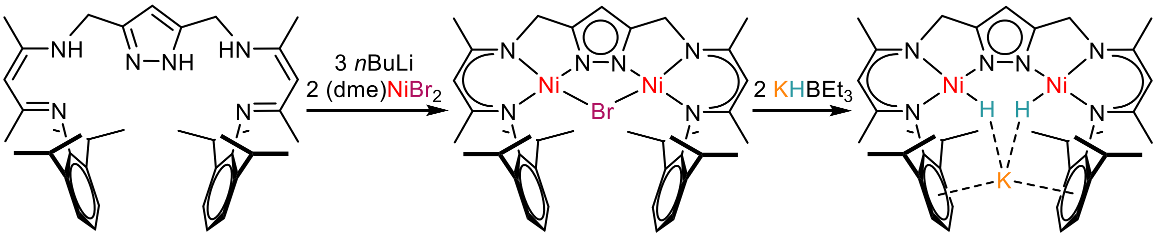

H$_3$L **1^{Br}** **2-K**

Figure 5: Stepwise synthesis of the dinickel dihydrido complex **2-K**.

Labelling experiments showed that these nickel(II) hydrides are able to eliminate H_2 from the bimetallic cleft. Exposing a degassed solution of **2-K** to an atmosphere of D_2 yields the labelled deuteride complex **2$^-$-d$_2$**. *Vice versa*, **2$^-$-d$_2$** incorporates H_2 under excess pressure of hydrogen gas. Monitoring the reaction with ^{1}H NMR and ^{2}H NMR experiments showed that the decrease of the amount of nickel hydride is coupled to the hydrogen release. The absence of molecular HD during the reaction indicated a pairwise H_2/D_2 exchange that involves both Ni–H moieties (Figure 6).

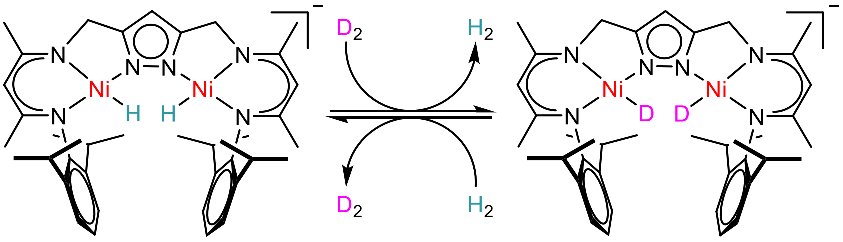

2$^-$ **2$^-$-d$_2$**

Figure 6: Pairwise H_2/D_2 exchange of the hydride complexes **2$^-$** and **2$^-$-d$_2$**.

Density functional theory (DFT) calculations suggest a two-step mechanism that initially involves the recombination of H_2 out of the Ni-bound hydrides and consecutive release from the binding pocket to leave two Ni^I centers with a vacant bimetallic cleft. The barrier for the hydrogen release is low in the absence of K$^+$ indicating a stabilizing effect from the interaction with the alkali cation. This was further explored by reacting **2-K** with 18-crown-6 ether which results in the removal of K$^+$ from the complex moiety. The complex was found to release hydrogen gas over time. Magnetic measurements of crystalline material that was exposed to vacuum indicated an antiferromagnetically coupled species with magnetic moment close to what is expected for two $S = ½$ systems suggesting the formation of a Ni^{I}Ni^I intermediate.

The application of **2-K** for reductive substrate activation was explored using phenyl acetylene. In the resulting complex, the phenyl acetylene moiety is found to be incorporated between the metal centers while showing structural parameters for a twofold reduction from a C–C triple-bond to a double bond (Figure 7). This shows the effectiveness of **2-K** for reductively binding unsaturated substrates. Spectroscopic and reactivity findings suggest that **2-K** can be viewed as masked Ni^{I}Ni^I complex. Since the utilization of the hydride **2-K** in reactions avoids the use of unstable low-valent metal species, it holds great potential as a powerful tool in small molecule and other substrate activation studies.[18]

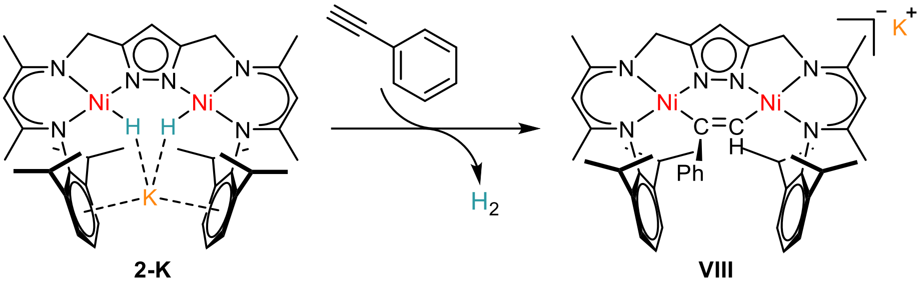

Figure 7: Reaction of **2-K** with the substrate phenyl acetylene under H_2 loss.

This was recently demonstrated by the reaction of **2-K** with the small molecules O_2 and NO. Treatment of **2-K** with one equivalent of O_2 results in the formation of the dinickel peroxo complex **IX**. Under an excess atmosphere of O_2, **IX** is further oxidized to a dinickel superoxo complex species. Electrochemical and reactivity studies showed that it was possible to readily interconvert them.[19] The reaction of two equivalents of NO with **2-K** yields compound **X**. Structural and spectroscopic characterization of **X** showed that, interestingly, the twofold reduction of the NO radical leads to its dimerization to a $[N_2O_2]^{2-}$ moiety (Scheme 2).[20]

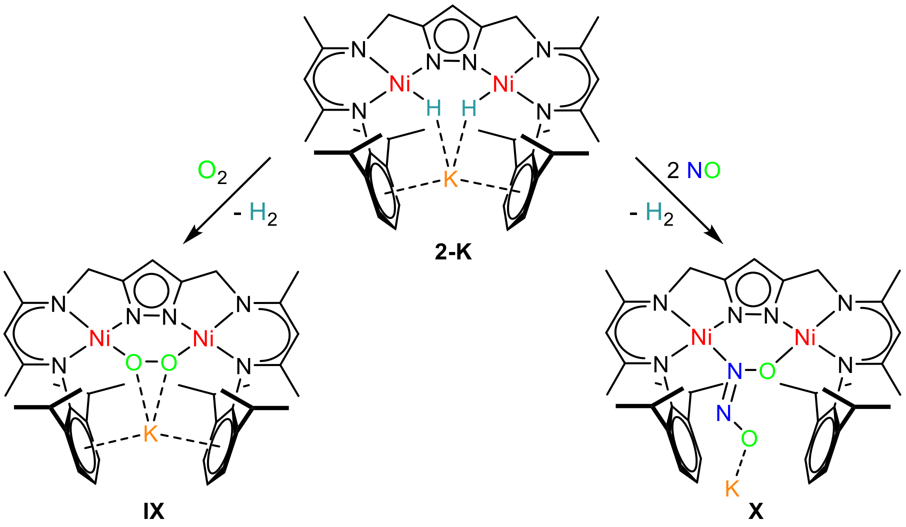

Scheme 2: Reactivity of **2-K** towards O_2 (left) and NO (right).

Establishing dinuclear nickel complexes with a pyrazole bridged bis(β-diketiminate) ligand represents an intriguing strategy for supporting low-valent species. The ability of the synthetic key compound **2-K** to bind substrates reductively is well documented. The following work focuses on continuing the application of **2-K** to serve as a masked Ni^INi^I complex for further reaction studies.

2 Thesis Outline

This work expands the recent achievements in the synthesis of a bis(β-diketiminate) pyrazole bridged ligand **H_3L** and its coordination chemistry regarding a new family of dinickel complexes. Following this, the substrate scope for the twofold reductive binding to the $[LNi_2]^-$ moiety is broadened. Furthermore, it will be shown that the bimetallic dinickel(II) dihydride complex is also suitable for single electron transfer reactions upon protonation, as suggested by the works of Dennis Manz[17] and Peng-Cheng Duan.[21]

The initial part of this thesis focuses on the reproduction and improvement of the synthesis of the already established dinickel dihydride complexes and a singly reduced dinickel dinitrogen complex. In the following chapter, the alkylation of the $[LNi_2]^-$ moiety and the competing single reduction pathway of N_2 will be discussed in detail. Continuing, the properties of the alkylation products are explored including the structural and spectroscopic characterization. Additionally, their ability to incorporate CO is probed in order to provide more insight on the proposed mechanism of the dinickel cofactor in the enzyme ACS.

Based on this, the reductive activation of further substrates with unsaturated C–O bonds including CO and CH_2O will be probed. The electrochemistry of the resulting species is studied, and it will be shown that it is possible to interconvert them chemically *via* proton coupled redox reactions. Additionally, further aldehyde derivatives are object to structural investigations.

The last chapter analyzes the unexpected chemoselectivity of the reduction of nitro functions over aldehyde groups. The resulting compounds represent a new family of dinickel stabilized dihydroxyl amines, which play an important role in the multistep reduction of nitro compounds to amines. These complexes are characterized and their counterion and substituent dependent stability is evaluated.

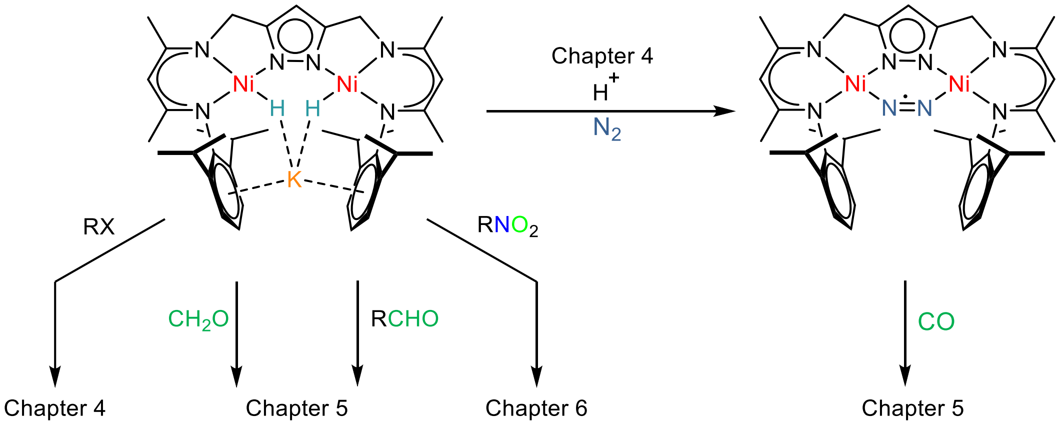

Scheme 3: Overview of the different studies of this work.

3 Reproduction and Improvement of the Synthesis of Dinickel Dihydride and Dinitrogen Complexes

3.1 Biological Inspiration behind the Hydrogen Release Coupled Substrate Reductions

As described above, metal hydrides can be a powerful tool for the activation of substrates. Also, nature has many examples where reducing equivalents are stored in metal hydride bonds. The most prominent active site of an enzyme showing this reactivity is the FeMo cofactor in nitrogenase (Figure 8).

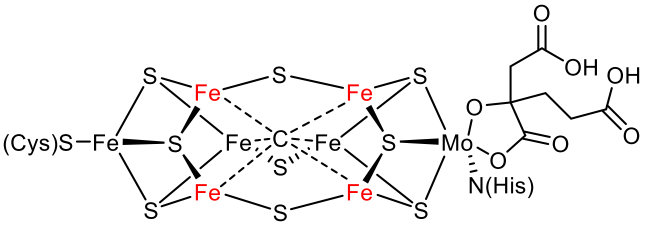

Figure 8: Structure of the resting state FeMo cofactor.

This microbial enzyme is responsible for the fixation of N_2, that due to the strong N–N triple bond (944.9 KJ/mol)[22] and lack of polarization generally shows low reactivity. To overcome this obstacle, nitrogenase provides a multimetallic Fe/S active site, which is charged with four electrons and four protons. The subsequent binding of N_2 is then preceded by the obligatory release of H_2.[23] These N_2 binding intermediates are denoted with E_4 according to the Lowe-Thorneley kinetic scheme for the nitrogenase function and represent the key stage in the process of N_2 reduction.[24] The structure of the initial complex E_4 (4H) is described with two metal-bridging hydrides between three iron centers. The two remaining protons are placed on the sulfur atoms coordinating these iron centers to obtain the electrostatic stabilization implicit in the required accumulation of one proton per electron in the FeMo cofactor.[25] Two separate mechanistic proposals for the nitrogen binding process starting with E_4 (4H) are shown in Scheme 4.

In the hydride protonation (***hp***) mechanism, N_2 binding is achieved by shifting one bridging hydride to an activated, terminal ligation mode and subsequent protonation by a sulfur bound proton to form dihydrogen which is substituted by N_2. The reductive elimination (***re***) pathway involves the initial shift of both bridging hydrides to the same metal center which are then reductively eliminated. The remaining iron center is left in a highly reduced, activated form and thus gains the ability to bind N_2. Several mechanistic constraints and studies on the photoinduced H_2 release from the E_4 complex suggest the ***re*** mechanism to be most likely to occur.[26]

The reason behind the obligatory production of an H_2 molecule upon binding and therefore wasting one quarter of the for the reaction required ATP, which do not directly contribute to the reduction of N_2 is yet not fully understood. However, it has been suggested that the concomitant H_2 evolution in the synthesis of ammonia from N_2 provides the entropic driving force for the highly disfavored N_2 binding.[27],[28] As it will be shown, this paradigm for the activation of different substrates can be applied to the nickel complexes of the a bis(β-diketiminate) pyrazole.

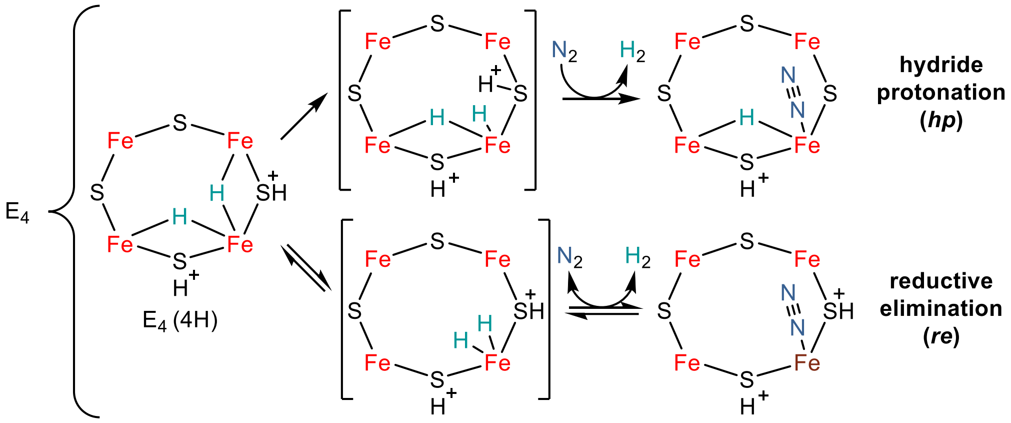
E4
E4 (4H)
N2
H2
hydride
protonation
(hp)
reductive
elimination
(re)

Scheme 4: Visualization of ***hp*** and ***re*** mechanisms for the H_2 release upon N_2 binding to E_4.

3.2 Synthesis of the Dinickel Dihydrido Complex 2-K

To obtain the dinickel dihydrido complex **2-K**, the ligand **H₃L** was synthesized according to literature (Scheme 5).[18] However, conditions were optimized in order to increase the overall yield and purity of the desired compound.

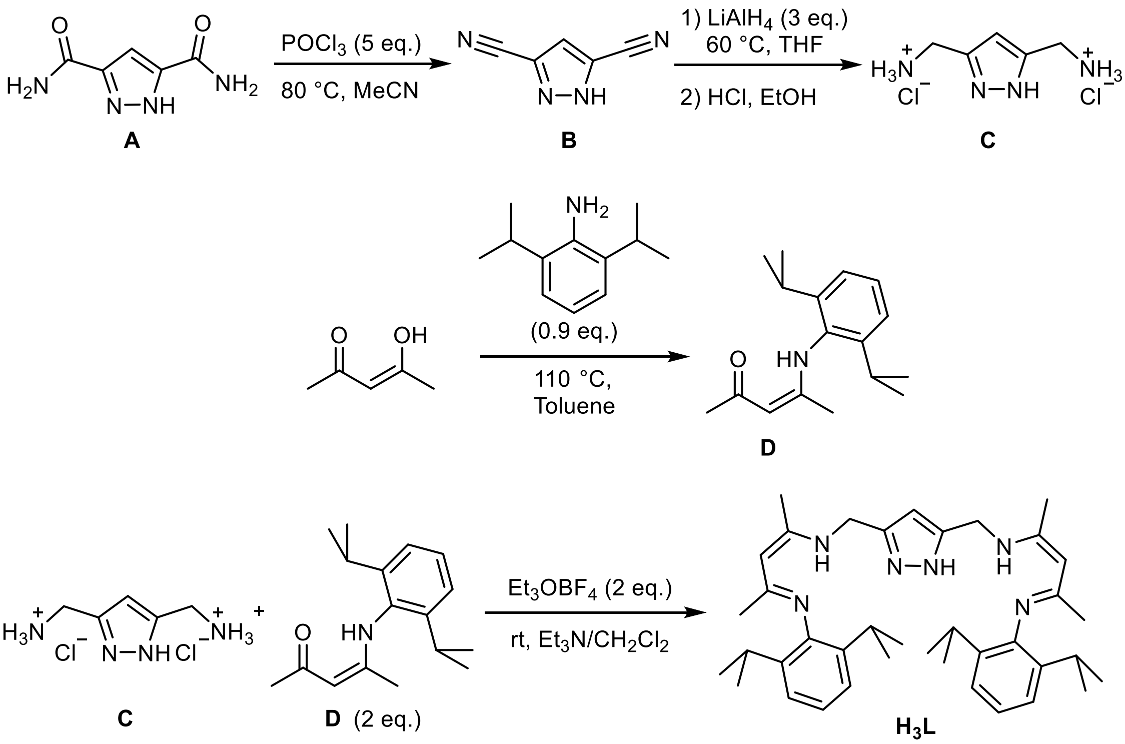
A
POCl3 (5 eq.)
80 °C, MeCN
B
1) LiAlH4 (3 eq.)
60 °C, THF
2) HCl, EtOH
C
(0.9 eq.)
110 °C,
Toluene
D
C
D (2 eq.)
Et3OBF4 (2 eq.)
rt, Et3N/CH2Cl2
H3L

Scheme 5: Multistep synthesis of the ligand system **H₃L**.

The initial dehydration reaction of **A** was done by adding $POCl_3$ stepwise, keeping the concentration of excess $POCl_3$ low over the course of the reaction time. This prevented the formation of degradation products and therefore increased the product yield. It should be noted that during the workup process, the organic phase was always kept at low pH values in order to contain the hydrolyzable nitrile functions, that otherwise would reform the starting material or the single dehydrated derivative. A final purification step using column chromatography yielded **B** as a fine yellow powder with a yield of 72%. Subsequent reduction using $LiAlH_4$ gave the corresponding amine. For purification purposes, the dihydrochloride was generated *via* protonation with a solution of HCl in Et_2O. The obtained dihydrochloride **C** proved to be easier to handle and was more stable towards decomposition compared to the free base congener. Due to the inexpensive starting materials and the simple reaction conditions, **D** could be synthesized at large scale. The purity of the condensation product was increased by distillation of the waxy solid at 100 °C and 10^{-3} mbar. The final step to produce the desired ligand **H_3L** involved addition of two equivalents of **D** to a solution of **C**. To ensure the formation of the product, **D** was activated with Et_3OBF_4 in CH_2Cl_2 over the course of 18 h. The solution was added to a suspension of **C** in Et_3N which not only led to the deprotonation of the dihydrochloric salt **C** but also neutralized any HBF_4 that was formed during the coupling reaction. Notably, CH_2Cl_2 was used in a three times larger volume compared to Et_3N to ensure that the pyrazole diamine unit remained in solution. Heating the mixture to 40 °C led to a significant decrease in reaction time from three days to 18 h. After extraction with toluene to separate the product from Et_3NHBF_4, the crude oil was mixed with EtOH in an ultrasonic bath to yield a fine powder. Washing with additional EtOH separated residues of unreacted **D**, which avoided the need for sublimation of the temperature sensitive ligand **H_3L** at 120 °C reported in literature. These optimized procedures gave the desired ligand **H_3L** in an overall yield of 30% (Scheme 5). Over a longer period of time **H_3L** readily decomposes at room temperature and thus should be kept at -20 °C.In order to form **1^{Br}**, **H_3L** was deprotonated with *n*-BuLi to form the corresponding lithium salt *in situ*. The formation of the trianionic species was indicated by a color change from light yellow to deep red upon addition of three equivalents of *n*-BuLi at -78 °C. Subsequent addition of two equivalents of $NiBr_2$(dme) afforded a thick brown suspension. Heating the reaction to 60 °C overnight showed a quantitative conversion. The reaction mixture was filtered affording the air stable dinickel μ-bromido complex **1^{Br}**, which was washed with acetone to remove minor impurities. Further purification was not necessary since subsequent reactions proved not to be susceptible to possible impurities. As mentioned above **1^{Br}** is insensitive to moisture and oxygen. Although the square planar coordination sphere of both nickel centers is distorted due to the insufficient size of the bridging anion, reactions with strong nucleophilic alkylating agents like MeMgBr or MeLi afforded predominant starting material **1^{Br}**. However, it was possible to exchange the bromide ligand with a cyanido bridge using NEt_4CN possibly due to the higher thermodynamic stability.

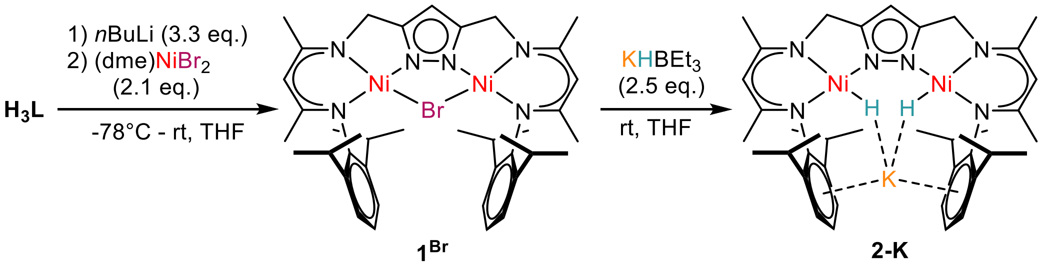

Scheme 6: Synthesis of dinickel dihydrido complex **2-K**.

Treatment of **1^{Br}** with the strong hydride transfer reagent, *viz*. $KHBEt_3$, led to the dinickel dihydrido complex **2-K**. Since the formation of a monohydrido complex could not be observed, at least two equivalents of $KHBEt_3$ were necessary for a complete conversion. Layering a concentrated THF solution of **2-K** with hexane resulted in a clean crystallization with a yield of up to 66% after four weeks. The complex proved to be highly sensitive towards moisture, and therefore the presence of trace amounts of H_2O resulted in the immediate formation of μ-hydroxido complex **3**. For this reason, the synthesis and all experiments involving **2-K** were done in a glove box under dinitrogen atmosphere (Scheme 6).

2-K appears as a compound of orange to light red color. It is soluble in THF but slightly less soluble in aromatic solvents such as toluene and benzene. The diamagnetic compound shows a highfield shifted signal at -24.16 ppm (in THF-d_8) for two protons in the ^1H NMR corresponding to both hydrido ligands bound to the Ni^{II} ions (Figure 9). For the hydrogen atoms at the α-position of the β-diketiminate subunits of the ligand, only one proton signal is found at 4.56 ppm. This indicates an identical coordination environment for both metal centers. Additionally, the protons of the methylene linkers between the central pyrazole and the β-diketiminate chelates show a singlet at 4.23 ppm, as it is expected for a square planar complex with a mirror plane within the coordination plane. The simplicity of the spectrum indicates a complex with C_{2v} symmetry in solution on the NMR timescale. This shows that the symmetry of the reported molecular structure found in solid state is retained in solution.[29]

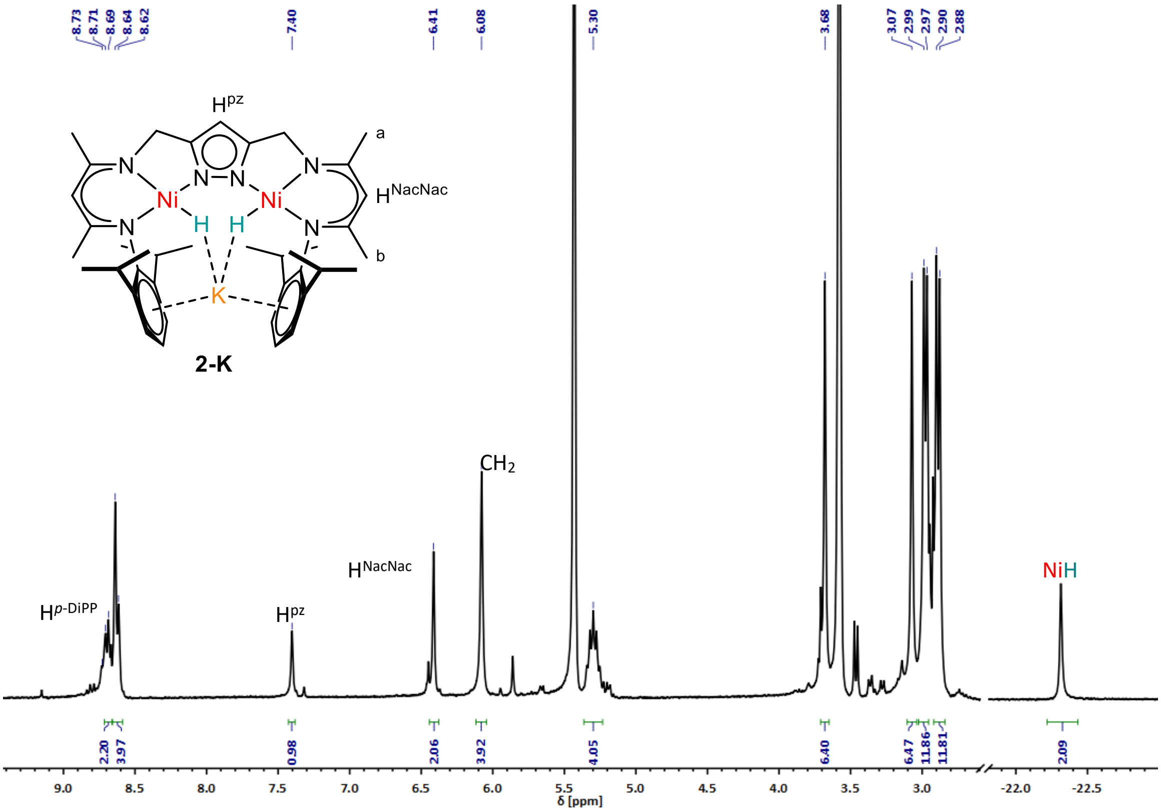

Figure 9: ^1H NMR spectrum of **2-K** in THF-d_8 at room temperature.

The UV/vis spectrum of **2-K** in THF shows bands that largely differ in intensity. In the UV region very strong absorptions were observed at 314 nm and 380 nm followed by weaker absorptions at 424 nm, 468 nm, 523 nm and 563 nm. Since the degradation product **3** also features strong bands in the UV region around 380 nm, both species are hard to distinguish *via* UV/vis spectroscopy, making this method unsuitable for monitoring reactions of **2-K** as the possible formation of **3** could not be excluded (Figure 10).

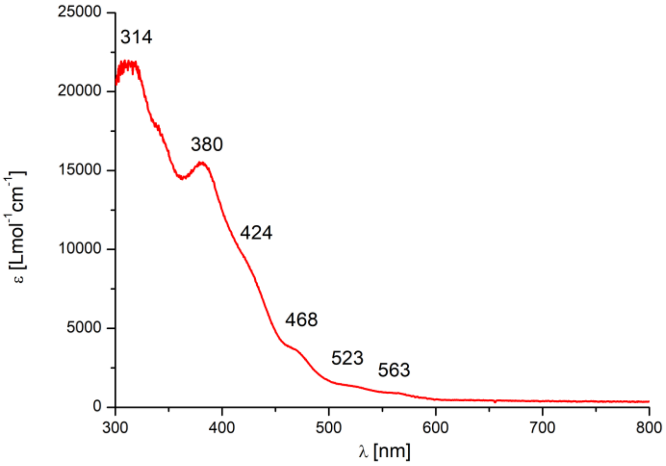

λ [nm]	ε [Lmol^{-1}cm^{-1}]
314	43650
380	16600
424	90000
468	5900
532	1400
563	900

Figure 10: UV/vis spectrum of **2-K** in THF at room temperature (left) and the table with extinction coefficients at different wavelength (right).

3.3 Abstraction of One Hydrido Ligand for the Single Reduction of Dinitrogen

As shown by Dennis Manz the dihydride complex **2-K** can be transformed into the dinickel dinitrogen complex **4**.[17] The works of Peng-Cheng Duan show, that the addition of one equivalent of a weak acid like HLutOTf[30] to a solution of **2-K** resulted in the evolution of 1.5 equivalents of H_2.[21] The reaction was not limited to Brønsted acids. Lewis acids like the commonly used hydride abstraction reagent Ph_3CBF_4 or PF_6 as well as Meerwein salts like Et_3OBF_4 also enabled access to nitrogen complex **4**. However, in these cases it is assumed that 0.5 equivalents of H_2 were generated. Using toluene as the solvent instead of THF simplified the separation of the byproduct KOTf, which was partially soluble in THF (Figure 11).

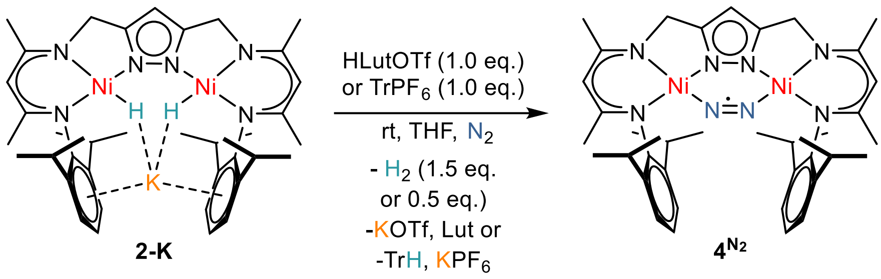

Figure 11: Synthesis of compound $\mathbf{4}^{N_2}$ from **2-K** with HLutOTf under evolution of 1.5 equivalents of H_2 or $TrPf_6$ under the evolution of 0.5 equivalents of H_2.

$\mathbf{4}^{\mathbf{N_2}}$ crystallizes in small rods of dark brown to black color. It is significantly less soluble in THF and aromatic solvents than its precursor **2-K**. The compound proved to be extremely sensitive towards moisture and therefore exclusion of any source of water was mandatory. As X ray diffraction analysis suggested a neutral complex, the bound N_2 moiety can formally be described as a negatively charged ligand coordinating two nickel(II) centers.[17] Using IR spectroscopy, a sharp band at 1896 cm^{-1} was detected which may be attributed to the stretching vibration of the activated N-N-bond. The ^1H NMR spectrum showed a limited number of very broad signals that could not be assigned to any protons suggesting that $\mathbf{4}^{\mathbf{N_2}}$ is of paramagnetic nature. It was not possible to record a spectrum without impurities of **3** since the diamagnetic compound shows sharper signals and thus even small amounts appear dominant. EPR experiments revealed a spin $S = ½$ ground state with an overall g value of 2.072. Since this is significantly larger than $g_e = 2.0023$, expected for a radical centered on light atoms such as nitrogen, a heavy atom contribution seems most probable. Therefore, the single electron is not only located at the bridging dinitrogen ligand but also distributed between both nickel centers. $\mathbf{4}^{\mathbf{N_2}}$ showed only weak absorptions in the UV/vis region. Bands between 300 nm and 500 nm seemed to be comparable to the electronic absorptions of **2-K**. However, the spectrum of dinitrogen complex $\mathbf{4}^{\mathbf{N_2}}$ features a broad but characteristic band at 698 nm, which probably derives from an electronic transition between the N_2 ligand and the Ni^{II} (Figure 12).

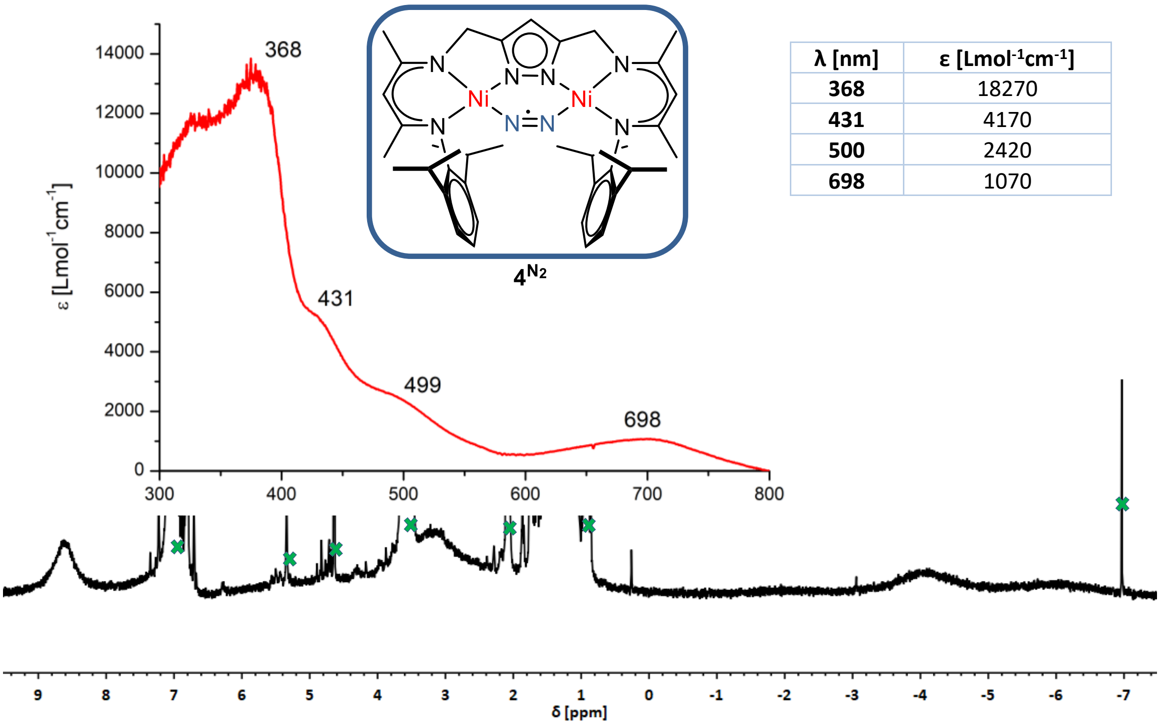

λ [nm]	ε [Lmol⁻¹cm⁻¹]
368	18270
431	4170
500	2420
698	1070

Figure 12: Spectral data of **4**^{N_2}. UV/vis in THF at room temperature (top, left) and the table with wavelength depended extinction coefficients (top, right). ^{1}H NMR spectrum in toluene-d$_8$ at room temperature (bottom). Impurities of **3** are marked by a green cross.

Notably, it was not possible to generate **4**^{N_2} by single reduction of **1**^{Br} by the use of strong reductants like KC$_8$. To provide further insight into the redox chemistry of **1**^{Br} cyclic voltametry (CV) of the compound was recorded in THF at room temperature using NBu$_4$PF$_6$ as electrolyte. Ferrocene was used as an internal standard and the presented potentials were referenced against the ferrocene/ferrocenium redox couple. The cyclic voltammograms were recorded under inert conditions in a nitrogen atmosphere glove box. The CV showed a reversible reduction at $E_{1/2}$ = -2.26 V and a second irreversible reduction at $E_{1/2}$ = -2.73 V (Figure 13). Although the potentials are low compared to literature values of β-diketiminate nickel(II) complexes,[31] the first wave was attributed to the Ni^{II}Ni^{II}/Ni^{II}Ni^{I} redox couple and the irreversible reduction was assigned to the second reduction event Ni^{II}Ni^{I}/Ni^{I}Ni^{I}. Upon oxidation, two waves are found at $E_{p,a}$ = -1.39 V and $E_{p,c}$ = -1.04 V which only appear after the potential for the irreversible reduction or potentials below were applied (-3.0 V). This suggests that the second oxidation in the electrochemical conversion of the Ni^{I}Ni^{I} species to the Ni^{II}/Ni^{II} compound occurs to some extend at elevated potentials, when compared to Ni^{II}Ni^{I}. In the stochiometric reaction with a strong reductant such as KC$_8$ a mixture of doubly reduced dinickel(I) complex **5** and the starting material was isolated, while milder reducing agents such as sodium amalgam (E = -2.36 V)[32] showed no conversion. Also using Mg^{I} reductants, which were likely to have a potential between both waves (E(Mg^{I}/Mg^{II}) = -2.29 V))[33] did not yield the desired single reduced dinitrogen complex **4**.

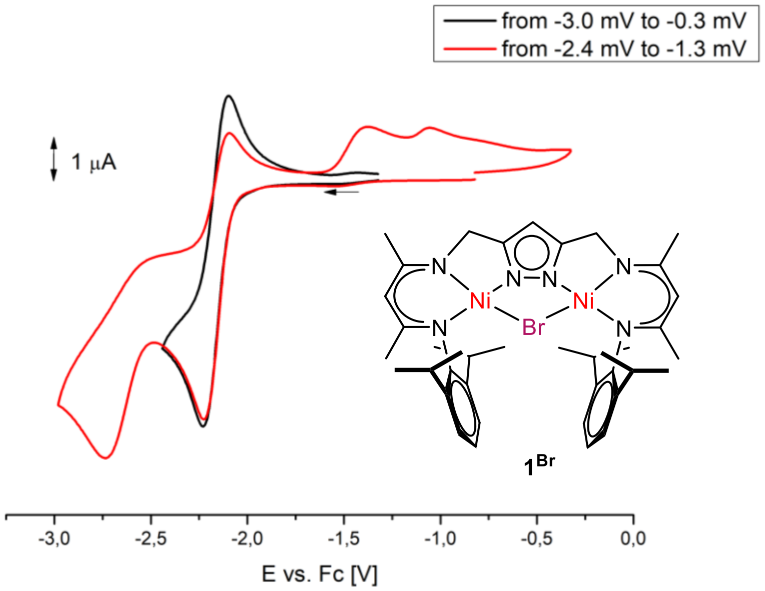

Figure 13: Cyclic voltammogram of $\mathbf{1^{Br}}$ in THF containing NBu_4PF_6 (0.1 M) at 298 K at 100m V/s referenced versus ferrocene. The reversible wave at -2.18 mV was measured starting from -1.3 V to - 2.4 V and back (black graph) and the full spectrum was measured from -0.8 V to -3.0 V and back.

This again reflects the high stability of $\mathbf{1^{Br}}$. The affinity for a bridging halide to maintain coordination to both metal centers causes the very low reduction potentials. While upon one electron reduction, the generated nickel(I) center prefers a T-shaped coordination geometry, the remaining nickel(II) center prefers a square planar coordination. The bromido ligand positioned in the overlapping binding site of both metal ions, forces the nickel(I) center to either yield an electron to attain the former oxidation state II, or the remaining nickel(II) center to also be reduced to nickel(I). The second reduction results in the elimination of the bromido ligand which is displayed by the irreversibility of the second reduction wave at $E_{p,a}$ = -2.73 V (Scheme 7). In case of a chemical reduction of $\mathbf{1^{Br}}$ with two equivalents KC_8, the precipitation of KBr provides enough driving force to generate the doubly reduced complex **5**. However, this does not occur in case of the single reduction of $\mathbf{1^{Br}}$ and therefore $\mathbf{4^{N_2}}$ was not accessible directly from $\mathbf{1^{Br}}$. The dinickel dinitrogen complex $\mathbf{4^{N_2}}$ was only obtained by using **2-K**, possibly due to the necessity of the accompanied dihydrogen evolution. As pointed out above, nature holds a prominent example for this type of reactivity as the nitrogenase catalyzed nitrogen fixation is also coupled to the formation of dihydrogen. It is assumed that this provides the sufficient driving force that is needed for the entropically disfavored nitrogen binding.[27]

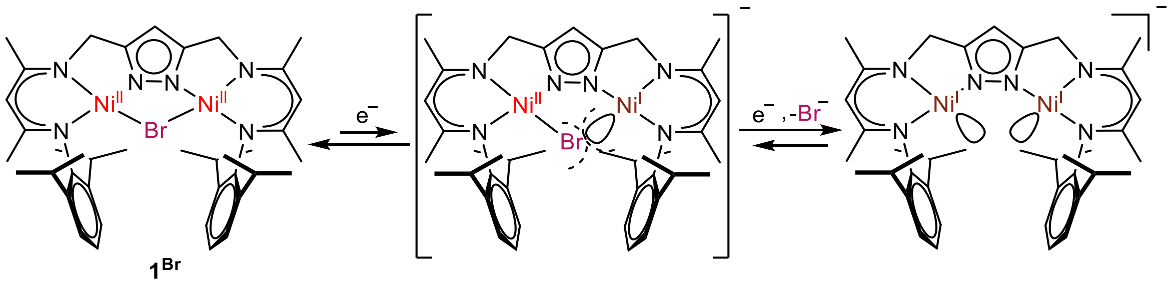

Scheme 7: Reaction scheme for the reduction of $\mathbf{1^{Br}}$. The single reduction product is probably an unstable intermediate which disproportionates to the starting material $\mathbf{1^{Br}}$ and the doubly reduced species under crystallization conditions.

4 Alkylation of a Bimetallic Dinickel Site and its Application as an Acetyl CoA Synthase Model

4.1 Introduction

4.1.1 Nickel alkyl complexes

The importance of nickel-alkyl complexes is ascribed to their general recognition as intermediates in catalytic transformations like olefin polymerization[34] or cross-coupling reactions.[35],[36] However, they are isolable and a great number of examples for this family of nickel complexes is known.[37],[38],[39] Due to the strong σ-donation of the alkyl ligand almost all of them adapt a square planar geometry in their Ni^{II} state. Nickel alkyl complexes are usually accessed *via* the reaction of the corresponding Ni^{II} halide complex with Grignard or lithium alkyl reagents (Figure 14).

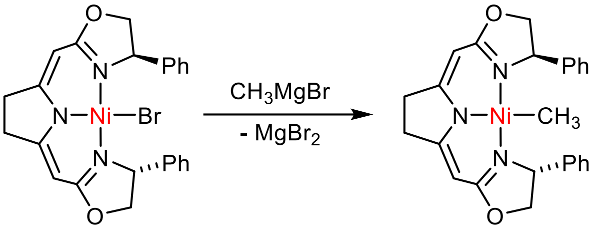

XI **XII**

Figure 14: Alkylation of nickel bromide complex **XI** of a pyrrole bridged bis(oxazolin) pincer system.[40]

Although it is considered an important step in catalytic cycles of cross coupling reactions examples for the of nickel alkyl complexes formed *via* oxidative addition of an alkyl halide to a Ni^0 compound are rare.[41]

The structural characterization of coordinatively unsaturated nickel alkyl complexes has been studied intensively, due to them being essential for the understanding of polymerization processes at molecular nickel centers.[42] Three coordinate nickel(II) ethyl complexes for example tend to saturate their coordination sphere *via* a β-agostic interaction. This makes them intermediate in structure between nonagostic monoalkyls and alkene hydride complexes, and thus they undergo a facile β-H-elimination/reinsertion equilibrium (Figure 15).[43]

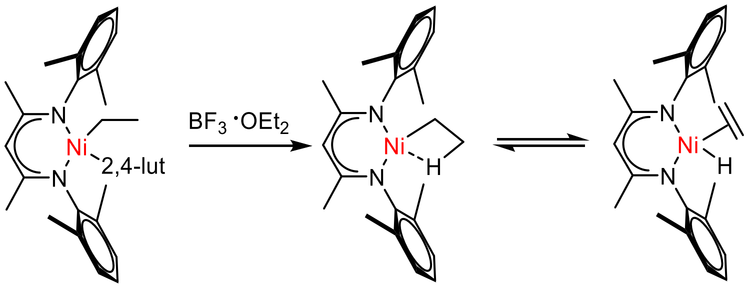

Figure 15: Synthesis of an unsaturated nickel ethyl complex and its β-H-elimination/reinsertion equilibrium.

4.1.2 Acetyl CoA Synthase

The importance of nickel alkyl complexes is not limited to technical applications. The most prominent example for an intermediate nickel alkyl species occurring in nature is the CO incorporating enzyme acetyl CoA synthase.

The reductive Wood-Ljungdahl pathway describes the CO/CO_2 fixation of anaerobic microorganisms. In acetogenic bacteria this complex mechanism revolves around an enzyme cluster containing two units of CO dehydrogenase (CODH) and acetyl CoA synthase (ACS), respectively. Both enzymes interact in a way that CODH reduces atmospheric CO_2 to CO passing it to the ACS which incorporates it into the metabolic key substrate acetyl CoA. This naturally occurring conversion presents a highly efficient biological analogue to a water gas shift (WGS) reaction coupled Monsanto process.[44]

ACS is a nickel dependent enzyme and its active site, the A-cluster, was among the first reported NiFeS clusters.[45] The A-cluster contains an Fe_4S_4 cluster which is linked to a nickel center commonly notated as Ni_p (for proximal nickel, Figure 16). The Ni_p itself is connected *via* two cysteinate bridges to the distal nickel center (Ni_d). The Ni_d is found to be square planar coordinated by a four donor chelating subunit of the surrounding protein containing the two cysteines and two back bone amides.[46]

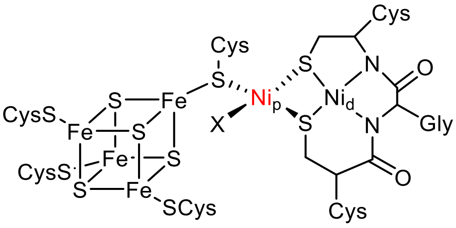

Figure 16: Active site of the nickel based enzyme acetyl CoA synthase (ACS). In the resting state X is a H_2O[47] ligand or an acetyl group[48] coordinating to the proximate nickel (Ni_p).

Despite the presence of six metal centers in the A-cluster the catalytic transformation of CO to acetyl CoA entirely occurs at the Ni_p while the Ni_d seems to only serve as an electronic modulator. Two scenarios are discussed for the mechanistic cycle, namely the diamagnetic mechanism involving a Ni^0 intermediate and the paramagnetic mechanism which involves a Ni^I intermediate.[46] In context of this work only the paramagnetic mechanism will be discussed.

Before substrate binding a reductive activation of the $[Fe_4S_4]^{2+}Ni_p^{2+}Ni_d^{2+}$ cluster to $[Fe_4S_4]^{2+}Ni_p^{+}Ni_d^{2+}$ must be achieved. It remains unclear if the first substrate to be bound is CO or CH_3^+. In fact there is strong evidence for a random binding meaning that both pathways are realized.[49] The methyl unit is provided by a methylcobalamin and binds to the Ni_p *via* an oxidative addition increasing the nickel oxidation state form +I to +III, while the cobalamin Co is reduced from Co^{III} to Co^I. The CO then inserts into the Ni–C bond forming a nickel bound acetyl group. Since the Ni_p^{III+} state is predicted to be highly unstable it must be reduced. This is probably achieved by an internal electron transfer from the nickel acetyl cleavage induced by the thiolate bearing coenzyme A. This step yields the product acetyl CoA and reforms the initial Ni^I intermediate (Scheme 8).

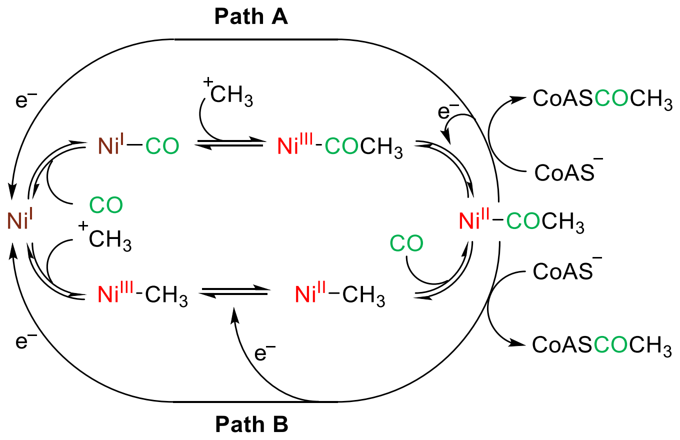
Path A
Path B
e⁻
e⁻
e⁻
e⁻
Ni^I
Ni^I–CO
Ni^{III}-COCH$_3$
Ni^{II}–COCH$_3$
Ni^{III}-CH$_3$
Ni^{II}–CH$_3$
$^+$CH$_3$
CO
$^+$CH$_3$
CO
CoASCOCH$_3$
CoAS$^-$
CoAS$^-$
CoASCOCH$_3$

Scheme 8: Paramagnetic mechanism of the ACS catalyzed synthesis of acetyl coA.[50]

4.1.3 Model Complexes for the Acetyl CoA Synthase

The mechanistic discussion for the ACS catalyzed reaction has inspired inorganic chemistry to find suitable models for the active site to support the different scenarios. Since the [Fe_4S_4] cluster and the Ni$_d$ are only modulators of the electronic and redox properties of the active site, modeling efforts for the ACS usually focus on imitating the Ni$_p$ or a bimetallic Ni$_p$-Ni$_d$ environment. It has been shown that either Ni^I or Ni^0 can bind CO or get methylated. Several examples for the methylation of a Ni^I unit have been reported.

The transfer of the methyl cation from methyl cobalamin to a nickel(I) center has been achieved in various cases. An example of a dinuclear nickel system is displayed in Scheme 9. The mixed valent bimetallic nickel system **XIII** reacts with a methylcobaloxime to the methyl complex **XIV**. Subsequent addition of CO gives an acetyl thioester from a reaction of the coordinated methylate and thiolate units. The rate limiting step is the electron transfer from the Ni^{II}Ni^I complex to the organocobalt compound which is followed by the Co–CH_3 bond homolysis and subsequent nickel methylation leading to the dinickel(II) methyl species. However, the reaction does not involve any Ni^{III} methyl intermediate as proposed for ACS, since the one electron steps generate a methyl radical which combines with the Ni^I moiety directly forming a Ni^{II} methyl unit.[51]

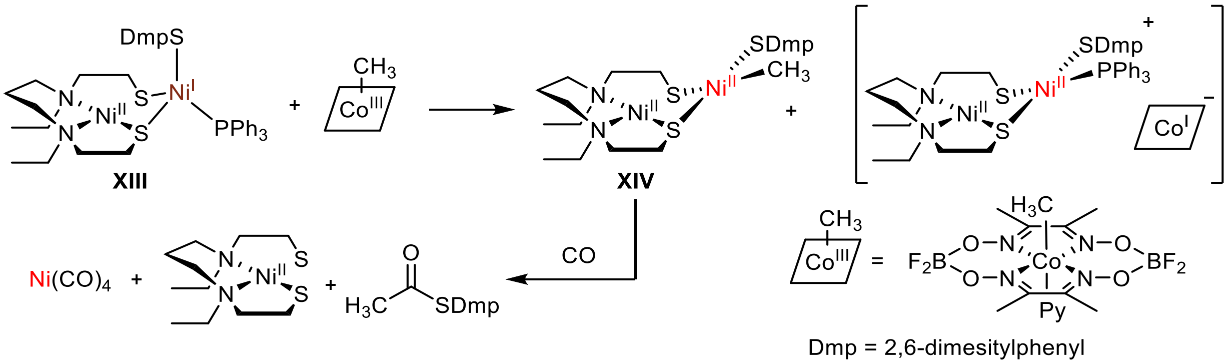
DmpS
Ni^I
Ni^{II}
PPh$_3$
XIII
CH$_3$
Co^{III}
XIV
SDmp
CH$_3$
Ni^{II}
SDmp
PPh$_3$
Co^I
CO
Ni(CO)$_4$
H$_3$C
SDmp
H$_3$C
F$_2$B
BF$_2$
Py
Dmp = 2,6-dimesitylphenyl

Scheme 9: Formation of an acetyl thioester form a nickel(I) thiolate complex **XIII** in the consecutive reaction with methylcobaloxamine and CO.[51]

The only notable example for an oxidative addition of a methyl cation to a nickel(I) moiety is shown in Figure 17. The Ni^I complex **XV** reacts with MeI and yields the neutral nickel(III) methyl complex **XVI**. The compound is thermally instable and decomposes in solution at ambient temperatures under the formation of ethane.[52] This supports the necessity of fast subsequent reduction of the high valent Ni^{III} species in Path B of the ACS catalytic cycle shown in Scheme 8.

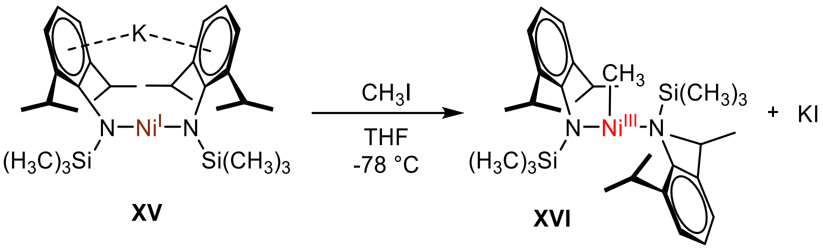

Figure 17: Oxidative addition of methyl iodide to Ni^{I} complex **XV**.

4.1.4 Objective

The following chapter subjects if the above introduced dinickel dihydride complex **2-K** is a potential functional mimic of acetyl CoA synthase (ACS). Since **2-K** can serve as a masked $Ni^{I}Ni^{I}$ complex it contains the necessary Ni^{I} center for the oxidative addition of a methyl cation provided by a suitable electrophilic methylation agent. The remaining Ni^{I} then offers the potential to serve as an electron reservoir transferring one electron to the instable Ni^{III} methyl species. Thus, reforming a stable Ni^{II} state. If a stable Ni^{II} methyl complex is isolated, the possibility of a CO insertion into the Ni–C bond shall be object of further investigation. Since it has be shown that the bimetallic cleft of the dinickel moiety in **2-K** readily incorporates two atomic substrate, it offers the potential to stabilize such an acetyl complex. This reaction sequence resembles Path B of the ACS activity in Scheme 8.

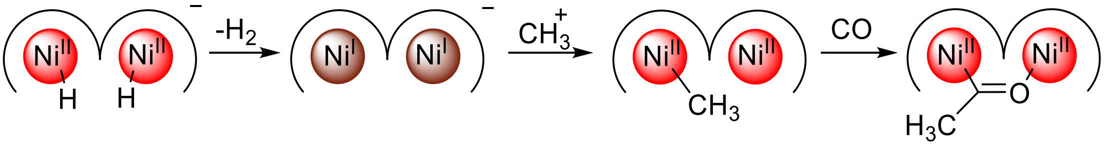

Scheme 10: Scheme for the application of the dinickel hydride complex as a functional model system for ACS.

4.2 Results and Discussion

4.2.1 Methylation of the Dinickel Moiety

In order to investigate the ability of the masked dinickel(I) complex **2-K** to perform oxidative additions of dipolar substrates, a series of electrophilic alkylating agents were applied. In a first attempt MeI was used in an *in situ* NMR experiment. The reaction with **2-K** showed an immediate color change of the THF solution to dark brown accompanied by the evolution of gas. After less than one hour a reaction control *via* ^{1}H NMR, revealed the formation of two distinct species in an approximate ratio of 1:3 (Figure 18, bottom). Both species showed only one singlet for the hydrogen atoms at the α-position of the β-diketiminate subunits of the ligand and for the protons of the methylene linkers between the central pyrazole and the β-diketiminate unit. Therefore, C_{2v} symmetry in solution was apparent for both complexes. Most interestingly, a proton signal at -3.16 ppm appeared for the major species with a relative integral of three. After 24 h the former major product was no longer detectable and solely the side product remained in the spectrum (Figure 18, top).

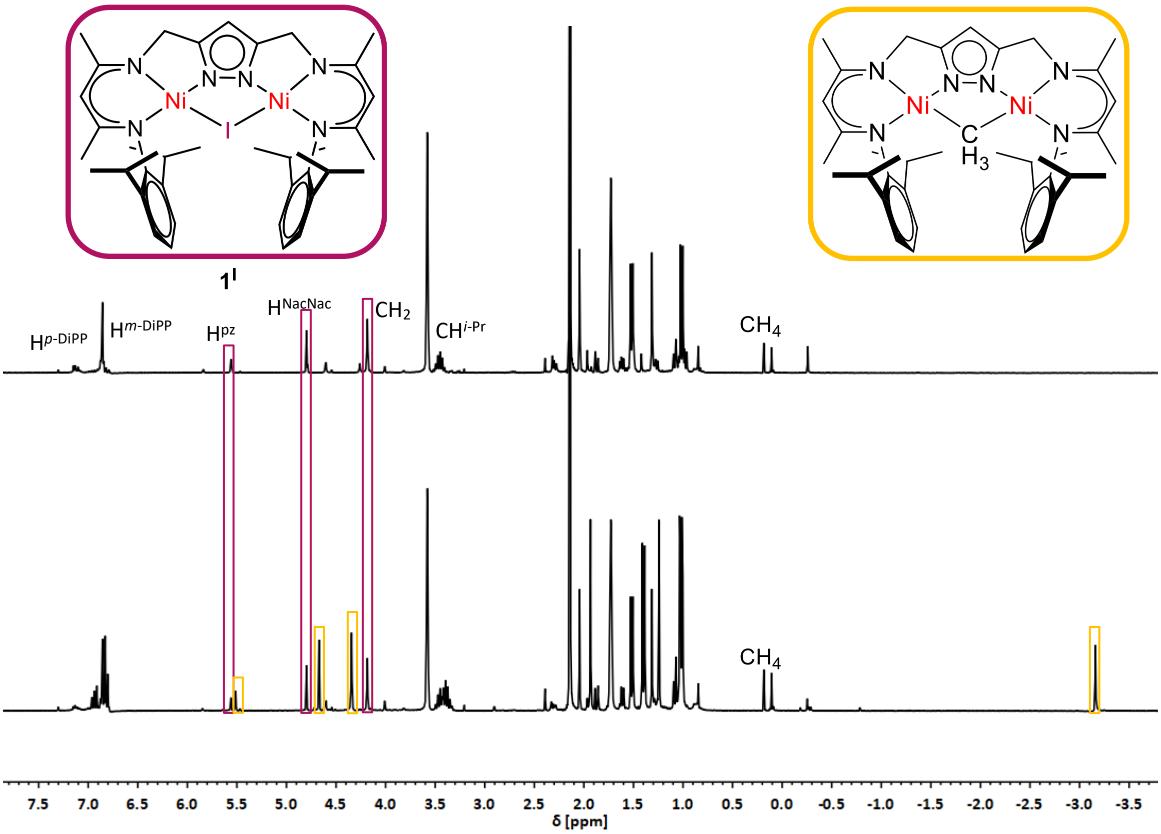

Figure 18: ^{1}H NMR spectra (300.13 MHz) of the reaction between **2-K** and MeI in THF-d_8 at the beginning (bottom) and after 24 h (top). Prominent signals, namely the pyrazole proton, NacNac-backbone protons, methylene bridges and the metal bound methyl group, are marked by rectangular frames of purple color for **1^{I}** and orange color for **6**.

A singlet at 0.19 ppm was assigned to methane.[53] Since the relative integral of the methane protons increased with the formation of the side product a connection to the evolution of methane seemed evident. Unfortunately, this could not be quantified due to the uncertain equilibrium between detectable methane in solution and in the gas phase (Figure 18). The high-field shifted singlet at -3.16 ppm and the decomposition of the main product accompanied by the evolution of methane suggested the oxidative addition of a methyl group to the bimetallic cleft of the pyrazolate based dinickel moiety.

The C_{2v} symmetry suggested the initial main product to be a diamagnetic dinickel complex bearing a bridging methyl group. The final product was identified as μ-iodido complex **1^I** due to its comparable proton shifts in respect to **1^{Br}**.[17] Dinickel methyl complex **6** seemed to be unstable in presence of the byproduct KI. This was probably caused by the iodide anions high affinity to bridge both metal centers which enabled an easy replacement of the methyl group. This behavior is also displayed by the already mentioned inertness of dinickel μ-bromido complex **1^{Br}** towards MeMgBr, MeLi or even stronger C nucleophiles like Me_3SiCH_2Li. The elimination of the methylate and the subsequent reaction with trace protons led to the formation of the observed methane.

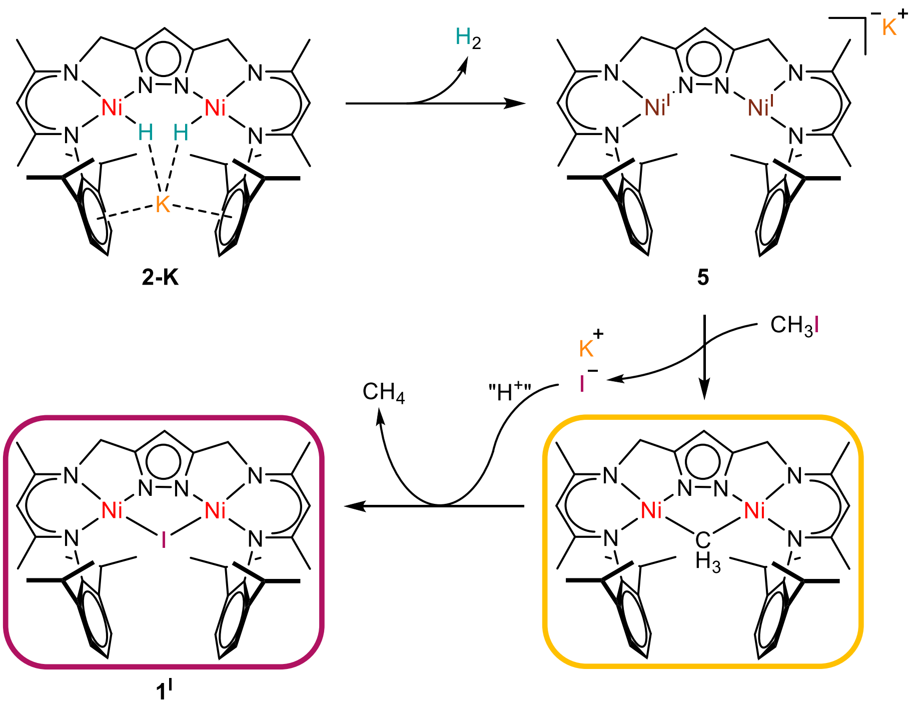

Scheme 11: Assumed reaction pathway of the conversion between **2-K** and MeI.

Even in toluene where KI has a lower solubility the formation of **1^I** was not fully suppressed. However, when KI was separated from the mixture by filtration no further change in ratio between **1^I** and **6** was observed according to ^1H NMR data recorded over the course of several days, suggesting that iodide salt causes the degradation of **6**. Unfortunately, it was not possible to separate both complexes since they showed similar crystallization properties (Scheme 11).

To explore if benzyl substrates provide complexes that do not co-crystallize with the corresponding halide complex, BnBr was tested as reagent. Unfortunately, the reaction only allowed the isolation of **1^{Br}**. Therefore, the focus was shifted to methylating agents bearing leaving groups that result in weakly coordinating anions, which were less likely to initiate a substitution reaction on **6**.

In an ^1H NMR experiment after adding MeOTf to a solution of **2-K** for the generation of **6**, no peaks for a diamagnetic byproduct were observed. However, broad signals at 8.61 ppm and -4.03 ppm suggested to formation of a paramagnetic species. The signals were in accordance with the

^{1}H NMR spectrum of dinitrogen radical compound **4**. Efforts to separate both species *via* crystallization proved to be unsuccessful. Like in the case of **1**$^{\mathrm{I}}$ the solid structures of **4**$^{\mathbf{N_2}}$ and **6** have a common unit cell (Figure 19).

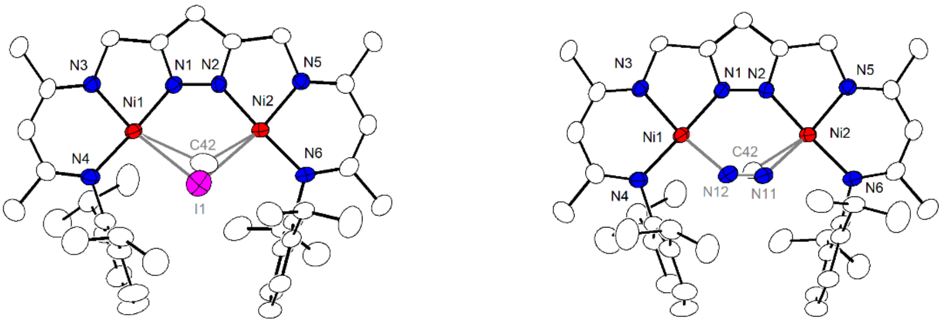

Cell [Å]	a = 17.1574(5)	b = 14.0433(3)	c = 17.3924(5)	a = 17.2078(4)	b = 14.1848(3)	c = 17.2635(4)
	β = 111.987(2)°	V = 3885.85(19) Å^3		β = 112.569(2)°	V = 3891.13(16) Å^3	

Figure 19: Molecular structures of **6** cocrystallized with **1**$^{\mathrm{I}}$ (left) and **4**^{N_2} (right). The iodide anion was found with a ratio of 0.48 (left) while N_2 moiety contributes in a ratio of 0.57 (right) to the structure relative to the methyl group. Hydrogen atoms are omitted for clarity.

As already mentioned, applying Meerwein salts[54] like Et$_3$O or Me$_3$OBF$_4$ to a solution of **2-K** solely led to the isolation of **4**. These results suggested a connection between the difference in product outcome and in the electrophilicity of used methylation reagents.

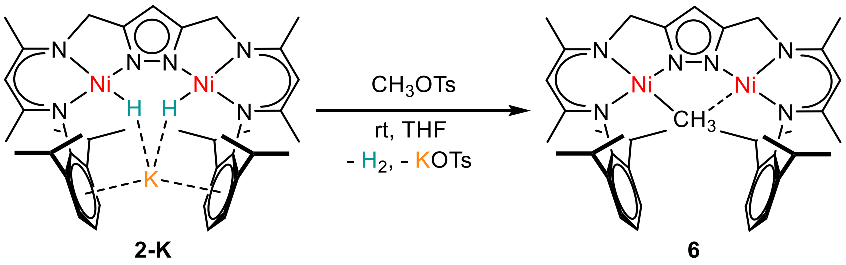

Figure 20: Synthesis of **6** with MeOTs.

Considering this, with MeOTs a weaker methylation agent which still fulfilled the requirement of a weakly coordinating leaving group was chosen. Initial ^{1}H NMR analysis of the product suggested a clean conversion to the desired compound **6** since neither broad signals indicative of **4**$^{\mathbf{N_2}}$ nor additional pyrazole proton signals were found. The accruing KOTs was insoluble in the used solvents toluene or THF and, therefore, easily filtered off. **6** was crystallized by slow diffusion of hexane into a THF solution of the complex yielding fine rods of dark brown to black color. Crystalline material shows poor solubility in THF and benzene, comparable to **4**$^{\mathbf{N_2}}$.

As already mentioned, NMR spectral data indicated a C_{2v} symmetrical species. The obvious structure deriving from that information is a methyl group coordinating both metal centers with an equal bond distance (Figure 18). Hence, the carbon atom bearing three hydrogen atoms and two nickel ions would form a 3 center 2 electron bond. However, also a fast intramolecular methyl exchange is consistent with the NMR data. This possible exchange could be described as an equilibrium between two chemically equivalent species, where the methyl group is bound to one nickel ion saturating the coordination sphere of the remaining nickel(II) center via an α-agostic interaction. Both possibilities and their schematic energy profiles are shown in Scheme 12. In case of an α-agostic interaction both chemically equivalent species are rapidly interconverting *via* a symmetrical transition state while in case of the μ-methylate complex the symmetrical species is the thermodynamic minimum. The equilibrium, however, would be temperature dependent and therefore was investigated by variable temperature experiments. ^{1}H NMR spectra at -60 °C in THF-d_8 showed no line broadening or signal splitting for the signal of the CH_3 group as it would be expected for an equilibrium between unsymmetrical species. The coupling constant between the methyl carbon nucleus and the connected protons $^1J_{H\text{-}C}$ = 120 Hz exceeded the usual range for α-agostic C-H coupling constants (75-100 Hz).[55] Even though this emphasized that the CH_3 group in methyl complex **6** was equally coordinated to both metal centers, reports of complexes with a bridging methyl unit suggests that a single metal-carbon bond is more accurate describing the binding mode, despite similar findings.[56],[57]

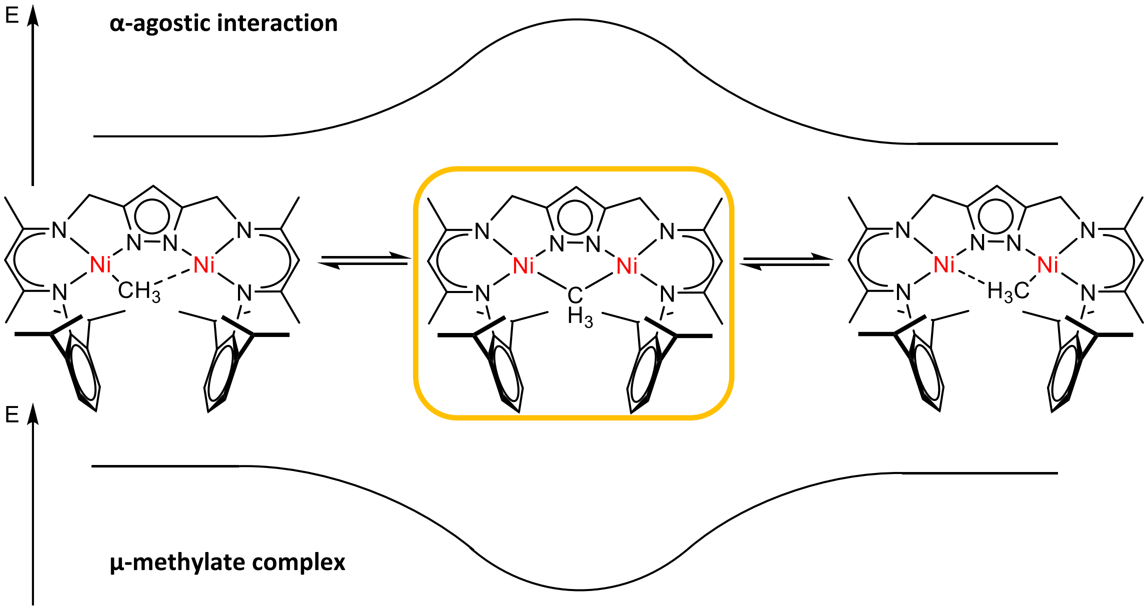

Scheme 12: Interaction of the methyl group in **6**. Schematic energy profiles for the two possibilities agnostic interaction (top) and μ-methylate complex.

NMR spectroscopy suggested that the reaction between deuterated MeOTs and **2-K** only resulted in the generation of methyl complex **6-d₃**. In comparison with **6** the ^{1}H NMR spectrum of **6-d₃** showed similar shifts for the proton signals of the dinucleating pyrazolate ligand **[L]**$^{3-}$. While the peak at -3.16 ppm was not found in the ^{1}H NMR spectrum a broad signal around that region (-3.13 ppm) appeared in the ^{2}H NMR spectrum, suggesting that the methyl group of MeOTs stays intact over the course of the reaction and no hydrogen transfer with **2-K** occurs. (Figure 21).

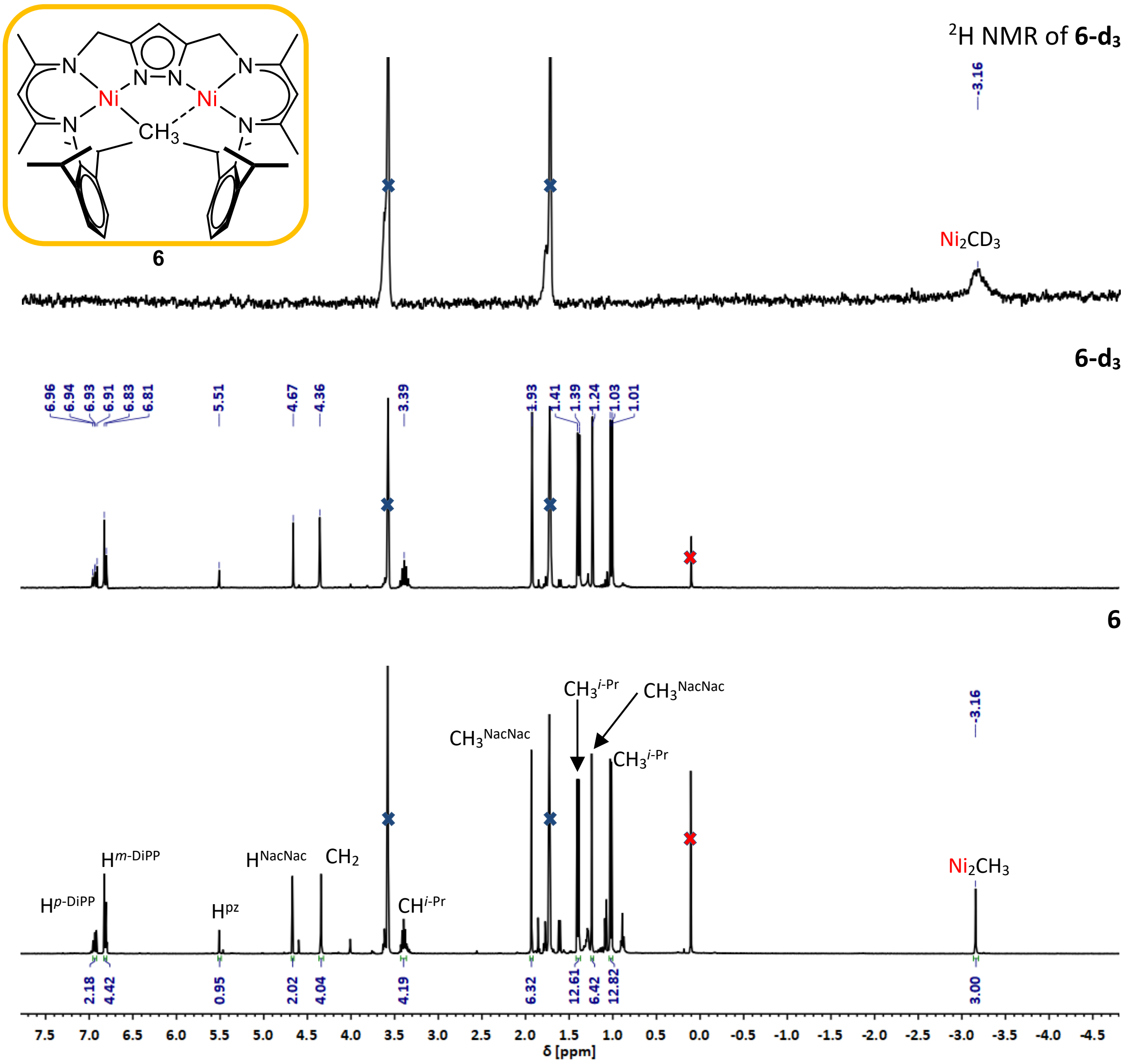

Figure 21: ^{1}H NMR spectrum (300.13 MHz) of **6** (bottom) and deuterium labeled methyl complex **6-d$_3$** (middle) in THF-d$_8$ and ^{2}H NMR spectrum of **6-d$_3$** (top) in THF at room temperature. Signals of silicon grease are marked by a red cross and solvent signals with a blue cross.

Geometry optimization using the BP86 functional and def2-TZVP basis set suggested that, indeed, the methylate ligand was bound unsymmetrical (Figure 23). Furthermore, the calculated IR spectrum predicted a significantly lowered C-H stretching at 2610 cm^{-1} (Figure 22). This almost matches a broad band at 2605 cm^{-1} in the experimental IR spectrum (Figure 22). This decrease in C–H bond strength is probably caused by the α-agostic interaction between the methyl group and the nickel(II) center. The band is not observed in the IR spectrum of the deuterated analogue **6-d$_3$** (Figure 22, bottom left) and the subtraction of the spectrum of **6** from the spectrum of **6-d$_3$** shows negative differences for 2607 cm^{-1}. However, due to the overlap with the absorption window of the ATR-IR crystal the positive difference at 1913 cm^{-1} which corresponds to the calculated isotopologue C–D stretching frequency was hard to detect (eq. 1).

Furthermore, the bands of the twelve methyl groups of the dinucleating pyrazolate ligand unit **[L]**$^{3-}$ in the region between 3000 cm^{-1} – 2800 cm^{1}, did not allow an identification of the remaining C–H stretching vibrations of the nickel bound methyl group. However, the main features in the remaining plot are still contained and only differ by the lower overall transmittance of the spectrum of **6**.

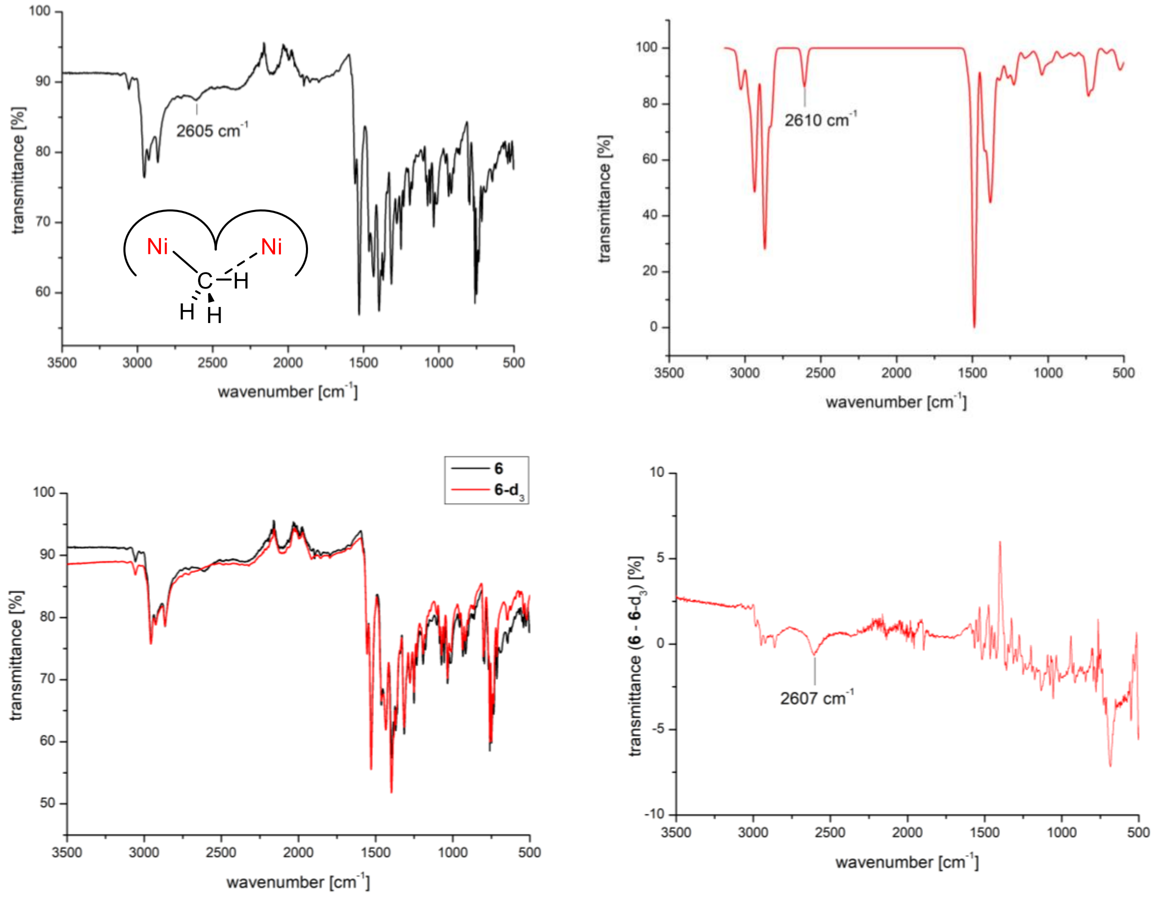

Figure 22: ATR-IR spectrum of solid **6** (top left) and simulated IR spectrum (top right) of **6** in gas phase. Stacked ATR-IR spectra of **6** and the labeled equivalent **6-d₃** (bottom left) and the subtraction of both spectra (bottom right).

Ultimately, XRD analysis of pure single crystals provided the molecular structure of **6**. The crystallographic data shows that, at least in solid state, **6** is unsymmetrical (Figure 23). The complex crystallizes in the monoclinic space group P 2_1/c. Both nickel centers are coordinated in a distorted square planar fashion with a metal-metal distance of 3.695 Å. As expected for the small carbon atom bound in the cavity, this is shorter than the distances for $\mathbf{1}^{\mathrm{Br}}$ with 3.807 Å and $\mathbf{4}^{\mathrm{N_2}}$ (3.950 Å). However, the metal-metal separation exceeds the reported distance for **3** with 3.470 Å significantly.[17] The distance of Ni(1)–C(40) with 1.997 Å is in accordance with examples for nickel(II) methyl complexes in literature.[58] However, the second nickel carbon distance Ni(2)–C(40) with 2.344 Å is significantly longer. This suggests the methyl group to hold a covalent bond to one nickel center while it has a weak interaction to the remaining $\mathrm{Ni}^{\mathrm{II}}$. This is also reflected by shorter metal ligand bonds at the second nickel ion (Ni(2)–N(2), Ni(2)–N(5), Ni(2)–N(6)). This difference is critical for the nitrogen-metal bond *trans* to the binding cavity, where the methyl function is located, displaying the compensation of the positive ion charge due to a lack of a strong σ-donation. Hence, the binding mode of the methylate function is best described as a covalent bond to one nickel center while saturating the open coordination sphere of the second nickel(II) ion *via* an α-agostic interaction (Figure 23). Values of structural parameters of **6** are presented in Table 1.

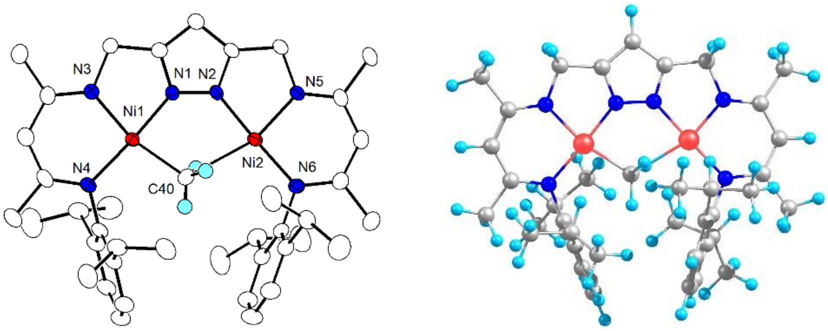

Figure 23: Molecular structure of methyl complex **6** (left) and calculated structure of methyl complex **6** (right). Solvent molecules and hydrogen atoms with exception to the methyl group were omitted for clarity.

Table 1: Selected bond lengths [Å] and angles [°] for methyl complex **6**.

Bond Lengths [Å]		Bond Angles [°]	
Ni(1)-N(1)	1.8293(17)	**N(1)-Ni(1)-C(40)**	84.41(8)
Ni(1)-N(3)	1.9168(17)	**N(4)-Ni(1)-C(40)**	99.22(9)
Ni(1)-N(4)	1.8958(17)	**N(3)-Ni(1)-C(40)**	165.79(8)
Ni(2)-N(2)	1.8240(17)	**N(1)-Ni(1)-N(3)**	81.39(7)
Ni(2)-N(5)	1.8739(16)	**N(4)-Ni(1)-N(3)**	94.98(7)
Ni(2)-N(6)	1.8753(18)	**N(2)-Ni(2)-C(40)**	78.97(7)
Ni(1)-C(40)	1.997(2)	**N(6)-Ni(2)-C(40)**	103.28(8)
Ni(2)-C(40)	2.344(2)	**N(5)-Ni(2)-C(40)**	161.06(7)
Ni(1)···Ni(2)	3.6956(5)	**N(5)-Ni(2)-N(6)**	95.39(8)
		N(2)-Ni(2)-N(5)	82.59(7)
		Ni(1)-C(40)-Ni(2)	116.51(10)

4.2.2 Mechanism of the Generation of the Dinickel Methylate Complex 6

As already mentioned, the reaction of dihydride complex **2-K** to methyl complex **6** competed with the generation of dinitrogen complex **4**$^{\mathrm{N_2}}$ in dependence of the used methylation agent. The strength of methylation reagents can be correlated with the relative rate constant for their solvolysis in water. Due to the fast reactivity of Me_3OBF_4 no data regarding comparison with the rate constant of MeOTf ($k_{rel} = 1.4 \cdot 10^8$) and MeOTs ($k_{rel} = 3.0 \cdot 10^4$) was available.[59],[60] However, Me_3OBF_4 is generally regarded as the strongest of the here applied methylation agents. The reaction of Me_3OBF_4 with **2-K** solely resulted in the formation of dinitrogen complex **4**$^{\mathrm{N_2}}$. The far weaker MeOTs cleanly yielded **6** and the moderately strong reagent MeOTf gave a mixture between both. Therefore, the more reactive the methylation agent, the more the formation of **4**$^{\mathrm{N_2}}$ is preferred and the less reactive the methylation agent, the more the formation **6** is preferred. Considering that the strength of methylation agent can be quantified by their reaction rates two mechanistic proposals for both pathways were made (Scheme 13).[59]

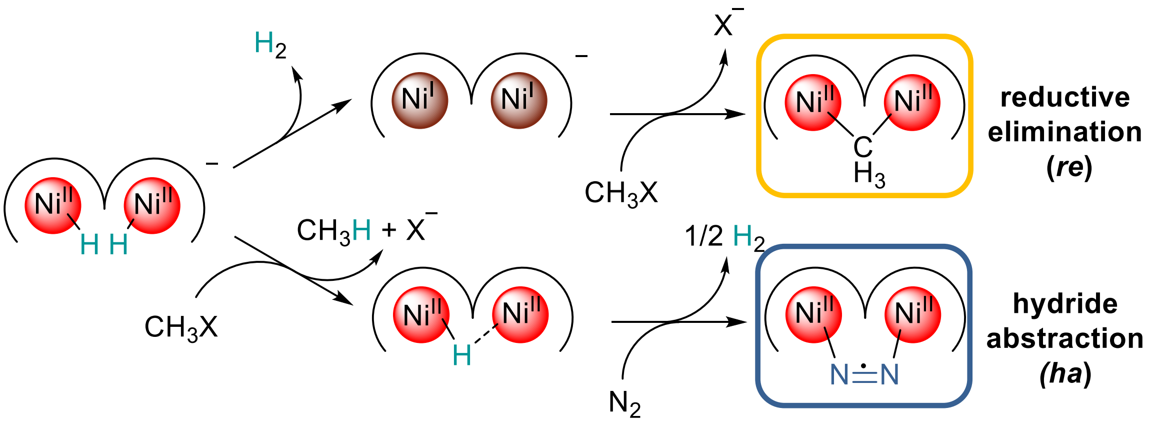

Scheme 13: Simplified illustration of both possible competing pathways for the reaction of **2-K** and general methylation reagents (CH_3X).

In earlier works it was shown that removing the K^+ counterion in **2-K** by chelating ligands like [2.2.2]crytand, triggered the release of dihydrogen to form the dinickel(I) complex **5**.[29] To investigate if this has an impact on the formation of **6**, a THF solution of dihydride complex **2-K** was treated with [2.2.2]cryptand prior to an addition of MeOTf. The ^{1}H NMR spectrum showed the indicative proton signal at -3.16 ppm for the nickel bound methylate group and solely one signal in the usual range of pyrazole protons at 5.51 ppm indicating that the reaction resulted only in one diamagnetic complex. The side product **4**$^{\mathbf{N_2}}$ was not detected. However, the complete absence of **4**$^{\mathbf{N_2}}$ was hard to prove by NMR, since its paramagnetic character led to broad indistinct signals, which are easily overseen. The decrease in amount of formed **4**$^{\mathbf{N_2}}$ was attributed to the *in situ* generation of **5**, since the reaction of **2-K** and MeOTf usually yielded a mixture of both products. Therefore, it seemed plausible to assume that the formation of **6** was linked to the intermediate **5**. This was supported by experiments using **5** directly generated *via* the reduction of **1**$^{\mathbf{Br}}$ with KC_8. In a follow up conversion with MeOTf the only product detected by ^{1}H NMR spectroscopy was **6**. This was also the case for Me_3OBF_4 which exclusively yields **4**$^{\mathbf{N_2}}$ upon reacting with **2-K**. Additionally, the previously discussed experiment with deuterated MeOTs indicated that the methyl group remains intact during the transfer, since no proton- deuterium exchange was observed. The mechanism deriving from these results is displayed in Scheme 13 and marked as *reductive elimination* (***re***). The initial step is the formation of the dinickel(I) complex **5** through the reductive elimination of dihydrogen from **2-K**. This is followed by a formal oxidative addition of a methyl cation, which is two-electron reduced in the process reforming the nickel(II) state for both metal centers.

There is less clear evidence for the mechanism of the competing transformation to **4**$^{\mathbf{N_2}}$**.** However, in respect to their usual reactivity in organic and organometallic chemistry[61],[62] the wide range of substrates, namely Ph_3CPF_6, HLuOTf, tris(pentafluorophenyl) borane,[21] Et_3OBF_4 and Me_3OBF_4 utilizable for the reaction suggested the initial step to be a *hydride abstraction* (***ha***) process. The possibility of a ligand protonation induced reductive elimination of dihydrogen was ruled out since DLutOTf did not show any hydrogen/deuterium exchange in the ligand backbone.

In a labeling experiment using **2-K-d₂** with the Meerwein salt Et_3OBF_4, the ^{2}H NMR spectrum showed two broad signals after 24 h reaction time. The signal at 4.58 ppm was assigned to molecular D_2 (Lit.: $\delta(H_2) = 4.55$ ppm)[53] and the signal at 1.02 ppm to DH_2CCH_3 (Lit.: $\delta(C_2H_6) =$

0.85 ppm)[53]. The significant difference in chemical shift of the DH_2CCH_3 signal compared to the literature value was probably caused by the broad linewidth due to the paramagnetic reaction product **4**^{N_2}. (Figure 24) The low quality of the ^2H NMR spectrum did not allow the determination of ratio between the two, but it was evident that both gases evolved during the reaction. This is in accordance with the ***ha*** mechanism displayed in Scheme 13, where one equivalent of CH_4 and half an equivalent of H_2 are formed. However, there is no evidence for the dinickel monohydride intermediate **7** presented. All attempts to detect it failed, including a synthesis *via* a σ-bond metathesis between dihydrogen and the structurally related **6**.

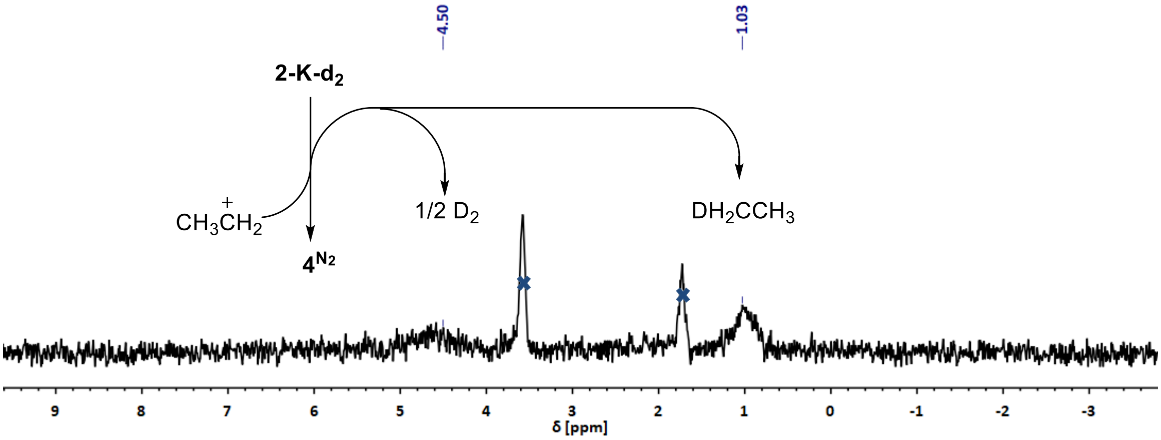

Figure 24: ^2H NMR spectrum (46.07 MHz) of the reaction of deuterium labeled dinickel dihydride complex 2-K-d2 and Et_3OBF_4 in THF showing approximate deuterium shifts for D_2 and DH_2CCH_3.[53] Solvent signals are marked by a blue cross.

Interestingly, the ***ha*** and the ***re*** mechanism resemble both mechanistic pathways that were discussed for the nitrogen binding at the FeMoco of nitrogenase in chapter 1.3.[23] Both mechanisms emanate from the Janus intermediate which holds two bridging hydride ligands between two iron centers and two protons on two bridging sulfide groups, respectively. According to the ***re*** mechanism H_2 is reductively eliminated and dinitrogen binds to the formally twice reduced iron center in the process. Subsequent proton shifts convert bound N_2 to diimide. In the hydride protonation (***hp***) pathway, (which is included in the ***ha*** mechanism for the reaction of **2-K** with one proton) one hydride ligand is protonated to release H_2 and N_2 binds to the vacant iron center. This is followed by a subsequent hydride and proton shift. In contrast to the reaction of **2-K** to **4**^{N_2}, the ***re*** mechanism seems to be operative for the N_2 binding in the FeMoco. However, an important difference is that in nitrogenase N_2 is reduced twice while in **4**^{N_2} it is only reduced by one electron. Either both the hydride abstraction with Meerwein salt and the protonation with a Brønsted acid provide additional entropic driving force upon elimination of a half equivalent of H_2 in comparison to the reductive elimination of dihydrogen. This seems to be necessary for the binding of dinitrogen.

This concludes that milder methylation agents transform **2-K** into methyl complex **6** due to a prior unimolecular hydrogen loss. Stronger reagents react faster than the formation of the intermediate nickel(I) complex **5** and therefore result in singly reduced dinitrogen complex **4**^{N_2}.

4.2.3 Synthesis of bridging Dinickel Alkylidene Complexes

In order to find a better understanding of the influence of the α-agostic interaction on the reactivity of the methyl group bound to the bimetallic cleft, the synthesis of a μ-methylidene bridged dinickel complex was attempted. To generate this complex **6** was treated with a variety of bases. KH and MeLi led to complex reaction mixtures possibly due to their ability to attack the weakly coordinated nickel(II) center nucleophilic. However, non-nucleophilic KHMDS also resulted in an undefined product mixture. Since the pK_a value of the nickel bound methyl group was expected to be very high (above $pK_a(CH_4)$ = 50-51)[63] no further attempts to deprotonate m **6** were made.

However, a μ-geminal alkylidene binding motive was accessible *via* a different strategy. **2-K** was treated with trimethylsilyldiazomethane as a carbene source (Figure 25).[64]

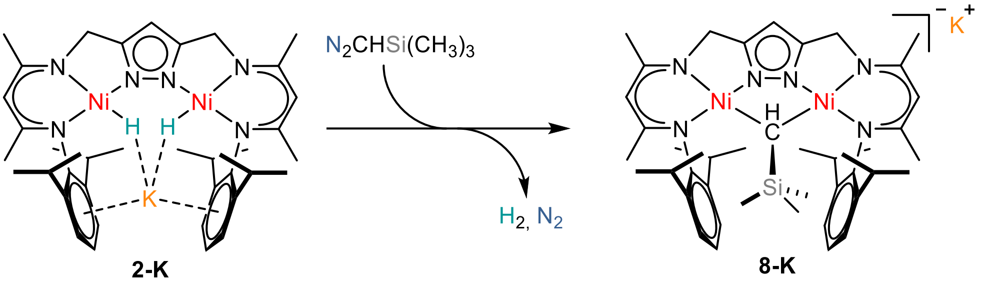

Figure 25: Reaction of **2-K** with trimethylsilyldiazomethane to **8-K**.

The immediate color change from bright orange to intense red was accompanied by vigorous gas evolution. The resulting compound was well soluble in THF, benzene, toluene, and even hexane. Crystalline material of **8-K** was obtained by cooling a concentrated THF/hexane solution of **8-K** to -35 °C for several days.

^{29}Si NMR spectroscopy of the product showed one signal at -6.94 ppm suggesting a single species containing a silicon nucleus. The ^{1}H NMR spectrum showed two doublets with an apparent roofing effect for the protons of the bridging methylene groups between the pyrazolate and the β-diketiminate subunits of the ligand. The measured coupling constant ($^2J_{H\text{-}H}$ = 15.9 Hz) is in the range of usual ^2J proton-proton coupling.[65] Therefore, the methylene protons above the coordination plane differ from their counterparts below. This break in symmetry was also observed for the signals of the four isopropyl groups resulting in two septets for the CH protons and four doublets for the CH_3 groups. Only one signal for the α-protons of the diketiminate units was found, suggesting the presence of a mirror plane orthogonal to the coordination plane. The diastereotropy of the methylene protons was attributed to the fact that the trimethylsilyl group was bend out of the coordination plane resulting in a C_s symmetry. The singlet at 0.35 ppm with a relative integral of nine was assigned to the Me_3Si group and the singlet at 0.14 ppm to the metal bound CH. As it will be shown later, complexes with a mirror plan inside the coordination plane also exhibit C_s symmetry. For reasons of differentiation complexes with a mirror plane orthogonal to the coordination plane, like **8-K** will be referred to as σ⊥xy-type complexes and complexes with a mirror plane parallel to the coordination plane will be referred to as σ‖xy-type complexes.

In THF-d_8 the CH proton of the dinickel bridging carbon atom appeared to be low field shifted at 0.14 ppm in comparison to the protons in **6** (δ = -3.17 ppm). Despite the electron donating influence of the Me_3Si group, the interaction with the K^+ counter ion seemed to significantly deshield at the proton resulting in the chemical shift difference. This was supported by the significant influence of the used NMR solvent on the observed proton shift. In C_6D_6 the proton signal for the metal bridging CH was found high field shifted (δ = -1.44 ppm) probably due to a different ion pair dissociation equilibrium. The ^{13}C NMR shows a resonance at δ = 19.2 ppm for the metal bridging carbon atom. These findings stand in strong contrast to literature reported values for nickel bridging alkylidenes were claimed shifts in the ^{1}NMR spectrum range from 14 – 4 ppm and shifts in the ^{13}C NMR spectrum are found at 274 ppm.[66] This suggests that the metal bound alkylidene **8-K** is rather described as a dianiconic $[CHSi(CH_3)_3]^{2-}$ ().

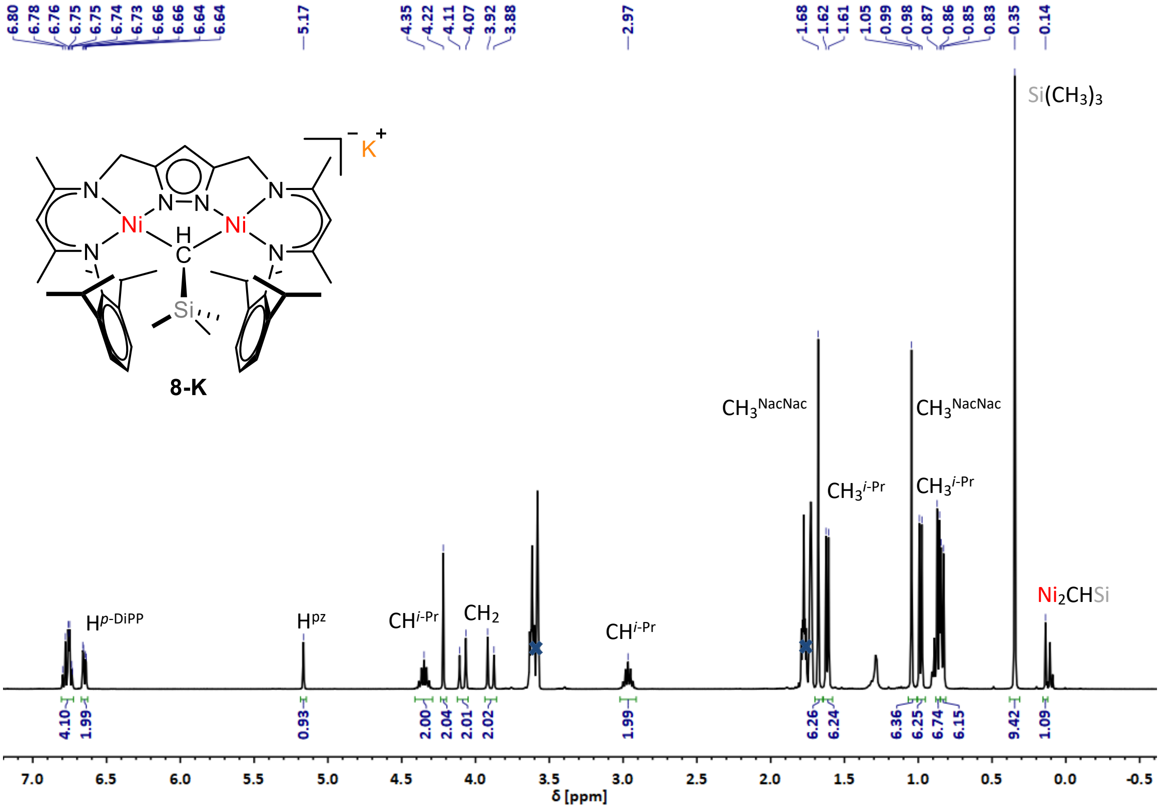

Figure 26: ^{1}H NMR spectrum (400.25 Hz) of μ-alkylidene complex **8-K** in THF-d_8.

As already mentioned, cooling a concentrated hexane/THF solution of **8-K** to -35 °C for several days gave crystals suitable for XRD analysis.

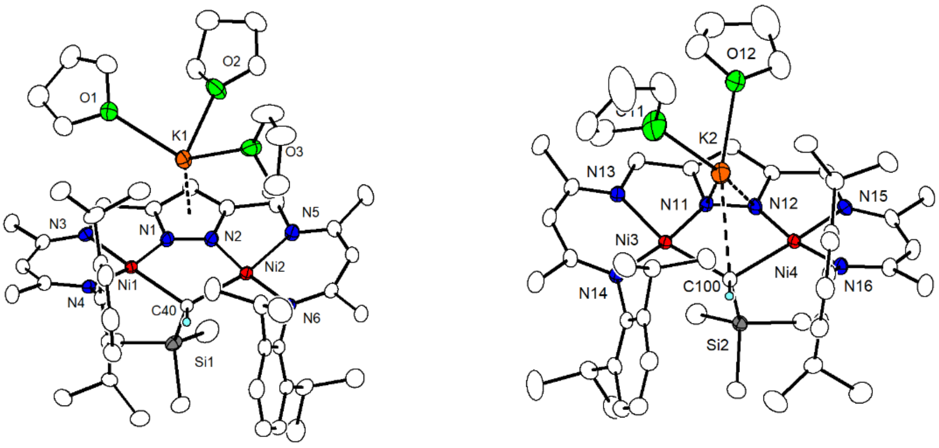

Si1 **Si2**

Figure 27: Molecular structures of **8-K** in with three (left) and two (right) coordinated THF molecules. Non-coordinated solvent molecules and hydrogen atoms except the one connected to the alkylidene carbon are omitted for clarity.

8-K crystallizes in the triclinic space group P $\bar{1}$. Two molecules are found in the asymmetric unit. In the solid state structure **Si1** the K^+ counter ion is coordinated by the pyrazolate π-system while binding three THF molecules. Structure **Si2** shows K^+ bound to only two THF molecules compensating the lack of the third THF by shortening the distance to both pyrazolate nitrogen atoms, the nickel centers and the alkylidene carbon atom. This results in slight elongations for coordinative bonds around the nickel centers with exception for the Ni-N bonds *trans* to the alkylidene ligand and the alkylidene ligand itself. For reasons of clarity only structure **Si1** will be discussed in detail (Figure 27).

Both nickel centers are found in a slightly distorted square planar coordination environment with a Ni···Ni distance of 3.4500(5) Å. The Me_3SiCH_2 carbon shares two bonds of similar distance to both metal centers, namely Ni(1)–C(40) with 2.0451 Å and Ni(2)–C(40) with 2.0549 Å. The similar distances suggest a µ-alkylidene binding motive for alkylidene complex **8-K**. Due to large steric demand the Me_3Si group is bend out of the coordination plane with an angle of 93.18° for Ni(1)–C(40)–Si(1) being almost rectangular and Ni(2)–C(40)–Si(1) with 109.36° which is very close to the tetrahedral angle. The wide angle for Ni(1)–C(40)–Si(1) with 114.59° results from the fixed nickel-nickel distance which is imposed by the ligand scaffold. The alkylidene function is best described as a double negatively charged Me_3SiCH_2coordinated to two nickel(II) ions. Despite the sharp angle in Ni(1)–C(40)–Si(1) the nickel bridging carbon atom is assumed to be mostly sp^3 hybridized. Angular deviations from the tetrahedral geometry might derive from crystallization induced distortions in the structure. A list of selected bond lengths and angles for both structures can be found in Table 2 and Table 3.

Table 2: Selected bond lengths [Å] for the molecular structures of **8-K**, namely **Si1** (left column) and **Si2** (right column).

Bond Lengths [Å] of (Si1) and (Si2)			
Ni(1)-N(1)	1.8041(17)	**Ni(3)-N(11)**	1.8230(16)
Ni(1)-N(3)	1.9837(16)	**Ni(3)-N(13)**	1.9755(17)
Ni(1)-N(4)	1.9263(17)	**Ni(3)-N(14)**	1.9283(16)
Ni(2)-N(2)	1.8111(17)	**Ni(4)-N(12)**	1.8070(17)
Ni(2)-N(5)	1.9823(18)	**Ni(4)-N(15)**	1.9682(16)
Ni(2)-N(6)	1.9317(16)	**Ni(4)-N(16)**	1.9237(17)
Ni(1)-C(40)	2.0451(19)	**Ni(3)-C(100)**	2.0776(19)
Ni(2)-C(40)	2.0549(19)	**Ni(4)-C(100)**	2.0562(19)
Ni(1)···Ni(2)	3.4500(5)	**Ni(3)···Ni(4)**	3.5058(5)

Table 3: Selected bond angles [°] for the molecular structures of **8-K**, namely **Si1** (left column) and **Si2** (right column).

Bond Angles [°] of Si1 and Si2			
N(1)-Ni(1)-C(40)	82.52(8)	**N(11)-Ni(3)-C(100)**	82.50(7)
N(4)-Ni(1)-C(40)	105.53(7)	**N(14)-Ni(3)-C(100)**	103.90(7)
N(3)-Ni(1)-C(40)	155.31(8)	**N(13)-Ni(3)-C(100)**	162.12(7)
N(1)-Ni(1)-N(3)	79.53(7)	**N(11)-Ni(3)-N(13)**	79.63(7)
N(4)-Ni(1)-N(3)	94.50(7)	**N(14)-Ni(3)-N(13)**	93.94(7)
N(2)-Ni(2)-C(40)	82.83(8)	**N(12)-Ni(4)-C(100)**	82.73(7)
N(6)-Ni(2)-C(40)	104.12(7)	**N(16)-Ni(4)-C(100)**	105.29(7)
N(5)-Ni(2)-C(40)	162.28(7)	**N(15)-Ni(4)-C(100)**	156.78(7)
N(5)-Ni(2)-N(6)	93.53(7)	**N(15)-Ni(4)-N(16)**	93.92(7)
N(2)-Ni(2)-N(5)	79.57(7)	**N(12)-Ni(4)-N(15)**	80.14(7)
Ni(1)-C(40)-Ni(2)	114.59(9)	**Ni(4)-C(100)-Ni(3)**	116.01(9)
Ni(1)-C(40)-Si(1)	93.18(8)	**Ni(3)-C(40)-Si(2)**	106.42(9)
Ni(2)-C(40)-Si(1)	109.36(9)	**Ni(4)-C(40)-Si(2)**	94.08(8)

Adding [2.2.2]cryptand to a THF solution of **8-K** resulted in the abstraction of the K^+. The solubility of the resulting alkylidene complex **8-cK** was significantly lower as it crystalized out of a THF/Et_2O mixture at room temperature. Crystalline material shaped as large rods of red color were subjected to XRD analysis.

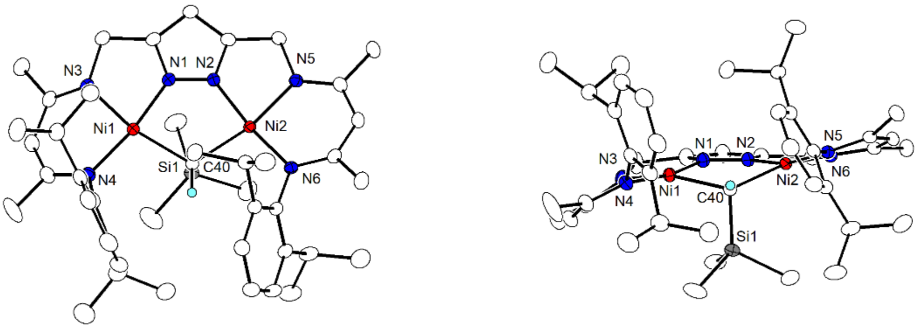

Figure 28: Molecular structure of **8-cK** in top view (left) and front view (right). [2.2.2] cryptand coordinated K$^+$, solvent molecules and hydrogen atoms except the one connected to the alkylidene carbon are omitted for clarity.

Alkylidene complex **8-cK** crystalizes in the monoclinic space group P2$_1$/c. In contrast to **8-K** the K$^+$ is removed from the dinickel complex moiety and encapsulated within the cavity of [2.2.2]cryptand. However, the overall appearance is similar to the structures found for the [2.2.2]cryptand free **8-K** (Figure 28). The nickel carbon distances are with 2.0176 Å for Ni(1)–C(40) and 2.0302 Å for Ni(2)–C(40) slightly contracted and the two Ni–C(40)–Si(1) angles are rather similar. Structural parameters are shown in Table 4.

As the CH$_3$ function in **6** was described as non-bridging and therefore only bound to one nickel(II) center the Ni···Ni distance appears to be significantly elongated with 3.6956 Å in comparison to the Ni···Ni distance in **8-cK** with 3.4412 Å. However, the Ni–C bond length of 1.997 Å in **6** appears to be decreased compared to the bond length found for both Ni–C bonds in **8-cK** (2.0176 Å, 2.0302 Å). All these parameters are longer than reported values for nickel carbon bonds in mononuclear nickel alkyl complexes bearing neutral (d(Ni–C) = 1.933 Å – 1.958 Å)[58] or anionic (d(Ni–C) = 1.9577 Å) ligands.

Table 4: Selected bond lengths [Å] and angles [°] for **8-cK**.

Bond Lengths [Å]		Bond Angles [°]	
Ni(1)-N(1)	1.8112(10)	**N(1)-Ni(1)-C(40)**	84.46(4)
Ni(1)-N(3)	1.9742(10)	**N(4)-Ni(1)-C(40)**	104.41(4)
Ni(1)-N(4)	1.9310(10)	**N(3)-Ni(1)-C(40)**	154.33(5)
Ni(2)-N(2)	1.8028(10)	**N(1)-Ni(1)-N(3)**	79.96(4)
Ni(2)-N(5)	1.9719(10)	**N(4)-Ni(1)-N(3)**	93.35(4)
Ni(2)-N(6)	1.9216(10)	**N(2)-Ni(2)-C(40)**	83.71(4)
Ni(1)-C(40)	2.0176(11)	**N(6)-Ni(2)-C(40)**	104.01(4)
Ni(2)-C(40)	2.0302(11)	**N(5)-Ni(2)-C(40)**	157.22(4)
Ni(1)···Ni(2)	3.4412(10)	**N(5)-Ni(2)-N(6)**	95.63(4)
		N(2)-Ni(2)-N(5)	79.84(4)
		Ni(1)-C(40)-Ni(2)	116.46(5)
		Ni(1)-C(40)-Si(1)	96.42(5)
		Ni(2)-C(40)-Si(1)	101.02(5)

4.2.4 Reactivity of the Dinickel Methyl Complex towards CO

Treating **6** with H_2 exclusively resulted in the formation of the hydrolysis product **3**, which was probably caused by traces of H_2O despite drying H_2 with sulfuric acid before use. In case of **8-K** reaction with H_2 also showed partially the formation of **3**. However, over longer periods of time the generation of the original starting material **2-K** accompanied by $SiMe_4$ was detected in the ^1H NMR spectrum.

When **6** was treated with CO, different reaction outcomes were observed depending on the pretreatment of the applied gas. First NMR experiments with CO that was dried over sulfuric acid showed the formation of an asymmetric complex **9** indicated by different proton shifts for the α-positions of the β-diketiminate units and **3**. Characteristic signals for the initially formed **3** disappeared over the course of a few days to leave the **9** as the only detectable species. Interestingly, the methylene brides between the pyrazolate and the β-diketiminate units gave two separate proton signals with one sharp singlet and one doublet coupling to a triplet at 10.87 ppm. This suggested the neighboring nitrogen donor of the β-diketiminate unit to be protonated (Figure 29).

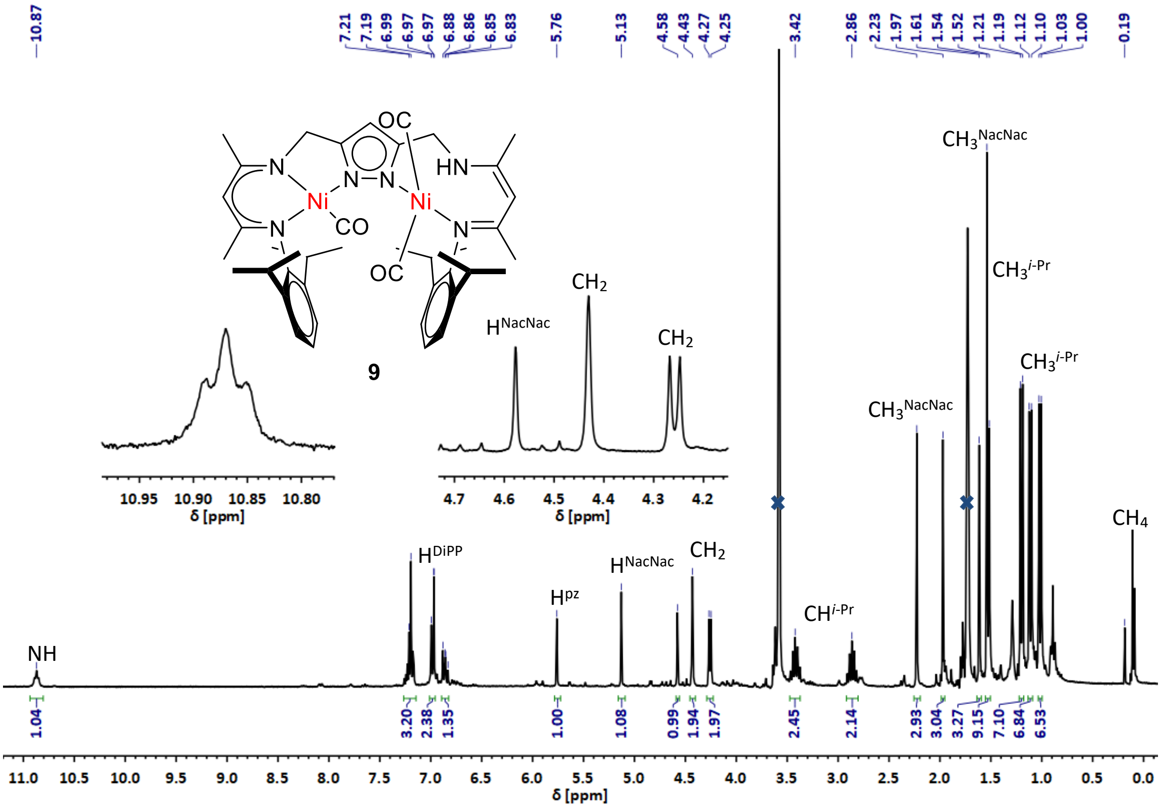

Figure 29: ^1H NMR spectrum (400.25 MHz) of **6** after treatment with ^{13}C labeled CO in THF-d_8 after one week. Besides the formed CO complex **9** only signal sets of minor impurities are visible.

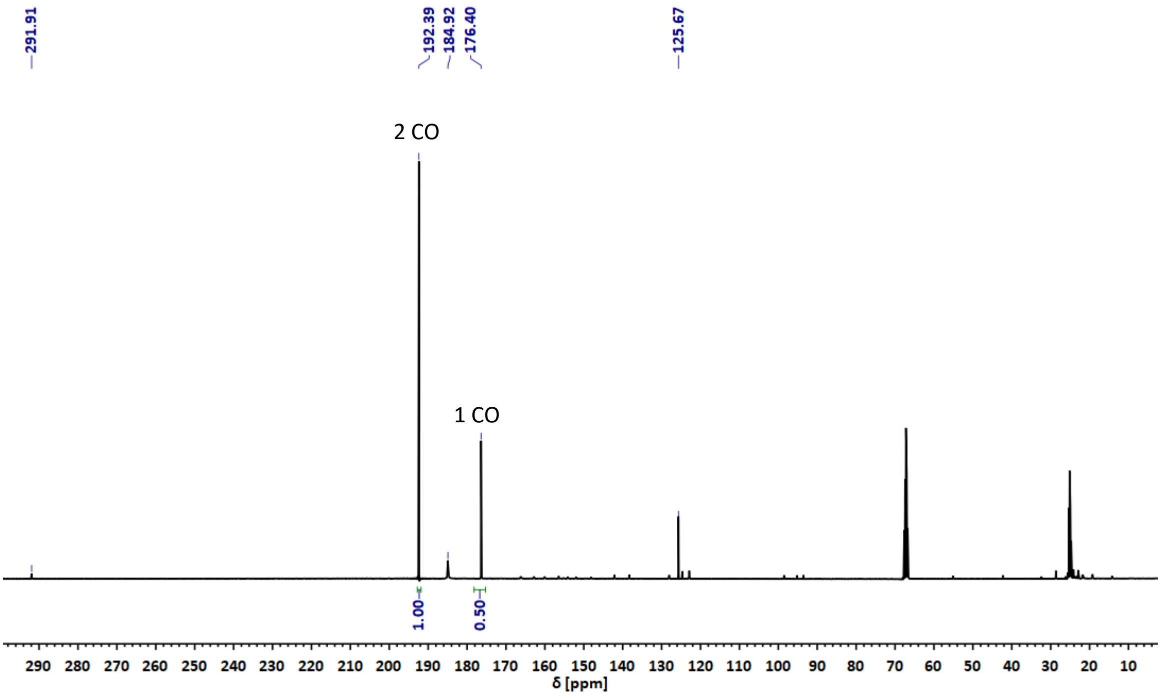

Figure 30: ^{13}C NMR spectrum (100.64 MHz) of **6** after treatment with ^{13}C labeled CO that was dried over H_2SO_4 in THF-d$_8$ after one week.

Carbon atoms deriving from CO were identified by their higher signal intensity in the ^{13}C NMR spectrum, when ^{13}CO was used for the reaction. Signals at 184.8 ppm and 124.7 ppm were assigned to excess CO[67] and CO_2,[53] respectively. Two Signals at 192.4 ppm and 176.4 ppm showed an exact relative integral ratio of 2:1 suggesting that they belonged to the same compound. Both carbon shifts were in the usual range of ^{13}C NMR signals for nickel carbonyl complexes.[68],[69],[70] This suggested the presence of three CO molecules in **9**. In the ^{1}H,^{13}C-HMBC spectrum the ^{13}C resonance at 176.4 ppm showed a correlation signal with the protons of the methylene bridging unit of the ligand at 4.43 ppm. This correlation derived from a *trans* coupling of the CO ligand through the nickel center (Figure 30). Unfortunately, it was not possible to isolate **9** and therefore, no additional spectral data was collected. A low intensity ^{13}C resonance at 292.0 ppm suggested the CO involved formation of a side product, although in trace amounts (Figure 31).

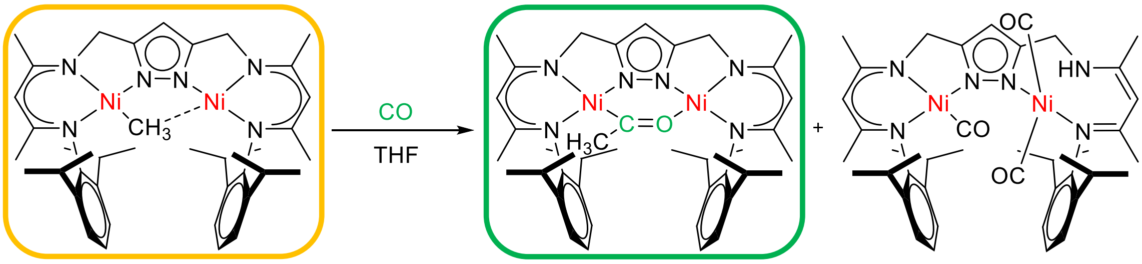

6 **10^{Me}** **9**

Figure 31: Reaction of **6** with dried CO to acetyl complex **10^{Me}** and CO complex **9**.

It remained unclear which mechanism led to **9**. The decreasing amount of initially observed **3** was probably involved. However, blind experiments showed that pure **3** remained stable and did not react under CO atmosphere. Hence, the presence of **6** was needed for the conversion.

Unfortunately, it was not possible to track the methylate ligand, or the deuterium labeled isotopologue by ^{1}H NMR or ^{2}H NMR spectroscopy. Literature presents different examples for coordination induced reductive elimination for nickel hydride complexes leading to comparable reaction outcomes (Figure 32).[71],[15]

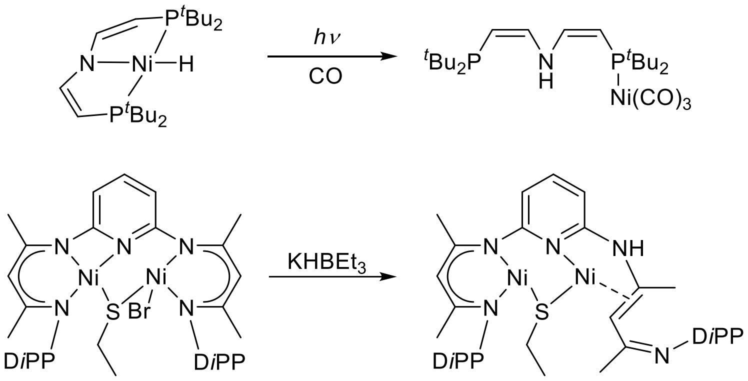

Figure 32: Examples for reductive amino ligand elimination. Photoinduced reductive elimination of the ligand in a PNP pincer nickel hydride complex leading to the protonated amino phosphine ligand coordinated to a nickel carbonyl complex (top).[71] Reductive elimination of a β-ketiminate moiety in a binuclear nickel complex over a hydride intermediate (bottom).[15]

Drying CO over molecular sieves (3 Å) resulted in a reaction where the minor species with the ^{13}C resonance at 292.0 ppm mentioned above became the major product as shown by a ^{13}C labeling experiment (Figure 33).

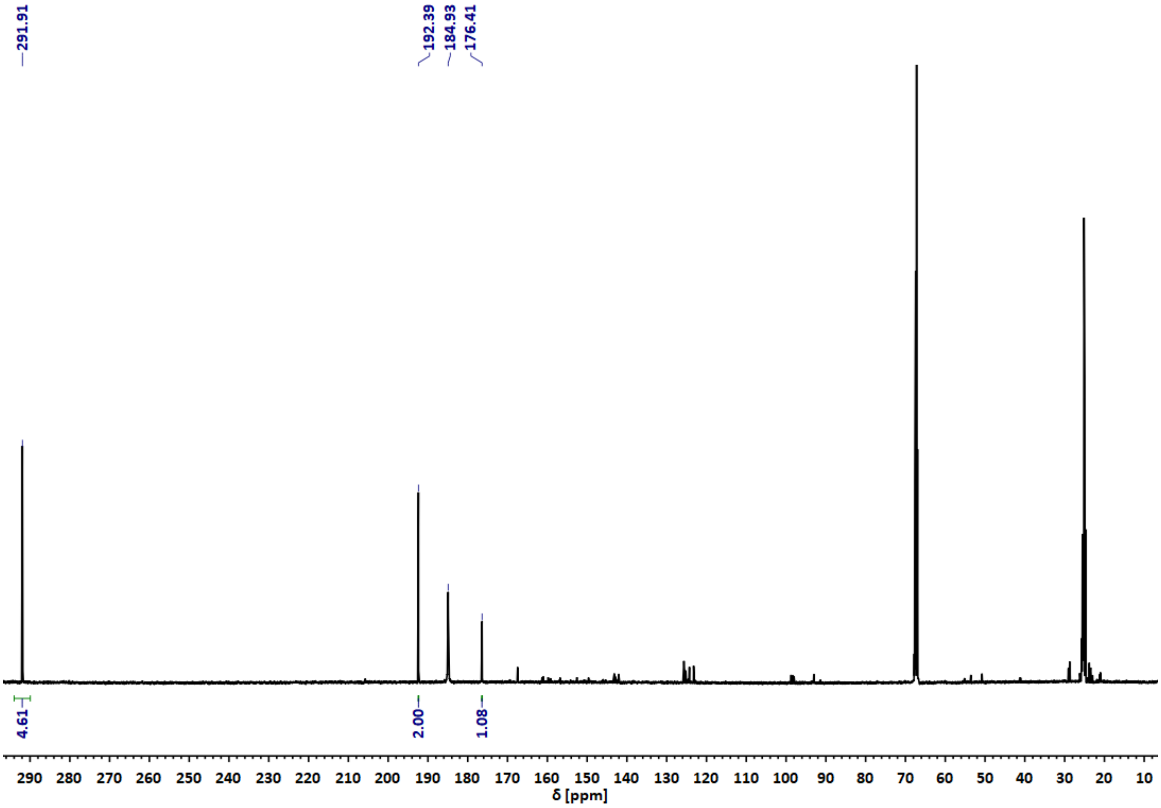

Figure 33: ^{13}C NMR spectrum (100.64 MHz) of methyl complex **6** in THF-d_8 after treatment with ^{13}C labeled CO that was dried over molecular sieves in THF-d_8 after one week.

In a ^{1}H,^{13}C-HMBC experiment the carbon signal at 292.0 ppm shows a correlation to a proton doublet at 1.83 ppm with a coupling constant of $^{3}J_{H,C}$ = 4.8 Hz (Figure 35). This suggested the alkylation of CO. The ^{1}H NMR spectrum showed two singlets for the α-protons of the β-diketiminate units of the ligand and two singlets for the protons of the methylene bridge.

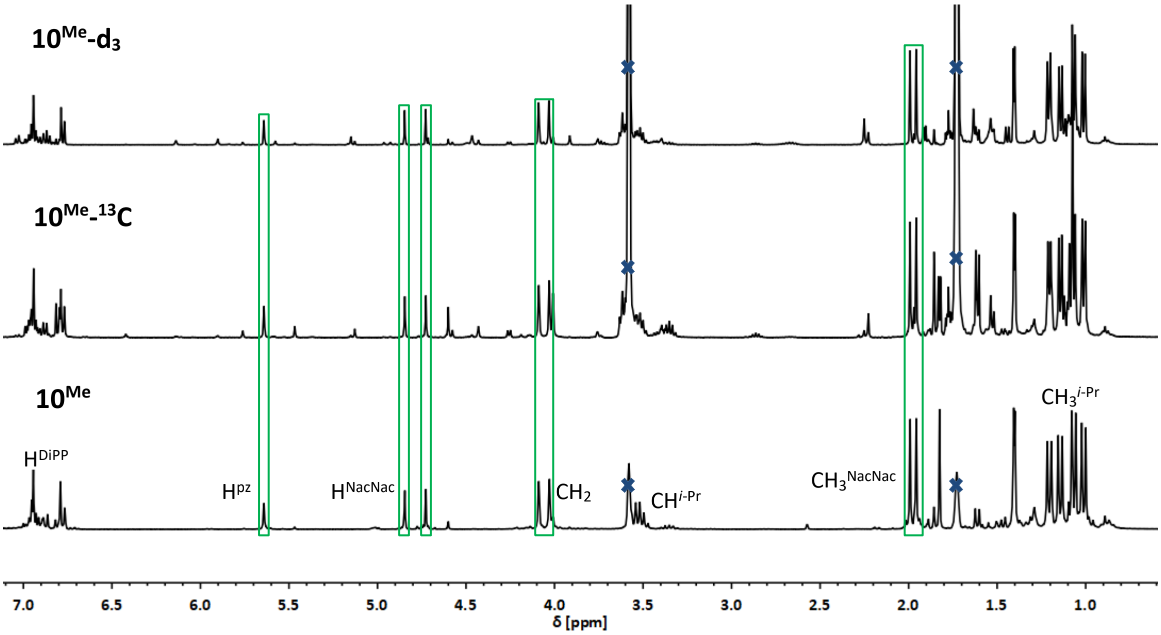

Figure 34: Stacked ^{1}H NMR spectra (400.25 MHz) of **10^{Me}** (bottom), ^{13}C labeled **10^{Me}** (middle), and deuterium labeled **10^{Me}-d_3** (top). Solvent signals are marked with a blue cross. Selected similar signals are marked by a green rectangle.

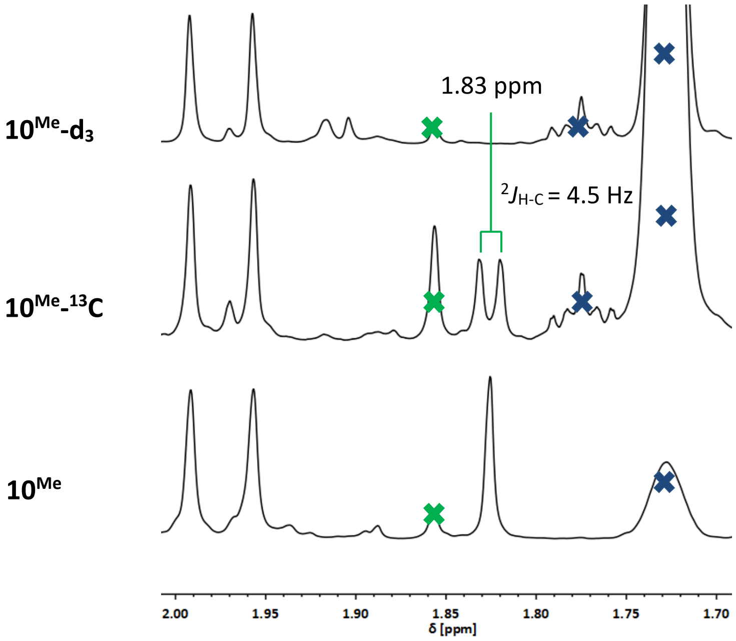

Figure 35: Stacked ^{1}H NMR spectra (400.25 MHz) of **10^{Me}** (bottom), ^{13}C labeled **10^{Me}** (middle), and deuterium labeled **10^{Me}-d_3** (top) around the region of the acetyl CH_3 group. Solvent signals are marked with a blue cross and signals of an impurity of **3** are marked with a green cross.

This signal set is observed for dinickel complexes of the pyrazolate bridging bis-β-diketiminate ligand **L** that have a mirror plane along the coordination plane but different coordination environments for the metal centers and therefore a C_s symmetry of the above defined σ‖xy-type.

To track the methyl group the same reaction was carried out with **6-d₃**. As shown in Figure 34 all signals of **10^{Me}** are visible in the ^{1}H NMR spectrum of the deuterium labeled analogue **10^{Me}-d$_3$** except the singlet at 1.83 ppm. Due to the low sensitivity of ^{2}H nucleus it was not possible to track the methyl group in an ^{2}H NMR experiment. However, the large difference in proton shift between **6** with -3.17 ppm and acetyl complex **10^{Me}** with 1.83 ppm indicated a chemical transformation that directly involved the nickel bound methylate. The solution structure of the acetyl complex **10^{Me}** according to above discussed NMR data is best described as an acetyl moiety bridging both metal centers in a *μ-κO,κC* fashion. The CO bound methyl group remains in the coordination plane as suggested by the mirror plane found in the ^{1}H NMR spectrum.

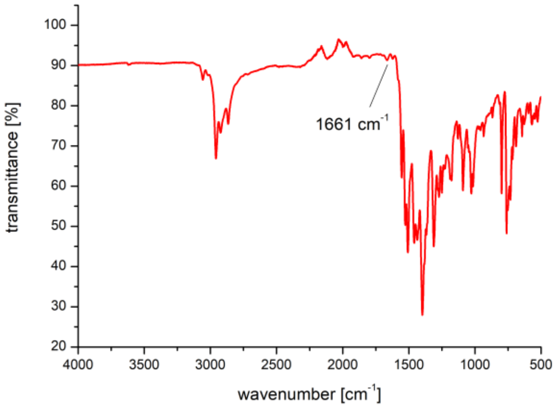

Figure 36: ATR-IR spectrum of **10^{Me}** in solid state.

The IR spectrum of **10^{Me}** shows a small feature at 1661 cm. This potentially belongs to the stretching mode of the C=O bond in the acetyl unit of the complex, since it is in the usual range for carbonyl group bands. The resonance is significantly lowered compared to the C–O stretching energy in free acetaldehyde [ν(C=O) = 1728 cm^{-1}] likely to be caused by the reducing character of the nickel bound to the carbon.[72] However, this has to be viewed with caution since the band has a very low intensity and therefore could also derive from minor impurities in the sample (Figure 36).

The insertion of CO into nickel carbon bonds represents a well-studied reaction due to the importance as a possible step in the metalloenzyme catalyzed acetyl CoA synthesis.[73],[74],[75]

4.3 Conclusion

In this chapter the synthesis of a new the dinickel methylate complex **6** was described. The ^{1}H NMR spectrum suggests a fast equilibrium in solution of the bridging methylate switching between the two nickel(II) center in the complex. The IR spectrum and solid state structure showed an α-agostic interaction of the nickel coordinating CH_3 group with the second Ni^{II} center, supported by DFT calculations.

The reaction mechanism of the alkylation of the **2-K** leading to **6** was investigated by isotope labeling and the analysis of the products. While reacting **2-K** with the weak methylation reagent MeOTs resulted in the formation of **6** *via* an ***oa*** mechanism, the strong methylation reagent Me_3OBF_4 led to the formation of $\mathbf{4^{N_2}}$ potentially *via* the proposed ***ha*** mechanism.

Furthermore, it was also possible to synthesize and characterize two new dinickel alkylidene complexes **8-K** and **8-cK** featuring a $[CHSi(CH_3)_3]^{2-}$ bridging unit within the bimetallic cleft. A structural comparison to **6** showed that unlike **6**, **8-K**/**8-cK** have two Ni–C bonds.

6 reacted readily with appropriately dried CO to the dinickel acetyl complex $\mathbf{10^{Me}}$. This was supported by ^{13}CO and CD_3 labeling experiments and NMR spectroscopy of the resulting products.

The reaction sequence of an oxidative addition of a methyl to a low-valent nickel(I) center and the following incorporation of CO into the Ni–C bond resembles the essential steps of the ACS catalytic cycle as emphasized in Scheme 14.

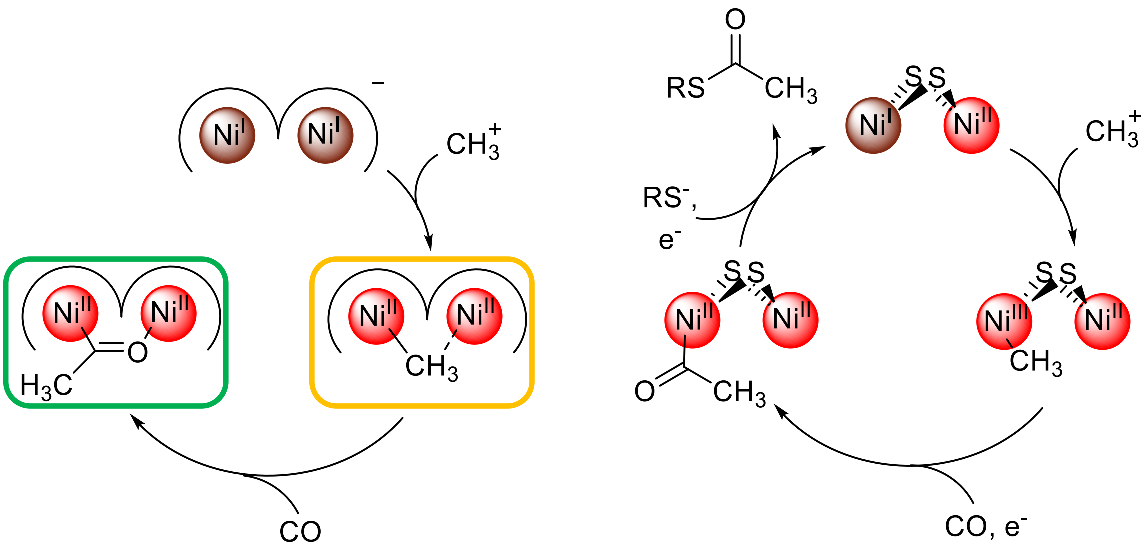

Scheme 14: Comparison between the reactivity of dinickel(I) complex **5** (left) and the proposed paramagnetic mechanism of acetyl CoA synthesis.

5 Activation of CO on a Dinickel Site and Proton Coupled Interconversion to a Reduced Formaldehyde Moiety

5.1 Introduction

5.1.1 CO as a Ligand in Metal Complexes

Due to its more reactive nature compared to CO_2, CO is a key C_1 building block in industrial chemistry. For example, it is used as a feedstock in industrial scale synthesis of methanol[76] and acetic acid.[77] As described in the previous chapter this strategy is also found in nature in the catalytic formation of acetyl CoA.

CO is a fundamental ligand in organometallic chemistry. It displays a rich coordination chemistry due to its exceptional binding properties. In addition to its σ-donor ability, the relatively low π* orbital energy enables CO to accept electron density and therefore establishes a π backbonding interactions with the metal center. This makes CO ideal for the stabilization of low-valent metal centers (Figure 37).

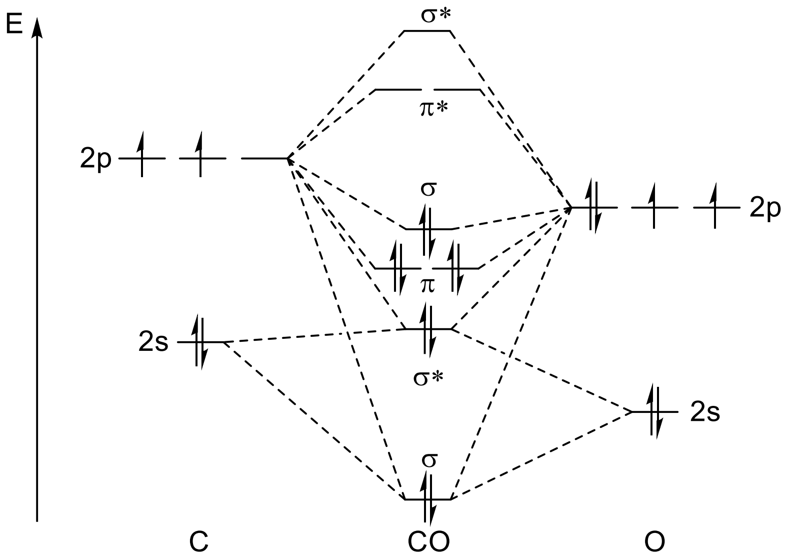

Figure 37: Molecular orbital diagram of CO.[78]

Due to the larger size of the π*-orbital at the carbon atom, CO generally coordinates to the metal *via* the carbon atom. It can bind to multiple metal centers at once and function as a bridging ligand with different binding modes. Even in these clusters containing two to three metal centers, CO tends to coordinate *via* the carbon atom (Figure 38). An exception is the μ-η^2 binding mode where it coordinates not only *via* the C atom to one metal center but also side-on *via* the π-orbital to a second metal center, thus acting as a four electron donor. [79]

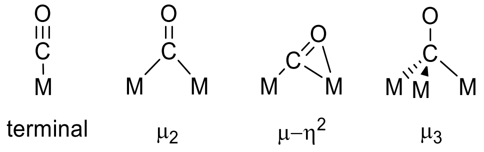

Figure 38: Different binding modes for CO in metal complexes.

The π backbond in several carbonyl complexes is well described, usually *via* vibration spectroscopy where the stretching frequency of free CO [ν(C–O) = 2143 cm^{-1}][80] is lowered.

5.1.2 Activation of CO in Nickel(I) Carbonyl Complexes

The first carbonyl complex discovered was $Ni(CO)_4$. It is used as an intermediate in the purification process of nickel which is named after Ludwig Mond who first described $Ni(CO)_4$ in 1889.[81] $Ni(CO)_4$ is readily available *via* the reaction of metallic nickel and CO. The formal nickel oxidation state of zero is retained in the tetrahedral complex and the C–O stretching vibration of 2057 cm^{-1} is found to be reduced in energy compared to free CO.[82] Since then many examples for nickel(0) complexes containing CO and preferably strong σ-donors like phosphines[68] or carbenes[83] have been reported.

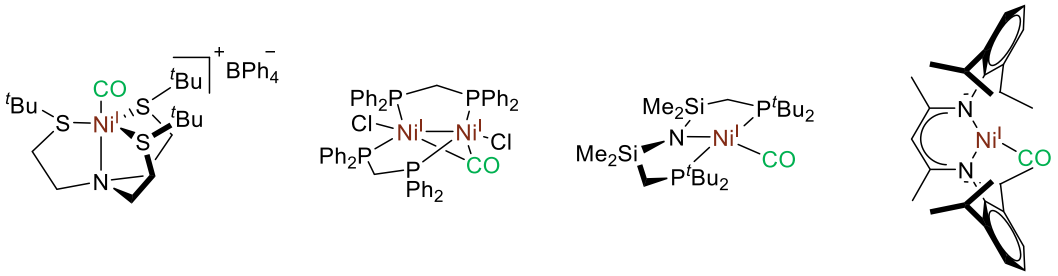

XVII **XVIII** **XIX** **XX**

Figure 39: Examples of nickel (I) carbonyl complexes.

As nickel(I) compounds are generally rarer, examples for CO containing nickel(I) complexes are rather scarce compared to their nickel(0) analogues. Figure 39 shows examples of nickel(I) carbonyl complexes in different coordination geometries. The first compound **XVII** is a trigonal bipyramidal complex synthesized by Holm *et al.*. The equatorial thiolate coordination environment was designed to functionally mimic the CODH/ACS active site. The CO complex is readily synthesized from the corresponding nickel(II) hydride and CO.[84] It was shown that the formation of **XVII** was probably linked to a Ni^{I} intermediate that was formed from the hydride *via* a H-atom transfer leading to $Ni(CO)_4$ and protonated ligand as observed byproducts.[85] The dinuclear complex **XVIII** was synthesized by a comproportionation reaction of the bis(diphenylphosphino)methane supported nickel(II) chloride and a dinickel(0) tricarbonyl complexes. The result was a dinuclear nickel(I) complex featuring a nickel-nickel bond and a bridging CO moiety.[86] The PNP-pincer system in **XIX** stabilizes a T-shaped nickel(I) complex which reacts reversibly with CO to give the non-planar complex **XIX**. The CO stretching frequency of 1940 cm^{-1} indicates some π backbonding.[87] The first three-coordinate nickel(I) carbonyl complex **XX** was reported by Holland *et al.* and involved the reaction of a Y-shaped β-diketiminate nickel(I) complex with CO.[88] The IR spectrum of **XX** showed a CO stretching band at 2022 cm^{-1} and thus suggested a weak π backbond. Another strategy for the generation of a β-diketiminate nickel(I) carbonyl reported by Limberg *et al.* is displayed in Scheme 15. In the bimetallic nickel(I) dinitrogen complex **XXI** the weakly coordinating N_2 can be substituted with CO. The structural parameters of the resulting monomeric nickel(I) carbonyl complex **XXII** are comparable to **XX**. It was possible to reduce **XXII** with KC_8 to give the diamagnetic nickel(0) carbonyl complex **XXIV**. An alternative synthetic pathway to **XXIV** included the initial reduction of **XXI** with KC_8 to a nickel(I) dinitrogen complex **XXII** and subsequent CO/N_2 exchange. CO stretching frequencies of 1782 cm^{-1} and 1742 cm^{-1} indicated that the CO is found to be significantly activated (Scheme 15).[89] This is demonstrated chemically by the reaction with MeI in a pursuit to mimic a reaction step in the proposed diamagnetic mechanism of the ACS catalyzed acetyl coA synthesis.[90]

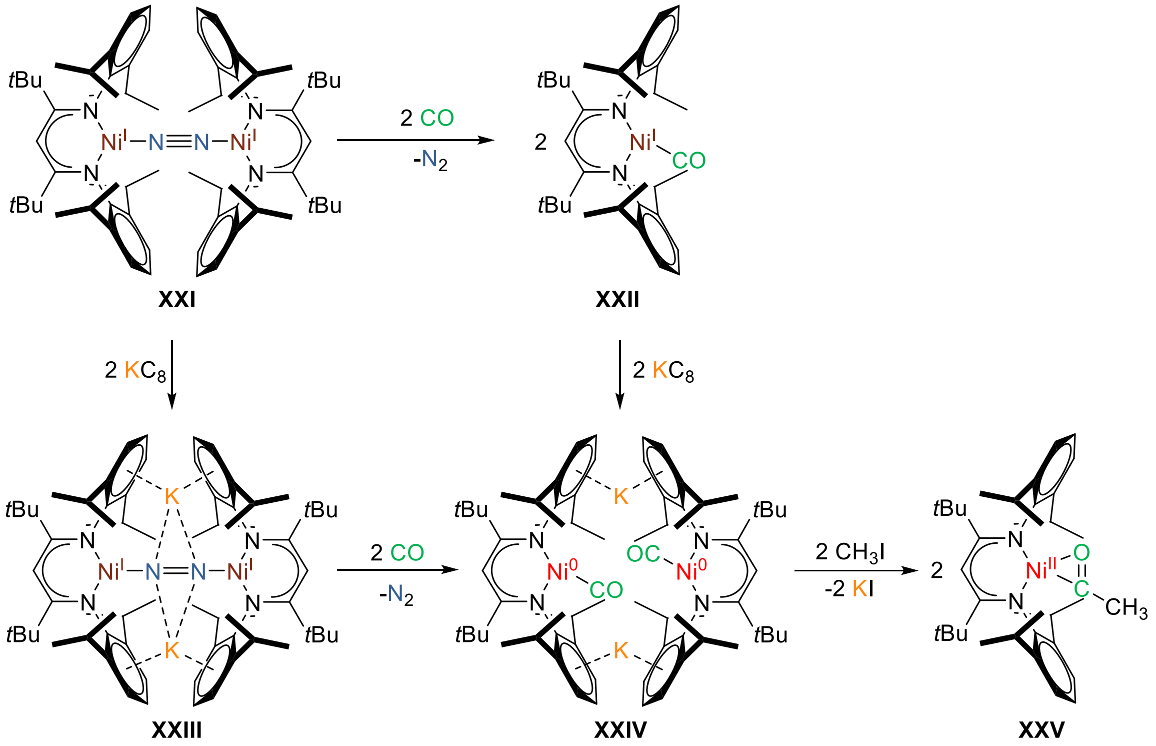

Scheme 15: Ligand substitution of N_2 with CO the example of the low-valent nickel complexes **XXI** and **XXIII** and the reductive conversion of **XXI** and **XXII** to **XXIV** and **XXV**, respectively.[89],[90]

5.1.3 Metal Mediated Reduction of CO

Besides the metal-mediated methylation of CO to acetyl functional groups, for example acetic acid, the hydrogenation of CO also presents a desirable reaction. Apart from the Fischer-Tropsch process, the most prominent example for a CO hydrogenation reaction is the conversion of CO to methanol. It belongs to the most important processes in petrochemistry as methanol serves as a basic C_1 building block in the production of a wide range of products including in the methanol-to-hydrocarbon processes.[91] Additionally, methanol has the potential to be a sustainable liquid fuel in the future.[92]

Modern approaches for industrial methanol production avoid high pressures and high temperatures, such as in the low-temperature solution-based methanol synthesis (LTMS). The most active catalysts for the LTMS are based on Ni or Cu. In the case of Ni, the catalyst is formed *in situ* from $Ni(CO)_4$. The active species has been identified as a monomeric or dimeric nickel hydride.[93] Two mechanisms have been discussed for the catalytic transformation of CO to methanol. The indirect mechanism which involves methyl formate as an intermediate and the direct mechanism that occurs *via* formaldehyde.

The first step of the direct mechanism is proposed to be a migratory CO insertion into the Ni–H bond resulting in a formyl species. This is followed by the reaction with hydrogen to form coordinated formaldehyde. Another insertion into the Ni–H bond gives a nickel methoxy complex which releases methanol upon reaction with H_2 (Scheme 16).[94]

Although, the initially formed nickel formyl species is a key intermediate, examples of nickel complexes functionalized by a formyl unit are rare,[95] and have not been structurally characterized. In general, formyl metal complexes are synthesized by the reaction of a hydride donor reagent with the respective metal carbonyl complex. However, in the catalytic mechanism of the Fischer-Tropsch process or the LTMS, migratory insertion of a metal bound hydride to a CO ligand to form the formyl unit has only been described scarcely in appropriate molecular model system, since this type of reaction is mostly thermodynamically uphill for d-metal complexes.[96],[97]

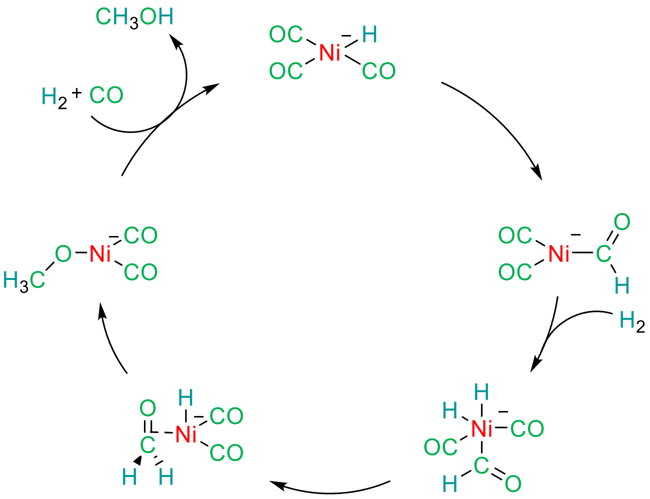

Scheme 16: Proposed mechanism of the direct hydrogenation of CO to methanol.[94]

The rate determining step of the catalytic cycle is the hydrogenation reaction of the formyl. The oxidative addition of H_2 results in a highly energetic intermediate which is likely to reductively eliminate formaldehyde almost immediate. Although, the resulting formaldehyde is likely to be an intermediate in the conversion, the reduction process cannot be stopped at the stage of the C=O double bond containing molecule and precedes to methanol. Consequently, in order to produce formaldehyde, methanol is partially oxidized or dehydrogenated, which consumes about 35% of produced methanol making it its main application.[98] This requirement of a reverse reaction causes a substantial decrease in energy efficiency.[99] Recent approaches for the selective hydrogenation of CO to formaldehyde involve heterogeneous catalysts.[100],[101] Developments in homogeneous catalysis mostly focus on the direct transformation of CO or CO_2 to methanol.[102],[103],[104] However, there are some examples for molecular systems that selectively produce silylated or borylated formaldehyde.[105],[106]

Generally, the hydrogenation of formaldehyde has a very low energetic barrier. Related works on the reduction of aldehydes mostly focus on functionalized substrates.[107],[108],[109]

5.1.4 Nickel-based Aldehyde Reduction

There is a general interest in the reduction of aldehydes since it has a widespread synthetic application. At the beginning, catalytic aldehyde reduction was mostly aimed towards the formation of alcohols; however modern achievements afforded various functionalizations including cross couplings.[110],[111]

To elucidate the mechanistic pathways of these reduction reactions, isolation of intermediates is required. Therefore, many studies have investigated stochiometric reactions to such compounds.

In 2009, Guan *et al.* synthesized the pincer ligand supported nickel(II) hydride complex **XXVI** as a reduction catalyst for aryl aldehydes. The nickel benzyloxy complex was identified as intermediate **XXVII** of the catalytic cycle by performing a stochiometric reaction between the respective nickel hydride complex and benzaldehyde (Figure 40). [112] The carbonyl group was inserted in the Ni–H bond of **XXVI** giving a stable the nickel benzyloxy complex **XXVII. XXVII** proved to be inert towards β-hydride elimination, which is often observed for late transition metal complexes.[113],[114]

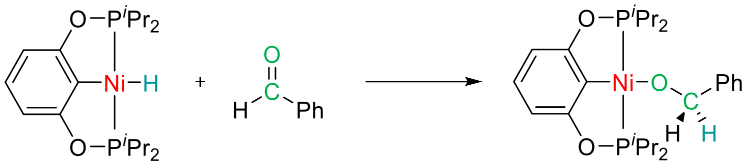

XXVI **XXVII**

Figure 40: Insertion of benzaldehyde into the Ni–H bond of nickel hydride **XXVI** to give nickel benzyloxy complex **XXVII**.[112]

Also, low-valent nickel(0) complexes can mediate the reduction of aldehyde. The first example for a low-valent nickel η^2-benzaldehyde complex is displayed in Figure 41. The complex was synthesized *via* substitution of C_2H_4 in **XXVIII** by benzaldehyde to yield **XXIX**[115] which was characterized by various spectroscopic and structural methods.[116] For instance, the C=O stretching vibration of 1600 cm^{-1} in **XXIX** is lower than in free benzaldehyde. However, it is still in the regime of typical IR bands for C–O double bonds.

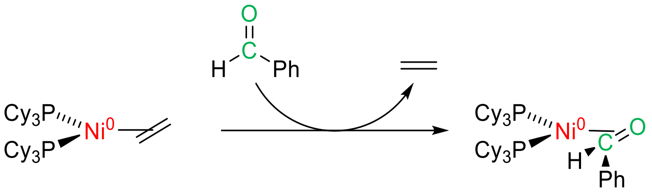

XXVIII **XXIX**

Figure 41: First example of a nickel benzaldehyde complex.[115]

The carbonyl functional group usually coordinates in a η^2-fashion to a nickel center and engages in a significant π-backbond interaction similar to what is described for olefins by the Dewar-Chatt-Duncanson model. In this, the actual oxidation state of the nickel can formally vary between 0 and +II depending on whether the aldehyde behaves as a neutral ligand or has formed a three membered metallacycle through an oxidative addition (Figure 42). However, usually the amount of electron density contributed from the metal center to the carbonyl moiety is not sufficient to change the oxidation states of metal and aldehyde.[117] Nonetheless, η^2-aldehyde complexes have been identified and utilized in various carbonyl group conversions including cyclisation [118] and direct esterification reactions.[119]

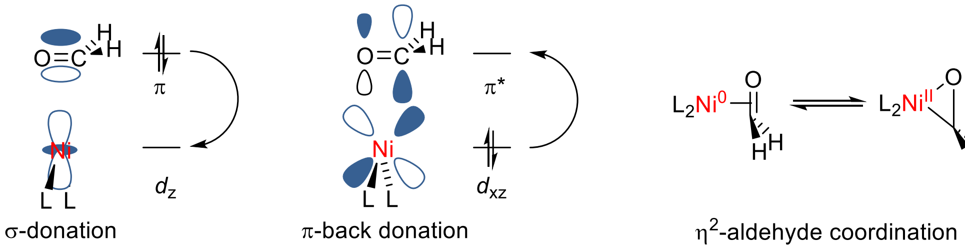

Figure 42: Bonding constitution between a low-valent nickel center and formaldehyde based on the Dewar-Chatt-Duncanson model (left) and Lewis formula description of the aldehyde complex between coordinated aldehyde and three membered metallacycle.[117]

The reaction in Figure 43 highlights how **XXX**, which features a similar scaffold to, **L**, is able to activate benzaldehyde. It was found that **XXX** is prone to intramolecular reductive elimination of the Ni–C and Ni–H bond resulting in an intermediate Ni^INi^I complex similar to the reductive elimination of H_2 in **2-K**. This Ni^INi^I intermediate readily reacts with benzaldehyde to give complex **XXXI**.[120] The molecular structure of **XXXI** revealed a significant C–O bond length increase of the carbonyl group from 1.212(3) Å in free benzaldehyde to 1.388(3) Å. Additionally, NMR data of the diamagnetic complex **XXXI** did not show a proton shift expected for an aldehyde function but a dramatic high-field shift to 2.03 ppm. These results suggest a reduction of the aldehyde moiety (Figure 43).

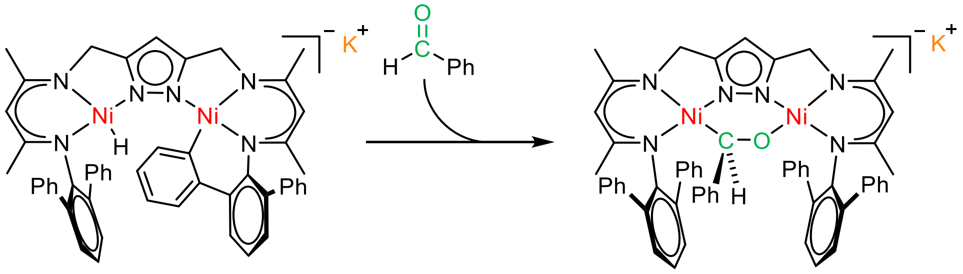

XXX **XXXI**

Figure 43: Benzaldehyde activation with the bis(diketiminate) pyrazolate dinickel complex **XXX**.

5.1.3 Objective

The previous chapter focused on the possible ACS model complex reactivity for the [LNi$_2$] complex motive, by isolating the respective complex **6** and studying the incorporation of CO leading to **10^{Me}**. As this scheme resembles Path A of the ACS paramagnetic mechanism, Path B describes a pathway where initially CO is bound to the nickel complex and then methylation of the bound CO leads to a similar product (Scheme 8). In a pursuit to resemble the reaction pattern of Path B, this chapter initially aims towards the isolation of an activated CO complex. As it was earlier shown N$_2$ could only be coordinated to the [LNi$_2$] complex motive if **2-K** was treated with one equivalent of a proton acid or hydride abstraction reagent. The resulting dinickel dinitrogen complex **4^{N_2}** featured a significantly reduced N$_2$ moiety. To synthesize the respective CO complex the same reaction conditions will be applied under CO atmosphere. Inspired by the synthesis of **XXIV** a substation of the N$_2$ ligand in **4^{N_2}** with the isoelectronic CO will be investigated (Scheme 15).

The activated CO moiety will be object to further reactivity studies. In view of the commercially interesting hydrogenation processes applied to CO, it will be investigated if the [LNi$_2$] complex motive is able to facilitate the CO hydrogenation and potentially allow the isolation of intermediate reaction products like formaldehyde. To gain more insight on the mechanism of the proton coupled CO reduction the direct formation of a new activated formaldehyde complex will be targeted. The degree of activation will be determined based on structural and spectroscopic properties.

As previously shown, complex **XXX** was able to reductively bind an aryl substituted aldehyde. This reactivity will also be investigated for **2-K**. Furthermore, in order to benchmark the influence of different substituents at the *para*-position of the arylaldehyde the reductive binding capability of **2-K** will be investigated with a consistent substrate pool of *para*-substituted arylaldehydes.

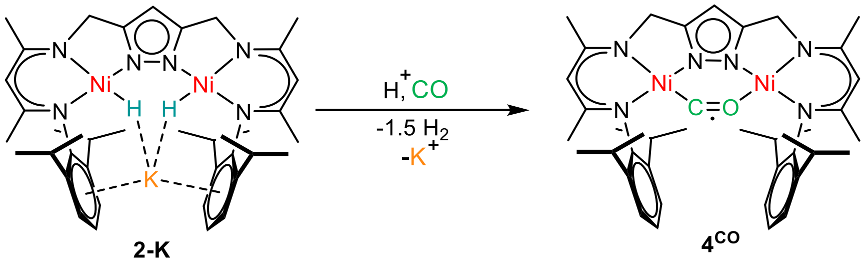

2-K

4^{CO}

Figure 44: Desired reaction of **2-K** with a proton under CO atmosphere.

5.2. Results and Discussion

5.2.1 CO activation via a single electron reduced dinickel complex

Applying an atmosphere of CO directly to a solution of **2-K** did not lead to any conversion and allowed the reisolation of the starting material **2-K**. For that reason, a different approach for the binding of CO was implemented.

As mentioned earlier, it was possible to generate the radical dinitrogen complex $\mathbf{4}^{\mathbf{N_2}}$ *via* protonation of **2-K** under dinitrogen atmosphere. Results from Peng-Cheng Duan suggested that these conditions were also applicable for the isoelectronic CO in order to synthesize a CO complex $\mathbf{4}^{\mathbf{CO}}$.[21] First attempts of synthesizing $\mathbf{4}^{\mathbf{CO}}$ involved the single protonation of **2-K** using one equivalent of HLutOTf. To remove any chance of the inclusion of adventitious dinitrogen, oxygen or moisture, extreme precautions and care were taken in the following reaction. All reagents and glassware were thoroughly dried using rigorous Schlenk techniques. THF was vacuum transferred to a Young ampoule at -196 °C which contained **2-K** ant HLutOTf. CO was transferred onto these frozen solids and the mixture was warmed slowly to -78 °C and stirred briefly. The solution was then warmed to room temperature and stirred overnight. The reaction mixture was filtered, and hexane layered on this to produce crystalline material. IR spectroscopy revealed a characteristic stretching band at 1735 cm^{-1} which was assigned to a C=O stretch vibration. Higher yields were obtained by optimizing the reaction conditions. To make the separation of the byproduct salt easier, toluene instead of THF was used as a solvent for the reaction. Furthermore, the Brønstedt acid HLutOTf was substituted by Et_3OBF_4, which functioned as a hydride abstractor and led to higher yields. The product was crystalized from THF/hexane solvent mixture at -35 °C as small brown cubes. It should be noted that no difference in reaction outcome was observed depending on whether the mixture of **2-K** and Et_3OBF_4 in toluene was prepared under exclusion of nitrogen or not. The crystalline material showed similar absorption in the IR spectrum.

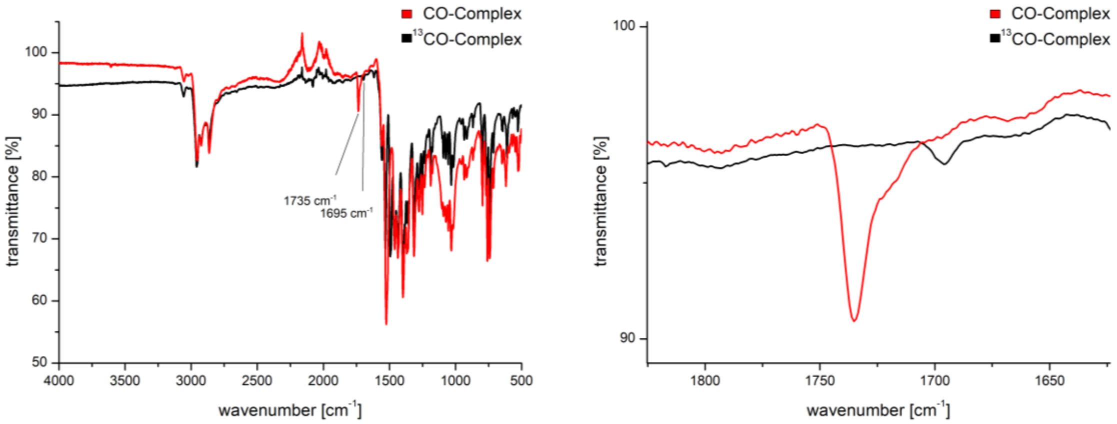

Figure 45: ATR-IR transmission spectra (left) and inlet of the area from 1850 cm^{-1} to 1675 cm^{-1} (right) of formyl complex $\mathbf{10}^{\mathbf{H}}$ (red line) and ^{13}C isotope labeled formyl complex $\mathbf{10}^{\mathbf{H}}$ (black line).

The IR spectra for the CO complex and its ^{13}C isotopologue are displayed in Figure 45. Except for the stretching band at 1735 cm^{-1} all absorption bands remain the same. However, in case of the ^{13}C labeled complex a small band at 1695 cm^{-1} was observed. This absorption matched the calculated value [calcd.: $v(^{13}CO)$ = 1696 cm^{-1}]. This shows that the band at 1735 cm^{-1} is indeed related to CO incorporated in the complex. Compared to free CO [*ν*(C–O) = 2143 cm^{-1}] or the CO complex **XX** [*ν*(C–O) = 2022 cm^{-1}],[88] the CO stretching vibration is significantly reduced in energy. This indicated a decreased bond order due to a reductive activation of the CO ligand.

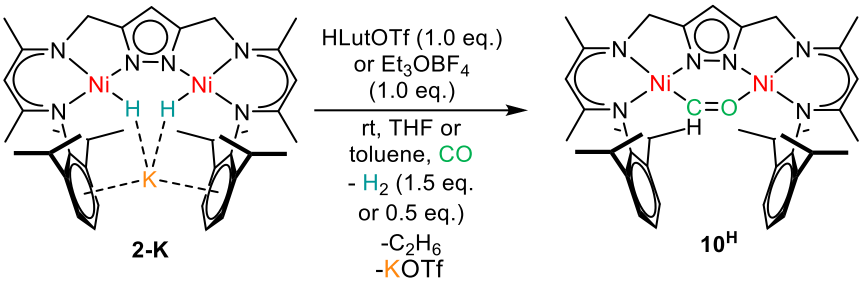

Figure 46: Synthesis of compound **10^H** from **2-K** with HLutOTf or Et_3OBF_4.

To obtain further information about the electronic structure the supposedly radical CO dinickel complex was analyzed in an EPR experiment. However, the substance proved to be EPR silent and therefore was subjected to NMR spectroscopy.

NMR spectroscopic data indicates the presence of a diamagnetic compounds. Two separate singlets for the α-protons of the β-diketiminate units and for the methylene bridge protons suggest a C_s symmetry of the σ||xy-type for the complex, similar to **10^{Me}**. Most prominent is a low field shifted singlet at 7.38 ppm, which is not assigned to any proton signals of **L**⁻. In the ^1H NMR spectrum of the complex generated with ^{13}C labeled CO the signal is split into a doublet with a coupling constant indicative for a ^1J coupling ($^1J_{H,C}$ = 147 Hz) (Figure 47). ^1H,^{13}C HSQC spectroscopy confirms the correlation of the low field shifted proton to a very low field shifted carbon at 275.9 ppm in the ^{13}C NMR spectrum. Using ^{13}C labeled CO in the reaction leading to the ^{13}C labeled complex proved that the carbon signal originated from CO as seen in Figure 48. These results suggested an H atom transfer to the carbon atom of the nickel coordinated CO resulting in a dinickel formyl complex **10^H**. Single crystals suitable for XRD analysis were obtained by slow diffusion of hexane into a THF solution of **10^H** at -35 °C.

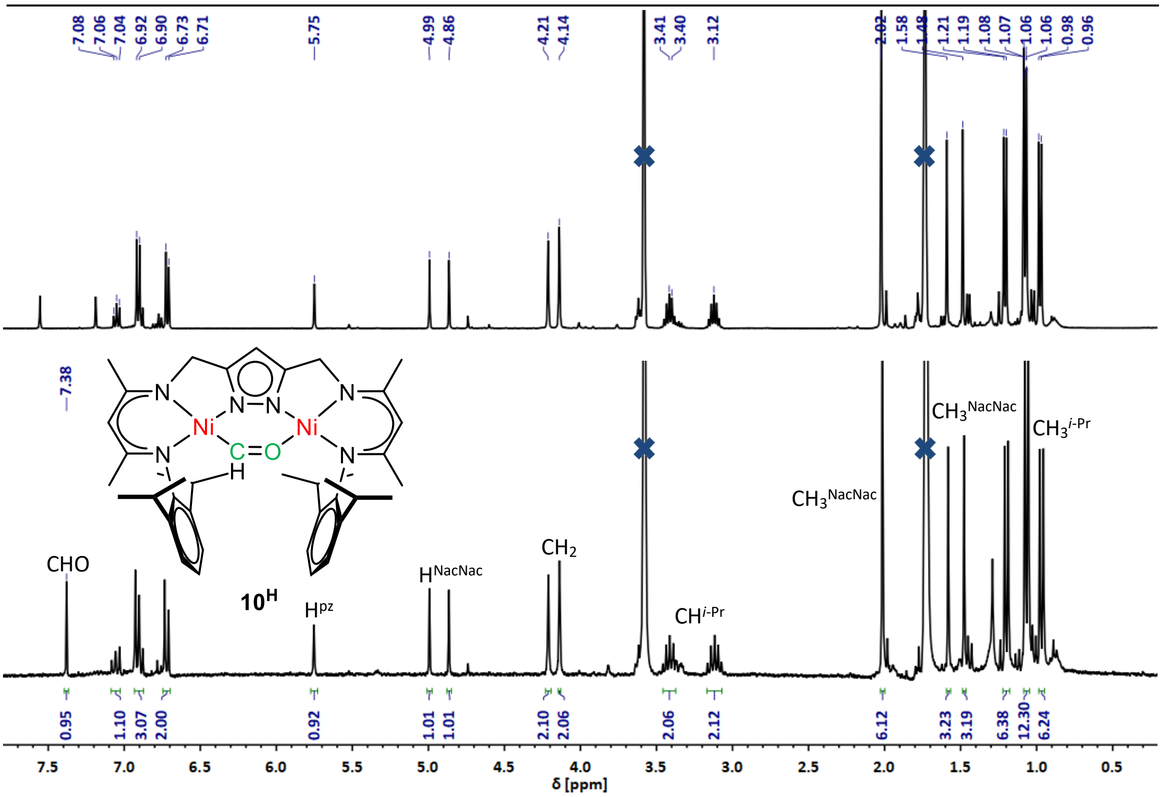

Figure 47: Stacked ^{1}H NMR spectra (400.25 MHz) of **10^{H}** (bottom) and ^{13}C labeled **10^{H}** (top) in THF-d_8. Solvent signals are marked with a blue cross.

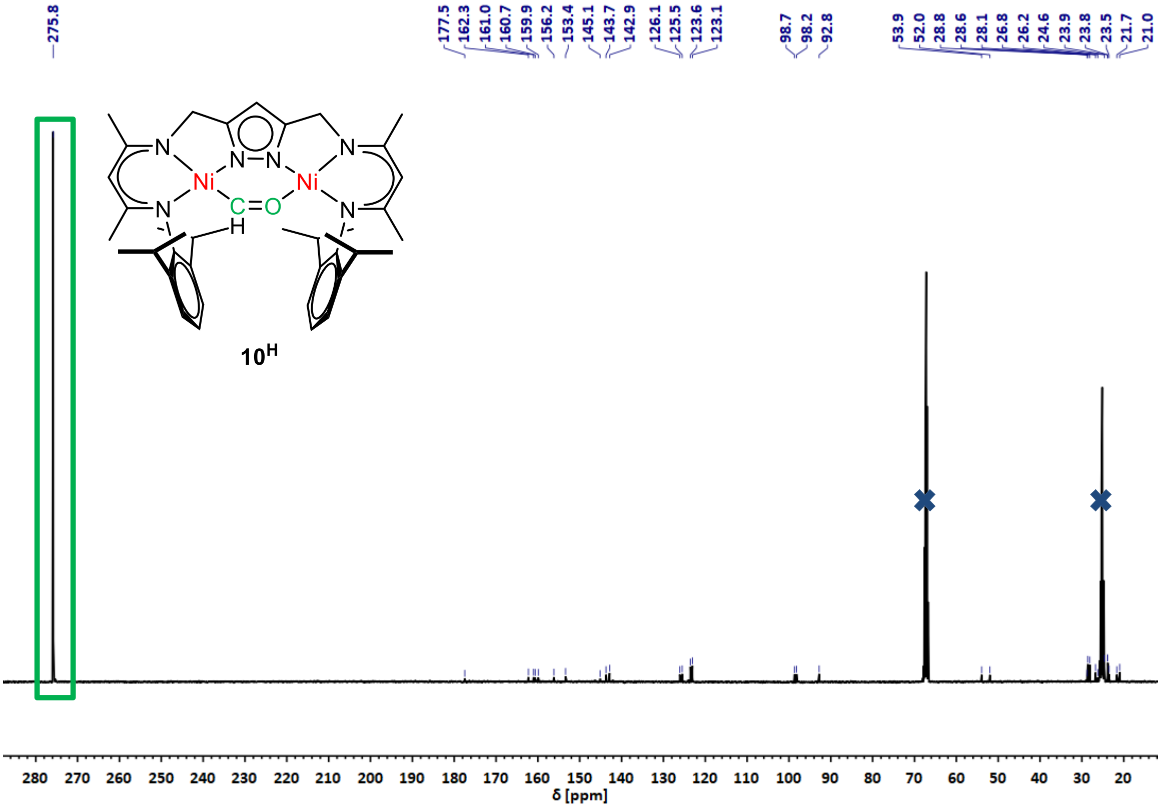

Figure 48: ^{13}C NMR spectrum (100.64 MHz) of ^{13}C labeled formyl complex **10^{H}** in THF-d_8. Solvent signals are marked with a blue cross and the formyl carbon is marked by a green box

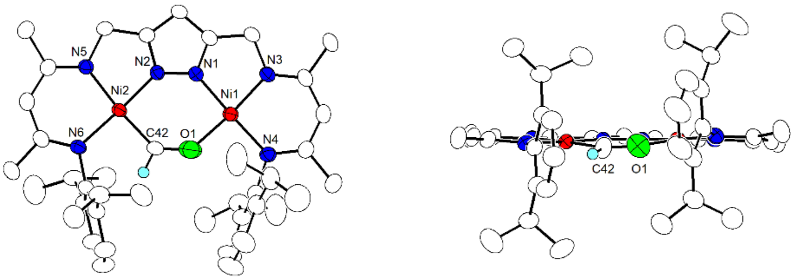

Figure 49: Top view of the molecular structure of **10**^{H} (left) and front view of the molecular structure of **10**^{H} (right). Solvent molecules and hydrogen atoms, except the H substituted on the bridging formyl ligand, are omitted for clarity.

As observed for many other dinickel complexes of **L**, **10**^{H} crystallizes in the monoclinic space group $P2_1/c$. Both nickel centers adopt a square planar coordination environment with a metal-metal distance of d(Ni···Ni) = 3.8777(5) Å. The formyl unit bridges them in a *μ-κC,κO* fashion. The Ni–C bond of 1.847(2) Å is significantly shorter than the corresponding bond distance in **6** [d(Ni–C) = 1.997(2) Å], probably due to the sp^2 hybridization of the involved carbon atom. However, the electronegative oxygen atom also shows a Ni–C bond shortening influence as indicated by comparison with a reported nickel alkyne complex of **L** [d(Ni–C) = 1.904(3) Å, 1.921(2) Å].[18] The Ni–O bond measures a distance of 1.858(2) Å. The C–O bond within the coordinated formyl unit of 1.227(3) Å is slightly elongated compared to C–O double bonds in aldehydes [formaldehyde: d(C–O) = 1.21 Å] (Figure 49).[121]

Table 5: Selected bond lengths [Å] and angles [°] for **10**^{H}.

Bond Lengths [Å]		Bond Angles [°]	
Ni(1)-N(1)	1.8426(17)	**N(1)-Ni(1)-O(1)**	90.92(8)
Ni(1)-N(3)	1.8826(17)	**N(4)-Ni(1)-O(1)**	91.49(9)
Ni(1)-N(4)	1.9049(18)	**N(3)-Ni(1)-O(1)**	171.38(9)
Ni(2)-N(2)	1.8475(17)	**N(1)-Ni(1)-N(3)**	83.68(8)
Ni(2)-N(5)	1.9074(17)	**N(4)-Ni(1)-N(3)**	94.32(8)
Ni(2)-N(6)	1.9107(17)	**N(2)-Ni(2)-C(42)**	91.06(9)
Ni(1)-O(1)	1.858(2)	**N(6)-Ni(2)-C(42)**	91.78(9)
Ni(2)-C(42)	1.847(2)	**N(5)-Ni(2)-C(42)**	173.18(9)
C(42)-O(1)	1.227(3)	**N(5)-Ni(2)-N(6)**	94.21(7)
Ni(1)···Ni(2)	3.8777(5) Å	**N(2)-Ni(2)-N(5)**	83.01(7)
		Ni(2)-C(42)-O(1)	135.15(19)
		Ni(1)-O(1)-C(42)	136.11(18)

Overall, the molecular structure of **10**^{H} resembles the one of the analogue N_2 complex **4**^{N_2}. Since in both structures the atoms C, N, O located in the bimetallic cleft only differ slightly in their electron count, they are hard to distinguish with X-ray diffraction methods. Additionally, the determined molecular structure provides no clear evidence for the H atom connected to the carbon in the bridging formyl unit. However, the C–O bond distance in **10**^{H} is significantly longer than the N–N bond in **4**^{N_2} [d(C–O) = 1.227(3) Å vs. d(N–N) = 1.106(3) Å]. This results in smaller angles between the nickel ions and the bound formyl unit, when compared to the corresponding angles spanned by the nickel ions and the N_2 moiety in **4**^{N_2} [∡(Ni–C–O) = 135.15(19)°; ∡(Ni–O–C) =

136.11(18)° vs. ∡(Ni–N–N) = 139.3(3)°, 140.6(3)°]. Important structural parameters of **10^H** are summarized in Table 5.

In conclusion, the bridging *μ-η^1,η^1*-[HC=O] in **10^H** is best described as a negatively charged formylate bound to one nickel ion *via* a Ni–C σ-bond and *via* a dative interaction of the free electron pair of the oxygen with the remaining Ni^{II}. The bond between the carbon and the oxygen atom can be classified as a double bond. The bond distance is very similar to that of free aldehydes, probably due to the bond elongating, electron donating effect of the metal-carbon bond and the bond shortening effect of the oxygen Ni^{II} Lewis acid interaction which cancel each other out in a push-pull effect. Usually formyl transition metal complexes tend to be unstable since the reaction to isomeric metal hydride carbonyl complexes is thermodynamically favored. However, it has been shown that it is possible to stabilize them *via* Lewis acid interactions on the formyl O atom.[96] This is the case for **10^H** as the second Ni^{II} ion serves as a Lewis acid on the formyl unit. This is the first time a formyl nickel complex was isolated and structurally characterized.

5.2.2 Mechanistic Studies of the CO Activation

As already described, applying the conditions for the generation of the radical complex **4^{N_2}** to **2-K** under CO atmosphere resulted in the formylation of the bimetallic cavity in the [LNi_2] complex motive to give the diamagnetic complex **10^H**. Since N_2 and CO are isoelectronic a different reaction outcome was unexpected and raised the question of the origin of the H atom in the formyl unit in **10^H**.

The reaction scheme displayed in Figure 46 suggests the possibility of an elimination of only one equivalent of dihydrogen after the protonation of a nickel bound hydrido ligand and the subsequent insertion of CO into the remaining nickel hydride bond. For this mechanism to occur the intermediate formation of dinickel monohydride complex **7** which was previously suggested as an intermediate for the reaction to **4^{N_2}** in Scheme 13 is required. However, there are only few examples in literature for the direct insertion of CO into a metal hydride.[97] This process is thermodynamically unfavorable, since formyl complexes of transition metals usually tend to revert back to carbonyl hydride complexes. However, it is possible to stabilize formyl transition metal complexes *via* a Lewis acid interaction with the formyl O atom as it is the case in the bimetallic cleft of **10^H** where one Ni^{II} ion binds the formyl unit *via* a Ni–C bond and the second Ni^{II} coordinates the formyl O atom *via* a Lewis acid interaction.[96] Experimental evidence for the exclusion of this mechanism was provided by labeling experiments. Using **2-K-d_2** for the reaction did not result in a deuterium formyl complex **10^H-d_1**. Furthermore, exposing a solution of **4^{N_2}** in THF or toluene to a CO atmosphere overnight also resulted in the same reaction outcome and led to the formation of **10^H**. This suggested that the mechanism for the generation of **10^H** was essentially the same as for **4^{N_2}** and that the initially formed radical CO complex **4^{CO}** reacted with an H atom subsequently. To further investigate the possible existence of the intermediate **4^{CO}** the reaction was monitored using an *in situ* EPR experiment. The analysis started with an EPR measurement of the starting material **4^{N_2}** in a frozen THF solution at 146 K. The nitrogen atmosphere in the sample tube then was exchanged with dried CO gas and the frozen solution was warmed to -78 °C. Upon thawing a slight color change from dark brown to light brown was observed within one min. The reaction was kept at -78 °C for about 5 min to ensure completion and then, again frozen at -196 °C. The reaction mixture was measured at 148 K.

The X-band EPR spectrum of **4**^{N_2} showed a rhombic signal centered around g = 2.073. The higher g-value compared to the g-value of a free electron (g_e = 2.0023) indicates a significant nickel contribution to the S = ½ spin system. The signal appears to be rather broad, probably due to the delocalization of the spin density over the bridging N_2 unit and both nickel centers. The unresolved hyperfine coupling due to the N_2 and six ligand nitrogen atoms potentially causes the signal broadening. The EPR spectrum of the reaction mixture of **4**^{N_2} and CO shows a signal set significantly different from the one found in the starting material. The lower g value of 2.057 and the lower g anisotropy of the signal pattern potentially indicate a less delocalized spin density compared to **4**^{N_2}. This is expected for **4**$^{\mathbf{CO}}$, since the CO ligand, unlike N_2 has a dipole momentum. As a result, the π* molecular orbital has a larger probability density at the carbon atom than at the oxygen atom and upon reduction the single electron is mostly localized on the carbon atom. Unfortunately, it was not possible to simulate the EPR spectrum of **4**$^{\mathbf{CO}}$ since the reaction outcome was not clean affording signals from multiple species in the measured spectrum and therefore the overall g-values are estimated by the central zero crossing of the signal line. However, repeating the above described experiment with ^{13}CO showed a partial signal splitting in the EPR spectrum as it would be expected for the hyperfine coupling to a *S* = ½ nucleus like ^{13}C (Figure 50). This clearly indicates a paramagnetic species which is somehow involved with the presence of CO and consequently highlighted the possibility of an intermediate radical dinickel CO complex. Thus, the assumed mechanism for the formation for **10**$^{\mathbf{H}}$ is first the reaction of **2-K** to **4**^{N_2}, or if N_2 is absent the initial formation of intermediate **7** which was already proposed for the formation of **4**^{N_2} and a subsequent ligand substitution with CO. The mechanistic pathways are displayed in Scheme 17.

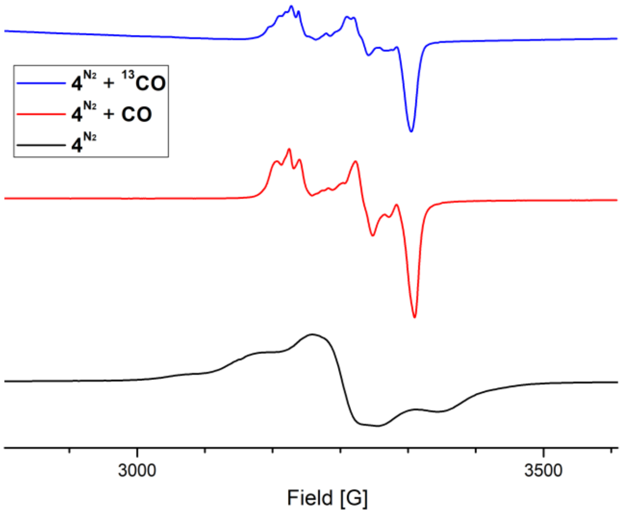

Figure 50: Stacked X-band EPR spectra (9.45 GHz; microwave power 10 mW) of **4**^{N_2} in THF at 146 K (black line), the reaction mixture of **4**^{N_2} and CO in THF at 148 K (red line) and the reaction mixture of **4**^{N_2} and CO in THF at 148 K (blue line).

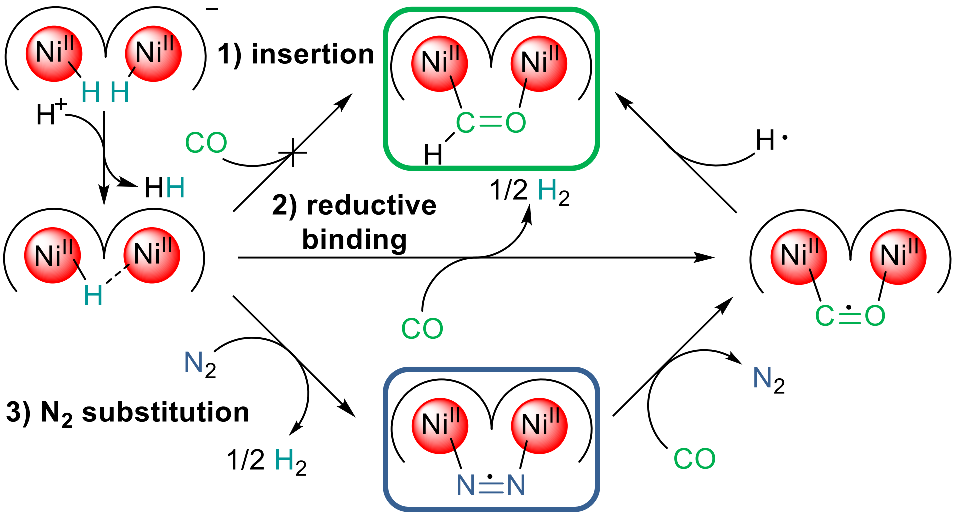

Scheme 17: Possible mechanistic pathways for the formation of **10^H**. 1) Insertion of CO into the Ni–H bond has been excluded; 2) Reductive binding of the CO coupled to the evolution of H_2, if N_2 is not present; 3) Substitution of N_2, when **2-K** was protonated under N_2 atmosphere.

As mentioned previously, **4^{CO}** could not be isolated due to the possibility of a more localized single e^- of the radical compound compared to the isolatable and isoelectronic **4^{N_2}**. The delocalization of spin density in **4^{N_2}** over the two nitrogen atoms and both nickel centers lowers the single occupied molecular orbital (SOMO) in energy, thus has a stabilizing effect. Since the delocalization is less prominent in **4^{CO}**, the SOMO is higher in energy, which results in an increased reactivity for the complex. The radical compound abstracts an H atom and forms the thermodynamically preferred C–H bond. The driving force for this reaction was reflected by failed attempts to perform the back reaction by generating **4^{CO}** out of the formyl complex **10^H**. Even by applying H atom abstractors such as TEMPO or the 2,4,6-tri-*tert*-butylphenoxy radical the C–H bond of the formyl unit stayed intact.

Since the reaction was performed in either toluene or THF, which are known to have relative small BDEs for their C–H bonds [BDE($PhCH_2$–H) = 370 KJ/mol; BDE(THF) = 385 KJ/mol][122],[123] that are comparable to the BDE of the formyl unit analogue formaldehyde [BDE(OHC–H) = 370 KJ/mol],[124] it was plausible that the solvent was the source of the H atom. However, *in situ* NMR experiments in toluene-d_8 still showed the characteristic proton signal of the formyl unit at 7.38 ppm. Consequently, it seemed unlikely that solvent molecules provide the H atom for the generation of **10^H**. The origin of the H atom remains unclear. It is possible that impurities in the applied CO gas are the source of H-atoms, since the reaction showed no clean conversion. Despite drying of the gas, a significant amount of **3** was still present in the ^{1}H NMR spectra of the crude reaction mixture. Another possibility was an intramolecular H atom transfer, since the C–H bond of the benzylic isopropyl group of the β-diketiminate unit of the ligand should have a lower BDE than toluene. Additionally, the isopropyl group is found in close proximity to the CO carbon atom(d(C–C) = 3.7114(30) Å), which increases the chance of an intramolecular H atom transfer. However, it was not possible to track a deuterium exchange in deuterated solvent by ^{1}H NMR, since the signals for the secondary protons of the isopropyl groups were partially covered by proton signals of the reaction side products.

5.2.3 Hydride Addition to the Dinickel Formyl Complex 10^H

As described above, the bond situation of the formylate found in **10^H** was determined to be consistent with a σ-bond between the Ni^{II} and the carbon and, additionally a dative interaction between the free electron pair of the oxygen and the other Ni^{II}. In an attempt to hydrogenate the formyl moiety within the bimetallic cleft one atmosphere of hydrogen was applied to a THF solution of **10^H**. However, the ^1H NMR spectrum showed no difference in signal pattern from the starting material. To increase the driving force of the proton coupled reduction the utilization of the hydride donor reagent $KHBEt_3$ was explored.

For this experiment one equivalent of a THF solution of $KHBEt_3$ (1 mol/L) was added to a THF-d_8 solution of **10^H**. The reaction was monitored by ^1H NMR spectroscopy. Initially, the changes in the ^1H NMR spectrum were only minor. However, a second proton signal at 6.65 ppm emerged in the region where signals for the proton of the pyrazolate unit of **L** are expected. This indicated a clean conversion of **10^H** to a new species. The reaction proved to be rather slow, as the starting material was only consumed after 72 h. Since the new species featured two singlets for either the α-protons of the β-diketiminate units and the methylene bridges of the ligand, the C_s symmetry of **10^H** was retained. However, while the proton signal of the formylate unit at 7.38 ppm decreased, a new signal at 2.31 ppm with a relative integral of two protons emerged (Figure 51). It seemed probable that this proton signal indicated a bridging alcoholate formed by a nucleophilic attack of the hydride on the carbon atom of the bridging formylate unit. The slow reaction progress was probably caused by a combination of the steric shielding of the diisopropyl aryls flanking the bimetallic binding pocket and the negative polarization of the nickel bound carbon atom (Figure 52).

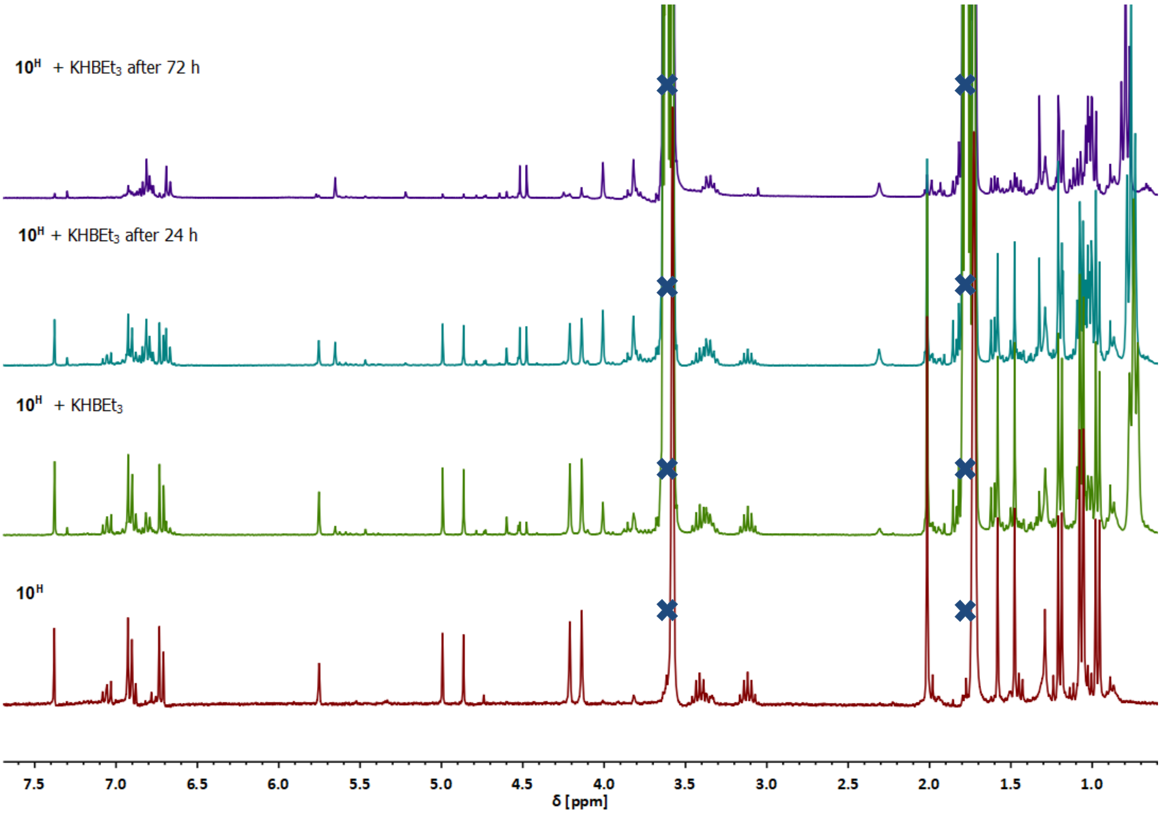

Figure 51: Stacked ^1H NMR (300.31 MHz) spectra of **10^H** (red line) and the reaction of **10^H** with $KHBEt_3$ initially (green line), after 24 h (cyan line), and after 72 h (purple line) in THF-d_8. Solvent signals are marked with a blue cross.

The low yield of **10^{H}** (13 %) made it difficult to isolate the reaction product **11-K** in decent amounts for further analysis. However, in the following part a different synthetic approach for **11-K** is presented, which avoids these issues.

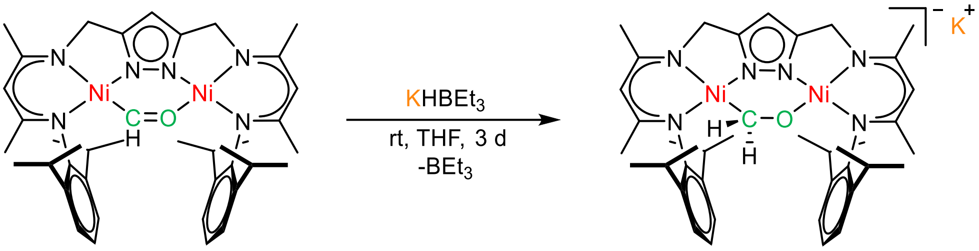

10^{H}

11-K

Figure 52: Synthesis of **11-K** by hydride donation to **10^{H}**.

5.2.4 Reductive Binding of Formaldehyde to the Dinickel Moiety

As described previously, it was not possible to execute the synthesis of **11-K** from **10^{H}** on a larger scale, since the reaction of **2-K** or **4^{N_2}** to the starting material **10^{H}** afforded low yields. A possible way to produce **11-K** in larger amounts was avoiding the protonation/hydride abstraction of **2-K**, which caused the low yields by using formaldehyde as a reagent where the carbon atom has a lower oxidation state.

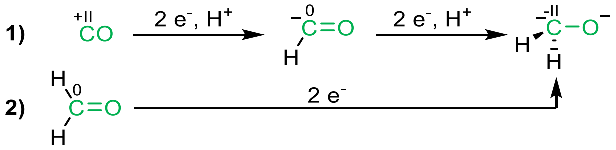

Scheme 18: Different approaches for the synthesis of the alcoholate bridge in **11-K** starting from CO (1) or from formaldehyde (2).

To a solution of **2-K** in THF, a suspension of three equivalents of paraformaldehyde in THF was slowly added resulting in a color change from orange to dark brown accompanied by a vigorous evolution of gas. The reaction mixture was stirred overnight to ensure a complete conversion. Slow diffusion of hexane into the filtered reaction mixture gave crystalline material of **11-K** in a yield of 56 %. The complex was well soluble in THF and slightly soluble in hexane.

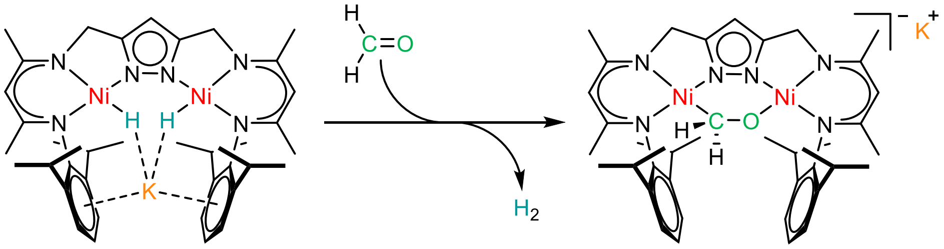

2-K

11-K

Figure 53: Reaction of **2-K** with formaldehyde to **11-K**.

The ^{1}H NMR spectrum of **11-K** provided evidence that it was the same reaction product as in the conversion of **10^{H}** with $KHBEt_3$, since both spectra featured similar proton shifts and relative signal intensities. As already outlined, the C_s symmetry of the σ‖xy-type was evident from the two singlets found for the α-protons of the β-diketiminate units. The mirror plane of the complex exists along the coordination plane, as indicated by the two singlets found for the CH_2 bridges between the β-diketiminate units and the pyrazolate. There is no proton signal resembling the chemical shift of an aldehyde unit [δ(formaldehyde) = 9.58],[125] but instead a broad singlet at 2.31 ppm with a relative integral of two (Figure 54). The signal broadening of the singlet at 2.31 ppm suggests a dynamic process with a slow exchange rate on the NMR timescale at room temperature.

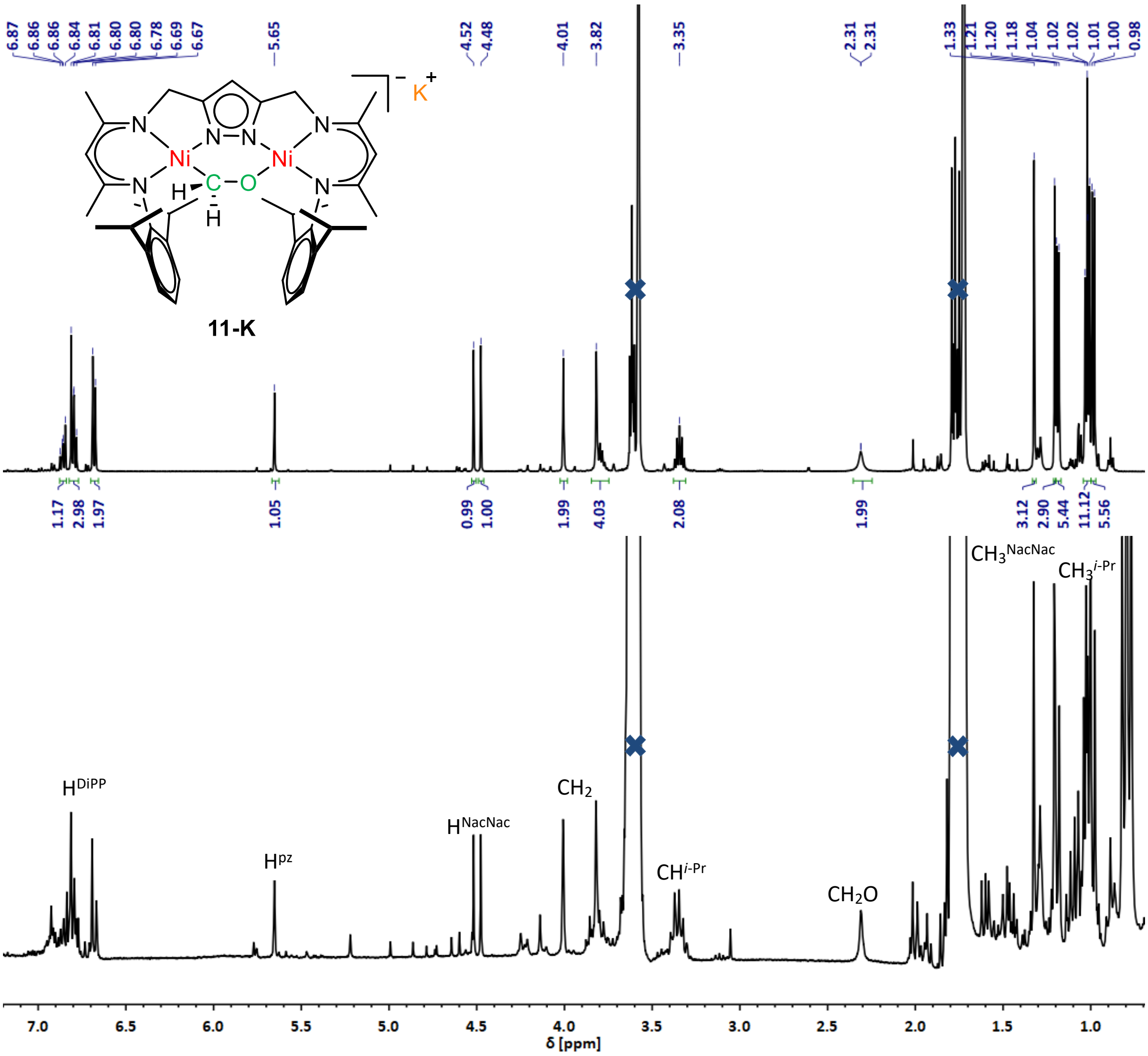

Figure 54: Stacked ^1H NMR (300.13 MHz) spectra of **11-K**, synthesized by the conversion of **10^H** with $KHBEt_3$ (bottom) and by the reaction of **2-K** with formaldehyde (top) in THF-d_8. Solvent signals are marked with a blue cross.

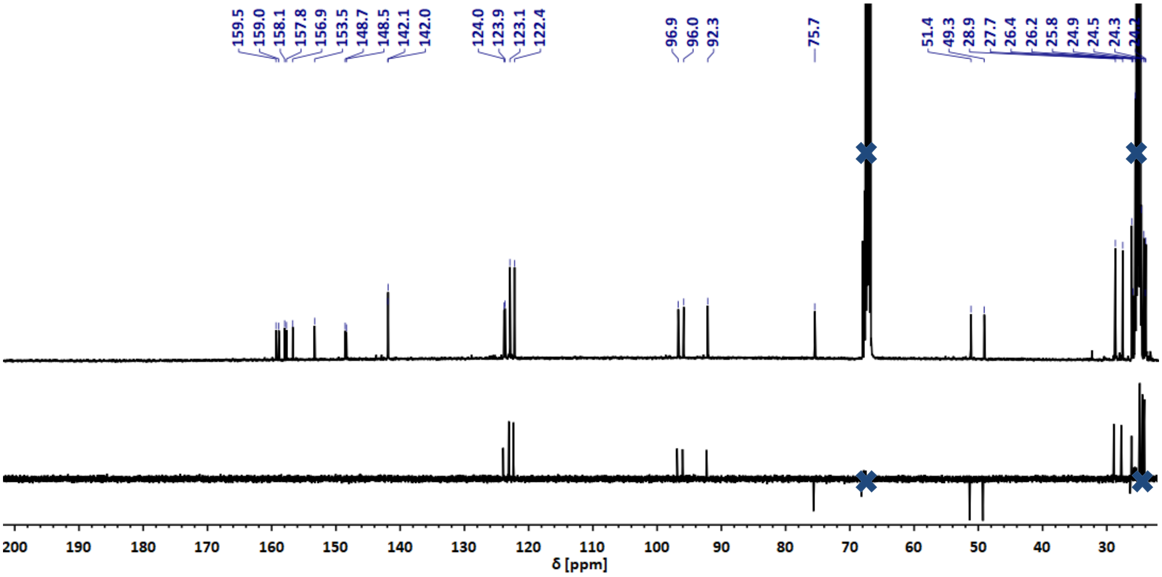

Figure 55: ^{13}C-DEPT NMR (100.64 MHz) spectrum of **11-K** (bottom) and ^{13}C NMR (100.64 MHz) of **11-K** (top) in THF-d_8. Solvent signals are marked with a blue cross.

The ^{13}C NMR spectrum shows no resonances in the region around the low field shifted signal at 275.8 ppm, which was assigned to the formylate group in the ^{13}C NMR spectrum of **10^{H}** nor a signal, which would be characteristic for a carbonyl group as found in formaldehyde [δ(formaldehyde) = 194 ppm].[125] A ^{13}C-DEPT experiment reveals three signals with a negative phase and therefore indicates carbon nuclei of three different CH_2 groups in the compound. ^{13}C shifts at 51.4 ppm and 49.3 ppm are identified as resonances of carbons in the methylene groups bridging the pyrazolate and the β-diketiminate units. An ^{1}H,^{13}C-HSQC spectrum shows that the ^{13}C signal at 75.7 ppm correlates to the proton signal at 2.31 ppm, which supports the assumption that the proton signal belongs to a nickel bound CH_2O moiety. Since the proton signal has a shift in a region where C-bound protons of alcohol functions are found, the spectral data supports the hypothesis that the product of the reaction between **10^{H}** and $KHBEt_3$, indeed bears a twice deprotonated alcohol in the dinickel binding site.

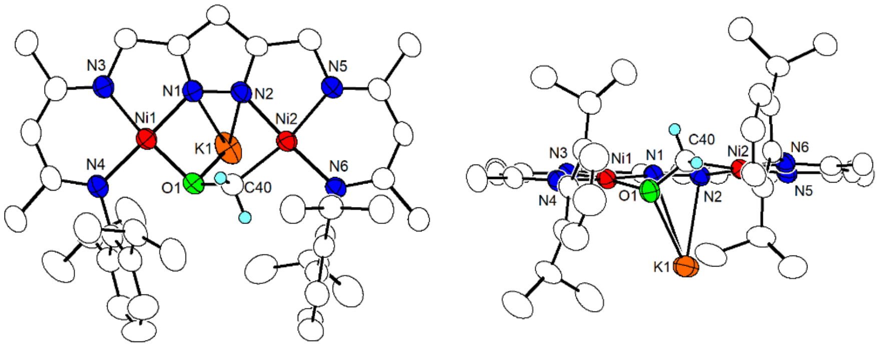

Figure 56: Top view of the molecular structure of **11-K** (left) and front view of the molecular structure of **11-K**. Solvent molecules and hydrogen atoms, except the H substituted on the bridging oxymethylene ligand, are omitted for clarity.

X-ray diffraction analysis of single crystals reveals that of **11-K** crystallizes in the monoclinic space group P 2_1/n; the molecular structure is shown in Figure 56. The sum of the angles of the Ni atom with the surrounding ligands are 360.18° and 359.96° for Ni(1) and Ni(2), respectively, confirming the presence of a square planar coordination environment. The dianionic CH_2O bridge found in the bimetallic cleft of the complex is bent out of the coordination plane. While the CH_2 unit is located above the plane, the oxygen is found on the opposite side underneath. This is reflected by a torsion angle of 84.72(23)° for θ(Ni(1)-O(1)-C(40)-Ni(2)). The C–O bond of the CH_2O unit of 1.397(4) Å is significantly longer than the analogue bond in **10^H** [1.227(3) Å] and thus shows a higher degree of reduction. The Ni–O distance of 1.828(2) Å is slightly shorter than the equivalent bond in **10^H** due to the ionic character of the oxygen atom in **11-K**. This is probably caused by the negative charge located at the O atom in **11-K** in contrast to the neutral O atom in **10^H**. The effect is probably extenuated by the K^+ coordinating to the oxygen with a K···O distance of 2.672(2) Å, compensating the negative charge. The sp^3 hybridization of the C atom in **11-K** results in an elongation for the Ni–C bond from 1.847(2) Å for the sp^2 hybridized C atom **10^H** to 1.974(3) Å. Thus, the Ni–C bond length in **11-K** mostly resembles the one found in **6** with 1.997 Å. Finally, the C–O distance measures 1.397(4) Å, which is an elongation of 0.17 Å compared to the respective bond of **10^H** with 1.227(3) Å. Therefore, the C–O bond within the $[CH_2O]^{2-}$ unit can be viewed as a single bond. This is in good agreement with the NMR data, which indicates a twice deprotonated alcohol function bound to the metal sites. The reduced formaldehyde unit can be described as an oxymethylene ligand, bridging two nickel centers, forming a six membered diazadinickeloxy cycle. Structural parameters for **11-K** are shown in Table 6.

Table 6: Selected bond lengths [Å] and angles [°] for **11-K**.

Bond Lengths [Å]		Bond Angles [°]	
Ni(1)-N(1)	1.855(2)	**N(1)-Ni(1)-O(1)**	89.50(10)
Ni(1)-N(3)	1.883(3)	**N(4)-Ni(1)-O(1)**	92.08(10)
Ni(1)-N(4)	1.898(3)	**N(3)-Ni(1)-O(1)**	170.50(10)
Ni(2)-N(2)	1.878(3)	**N(1)-Ni(1)-N(3)**	83.73(11)
Ni(2)-N(5)	1.976(2)	**N(4)-Ni(1)-N(3)**	94.87(11)
Ni(2)-N(6)	1.906(2)	**N(2)-Ni(2)-C(40)**	87.36(12)
Ni(1)-O(1)	1.838(2)	**N(6)-Ni(2)-C(40)**	96.11(12)
Ni(2)-C(40)	1.974(3)	**N(5)-Ni(2)-C(40)**	168.34(12)
C(40)-O(1)	1.397(4)	**N(5)-Ni(2)-N(6)**	94.32(10)
Ni(1)···Ni(2)	3.9282(6)	**N(2)-Ni(2)-N(5)**	82.17(10)
K(1)···O(1)	2.672(2)	**Ni(2)-C(40)-O(1)**	118.4(2)
K(1)···N(1)	3.179(3)	**Ni(1)-O(1)-C(40)**	118.52(19)
K(1)···N(2)	3.000(3)	**Ni(1)-O(1)-C(40)-Ni(2)**	84.72(23)

The reaction of **2-K** with formaldehyde to **11-K** is best described as a twofold reduced formaldehyde activation accompanied by a reductive elimination of dihydrogen, as it is shown in Figure 53.

Addition of [2.2.2]cryptand to solution of **2-K** before adding paraformaldehyde addition resulted in the formation of **11-cK**. Slow diffusion of hexane into a THF solution of the complex yielded light brown needles. Since **11-cK** showed significantly worse solubility, especially in hexane, the yield of the reaction was increased from 56 % to 75 % compared to **11-K**.

While the main features of the ^1H NMR spectrum of **11-cK** resemble the ones of the spectrum of **11-K**, the signals generally appear to be shifted to higher field. This is probably a result of the cryptand suppressing the cation interaction by encapsulating the K^+ and thus deshielding the complex. Additional proton signals for the potassium [2.2.2]cryptate are found as a singlet at 3.64 ppm and two multiplets at 3.59 ppm and 2.57 ppm. The proton signal at 2.19 ppm originating from the CH_2 group of the oxymethylene unit is better resolved and narrower. While the K^+ coordinating the oxymethylene unit probably causes an increased energetic barrier for the ring flip of the six membered diazadinickeloxy cycle in **11-K**, the abstraction of the K^+ with [2.2.2]cryptand includes a faster ring flip dynamic (Figure 57).

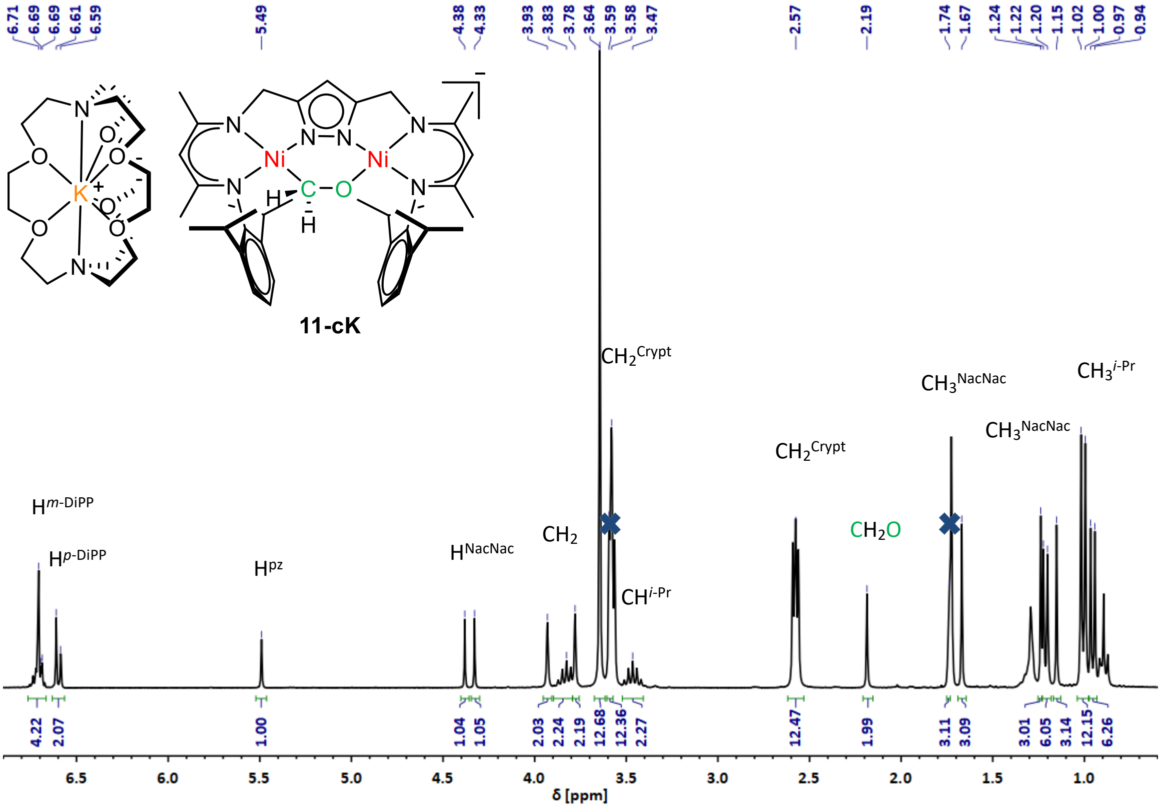

Figure 57: ^1H NMR (400.25 MHz) spectrum of **11-cK** in THF-d_8. Solvent signals are marked by blue cross.

5.2.5 Hydride Transfer Reactivity of 2-K towards Formaldehyde in Benzene

An interesting observation of the reaction of **2-K** with formaldehyde was made, when benzene instead of THF was used as a solvent. The addition of three equivalents of paraformaldehyde to a solution of **2-K** in benzene resulted in a color change from orange to green instead of brown, as it was observed for a THF. Additionally, there was no gas evolution observed, which usually indicated the loss of hydrogen in **2-K** upon exposure to substrates. The ^1H NMR of the solution suggests a compound with C_s symmetry of the σ⊥xy-type, where the mirror plane is orthogonal to the coordination plane of the nickel centers, similar to **8-K**, indicating that the reaction product was different from **11-K**. The most prominent signals in the ^1H NMR are a doublet at 2.77 ppm with a coupling constant of 1.6 Hz and an integral of six relative to the proton of the pyrazolate unit of the ligand, as well as a low field shifted resonance at 12.19 ppm with a poorly resolved septet pattern with an integral of one. A ^1H,^1H-COSY experiment confirms the correlation between both signals. Interestingly, the ^{1}H,^{13}C-HSQC correlation spectrum shows no ^1J coupling to a carbon nucleus for the septet at 12.19 ppm. This and the large low field shift suggested the proton to be bound to a hetero atom.

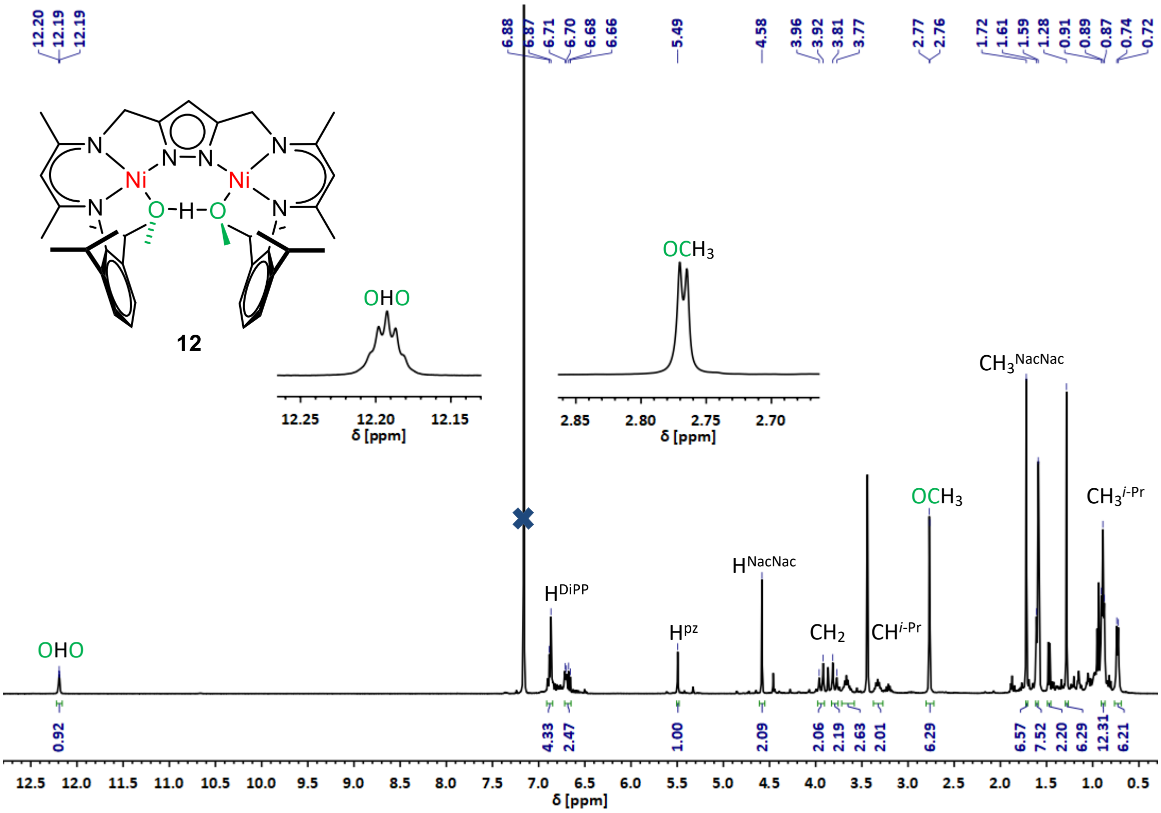

Figure 58: ^{1}H NMR of **12** in benzene-d$_6$.

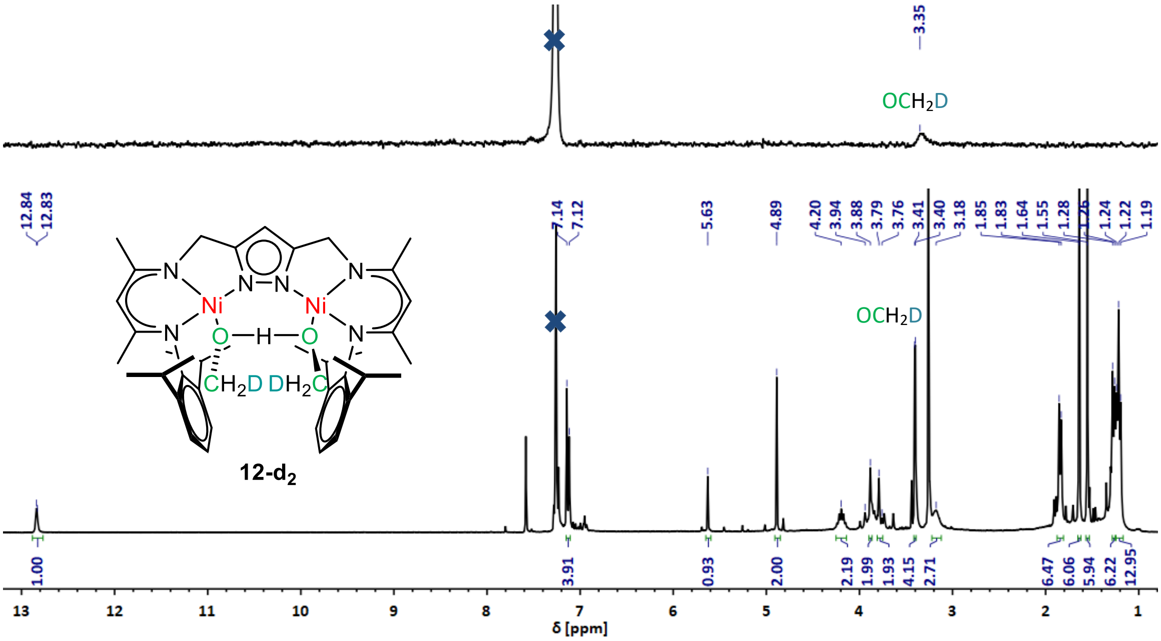

Figure 59: ^{1}H NMR spectra of **12-d$_2$** in benzene-d$_6$ (bottom) and ^{2}H NMR spectrum of **12-d$_2$** in benzene.

To further investigate the reaction, a benzene solution of the deuterium labeled hydride complex **2-K-d$_2$** was reacted with formaldehyde in an *in situ* NMR experiment. The ^{1}NMR spectrum showed proton signals shifted probably due to impurities in solution. However, the overall signal pattern remained the same. Interestingly, the doublet at 3.41 ppm coupling to the low field shifted septet showed a decreased integral from six to four in comparison to the corresponding signal found in the ^{1}H NMR spectrum of **12**. To identify the fate of the deuterides of **2-K-d$_2$** a ^{2}H NMR experiment was performed. Besides the signal for benzene the spectrum shows a single broad resonance at 3.35 ppm, which is in the range of the doublet at 3.41 ppm in the ^{1}H NMR spectrum of **12**. Unfortunately, it was not possible to determine coupling constants between the protons and the deuterium, due to signal broadening. The similar shift and the decreased integral both suggest that the two hydrogen atoms were substituted by two deuterium atoms originating from **2-K** (Figure 59).

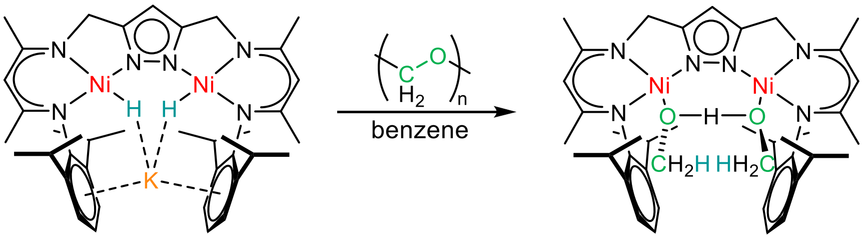

2-K **12**

Figure 60: Reaction of **2-K** with paraformaldehyde in benzene. Both hydrido ligands of **2-K** behave as nucleophiles by attacking the carbon atoms of formaldehyde which lead to the reduction to methanolate observed in **12**.

This concluded that in the reaction with paraformaldehyde in benzene, **2-K** did not reductively eliminate H_2 as it was usually observed in the presence of electrophilic substrates like formaldehyde in THF. Instead an insertion of two formaldehyde into the Ni–H bonds is observed forming two methanolate units. Both methanolates coordinate the nickel ions and bind to an additional proton (Figure 60). Layering a solution of **12** in THF with hexane yielded green single crystals suitable for X-ray diffraction analysis. The molecular structure is displayed in Figure 61.

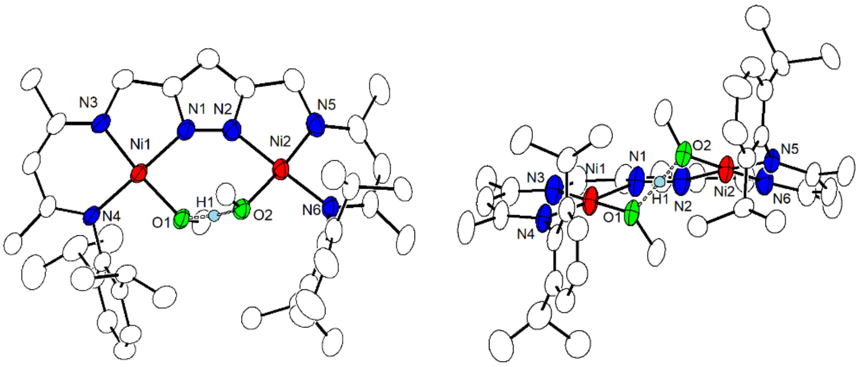

Figure 61: Top (left) and front (right) view of the molecular structure of **12**. Solvent molecules and hydrogen atoms, except the H coordinated by the methanolate ligands, are omitted for clarity.

12 crystallizes in the triclinic unit space group P $\overline{1}$ with a large nickel-nickel distance of 4.2490(6) Å. Both metal centers are found in a distorted square planar geometry. Their coordination planes are twisted away from each other, in order to evade the steric demand of the two methanolate ions bound to the bimetallic cleft. The bond distance between the metal centers and the methanolate oxygens of 1.8739(18) Å and 1.8812(19) Å are longer than the one for the Ni–O bond in **11-K** with 1.838(2) Å. The C–O bonds in the methanolate ligands are in range of the usual bond length found for free methanol [d(C–O) = 1.427(4) Å; 1.416(4) Å vs. 1.42 Å].[126] To compensate the negative charge of the neighboring methanolate ions, a proton is incorporated between them. The distance between the oxygen atoms is 2.4005(34) Å. This is comparable to the O···O distance of reported bimetallic nickel(II) complexes with a OHO bridge between the metal ions [d(O···O]) = 2.432][127] and results in a significant steric demand. Considering the large oxygen-oxygen distance and the torsion angle between the nickel centers and both oxygen atoms [θ(Ni(1)-O(1)-O(2)-Ni(2)) = 86.254(125) Å] the alignment of the separate nickel coordination planes is found to be highly perturbed. The methanolate methyl groups are directed away from the binding pocket, reaching in opposite directions. As a result, **12** is found to have C_2 symmetry instead of σ⊥xy-type C_s symmetry, which is also consistent with the ^{1}H NMR data. As the structure appears to be significantly different from the C_{2V} symmetric molecular structure of the hydroxide analogue complex **3**,[19] the question arises why one methanol was not eliminated from **12** to form a complex similar in geometry to **3**. The reason is probably found in the steric demand of the methanolate methyl group. While the flanking aryls of the organic ligand prohibit the methyl group to reach into the space between them, perturbation of the parallel coordination planes of the nickel ions leads to a misalignment of the aryl groups. This widens the pocket and allows the coordination of two methanolates. By bending their methyl groups away from the flanking aryl groups into the unoccupied space above and underneath them, they evade the steric pressure effectively.

Table 7: Selected bond lengths [Å] and angles [°] for **12**.

Bond Lengths [Å]		Bond Angles [°]	
Ni(1)-N(1)	1.905(3)	**N(1)-Ni(1)-O(1)**	90.34(10)
Ni(1)-N(3)	1.866(2)	**N(4)-Ni(1)-O(1)**	90.60(9)
Ni(1)-N(4)	1.896(3)	**N(3)-Ni(1)-O(1)**	174.13(10)
Ni(2)-N(2)	1.906(3)	**N(1)-Ni(1)-N(3)**	84.39(11)
Ni(2)-N(5)	1.861(2)	**N(4)-Ni(1)-N(3)**	94.75(11)
Ni(2)-N(6)	1.891(2)	**N(2)-Ni(2)-O(2)**	91.30(9)
Ni(1)-O(1)	1.8739(18)	**N(6)-Ni(2)-O(2)**	91.05(9)
Ni(2)-O(2)	1.8812(19)	**N(5)-Ni(2)-O(2)**	173.96(11)
O(1)-C(40)	1.427(4)	**N(5)-Ni(2)-N(6)**	94.32(10)
O(2)-C(41)	1.416(4)	**N(2)-Ni(2)-N(5)**	83.92(11)
O(1)-H(1)	1.2893(587)	**Ni(1)-O(1)-C(40)**	116.82(17)
O(2)-H(1)	1.1142(567)	**Ni(2)-O(2)-C(41)**	114.90(18)
Ni(1)···Ni(2)	4.2490(6)	**Ni(1)-O(1)-O(2)-Ni(2)**	86.254(125)

The origin of the proton between the methanolates remains unclear. Since the low-field shifted septet at 12.19 ppm/12.84 ppm was even observed in *insitu* ^{1}H NMR experiments in deuterated solvents it was unlikely that the solvent was the source. It is possible that it originates from trace impurities of water in the reagent paraformaldehyde, as a putative $[LNi_2(O(CH_3))_2]^-$ would likely be very basic.

Based on these experiments the truly remarkable observation is that the outcome of the reaction of **2-K** with formaldehyde can be controlled by the choice of solvent. The hydrogen evolution for the reductive binding of formaldehyde in THF indicates the formation of an intermediate Ni^INi^I complex, similar to other substrate activation reactions of **2-K**.[29] The Ni^INi^I complex then provides two electrons for the reduction of formaldehyde, binding it as an oxymethylene in the bimetallic cavity. In benzene there is no hydrogen evolution observed and **2-K** reacts with two equivalents of formaldehyde, *via* a 1,2-insertion of the substrate in the Ni–H bond. This requires the insertion of formaldehyde to be faster than the reductive hydrogen loss. The two different pathways can be affected by the change in solvent in two different ways. First, it is known that paraformaldehyde tends to form its monomer faster in nonpolar solvents.[128] This results in a higher concentration of formaldehyde in benzene which then reacts with **2-K** before the complex is able to release dihydrogen. Furthermore, the polar solvent THF is able to coordinate the K^+, which is then abstracted from the complex cavity. It was shown that the K^+ has a stabilizing effect on the dinickel dihydride moiety of **2-K**.[18] Consequently, the complex is more stable towards the reductive elimination of dihydrogen in a nonpolar solvent like benzene and might react with substrates before the H_2 release. As it will be shown later this change in solvent has no effect on benzaldehyde derivates and might be limited to small substrates, which are not prevented to enter the sterically crowded complex cavity. Interestingly, both reaction pathways resemble the reductive elimination (***re***) and the 1,2-insertion which corresponds to the hydride abstraction (***ha***) pathways discussed for the reaction of different methylation agents with **2-K** as shown in Scheme 19.

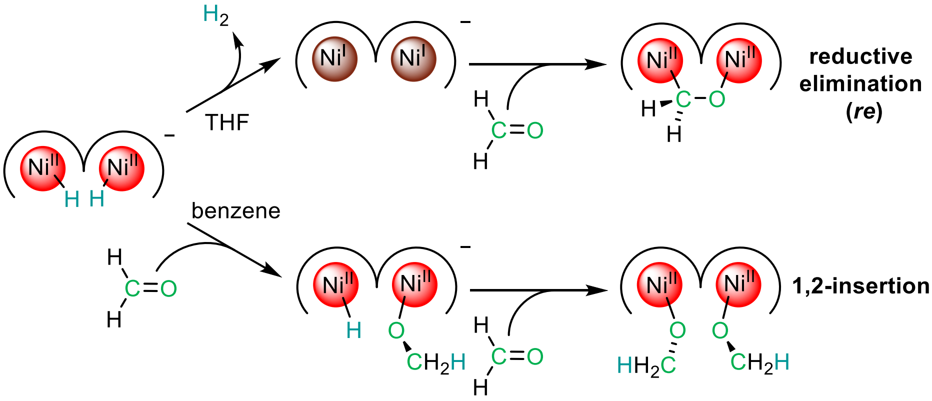

Scheme 19: Solvent dependent mechanistic pathways for the reaction of **2-K** with formaldehyde.

5.2.6 Oxidation of the oxymethylene unit in 11-K

To gain insight into the redox properties of **11-K**, the cyclic voltammogram of the compound was recorded in THF at room temperature using NBu_4PF_6 as electrolyte. Since ferrocene interfered with the redox processes of the complex, $Cp_2{}^*Fe$ was used as an internal standard and the spectrum was corrected to show potentials against ferrocene.[129] The CVs were recorded under inert conditions in a nitrogen atmosphere glove box.

The cyclic voltammogram displayed in Figure 62 shows three main redox processes between $E = -2.5$ V and $E = -0.3$ V. The first anodic process at $E_{1/2} = -1.40$ V is reversible. A second irreversible oxidation is observed at $E_{p,c} = -0.45$ V indicating a major structural change in the complex after being oxidized twice. The intensity of the reduction peak of the first oxidation at -1.47 V decreases in the event of a second reduction, as the wave for the irreversible reduction at $E_{p,a} = -2.31$ V increases. The small reversible wave at $E_{p,a} = -2.2$ V probably originates from impurities. The voltammogram suggested that it was possible to oxidize **11-K** twice, reverting the reaction of **10^H** with KHBEt$_3$.

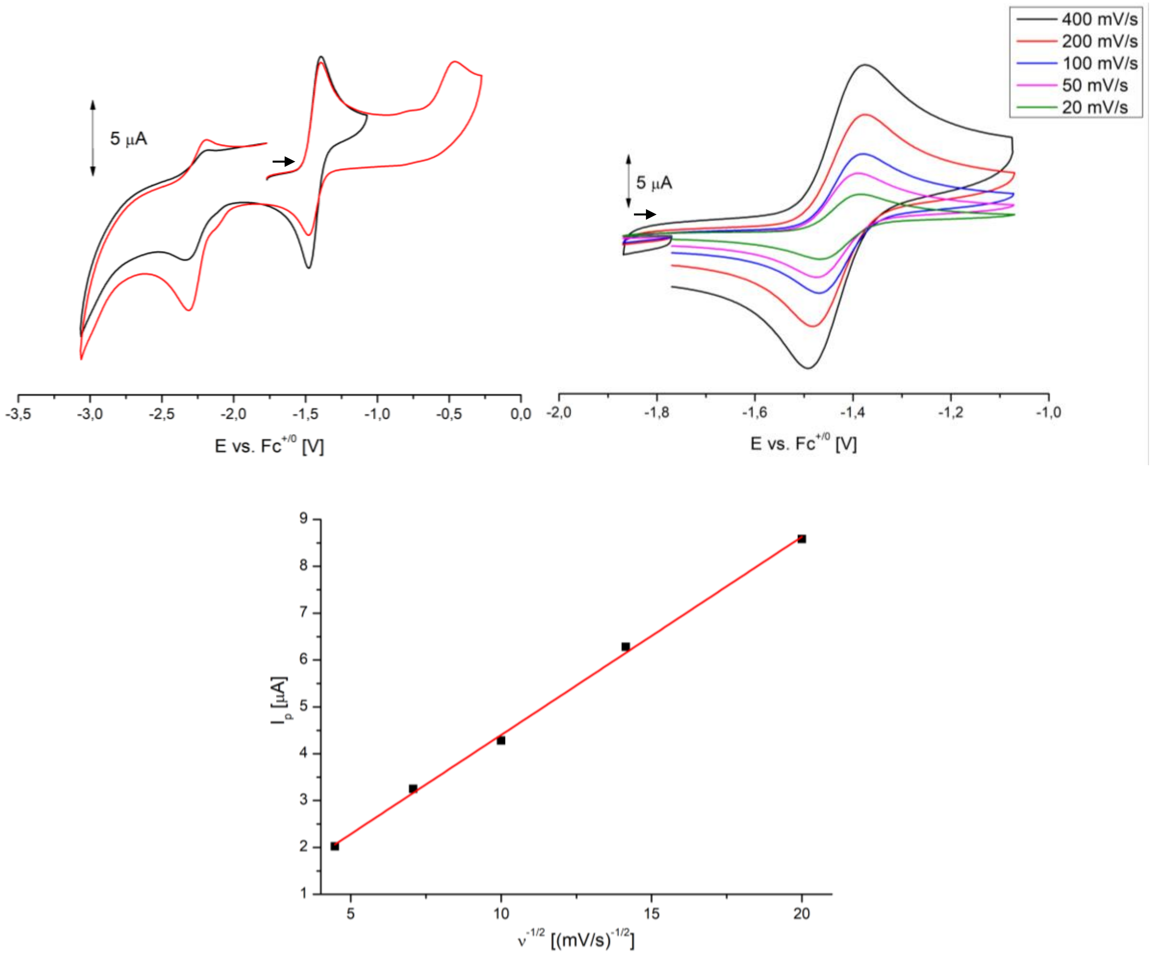

Figure 62: Cyclic voltammogram of **11-K** in THF (top, left), 0.1 M ^{n}Bu$_4$NPF$_6$ at 100 mVs^{-1} at 25 °C from -3.1 V to -1.1 V (black line) and from -3.1 V to -0.3 V (red line). The reversible wave around -1.43 V was measured at different scan rates (top, right). Intensity of the reversible oxidation plotted *vs*. the square root of the scan rate (bottom).

Since **11-K** was formed by the reaction of **10^H** with the hydride donor KHBEt$_3$, it seemed feasible to utilize a hydride abstractor reagent such as Ph$_3$CPF$_6$ to revert the reaction. Surprisingly, after 24 h the ^{1}H NMR of the reaction mixture showed paramagnetic signals resembling the ones of the dinitrogen radical complex **4^{N_2}**. This is probably a result of the preference of the tritylium to cleave Ni–C or Ni–O bond instead of the C–H bond of the oxymethylene unit bridging between the nickel centers. The mechanism behind the formation of **4^{N_2}** remains unclear.

To meet the requirements of a two electron oxidant and a base to abstract one proton and one K$^+$, DDQ was used for the successful reaction to **10^H**. In an ^{1}H NMR experiment the reaction between a solution of **11-K** and DDQ showed the formation of **10^H** indicated by the characteristic formyl proton signal (Figure 63).

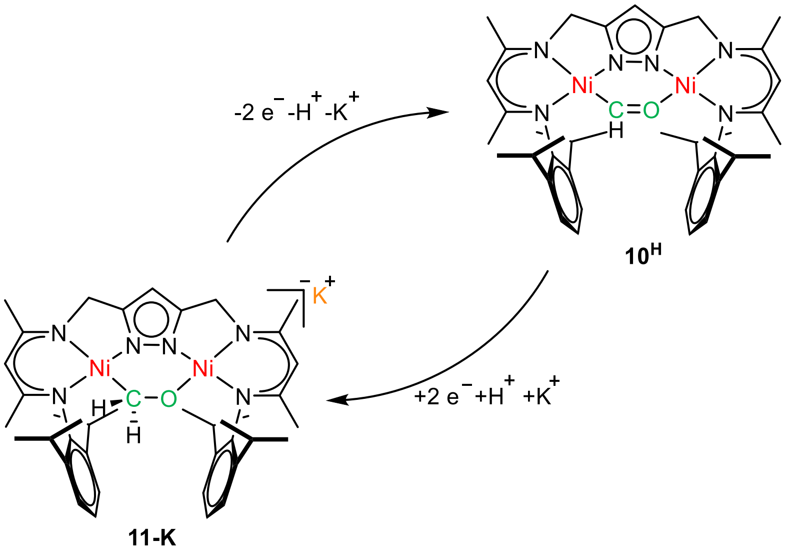
-2 e⁻ -H⁺ -K⁺
10H
+2 e⁻ +H⁺ +K⁺
11-K
K⁺
Ni
Ni
N
C
O
H

Figure 63: Oxidation of **11-K** to $\mathbf{10^H}$ and the reverse reduction.

5.2.7 Reductive Binding of Benzaldehyde

To further explore the reactivity of **2-K** towards carbonyl functional groups, additional substrates were tested. The substrate scope appeared to be rather limited, as acetone showed no reactivity towards **2-K**, probably due to steric shielding of the carbonyl function. **2-K** also proved to be inert towards the acetaldehyde trimer paraldehyde and monomeric acetaldehyde in DMF solution. However, the electronic effect of the phenyl substituent in benzaldehyde was expedient in a thermodynamic matter, as **2-K** showed a rapid reaction upon being exposed to the aryl aldehyde (Figure 64).

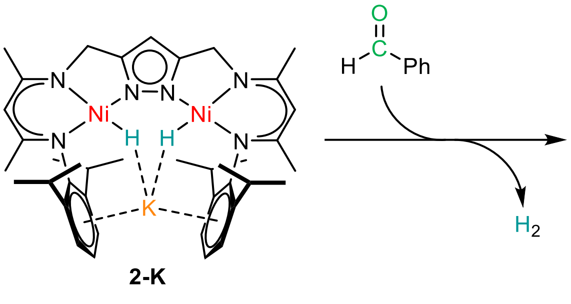

Figure 64: Reaction of **2-K** with benzaldehyde to **13-K**.

Adding one equivalent of dry benzaldehyde to a solution of **2-K** in THF or benzene led to a color change from orange to deep red, accompanied by vigorous hydrogen evolution. The reaction product is well soluble in THF and benzene and mostly insoluble in hexane.

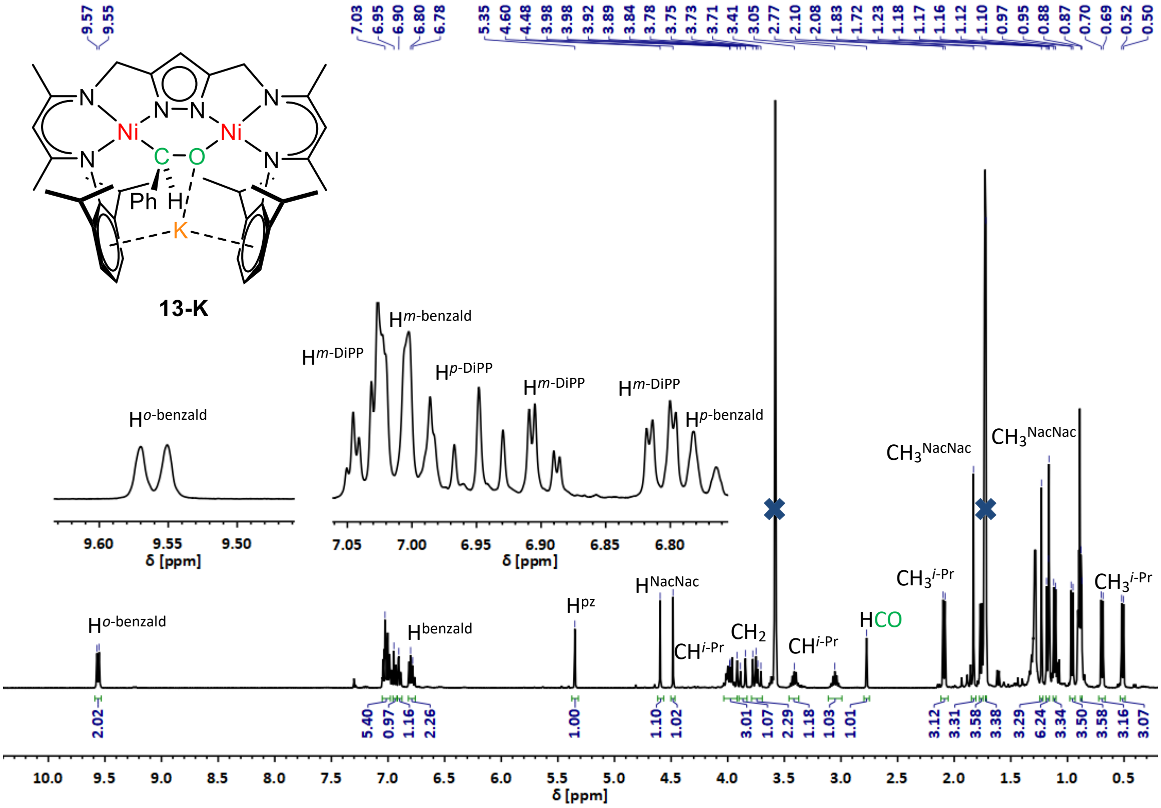

Figure 65: ^1H NMR spectrum (400.24 MHz) of **13-K** in THF-d_8. The inset shows the signals of the aryl protons. Solvent signals are marked by a blue cross.

The ^{1}H NMR spectrum shows shifts expected for a diamagnetic complex (Figure 65). For the α-protons of the β-diketiminate unit, two singlets at 4.60 ppm and 4.48 ppm are found indicating an unsymmetrical complex. However, the protons of the methylene units bridging the β-diketiminate units and the pyrazolate show a pronounced signal pattern caused by the inequality of all four protons overlapping with two septets of the secondary isopropyl group protons. The coupling constants around 17.7 Hz are indicative for ^{1}J couplings (Figure 66). According to the NMR spectroscopic data the symmetry of the complex is C_1.

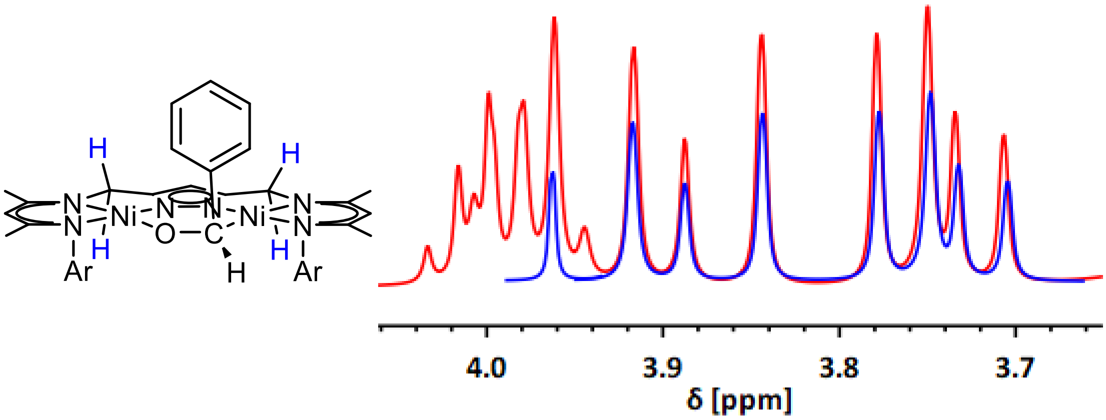

Figure 66: ^{1}H NMR spectrum (400.24 MHz) of the of the methylene groups bridging the pyrazolate and β-diketiminate units. The red line shows the original spectrum and the blue line shows the clean methylene group coupling pattern.

Most prominent is a far low field shifted doublet at 9.56 ppm. Since it showed a correlation to two protons of the isopropyl units in a $^{1}H,^{1}H$ NOESY experiment, it was assigned to the *ortho*-protons of the phenyl group. The noticeable low field may be explained by an anagostic interaction with the Ni^{II} ions. As the hydrogen atoms reach into the periphery of the low energetic d_{z^2} orbitals, the electron density is decreased through a C–H bond elongation, which results in a significant deshielding and consequently can be observed by a large low-field shift in the ^{1}H NMR spectrum.[130]

Another signal of interest is the resonance at 2.77 ppm, which has a relative integral of one and is not assigned to any protons of **L**$^{3-}$, but to the proton connected to the benzaldehyde carbonyl group. The large high field shift in comparison to the carbonyl group proton of benzaldehyde was a first indicator for a reductive activation of the substrate.

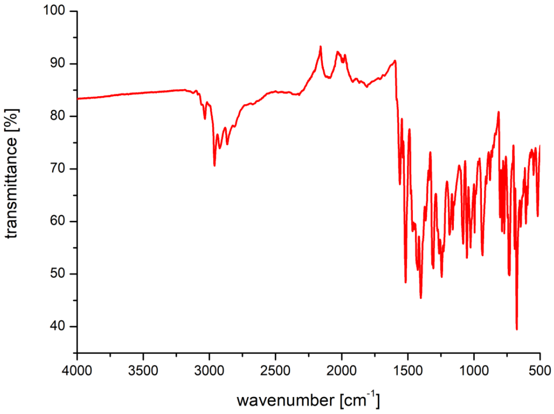

Figure 67: ATR-IR spectrum of **13-K** in solid state.

The IR spectrum of **13-K** shows no band indicative for a C=O unit in the region between 1760 cm^{-1} and 1640 cm^{-1}.[131] This suggests a significant degree of reduction in the double bond, as the band is most likely shifted to lower wavenumbers, where it is covered by other bands (Figure 67).

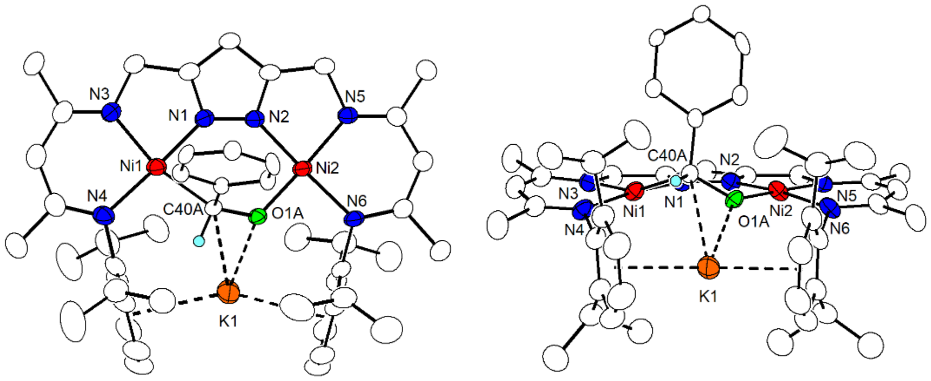

Figure 68: Molecular structure of **13-K** in top view (left) and front view (right). Solvent molecules and hydrogen atoms, except the H bound to the benzaldehyde carbonyl carbon, are omitted for clarity.

Slow diffusion of hexane into a solution of **13-K** in THF at -35 °C gave red cubes as single crystals suitable for X-ray diffraction analysis (Figure 68). The complex crystalizes in the triclinic unit cell $P\,\bar{1}$. The metal centers are separated by a distance of 3.9349(5) Å and the *μ-κC,κO* bound [PhCHO]$^{2-}$ unit in between them is disordered. Both Ni ions are coordinated by **L**$^{3-}$ and the [PhCHO]$^{2-}$ carbon or oxygen atom to adopt a square planar environment. The C–O bond of the nickel bound benzaldehyde moiety is 1.414(5) Å long, which is significantly longer than the respective bond in free benzaldehyde which measures about 1.26 Å[132] but comparable to the reduced C–O bond length of the formaldehyde unit in **11-K** with 1.394(4) Å. While the distance between the nickel center and the bound substrate carbon atom is with 2.071(5) Å longer compared to the Ni–C bond in **11-K** [1.974(3) Å], the Ni–O bond is found to be contracted in **13-K** [d(Ni–O) = 1.787(3) Å vs. 1.838(2) Å]. This may be a result of the phenyl group substituent at the nickel bound carbon, which weakens the Ni–C by increasing the steric pressure. Moreover, it might also be result of the closer proximity of the oxygen atom to the K$^+$ cation [d(K···O) = 2.467(3) Å vs. 2.672(3) Å]. In contrast to what was found for **11-K**, the K$^+$ in **13-K** is encapsulated in between the flanking diisopropylphenyl units around the bimetallic cleft, probably through a Lewis acid interaction with the π-system. The distance of the cation to the centroids of these aryl units measures 2.8286(8) Å and 2.8138(8) Å. As a result, they are bend out of the plane spanned by **L**$^{3-}$ and the nickel centers in the opposite direction of the phenyl group of the bound PhCHO unit, which is almost orthogonal to the plane of the pyrazole moiety. As the NMR data and the IR spectrum implied, the bridging moiety in **13-K** is best described as a $[PhCHO]^{2-}$ with a C–O single bond. Therefore, the benzaldehyde moiety in the dinickel complex is twofold reduced. A selection of structural parameters of **13-K** is given in Table 8.

Table 8: Selected bond lengths [Å] and angles [°] for **13-K**.

Bond Lengths [Å]		Bond Angles [°]	
Ni(1)-N(1)	1.8522(16)	**N(1)-Ni(1)-C(40A)**	85.48(14)
Ni(1)-N(3)	1.9227(16)	**N(4)-Ni(1)-C(40A)**	100.32(15)
Ni(1)-N(4)	1.9284(17)	**N(3)-Ni(1)-C(40A)**	157.40(16)
Ni(2)-N(2)	1.8572(16)	**N(1)-Ni(1)-N(3)**	83.41(7)
Ni(2)-N(5)	1.9177(16)	**N(4)-Ni(1)-N(3)**	93.14(7)
Ni(2)-N(6)	1.9333(16)	**N(2)-Ni(2)-O(1A)**	93.92(10)
Ni(1)-C(40A)	2.071(5)	**N(6)-Ni(2)-O(1A)**	89.18(10)
Ni(2)-O(1A)	1.787(3)	**N(5)-Ni(2)-O(1A)**	176.59(10)
O(1A)-C(40A)	1.414(5)	**N(5)-Ni(2)-N(6)**	93.50(7)
C(40A)-C(41A)	1.523(9)	**N(2)-Ni(2)-N(5)**	83.17(7)
K(1)-Aryl(1)	2.8286(8)	**Ni(1)-C(40A)-O(1A)**	120.2(3)
K(1)-Aryl(2)	2.8138(8)	**Ni(2)-O(1A)-C(40A)**	122.4(3)
K(1)-C(40A)	2.980(5)	**Ni(1)-C(40A)-C(41A)**	106.3(3)
K(1)-O(1A)	2.476(3)	**O(1A)-C(40A)-C(41A)**	114.0(6)
Ni(1)···Ni(2)	3.9349(5)	**Ni(1)-C(40A)-O(1A)-Ni(2)**	72.265(467)

In order to clarify the mechanism of the reductive activation of the substrate, the reaction between benzaldehyde and the dideuteride isotopologue of **2-K**, *viz*. **2-K-d$_2$** was monitored by ^{2}H NMR spectroscopy (Figure 69).

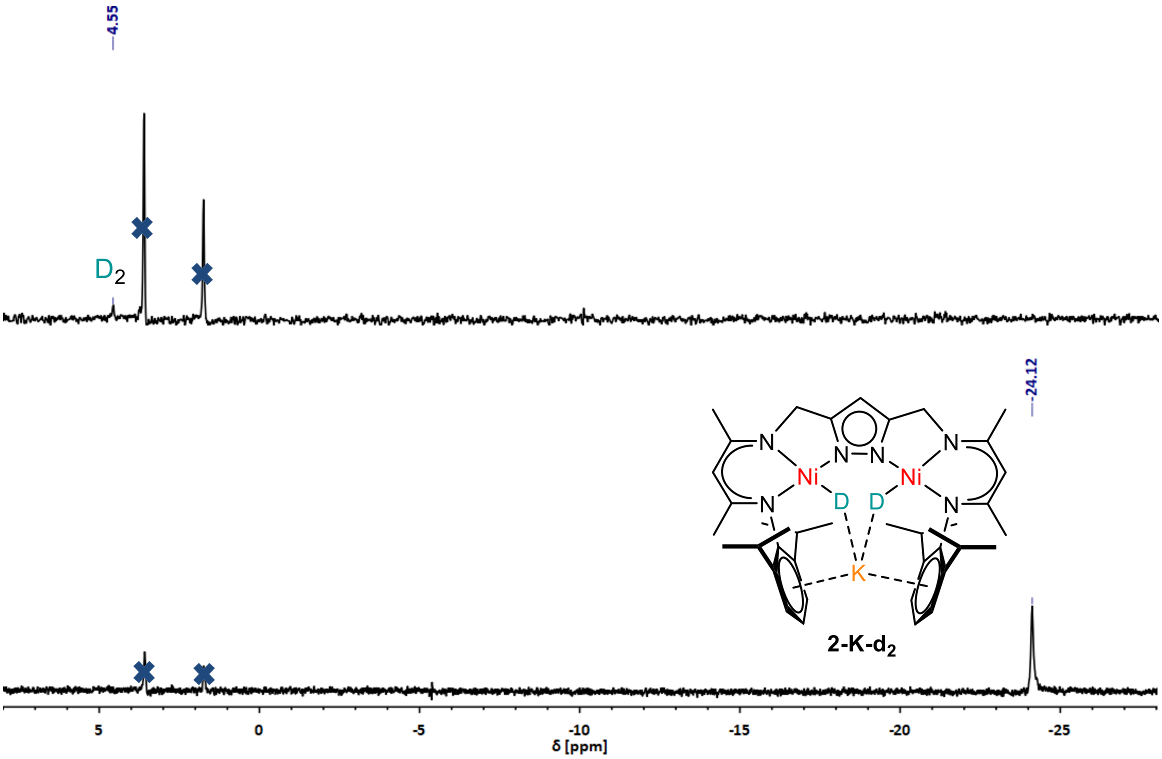

Figure 69: ^{2}H NMR spectrum of **2-K-d₂** (bottom) and the reaction of **2-K-d₂** with benzaldehyde. Solvent signals are marked by blue crosses.

The high field shifted signal of the nickel bound deuterium at -24.12 ppm disappears upon addition of the benzaldehyde substrate while a sharp singlet at 4.55 ppm for formed D_2 emerges. Since there is no evidence for HD evolution which would be indicated by a widely spilt doublet around 4.55 ppm this experiment supports the assumed mechanism that the activating $Ni^{I}Ni^{I}$ complex species is formed by a reductive elimination of H_2, to then reductively bind benzaldehyde.

5.2.8 Reactivity of the Dinickel Benzaldehyde Complex Towards Dihydrogen

With promise for an application of **2-K** as a catalyst for the reduction of benzaldehyde, the reactivity of **13-K** towards H_2 was probed. Exposing a THF solution of **13-K** to one atmosphere of H_2 results in a color change from deep red to orange. The reaction was monitored by ^{1}H NMR spectroscopy. An NMR measurement after one hour surprisingly indicated the partial reformation of **2-K** with high field shifted singlet at -24.16 ppm. Additionally, a signal at 9.97 ppm for a carbonyl group proton suggests the formation of free benzaldehyde. An OH proton of the decomposition species **3** is observed at -7.27 ppm, which is probably formed by a reaction with trace amounts of water in the applied hydrogen gas despite drying it over H_2SO_4 for 24 h before usage. Heating the reaction to 60 °C for 24 h results in a complete consumption of **13-K**, as indicated by the absence of the characteristic signal for the proton of the pyrazolate unit at 5.35 ppm. The two dominant species in the ^{1}H NMR spectrum are **2-K** and **3**. However, a singlet at 4.54 ppm suggests the formation of the desired benzaldehyde reduction product benzyl alcohol, as literature assigns a proton shift of 4.54 ppm for its CH_2 group in $CDCl_3$ (Figure 70).[133] Unfortunately, an excess of benzaldehyde in the presence of **2-K** under H_2 atmosphere did not show catalytic conversion to benzyl alcohol.

The experiment shows that the H_2 formation coupled reaction of **2-K** with benzaldehyde is reversible (Figure 71). This again suggests that a Ni^{I}Ni^{I} intermediate, is able to twofold reduce and bind both, H_2 and benzaldehyde. Unfortunately, the requirements of extremely dry hydrogen gas did not allow reactions at higher pressures to enforce a complete conversion, since it was only possible to dry the gas sufficiently at 1 atm. However, at elevated temperatures of 60 °C a different mechanism takes place. Since the formation of **3** is observed it is possible, that a reaction of the reduced $[PhCHO]^{2-}$ moiety in **13-K** with protons of trace amounts of H_2O leads to the formation of benzyl alcohol. Another possible mechanistic scenario is direct hydrogenation of the Ni–C bond as previously described for a Ni–C bond in a system with a similar ligand scaffold.[120] Furthermore, higher temperatures could induce a hydride transfer reaction *via* an 1,2 insertion of benzaldehyde into the Ni–H bond in **2-K**, like it was observed in the reaction of formaldehyde an **2-K** in benzene (see above). Although, the sterical hinderance of the aldehyde phenyl substituent would lead to a high barrier for an insertion reaction, this would align with the observation that after reacting **13-K** with H_2 for 24 h at 60 °C all of **13-K** is consumed and no free benzaldehyde is visible in the ^1H NMR spectrum while the two dinickel complex species **2-K** and **3** remain in an approximate 1:1 ratio. Since one molecule of **2-K** bears two hydride ligands, it potentially can reduce two molecules of benzaldehyde to benzyl alcoholate. Due to the steric demand the benzyl alcohol is forced out of the bimetallic binding pocket and substituted by a hydroxide which may originate from trace amounts of H_2O. Although **2-K** proved to be an insufficient tool for the catalytic reduction of benzaldehydes these findings yet again demonstrate the ability to stabilize highly reduced substrate intermediates.

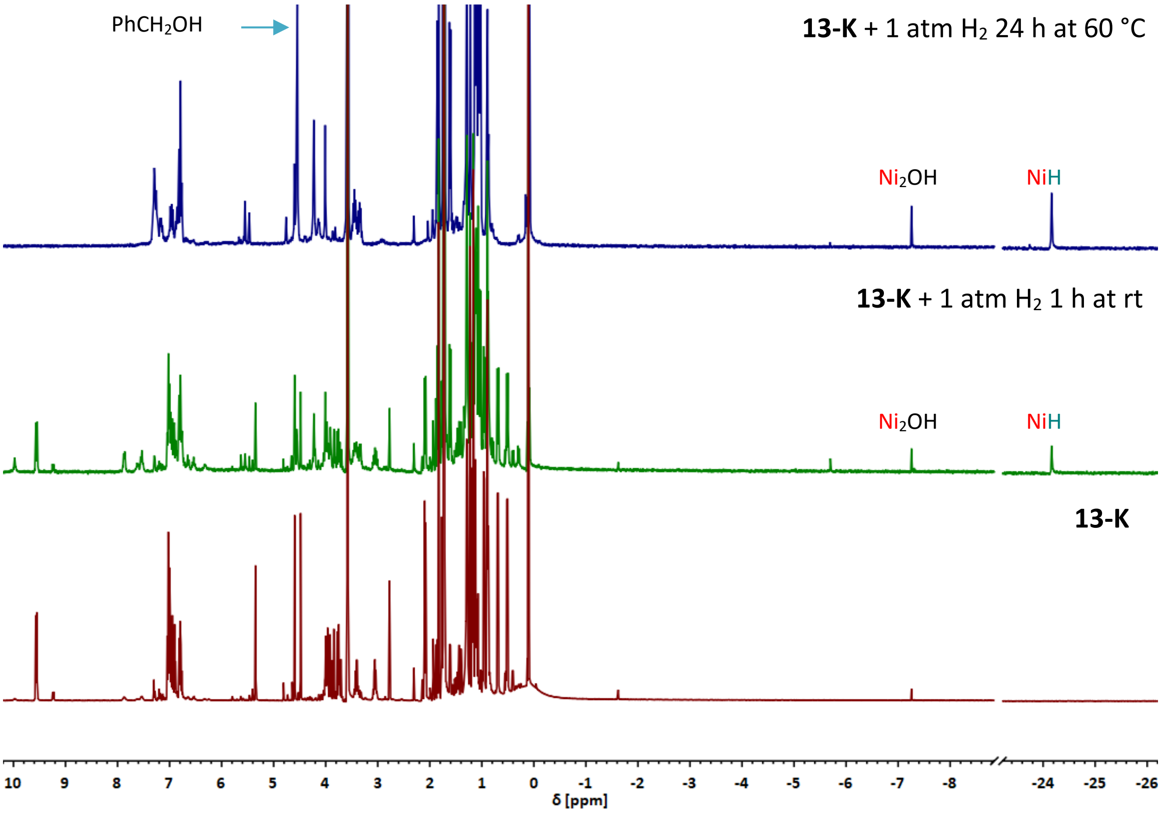

Figure 70: Stacked ^1H NMR spectra (300.13 MHz) of **13-K** (red line), **13-K** under 1 atm H_2 after 1 h (green line) and **13-K** under 1 atm H_2 after 24 h at 60 °C (blue line) in THF-d_8.

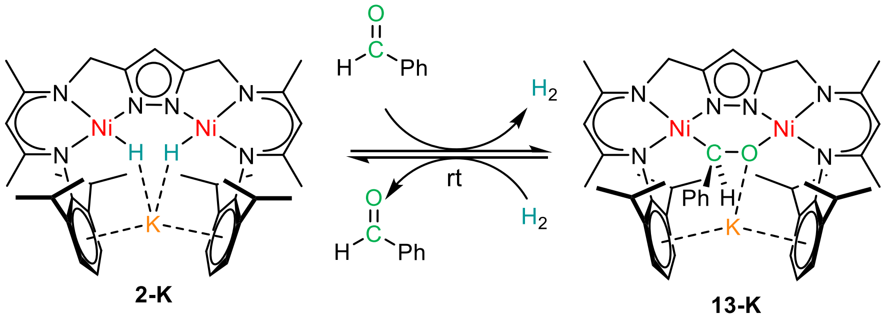

Figure 71: Reversible H_2 release coupled reaction of **2-K** with benzaldehyde.

5.2.9 The Cation Influence on the Structure of Dinickel Benzaldehyde Complex 13-K

Adding one equivalent of [2.2.2]cryptand to a **2-K** solution in THF followed by one equivalent of benzaldehyde led to the formation of **13-cK**, indicated by a color change to intense red. Layering a solution of **13-cK** in THF with hexanes yields crystalline material in the shape of red cubes.

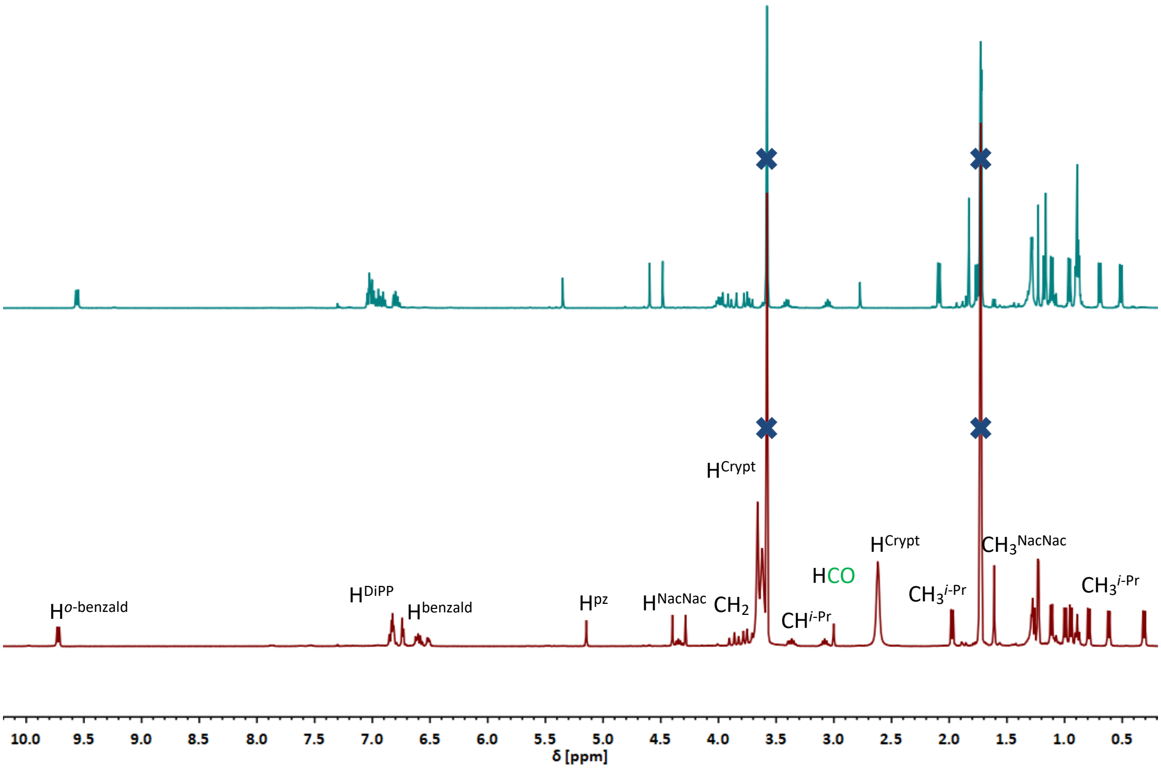

Figure 72: Stacked ^{1}NMR spectra of **13-K** (cyan line) and **13-cK** (red line) in THF-d_8.

Analysis of the ^1H NMR spectrum of **13-cK** reveals a general high field shift for most of the protons of the [LNi_2] unit compared to **13-K**, as expected for the suppression of the influence of the K^+ on the complex. Exception is one proton of the secondary isopropyl positions. Interestingly, proton shifts of the bound benzaldehyde substrate, which are located closely to the bimetallic core of the complex, namely the *ortho* protons of the phenyl and the proton of the CHO-bridging unit, are significantly increased [$\delta_{o\text{-Ph}} = 9.56$ ppm vs. 9.72 ppm; $\delta_{CHO} = 2.77$ ppm vs. 3.00 ppm]. This low field shift is probably caused by a relaxation of the strained complex structure upon suspending the interaction of the K^+ and the π-systems of the dipp groups.

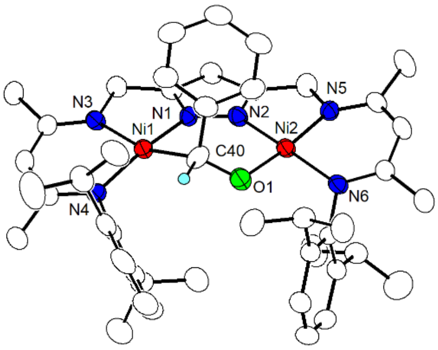

Figure 73: Molecular structure of **13-cK**. Solvent molecules, the [2.2.2]cryptand coordinated K⁺ counterion and hydrogen atoms, except the H bound to the benzaldehyde carbonyl carbon, are omitted for clarity.

13-cK crystallizes in the monoclinic space group *P* 2_1/C. The overall appearance resembles the one found for **13-K** (Figure 73). The crucial difference is the location of the K^+, which is encapsulated in the [2.2.2]cryptand binding pocket and not held in between the flanking aryl groups of the β-diketiminate units, resulting in an ionic compound. The Ni···Ni distance of 3.8675(11) Å is significantly contracted compared to the potassium coordinated analogue [d(Ni···Ni) = 3.9349(5) Å]. As already described for the structure of the dinickel nitrosobenzene complex,[134] the interaction with the K^+ seems to have a bond weakening effect on the bound substrate.

Table 9: Selected bond lengths [Å] and angles [°] for **13-cK**.

Bond Lengths [Å]		Bond Angles [°]	
Ni(1)-N(1)	1.856(5)	**N(1)-Ni(1)-C(40)**	87.9(2)
Ni(1)-N(3)	1.960(5)	**N(4)-Ni(1)-C(40)**	97.9(2)
Ni(1)-N(4)	1.925(5)	**N(3)-Ni(1)-C(40)**	163.1(3)
Ni(2)-N(2)	1.851(5)	**N(1)-Ni(1)-N(3)**	82.5(2)
Ni(2)-N(5)	1.895(5)	**N(4)-Ni(1)-N(3)**	94.4(2)
Ni(2)-N(6)	1.909(5)	**N(2)-Ni(2)-O(1)**	93.7(2)
Ni(1)-C(40)	2.000(7)	**N(6)-Ni(2)-O(1)**	90.0(2)
Ni(2)-O(1)	1.842(4)	**N(5)-Ni(2)-O(1)**	175.0(2)
O(1)-C(40)	1.366(8)	**N(5)-Ni(2)-N(6)**	93.5(2)
C(40)-C(41)	1.542(10)	**N(2)-Ni(2)-N(5)**	83.2(2)
Ni(1)···Ni(2)	3.8674(11)	**Ni(1)-C(40)-O(1)**	119.3(5)
		Ni(2)-O(1)-C(40)	122.2(4)
		Ni(1)-C(40)-C(41)	107.3(4)
		O(1A)-C(40)-C(41)	112.9(6)
		Ni(1)-C(40)-O(1)-Ni(2)	72.999(597)

This is indicated by the contraction of the C–O bond in **13-cK**, when compared to **13-K**, where the K^+ is in close proximity to the $[PhCHO]^{2-}$ unit [d(C–O) = 1.366(8) Å vs. 1.414(5) Å]. For the atoms directly bound to the metal ions an alternating effect for the bond distance change was observed, in which the Ni–O bond length increased from 1.787(3) Å to 1.842(4) Å, while the Ni–C bond contracted from 2.071(5) Å to 2.000(7) Å. This is a consequence of the K^+ being mainly coordinated to the oxygen atom in **13-K**. Selected structural parameters of **13-cK** are listed in Table 9.

Crystallographic and NMR data show the significant impact of the counterion on the interaction between the complex and the bound substrate. The influence is expressed by an increase in C–O bond length, when the K^+ is bound to the complex and in close proximity to the $[PhCHO]^{2-}$ unit. The polarizing effect of the K^+ results in a withdrawal of electron density from the metal ions to the coordinated $[PhCHO]^{2-}$ unit, weakening the C–O bond. The above mentioned anagostic interaction of the Ni^{II} centers and the *ortho* protons is amplified in the case of **13-cK** as indicated by the increased shielding of the protons according to the ^1H NMR data. Removal of the K^+ between the dipp groups results in a decrease of strain in the molecular structure of **13-cK** causing a shorter distance between the *ortho* protons and the Ni^{II} ions. In the following part further approaches for the manipulation of the electronic structure of these dinickel benzaldehyde complexes are presented by altering the electronic properties of the aryl unit.

5.2.10 Effects of the *para* Substituents in Dinickel Arylaldehydes

Similar to the synthesis of the **13-K**, **2-K** forms various dinickel arylaldehyde complexes upon reaction with different *para* substituted arylaldehyde derivatives. The selection of substituents covered mesomeric and inductive electron withdrawing (-M, -I) and electron donating (+M, +I) functional groups, *viz*. Me_2N-, MeO-, F-, F_3C- and nitro substituents.

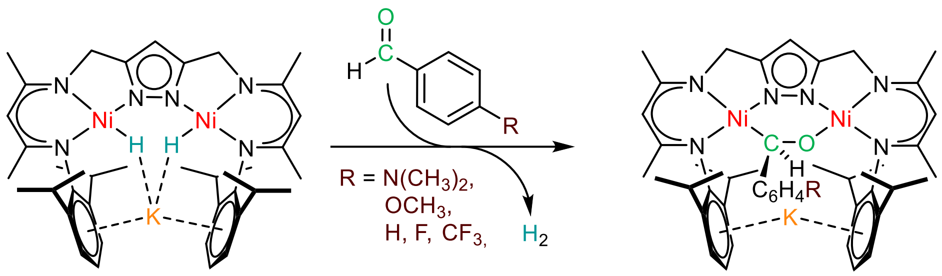

2-K

13^{NMe_2}-K **13^{F}-K**
13^{OMe}-K **13-K** **13^{CF_3}-K**

Figure 74: Reaction of **2-K** with various *para* arylaldehydes.

As expected, all aldehydes reacted instantaneously upon addition to a solution of **2-K**. In every case the evolution of H_2 was observed, which indicated a twofold reduction of the carbonyl functional groups (Figure 74). The resulting dinickel complexes feature similar colors of dark red to brown with exception of the blue dinickel nitrobenzaldehyde complex. The compounds of this complex family show modest to good solubility in THF and benzene. However, exceptions are the products of the reaction with 4-fluorobenzaldehyde and 4-nitrobenzaldehyde, which are only sufficiently soluble in only DMSO.

The proton signal shifts of the $[LNi_2]$ unit in the ^1H NMR spectra are similar. While all complexes of the *para* substituted benzaldehyde derivatives obviously lack one proton in the chemical shift region between 7.5 ppm and 6.5 ppm compared to the unsubstituted complex **13-K**, the Me_2N derivate has a six proton singlet at 2.82 ppm and 4-anisaldehyde derivative shows three proton signal at 3.69 ppm. The 4-trifluoromethyl benzaldehyde shows a signal at -62.1 ppm in the ^{19}F NMR spectrum.

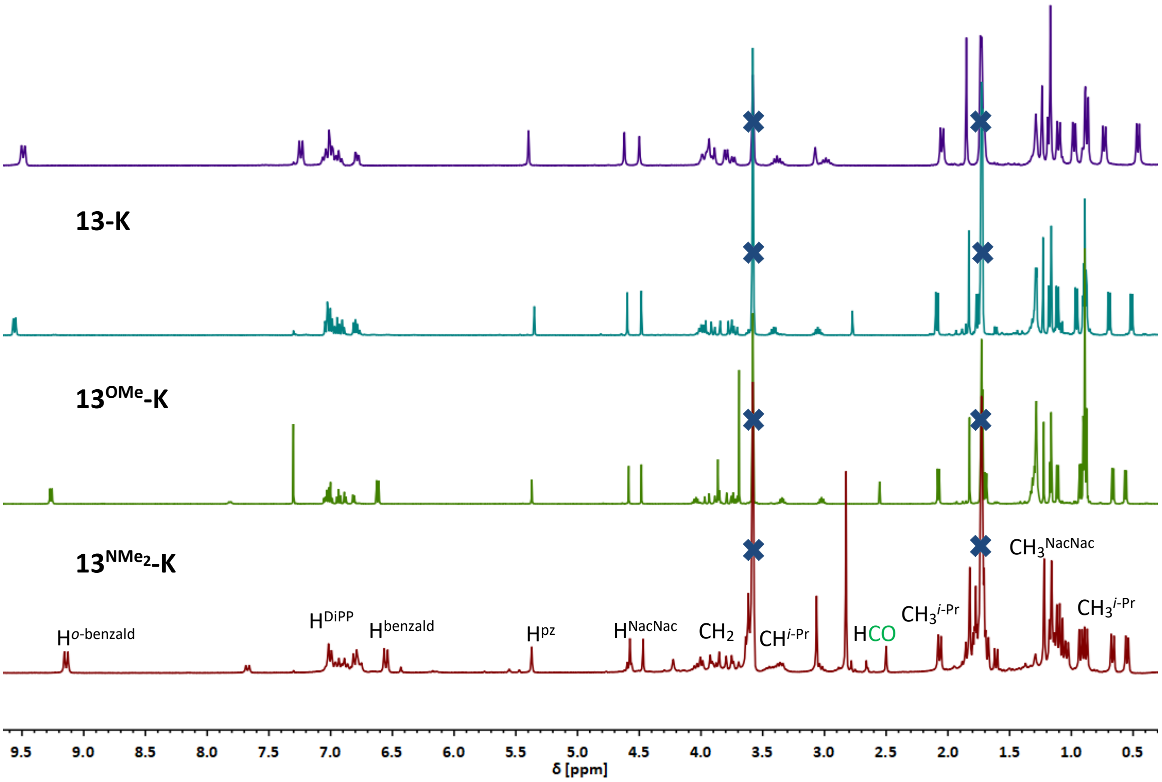

Figure 75: Stacked ^{1}H NMR spectra (300.13 MHz) of **13^{CF_3}-K**, **13-K**, **13^{OMe}-K** and **13^{NMe_2}-K** in THF-d_8

The change in the complexes' electronic structure depending on the *para* substituents is expressed most significantly through the chemical shift difference of the corresponding aryl *ortho* protons and the proton bound to the OCH bridging unit. As expected for the electron donating functional groups of the complexes **13^{NMe_2}-K** and **13^{OMe}-K** the signals of the aryl *ortho* protons experience a high field shift with respect to **13-K** from 9.56 ppm to 9.13 ppm for the Me_2N derivative and to 9.26 ppm for the MeO derivative. A similar trend is observed for the CHO bridge protons with a signal shift from 2.77 ppm for **13-K**, to 2.50 ppm for **13^{NMe_2}-K** and 2.55 ppm for **13^{OMe}-K**. For the CHO bridge proton in **13^{CF_3}-K** with the electron withdrawing F_3C substituted the opposite effect is observed, as the resonance undergoes a low field shift to 3.07 ppm. However, this does not apply to the aryl *ortho* proton, as the doublet shows a small shift from 9.56 ppm to 9.49 ppm (Figure 75). This counterintuitive observation is probably a result of less a pronounced interaction of the arlyl *ortho* protons with the Ni^{II} ions. As previously described, the large downfield shift of the protons in the *ortho* position of the aromatic system is attributed to an anagostic interaction with the nickel centers. The electron withdrawing effect of the CF_3 group might lead to a sufficient contraction of the aryl C–H bonds to weaken the anagostic interaction negating the expected trend for the aryl *ortho* proton signal drift.[130]

To parametrize these findings, the chemical shifts (δ) of the discussed proton signals are plotted against the Hammett constant of the corresponding *para* substituent in the dinickel arylaldehyde complexes in Figure 76.[135] The chemical shift differences of the mentioned protons in the dinickel arylaldehyde complexes are roughly in accordance with the estimated values (Table 10).

Table 10: List of *para* substituents in the dinickel arylaldehyde complexes ($KLNi_2C_6H_4R$) and the corresponding Hammett constants as well as the corresponding proton shifts for the aryl *ortho* protons and the CHO bridging unit protons.

para Substituent R	Hammett constant σ	$\delta_{o\text{-}Ar}$ [ppm] in $KLNi_2C_6H_4R$	δ_{CHO} [ppm] in $KLNi_2C_6H_4R$
***N*,*N*-Dimethylamino ($N(CH_3)_2$)**	-0.83	9.13	2.50
Methoxy (OCH_3)	-0.27	9.26	2.55
None (H)	0.00	9.56	2.77
Trifluoromethyl (CF_3)	0.54	9.49	3.07

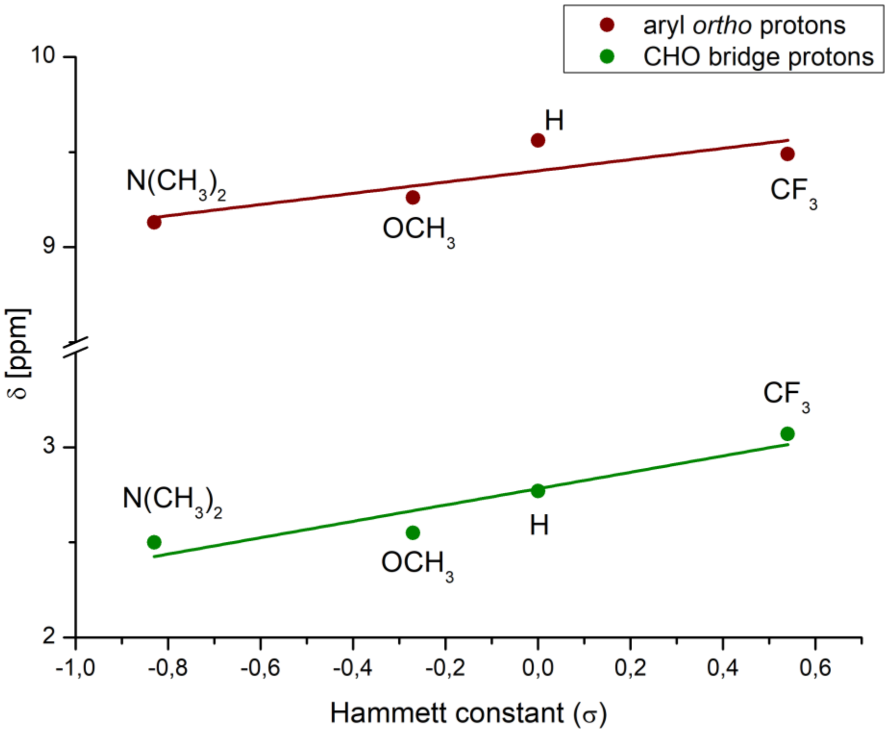

Figure 76: Chemical shifts of the different aryl *ortho* protons (brown line) and of the CHO bridge protons (green line) plotted against the corresponding Hammett parameters.[135]

In the case of $\mathbf{13^{NMe_2}}$**-K** multiple crystallization attempts by slow diffusion of hexane into a solution of the complex in benzene afforded single crystals suitable for XRD analysis. In solid state the complex with the Me_2N substituent crystalizes in the monoclinic space group $P\,2_1/n$ and features a nickel-nickel distance of 3.9368(5) Å, which resembles the one of **13-K** with 3.9349(5) Å.

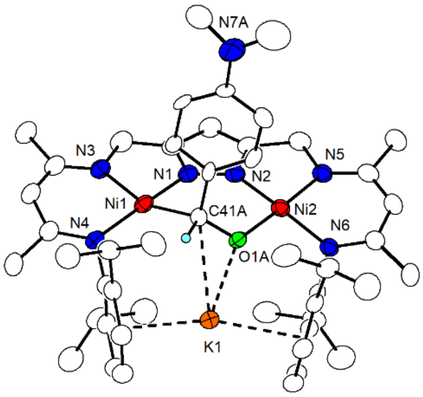

Figure 77: Molecular structure of **13$^{\mathrm{NMe_2}}$-K**. Solvent molecules and hydrogen atoms, except the H bound to the *N*,*N*-dimethylamino benzaldehyde carbonyl carbon, are omitted for clarity.

The main difference of the molecular structure of **13$^{\mathrm{NMe_2}}$-K** compared to **13-K** is the Me$_2$N function at the *para* position to the metal bound aldehyde function. In comparison to **13-K**, all bond length differences fall within the error including the C–O bond length. Therefore, the impact of the *para* substituent seems to be unsubstantial for the molecular structure of the dinickel arylaldehyde complexes. For that reason, no further efforts in analyzing the solid state structures of **13$^{\mathrm{OMe}}$-K**, **13$^{\mathrm{CF_3}}$-K** or **13$^{\mathrm{F}}$-K** were made (Figure 77).

Table 11: Selected bond lengths [Å] and angles [°] for **13$^{\mathrm{NMe_2}}$-K**.

Bond Lengths [Å]		Bond Angles [°]	
Ni(1)-N(1)	1.8578(17)	**N(2)-Ni(2)-C(41B)**	86.34(17)
Ni(1)-N(3)	1.9267(17)	**N(6)-Ni(2)-C(41B)**	99.31(18)
Ni(1)-N(4)	1.9322(18)	**N(5)-Ni(2)-C(41B)**	157.9(2)
Ni(2)-N(2)	1.8588(17)	**N(1)-Ni(1)-N(3)**	83.26(7)
Ni(2)-N(5)	1.9243(17)	**N(4)-Ni(1)-N(3)**	92.87(7)
Ni(2)-N(6)	1.9247(17)	**N(1)-Ni(1)-O(1B)**	93.82(12)
Ni(2)-C(41B)	2.061(7)	**N(4)-Ni(1)-O(1B)**	89.81(13)
Ni(1)-O(1B)	1.811(3)	**N(5)-Ni(1)-O(1B)**	176.59(10)
O(1A)-C(41B)	1.406(7)	**N(5)-Ni(2)-N(6)**	93.50(7)
C(41B)-C(42B)	1.505(12)	**N(2)-Ni(2)-N(5)**	83.33(7)
K(1)-Aryl(1)	2.8229(5)	**Ni(2)-C(41B)-O(1B)**	120.8(5)
K(1)-Aryl(2)	2.8170(5)	**Ni(1)-O(1A)-C(41B)**	123.5(4)
K(1)-C(41B)	2.965(7)	**Ni(2)-C(41B)-C(41B)**	104.3(4)
K(1)-O(1B)	2.510(4)	**O(1A)-C(41A)-C(41B)**	114.2(9)
Ni(1)···Ni(2)	3.9368(5)	**Ni(2)-C(41A)-O(1B)-Ni(1)**	78.820(475)

However, in the case of the reaction of **2-K** with 4-nitrobenzaldehyde, a very different reaction outcome was observed. The characterization of the reaction product **14$^{\mathrm{Bna}}$-K** will be discussed in the following chapter.

5.3 Conclusion

In this chapter the reductive binding of CO to a bimetallic nickel site was discussed. As the twofold reduction with **2-K** proved to be unsuccessful **4^{N_2}** was utilized in a ligand exchange reaction with CO. The reaction outcome was the new dinickel formyl complex **10^{H}** featuring a *μ-κC,κO*-formyl bridge in between the metal centers. This represents the first example for a structurally characterized nickel formyl complex. Monitoring the reaction by EPR suggests a CO radical intermediate **4^{CO}** isoelectronic to **4^{N_2}**. Although, the highly reactive compound **4^{CO}** could not be isolated due to the strong tendency to abstract an H-atom, the resulting dinickel formyl complex **10^{H}** represents an important intermediate in context of the commercially relevant CO hydrogenation.

To further explore the concept of CO reduction on a bis(β-diketiminate) pyrazolate dinickel systemcomplex **10^{H}** treated with $KHBEt_3$ to yield **11-K**. An alternative synthesis for **11-K** was established by treatment of **2-K** with formaldehyde in THF, which led to the direct twofold reduction of the carbonyl functional group. It was shown that it was possible to oxidize **11-K** to **10^{H}** proving that the concept of micro reversibility was applicable to the reaction. Interestingly, the reaction of **2-K** with formaldehyde resulted in the dinickel dimethanolate complex **12** when benzene was used as a solvent, suggesting a nickel hydride rather than a $Ni^{I}Ni^{I}$ reactivity.

In the final part, the substrate scope for the activation of aldehydes was extended to benzaldehyde and respective derivatives. Although, dinickel benzaldehyde complex **13-K** proved to be an insufficient catalyst for the hydrogenation of benzaldehyde, it was shown that the reaction between **2-K** and benzaldehyde is reversible under hydrogen atmosphere. For the reductive binding of benzaldehyde derivatives, different *para* substituents were chosen in view of their electronic properties. While the influence on the degree of activation was not notable in the solid structure of **13^{NMe_2}-K**, changes in the respective ^{1}H NMR spectra were evaluated by comparison to the according Hammet parameters.

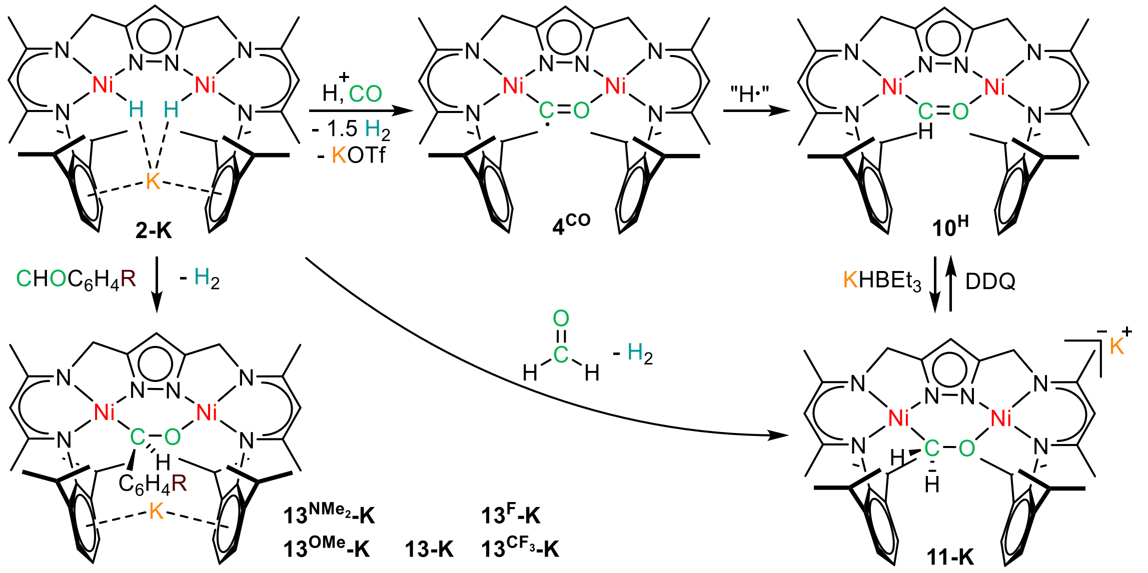

Scheme 20: Overview of the dinickel mediated activation of CO multiple bonds and interconversion of the resulting complexes.

6 Reductive Binding of Nitro Substrates on a Bimetallic Dinickel Site

Parts of this chapter have been published: T. Kothe, U-H. Kim, S. Dechert, F. Meyer, *Inorg. Chem.* **2020**, *59*, 14207–142176.

6.1.1 Reduction of Nitro Compounds to Amines

The nitro group represents a valuable functional group in synthetic organic chemistry. The by far most important conversion is the reduction to anilines. In particular, the transformation of aromatic nitro compounds is of significant interest, due to the high demand of aryl amines which are essential chemicals for the industrial production of polymers, dyes, pigments, pharmaceuticals and herbicides.[136]

For a long time, the use of metallic iron in acidic media in stoichiometric amounts was the main manufacturing process for the production of aniline from nitrobenzene, which was introduced by Béchamp in 1854.[136] Catalytic reductions with H_2 were first established with noble metals like palladium as heterogeneous catalysts.[137] Modern approaches focus on utilizing abundant 3d metals like Fe,[138] Co[139] or Ni[140] which are also represented in a broad range of homogeneous systems using H_2,[141] silanes[142] or formic acid[143] as reductants. Major goals of recent studies in the field are not only limited to the improvement in activity of catalysts but also the conversion of aliphatic nitro compounds which are harder to reduce than nitroaryl substrates.[144] Broadening the substrate scope and tolerance towards other easily reducible functional groups as esters, ketones or nitriles is another goal of current research. Although some of the catalytic systems have been quite effective in these regards, mechanistic insight is often lacking and possible intermediates have rarely been identified.[139]

Despite the importance of the reduction of nitro compounds to anilines only a limited number of studies on the reaction mechanism have been reported. The generally accepted mechanism continues to be the one from Haber which was proposed based on electrochemical experiments in 1898.[145] During the reduction the formal oxidation state of the nitro group nitrogen atom is lowered from +III to -III. Consequently, the reaction features several sequential one electron reduction steps which are usually coupled to protonation of the nitro group's N and O atoms.[146]

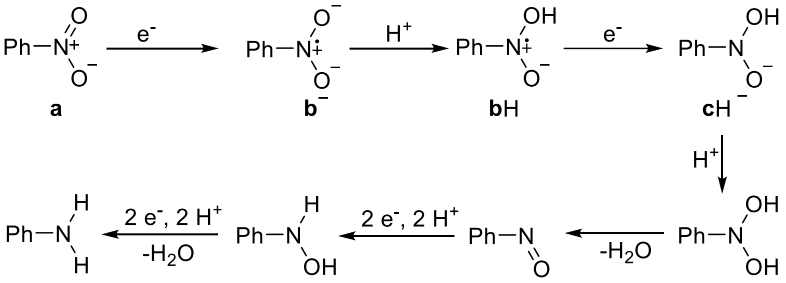

Scheme 21: Sequential proton-coupled reduction of nitrobenzene to aniline.

Some of the intermediates in Scheme 21 like hydroxyl aniline (**e**H_2) and nitrosobenzene (**d**) are rather stable and therefore can be isolated. In some cases of catalytic nitrobenzene reductions, an accumulation of phenylhydroxylamine is observed rendering its reduction the rate determining step.[147] Although, nitrosobenzene is also stable, it reacts fast to aniline under reduction conditions .

The reduction products preceding the elimination of the first oxygen atom are highly reactive. The nitrobenzenide anion (**b**$^-$) is accessible *via* alkali metal reduction, although the corresponding K$^+$, Cs$^+$ and Rb$^+$ salts are highly air sensitive and only thermally stable if [2.2.2]cryptand or crown ethers shield the cation from the radical anion.[148] The subsequent formation of dihydroxylamine (**c**H$_2$) was observed in electrochemical experiments, however yet needs to be confirmed structurally.[149]

6.1.2 Derivatives of Dihydroxylamines

Although, dihydroxylamines (**c**H$_2$) have been detected under some reaction conditions they have not yet been isolated and fully characterized, due to their instability. However, there are some examples where the oxygen atom is functionalized leading to more or less stable compounds.

One strategy is to stabilize the dihydroxylamine moiety in an 1,3,2-dialkoxazolidine. These heterocyclic compounds are usually accessible *via* photochemical 1,3 cycloaddition reactions of nitro compounds with alkenes. Due to their instability, 1,3,2-dialkoxazolidines were first identified by their decomposition products being carbonyl compounds, azobenzene and other substances. At low temperatures it was possible to observe them *via* ^{1}H NMR spectroscopy. However, the stable derivative **XXXII** was supplied with bulky adamantyl groups, which allowed the first structural characterization of these compounds.[150]

Another approach is the substitution of dihydroxylamines with heavier carbon homologues , e. g. silicon. This was demonstrated by the synthesis of *N*,*N*-bis(silyloxy)enamines. The conversion involves the treatment of aliphatic nitro compounds with trimethylsilyl bromide in presence of a base.[151] Their instability and tendency to rearrange to bis(trimethylsilyl) α-hydroxyoximes was suppressed by substitution with an electron poor aromatic nitro system.[152]

Tetramethyl digermene binds nitromethane *via* an 1,3 cycloaddition. The structure of the resulting 1,3,2-dioxazolidine **XXXIV** was determined by XRD analysis. **XXXIV** cleanly isomerizes to the oxime derivative **XXXV** at lower concentrations (Figure 78).[153]

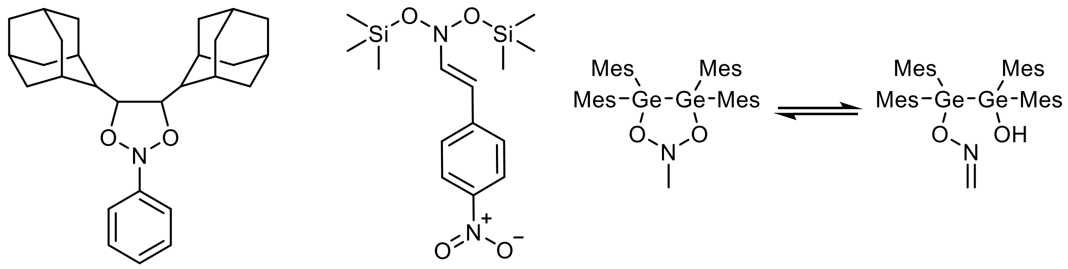

XXXII **XXXIII** **XXXIV** **XXXV**

Figure 78: Selected derivatives of dihydroxylamines and the equilibrium between **XXXIV** and **XXXV**.

6.1.3 Nickel Complexes of Nitro Group Reduction Intermediates

Studies on the coordination chemistry of nitro compounds to transition metals remain scarce. The only known example for a nickel complex bearing a nitro aryl ligand was presented by Kersting *et al.*. The macrocyclic dinickel complex **XXXII** was obtained by the reaction of its precursor chloride complex with 4-nitrophenolate. **XXXII** features a *κO*,*κO'*-bridging nitro aryl unit which is found to have a notable increase in N–O bond length because of its predominant aci-nitro resonance form (Figure 79).[154] Though this is technically not a reduction, it demonstrates the utility of a bimetallic nickel coordination environment for altering the nitro function N–O bond order within aryl nitro compounds.

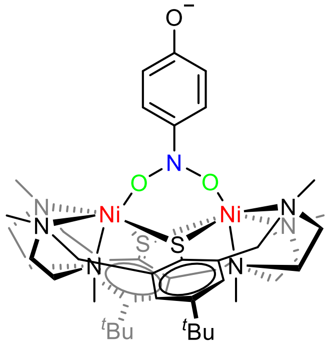

XXXII

Figure 79: Structure of the macrocyclic dinickel nitrophenolate complex **XXXII**.

The approach of a stabilizing bimetallic dinickel site was also used for nitrosobenzene (**d**) which represents one of the nitrobenzene reduction intermediate.

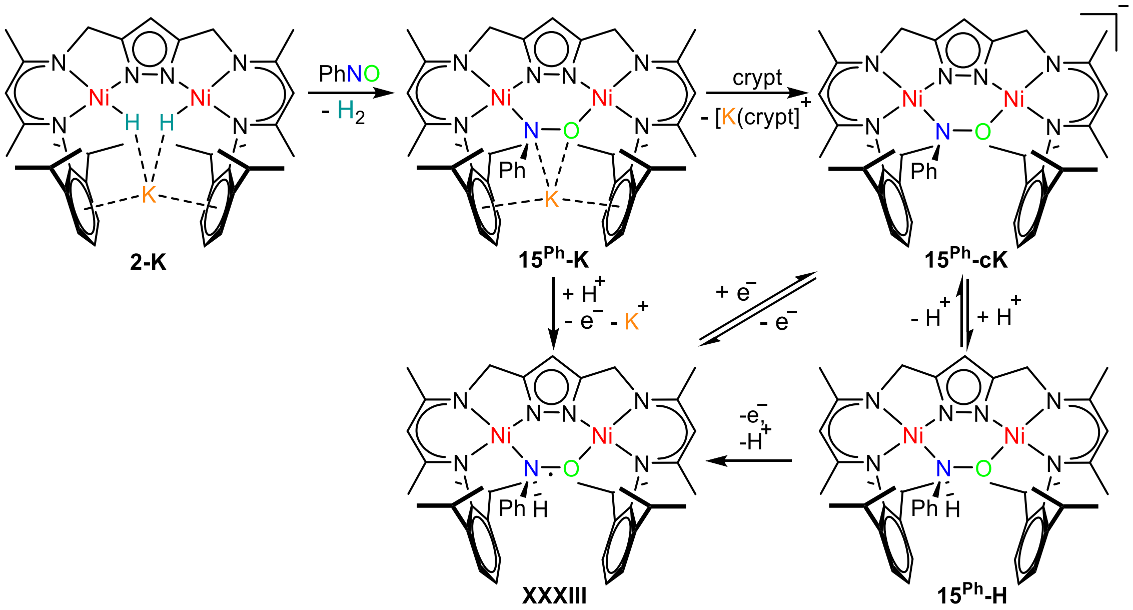

Scheme 22: Synthesis and interconversion reactions of the reductively bound nitrosobenzene substrate.

It was demonstrated that the bis(β-diketiminate) pyrazolate dinickel system [LNi_2] can stabilize the twofold reduced nitrosobenzene (**d**). Treatment of **2-K** with nitrosobenzene resulted in the formation of **15^{Ph}-K** under concomitant H_2 evolution. The N,O bridging twofold reduced PhNO moiety in complex **15^{Ph}-K** was described as a doubly deprotonated *N*-phenylhydroxylamine (**e**$^{2-}$). The incorporated K^+ in the molecule was found to have a significant N–O bond destabilizing effect as was shown by the cation removal with [2.2.2]cryptand. The reversible protonation of the resulting anionic complex **15^{Ph}-cK** led to compound **15^{Ph}-H** which featured a singly deprotonated *N*-phenylhydroxylamine (**e**H^-). Treatment of **15^{Ph}-H** with the 2,4,6 tri-*tert*-butyl phenoxy radical gave the radical monoreduced PhNO unit coordinated in the bimetallic cleft of complex **XXXIII** which was also accessible *via* the oxidation of **15^{Ph}-K** with $Cp_2{}^*FePF_6$ (Scheme 22).[155]

6.1.4 Objective

This chapter examines the reductive binding of nitro compounds to the bis(β-diketiminate) pyrazolate dinickel moiety [LNi_2]. As demonstrated for example in the synthesis of **15^{Ph}-K**, **2-K** can act as a masked Ni^INi^I complex, which releases H_2 in a reductive elimination and is able to subsequently twofold reduce substrates. Applying this concept to nitro groups should result in a doubly deprotonated dihydroxylamine (**c**$^{2-}$). Although, derivatives of **c**H_2 exist, they are often described as unstable despite their covalent bonds to heavy carbon analogues at the oxygen atoms. Literature suggests that a dinickel binding site potentially stabilizes such a reduced nitro moiety.[147] As dihydroxylamine (**c**H_2) and deprotonated dihydroxylamine (**c**H^-) present observed intermediates in the commercially relevant nitrobenzene reduction to aniline, this could provide more insight for the actual reduction pathway.

Preliminary results presented in the previous chapter suggested that the treatment of **2-K** with 4-nitrobenzaldehyde led cleanly to a nitro group bound nickel complex despite the presence of an aldehyde function. Based on this, the substrate scope will be extended to unfunctionalized nitrobenzene and aliphatic nitromethane to evaluate the reductive versatility of **2-K**.

Furthermore, these compounds should be convertible to subsequent intermediates beyond dihydroxylamine (**c**H_2) following the reduction sequence shown in Scheme 21 as for example nitroso compounds (**d**). In this context the bond weakening cation influence suggested by the observations for **15^{Ph}-K** and **15^{Ph}-cK** will be investigated. To provide a broader survey, the cation selection will include Na^+, in addition to K^+ and [K^+(cryptand)], which would be accessible *via* **2-Na**.

6.2 Results and Discussion

6.2.1 Chemoselective Reduction of a Nitro Function in Presence of a Carbonyl function

In contrast to the red to brown color of THF solutions containing the different dinickel complexes bound benzaldehyde derivatives, adding 4-nitrobenzaldehyde to a solution of **2-K** in THF led to an immediate color change from bright orange to deep blue.

In an ESI-MS experiment a peak with *m/z* 872.2 in accord with a cation containing two nickel atoms assigned by the characteristic isotopic pattern, is proposed to be $[LNi_2O_2NC_6H_4CHO]^+$. Interestingly, a second, less dominant peak with a value of *m/z* 856.3 was observed, approximately 16.0 u smaller than the major peak at *m/z* 872.2. This suggested an ionization induced loss of one oxygen atom to form $[LNi_2ONC_6H_4CHO]^+$. As it will be pointed out later, this represents an important transformation for this class of complexes (Figure 80).

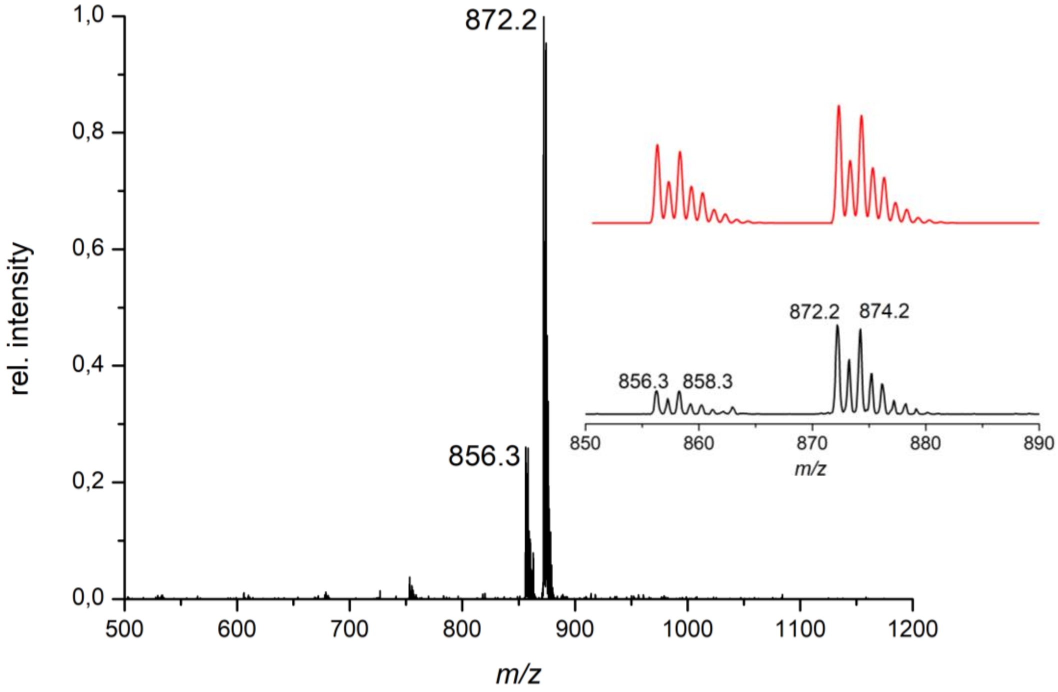

Figure 80: ESI$^+$ mass spectrum of $\mathbf{14^{Bna}}$**-K**. The inset shows the experimental (black line) and simulated (red line) isotope pattern for the major peak around *m/z* = 872.2 (1.0) $[M]^+$.

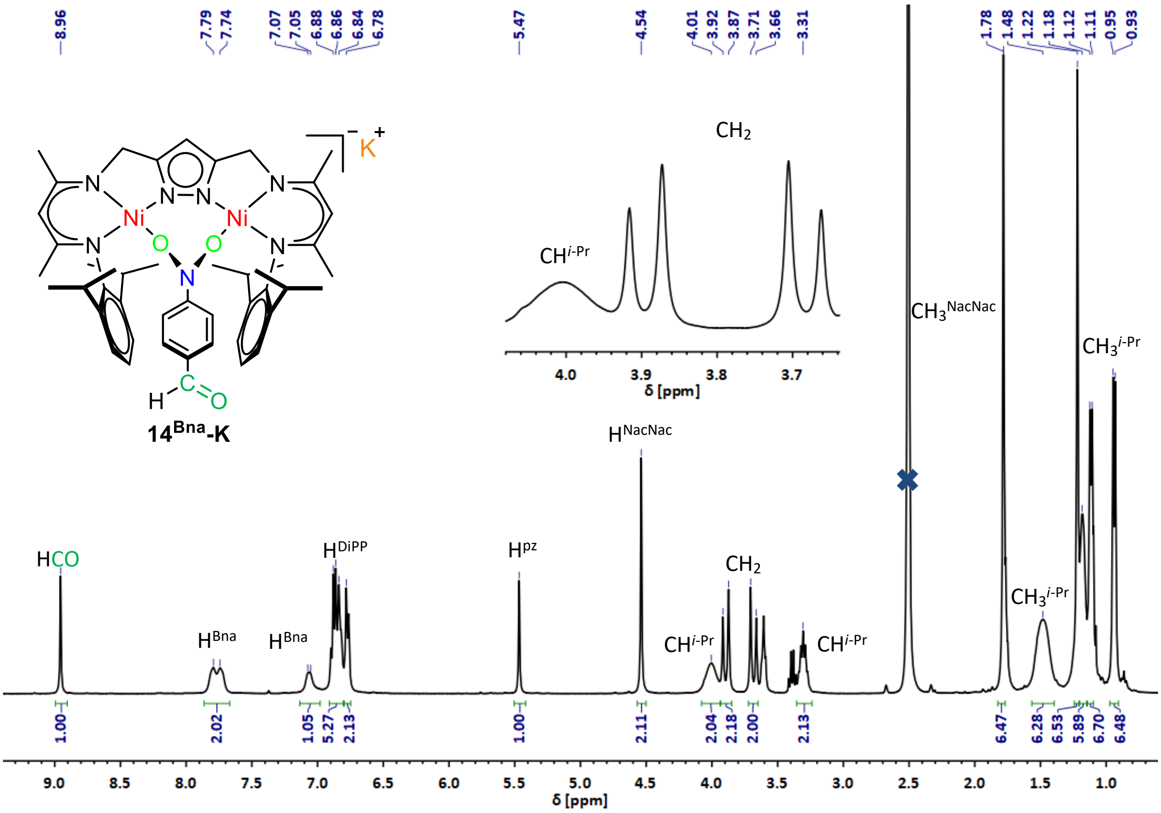

Figure 81: ^{1}H NMR spectrum (400.25 MHz) of **14^{Bna}-K** in DMSO-d$_6$. The solvent signal is marked by a blue cross.

Since the obtained compound is barely soluble in THF, NMR spectral data had to be recorded in DMSO-d$_6$. The ^{1}H NMR spectrum of the deep blue complex did not show the pronounced signal pattern for the CH$_2$ bridges between the pyrazolate and the β-diketiminate units of **L** which were observed for the C_1 symmetric **13-K** and its functionalized derivatives, but a simpler pattern similar to the one found for **8-K**, indicating C_s symmetry of the σ⊥xy-type. Additionally, a sharp singlet at 8.96 ppm was assigned to a carbonyl proton, suggesting that the aldehyde function of 4-nitrobenzaldehyde was not directly involved in the reaction with **2-K** (Figure 81). Hence, the NMR data suggested the pyrazolate bis(β-diketiminate) coordinated dinickel moiety [LNi$_2$] of **2-K** to bind the nitro instead of the carbonyl function (Figure 82).

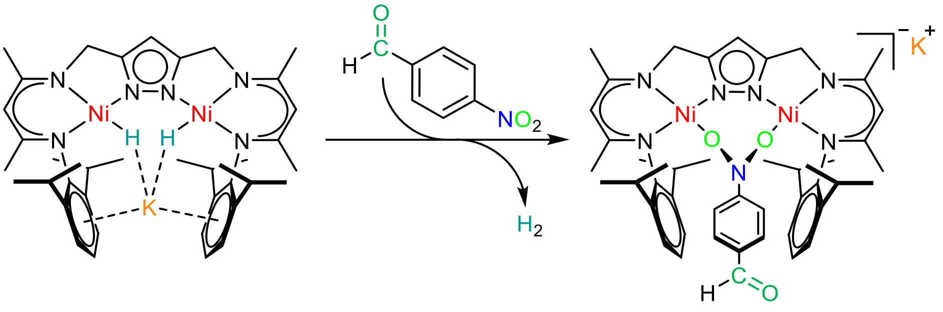

2-K

14^{Bna}-K

Figure 82: Reaction of **2-K** with 4-nitrobenzaldehyde.

Proton signals of the aromatic unit of the bound nitrobenzaldehyde substrate and the isopropyl units directed towards it, appeared to be significantly broadened, showing an intramolecular dynamic process. This was most prominent for the secondary isopropyl proton at 4.01 ppm, which instead of giving a clear septet only appeared as a broad signal, as well as the proton signals for the CH_3 groups of the isopropyl units at 1.48 ppm and 1.18 ppm, which also lacked sufficient resolution to observe their doublet structure.

The UV/vis spectrum of **14^{Bna}-K** showed a prominent absorption at 266 nm, which was within the region for the ligand to nickel charge transfer (MLCT) band of [LNi_2] complexes. Electronic transitions around 370 nm, 384 nm and 408 nm were assigned to charge transfer from the pyrazolate ligand to the nickel(II) metal centers, as similar bands were also observed in the UV/vis spectra of **2-K** and **4^{N_2}**. The broad band at 588 nm was assigned to a charge transfer between the $[O_2NC_6H_4CHO]^{2-}$ π* and the Ni^{II} ions (Figure 83).[156]

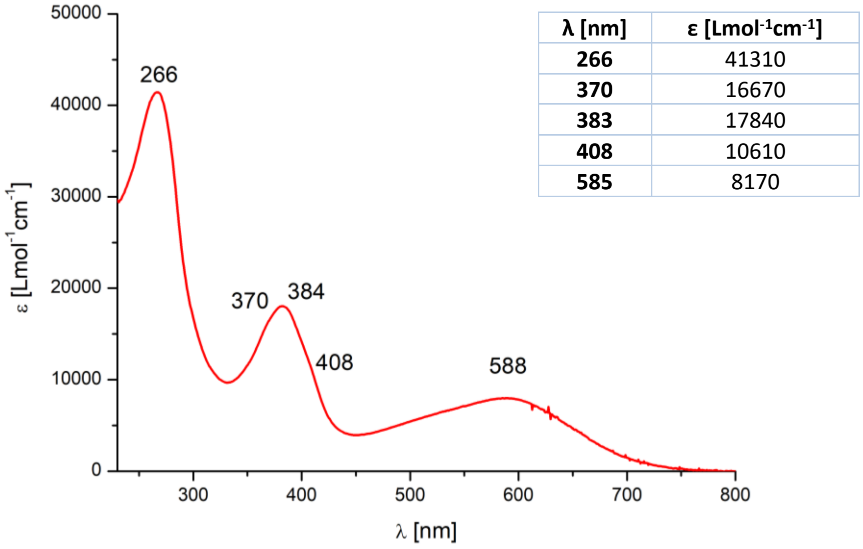

λ [nm]	ε [$Lmol^{-1}cm^{-1}$]
266	41310
370	16670
383	17840
408	10610
585	8170

Figure 83: UV/vis spectrum of **14^{Bna}-K** recorded at room temperature in THF and table listing the wavenumbers of the electronic transitions and their corresponding extinction coefficient.

The limited solubility of **14^{Bna}-K** in solvents like THF or benzene did not allow the successful isolation of crystalline material suitable for XRD analysis. To increase the solubility of the complex a solution of **2-K** in THF was treated with one equivalent of [2.2.2]cryptand prior to the addition of 4-nitrobenzaldehyde. This resulted in a color change to bright blue. The resulting complex **14^{Bna}-cK** was sufficiently soluble in THF to record NMR data. Removal of the K^+ cation from the $[LNi_2ONC_6H_4CHO]^-$ anion seems to induce a better resolution for the proton signals of the isopropyl groups directed towards the bound nitrobenzaldehyde substrate, suggesting that the K^+ slows a dynamic effect around the bound substrate. (Figure 84).

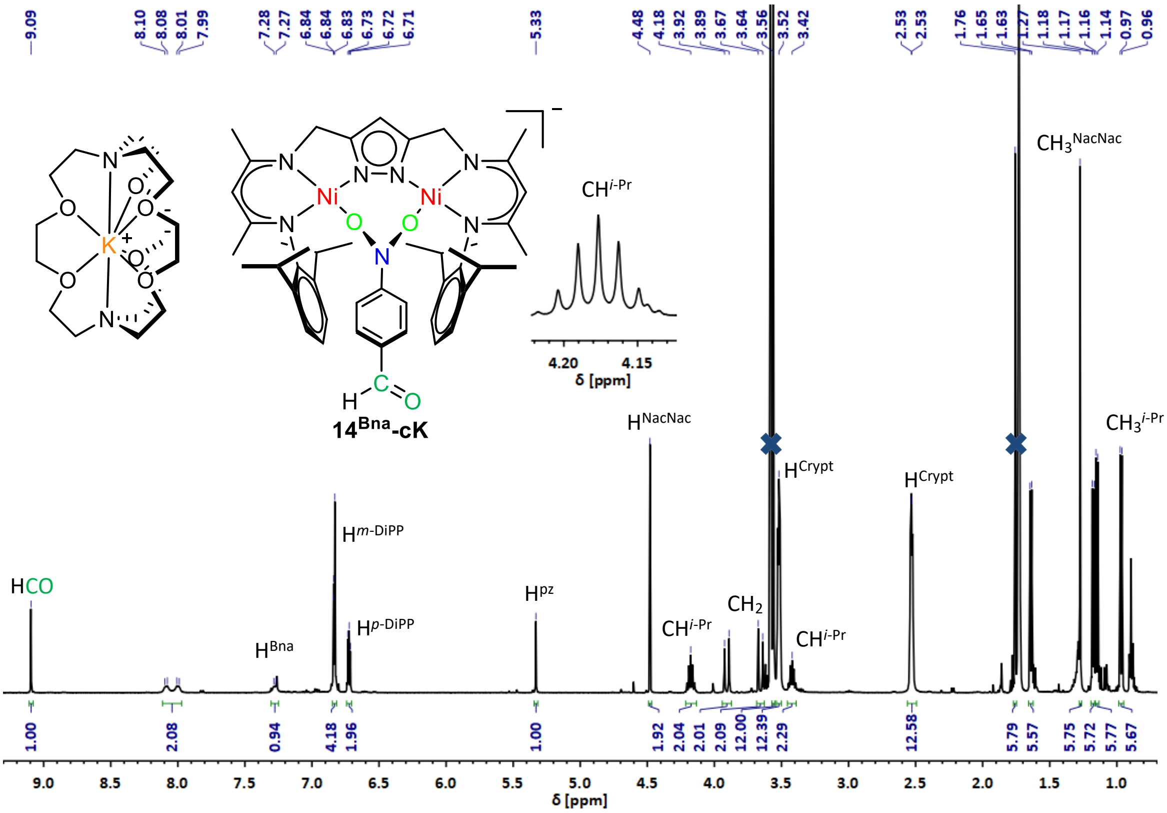

Figure 84: ^1H NMR spectrum (400.25 MHz) of **14^{Bna}-cK** in THF-d$_6$.

Diffusion of hexane into a solution of **14^{Bna}-cK** in THF resulted in the formation of single crystals, which were analyzed by X-ray diffraction analysis (Figure 85).

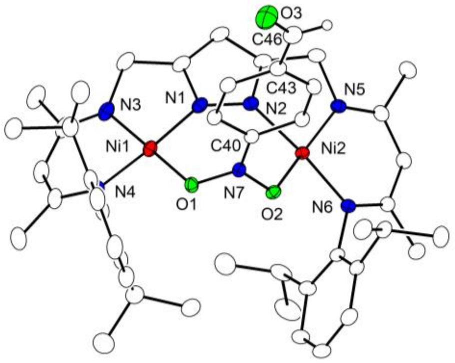

Figure 85: Molecular structure of **14^{Bna}-cK**. Solvent molecules, the [2.2.2]cryptand coordinated K$^+$ counterion and hydrogen atoms are omitted for clarity.

The molecular structure of **14^{Bna}-cK** confirms the structure suggested by the NMR data, as the aldehyde function is not involved in a direct coordination to the metal centers. Instead, the nitro function of the 4-nitrobenzaldehyde substrate is found to bridge both nickel ions in *μ*-*κ*O,*κ*O' binding mode. The unit cell of **14^{Bna}-cK** in solid state is P$\bar{1}$. Both nickel ions are separated 4.1439(6) Å, which is significantly higher than for other nickel complexes of **L**. The major difference is caused by higher steric demand of the three atom bridging nitro function coordinated to the metal centers. This is only exceeded by the bis-methanolate complex **12**, which also features a three atom bridge resulting in a Ni···Ni separation of 4.2490(6) Å. Both metal centers show bond lengths and bond angles expected for Ni^{II}. The oxygen atoms of the 4-nitrobenzaldehyde nitro function coordinate both nickel centers with similar bond distances of 1.8527(11) Å for Ni(1)–O(1) and 1.8555(10) Å for Ni(2)–O(2), which is comparable to the value of 1.842(4) Å found for the Ni–O bond between the Ni^{II} ion and the formally negatively charged alcoholate oxygen in **13-cK**. This hints towards a possible twofold nitro group reduction to give a dihydroxyl aniline derivative, which is further supported by the elongation of the N–O bond distances in **14^{Bna}-cK**, when compared to free 4-nitrobenzaldehyde [d(N–O) = 1.3406(16) Å, 1.3481(16) Å vs. d(N–O) = 1.248(6) Å, 1.236(7) Å].[157] Similar to the nonreduced 4-nitrobenzaldehyde, the angles between atoms surrounding the nitro group nitrogen in **14^{Bna}-cK** are around 120°. However, although nitrogen atoms bearing the formal oxidation state -III usually adapt a tetrahedral geometry, this does not contradict the possibility of a twofold reduction, considering that in aniline derivatives the amine nitrogen atoms are also found in a trigonal planar geometry, since their nitrogen lone pair resonates into the aromatic π-system.[158] In case of the dinickel bound 4-nitrobenzaldehyde in **14^{Bna}-cK**, the donation of the electron density leads to a significant decrease in aromaticity of the benzaldehyde moiety, as indicated by the alternating C–C bond length of the six membered carbon cycle (Figure 86). A list of selected structural parameters is given in Table 12.

Table 12: Selected bond lengths [Å] and angles [°] for **14^{Bna}-cK**.

Bond Lengths [Å]		Bond Angles [°]	
Ni(1)-N(1)	1.9059(14)	**N(1)-Ni(1)-O(1)**	97.94(5)
Ni(1)-N(3)	1.8832(14)	**N(4)-Ni(1)-O(1)**	86.15(5)
Ni(1)-N(4)	1.9004(14)	**N(3)-Ni(1)-O(1)**	178.17(5)
Ni(2)-N(2)	1.9002(13)	**N(1)-Ni(1)-N(3)**	83.28(6)
Ni(2)-N(5)	1.8845(13)	**N(4)-Ni(1)-N(3)**	92.64(6)
Ni(2)-N(6)	1.8923(13)	**N(2)-Ni(2)-O(2)**	95.84(5)
Ni(1)-O(1)	1.8527(11)	**N(6)-Ni(2)-O(2)**	87.56(5)
Ni(2)-O(2)	1.8555(10)	**N(5)-Ni(2)-O(2)**	167.97(5)
O(1)-N(7)	1.3406(16)	**N(5)-Ni(2)-N(6)**	94.49(5)
O(2)-N(7)	1.3481(16)	**N(2)-Ni(2)-N(5)**	84.40(6)
C(40)-N(7)	1.331(2)	**O(1)-N(7)-O(2)**	115.92(11)
C(46)-O(3)	1.214(2)	**O(1)-N(7)-C(40)**	121.41(12)
C(46)-C(43)	1.425(2)	**O(2)-N(7)-C(40)**	122.59(12)
Ni(1)···Ni(2)	4.1439(6)	**O(3)–C(43)–C(46)**	127.83(19)

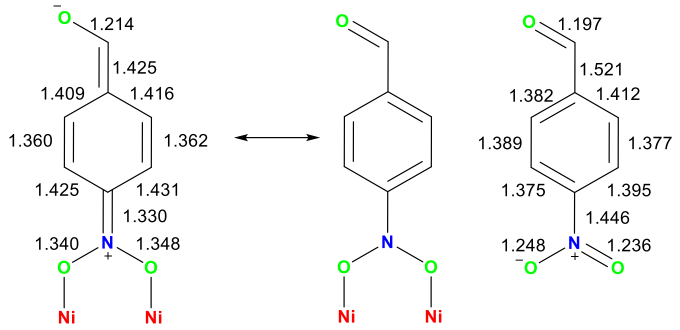

Figure 86: Comparison of the bond distances [Å] in free 4-nitrobenzaldehyde (right) and both resonance structures of the reductively bound 4-nitrobenz-aldehyde in the dinickel complex **14$^{\mathrm{Bna}}$-cK** (left).

As shown in Figure 86, the C–N bond of the 4-nitrobenzaldehyde moiety in **14$^{\mathrm{Bna}}$-cK** is significantly shortened with respect to the analogous bond distance in free 4-nitrobenzaldehyde. Although, the C–C bonds of the aryl ring in free 4-nitrobenzaldehyde are also found to alternate in length, the differences are far less pronounced than in **14$^{\mathrm{Bna}}$-cK**. Additionally, the C–C bond connecting the aldehyde function to the aryl ring is contracted, while the C–O bond is elongated, suggesting that the aldehyde function in **14$^{\mathrm{Bna}}$-cK** has significant enolate character. Therefore, the reduction of the 4-nitrobenzaldehyde moiety induces a significant structural change to compensate the additional negative charge. The increased electron density at the aldehyde function is also reflected by its reactivity. **14$^{\mathrm{Bna}}$-cK** did not react with an excess of the starting material **2-K**, showing that it was not possible to further reduce the aldehyde function.

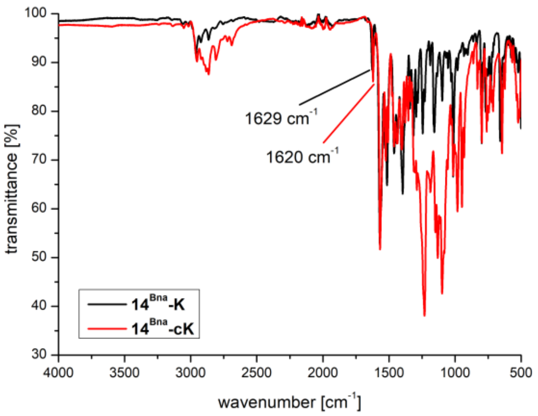

Figure 87: Stacked ATR-IR spectra of solid **14$^{\mathrm{Bna}}$-K** (black line) and **14$^{\mathrm{Bna}}$-cK** (red line).

Additional evidence for the reduction induced decrease of bond strength of the dangling aldehyde function was provided by IR spectroscopy. The IR spectra of **14$^{\mathrm{Bna}}$-K** and **14$^{\mathrm{Bna}}$-cK** are both presented in in Figure 87. For both compounds the usual C–H stretching vibrations for the ligand framework **L** are observed around 3000 cm^{-1}. In case of **14$^{\mathrm{Bna}}$-cK** additional overlapping bands of C–H vibrations of the [2.2.2]cryptand unit lead to a lower transmittance. This effect is also observed in the fingerprint region below 1600 cm^{-1}. The band at 1629 cm^{-1} in the spectrum of **14$^{\mathrm{Bna}}$-K**, which is assigned to the stretching vibration of the C–O bond within the aldehyde function, is the most indicative. The value is significantly decreased compared to the one found for free 4-nitrobenzaldehyde with 1714 cm^{-1}. This clearly reflects the proposed decrease in bond order.[159] The effect is slightly stronger for **14$^{\mathrm{Bna}}$-cK**, as the IR spectrum features the same band at a lower energy of 1620 cm^{-1}. Removal of the K$^+$ from the [$LNi_2ONC_6H_4CHO$]$^-$ anion with [2.2.2]-cryptand negates the polarizing effect of the cation on the nickel(II) bound nitro function. As a result, the quinoid form of the bound substrate shown in Figure 86, where the C–O bond has decreased bond order is more dominant in **14^{Bna}-cK**.

The general interest in selective reductions of nitro compounds highlights the reaction of 4-nitrobenzaldehyde and **2-K**. However, truly remarkable is that even in presence of a highly electrophilic group like the aldehyde function the nitro group is reduced exclusively. This chemoselectivity is underlined by good yields (61 %) of the reaction and the purity of the product which was confirmed by elemental analysis.

In order to further explore the nature of the twofold reduced nitro function and potential follow up reactivity without an interference of the aldehyde function, nitrobenzene was used as a substrate for the reaction.

6.2.2 Reductive Binding of Nitrobenzene

Adding one equivalent of dry and oxygen free nitrobenzene to a THF solution of **2-K** resulted in an immediate color change from bright orange to deep purple (Figure 88). The reaction product **14^{Ph}-K** exhibited moderate solubility in THF and benzene, but was well soluble in CH_2Cl_2, in which it was stable over several days. The same procedure was applied to **2-Na** to obtain **14^{Ph}-Na**. Crude **14^{Ph}-Na** from the reaction showed a better solubility in THF than **14^{Ph}-K**, while crystalline material was comparably soluble.

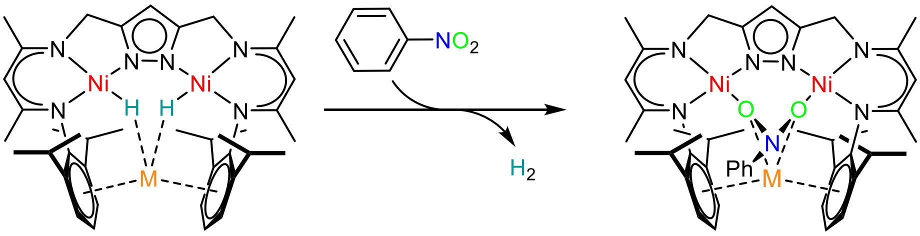

2-K
2-Na

M = K
M = Na

14^{Ph}-K
14^{Ph}-Na

Figure 88: Reaction of nitrobenzene with **2-K** or **2-Na**.

The ^{1}H NMR data of **14^{Ph}-K** suggests a C_s symmetry of the σ⊥xy-type similar to **14^{Bna}-K**, indicated by the two widely coupled doublets at 3.72 ppm und 3.63 ppm for the protons of the methylene bridge of **L**, which is only partially covered by the THF solvent signal. In the region above 6.40 ppm a total of eleven aryl bound protons are found. The most upfield shifted of these proton signals is a triplet at 6.49 ppm, which is assigned to the *para* proton of the nitrobenzene aromatic ring.

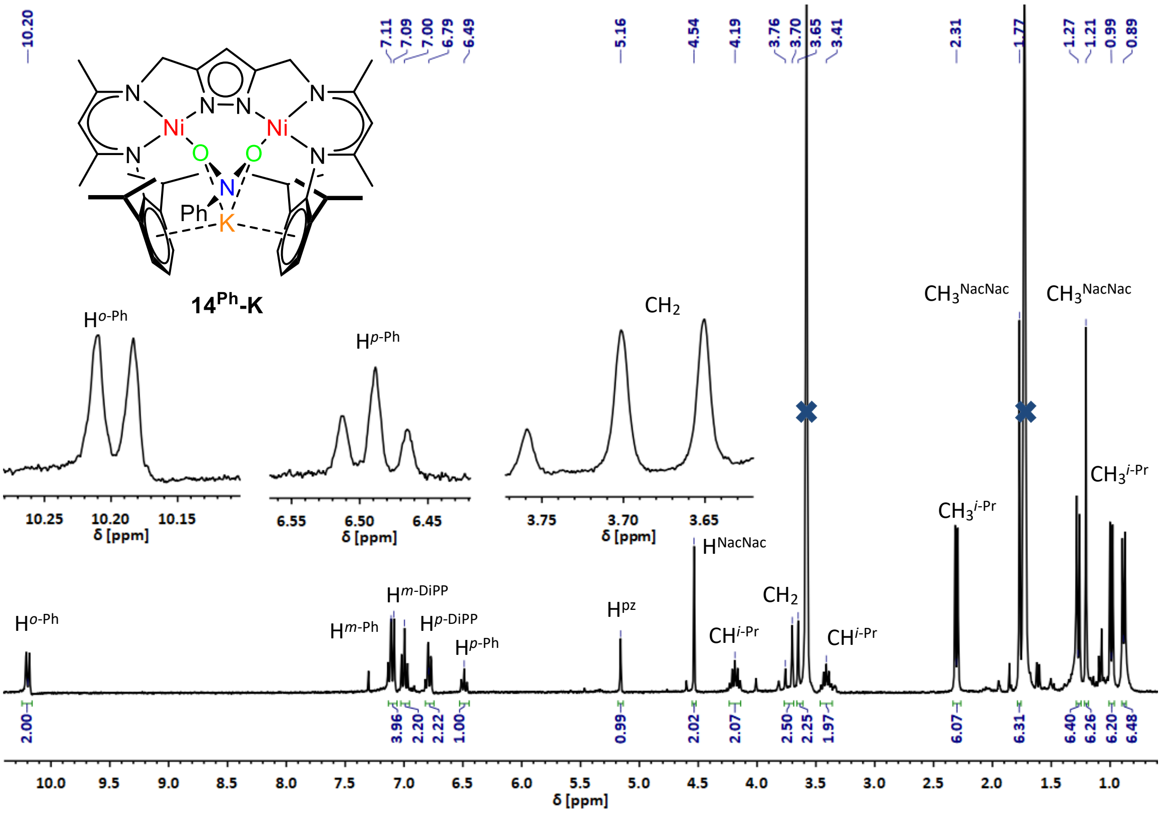

Figure 89: ^{1}H NMR spectrum of **14^{Ph}-K** in THF-d$_8$.

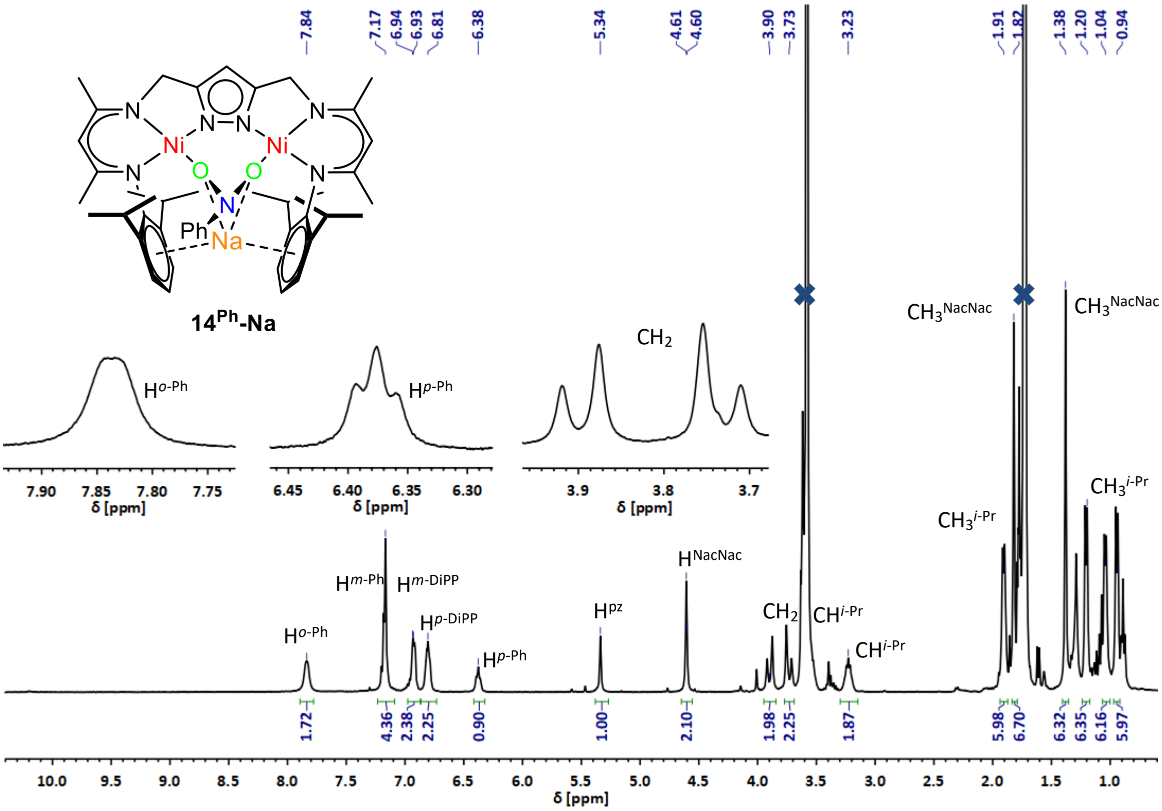

Figure 90: ^{1}H NMR spectrum of **14^{Ph}-Na** in THF-d$_8$.

The protons in *ortho* position to the nitro group experience a significant low-field shift to 10.20 ppm. Similar to what was discussed for the *ortho* proton signal of **13-K** this is potentially caused by an anagostic interaction between the aryl bound protons and the nickel centers. However, in the case of **14^{Ph}-K** this interaction seems to be pronounced, since the *ortho* protons of the nickel bound benzaldehyde moiety in **13-K** experienced a less dramatic shift of only 9.56 ppm (Figure 89).

The general signal pattern is preserved in the ^{1}H NMR spectrum of the **14^{Ph}-Na**. Nevertheless, the nitrobenzene *ortho* protons give a signal at 7.84 ppm, which is significantly different from the signal at 9.56 ppm for the respective protons in **14^{Ph}-K**, suggesting that the counterions K^+/Na^+ have a considerable impact on the electronic structure of the dinickel nitrobenzene complexes (Figure 90).

Adding NaOTf to a THF-d_8 solution of **14^{Ph}-K** did not result in any spectral changes. However, adding KPF_6 to a solution of the sodium analogue **14^{Ph}-Na** resulted in the direct formation of **14^{Ph}-K** (Figure 91). This suggested a stronger binding for K^+ compared to Na^+. Adding the corresponding cation in excess to the complex **14^{Ph}-K** or **14^{Ph}-Na** did not result in any shift of the proton signals. This indicated that both complexes **14^{Ph}-K** and **14^{Ph}-Na** are not dissociating upon being dissolved and that the solution structures are represented by a contact ion pair of K^+/Na^+ and the anionic dinickel unit.

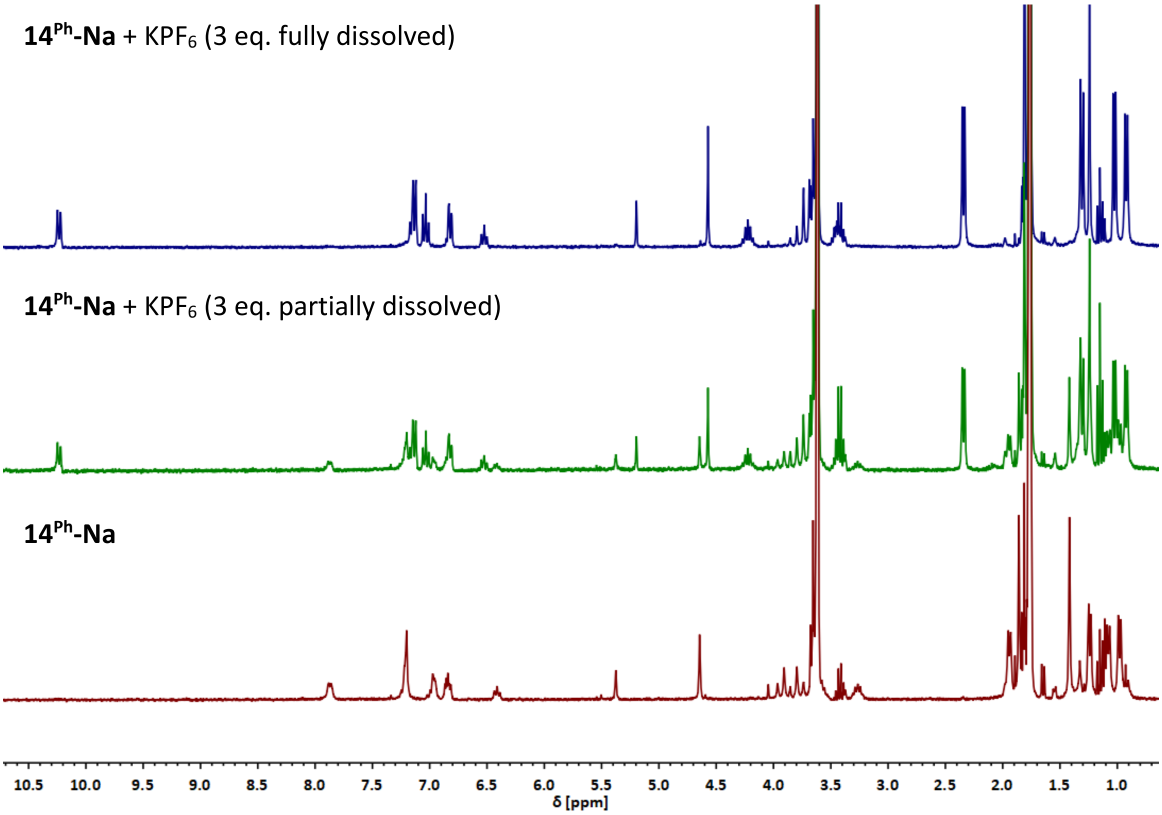

Figure 91: Stacked ^{1}H NMR spectra of **14^{Ph}-Na** + KPF_6 (3eq.) (top, blue line), **14^{Ph}-Na** + KPF_6 (3 eq., only partially dissolved) (middle, green line) and **14^{Ph}-Na** (bottom, red line) in THF-d_8.

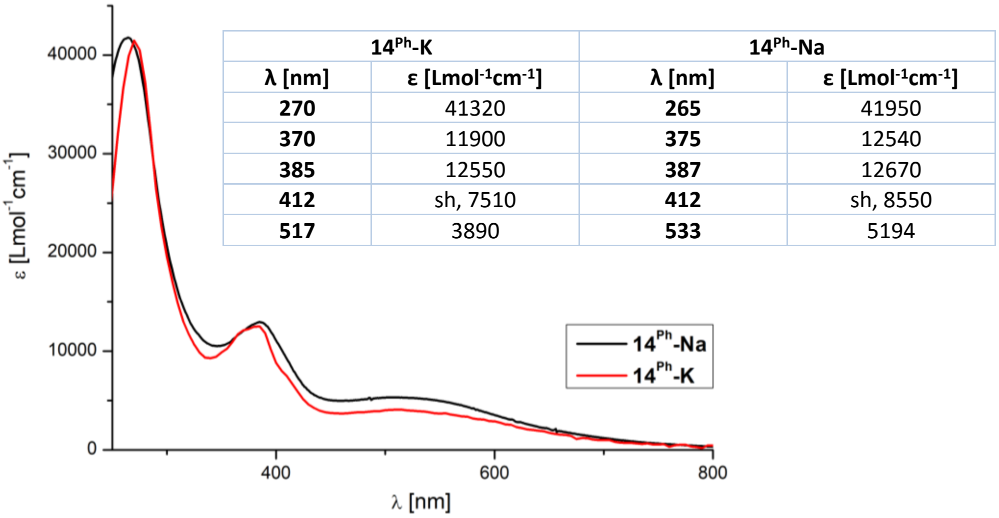

14^{Ph}-K		14^{Ph}-Na	
λ [nm]	**ε [Lmol^{-1}cm^{-1}]**	**λ [nm]**	**ε [Lmol^{-1}cm^{-1}]**
270	41320	**265**	41950
370	11900	**375**	12540
385	12550	**387**	12670
412	sh, 7510	**412**	sh, 8550
517	3890	**533**	5194

Figure 92: UV/vis spectra of **14^{Ph}-K** and **14^{Ph}-Na** in THF at room temperature and table listing the wavelength of the electronic transitions and their corresponding extinction coefficient.

The electronic absorption spectra of **14^{Ph}-K** and **14^{Ph}-Na** show only minor differences as both complexes have bands similar in wavelength and absorption. Comparable to the UV/vis spectrum of **14^{Bna}-K** an intense band at 270 nm is assigned to a LMCT between the **L**$^{3-}$ and the nickel(II) centers. The weaker transitions around 370 nm, 385 nm and 412 nm are also attributed to an electron transfer between the pyrazolate and the metals. Although, the broadness of the [PhNO$_2$]$^{2-}$ π* → Ni^{II} transition bands at 517 nm for **14^{Ph}-K** and 533 nm for **14^{Ph}-Na** makes an exact comparison between these features difficult, the counterion influence on the electronic transition seems minimal. The features differ largely in their shape and intensity compared to the respective transition in the spectrum of **14^{Bna}-K**. The band for the aldehyde functionalized derivative appears at a higher wavelength of 588 nm and with a higher extinction coefficient of 8170 Lmol^{-1}cm^{-1}. This is potentially caused by the extension of the π-system of the bound nitro substrate by the electron withdrawing carbonyl function, which could lead to an energetic stabilization of the occupied π* orbitals and consequently to a lower energy gap between the Ni^{II} d orbitals and the π* orbitals. As a result, the transition has a maximum at higher wavelength.

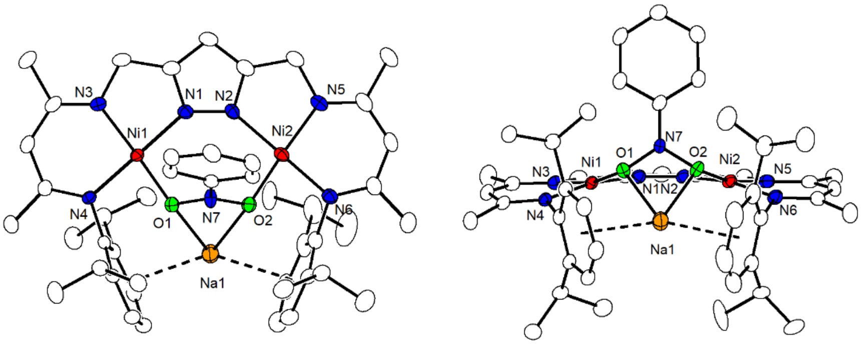

Figure 93: Top (left) and front (right) view of the molecular structure of **14^{Ph}-Na**. Solvent molecules and hydrogen atoms are omitted for clarity.

The better solubility of crude **14^{Ph}-Na** allowed to obtain single crystals from slow diffusion of hexane into a THF solution of the complex. XRD analysis of the material showed the identical triclinic unit cell $P\bar{1}$ for **14^{Ph}-Na** as for the aldehyde functionalized complex **14^{Bna}-cK**. However, in contrast to what is found for the potassium [2.2.2]cryptate containing complex **14^{Bna}-cK**, in the molecular structure of **14^{Ph}-Na** the Na$^+$ counterion is encapsulated in between the flanking aromatic rings of β-diketiminate units of the ligand with a distance of 2.7107(14) Å and 2.7035(15) Å between the Na$^+$ and the centroids of the rings. Additionally, the cation is coordinated by the oxygen atoms of the nitro function with distances of 2.313(2) Å and 2.304(2) Å. The twist of the aryl units induced by the coordination Na$^+$ results in larger separation of the metal centers for the complex when compared to **14^{Bna}-cK** [d(Ni···Ni) = 4.2411(6) Å vs. 4.1439(6) Å]. Both nickel coordination environments resemble a square planar geometry with bond lengths and bond angles typical for Ni^{II} complexes of **L**. Similar to **14^{Bna}-cK**, the aryl nitro compound is coordinating *via* a three membered bridging NO_2 unit in a μ-κO,κO′ mode. The nitrobenzene phenyl substituent aligns with the nitro group and is directed almost orthogonal to the coordination plane of the metal centers and reaches in the opposite direction of the Na$^+$ [∡ = 83.7°]. As already discussed for **14^{Bna}-cK** the nitrogen of the aryl substituted nitro compound is surrounded by angles close to 120° and therefore has a trigonal planar geometry. The Ni–O bond distances are with 1.350(5) Å and 1.355(5) Å significantly shorter than the analogous bonds in **14^{Bna}-cK** [d(Ni–O) = 1.8527(11) Å, 1.8555(10) Å], indicating stronger interaction between the bimetallic binding site and the substrate. This is also reflected by the in contrast to **14^{Bna}-cK** slightly elongated N–O bonds [d(N–O) = 1.350(3) Å, 1.355(3) Å vs. 1.3406(16) Å, 1.3481(16) Å]. As the absence of an electron withdrawing substituent at the aromatic ring might contribute to this, the main reason for the stronger substrate activation is probably the association of the $[RNO_2]^{2-}$ unit with the Lewis acidic Na$^+$. As the bond weakening influence of K$^+$ was already described for **13-K**, it seems likely that Na$^+$ has a similar effect when being located in close proximity to the bimetallic pocket. However, since the carbonyl function is not present in **14^{Ph}-Na** the partial loss of aromaticity within the benzaldehyde unit of **14^{Bna}-cK** is not observed for the phenyl substituent of the bound nitrobenzene. Similar to what was discussed above for **14^{Bna}-cK**, the unfunctionalized analogue **14^{Ph}-Na** can be described as a dinickel complex coordinated by twice deprotonated aryl dihydroxylamine, which represents **c**$^{2-}$ in the nitrobenzene reduction pathway displayed in Scheme 21. Structural parameters of **14^{Ph}-Na** are listed in Table 13.

Table 13: Selected bond lengths [Å] and angles [°] for **14^{Ph}-Na**.

Bond Lengths [Å]		Bond Angles [°]	
Ni(1)-N(1)	1.900(2)	**N(1)-Ni(1)-O(1)**	96.82(8)
Ni(1)-N(3)	1.885(2)	**N(4)-Ni(1)-O(1)**	86.44(8)
Ni(1)-N(4)	1.908(2)	**N(3)-Ni(1)-O(1)**	167.62(8)
Ni(2)-N(2)	1.913(2)	**N(1)-Ni(1)-N(3)**	85.40(9)
Ni(2)-N(5)	1.881(2)	**N(4)-Ni(1)-N(3)**	93.51(9)
Ni(2)-N(6)	1.907(2)	**N(2)-Ni(2)-O(2)**	97.70(8)
Ni(1)-O(1)	1.8657(17)	**N(6)-Ni(2)-O(2)**	85.82(8)
Ni(2)-O(2)	1.8614(17)	**N(5)-Ni(2)-O(2)**	167.94(9)
O(1)-N(7)	1.350(3)	**N(5)-Ni(2)-N(6)**	93.65(9)
O(2)-N(7)	1.355(3)	**N(2)-Ni(2)-N(5)**	85.00(9)
C(42)-N(7)	1.358(3)	**O(1)-N(7)-O(2)**	113.90(19)
Na(1)-O(1)	2.313(2)	**O(1)-N(7)-C(42)**	123.2(2)
Na(1)-O(2)	2.304(2)	**O(2)-N(7)-C(42)**	122.4(2)
Na(1)–Aryl(1)	2.7107(14)	**Ni(1)-O(1)–Na(1)**	124.91(9)
Na(1)–Aryl(2)	2.7035(15)	**Ni(2)-O(2)–Na(1)**	123.68(9)
Ni(1)···Ni(2)	4.2411(6)	**Aryl(1)–Na(1)–Aryl(2)**	140.42(5)

The IR spectra of **14^{Ph}-K** and **14^{Ph}-Na** show the typical bands for the C–H stretching vibrations of the ligand framework **L** between 3060 cm^{-1} and 2760 cm^{-1}. As expected, there is no band around 1630 cm^{-1} like it was observed for the spectra of **14^{Bna}-K** and **14^{Bna}-cK**, confirming that this band originates from the C=O vibration of the aldehyde function (Figure 87). Besides minor differences in intensity the spectra of the alkali metal derivatives **14^{Ph}-K** and **14^{Ph}-Na** are almost identical, suggesting that the counterion only has limited effect on the bond strength within the reduced nitrobenzene substrate. However, due to multiple overlaps of resonances in the fingerprint region below 1000 cm^{-1} this is hard to evaluate (Figure 94).

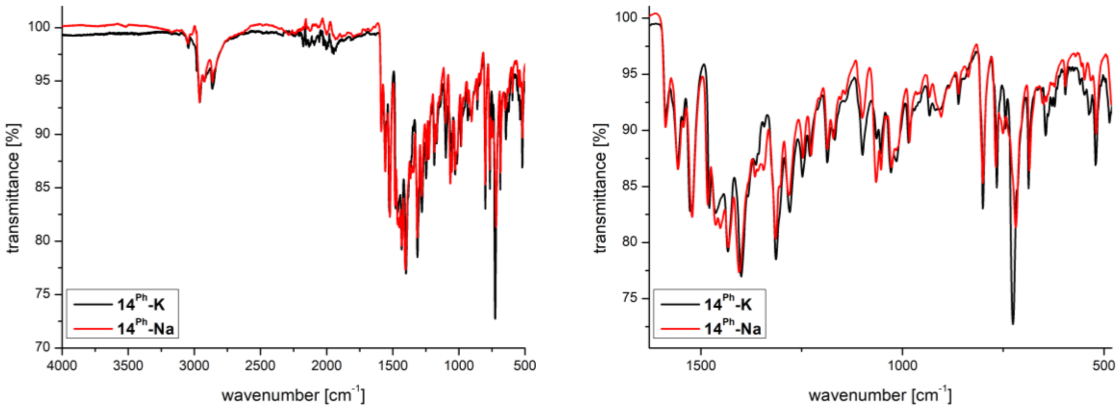

Figure 94: Stacked ATR-IR spectra of solid **14^{Ph}-K** (black line) and **14^{Ph}-Na** (red line) from 4000 cm^{-1} to 500 cm^{-1} (left) and from 1600 cm^{-1} to 500 cm^{-1} (right).

6.2.3 Formal Deoxygenation of the Dinickel Nitrobenzene Complex 14^{Ph}-K

In order to investigate the counterion influence on the dinickel complex moiety further, the interaction of the K^+ with the $[LNi_2O_2NPh]^-$ core was suppressed by binding it into the cavity of [2.2.2]cryptand. Adding [2.2.2]cryptand to a solution of **14^{Ph}-K** resulted in an immediate color change from purple to cyan. Surprisingly, this resulted in three new species, as indicated by three close but distinct NMR signals for protons of the pyrazolate unit at 5.47 ppm, 5.28 ppm and 5.26 ppm. The signals of the species with a pyrazolate proton resonance at 5.47 ppm were assigned to **3**, which was only present in small amounts of approximately 8 %. The remaining complexes are found in a relative ratio of approximately 2:1 to each other. The initial ratio did not change over a period of three days and even after heating at 60 °C only showed minor changes (Figure 95).

Singlets at 4.43 ppm, 4.41 ppm and 4.40 ppm were attributed to the α-protons of the β-diketiminate units. As one of these singlets belonged to the minor species, the other two were assigned to the major species indicating that both nickel centers within the complex no longer share a common coordination by the nitrobenzene oxygen atoms like in **14^{Ph}-K**. Although, it was not possible to identify the symmetry of the complexes by the coupling patterns of the proton signals for the methylene bridge between the pyrazolate moiety and the β-diketiminate units, due to the overlap of multiple signals in the region between 3.95 ppm and 3.70 ppm, four different resonances for the secondary protons of the isopropyl groups of the β-diketiminate units at 4.61 ppm, 3.47 ppm, 3.15 ppm and 3.06 ppm indicated a C_1 symmetry for the major species similar to **13-K**. The compound was identified as **15^{Ph}-cK**, as the proton shifts matched the ones found for the pure compound published previously (Figure 95).[155] This was also confirmed by XRD analysis of crystals of **15^{Ph}-cK** manually selected from a mixture obtained from slow diffusion of hexane into a solution of the reaction mixture that had been washed with hexane. The minor species showed only two signals for the secondary protons of the isopropyl groups at and 4.29 ppm and 3.41 ppm suggesting a C_s symmetry like in **14^{Ph}-K**. Although, the proton shifts were different from the ones found for **14^{Ph}-K**, the general signal pattern was preserved in the ^{1}H NMR spectrum suggesting that the dinickel complex moiety remained intact. The signal shifts were probably caused by the [2.2.2]cryptand induced abstraction of the K^+, like it was observed for compound **13-cK** earlier. However, since it was not possible to isolate pure **14^{Ph}-cK**, no direct comparison was made.

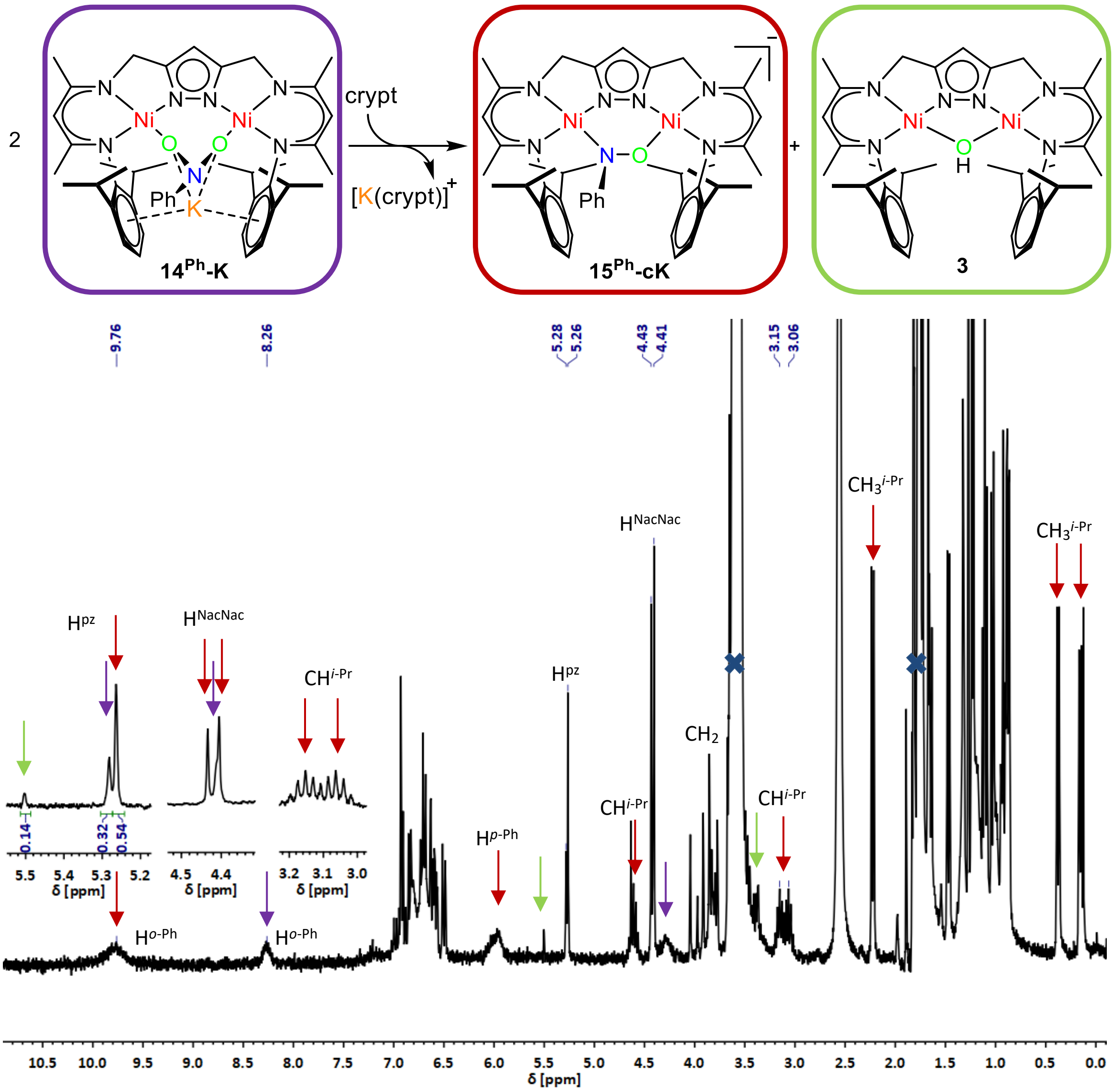

Figure 95: Degradation of **14$^{\text{Ph}}$-K** upon addition of [2.2.2]cryptand (top) and corresponding the ^{1}H NMR spectrum in THF-d$_8$. Selected signals of **14$^{\text{Ph}}$-cK** (purple) and **15$^{\text{Ph}}$-cK** (red) are marked arrows. Solvent signals are marked by a blue cross.

These results indicated that the removal of the K$^+$ with [2.2.2]cryptand from the dinickel complex moiety induced a degradation to **15$^{\text{Ph}}$-cK**, which formally can be described as a twice deprotonated hydroxylamine (**e**$^{2-}$ in Scheme 21). To exclude the possibility of a reaction with minor impurities in the used [2.2.2]cryptand, the same reaction was carried out with a crown ether. Monitoring the reaction of **14$^{\text{Ph}}$-K** with dibenzo-18-crown-6 by ^{1}H NMR did not show any conversion of the complex. However, this was attributed to the weaker affinity of dibenzo-18-crown-6 to encapsulate the K$^+$ compared to [2.2.2]cryptand. Exchange of the Lewis acidic K$^+$ with the weakly coordinating bis(triphenylphosphine)iminium cation by adding the corresponding chloride salt to a solution of **14$^{\text{Ph}}$-K** in THF resulted in the same color change from purple to cyan, that was observed for the reaction with [2.2.2]cryptand. The ^{1}H NMR of the reaction mixture showed six different species including one with two different proton signals for the α-protons of the β-diketiminate units similar to **15$^{\text{Ph}}$-cK**.

As already discussed above, the nitrobenzene unit in **14$^{\text{Ph}}$-K** and the nitrosobenzene unit in **15$^{\text{Ph}}$-K** both are best described as twofold reduced. Consequently, the transformation of **14$^{\text{Ph}}$-K** to **15$^{\text{Ph}}$-K** corresponds to a formal loss of an oxygen atom. As an elimination of molecular O_2 seems unlikely the possibility of a further reduction of **14^{Ph}-K** and a subsequent abstraction of a O^{2-} will be further evaluated. An indication for this kind of degradation mechanism is the concomitant generation of **3** in the reaction. This points towards a formal disproportionation mechanism taking place during the reaction. Hence, the abstraction of the K^+ from the complex moiety induces a reduction of the nitrobenzene moiety to nitrosobenzene forming **3** in the process. Released nitrosobenzene then reacts with **14^{Ph}-cK** to the observed dinickel nitroso complex **15^{Ph}-cK**. (Scheme 23).

The abrupt end of the degradation progress of **14^{Ph}-K** in presence of [2.2.2]cryptand, is probably caused by the limited availability of trace protons present in the reaction mixture that are required for the formation of **3**. However, the absence of proton signals for free nitrobenzene in the ^{1}H NMR spectrum contradicts this mechanism.

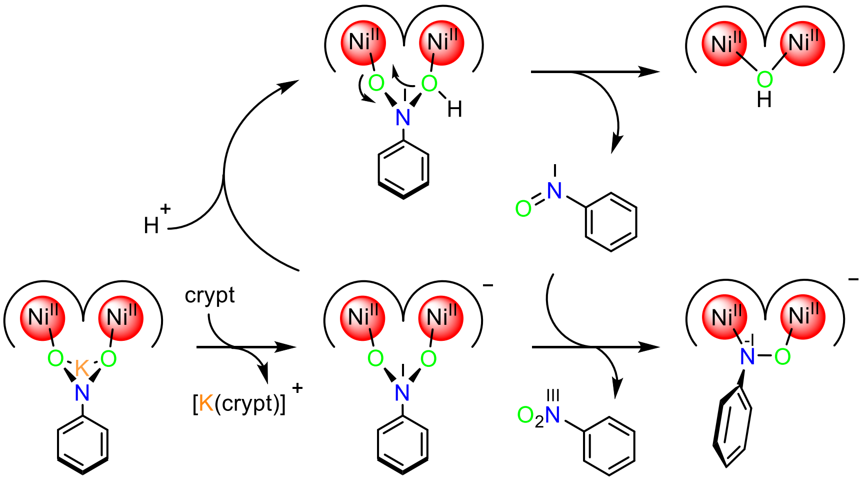

Scheme 23: Proposed mechanism for the formation of **15^{Ph}-K** out of **14^{Ph}-K**.

The role of the proton was further investigated by treating **14^{Ph}-K** directly with one equivalent of HLutOTf. An *in situ* ^{1}H NMR experiment showed the formation of several species. Due to overlapping and in some cases broadness of the proton signals none of the compounds was identified. However, the subsequent addition of [2.2.2]cryptand resulted in the formation of **3** and **15^{Ph}-H** as indicated by comparison with reported ^{1}H NMR data.[155] Both complex species were found in an approximate ratio of 1:1 to each other. In addition, the formation of free nitrobenzene was observed in the ^{1}H NMR spectrum (Figure 96). These observations point towards the mechanism shown in Scheme 23 where nitrosobenzene is formed by protonation of **14^{Ph}-cK** accompanied by the generation of **3**. Nitrosobenzene then substitutes the nitrobenzene moiety of **14^{Ph}-K** to form the thermodynamically preferred **15^{Ph}-cK.** In contrast to the reaction shown in Figure 95 the product of the protonation of **14^{Ph}-K** in presence of [2.2.2]cryptand is **15^{Ph}-H** which derives from the protonation of initially formed **15^{Ph}-cK**. This shows that a clean conversion of **14^{Ph}-K** to **15^{Ph}-cK/H** and **3** not only requires a proton source but also the abstraction of the K^+. Suppressing the ion pair assembly between K^+ and the dinickel bound substrate moiety probably increases the affinity of the anionic complex unit to accept a proton.

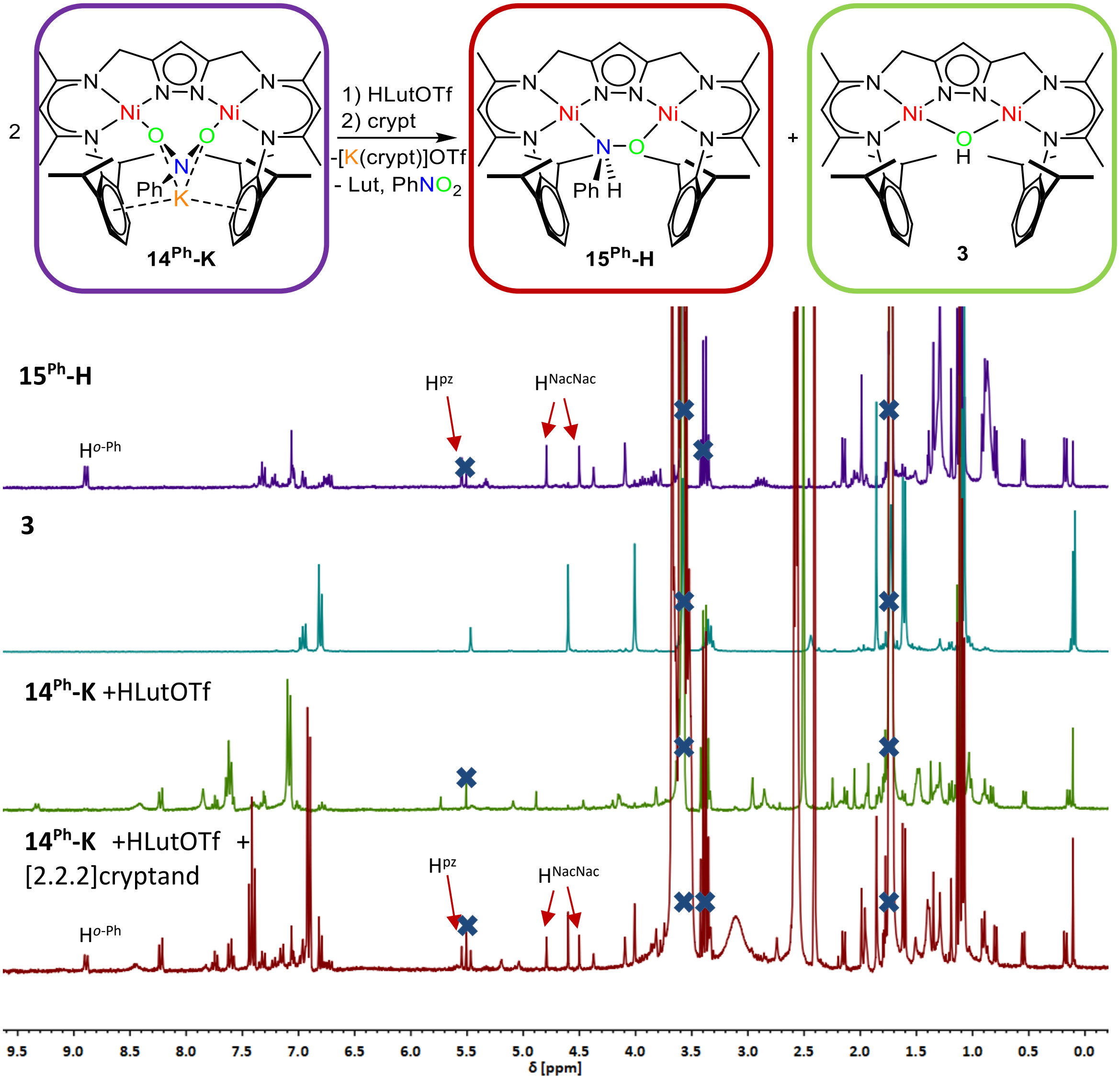

Figure 96: Reaction of **14^{Ph}-K** with HLutOTf and [2.2.2]cryptand (top) and stacked ^{1}H NMR spectra of **15^{Ph}-H** (purple line), 3 (cyan line), the reaction mixture of **14^{Ph}-K** with [HLut]OTf (green line), and reaction mixture of **14^{Ph}-K** with [HLut]OTf after the addition of [2.2.2]cryptand (red line) in THF-d_8 (bottom). Solvent signals are marked by a blue cross.

As reagent fulfilling both requirements for the conversion of **14^{Ph}-K**, 3,5-di-*tert*-butylcatechol (3,5-DCTB) was chosen since the deprotonated catechol readily forms alkali metal complexes for the necessary K^+ abstraction.[160] For the reaction a suspension of **14^{Ph}-K** was treated with one equivalent of the catechol and stirred for 1 h at room temperature to undergo a color change from purple to brown. The solvent was removed *in vacuo* and the residue was washed with hexane and analyzed by ^{1}H NMR spectroscopy.

The spectral data showed a complete consumption of the starting material **14^{Ph}-K** since the characteristic signals at 10.19 ppm for the *ortho* protons of the nitrobenzene unit or the pyrazolate proton at 5.16 ppm were not retained in the spectrum of the reaction mixture. The pyrazolate proton signal at 5.46 ppm and the high-field shifted hydroxide proton at -7.26 ppm indicated the presence of **3** in the product mixture. Additional signals between 8.3 ppm and 7.5 ppm were attributed to free nitrobenzene. The residual signal set belonged to one species that showed two singlets for the α-protons of the β-diketiminate subunit of the ligand, indicating a different coordination for the Ni^{II} centers as in **15^{Ph}-K**. Similar to the reaction of **14^{Ph}-K** with

HLutOTf in presence of [2.2.2]cryptand the signal shifts matched the ones reported for **15^{Ph}-H**. (Figure 97).

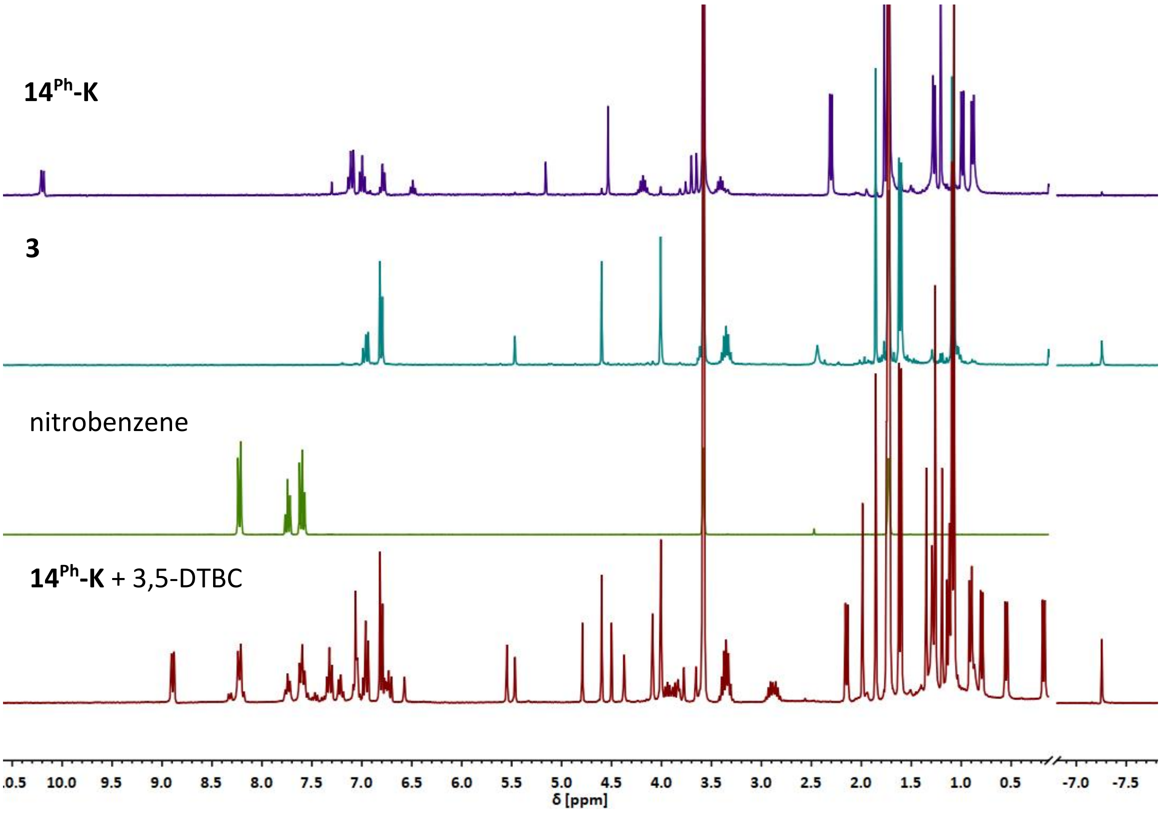

Figure 97: Stacked ^1H NMR spectra of **14^{Ph}-K** (purple line), **3** (cyan line), nitrobenzene (green line) and the reaction mixture of **14^{Ph}-K** and 3,5-DTBC after workup (red line) in THF-d_8.

Based on this data the reaction follows the mechanism displayed in Scheme 23 with the exception that the produced catecholate binds the K^+ instead of additional [2.2.2]cryptand. The approximate 1:1 ratio between **3** and **15^{Ph}-H** found for the reaction of **14^{Ph}-K** with HLutOTf and [2.2.2]cryptand is also found in the reaction mixture of **14^{Ph}-K** and 3,5-DTCB. However, since ^1H NMR data was collected from a sample after a workup, the determined ratio potentially deviates from the actual ratio deriving from the reaction. This transformation corresponds to the first N-O bond cleaving step in the nitrobenzene reduction displayed in Scheme 21 where dihydroxyl aniline (**c**H_2) is converted to hydroxyl aniline (**e**H^-) (Scheme 24). In the case of **14^{Ph}-K** the protonation triggers a disproportionation following the reaction equation: $2\ \mathbf{c}^{2-} + 2\ H^+ \rightarrow \mathbf{e}H^- + \mathbf{a} + OH^-$.

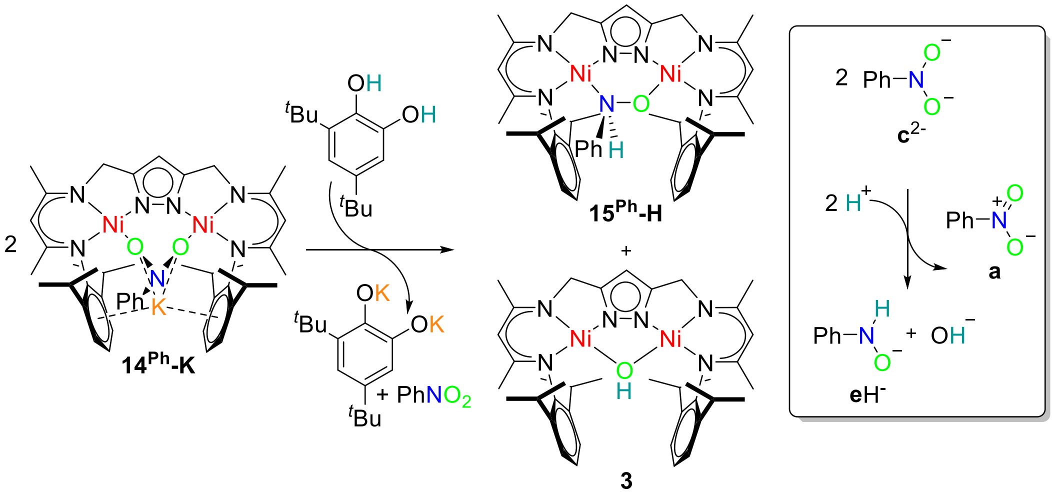

Scheme 24: Reaction of **14^{Ph}-K** with 3,5-DTBC and the corresponding transformation in the nitrobenzene reduction mechanism.

In order to provide deeper insight into the redox conversion of **14^{Ph}-K** to **15^{Ph}-K**, the electrochemical potentials of **14^{Ph}-K** were determined by a cyclic voltammetry (CV) experiment.

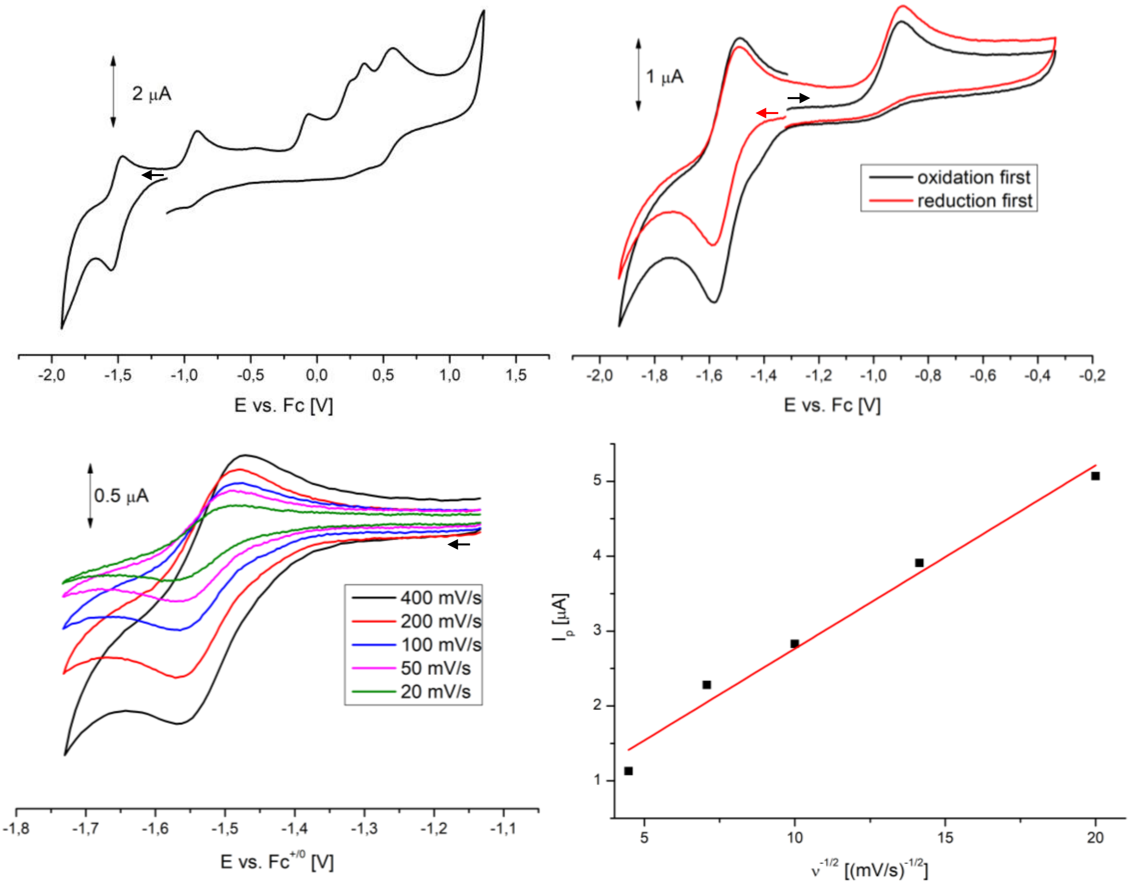

Figure 98: Cyclic voltammogram of compound **14^{Ph}-K** recorded in CH_2Cl_2 at room temperature measured at 100 mV/s scan rate (top, left), around the reversible reduction wave around E = -1.51 V and the first oxidation wave around E = -0.90 V at 100 mV/s scan rate (top, right), the reversible reduction wave around E = -1.51 V measured at different scan rates (bottom, left) and the intensity of the reversible reduction plotted *vs.* the square root of the scan rate.

Due to limited solubility of **14^{Ph}-K** in THF the electro chemistry measurements were performed in CH_2Cl_2 with NBu_4PF_6 (0.1 M) as an electrolyte. Values were referenced against the Fc/Fc^+ redox couple after a post measurement correction of the potentials against the internal standard $FeCp*_2$/ $[FeCp*_2]^+$ to prevent interference with the complex redox processes.[129] All cyclic voltammograms were recorded under inert conditions in a nitrogen atmosphere glovebox at room temperature.

The CV of **14^{Ph}-K** features only one wave in the reductive regime at $E_{1/2}$ = -1.51 V within the scan range permitted by the solvent. The reduction appears to be reversible according to the linear relation between peak intensity and the square root of the scan rate and is similar to the first reduction event found for **1^{Br}** ($E_{1/2}$ = -2.26 V). However, it remains unclear, if the reduction is metal based. The first oxidation event at E_{pos} = -0.90 V is a represented by an irreversible redox wave. When the oxidation regime is scanned prior to the reduction, the reductive wave increases in intensity. This presumably indicates that the nitrobenzene moiety is involved in the single oxidation process by a transition of $[PhNO_2]^{2-} \rightarrow [PhNO_2]^-$. The additional oxidation features above a potential of E = 0 V are probably related to oxidations on the pyrazolate bis(β-diketiminate) ligand or a further oxidation of the nitrobenzene moiety, *viz.* $[PhNO_2]^- \rightarrow [PhNO_2]$ (Figure 98).

Due to the low potentials required for the reduction, attempts to convert **14^{Ph}-K** cleanly to **15^{Ph}-K** requires strong reductants such as KC_8 and sodium naphthalenide in THF. However, these reactions only led to the reisolation of **14^{Ph}-K** as well as a partial decomposition. Other experiments to abstract one of the nitro group oxygen atoms involved the use of oxophilic reagents like PPh_3, PMe_3, $[Cu(NCMe)_4]ClO_4$ and KBn, which in case of the phosphines showed no reaction and in case of $[Cu(NCMe)_4]ClO_4$ and KBn led to decomposition. As the further reduction of an already twice reduced $[PhNO_2]^{2-}$ moiety proved to be difficult, following approaches of the reduction included coupling it to a protonation; hence, performing an H atom transfer. The obvious chemical for such a reaction was H_2, since it essentially provides two electrons and two protons. However, monitoring the conversion by ^1H NMR revealed a slow formation of **3** after 18 h. This seemed unsurprising, as the coupling product of the reaction was H_2O, which readily reacts with **14^{Ph}-K** or **15^{Ph}-K** to **3**. In an *in situ* NMR experiment an excess of the H atom transfer reagent TEMPO-H led to no reaction with **14^{Ph}-K**. Hydride transfer reagent as $KHBEt_3$ or $PhSiH_3$ did not show any reactivity towards **14^{Ph}-K**. Also, more electrophilic reagents like the protic $(EtO)_3SiH$ showed no conversion, while the Lewis acidic $BH_3 \cdot THF$ led to the formation of several unidentified products.

Reactions that did not aim towards the reduction of **14^{Ph}-K** as for example the oxidation with $[FeCp*_2]PF_6$ led to decomposition and mainly the formation of **3**.

6.2.4. Reductive Binding of Nitromethane

With respect of the counterion dependent stability of the $[RNO_2]^{2-}$ moiety, the substrate scope was extended to nitromethane in order to further evaluate the influence of the substituent. Treating a THF solution of **2-Na** with one equivalent of nitromethane at room temperature results in an immediate color change from orange to deep red accompanied by the evolution of H_2. In an ESI-MS experiment of a fresh solution of the product a peak with *m/z* 806.4 was assigned to $[LNi_2O_2NCH_3 + Na]^+$ (Figure 99). This suggests the binding of one nitromethane molecule to the bimetallic cleft resulting in **14^{Me}-Na** similar to what was found for the $PhNO_2$ substrate. The same procedure was applicable to **2-K** yielding **14^{Me}-K** (Figure 100).

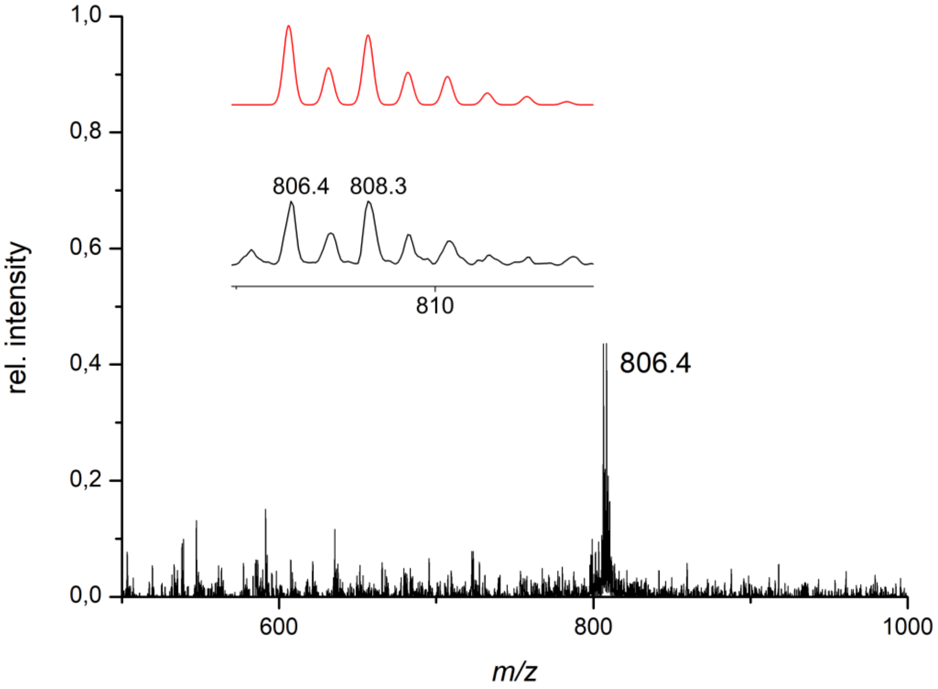

Figure 99: ESI$^+$ mass spectrum of **14^{Me}-Na** in THF. The inset shows the experimental (black line) and the simulated (red line) isotope pattern for the major peak around *m/z* = 806.4 $[M^- + Na]^+$.

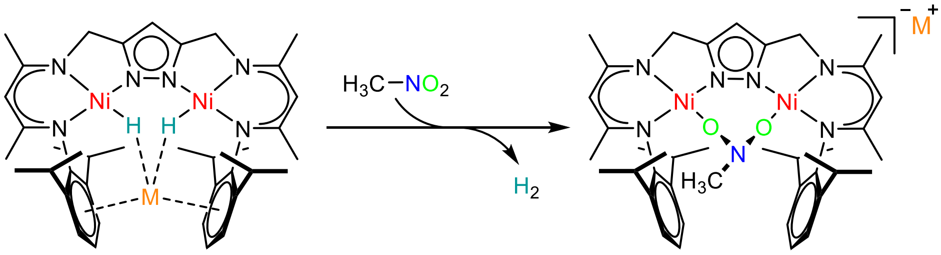

2-K
2-Na

M = K
M = Na

14^{Me}-K
14^{Me}-Na

Figure 100: Reaction of **2-K** with nitromethane to give **14^{Me}-K**.

Single crystals of **14^{Me}-Na** and **14^{Me}-K** suitable for X-ray diffraction analysis were obtained within a few days by slow diffusion of hexane into a THF solution of the product at -35 °C. Crystalline material of **14^{Me}-K** is stable at -35 °C for several weeks but decomposes at room temperature.

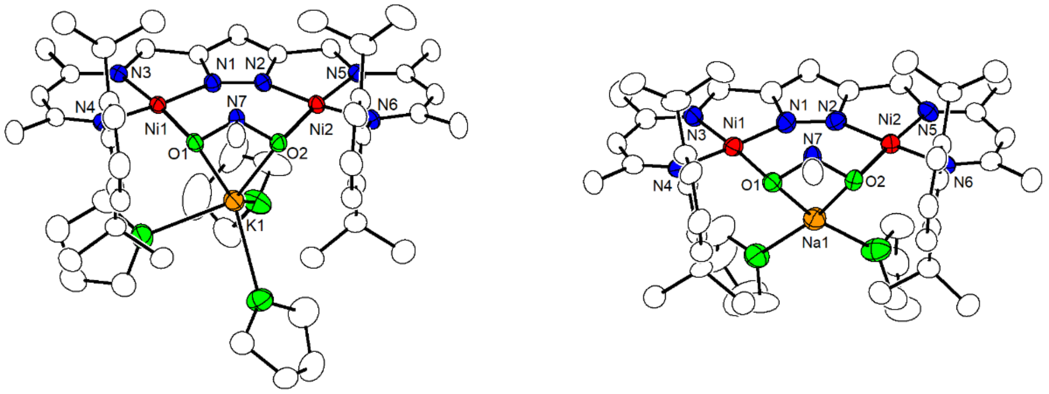

Figure 101: Molecular structures of **14^{Me}-K** (left) and **14^{Me}-Na** (right). Hydrogen atoms and non-coordinated solvent molecules (THF) are omitted for clarity.

In solid state complex **14^{Me}-K** is found in the triclinic unit cell P $\bar{1}$ and features a Ni···Ni distance of 4.3436(3) Å, which is significantly longer than the respective distances found for **14^{Ph}-Na** and **14^{Bna}-cK** [4.2411(6) Å, 4.1439(6) Å]. Both metal centers show typical bond lengths and bond angles for low spin nickel(II) in a square planar coordination. The [CH$_3$NO$_2$] unit bridges them in a *μ*-*κ*O,*κ*O′ binding mode similar to the aryl substituted nitro compounds in the dinickel complexes **14^{Ph}-Na** and **14^{Bna}-cK**. However, in strong contrast to them the oxygen bound N7 is not found to be trigonal planar, but adapts a pyramidal geometry with a significant smaller angle of 106.15(12)° for O1−N7−O2 compared to free nitromethane [124.1(4)°][161] or to the aryl derivatives **14^{Ph}-Na** and **14^{Bna}-cK** [113.90(19)°, 115.92(11)°]. Additionally, the angles between the methyl substituent and the oxygen atoms are with 103.60(13)° and 104.46(13)° in the range of the tetrahedral bond angle of 109.5°. Furthermore, the N−O bond lengths for O1−N7 and O2−N7 are with 1.4298(19) Å and 1.4284(19) Å significantly longer than in nitromethane [1.198(6) Å, 1.226(7) Å],[161] respectively, and comparable to the length of the N−O single bond in hydroxylamine [d(N−O) = 1.476(3) Å].[162] The [CH$_3$NO$_2$]$^{2-}$ dianion binds to the nickel(II) centers *via* both oxygen atoms, while the nitrogen lone pair reaches out of the complex plane and remains uninvolved in any coordination. The methyl group is directed towards the space between the two flanking aryl substituents of the β-diketiminato units and has essentially the same N−C bond length to the nitrogen atom as its analogue in nitromethane [d(N−O) = 1.478(2) Å vs. 1. 481(3) Å].[161] The K$^+$ in the molecular structure of **14^{Me}-K** is located in the opposite direction of the nitro group nitrogen atom, coordinated by the two oxygen atoms in addition to three molecules of THF. This stands in contrast to what was found for the solid state structure of **14^{Ph}-Na** where the Na$^+$ is encapsulated between the aromatic rings of the β-diketiminato units, and therefore results in longer distances between the Lewis acidic cation and the oxygens [2.6734(13) Å, 2.7289(13) Å vs. 2.313(2) Å, 2.304(2) Å].

Table 14: Selected bond lengths [Å] and angles [°] for **14^{Me}-K** and **14^{Me}-Na**.

Bond Lengths [Å]	K	Na	Bond Angles [°]	K	Na
Ni(1)-N(1)	1.9391(15)	1.939(5)	**N(1)-Ni(1)-O(1)**	95.14(6)	93.8(2)
Ni(1)-N(3)	1.9003(15)	1.884(5)	**N(4)-Ni(1)-O(1)**	87.54(6)	88.9(2)
Ni(1)-N(4)	1.9213(15)	1.930(5)	**N(3)-Ni(1)-O(1)**	171.57(6)	172.8(2)
Ni(2)-N(2)	1.9277(15)	1.939(5)	**N(1)-Ni(1)-N(3)**	84.65(6)	85.3(2)
Ni(2)-N(5)	1.8979(14)	1.883(5)	**N(4)-Ni(1)-N(3)**	93.05(6)	92.2(2)
Ni(2)-N(6)	1.9090(15)	1.922(5)	**N(2)-Ni(2)-O(2)**	94.64(6)	94.4(2)
Ni(1)-O(1)	1.8255(12)	1.835(4)	**N(6)-Ni(2)-O(2)**	88.76(6)	87.2(2)
Ni(2)-O(2)	1.8351(12)	1.824(4)	**N(5)-Ni(2)-O(2)**	170.94(6)	173.9(2)
O(1)-N(7)	1.4298(19)	1.431(6)	**N(5)-Ni(2)-N(6)**	92.39(6)	93.5(2)
O(2)-N(7)	1.4284(19)	1.433(6)	**N(2)-Ni(2)-N(5)**	84.96(6)	85.0(2)
C(40)-N(7)	1.478(2)	1.480(8)	**O(1)-N(7)-O(2)**	106.15(12)	105.4(4)
M(1)-O(1)	2.6734(13)	2.319(5)	**O(1)-N(7)-C(40)**	103.60(13)	103.7(5)
M(2)-O(2)	2.7289(13)	2.299(5)	**O(2)-N(7)-C(40)**	104.46(13)	104.0(5)
Ni(1)···Ni(2)	4.3436(3)	4.3832(12)	**Ni(1)-O(1)–M(1)**	97.68(5)	96.06(19)
			Ni(2)-O(2)–M(1)	100.75(5)	94.14(19)

As already mentioned, replacing **2-K** by **2-Na** led to similar color change from orange to deep red when reacted with nitromethane. Comparing both molecular structures, shows that the bond distances within the dinickel complexes moiety of **14^{Me}-K** and **14^{Me}-Na** are essentially equivalent. Notable differences are found for the $[CH_3NO_2]^{2-}$ bound to the cations. While in **14^{Me}-K** the K^+ is coordinated by three THF molecules, the analogue Na^+ in **14^{Me}-Na** is only coordinated by two. This causes a significant difference in distance between the alkali metal ions and the nitromethane oxygen atoms [2.299(5) Å, 2.319(5) Å for Na^+ vs. 2.6734(16) Å, 2.7289(13) Å for K^+] and consequently suggests a stronger association of the Na^+ cation with the $[LNi_2O_2NCH_3]^-$ anion of **14^{Me}-Na** compared with the K^+ analogue in **14^{Me}-K**. The molecular structures of **14^{Me}-K** and **14^{Me}-Na** are presented in Figure 101, and selected bond distances and angles are listed in Table 14. Bond angles and bond lengths around the N7 indicate that the $[H_3CNO_2]^{2-}$ bridge between the nickel(II) ions is best described as a doubly deprotonated dihydroxyl methyl amine.

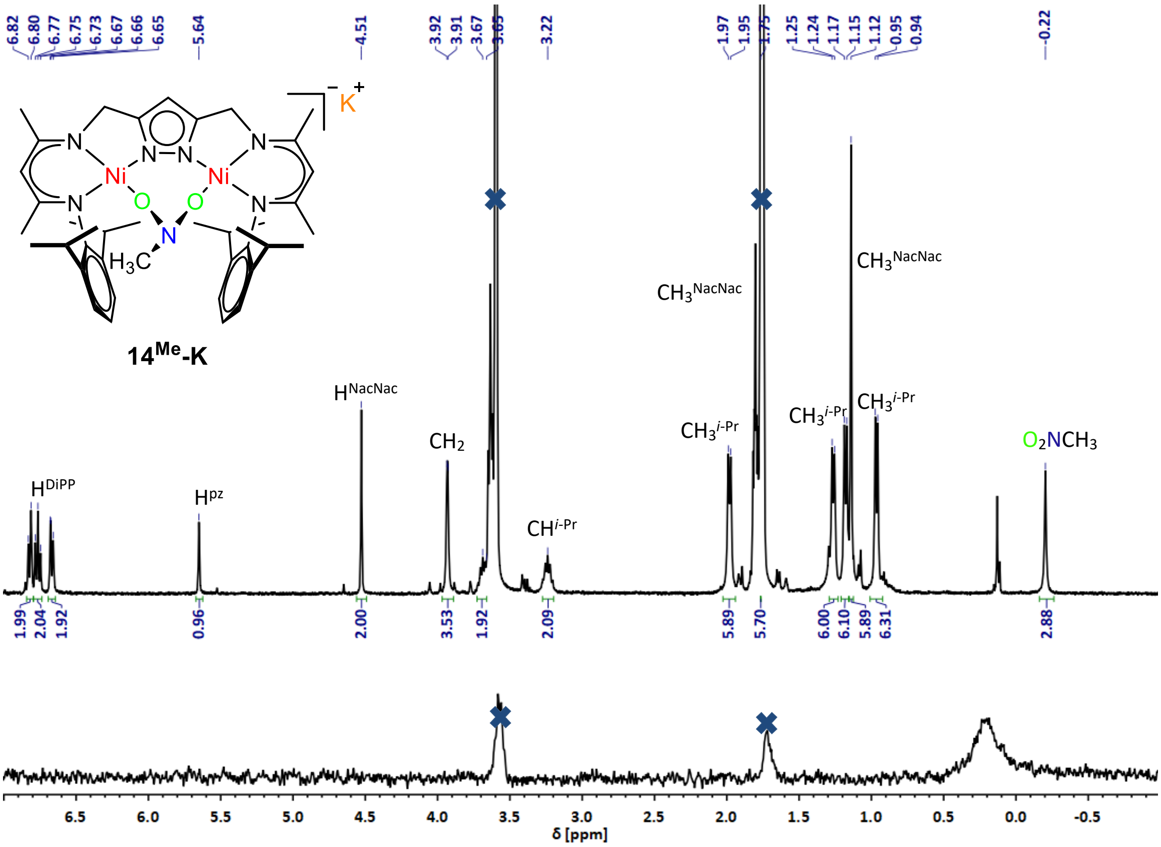

Figure 102: ^{1}H NMR spectrum of **14^{Me}-K** in THF-d$_8$ (top) and ^{2}H NMR spectrum of **14^{Me}-K-d$_3$** in THF (bottom) at -40 °C. Solvent signals are marked by a blue cross

The ^{1}H NMR spectrum of **14^{Me}-K** corresponds to a diamagnetic complex. One singlet for the α-protons of the β-diketiminato units at 4.51 ppm suggests C_s symmetry. However, only one singlet for the protons of the methylene bridging unit in **L** is found at 3.91 ppm, which contradicts the C_s symmetry indicated by the X ray analysis data. In spectra recorded at room temperature it was not possible to assign a resonance to the nitro function methyl unit. Low temperature NMR experiments in THF-d$_8$ at -40°C revealed a high-field-shifted resonance at -0.22 ppm corresponding to the substrate's methyl group. This was confirmed by recording a ^{2}H NMR spectrum of the deuterium labeled analogue **14^{Me}-K-d$_3$** in THF at room temperature. **14^{Me}-K-d$_3$** showed only one resonance at 0.20 ppm. (Figure 102).

Signal broadening at elevated temperatures suggested a barrier for the dynamic inversion of the methyl bound nitrogen atom. Variable-temperature ^{1}H NMR shows the signal to shift low-field upon heating while broadening, which is a common observation for a fast dynamic process.[163] Additionally, the protons of the methylene bridge between the pyrazolate and the β-diketiminato units appear as two doublets with a pronounced roof effect at lower temperatures. Upon elevating the temperature, they merge to a singlet indicating an increase in symmetry from C_s to C_{2v}. However, the temperature sensitivity of **14^{Me}-K** did not allow an identification of the coalescence point. Therefore, no activation energies for the inversion barrier were determined (Figure 103). Despite the major difference in counterion interaction found in the solid state structures of **14^{Me}-K** and **14^{Me}-Na**, both compounds showed essentially the same proton shifts in the NMR.

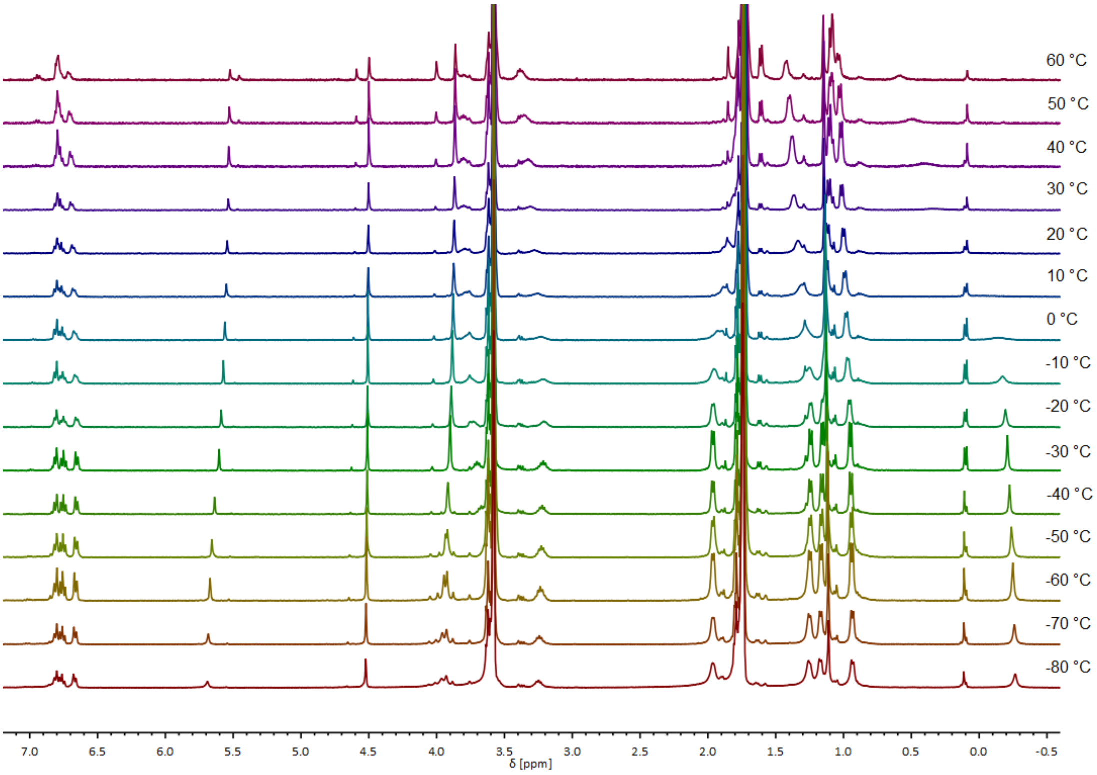

Figure 103: Variable temperature ^{1}H NMR data of **14$^{\text{Me}}$-K** in THF-d$_8$.

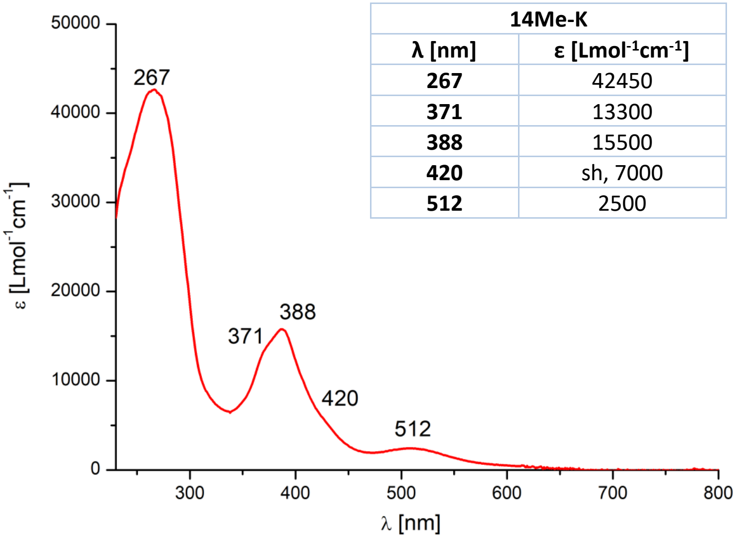

14Me-K	
λ [nm]	**ε [Lmol^{-1}cm^{-1}]**
267	42450
371	13300
388	15500
420	sh, 7000
512	2500

Figure 104: UV/vis spectra of **14$^{\text{Me}}$-K** in THF at -40 °C and table listing the wavenumbers of the electronic transitions and their corresponding extinction coefficient.

The electronic absorption spectrum of **14$^{\text{Me}}$-K** is comparable to the ones found for **14$^{\text{Ph}}$-K**, **14$^{\text{Ph}}$-Na** and **14$^{\text{Bna}}$-K**. The major difference is found for the transition at 512 nm. For **14$^{\text{Me}}$-K** the absorption band appears at lower wavelength and has a reduced extinction coefficient. This is probably caused by the lack of an extended π system, which distributes the electron density more effectively and results in an energetic stabilization in the cases of **14$^{\text{Ph}}$-K**, **14$^{\text{Ph}}$-Na** and **14$^{\text{Bna}}$-K** (Figure 104).

6.2.5 Alkali Metal Cation Dependent Thermal Stability of the Dinickel Nitromethane complexes

At room temperature a solution of **14^{Me}-K** in THF-d_8 decomposes to a species with C_s symmetry according to the ^{1}H NMR spectrum and **3**. The identical decomposition is observed for **14^{Me}-Na**. An ESI-MS of a two day old solution of **14^{Me}-Na** showed a peak at *m/z* 788.4 with an isotope pattern expected for a dinickel complex. The signal corresponded to a dinickel methyloxim complex **16** with the formula $C_{40}H_{55}N_7NaNi_2O$.

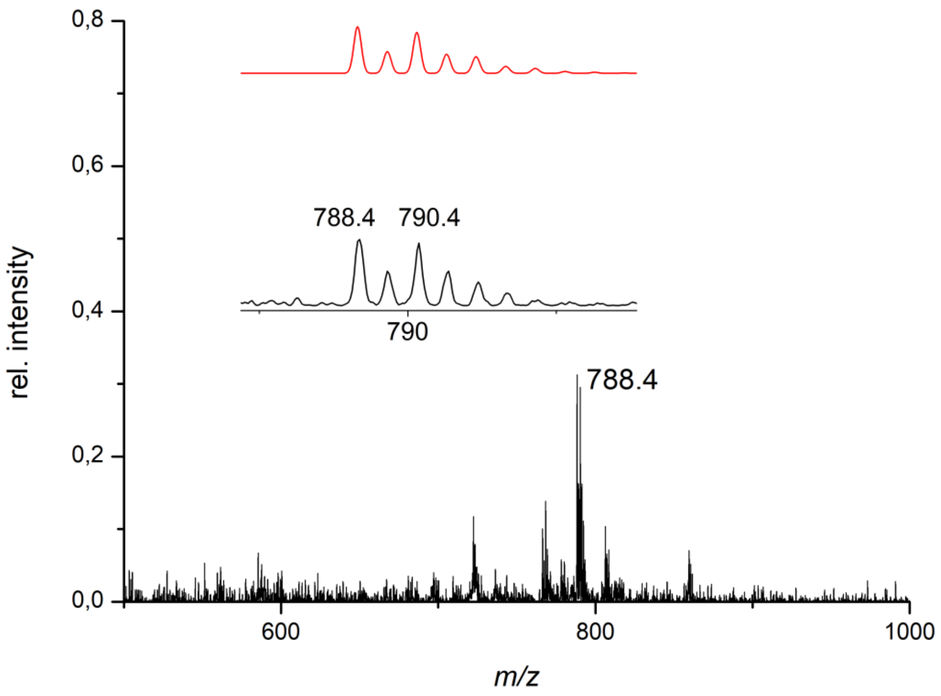

Figure 105: ESI$^+$ mass spectrum of **16** in THF. The inset shows the experimental (black line) and the simulated (red line) isotope pattern for the peak around *m/z* = 788.4 $[M^-+Na]^+$.

Single crystals of **16** were obtained by manually separation of a crystal mixture of **16** and **3** that was afforded by slow diffusion of hexanes into a THF solution of the crude reaction mixture.

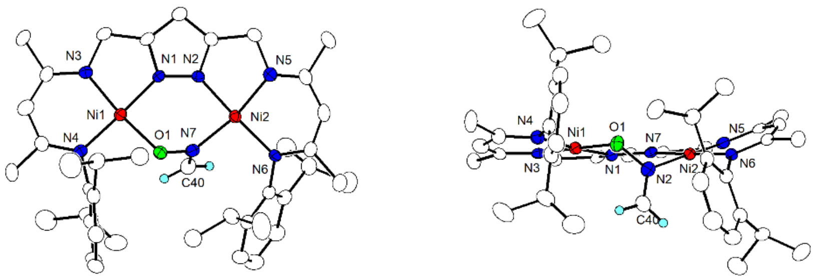

Figure 106: Top view of the molecular structure of **16** (left) and front view of the molecular structure of **16**. Solvent molecules and hydrogen atoms, except the H substituted on oxime unit CH_2 group, are omitted for clarity.

Dinickel complex **16** crystalizes in the triclinic unit cell P $\bar{1}$ and exhibits a metal-metal distance of 3.9005(12) Å (Figure 106). The nickel-nickel separation is found to be significantly contracted compared to the ones determined for the dinickel nitromethane complexes **14^{Me}-K** and **14^{Me}-Na** with d(Ni···Ni) = 4.3436(3) Å and 4.3832(12) Å, due to the decrease in bridging unit atom count from three to two. **16** features an anionic $[ONCH_2]^-$ unit within the bimetallic cleft. The nickel(II) centers are bridged by it in *μ*-*κ*O,*κN* fashion. The N–O bond is with 1.387(3) Å significantly shorter than the ones for **14^{Me}-K** and **14^{Me}-Na**, which range from 1.4284(19) Å to 1.433(6) Å. This potentially originates from the absence of the bond weakening K^+/Na^+ cations which result in a different N–O distances, depending on their alkali metal-oxygen distances. The methylene group is directed almost orthogonal out of the coordination plane and has a significant shortened N–C bond when compared to **14^{Me}-K** and **14^{Me}-Na** [d(N–C) = 1.268(4) Å vs. 1.478(2) Å, 1.480(8) Å]. This distance is in the usual range for a N–C double bonds. Additionally, angles of 115.63(18)°, 115.6(3)° and 125.0(3)° around the $[ONCH_2]^-$ nitrogen indicate a sp^2 hybridized N atom and therefore, **16** is best described as a dinickel complex with a monoanionic formaldoximate bridging unit in between the metal centers.

Table 15: Selected bond lengths [Å] and angles [°] for **16**.

Bond Lengths [Å]		Bond Angles [°]	
Ni(1)-N(1)	1.861(3)	**N(1)-Ni(1)-O(1)**	90.20(10)
Ni(1)-N(3)	1.883(3)	**N(4)-Ni(1)-O(1)**	91.68(11)
Ni(1)-N(4)	1.893(3)	**N(3)-Ni(1)-O(1)**	173.35(11)
Ni(2)-N(2)	1.849(3)	**N(1)-Ni(1)-N(3)**	83.15(11)
Ni(2)-N(5)	1.886(3)	**N(4)-Ni(1)-N(3)**	94.94(12)
Ni(2)-N(6)	1.905(3)	**N(2)-Ni(2)-N(7)**	85.39(11)
Ni(1)-O(1)	1.893(2)	**N(6)-Ni(2)-N(7)**	97.88(11)
Ni(2)-N(7)	1.919(3)	**N(5)-Ni(2)-N(7)**	167.63(12)
O(1)-N(7)	1.387(3)	**N(5)-Ni(2)-N(6)**	93.75(11)
N(7)-C(40)	1.268(4)	**N(2)-Ni(2)-N(5)**	83.04(12)
Ni(1)···Ni(2)	3.9005(12)	**Ni(2)-N(7)-O(1)**	118.3(2)
		Ni(1)-O(1)-N(7)	115.63(18)
		O(1)-N(7)-C(40)	115.6(3)
		Ni(2)-N(7)-C(40)	125.0(3)

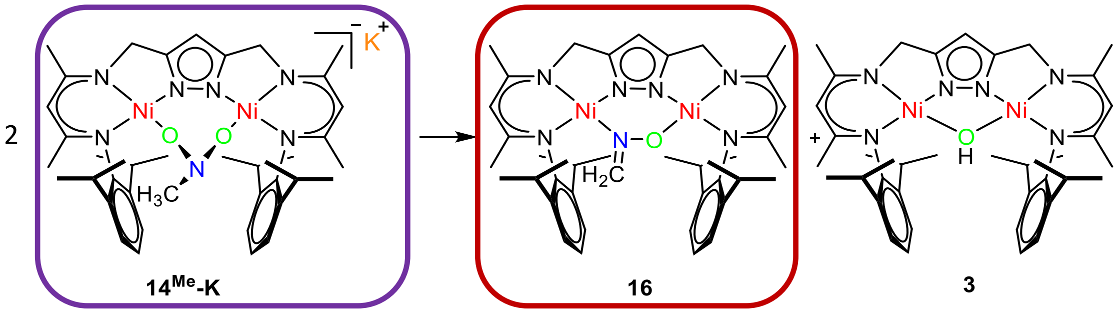

Figure 107: Thermal decomposition of **14^{Me}-K** to **14^{Me}-K** and **3**.

The progress of the decomposition reaction of **14^{Me}-K** at room temperature was monitored by ^{1}H NMR spectroscopy. Kinetic parameters of the reaction were calculated from the relative ratios of **14^{Ph}-K**, **16** and **3** determined by the integral of the α-protons signal of the β-diketiminate unit (Figure 108).

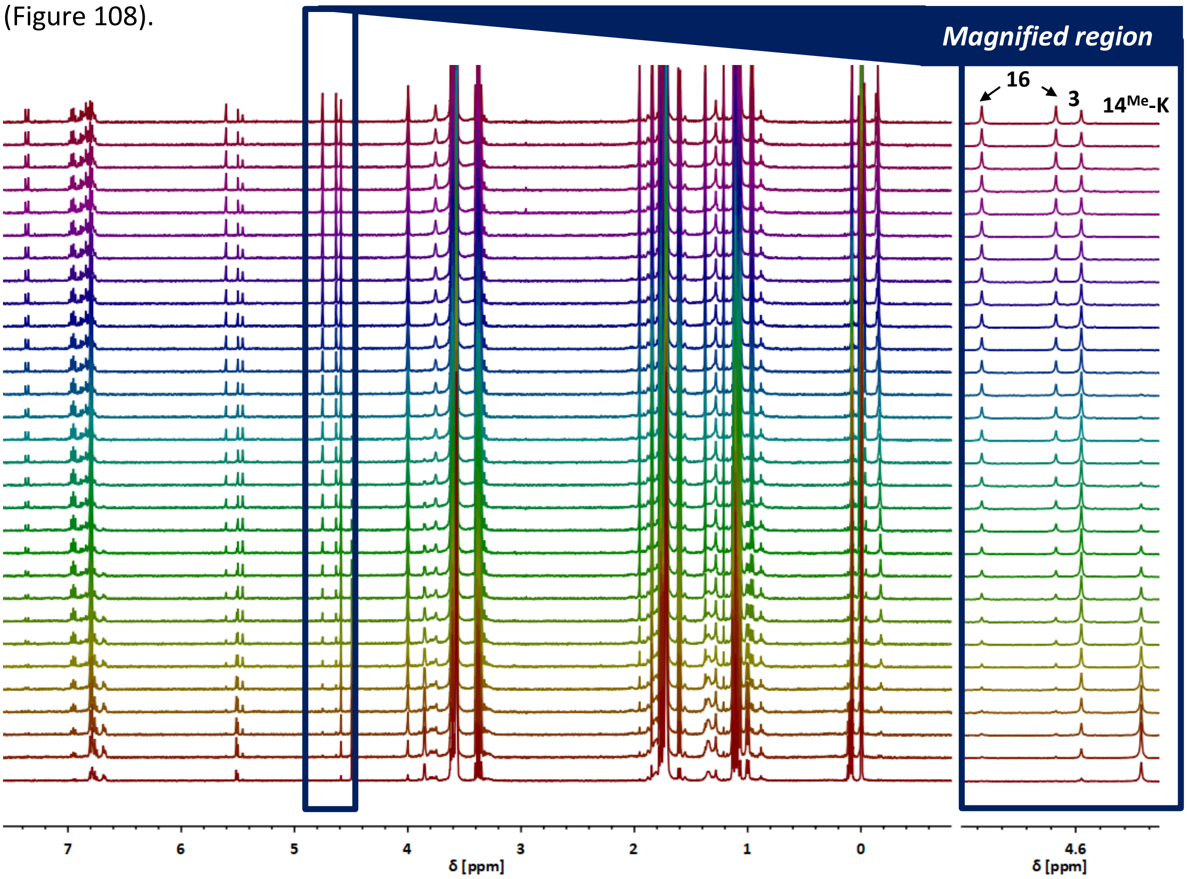

Figure 108: Time dependent ^{1}H NMR measurements for the decomposition of **14^{Me}-K** in THF-d_8 at rt. Spectra shown were recorded every 12.6 min. Magnified region (4.78 ppm – 4.45 ppm) of α-protons of the β-diketiminato units of the complexes **14^{Me}-K**, **16**, and **3**.

Although, two different reaction products suggest a complex mechanism, the decay of **14^{Me}-K** follows a first order rate law with a rate constant $k = 2.38 \pm 0.03 \cdot 10^{-4}\ s^{-1}$ which corresponds to a half-life of 48.0 min (Figure 109). The exchange of the K^+ counter ion with Na^+ appears to have a major impact on the complex stability since the rate constant for the decay of **14^{Me}-Na** is with two orders of magnitude slower ($k = 4.69 \pm 0.06 \cdot 10^{-6}\ s^{-1}$) which corresponds to a half-life of 41 h (Figure 110).

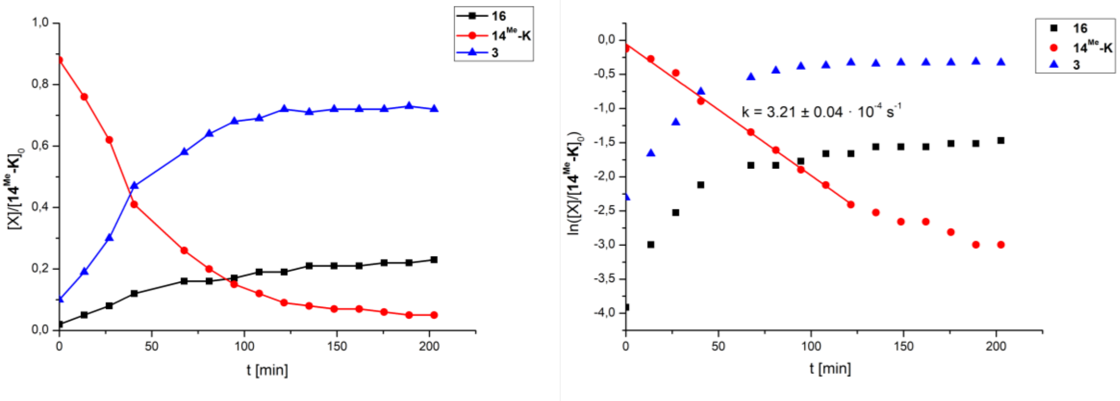

Figure 109: Concentrations (left) and logarithmic concentrations (right) of **14^{Me}-K** (red line/circles), **16** (black squares), **3** (blue triangles), and sum of **14^{Me}-K**, **16**, and **3** relative to the initial concentration of **14^{Me}-K** plotted against time.

Relative concentrations were determined by the integrals of the α-proton of the β-diketiminato subunits in **14^{Me}-K**, **16**, and **3** in the ^{1}H NMR spectrum recorded in THF-d_8.

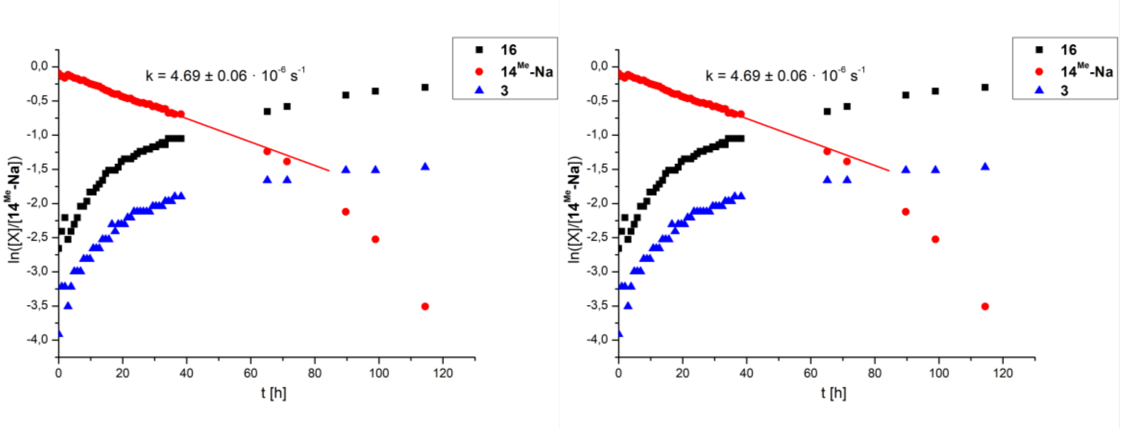

Figure 110: Concentrations (left) and logarithmic concentrations (right) of **14^{Me}-Na** (red circles), **16** (black squares), and **3** (blue triangles) relative to the initial concentration of **14^{Me}-Na** plotted against time. Relative concentrations were determined by the integrals of the α-proton of the β-diketiminate subunits in **14^{Me}-Na**, **16**, and **3** in the ^{1}H NMR spectrum in THF-d_8.

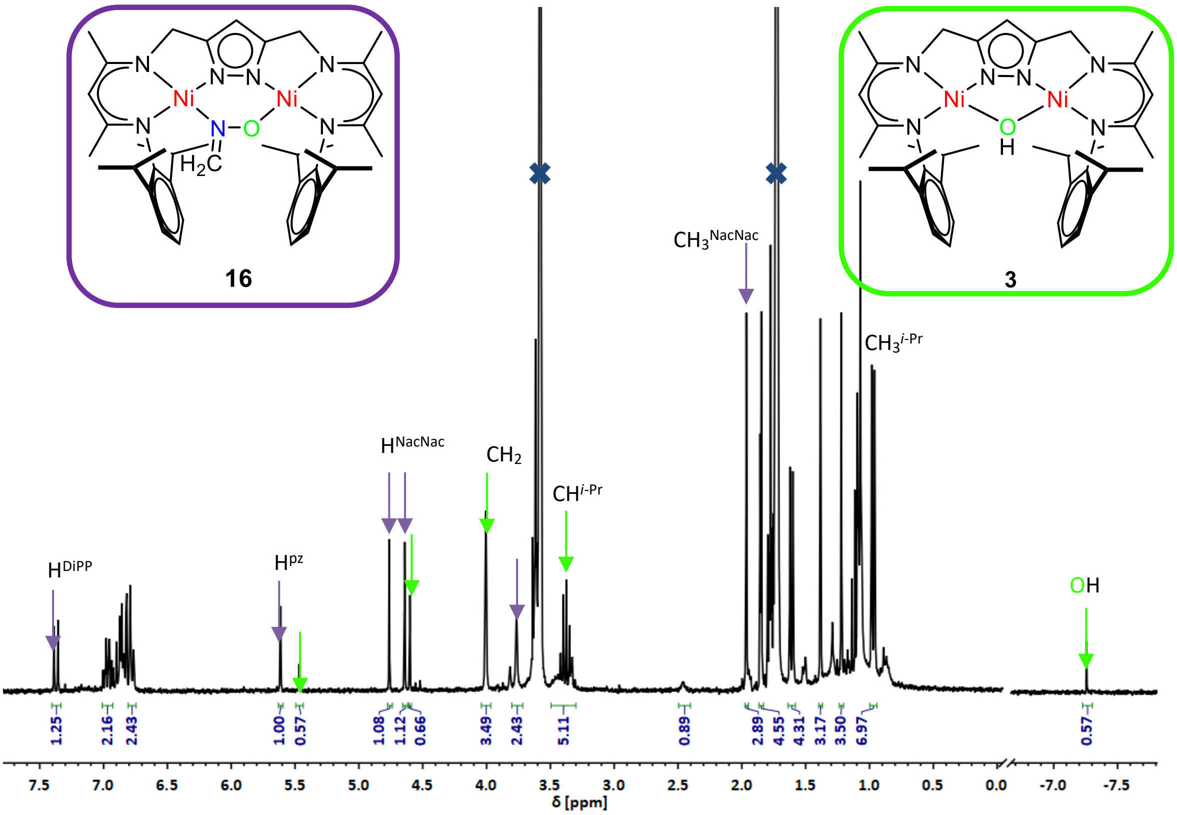

Figure 111: ^{1}H NMR spectrum (300.13 MHz) of the decomposition of **14^{Ph}-Na** in THF-d_8 after 114 h at rt. Characteristic proton signals of **14^{Ph}-Na** (purple arrows) and **3** (green arrows) are marked. Solvent signals are marked with a blue cross.

The product outcome involving **16** and **3** is redolent of germinyl nitromethane compound found in the equilibrium between **XXXIV** and **XXXV** as shown in Figure 78. Although, due to the complex product mixture mechanistic proposals are difficult, the first order law found for the degradation reaction of **14^{Me}-K** and **14^{Me}-Na** suggests the rate determining step to be unimolecular. This would imply that **14^{Me}-K** slowly forms a reactive species which further reacts to the products **16** and **3** accompanied by the elimination of either OH^- or $[ONCH_2]^-$. The overall concentration of the involved species **14^{Me}-K**, **16** and **3** remains the same over the course of the reaction as indicated by the relative ratios of the α-proton of the β-diketiminato subunits to the signal of CH_2Cl_2 in the ^1H NMR spectra. Furthermore, **3** slowly converts to **16** after **14^{Me}-K** is fully consumed, suggesting that a secondary process occurs which is likely to be a substitution reaction of $[ONCH_2]^-$ with **3**. The intermediate displayed in Scheme 25 is based on the structure of **XXXV**. However, no spectroscopical evidence for its existence was obtained.

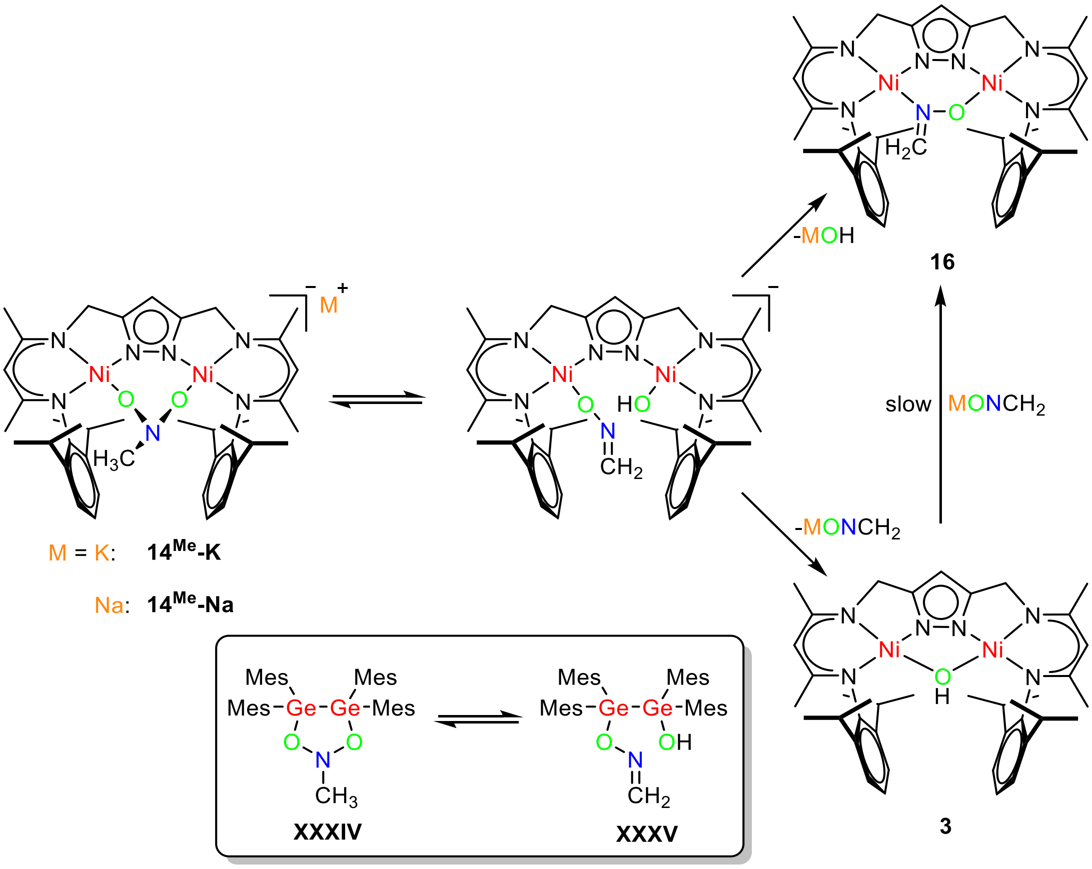

Scheme 25: Proposed mechanism for the decomposition of **14^{Me}-Na**/**14^{Me}-Na** based on the isomerization observed for **XXXIV** and **XXXV**.

This mechanism explains the observation that the final ratio between **16** and **3** greatly differed depending on the alkali metal cation (Figure 111). For the decomposition of **14^{Me}-K, 3** was found in excess with a product ratio of 1:3 for **16**/**3**. In case of the sodium analogue **14^{Me}-Na** the hydroxido complex is the minor reaction product with approximate ratio of 3:1 for **16**/**3**. Since the elimination of either OH^- or H_2CNO^- is associated with the corresponding alkali metal ion, it potentially has a significant impact on the product outcome. During the decomposition a colorless precipitate formed which possibly indicates the MOH^- and $MONCH_2$. Unfortunately, it was not possible to track the $MONCH_2$ probably due to it being insoluble. The change in rate law at lower concentrations of **14^{Me}-K** and **14^{Me}-Na** suggests that the secondary process becomes more relevant at low concentrations. This is supported by the observation that the **16**/**3** ratio after consumption of **14^{Me}-K** is higher when initial concentration of **14^{Me}-K** is low. These kinetic investigations showed a crucial dependency of the alkali metal ion on the thermal stability of the complexes **14^{Me}-K** and **14^{Me}-Na**. Both molecular structures showed that the interaction between the alkali metal ion and the reduced nitromethane moiety within the bimetallic cleft is stronger in the case of Na^+, indicated by shorter bond distances and a missing THF ligand compared to **14^{Me}-K**. This closer interaction compensates the electron density on the nitromethane substrate more efficiently than in the case of **14^{Me}-K**. As a result, its tendency to eliminate $MONCH_2$ is lowered and the decomposition proceeds slower.

6.3 Conclusion

This chapter examined the reductive binding of nitro compounds to a dinickel complex moiety using **2-K** and **2-Na**. The resulting series of new complexes has been characterized structurally and spectroscopically. The reaction of **2-K** and 4-nitrobenzaldehyde led to a clean activation of the nitro group in complex **14**$^{\mathrm{Bna}}$-K despite the presence of an easily reducible aldehyde function, demonstrating the high chemoselectivity of the dinickel binding site. The increase in electron donation of the reduced nitro group resulted in a partial loss of aromaticity within the six membered ring of the coordinated 4-nitrobenzaldehyde as indicated by XRD analysis. The study was extended to unfunctionalized nitrobenzene complexes. The alkali metal derivatives **14$^{\mathrm{Ph}}$-K** and **14$^{\mathrm{Ph}}$-Na** showed a significant shift difference in the ^{1}H NMR with a strong low field shift for the *ortho* protons of the coordinated nitrobenzene. Cation exchange experiments showed that the complexes **14$^{\mathrm{Ph}}$-K** and **14$^{\mathrm{Ph}}$-Na** barely dissociate in THF and that K^+ binds stronger than Na^+. Additionally, the alkali metal cations have an important influence on the complex stability since the addition of [2.2.2]cryptand in presence of trace protons resulted in the partial formation to **3** and **15$^{\mathrm{Ph}}$-cK**. Furthermore, it was possible to provide mechanistic insight into the clean proton induced formation of **15$^{\mathrm{Ph}}$-H** from **14$^{\mathrm{Ph}}$-K** by using 3,5-DTBC as acid. The structure **14$^{\mathrm{Me}}$-K** and **14$^{\mathrm{Me}}$-Na** revealed a significant reduction of the nitro group as the nitro group N atom showed a pyramidal geometry for the surrounding substituents and the N−O bond length was significantly increased. Therefore, the reduced nitro moiety is best described as a doubly deprotonated dihydroxyl amine. Complexes **14$^{\mathrm{Me}}$-K** and **14$^{\mathrm{Me}}$-Na** showed thermal instability in solution and decomposed to **16** and **3**. **16** was structurally characterized and the decomposition reaction was monitored by time dependent ^{1}H NMR spectroscopy. The kinetic parameters resulting from these measurements were heavily dependent on the respective alkali metal ion employed in the starting material **14$^{\mathrm{Me}}$-K/14$^{\mathrm{Me}}$-Na** rendering **14$^{\mathrm{Me}}$-Na** more stable with a rate constant almost two orders of magnitude smaller than the analogue potassium complex [$k = 4.69 \pm 0.06 \cdot 10^{-6}\ s^{-1}$ vs. $3.21 \pm 0.04 \cdot 10^{-4}\ s^{-1}$]. The general tendency of the twofold reduced nitro group to lose one oxygen will contribute to a better understanding of catalytic reduction processes of arylic as well as aliphatic nitro compounds.

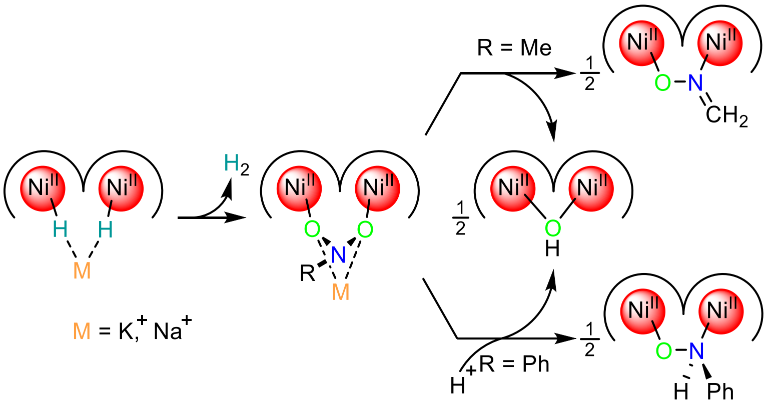

Scheme 26: Reductive binding of nitro compounds and subsequent

7 Experimental Part

7.1 Materials and Methods

Manipulations involving air- and moisture-sensitive compounds were conducted under an atmosphere of dried (phosphorus pentoxide on solid support [Sicapent, Merck]) argon (5.0) using standard Schlenk techniques or in a MBraun glovebox (O_2< 0.5 ppm and H_2O < 0.5 ppm) filled with dinitrogen atmosphere. THF, THF-d_8, toluene-d_8, diethyl ether, cyclohexane, benzene, C_6D_6, and pentane were dried over potassium or potassium sodium alloy and degassed applying at least three freeze-pump-thaw cycles using liquid nitrogen and are labeled as absolute (abs.). Toluene, hexane, acetonitrile, and dichloromethane were dried with an Mbraun Solvent purification system (SPS). All solvents were stored over molecular sieves (3Å).

Hydrogen, carbon monoxide gas and deuterium gas were purchased from Linde. Chemicals used were either present in the working group or purchased from commercial sources, or their synthesis is described. Benzaldehyde, *p*-anisaldehyde, *p*-trifluoromethyl benzaldehyde, *p*-fluorobenzaldehyde, and nitrobenzene were dried over $CaCl_2$ and distilled prior to use. NMR experiments of air- and moisture-sensitive compounds were conducted in J. Young NMR tube. Gases HD, D_2, and H_2 were rigorously dried by storing them over concentrated H_2SO_4 for around 1 day. CO and ^{13}CO were dried molecular sieves (3 Å) for at least 3 days. CD_3OTs[164] and HLutOTf[30] were synthesized according to literature procedures.

7.2 Instrumentation

^{1}H NMR,^{2}H NMR, ^{13}C NMR, ^{1}H–^{1}H COSY, ^{1}H–^{13}C HSQC, and ^{1}H–^{13}C HMBC spectra were recorded on Bruker Avance spectrometers (300, 400, and 500 MHz) at room temperature unless otherwise noted. Chemical shifts are reported in parts per million relative to residual proton and carbon signals of the solvent ($CDCl_3$,δ(H) = 7.26,δ(C) = 77.16 ppm; THF-d_8, δ(H) = 1.72 and 3.58;δ(C) = 25.31 and 67.21 ppm).[53] Peaks are labeled according to their multiplicity and abbreviated as follows: s (singlet), d (doublet), t (triplet), sep (septet), m (multiplet) and an additional b in case of broad signals that prevent the determination of coupling constants (J [Hz]). ^{1}H–^{1}H NOESY spectra were recorded at 400 MHz using a mixing time of 0.5 s. For traceability, NMR data is labeled with the spectrum identification [experiment number, NMR experiment number].

Electron ionization (EI) and electrospray ionization (ESI) mass spectra were collected on a Bruker HCTultra instrument. Moisture- or oxygen-sensitive samples were prepared in a glovebox (MBRAUN UNIlab) under an argon atmosphere and injected into the Bruker HTCultra instrument *via* a direct Peek tubing connection.

Elemental analyses were carried out with an Elementar 4.1 vario EL 3 instrument by the analytical department of the University of Göttingen.

IR spectra of solid samples were measured with a Cary 630 FTIR spectrometer equipped with a DialPath and Diamond ATR accessory (Agilent) placed in a glovebox (MBRAUN UNIlab, argon atmosphere). IR bands were labeled according to their relative intensities with vs (very strong), s(strong), m (medium), w (weak), and very weak (vw). The calculated isotope shifts were obtained by using the following equation:

$$\frac{\nu}{\nu'} = \sqrt{\frac{\frac{m_A \cdot m_B}{m_A + m_B}}{\frac{m'_A \cdot m'_B}{m'_A + m'_B}}} \quad (eq. 1)$$

ν = wavenumber
ν' = wavenumber of the isotopologue
m_A = mass of atom A
m_B = mass of atom B
m'_A = mass of atom A in the isotopologue
m'_B = mass of atom B in the isotopologue

UV/Vis spectra were recorded using a Varian Cary 5000 or Varian Cary 60 with quartz cells (1 cm) in the solvents indicated and the temperature control was performed with a cryostat from UNISOKU SCIENTIFIC INSTRUMENTS (Japan).

Cyclic voltammograms were measured under inert conditions with a Gamry Interface 1000b potentiostat controlled by Gamry Framework software. The samples were measured in THF or CH_2Cl_2 solutions at a concentration of 1 mM of complex and 0.1 M of Bu_4NPF_6 as electrolyte. A glassy carbon electrode was used as working electrode, a platinum wire as counter electrode and a silver wire as a pseudo-reference electrode. Fc or $Cp_2{}^*Fe$ was added as an internal standard and all spectra were referenced to the ferrocene/ferrocenium redox couple (Fc/Fc^+).

X-band EPR spectra were obtained with a Bruker E500 ELEXSYS spectrometer equipped with a standard cavity (ER4102ST, 9.45 GHz). The temperature was regulated with an Oxford Instruments Helium flow cryostat (ESP910) and an Oxford temperature controller (ITC-4). The microwave frequency was measured with the built-in frequency counter and the magnetic field was calibrated using an NMR field probe (Bruker ER035M).

X-ray data were collected on a STOE IPDS II or a BRUKER D8-QUEST diffractometer (monochromated Mo-K_α radiation, $\lambda = 0.71073$ Å) by use of ω or ω and ϕ scans at –140 °C or –173 °C. The structures were solved with SHELXT and refined on F^2 using all reflections with SHELXL-18.[165],[166] Non-hydrogen atoms were refined anisotropically. Hydrogen atoms were placed in calculated positions and assigned to an isotropic displacement parameter of 1.5/1.2 $U_{eq}(C)$. Face-indexed absorption corrections were performed numerically with the program X-RED[167] or by the multi-scan method with SADABS.[168]

7.3 Synthetic Procedures

3,5-Dicyano-1*H*-pyrazole (B)

The following synthesis is a modification of the procedure reported in literature:[29] In a dried 1 L Schlenk flask with reflux condenser and overpressure valve **A** (20 g, 0.13 mol, 1.00 eq.) was suspended in acetonitrile (500 mL, dry) and cooled to 0 °C. Then $POCl_3$ (15 mL, 24.7 g, 0.160 mol, 1.20 eq.) was slowly added over 5 min. Then the reaction mixture was stirred at 80 °C for 8 h and cooled to 0 °C again to add $POCl_3$ (10 mL, 16.5 g, 0.110 mol, 0.80 eq.). The mixture was heated to 80 °C. This was repeated another four times to add $POCl_3$ (55 mL, 90.5 g, 0.590 mol, 4.5 eq.) in total. After complete addition the reaction mixture turned into a black solution which was carefully quenched with ice water and stirred overnight. The mixture was extracted with EtOAc (3 x 300 mL) and the combined organic layers were dried over $MgSO_4$. The solvent was removed on a rotary evaporator. The resulting brown powder was subjected to column chromatography (300 g silica, EtOAc/ hexane 3:7, 100 mL fractions, $R_F = 0.44$) to yield **B** as a light-yellow powder. (11.1 g, 0.094 mol, 72%)

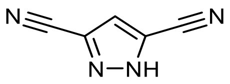

B

^{1}H NMR (300.13 MHz, DMSO-d^6): δ [ppm] = 7.89 (s, 1H, H^{pz}). [TK478, 152]

Spectral data matches the data reported in literature.[29]

3,5-Bis(aminomethylene)-1*H*-pyrazole dihydrochloride (C)

The following synthesis is a modification of the procedure reported in literature:[29] In a dried 1 L Schlenk flask **B** (4.56 g, 38.6 mmol, 1.0 eq.) was dissolved in THF (500 mL, dry) and cooled to 0 °C. A solution of $LiAlH_4$ (2.0 M, 38 mL, 77.2 mmol, 2.0 eq.) was added over 10 min. The reaction mixture was heated to 60 °C and stirred for 48 h. The resulting white slurry was cooled to 0 °C and H_2O (150 mL) was added carefully. All solvent was removed until a sticky solid was obtained. The solid was subjected to Soxhlet extraction with THF (250 mL) overnight. After solvent removal with a rotary evaporator the obtained oil was dissolved in EtOH (50 mL), cooled to 0 °C. Addition of etheric HCl led to precipitation of the hydrochloride salt. The solid was filtered off with a Büchner funnel and washed with Et_2O. After drying *in vacuo* **C** was obtained as a fine white powder. (6.25 g, 31.4 mmol, 81%)

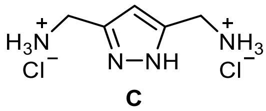

C

^{1}H NMR (300.13 MHz, DMSO-d^6): δ [ppm] = 12.96 (bs, 1H, NH^{pz}), 7.79 (bs, 4H, NH_3^+), 6. 42 (s, 1H, H^{pz}), 3.96 (s, 4H, CH_2). [TK479, 157]

Spectral data matches literature.[29]

4-((2,6-diisopropylphenyl)amino)pent-3-en-2-one (D)

The following synthesis is a modification of the procedure reported in literature:[29] In a 250 mL round-bottom flask with Dean-Stark apparatus and reflux condenser acetyl acetone (11.7 g, 12.0

mL, 116 mmol, 1.10 eq) and diisopropyl aniline (18.79 g, 20 mL, 106 mmol, 1.00 eq) were dissolved in toluene (100 mL, wet). After addition of *p*-TsOH (0.5 g, 2.63 mmol, 2.5 mol%) the reaction mixture was refluxed for 6 h. The solvent was removed on a rotary evaporator and the resulting brown oil was washed with water (30 mL) and extracted with Et_2O (3 x 40 mL). Hydrochloric acid (1 M, 5mL) was added to the combined organic phases to precipitate the hydrochloride salt of unreacted diisopropyl aniline. After filtration the solution was washed with H_2O (30 mL) again. The organic phase was dried over Na_2SO_4 and the solvent was removed on a rotary evaporator. The brown residue was distilled at 100 °C at 10^{-3} mbar giving a light-yellow oil which forms sharp needles. The solid was dissolved in hexane and crystallized at -20 °C yielding **D** as large rods. (11.8 g, 46 mmol, 43 %)

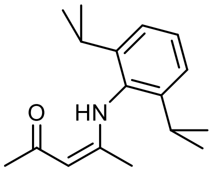

D

^{1}H NMR (300.13 MHz, $CDCl_3$): δ [ppm] = 12.05 (s, 1H, NH), 7.30 (dd, $^3J_{\text{H-H}}$ = 8.5 Hz, $^3J_{\text{H-H}}$ = 7.1 Hz, 1H, H-DiPP^{p}), 7.17 (d, $^3J_{\text{H-H}}$ = 7.2 Hz, 2H, H-DiPP^{m}), 5.21 (s, 1H, H$^{\text{Nacnac}}$), 3.03(sep, $^3J_{\text{H-H}}$ = 6.9 Hz, 2H, CH$^{i\text{Pr}}$), 2.13 (s, 3H, CH_3), 1.63 (s, 3H, CH_3), 1.22 (d, 6H, $^3J_{\text{H-H}}$ = 6.9 Hz, CH_3^{Nacnac}), 1.15 (d, 6H, $^3J_{\text{H-H}}$ = 6 Hz, CH_3^{Nacnac}). [TK385, 96]

Spectral data matches literature.[29]

H_3L

The following synthesis is a modification of the procedure reported in literature:[29] In a dried 100 mL Schlenk flask **D** (2.61 g, 10.0 mmol, 2.0 eq.) was dissolved in CH_2Cl_2 (30 mL, dry) and Et_3OBF_4 (2.85 g, 15.0 mmol, 3.1 eq.) was added. After a color change to yellow was observed the reaction mixture was stirred overnight. The solution was added to a suspension of **C** (1.0 g, 5.0 mmol, 1.0 eq.) in Et_3N (10 mL, dry) in a 100 mL Schlenk flask. The cloudy reaction mixture was stirred at 40 °C overnight. The solvent was removed on a rotary evaporator and the gooey residue was extracted with toluene (3 x 30 mL). After evaporation of the solvent **H_3L** was obtained as a crude oil which after addition of EtOH (10mL) and exposure to a ultrasonic bath gave a suspension of a white powder. Filtration and washing with cold EtOH afforded **H_3L** as a white powder. (1.58 g, 2.6 mmol, 52%)

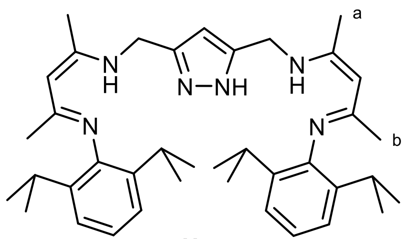

H_3L

^{1}H NMR (300.13 MHz, $CDCl_3$): δ [ppm] = 7.09 (d, $^3J_{\text{H-H}}$ = 8.5 Hz, 2H, H$^{\text{DiPP-}m}$), 7.08(d, $^3J_{\text{H-H}}$ = 7.1 Hz, 2H, H$^{\text{DiPP-}m}$), 7.01 (d, $^3J_{\text{H-H}}$ = 8.8 Hz, ^3J = 6.0 Hz, 2H, H-DiPP^{p}), 6.00 (s, 1H, H$^{\text{pz}}$), 4.72 (s, 2H, CH$^{\text{NacNac}}$), 4.39 (s, 4H, CH_2), 2.84 (sep, $^3J_{H\text{-}H}$ = 6.9 Hz, 4H, CH^{iPr}), 1.95 (s, 6H, $CH_3^{NacNac\text{-}a}$), 1.64 (s, 6H, $CH_3^{NacNac\text{-}b}$), 1.15 (d, 12H, $^3J_{H\text{-}H}$ = 6.9 Hz, CH_3^{iPr}), 1.06 (d, 12H, $^3J_{H\text{-}H}$ = 6.9 Hz, CH_3^{iPr}). [TK399, 121]

Spectral data matches literature.[29]

LNi_2Br (1^{Br})

The following synthesis is a modification of the procedure reported in literature:[29] In a dried 50 mL Schlenk flask $\mathbf{H_3L}$ (8.24 g, 13.5 mmol, 1.0 eq.) was dissolved in THF (50 mL, abs) and cooled to -78 °C. After dropwise addition of *n*-BuLi (17.9 mL, 44.7 mmol, 3.3 eq.) a color change to deep-red was observed, and the solution was slowly heated to room temperature over 25 min. Solid $NiBr_2$(dme) (9.08 g, 29.7 mmol, 2.2 eq) was added under an argon stream. The dark brown suspension was stirred at 60 °C overnight. The precipitate was separated with a centrifuge and the THF solution was discarded. The light-brown powder was washed with acetone three times until the washing solution remained colorless. $\mathbf{1^{Br}}$ was obtained as a brown powder. (10.1 g, 12.6 mmol, 93%)

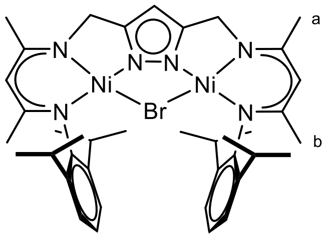

$\mathbf{1^{Br}}$

^{1}H NMR (300.13 MHz, $CDCl_3$): δ [ppm] = 6.92 (dd, $^3J_{H\text{-}H}$ = 8.4 Hz, $^3J_{H\text{-}H}$ = 6.8 Hz, 2H, $H^{DiPP\text{-}p}$), 6.80 (d, $^3J_{H\text{-}H}$ = 7.5 Hz, 4H, $H^{DiPP\text{-}m}$), 5.54 (s, 1H, H^{pz}), 4.77 (s, 2H, CH^{NacNac}), 4.15 (s, 4H, CH_2), 3.37 (sep, $^3J_{H\text{-}H}$ = 6.8 Hz, 4H, CH^{iPr}), 2.01 (s, 6H, $CH_3^{NacNac\text{-}a}$), 1.47 (d, 12H, $^3J_{H\text{-}H}$ = 6.9 Hz, CH_3^{iPr}), 1.30 (s, 6H, $CH_3^{NacNac\text{-}b}$), 1.01 (d, 12H, $^3J_{H\text{-}H}$ = 6.9 Hz, CH_3^{iPr}). [TK485, 84]

Spectral data matches literature.[29]

$KLNi_2H_2$ (2-K)

The following synthesis is a modification of the procedure reported in literature:[29] In a 40 mL screw cap vial in a glove box $\mathbf{1^{Br}}$ (1.00 g, 1.25 mmol, 1.00 eq.) was suspended in THF (30 mL, abs.) and $KHBEt_3$ solution in THF (2.80 mL, 1 M, 2.80 mmol, 2.25 eq.) was added dropwise. After 45 min reaction time at room temperature the darkened mixture was filtered and concentrated *in vacuo*. The residual sticky solid was washed with hexane (3 x 20 mL) until the washing solution remained colorless and a fine orange powder was obtained. The solid was dissolved in THF and overlayered with hexane. After four weeks crystallization **2-K** was isolated as large cubes. (0.65 g, 0.82 mmol, 66%)

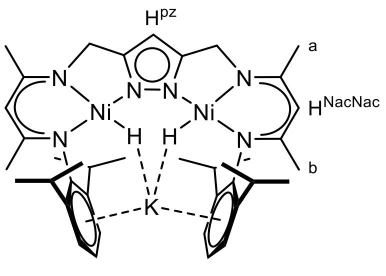

2-K

^{1}H NMR (300.13 MHz, THF-d$_8$):δ [ppm] = 6.86 (dd, $^{3}J_{H,H}$ = 8.3 Hz, $^{3}J_{H\text{-}H}$ = 6.5 Hz, 2H, H$^{DiPP\text{-}p}$), 6.78 (d, $^{3}J_{H\text{-}H}$ = 7.1 Hz, 4H, H$^{DiPP\text{-}m}$), 5.55 (s, 1H, H^{pz}), 4.56 (s, 2H, CH^{NacNac}), 4.23 (s, 4H, CH$_2$), 3.45 (sep, $^{3}J_{H,H}$ = 6.8 Hz, 4H, CH^{iPr}), 1.83 (s, 6H, CH$_3^{NacNac\text{-}a}$), 1.22 (s, 6H, CH$_3^{NacNac\text{-}b}$), 1.13 (d, $^{3}J_{H\text{-}H}$ = 6.9 Hz, 12H, CH$_3^{iPr}$), 1.03 (d, $^{3}J_{H\text{-}H}$ = 6.9 Hz, 12H, CH$_3^{iPr}$), -24.17 (s, 2H, NiH). [TK391, 31]

UV-Vis (THF): λ [nm] (ε = L·mol^{-1}·cm^{-1}) = 314 (43630), 380 (16570), 424 (8990), 468 (5900), 532 (1410), 563 (900).

Spectral data matches literature.[29]

NaLNi$_2$H$_2$ (2-Na)

The following synthesis is a modification of the procedure reported in literature:[29] In a 40 mL screw cap vial in a glove box **1^{Br}** (1.2 g, 1.5 mmol, 1.0 eq.) was suspended in THF (30 mL, abs.) and NaHBEt$_3$ solution in THF (2.3 mL, 1 M, 3.3 mmol, 2.2 eq.) was added dropwise. After 45 min reaction time at room temperature the darkened mixture was filtered and concentrated *in vacuo*. The residual sticky solid was washed with hexane (3 x 20 mL) until the washing solution remained colorless and a fine orange powder was obtained. The solid was dissolved in THF and overlayered with hexane. After four weeks crystallization **2-Na** was isolated as large cubes. (0.8 g, 0.9 mmol, 64%)

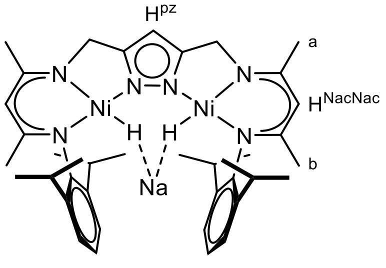

2-Na

KLNi$_2$H$_2$ (2-K-d$_2$)

In a 50 mL Teflon valve sealed flask in a glove box **2-K** (98 mg, 0.12 mmol, 1.00 eq.) was dissolved in THF (15 mL, abs.) The solution was degassed with two freeze pump thaw cycles and D$_2$ gas (1atm, dry) was added. After stirring 3 days the reaction mixture was filtered and overlayered with hexane. After four weeks crystallization at room temperature **2-K-d$_2$** was isolated as large red cubes. (755 mg, 0.94 mmol, 77%)

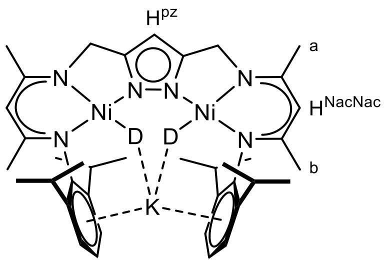

2-K-d$_2$

^{2}H NMR (46.07 MHz, THF): δ [ppm] = -24.13 (s, 2D, NiD). [TK582, 265]

Spectral data matches literature.[29]

LNi$_2$N$_2$ (4^{N_2})

In a 20 mL screw cap vial in a nitrogen filled glove box **2-K** (20 mg, 25 µmol, 1 eq.) was dissolved in toluene (7 mL). Ph$_3$CPF$_6$ (10 mg, 25 µmol, 1 eq.) was added to give a quick color change to dark brown. The reaction mixture was stirred overnight and precipitated KPF$_6$ was filtered off. The solvent was evaporated *in vacuo* and the residue dissolved in THF. Then the solution was overlayered with hexane. After 2 weeks at -35 °C crystallization **4^{N_2}** was isolated as small black rods. (12 mg, 16 µmol, 65 %)

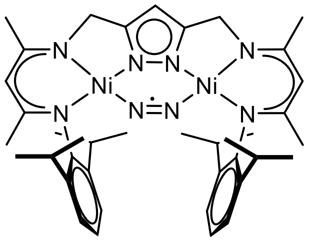

4^{N_2}

^{1}H NMR (300.13 MHz, toluene-d$_8$): δ [ppm]= 8.61 (bs), 3.17 (bs), -4.03 (bs), -5.96 (bs). [TK584, 187]

FT-IR (ATR): $\tilde{\nu}$ [cm^{-1}] = 3050 (w), 2957 (m), 2921 (m), 2866 (m), 1896 (m), 1549 (m), 1528 (s), 1457 (s), 1436 (s), 1395 (s), 1368 (m), 1360 (m), 1320 (m), 1310 (s), 1291 (w), 1277 (w), 1252 (m), 1234 (w), 1207 (w), 1186 (m), 1176 (w), 1159 (w), 1145 (w), 1138 (w), 1105 (w), 1090 (m), 1055 (m), 1030 (s), 1011 (m), 936 (w), 916 (m), 866 (w), 844 (m), 794 (s), 764 (w), 759 (m), 748 (s), 743 (s), 715 (w), 644 (w), 632 (w), 628 (w), 623 (w), 541 (w), 520 (s), 480 (s), 463 (w), 456 (m), 449 (w), 442 (w), 437 (w), 431 (w), 424 (m), 420 (m), 417 (m), 414 (m), 410 (vw), 406 (m), 402 (m) cm^{-1}.

UV-Vis (THF): λ [nm] (ε = L·mol^{-1}·cm^{-1}) = 368 (18270), 431 (4170), 500 (2420), 698 (1070).

LNi$_2$CH$_3$ (6)

Method A: In a 20 mL screw cap vial in a glove box **1^{Br}** (100 mg, 125 µmol, 1.00 eq.) was suspended in THF (15 mL, abs.) and KC$_8$ (38 mg, 274 µmol, 2.20 eq.) was added. Immediately a deep red color emerged, and the reduction was continued overnight to ensure completion. After filtration, CH$_3$OTs (23 mg, 125 µmol, 1.00 eq.) was added, giving a brown suspension. The reaction mixture was stirred for 1 h at room temperature and filtered. The brown THF solution was overlayered with hexane. After three weeks crystallization **6** was isolated as dark brown rods. (18 mg, 24 µmol, 19.5%)

Method B: In a 20 mL screw cap vial in a glove box **1-K** (50 mg, 63 µmol, 1 eq.) was dissolved in toluene (7 mL, abs.) and CH_3OTs (11.7 mg, 63 µmol, 1 eq.) was added. After stirring for 4 h at room temperature formed KOTs was filtered off and the solvent was removed *in vacuo*. The residue was dissolved in THF and overlayered with hexane. After one week crystallization **6** was isolated as dark brown rods. (16.9 mg, 22.7 µmol, 36.0 %)

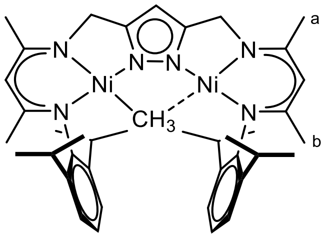

6

^{1}H NMR (400.25 MHz, THF-d_8): δ [ppm] = 6.94 (t, $^3J_{H\text{-}H}$ = 7.6 Hz, 2H, H-DiPP^{p}), 6.82 (t, $^3J_{H\text{-}H}$ = 7.6 Hz, 4H, H-DiPP^{m}), 5.51 (s, 1H, H^{pz}), 4.67 (s, 2H, CH^{NacNac}), 4.34 (s, 4H, CH_2), 3.40 (sep, $^3J_{H\text{-}H}$ = 6.8 Hz, 2H, CH^{iPr}), 1.93 (s, 6H, $CH_3^{NacNac\text{-}a}$), 1.40 (d, $^3J_{H\text{-}H}$ = 6.9 Hz, 12H,$CH_3^{iPr\text{-}a}$), 1.24 (s, 6H, $CH_3^{NacNac\text{-}b}$), 1.02 (d, $^3J_{H\text{-}H}$ = 6.9 Hz, 12H,$CH_3^{iPr\text{-}b}$), -3.16 (s, 3H, CH_3^{Ni}). [TK519, 2]

^{13}C NMR (100.64 MHz, THF-d_8): δ [ppm] = 160.5 (Cq, C$^{NacNac\text{-}a}$), 158.5 (Cq) C$^{NacNac\text{-}b}$), 152.2 (Cq, C^{pz}), 148.1 (Cq, C-DiPP^{i}), 141.9 (Cq, C-DiPP^{o}), 126.0 (CH, HC-DiPP^{p}), 124.3 (CH, HC-DiPP^{m}), 98.3 (CH, HC^{NacNac}), 92.5 (CH, HC^{pz}), 55.5 (CH_2, CH_2), 28.5 (CH, CH^{iPr}), 25.1 (CH_3, $CH_3^{iPr\text{-}a}$), 24.2(CH_3, $CH_3^{iPr\text{-}b}$), 23.4 (CH_3, $CH_3^{NacNac\text{-}b}$), 21.4 (CH_3, $CH_3^{NacNac\text{-}a}$), -15.0 (CH_3, CH_3^{Ni}). [TK519, 9]

FT-IR (ATR): $\tilde{\nu}$ [cm^{-1}] = 3057 (w), 2954 (m), 2924 (m), 2885 (m), 2864 (m), 2807 (w), 2804 (w), 2619 (w), 1555 (w), 1528(s), 1463 (s), 1432 (s), 1396(s), 1381 (w), 1368 (m), 1361 (w), 1341 (w), 1314 (s), 1278 (m), 1251 (s), 1233 (w), 1192 (w), 1177 (w), 1158 (w), 1145 (w), 1102 (w)1084 (w), 1073 (m), 1055 (m), 1033 (m), 1018 (m), 955 (w), 933 (m), 917 (m), 872 (w), 862 (w), 845 (w), 801 (m), 794 (m), 767 (m), 759 (s), 748 (s), 734 (s), 713 (m), 691 (w), 685 (w), 662 (w), 643 (w), 621 (w), 615 (w), 567 (w), 550 (w), 541 (w), 526 (w), 503 (w), 478 (w), 451 (w), 430 (s), 419 (m), 401 (m).

Elemental Analysis: calc. for $C_{39}H_{54}N_6Ni_2$: C 64.67, H 7.52, N 11.60; found C 63.80, H 7.73, N 11.20.

LNi_2CD_3 (6-d_3)

In a 20 mL screw cap vial in a glove box **1^{Br}** (100 mg, 125 µmol, 1.00 eq.) was suspended in THF (15 mL, abs.) and KC_8 (38 mg, 274 µmol, 2.20 eq.) was added. An immediate color change to deep red was observed. The reduction was stirred overnight to ensure completion. After filtration, CD_3OTs (23 mg, 125 µmol, 1.00 eq.) was added, giving a brown suspension. The reaction mixture was stirred overnight at room temperature and filtered. The brown THF solution was overlayered with hexane. After three weeks crystallization yielded **6** was isolated as dark brown rods. (21 mg, 27.5 µmol, 22%)

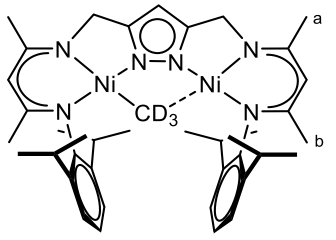

6-d$_3$

^{1}H NMR (400.25 MHz, THF-d$_8$): δ [ppm] = 6.94 (t, $^3J_{\text{H-H}}$ = 7.6 Hz, 2H, H-DiPP^p), 6.82 (t, $^3J_{\text{H-H}}$ = 7.6 Hz, 4H, H-DiPP^m), 5.51 (s, 1H, H$^{\text{pz}}$), 4.67 (s, 2H, CH$^{\text{NacNac}}$), 4.34 (s, 4H, CH$_2$), 3.40 (sep, $^3J_{\text{H-H}}$ = 6.8 Hz, 2H, CH$^{i\text{Pr}}$), 1.93 (s, 6H, CH$_3$$^{\text{NacNac-a}}$), 1.40 (d, $^3J_{\text{H-H}}$ = 6.9 Hz, 12H,CH$_3$$^{i\text{Pr-a}}$), 1.24 (s, 6H, CH$_3$$^{\text{NacNac-b}}$), 1.02 (d, $^3J_{\text{H-H}}$ = 6.9 Hz, 12H,CH$_3$$^{i\text{Pr-b}}$). [TK555, 159]

^{2}H NMR (46.07 MHz, THF): δ [ppm] = -3.18 (s, 3D, NiCD$_3$). [TK555, 169]

KLNi$_2$CHSi(CH$_3$)$_3$ (8-K)

In a 20 mL screw cap vial in a glove box **2-K** (20 mg, 25 µmol, 1.0 eq.) was dissolved in THF (3 mL, abs.) and trimethylsilyl diazomethane solution in hexane (12.5 µL, 2 M, 25 µmol, 1.0 eq.) was added. After 10 min stirring at room temperature the deep red reaction mixture was filtered and overlayered with hexane. After two weeks at -35 °C crystallization **8-K** was isolated as large red rods. (11.7 mg, 13.5 µmol, 54 %)

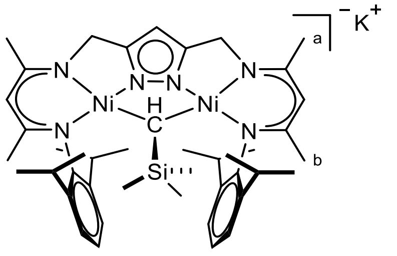

8-K

^{1}H NMR (400.25 MHz, THF-d^8) δ [ppm] = 6.81 – 6.73 (m, 4H, H-DiPP^m), 6.65 (dd, $^3J_{\text{H-H}}$ = 7.1 Hz, $^4J_{\text{H-H}}$ = 2.5 Hz, 2H,H-DiPP^p), 5.17 (s, 1H, CH$^{\text{pz}}$), 4.35 (sep, $^3J_{\text{H-H}}$ = 6.9 Hz, 2H, CH$^{i\text{Pr-H}}$), 4.22 (s, 2H, CH$^{\text{NacNac}}$), 4.09 (d, $^2J_{\text{H-H}}$ = 16.9 Hz, 2H, CH$_2$), 3.90 (d, $^2J_{\text{H-H}}$ = 16.9 Hz, 2H, CH$_2$), 2.97 (sep, $^3J_{\text{H-H}}$ = 6.8 Hz, 2 H, CH$^{i\text{Pr-Si}}$), 1.68 (s, 6H, CH$_3$$^{\text{NacNac-a}}$), 1.62 (d, $^3J_{\text{H-H}}$ = 6.9 Hz, 6H, CH$_3$$^{i\text{Pr-H-in}}$), 1.05 (s, 6H, CH$_3$$^{\text{NacNac-b}}$), 0.98 (d, $^3J_{\text{H-H}}$ = 6.9 Hz, 6H, CH$_3$$^{i\text{Pr-H-out}}$), 0.86 (d, $^3J_{\text{H-H}}$ = 6.8 Hz, 6H, CH$_3$$^{i\text{Pr-Si-out}}$), 0.84 (d, $^3J_{\text{H-H}}$ = 6.8 Hz, 6H, CH$_3$$^{i\text{Pr-Si-in}}$), 0.35 (s, 9H, Si(CH$_3$)$_3$), 0.14 (s, 1H, Ni$_2$CHSi). [TK537, 27]

^{13}C NMR (100.64 MHz, THF-d^8): δ [ppm] = 158.3 (Cq, C$^{\text{NacNac-b}}$), 156.8 (Cq, C$^{\text{NacNac-a}}$), 152.6 (Cq, HC-DiPP^i), 149.7 (Cq, C$^{\text{pz}}$), 143.2 (Cq, DiPP$^{o\text{-H}}$), 140.7 (Cq, Cq, C-DiPP$^{o\text{-Si}}$), 123.7 (CH, HC-DiPP^m), 123.3 (CH, HC-DiPP^p), 123.1 (CH, HC-DiPP^m), 96.04 (CH, HC$^{\text{NacNac}}$), 89.4 (CH, HC$^{\text{pz}}$), 52.9 (CH$_2$, CH$_2$), 28.6 (CH, CH$^{i\text{Pr-H}}$), 27.4 (CH, CH$^{i\text{Pr-Si}}$), 27.2 (CH$_3$, H$_3$C$^{i\text{Pr-Si-in}}$), 26.2(CH$_3$, H$_3$C$^{i\text{Pr-H-in}}$), 25.1 (CH$_3$, H$_3$C$^{i\text{Pr-Si-out}}$), 25.1 (CH$_3$, H$_3$C$^{\text{NacNac-b}}$), 24.6 (CH$_3$, H$_3$C$^{i\text{Pr-H-out}}$) 21.1 (CH$_3$, H$_3$C$^{\text{NacNac-a}}$), 19.2 (CH, Ni$_2$CHSi), 7.2 (CH$_3$, Si(CH$_3$)$_3$). [TK537, 29]

^{1}H NMR (300.13 MHz, C$_6$D$_6$): δ [ppm] = 6.90 (dd, $^3J_{\text{H-H}}$ = 6.8 Hz, $^4J_{\text{H-H}}$ = 2.4 Hz, 2H, H-DiPP^m), 6.79 (t, $^3J_{\text{H-H}}$ = 7.3 Hz, 2H, H-DiPP^p) 6.76 (dd, $^3J_{\text{H-H}}$ = 6.8 Hz, $^4J_{\text{H-H}}$ = 2.4 Hz, 2H, 2H,H-DiPP^p), 5.64 (s, 1H, CH$^{\text{pz}}$), 4.82 (s, 2H, CH^{NacNac}), 4.21 (d, $^2J_{H\text{-}H}$ = 17.9 Hz, 2H, CH$_2$), 3.99 (d, $^2J_{H\text{-}H}$ = 17.9 Hz, 2H, CH$_2$), 3.87 (sep, $^3J_{H\text{-}H}$ = 6.6 Hz, 2H, CH$^{iPr\text{-}H}$), 3.26 (sep, $^3J_{H\text{-}H}$ = 6.9 Hz, 2 H, CH$^{iPr\text{-}Si}$), 1.80 (d, $^3J_{H\text{-}H}$ = 6.9 Hz, 6H, CH$_3^{iPr\text{-}H\text{-}in}$), 1.66 (s, 6H, CH$_3^{NacNac\text{-}a}$), 1.44 (s, 6H, CH$_3^{NacNac\text{-}b}$), 1.30 (d, $^3J_{H\text{-}H}$ = 6.9 Hz, 6H, CH$_3^{iPr\text{-}H\text{-}out}$), 1.09 (d, $^3J_{H\text{-}H}$ = 6.6 Hz, 6H, CH$_3^{iPr\text{-}Si\text{-}out}$), 1.02 (d, $^3J_{H\text{-}H}$ = 6.6 Hz, 6H, CH$_3^{iPr\text{-}Si\text{-}in}$), 1.02 (s, 9H, Si(CH$_3$)$_3$), -1.44 (s, 1H, Ni$_2$CHSi). [TK555b, 261]

^{29}Si NMR (99.39 MHz, C$_6$D$_6$): δ [ppm] = -6.9 (Si(CH$_3$)$_3$). [TK555b, 1]

FT-IR (ATR): ν [cm^{-1}] = 3055 (w), 2958 (m), 2865 (m), 1560 (m), 1512 (s), 1459 (w), 1436 (vs), 1400 (vs), 1358 (m), 1341 (w), 1317 (w), 1309 (m), 1253 (m), 1237 (w), 1223 (w), 1182 (m), 1105 (m), 1076 (m), 1046 (s), 1025 (m), 1019 (m), 994 (w), 961 (vw), 937 (w), 887 (m), 843 (s), 822 (m), 793 (m), 757 (s), 719 (s), 704 (m), 689 (m), 651 (s), 623 (w), 592 (w), 545 (w), 524 (m), 520 (w).

UV-Vis (THF): λ [nm] (ε = L·mol^{-1}·cm^{-1}) = 282 (25830), 303 (sh, 21240), 388 (8620), 458 (sh, 5340).

MS (ESI$^+$, THF) *m/z*: [H$_2$LNi$_2$CHSi(CH$_3$)$_3$]$^+$ = 809.44, [LNi$_2$CHSi(CH$_3$)$_3$ + THF]$^+$ = 879.42.

(K[2.2.2]-cryptand)KLNi$_2$CHSi(CH$_3$)$_3$ (8-cK)

In a 20 mL screw cap vial in a glove box **2-K** (20 mg, 25 µmol, 1.0 eq.) was dissolved in THF (3 mL, abs.) and trimethylsilyl diazomethane solution in hexane (12.5 µL, 2 M, 25 µmol, 1.0 eq.) and [2.2.2]cryptand (9.4 mg, 25 µmol, 1.0 eq.) were added. After 10 min stirring at room temperature the deep red reaction mixture was filtered and overlayered with hexane. After two weeks at -35 °C crystallization **8-cK** was isolated as large red rods. (13 mg, 10 µmol, 40 %)

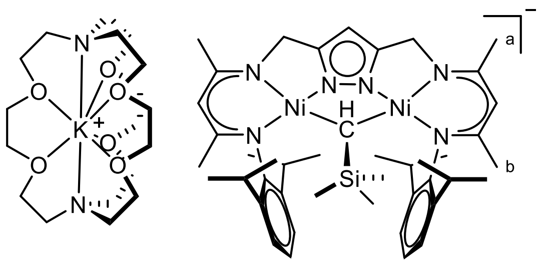

8-cK

^{1}H NMR (400.25 MHz, THF-d^8): δ [ppm] = 6.80 – 6.72 (m, 4H, H-DiPP^m), 6.65 (dd, $^3J_{H\text{-}H}$ = = 7.1 Hz, $^4J_{H\text{-}H}$ = 2.5 Hz, 2H,H-DiPP^p), 5.16 (s, 1H, CH^{pz}), 4.33 (sep, J = 6.9 Hz, 2H, CH$^{iPr\text{-}H}$), 4.21 (s, 2H, CH^{NacNac}), 4.09 (d, $^2J_{H\text{-}H}$ = 16.9 Hz, 2H, CH$_2$), 3.90 (d, $^2J_{H\text{-}H}$ = 16.9 Hz, 2H, CH$_2$), 3.59 (m, 12H, crypt-H),3.55 (m, 12H, crypt-H), 2.97 (sep, $^3J_{H\text{-}H}$ = 6.8 Hz, 2 H, CH$^{iPr\text{-}Si}$), 2.56 (m, 12H, crypt-H), 1.68 (s, 6H, CH$_3^{NacNac\text{-}a}$), 1.62 (d, $^3J_{H\text{-}H}$ = 6.9 Hz, 6H, CH$_3^{iPr\text{-}H\text{-}in}$), 1.04 (s, 6H, CH$_3^{NacNac\text{-}b}$), 0.98 (d, $^3J_{H\text{-}H}$ = 6.9 Hz, 6H, CH$_3^{iPr\text{-}H\text{-}out}$), 0.86 (d, $^3J_{H\text{-}H}$ = 6.8 Hz, 6H, CH$_3^{iPr\text{-}Si\text{-}out}$), 0.84 (d, $^3J_{H\text{-}H}$ = 6.8 Hz, 6H, CH$_3^{iPr\text{-}Si\text{-}in}$), 0.35 (d, $^3J_{H\text{-}H}$ = 0.5 Hz, 9H, Si(CH$_3$)$_3$), 0.14 (d, $^3J_{H\text{-}H}$ = 0.5 Hz, 1H, Ni$_2$CHSi). [TK549, 160]

LNi$_2$CCH$_3$O (10^{Me})

In a 40 mL Teflon valve sealed flask in the glovebox **6** (20 mg, 27 µmol, 1.0 eq.) was dissolved in THF (5 mL, abs.). The solution was degassed with freeze-pump-thaw cycle three times and then over molecular sieves (3 Å) dried CO was added. The reaction mixture was stirred for three days for complete conversion. The solvent was removed *in vacuo* and the dark brown residue was washed with hexane and filtered. Acetyl complex **10$^{\mathrm{Me}}$** was obtained as a powder of light beige color. (2.3mg, 3 µmol, 12 %)

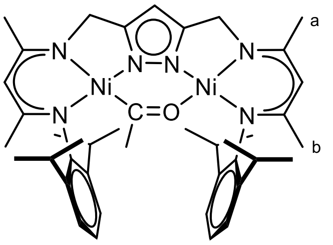

10$^{\mathrm{Me}}$

^{1}H NMR (400.25 MHz, THF-d^8): δ [ppm]= 6.99-6.92 (m, 3H, H-DiPP^{p}), 6.91-6.86 (m, 1H, H-DiPP^{m}), 6.78 (d, J = 7.7 Hz, 2H, H-DiPP^{p}), 5.64 (s, 1H, H$^{\mathrm{pz}}$), 4.85 (s, 1H, CH$^{\mathrm{NacNac}}$), 4.73 (s, 1H, CH$^{\mathrm{NacNac}}$), 4.09 (s, 2H, CH$_2$), 4.03 (s, 2H, CH$_2$), 3.57-3.48 (m, 2H, CH$^{i\mathrm{Pr}}$), 1.99 (s, 3H, CH$_3^{\mathrm{NacNac\text{-}a}}$), 1.96 (s, 3H, CH$_3^{\mathrm{NacNac\text{-}a}}$), 1.83 (s, 3H, OCCH$_3$), 1.41 (s, 3H, CH$_3^{\mathrm{NacNac\text{-}b}}$), 1.40 (s, 3H, CH$_3^{\mathrm{NacNac\text{-}b}}$), 1.21 (d, $^3J_{\mathrm{H\text{-}H}}$ = 6.8 Hz, 3H, CH$_3^{i\mathrm{Pr}}$), 1.14 (d, $^3J_{\mathrm{H\text{-}H}}$ = 6.8 Hz, 6H, CH$_3^{i\mathrm{Pr}}$), 1.07 (d, $^3J_{\mathrm{H\text{-}H}}$ = 6.8 Hz, 6H, CH$_3^{i\mathrm{Pr}}$), 1.01 (d, $^3J_{\mathrm{H\text{-}H}}$ = 6.8 Hz, 6H, CH$_3^{i\mathrm{Pr}}$). [TK599, 138]

^{13}C NMR (100.64 MHz, THF-d^8): δ [ppm] = 292.0 (CH, CO), 161.3 (Cq, C$^{\mathrm{NacNac\text{-}b}}$), 161.1 (Cq, C$^{\mathrm{NacNac\text{-}a}}$), 161.0 (Cq, C$^{\mathrm{NacNac\text{-}a}}$), 159.8 (Cq, C$^{\mathrm{NacNac\text{-}b}}$), 156.8 (Cq, C$^{\mathrm{pz}}$), 152.6 (Cq, C$^{\mathrm{pz}}$), 150.9 (Cq, C-DiPP^{i}), 146.0 (Cq, C-DiPP^{i}), 143.2 (Cq, C-DiPP^{o}), 143.0 (Cq, C-DiPP^{o}), 125.8 (CH, C-DiPP^{p}), 125.5 (CH, C-DiPP^{p}), 124.3 (CH, C-DiPP^{m}), 123.2 (CH, C-DiPP^{m}), 98.7 (CH, CH$^{\mathrm{NacNac}}$), 98.3 (CH, CH$^{\mathrm{NacNac}}$), 93.0 (CH, C$^{\mathrm{pz}}$), 53.6 (CH$_2$, CH$_2$), 50.8 (CH$_2$, CH$_2$), 41.2 (CH$_3$, COCH$_3$) 28.7 (CH, CH$^{i\mathrm{Pr}}$), 28.7 (CH, CH$^{i\mathrm{Pr}}$), 25.6 (CH$_3$, CH$_3^{i\mathrm{Pr}}$), 25.2 (2 CH$_3$, CH$_3^{i\mathrm{Pr}}$), 23.8 (CH$_3$, CH$_3^{i\mathrm{Pr}}$), 23.6 (CH$_3$, CH$_3^{\mathrm{NacNac\text{-}b}}$), 23.4 (CH$_3$, CH$_3^{\mathrm{NacNac\text{-}b}}$), 21.0 (CH$_3$, CH$_3^{\mathrm{NacNac\text{-}a}}$), 20.9 (CH$_3$, CH$_3^{\mathrm{NacNac\text{-}a}}$). [TK542, 38]

FT-IR (ATR): $\tilde{\nu}$ [cm^{-1}] = 3058 (w), 2951 (m), 2921 (m), 2866 (m), 1668 (vw), 1621 (vw), 1555 (m), 1527 (s), 1508 (s), 1456 (s), 1433 (s), 1394 (vs), 1366 (w), 1312 (s), 1280 (vw), 1273 (w), 1247 (m), 1230 (w), 1187 (m), 1174 (m), 1129 (w), 1088 (m), 1029 (m), 1014 (m), 932 (w), 866 (w), 801 (s), 760 (s), 751 (w), 730 (s), 714 (m), 690 (m), 645 (m), 624 (w), 595 (w), 570 (w), 559 (w), 544 (w), 528 (w).

LNi$_2$CHO (10$^{\mathrm{H}}$)

In a Teflon valve sealed 20 mL glass tube **2-K** (50 mg, 63 µmol, 1 eq.) and Et$_3$OBF$_4$ (13 mg, 63 µmol, 1 eq.) were suspended in toluene (10 mL, abs.). Upon stirring under a nitrogen atmosphere, the orange mixture changed to dark brown indicating the formation of **4**. The reaction mixture was degassed with two freeze-pump-thaw cycles vile the atmosphere was exchanged with CO (1 atm) after the last cycle. The color lightened faintly, and the reaction was stirred at room temperature overnight. The byproduct KBF$_4$ was filtered off and the solvent was removed *in vacuo*. The brown residue was dissolved in THF (abs.) and overlayered with hexane. After one week at -35 °C crystallization **10$^{\mathrm{Me}}$** was isolated as dark brown cuboids. (6 mg, 8 µmol, 12.7%)

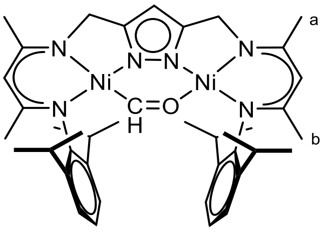

10^{H}

^{1}H NMR (300.13 MHz, THF-d^8): δ [ppm]= 7.38 (s, 1H, HCO), 7.06 (t, *J* = 7.7 Hz, 1H, H-DiPP^{p}), 6.91 (d, J = 7.8 Hz, 3H, H-DiPP^{m}), 6.72 (d, J = 7.9 Hz, 2H, H-DiPP^{p}), 5.75 (s, 1H, H^{pz}), 4.99 (s, 1H, CH$^{NacNac-CH}$), 4.86 (s, 1H, CH$^{NacNac-O}$), 4.21 (s, 2H, CH$_2$), 4.14 (s, 2H, CH$_2$), 3.42 (sep, *J* = 6.9 Hz, CH^{iPr-O}), 3.12 (sep, *J* = 6.9 Hz, CH^{iPr-HC}), 2.02 (s, 3H, CH$_3^{NacNac-a/CH}$), 2.02 (s, 3H, CH$_3^{NacNac-a/ O}$), 1.58 (s, 3H, CH$_3^{NacNac-b/CH}$), 1.48 (s, 3H, CH$_3^{NacNac-b/O}$), 1.20 (d, *J* = 6.9 Hz, 3H, CH$_3^{iPr-O}$), 1.07 (d, *J* = 6.9 Hz, 6H, CH$_3^{iPr}$), 1.07 (d, *J* = 6.9 Hz, 6H, CH$_3^{iPr-HC}$), 0.97 (d, *J* = 7.1 Hz, 6H, CH$_3^{iPr-HC}$). [TK533, 135]

^{13}C NMR (100.64 MHz, THF-d^8): δ [ppm] = 275.9 (CH, HCO), 162.3 (Cq, C$^{NacNac-a}$), 161.1 (Cq, C$^{NacNac-a}$), 160.7 (Cq, C$^{NacNac-b/CH}$), 159.9 (Cq, C$^{NacNac-b/O}$), 156.2 (Cq, C^{pz}), 153.4 (Cq, C^{pz}), 146.3 (Cq, C-DiPP^{i-}), 145.1 (Cq, C-DiPP^{i-}), 143.7 (Cq, C-DiPP^{o-CH}), 142.9 (Cq, C-DiPP^{o-O}), 126.1 (CH, C-DiPP^{p}), 125.5 (CH, C-DiPP^{p}), 123.6 (CH, C-DiPP^{m}), 123.1 (CH, C-DiPP^{m}), 98.7 (CH, CH$^{NacNac-CH}$), 98.2 (CH$^{NacNac-O}$), 92.8 (CH, C^{pz}), 54.0 (CH$_2$, CH$_2$), 52.0 (CH$_2$, CH$_2$), 28.6 (CH, CH^{iPr-O}), 28.1 (CH, CH^{iPr-CH}), 26.8 (CH$_3$, CH$_3^{NacNac-b/CH}$), 25.2 (CH$_3$, CH$_3^{NacNac-b/O}$), 24.4 (CH$_3$, CH$_3^{iPr-O}$), 23.9 (CH$_3$, CH$_3^{iPr-HC}$), 23.8 (CH$_3$, CH$_3^{iPr-HC}$), 23.5 (CH$_3$, CH$_3^{NacNac-b/O}$), 21.7 (CH$_3$, CH$_3^{NacNac-a/O}$), 21.0 (CH$_3$, CH$_3^{NacNac-a/CH}$). [TK542, 38]

FT-IR (ATR): $\tilde{\nu}$ [cm^{-1}]: = 3054 (w), 2954 (m), 2923 (m), 2890 (m), 2864 (m), 1735 (m), 1558 (w), 1525 (s), 1461 (s), 1436 (s), 1398 (s), 1381 (w), 1369 (w), 1362 (w), 1359 (m), 1315 (m), 1277 (m), 1252 (m), 1234 (m), 1211 (m), 1188 (m), 1175 (m), 1159 (m), 1153 (m), 1142 (m), 1102 (w), 1092 (m), 1073 (m), 1055 (m), 1033 (m), 1020 (s), 965 (m), 957 (w), 954, 78, 935 (w), 917, (w), 902, (m), 828 (w),, 815 (w), 796 (w), 769 (s), 760 (m), 742 (w), 714 (w), 649 (w), 640 (w), 619 (w) , 597 (w), 594 (w), 590 (w), 586 (w), 582 (w), 579 (w), 575 (w), 568 (w), 560 (w), 556 (w), 553 (w), 549 (w), 539 (w), 534 (w), 527 (w), 523 (w), 513 (w), 509 (w), 501 (w), 498 (w), 494 (w), 490 (w), 486 (w), 483 (w), 480 (w), 476 (w), 472 (w), 469 (w), 465 (w), 458 (m), 454 (w), 443 (s), 439 (s), 435 (s), 431 (s), 428 (w), 424 (s), 420 (s), 417 (s), 414 (s), 409 (m), 406 (m), 403 (s) cm^{-1}.

KLNi$_2$CH$_2$O (11-K)

In a 20 mL screw cap vial in a glove box **2-K** (20 mg, 25 µmol, 1.0 eq.) was dissolved in THF (2 mL, abs.). A suspension of paraformaldehyde (0.8mg, 75 µmol, 3 eq.) in THF (0.2 mL, abs.) was added leading to a color change to dark brown. After stirring for 18 h, the reaction mixture was filtered and overlayered with hexane. After 4 weeks crystallization **11-K** was isolated as red cubes. (11 mg, 14 µmol, 56 %)

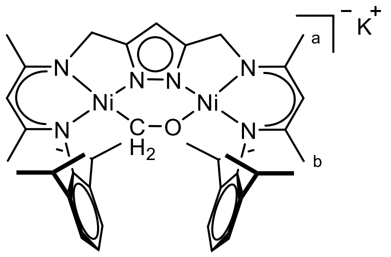

11-K

^{1}H NMR (500.25 MHz, THF-d^{8}): δ [ppm] = 6.86 (dd, $^{3}J_{H\text{-}H}$ = 8.8 Hz, $^{3}J_{H\text{-}H}$ = 6.7 Hz, 1H, H-DiPP), 6.80 (dd, 3H, $^{3}J_{H\text{-}H}$ = 8.8 Hz, $^{3}J_{H\text{-}H}$ = 6.7 Hz, H-DiPP), 6.68 (d, $^{3}J_{H\text{-}H}$ = 7.7 Hz, 2H, H-DiPP^{p}), 5.65 (s, 1H, H^{pz}), 4.52 (s, 1H, CH^{NacNac}), 4.48 (s, 1H, CH^{NacNac}), 4.01 (s, 2H, CH$_2$), 3.82 (s, 2H, CH$_2$), 3.80 (sep, $^{3}J_{H\text{-}H}$ = 6.8 Hz, 2H, CH^{iPr}), 3.35 (sep, $^{3}J_{H\text{-}H}$ = 6.8 Hz, CH^{iPr}), 2.31 (s, 2H, CH$_2$O), 1.80 (s, 3H, CH$_3^{NacNac\text{-}a}$), 1.75 (s, 3H, CH$_3^{NacNac\text{-}a}$), 1.33 (s, 3H, CH$_3^{NacNac\text{-}b}$), 1.20 (s, 3H, CH$_3^{NacNac\text{-}b}$), 1.19 (d, $^{3}J_{H\text{-}H}$ = 6.8 Hz, 3H, CH$_3^{iPr}$), 1.03 (d, $^{3}J_{H\text{-}H}$ = 6.8 Hz, 6H, CH$_3^{iPr}$), 1.02 (d, $^{3}J_{H\text{-}H}$ = 6.8 Hz, 6H, CH$_3^{iPr}$), 0.99 (d, $^{3}J_{H\text{-}H}$ = 6.9 Hz, 6H, CH$_3^{iPr}$). [TK560, 1]

^{13}C NMR (125.79 MHz, THF-d^{8}): δ [ppm] = 159.5 (Cq, C$^{NacNac\text{-}a}$), 159.0 (Cq, C$^{NacNac\text{-}b}$), 158.1 (Cq, C$^{NacNac\text{-}a}$), 157.8 (Cq, C$^{NacNac\text{-}b}$), 156.9 (Cq, C^{pz}), 153.5 (Cq, C^{pz}), 148.7 (Cq, C-DiPP^{i}), 148.5 (Cq, C-DiPP^{i}), 142.1 (Cq, C-DiPP^{o}), 142.1 (Cq, C-DiPP^{o}), 124.0 (CH, HC-DiPP^{m}), 123.9 (CH, HC-DiPP^{m}), 123.1 (CH, HC-DiPP^{m}), 122.4 (CH, HC-DiPP^{p}), 96.9 (CH, HC^{NacNac}), 96.0 (CH, HC^{NacNac}), 92.3 (CH, HC^{pz}), 75.7 (CH$_2$, H$_2$CO), 51.4 (CH$_2$, CH$_2$), 49.3 (CH$_2$, CH$_2$), 28.9 (CH, CH^{iPr}), 27.8 (CH, CH^{iPr}), 26.4 (CH$_3^{NacNac\text{-}b}$), 24.9 (CH$_3$, CH$_3^{iPr}$), 24.5 (CH$_3^{iPr}$). 24.3 (CH$_3$, CH$_3^{NacNac\text{-}a}$), 24.2 (CH$_3^{iPr}$), 21.7 (CH$_3^{NacNac\text{-}a}$), 21.4 (CH$_3^{NacNac\text{-}b}$). [TK560, 2]

FT-IR (ATR): $\tilde{\nu}$ [cm^{-1}]: = 3060 (w), 3015 (vw), 2950 (m), 2921 (m), 2861 (m), 2740 (w), 1612 (vw), 1592 (vw), 1556 (m), 1523 (s), 1512 (s), 1455 (m), 1431 (s), 1394 (vs), 1366 (s), 1307 (s), 1275 (m), 1262 (w), 1249 (m), 1228 (m), 1186 (m), 1144 (w), 1078 (w), 1052 (s), 1031 (m), 978 (vs), 916 (vw), 894 (m), 865 (w), 799 (m), 791 (w), 765 (w), 752 (vs), 726 (s), 710 (m), 660 (w), 644 (w), 635 (vw), 616 (vw), 553 (m), 526 (m), 466 (w), 446 (w), 422 (m), 405 (m).

(K[2.2.2]-cryptand)LNi$_2$CH$_2$O (10-cK)

In a 20 mL screw cap vial in a glove box **2-K** (20 mg, 25 µmol, 1.0 eq.) and [2.2.2]-cryptand (9.4 mg, 25 µmol, 1.0 eq.) were dissolved in THF (2 mL, abs.). A suspension of paraformaldehyde (0.8mg, 75 µmol, 3 eq.) in THF (0.2 mL, abs.) was added leading to a color change to dark brown. After stirring for 18 h, the reaction mixture was filtered and overlayered with hexane. After 4 weeks crystallization **10-cK** was isolated as light brown needles. (22 mg, 19 µmol, 75%)

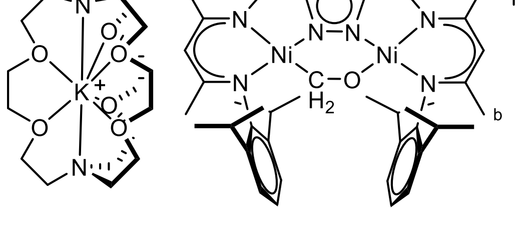

11-cK

^{1}H NMR (400.25 MHz, THF-d^{8}): δ [ppm] = 6.74-6.64 (m, 4H, H-DiPP^{m}), 7.06 (d, $^{3}J_{\text{H-H}}$ = 7.7 Hz, 2H, H-DiPP^{p}), 5.48 (s, 1H, H$^{\text{pz}}$), 4.38 (s, 1H, CH$^{\text{NacNac}}$), 4.32 (s, 1H, CH$^{\text{NacNac}}$), 3.92 (s, 2H, CH$_2$), 3.82 (sep, $^{3}J_{\text{H-H}}$ = 6.9 Hz, 2H, CH$^{i\text{Pr}}$) 3.77 (s, 2H, CH$_2$), 3.64 (s, 12H, crypt-H), 3.56 (m, 12H, crypt-H), 3.46 (sep, $^{3}J_{\text{H-H}}$ = 6.9 Hz, CH$^{i\text{Pr}}$), 2.57 (m, 12H, cryptH), 2.18 (s, 2H, CH$_2$O), 1.71 (s, 3H, CH$_3^{\text{NacNac-a}}$), 1.66 (s, 3H, CH$_3^{\text{NacNac-a}}$), 1.23 (s, 3H, CH$_3^{\text{NacNac-b}}$), 1.21 (d, $^{3}J_{\text{H-H}}$ = 6.9 Hz, 3H, CH$_3^{i\text{Pr}}$), 1.15 (s, 3H, CH$_3^{\text{NacNac-b}}$), 1.00 (d, $^{3}J_{\text{H-H}}$ = 6.9 Hz, 6H, CH$_3^{i\text{Pr}}$), 1.00 (d, $^{3}J_{\text{H-H}}$ = 6.9 Hz, 6H, CH$_3^{i\text{Pr}}$), 0.95 (d, $^{3}J_{\text{H-H}}$ = 7.0 Hz, 6H, CH$_3^{i\text{Pr}}$). [TK563, 71]

^{13}C NMR (100.64 MHz, THF-d^{8}): δ [ppm] = 158.1 (Cq, C$^{\text{NacNac-a}}$), 157.9 (Cq, C$^{\text{NacNac-b}}$), 155.9 (Cq, C$^{\text{NacNac-a}}$), 155.8 (Cq, C$^{\text{NacNac-b}}$), 153.9 (Cq, C$^{\text{pz}}$), 151.0 (Cq, C$^{\text{pz}}$), 150.1 (Cq, C-DiPP^{i}), 149.0 (Cq, C-DiPP^{i}), 141.9 (Cq, C-DiPP^{o}), 122.3 (CH, HC-DiPP^{m}), 121.7 (CH, HC-DiPP^{p}), 96.0 (CH, HC$^{\text{NacNac}}$), 95.0 (CH, HC$^{\text{NacNac}}$), 90.5 (CH, HC$^{\text{pz}}$), 77.7 (CH$_2$, H$_2$CO), 71.3 (CH$_2$, crypt-C), 68.4 (CH$_2$, crypt-C), 54.7 (CH$_2$, crypt-C), 51.1 (CH$_2$, CH$_2$), 49.3 (CH$_2$, CH$_2$), 28.6 (CH, CH$^{i\text{Pr}}$), 27.6 (CH, CH$^{i\text{Pr}}$), 26.2 (CH$_3$, CH$_3^{\text{NacNac-b}}$), 25.3 (CH$_3$, CH$_3^{i\text{Pr}}$), 25.2 (CH$_3$, CH$_3^{i\text{Pr}}$), 24.4 (CH$_3$, CH$_3^{i\text{Pr}}$), 24.3 (CH$_3$, CH$_3^{\text{NacNac-b}}$), 24.1 (CH$_3$, CH$_3^{i\text{Pr}}$), 21.7 (CH$_3$, CH$_3^{\text{NacNac-a}}$), 21.2 (CH$_3$, CH$_3^{\text{NacNac-a}}$). [TK563, 72]

KLNi$_2$(OCH$_3$)$_2$H (12)

In a 20 mL screw cap vial in a glove box **2-K** (20 mg, 25.2 µmol, 1.0 eq.) was dissolved in benzene (3 mL, abs.) and paraformaldehyde (3.2 mg, 100.8 µmol, 4 eq.) was added resulting in a color change from orange to green. After the reaction mixture was stirred for 18 h the solvent was removed *in vacuo*. The residue was dissolved in THF, filtered and overlayered with hexane. After 10 days crystallization at room temperature gave **12** as green cubes. (4.4 mg, 5.5 µmol, 22 %)

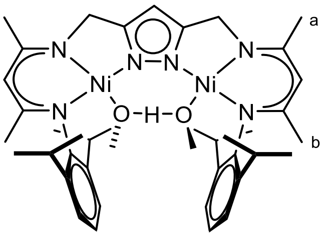

12

^{1}H NMR (benzene-d$_6$, 400.25 MHz): δ [ppm] = 12.21 (sept, ^{1}H, $^{3}J_{\text{H-H}}$ = 2.1 Hz, OHO),6.91-6.65 (m, 6H, CHAr), 5.50 (s, 1H, CH$^{\text{pz}}$), 4.58 (s, 2H, CH$^{\text{NacNac}}$), 3.94 (d, 2H,$^{2}J_{\text{H-H}}$ = 17.2 Hz, CH$_2$), 3.79 (d, 2H, $^{2}J_{\text{H-H}}$ = 17.3 Hz, CH$_2$), 3.67 (sept, 2H, $^{3}J_{\text{H-H}}$ = 6.9 Hz, CH$^{i\text{Pr}}$), 3.33 (sept, 2H, $^{3}J_{\text{H-H}}$ = 6.8 Hz, CH$^{i\text{Pr}}$), 2.77 (d, 6H, $^{3}J_{\text{H-H}}$ = 2.2 Hz, OCH$_3$), 1.72 (s, 6H, CH$_3^{\text{NacNac-a}}$), 1.61 (d, 6H, $^{3}J_{\text{H-H}}$ = 7.6 Hz, CH$_3^{i\text{Pr}}$), 1.29 (s, 6H, CH$_3^{\text{NacNac-b}}$), 0.90 (d, 6H, $^{3}J_{\text{H-H}}$ = 6.4 Hz, CH$_3^{i\text{Pr}}$), 0.88 (d, 6H, $^{3}J_{\text{H-H}}$ = 6.4 Hz, CH$_3^{i\text{Pr}}$), 0.73 (d, 6H, $^{3}J_{\text{H-H}}$ = 6.7 Hz, CH$_3^{i\text{Pr}}$). [TKUHK23, 36]

^{13}C NMR (THF-d8, 100.65 MHz): δ [ppm] = 160.5 (Cq, C$^{\text{NacNac-a}}$), 160.0 (Cq, C$^{\text{NacNac-b}}$), 157.4 (Cq, C$^{\text{pz}}$), 146.5 (Cq, C-DiPP), 145.8 (Cq, C$^{\text{pz}}$), 142.2 (Cq, C-DiPP^{o}), 125.5 (CH, C-DiPP^{m}), 123.6 (CH, C-DiPP^{m}), 123.4 (CH, C-DiPP^{p}),99.0 (CH, C$^{\text{NacNac}}$), 92.4 (CH, C$^{\text{pz}}$), 52.9 (CH$_2$, CH$_2$), 51.7 (CH$_3$, OCH$_3$), 29.5 (CH, CH$^{i\text{Pr}}$), 29.1 (CH, CH$^{i\text{Pr}}$), 25.6 (CH$_3$, CH$_3^{i\text{Pr}}$), 25.4 (CH$_3$, CH$_3^{i\text{Pr}}$), 25.0 (CH$_3$, CH$_3^{i\text{Pr}}$), 24.9 (CH$_3$, CH$_3^{i\text{Pr}}$), 24.0 (CH$_3$, CH$_3^{\text{NacNac-b}}$), 19.9 (CH$_3$, CH$_3^{\text{NacNac-a}}$). [TKUHK23, 39]

KLNi$_2$(CHOPh) (13-K)

In a 20 mL screw cap vial in a glove box **2-K** (40 mg, 50 µmol, 1.0 eq.) was dissolved in THF (1 mL, abs.) and benzaldehyde (5.1 µL, 5.3 mg, 50 µmol, 1.0 eq.) was added leading to a color change from bright orange to intense red. After 5 min stirring at room temperature the solution was overlayered with hexane. After one week crystallization at -35 °C **13-K** was isolated as red rods. (37 mg, 42.6 µmol, 85 %)

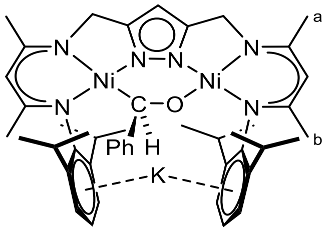

13-K

^{1}H NMR (400.25 MHz, THF-d^8): δ [ppm]= 9.56 (d, ^3J = 7.9 Hz, 2H, CH$^{o\text{-benzald}}$), 7.05-7.01 (m, 2H, H-DiPP^{m}), 7.02-6.96 (m, 2H, CH$^{m\text{-benzald}}$), 6.99-6.96 (m, 1H, H-DiPP^{p}), 6.94 (d, ^3J = 7.4 Hz, 1H, 1H, H-DiPP^{p}), 6.90 (dd, ^3J = 7.7 Hz, ^4J = 1.8 Hz, 1H, H-DiPP^{m}), 6.81 (dd, ^3J = 7.2 Hz, ^4J = 1.7 Hz, 1H, H-DiPP^{m}), 6.80-6.76 (m, 1H, CH$^{p\text{-benzald}}$), 5.35 (s, 1H, CH$^{\text{pz}}$), 4.60 (s, 1H, CH$^{\text{NacNacCHPh}}$), 4.48 (s, 1H, CH$^{\text{NacNac-O}}$), 4.00 (sep, ^3J = 6.4 Hz, 1H, CH$^{i\text{Pr-H/O}}$), 3.99 (sep, J = 6.1 Hz, 1H, CH$^{i\text{Pr-H/CHPh}}$) 3.94 (d, ^2J = 18 Hz, 1H, CH$_2^{\text{CHPh}}$), 3.87 (d, ^2J = 17.3 Hz, 1H, CH$_2^{\text{O}}$), 3.76 (d, ^2J = 17.9 Hz, 1H, CH$_2^{\text{CHPh}}$), 3.73 (d, ^2J = 17.7 Hz, 1H, CH$_2^{\text{O}}$), 3.41 (sep, J = 6.8 Hz, 1H, CH$^{i\text{Pr-Ph/CHPh}}$), 3.05 (sep, ^3J = 6.7 Hz, 1H, CH$^{i\text{PrPh/O}}$), 2.77 (s, 1H, NiCH), 2.09 (d, ^3J = 6.8 Hz, 3H, CH$_3^{i\text{Pr-H/O}}$), 1.83 (s, 3H, CH$_3^{\text{NacNac-a/CHPh}}$), 1.76 (d, ^3J = 6.8 Hz, 3H, CH$_3^{i\text{Pr-H/CHPh}}$), 1.72 (s, 3H, CH$_3^{\text{NacNac-a/O}}$), 1.23 (s, 3H, CH$_3^{\text{NacNac-b/O}}$), 1.18 (d, ^3J = 7.0 Hz, 3H, CH$_3^{i\text{Pr-H/O}}$), 1.16 (s, 3H, CH$_3^{\text{NacNac-b/CHPh}}$), 1.11 (d, ^3J = 6.9 Hz, 3H, CH$_3^{i\text{Pr-H/CHPh}}$), 0.96 (d, ^3J = 6.8 Hz, 3H, CH$_3^{i\text{PrPh/O}}$), 0.89 (d, ^3J = 6.8 Hz, 3H, CH$_3^{i\text{Pr-Ph/CHPh}}$), 0.69 (d, ^3J = 6.8 Hz, 3H, CH$_3^{i\text{PrPh/O}}$), 0.51 (d, ^3J = 6.8 Hz, 3H, CH$_3^{i\text{Pr-Ph/CHPh}}$). [TK457, 1]

^{13}C NMR (100.64 MHz, THF-d^8): δ [ppm]= 160.5 (Cq, C$^{\text{NacNac-a/CHPh}}$), 159.0 (Cq, C$^{\text{NacNac-a/O}}$), 159.0 (Cq, C$^{\text{NacNac-b/CHPh}}$), 157.9 (Cq, C$^{\text{NacNac-b/O}}$), 155.4 (Cq, C$^{i\text{-benzald}}$), 154.3 (Cq, C$^{\text{pz-O}}$), 151.9 (Cq, C-DiPP$^{i\text{-CHPh}}$), 151.6 (Cq, C$^{\text{pz-CHPH}}$), 150.4 (Cq, C-DiPP$^{i\text{-O}}$), 147.1 (Cq, C$^{i\text{Pr-Ph/CHPh}}$), 145.6 (Cq, C$^{i\text{Pr-H/CHPh}}$), 144.3 (Cq, C$^{i\text{PrPh/O}}$), 143.5 (Cq, C$^{i\text{Pr-H/O}}$), 126.7 (CH, CH$^{m\text{-benzald}}$), 126.5 (CH, CH$^{o\text{-benzald}}$), 124.6 (CH, C-DiPP^{p}), 124.0 (CH, C-DiPP^{p}), 123.7 (CH, C-DiPP^{m}), 123.5 (CH, C-DiPP^{m}), 123.4 (CH, C-DiPP^{m}), 123.3 (CH, C-DiPP^{m}), 120.8 (CH, CH$^{p\text{-benzald}}$), 98.0 (CH, C$^{\text{NacNac-CHPh}}$), 97.1 (CH, C$^{\text{NacNac-O}}$), 91.2 (CH, C$^{\text{pz}}$), 76.6 (CH, NiC), 52.1 (CH$_2$,CH$_2^{\text{O}}$), 50.3 (CH$_2$,CH$_2^{\text{CHPh}}$), 28.8 (CH, CH$^{i\text{Pr-H/O}}$), 28.5 (CH, CH$^{i\text{Pr-H/CHPh}}$), 28.3 (CH, CH$^{i\text{Pr-Ph/CHPh}}$), 27.8 (CH, CH$^{i\text{PrPh/O}}$), 26.1 (CH$_3$, CH$_3^{i\text{Pr-H/CHPh}}$), 25.8 (CH$_3$, CH$_3^{i\text{Pr-H/O}}$), 25.4 (CH$_3$, CH$_3^{\text{NacNac-b/O}}$), 25.1 (CH$_3$, CH$_3^{i\text{Pr-Ph/O}}$), 25.1 (CH$_3$, CH$_3^{i\text{Pr-Ph/CHPh}}$), 24.8 (CH$_3$, CH$_3^{i\text{PrPh/O}}$), 24.1 (CH$_3$, CH$_3^{\text{NacNac-b/CHPh}}$), 24.1 (CH$_3$, CH$^{i\text{Pr-Ph/O}}$) 23.8 (CH$_3$, CH$_3^{i\text{Pr-H/CHPh}}$), 23.2 (CH$_3$, CH$_3^{i\text{Pr-H/O}}$), 21.3 (CH$_3$, CH$_3^{\text{NacNac-a/O}}$), 21.2 (CH$_3$, CH$_3^{\text{NacNac-a/CHPh}}$). [TK457, 4]

FT-IR (ATR): $\tilde{\nu}$ [cm^{-1}] = 3034 (w), 2962 (w), 2922 (w), 2866 (w), 2810 (w), 1560 (m), 1516 (s), 1465 (s), 1425 (s), 1402 (s), 1364 (s), 1340 (m), 1307 (s), 1264 (s), 1244 (s), 1230 (s), 1184 (s), 1160 (s), 1082 (s), 1053 (s), 1026 (s), 996 (s), 936 (s), 803 (s), 788 (s), 771 (s), 732 (vs), 693 (s), 677 (vs), 647 (s), 608 (s), 595 (s), 569 (m), 550 (m), 518 (s), 488 (s), 472 (m), 462 (m), 445 (s), 417 (m).

UV-Vis (THF): λ [nm] (ε = L·mol^{-1}·cm^{-1}) = 267 (2311), 295 (2592), 382 (1512), 475 (sh, 367).

(K[2.2.2]cryptand)LNi$_2$(CHOPh) (13-cK)

In a 20 mL screw cap vial in a glove box **2-K** (20 mg, 25 µmol, 1 eq.) and [2.2.2]-cryptand were dissolved in THF (2 mL, abs.). Benzaldehyde (1.1 µL, 1.2 mg, 12.5 µmol, 1 eq.) was added leading to a color change from bright orange to intense red. After stirring for 1 h at room temperature the solution was filtered and overlayered with hexane. After one week at room temperature crystallization **13-cK** was isolated as red cubes. (28.5 mg, 22 µmol, 88 %)

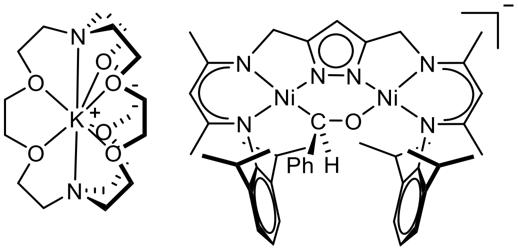

13-cK

^{1}H NMR (400.25 MHz, THF-d$_8$): δ [ppm] = 9.75 (d, 2H, $^3J_{\text{H-H}}$ = 7.8 Hz, CH$^{o\text{-benzald}}$), 6.86-6.80 (m, 4H, H-DiPP), 6.76-6.71 (m, 2H, CH$^{m\text{-benzald}}$), 6.64-6.56 (m, 2H, H-DiPP), 6.53-6.49 (m, 1H, CH$^{p\text{-benzald}}$), 5.14 (s, 1H, CH$^{\text{Pz}}$), 4.40 (s, 1H, CH$^{\text{NacNac-O}}$), 4.36 (sept, $^3J_{\text{H-H}}$ = 6.8 Hz, 2H, CH$^{i\text{Pr}}$), 4.28 (s, 1H, CH$^{\text{NacNac-Ph}}$), 3.88 (d, $^2J_{\text{H-H}}$ = 17.4 Hz, 1H, CH$_2$), 3.80 (m, 1H,CH$_2$), 3.73 (m, 1H, CH$_2$), 3.67 (s, 24H, crypt), 3.65 (m, 1H, CH$_2$), 3.64 (m, 1H, CH$^{i\text{Pr}}$), 3.37 (m, $^3J_{\text{H-H}}$ = 6.9 Hz, 2H, CH$^{i\text{Pr}}$), 3.08 (sept, 1H, $^3J_{\text{H-H}}$ = 6.6 Hz, CH$^{i\text{Pr}}$), 3.01 (s, 1H, NiCH), 2.66 (s, 12H, crypt), 1.97 (d, 3H, $^3J_{\text{H-H}}$ = 6.8 Hz, CH$_3^{i\text{Pr}}$), 1.73 (s, 3H, CH$_3^{\text{NacNac-a}}$), 1.61 (s, 3H, CH$_3^{\text{NacNac-a}}$), 1.28 (d, 3H, $^3J_{\text{H-H}}$ = 6.8 Hz, CH$_3^{i\text{Pr}}$), 1.24 (s, 3H, CH$_3^{\text{NacNac-b}}$), 1.23 (s, 3H, CH$_3^{\text{NacNac-b}}$), 1.11 (d, 3H, $^3J_{\text{H-H}}$ = 6.9 Hz, CH$_3^{i\text{Pr}}$), 0.99 (d, 3H, $^3J_{\text{H-H}}$ = 6.9 Hz, CH$_3^{i\text{Pr}}$), 0.95 (d, 3H, $^3J_{\text{H-H}}$ = 6.7 Hz, CH$_3^{i\text{Pr}}$), 0.79 (d, 3H, $^3J_{\text{H-H}}$ = 6.8 Hz, CH$_3^{i\text{Pr}}$), 0.61 (d, 3H, $^3J_{\text{H-H}}$ = 6.7 Hz, CH$_3^{i\text{Pr}}$), 0.32 (d, 3H, $^3J_{\text{H-H}}$ = 6.7 Hz, CH$_3^{i\text{Pr}}$). [UHK20, 47]

^{13}C NMR (100.65 MHz, THF-d$_8$): δ [ppm] = 160.2 (Cq, C-DiPP^i), 158.9 (Cq, C$^{\text{NacNac-b}}$), 158.6 (Cq, C$^{\text{NacNac-b}}$), 157.7 (Cq, C$^{\text{NacNac-a}}$), 156.4 (Cq, C$^{\text{NacNac-a}}$), 152.5 (CH, C$^{\text{q-Pz}}$), 151.4 (Cq, C$^{i\text{-benzald}}$), 151.2 (Cq, C$^{\text{Pz}}$), 145.5 (Cq, C$^{i\text{Pr}}$), 144.8 (Cq, C$^{i\text{Pr}}$), 142.7 (Cq, C$^{\text{DIPP}}$), 142.4 (Cq, C$^{i\text{Pr}}$), 141.6 (Cq, C$^{i\text{Pr}}$), 129.9 (CH, CH$^{p\text{-benzald}}$), 127.3 (CH, CH$^{o\text{-benzald}}$), 125.9 (CH, CH$^{p\text{-DIPP}}$), 125.4 (CH, CH$^{m\text{-benzald}}$) 122.2 (CH, C$^{p\text{-DIPP}}$), 96.7 (CH, CH$^{\text{NacNac}}$), 95.8(CH, CH$^{\text{NacNac}}$), 90.0 (CH, CH$^{\text{Pz}}$), 79.5 (CH, NiC), 71.4 (CH$_2$, Crypt), 68.6 (CH$_2$, Crypt), 55.1 (CH$_2$, Crypt), 52.4 (CH$_2$, CH$_2$), 50.9 (CH$_2$, CH$_2$), 29.0 (CH, CH$^{i\text{Pr}}$), 28.8 (CH, CH$^{i\text{Pr}}$), 28.8 (CH, CH$^{i\text{Pr}}$), 27.7 (CH, CH$^{i\text{Pr}}$), 27.3 (CH$_3$, CH$_3^{i\text{Pr}}$), 26.3 (CH$_3$, CH$_3^{i\text{Pr}}$), 26.0 (CH$_3$, CH$_3^{\text{NacNac}}$), 25.9 (CH$_3$, CH$_3^{i\text{Pr}}$), 25.7 (CH$_3$, CH$_3^{i\text{Pr}}$), 25.6 (CH$_3$, CH$_3^{i\text{Pr}}$), 25.2(CH$_3$, CH$_3^{i\text{Pr}}$), 24.6 (CH$_3$, CH$_3^{i\text{Pr}}$), 24.4 (CH$_3$, CH$_3^{\text{NacNac}}$), 23.8 (CH$_3$, CH$_3^{i\text{Pr}}$), 23.7 (CH$_3$, CH$_3^{\text{NacNac}}$), 23.4 (CH$_3$, CH$_3^{\text{NacNac}}$), 20.1 (CH$_3$, CH$_3^{\text{NacNac}}$). [UHK20, 2]

FT-IR (ATR): $\tilde{\nu}$ [cm^{-1}] = 3038 (w), 2956 (m), 2899 (m), 2862 (m), 2813 (m), 1554 (w), 1519 (s), 1477 (m), 1464 (m), 1434 (s), 1405 (s), 1354 (m), 1315 (m), 1300 (m), 1258 (m), 1184 (w), 1173 (w), 1154 (w), 1131 (m), 1103 (vs), 1088 (s), 1081 (s), 1063 (m), 1024 (m), 997 (m), 944 (s), 933 (s), 832 (w), 795 (w), 779 (w), 759 (m), 743 (m), 722 (s), 697 (s), 684 (vs), 645 (w), 603 (w), 519 (m), 484 (w), 413 (w), 408 (w).

KLNi$_2$(CHOC$_6$H$_5$N(CH$_3$)$_2$) (13$^{\text{NMe}_2}$-K)

In a 20 mL screw cap vial in a glovebox **2-K** (40 mg, 50 µmol, 1.0 eq.) was dissolved in THF (3 mL, abs.) and 4-*N,N*-dimethylaminobenzaldehyd (7.5 mg, 50 µmol, 1.0 eq.) was added. An immediate color change from orange to dark-red was observed. After stirring overnight, the mixture was filtered, and the filtrate was layered with hexane. Crystallization for 10 days at room temperature gave **13$^{\text{NMe}_2}$-K** as dark red needles suitable for X-ray diffraction. (18.5 mg, 19.5 µmol, 39 %)

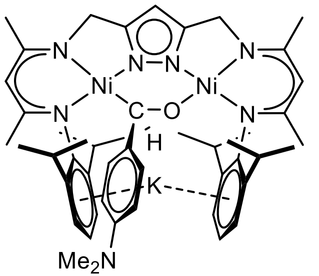

$\mathbf{13^{NMe_2}}$-K

^{1}H NMR (500.25 MHz, THF-d_8): δ [ppm] = 9.13 (d, $^{3}J_{\mathrm{H\text{-}H}}$ = 8.8 Hz, 2H, $\mathrm{CH}^{o\text{-}\mathrm{ald}}$), 7.66 (d, $^{3}J_{\mathrm{H\text{-}H}}$ = 8.8 Hz, 1H, $\mathrm{CH}^{m\text{-}\mathrm{ald}}$), 7. 66 (d, 2H, $^{3}J_{\mathrm{H\text{-}H}}$ = 8.8 Hz, $\mathrm{CH}^{m\mathrm{ald}}$), 7.01-6.74 (m, 8H, $\mathrm{CH}^{\mathrm{Ar}}$), 5.37 (s, 1H, $\mathrm{CH}^{\mathrm{Pz}}$), 4.58 (s, 1H, $\mathrm{CH}^{\mathrm{NacNac\text{-}O}}$), 4.47 (s, 1H, $\mathrm{CH}^{\mathrm{NacNac}}$), 4.04 (m, 1H, $\mathrm{CH}^{i\mathrm{Pr}}$), 3.90 (m, 1H, $\mathrm{CH}^{i\mathrm{Pr}}$), 3.80 (m, $\mathrm{CH_2}$), 3.74 (m, $\mathrm{CH_2}$), 3.06 (s, 3H, $\mathrm{N(CH_3)_2}$), 2.99 (m, 1H, $\mathrm{CH}^{i\mathrm{Pr}}$), 2.99 (m, 1H, $\mathrm{CH}^{i\mathrm{Pr}}$), 2.50 (s, 1H, $\mathrm{CHO}^{\mathrm{ald}}$), 2.07 (d, 3H, $^{3}J_{\mathrm{H\text{-}H}}$ = 7.0 Hz, $\mathrm{CH_3}^{i\mathrm{Pr\text{-}Ar/CHAr}}$), 1.82 (s, 3H, $\mathrm{CH_3}^{\mathrm{NacNac}}$), 1.61 (d, 3H, $^{3}J_{\mathrm{H\text{-}H}}$ = 6.0 Hz, $\mathrm{CH_3}^{i\mathrm{Pr}}$), 1.22 (s, 3H, $\mathrm{CH_3}^{\mathrm{NacNac}}$), 1.17 (d, 3H, $^{3}J_{\mathrm{H\text{-}H}}$ = 6.4 Hz, $\mathrm{CH_3}^{i\mathrm{Pr}}$), 1.13 (d, 3H, $^{3}J_{\mathrm{HH}}$ = 6.5 Hz, $\mathrm{CH_3}^{i\mathrm{Pr}}$), 1.09 (s, 3H, $\mathrm{CH_3}^{\mathrm{NacNac}}$), 1.07 (s, 3H, $\mathrm{CH_3}^{\mathrm{NacNac}}$), 0.90 (d, 3H, $^{3}J_{\mathrm{HH}}$ = 6.7 Hz, $\mathrm{CH_3}^{i\mathrm{Pr}}$), 0.88 (d, 3H, $^{3}J_{\mathrm{HH}}$ = 6.5 Hz, $\mathrm{CH_3}^{i\mathrm{Pr}}$), 0.67 (d, 3H, $^{3}J_{\mathrm{HH}}$ = 6.8 Hz, $\mathrm{CH_3}^{i\mathrm{Pr}}$), 0.55 (d, 3H, $^{3}J_{\mathrm{HH}}$ = 6.7 Hz, $\mathrm{CH_3}^{i\mathrm{Pr}}$). [UHK07, 77]

FT-IR (ATR): $\tilde{\nu}$ [$\mathrm{cm^{-1}}$]: = 3608 (w), 3053 (w), 2958 (m), 2922 (m), 2865 (m), 1661 (w), 1524 (s), 1463 (s), 1432 (s), 1399 (vs), 1316 (s), 1274 (m), 1251 (m), 1231 (m), 1194 (m), 1163 (m), 1090 (m), 1057 (m), 1029 (m), 944 (m), 802 (s), 771 (m), 732 (s), 639 (m), 622 (m), 595 (m), 575 (m), 551 (m), 512 (m), 460 (m), 432 (m), 416 (m), 400 (m).

$\mathbf{KLNi_2(CHOC_6H_5OCH_3)}$ ($\mathbf{13^{OMe}}$-K)

In a 20 mL screw cap vial in a glovebox **2-K** (20.8 mg, 25 µmol, 1.0 eq.) was dissolved in benzene (3 mL, abs.) and 4-methoxybenzaldehyde (3.0 µL, 3.4 mg, 25 µmol, 1.0 eq.) was added. An immediate color change from orange to dark-red was observed. After stirring for 5 h, the mixture was filtered and overlayered with hexane. Crystallization for 10 days at room temperature gave **$\mathbf{13^{OMe}}$-K** as black needles. (7.7 mg, 8.3 µmol, 33 %)

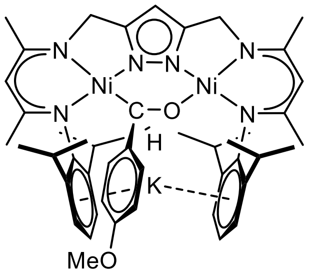

$\mathbf{13^{OMe}}$-K

^{1}H NMR (500.25 MHz, THF-d_8): δ [ppm] = 9.27 (d, $^{3}J_{\mathrm{H\text{-}H}}$ = 8.6 Hz, 2H, $\mathrm{CH}^{o\text{-}\mathrm{ald}}$), 7.05-6.98 (m, 3H, H-DiPP), 6.94 (t, $^{3}J_{\mathrm{H\text{-}H}}$ = 7.6 Hz, 1H, HDiPP^{p}), 6.88 (dd, $^{3}J_{\mathrm{H\text{-}H}}$ = 7.7 Hz, $^{4}J_{\mathrm{H\text{-}H}}$ = 1.7 Hz, 1H, $\mathrm{H\text{-}DiPP}^{m}$), 6.81 (dd, $^{3}J_{\mathrm{H\text{-}H}}$ = 7.3 Hz, $^{4}J_{\mathrm{H\text{-}H}}$ = 1.8 Hz, 1H, HDiPP^{m}) 6.62 (d, 2H, $^{3}J_{\mathrm{H\text{-}H}}$ = 8.8 Hz, $\mathrm{CH}^{m\mathrm{ald}}$), 5.37 (s, 1H, $\mathrm{CH}^{\mathrm{Pz}}$), 4.58 (s, 1H, $\mathrm{CH}^{\mathrm{NacNac\text{-}O}}$), 4.48 (s, 1H, $\mathrm{CH}^{\mathrm{NacNac\text{-}CHAr}}$), 4.04 (sept, 1H, $^{3}J_{\mathrm{H\text{-}H}}$ = 6.9 Hz, $\mathrm{CH}^{i\mathrm{PrH/O}}$), 3.95 (d, 1H, $^{2}J_{\mathrm{H\text{-}H}}$ = 17.9 Hz, $\mathrm{CH_2}^{\mathrm{O}}$), 3.87 (d, 1H, $^{2}J_{\mathrm{H\text{-}H}}$ = 17.5 Hz, $\mathrm{CH_2}^{\mathrm{CHAr}}$), 3.86 (m, 1H, $\mathrm{CH}^{i\mathrm{Pr\text{-}H/CHAr}}$), 3.77 (d, 1H, $^{2}J_{\mathrm{HH}}$ = 17.9 Hz, $\mathrm{CH_2}^{\mathrm{O}}$), 3.72 (d, 1H, $^{2}J_{\mathrm{H\text{-}H}}$ = 17.3 Hz, $\mathrm{CH_2}^{\mathrm{CHAr}}$), 3.69 (s, 3H, $\mathrm{OCH_3}$), 3.34 (sept, 1H, $^{3}J_{\mathrm{H\text{-}H}}$ = 6.8 Hz, $\mathrm{CH}^{i\mathrm{PrAr/O}}$), 3.02 (sept, 1H, $^{3}J_{\mathrm{H\text{-}H}}$ = 6.8 Hz, $\mathrm{CH}^{i\mathrm{Pr\text{-}Ar/CHAr}}$), 2.55 (s, 1H, $\mathrm{CHO}^{\mathrm{ald}}$), 2.08 (d, 3H, $^{3}J_{\mathrm{H\text{-}H}}$ = 6.9 Hz, $\mathrm{CH_3}^{i\mathrm{Pr\text{-}H/O}}$), 1.82 (s, 3H, $\mathrm{CH_3}^{\mathrm{NacNac\text{-}a/O}}$), 1.72 (s, 3H, $\mathrm{CH_3}^{\mathrm{NacNac\text{-}a/CHAr}}$), 1.70 (d, 3H, $^{3}J_{\mathrm{H\text{-}H}}$ = 6.8 Hz,

$CH_3^{iPr-H/CHAr}$), 1.22 (s, 3H, $CH_3^{NacNac-b/CHAr}$), 1.17 (d, 3H, $^3J_{HH}$ = 6.8 Hz, $CH_3^{iPr-H/O}$) 1.16 (s, 3H, $CH_3^{NacNac-b/O}$), 1.11 (d, 3H, $^3J_{HH}$ = 6.9 Hz, $CH_3^{iPr-H/CHAr}$), 0.93 (d, 3H, $^3J_{H-H}$ = 6.8 Hz, $CH_3^{iPr-Ar/CHAr}$), 0.90 (d, 3H, $^3J_{H-H}$ = 6.8 Hz, $CH_3^{iPr-Ar/O}$), 0.88 (s, 3H, CH_3^{NacNac}), 0.67 (d, 3H, $^3J_{H-H}$ = 6.8 Hz, $CH_3^{iPr-Ar/CHAr}$), 0.56 (d, 3H, $^3J_{H-H}$ = 6.8 Hz, $CH_3^{iPr-Ar/O}$). [UHK08, 1]

^{13}C NMR (125.80 MHz, THF-d_8): δ [ppm] = 160.4 (Cq, $C^{NacNac-a/O}$), 159.0 (Cq, $C^{NacNac-b/O}$), 158.8 (Cq, $C^{NacNac-a/CHAr}$), 157.9 (Cq, $C^{NacNac-b/CHAr}$), 155.3 (Cq, C^{i-ald}), 154.4 (Cq, $C^{pz-CHAr}$), 151.7 (Cq, C-$DiPP^{i-CHAr}$), 151.6 (Cq, C^{pz-O}), 150.3 (Cq, C-$DiPP^{i-O}$), 147.8 (Cq, $\underline{C}OCH_3$), 147.0 (Cq, $C^{iPrAr/O}$), 145.2 (Cq, $C^{iPr-H/CHAr}$), 144.3 (Cq, $C^{iPr-Ar/CHAr}$), 143.4 (Cq, $C^{iPrH/O}$), 127.4kk (CH, CH^{o-ald}), 123.8 (CH, C-DiPP), 123.8 (CH, C-$DiPP^{p}$), 123.4 (CH, C-$DiPP^{m}$), 123.4 (CH, C-$DiPP^{m}$), 123.2 (CH, C-DiPP), 123.3 (CH, C-DiPP), 112.2 (CH, CH^{m-ald}), 98.0 (CH, $C^{NacNac-CHAr}$), 97.0 (CH, $C^{NacNac-O}$), 91.2 (CH, C^{pz}), 76.8 (CH, NiC), 54.7 (CH_3, OCH_3), 52.0 (CH_2,CH_2^{CHAr}), 50.2 (CH_2,CH_2^{O}), 28.8 (CH, $CH^{iPr-H/O}$), 28.4 (CH, $CH^{iPr-H/CHAr}$), 28.3 (CH, $CH^{iPr-Ar/O}$), 27.7 (CH, $CH^{iPrAr/CHAr}$), 26.0 (CH_3, $CH_3^{iPr-H/CHAr}$), 25.8 (CH_3, $CH_3^{iPr-H/O}$), 25.6 (CH_3, $CH_3^{NacNac-b/CHAr}$), 25.4 (CH_3, $CH_3^{NacNac-a/CHAr}$), 25.2 (CH_3, $CH_3^{iPr-Ar/O}$), 25.1 (CH_3, $CH_3^{iPr-Ar/CHAr}$), 24.5 (CH_3, $CH_3^{iPrAr/CHAr}$), 24.1 (CH_3, $CH^{iPr-H/O}$) 23.8 (CH_3, $CH_3^{iPr-H/CHAr}$), 23.3 (CH_3, $CH_3^{iPr-H/O}$), 21.3 (CH_3, $CH_3^{NacNac-a/O}$), 21.2 (CH_3, $CH_3^{NacNac-a/CHAr}$). [UHK08, 4]

FT-IR (ATR): $\tilde{\nu}$ [cm^{-1}] = 3050 (w), 2962 (m), 2923 (m), 2861 (m), 2825 (m), 1681 (w), 1598 (w), 1557 (s), 1517 (s), 1497 (s), 1426 (s), 1402 (vs), 1308 (s), 1231 (vs), 1180 (s), 1158(s), 1089 (s), 1063 (s), 1049 (s), 1030 (s), 943 (s), 915 (s), 815(s), 799 (s), 773 (s), 741 (s), 678 (vs), 624 (s), 578 (s), 550 (s), 525 (s), 503 (s), 466 (s), 424 (s).

KLNi$_2$(CHOC$_6$H$_5$F) (13^F-K)

In a 20 mL screw cap vial in a glovebox hydride complex **2-K** (10.0 mg, 12.6 µmol, 1.00 eq.) was dissolved in benzene (3 mL, abs.) and 4-fluorobenzaldehyde (1.3 µL, 1.5 mg, 12.6 µmol, 1.00 eq.) was added. An immediate color change from orange to brown was observed. After stirring for 2 h, the mixture was filtered, and the solvent was removed *in vacuo*. **13^F-K** was obtained as a brown powder (3.5 mg, 4.0 µmol, 32 %)

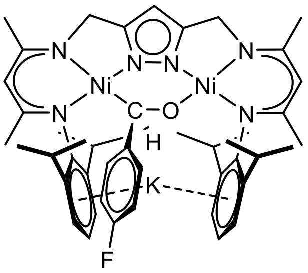

13^F-K

^{1}H NMR (400.25 MHz, DMSO-d_6): δ [ppm] = 9.21 (dd, $^3J_{H-H}$ = 8.6 Hz, $^2J_{H-F}$ = 8.6 Hz, 2H, CH^{o-ald}), 6.84-6.48 (m, 8H, CH^{Ar}), 5.31 (s, 1H, CH^{Pz}), 4.42 (s, 1H, $CH^{NacNac-O}$), 4.29 (s, 1H, CH^{NacNac}), 4.06 (m, 1H, CH^{iPr}), 3.90-3.61 (m, 4H, CH_2), 3.90 (m, 1H, CH^{iPr}), 4.52 (sept, $^3J_{H-H}$ = 6.8 Hz, 1H, CH^{iPr}), 3.90 (sept, $^3J_{H-H}$ = 6.7 Hz, 1H, CH^{iPr}), 2.84 (sept, $^3J_{H-H}$ = 6.5 Hz, 1H, CH^{iPr}), 2.70 (s, 1H, CHO^{ald}), 1.88 (d, 3H, $^3J_{H-H}$ = 6.9 Hz, CH_3^{iPr}), 1.74 (s, 3H, $CH_3^{NacNac-a}$), 1.61 (s, 3H, $CH_3^{NacNac-a}$), 1.14 (s, 6H, $CH_3^{NacNac-b}$), 1.07 (d, 3H, $^3J_{HH}$ = 6.9 Hz, CH_3^{iPr}), 0.99 (d, 3H, $^3J_{HH}$ = 6.7 Hz, CH_3^{iPr}), 0.93 (d, 3H, $^3J_{HH}$ = 6.7 Hz, CH_3^{iPr}), 0.88 (d, 3H, $^3J_{HH}$ = 6.7 Hz, CH_3^{iPr}), 0.74 (d, 3H, $^3J_{HH}$ = 6.8 Hz, CH_3^{iPr}), 0.52 (d, 3H, $^3J_{HH}$ = 6.7 Hz, CH_3^{iPr}), 0.24 (d, 3H, $^3J_{HH}$ = 6.6 Hz, CH_3^{iPr}). [UHK14, 14]

^{19}F NMR (100.65 MHz, DMSO-d$_6$): δ [ppm] = -125.8 (Ar-F). [UHK14, 15]

FT-IR (ATR): $\tilde{\nu}$ [cm^{-1}]: = 3051 (w), 2959 (w), 2924 (w), 2868 (w), 2809 (vw), 1561 (m), 1518 (vs), 1488 (s), 1428 (vs), 1403 (vs), 1365 (m), 1317 (s), 1274 (m), 1265 (s), 1246 (s), 1225 (m), 1192 (s), 1163 (m), 1147 (m), 1092 (m), 1066 (s), 1024 (m), 1009 (m), 948 (s), 919 (m), 905 (m), 822 (m), 815 (s), 799 (s), 767 (s), 744 (vs), 732 (s), 677 (m), 631 (m), 623 (m), 595 (m), 576 (s), 553 (m), 514 (m), 493 (m), 460 (w), 444 (m), 420 (m), 399 (s).

KLNi$_2$(CHOC$_6$H$_5$CF$_3$) (13$^{\mathrm{CF_3}}$-K)

In a 20 mL screw cap vial in a glovebox **2-K** (10.0 mg, 12.6 µmol, 1.00 eq.) was dissolved in benzene (3 mL, abs.) and 4-fluorobenzaldehyde (1.3 µL, 1.5 mg, 12.6 µmol, 1.00 eq.) was added. An immediate color change from orange to brown was observed. After stirring for 2 h, the mixture was filtered, and the solvent was removed *in vacuo*. **13$^{\mathrm{CF_3}}$-K** was obtained as a brown powder (3.5 mg, 4.0 µmol, 32 %)

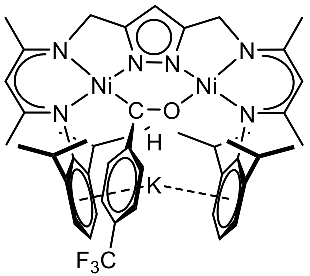

13$^{\mathrm{CF_3}}$-K

^{1}H NMR (400.25 MHz, THF-d$_8$): δ [ppm] = 9.49 (d, $^3J_{\text{H-H}}$ = 8.0 Hz, 2H, CH$^{o\text{-ald}}$), 7.24 (d, 2H, ^{3}J$_{\text{H-H}}$ = 7.9 Hz, CH$^{m\text{-Ald}}$), 7.23-6.78 (m, 6H, CH$^{\text{Ar}}$), 5.40 (s, 1H, CH$^{\text{Pz}}$), 4.62 (s, 1H, CH$^{\text{NacNac-O}}$), 4.50 (s, 1H, CH$^{\text{NacNac}}$), 3.96 (d, $^3J_{\text{H-H}}$ = 17.7 Hz, 1H, CH$_2$), 3.96 (m, 1H, CH$^{i\text{Pr}}$), 3.93 (m, 1H, CH$^{i\text{Pr}}$), 3.92 (d, $^3J_{\text{H-H}}$ = 17.3 Hz, 1H, CH$_2$), 3.78 (d, $^3J_{\text{H-H}}$ = 17.3 Hz, 1H, CH$_2$), 3.76 (d, $^3J_{\text{H-H}}$ = 17.4 Hz, 1H, CH$_2$), 3.38 (sept, $^3J_{\text{H-H}}$ = 6.7 Hz, 1H, CH$^{i\text{Pr}}$), 3.07 (s, 1H, CHO$^{\text{ald}}$), 2.99 (sept, $^3J_{\text{H-H}}$ = 6.9 Hz, 1H, CH$^{i\text{Pr}}$), 2.05 (d, 3H, $^3J_{\text{HH}}$ = 6.8 Hz, CH$_3$$^{i\text{Pr}}$), 1.85 (s, 3H, CH$_3$$^{\text{NacNac-a}}$), 1.29 (s, 3H, CH$_3$$^{\text{NacNac-a}}$), 1.24 (s, 3H, CH$_3$$^{\text{NacNac-b}}$), 1.18 (d, 3H, $^3J_{\text{HH}}$ = 6.3 Hz, CH$_3$$^{i\text{Pr}}$), 1.17 (s, 3H, CH$_3$$^{\text{NacNac-b}}$), 1.10 (d, 3H, $^3J_{\text{HH}}$ = 6.8 Hz, CH$_3$$^{i\text{Pr}}$), 0.98 (d, 3H, $^3J_{\text{HH}}$ = 6.8 Hz, CH$_3$$^{i\text{Pr}}$), 0.90 (d, 3H, $^3J_{\text{HH}}$ = 6.5 Hz, CH$_3$$^{i\text{Pr}}$), 0.87 (d, 3H, $^3J_{\text{HH}}$ = 6.9 Hz, CH$_3$$^{i\text{Pr}}$), 0.73 (d, 3H, $^3J_{\text{HH}}$ = 6.7 Hz, CH$_3$$^{i\text{Pr}}$), 0.46 (d, 3H, $^3J_{\text{HH}}$ = 6.7 Hz, CH$_3$$^{i\text{Pr}}$). [UHK15, 55]

^{13}C NMR (125.80 MHz, THF-d$_8$): δ [ppm] = 161.4 (Cq, $\underline{\text{C}}$CF$_3$), 161.0 (Cq, C$^{\text{NacNac-a}}$), 160.1 (Cq, C$^{i\text{-ald}}$), 159.6 (Cq, C$^{\text{NacNac-b}}$), 158.5 (Cq, C$^{\text{NacNac-a}}$), 154.9 (Cq, C$^{\text{pz}}$), 154.4 (Cq, C$^{i\text{Pr}}$), 152.5 (Cq, C$^{\text{pz}}$), 150.0 (Cq, C-DiPP^{i}), 146.9 (Cq, C$^{i\text{Pr}}$), 145.7 (Cq, C$^{i\text{Pr}}$), 143.8 (Cq, C$^{i\text{Pr}}$), 143.3 (Cq, C$^{i\text{Pr}}$), 126.2 (CH, CH$^{o\text{-ald}}$), 125.7 (CH, C-DiPP^{m}), 125.6 (CH, C-DiPP^{m}), 125.2 (CH, C-DiPP^{m}), 124.4 (CH, C-DiPP^{p}), 123.9 (CF$_3$), 123.4 (CH, CH$^{m\text{-ald}}$), 123.2 (CH, C-DiPP^{p}), 122.8 (CH, C-DiPP^{m}), 98.2 (CH, C$^{\text{NacNac}}$), 97.1 (CH, C$^{\text{NacNac}}$), 92.1 (CH, C$^{\text{pz}}$), 77.0 (CH, NiC), 52.6 (CH$_2$,CH$_2$), 50.7 (CH$_2$,CH$_2$), 29.4 (CH$_3$, CH$_3$$^{\text{NacNac-a}}$), 29.1 (CH, CH$^{i\text{Pr}}$), 29.1 (CH, CH$^{i\text{Pr}}$), 28.3 (CH, CH$^{i\text{Pr}}$), 28.1 (CH, CH$^{i\text{Pr}}$), 25.9 (CH$_3$, CH$_3$$^{i\text{Pr}}$), 25.8 (CH$_3$, CH$_3$$^{i\text{Pr}}$), 24.5 (CH$_3$, CH$_3$$^{\text{NacNac-a}}$), 24.3 (CH$_3$, CH$_3$$^{i\text{Pr}}$), 23.8 (CH$_3$, CH$_3$$^{i\text{Pr}}$), 23.8 (CH$_3$, CH$_3$$^{i\text{Pr}}$), 23.1 (CH$_3$, CH$_3$$^{i\text{Pr}}$), 22.8 (CH$_3$, CH$_3$$^{i\text{Pr}}$), 21.9 (CH$_3$, CH$_3$$^{\text{NacNac-a}}$), 21.7 (CH$_3$, CH$_3$$^{i\text{Pr}}$), 21.5 (CH$_3$, CH$_3$$^{\text{NacNac-a}}$). [UHK15, 56]

^{19}F NMR (100.65 MHz, THF-d$_8$): δ [ppm] = -62.1 (CF$_3$). [UHK14, 15]

FT-IR (ATR): $\tilde{\nu}$ [cm^{-1}]: = 3051 (w), 2959 (w), 2924 (w), 2868 (w), 1560 (m), 1518 (vs), 1488 (s), 1465 (s), 1430 (s), 1402 (vs), 1317 (s), 1275 (m), 1265 (m), 1246 (m), 1092 (m), 1066 (s), 1024 (m), 1009 (m), 948 (s), 919 (m), 904 (m), 849 (w), 814 (s), 800 (s), 767 (s), 745 (vs), 732 (s), 678 (m), 632 (m), 623 (m), 576 (s), 513 (m), 493 (m), 444 (m), 420 (m), 399 (s).

$KLNi_2O_2NC_6H_4CHO$ (14^{Bna}-K)

In a 20 mL screw cap vial in a glove box **2-K** (40 mg, 63 µmol, 1.0 eq.) was dissolved in THF (3 mL, abs.) and nitrobenzaldehyde (9.5 mg, 63 µmol, 1.0 eq.) was added. An immediate color change from bright orange to deep blue was observed. To ensure completion of the reaction the mixture was stirred overnight. The suspension was filtered and the remaining solid washed with THF and dried *in vacuo.* **14^{Bna}-K** was isolated as a dark blue powder. (28 mg, 30.7 µmol, 61%)

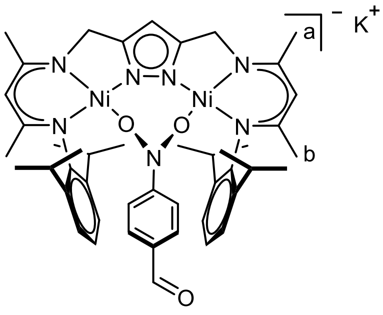

14^{Bna}-K

^{1}H NMR (400.25 MHz, DMSO-d$_6$): δ [ppm] = 9.96 (s, 1H, CHO), 7.79 (bs, 1H, CH$^{o\text{-Nitrobenzald}}$), 7.74 (bs, 1H, CH$^{o\text{-Nitrobenzald}}$), 7.06 (bs, 1H, C$^{m\text{-Nitrobenzald}}$), 6.90-6.81 (m, 4H, H-DiPP), 6.84 (bs, 1H,C$^{m\text{-Nitrobenzald}}$), 6.77 (d, $^3J_{H\text{-}H}$ = 7.3 Hz, 2H, H-DiPP^m), 5.47 (s, 1H, CH^{pz}), 4.54 (s, 2H, CH^{NacNac}), 4.01 (bs, 2H, CH^{iPr}), 3.72 (d, $^2J_{H\text{-}H}$ = 17.3 Hz, 2H, CH$_2$), 3.68 (d, $^2J_{H\text{-}H}$ = 17.3 Hz, 2H, CH$_2$), 3.31 (sep, $^3J_{H\text{-}H}$ = 7.1 Hz, 2H, CH^{iPr}), 1.78 (s, 6H, CH$_3^{NacNac}$), 1.48 (bs, 6H, CH$_3^{iPr}$), 1.22 (s, 6H, CH$_3^{NacNac}$), 1.18 (bs, 6H, CH$_3^{iPr}$), 1.12 (d, $^3J_{H\text{-}H}$ = 7.1 Hz, 6H, CH$_3^{iPr}$), 0.93 (d, $^3J_{H\text{-}H}$ = 7.1 Hz, 6H, CH$_3^{iPr}$). [TK609, 144]

^{13}C NMR (100.65 MHz, DMSO-d$_6$): δ [ppm] = 181.8 (CH, CHO), 157.9 (Cq, C^{NacNac}), 157.8 (Cq, C^{NacNac}), 153.1 (Cq, C^{Pz}), 143.9 (Cq, C-DiPP^o), 142.4 (Cq, C-DiPP^o), 133.4 (CH, C$^{m\text{-Nitrobenzald}}$), 124.7 (CH, C$^{m\text{-Nitrobenzald}}$), 123.7 (CH, C-DiPP^m), 122.2 (CH, C-DiPP^p), 121.6 (CH, C-DiPP^m), 116.7 (Cq, C$^{p\text{-Nitrobenzald}}$)111.7 (CH, C$^{o\text{-Nitrobenzald}}$), 108.7 (CH, C$^{o\text{-Nitrobenzald}}$), 96.8 (CH, CH^{NacNac}), 92.3 (CH, CH^{pz}), 49.8 (CH$_2$, CH$_2$), 27.8 (CH, CH^{iPr}), 27.5 (CH, CH^{iPr}), 25.5 (CH$_3$, CH$_3^{iPr}$), 25.0 (CH$_3$, CH$_3^{iPr}$), 24.3(CH$_3$, CH$_3^{iPr}$), 24.3(CH$_3$, CH$_3^{iPr}$), 23.7 (CH$_3$, CH$_3^{NacNac}$), 21.0 (CH$_3$, CH$_3^{NacNac}$). [TK609, 149]

UV-Vis (THF): λ [nm] (ε = L·mol^{-1}·cm^{-1}) = 266 (41310), 370 (16670), 383 (17840), 408 (10610), 585 (8170).

FT-IR (ATR): $\tilde{\nu}$ [cm^{-1}] = 3060 (vw), 3020 (wv), 2986 (vw), 2961 (m), 2922 (m), 2864 (m), 2821 (w), 1628 (m), 1597 (w), 1569 (vs), 1530 (m), 1515 (s), 1461 (s), 1436 (m’), 1396 (s), 1370 (w), 1341 (m), 1314 (m), 1294 (m), 1282 (m), 1245 (m), 1230 (m), 1208 (w), 1188 (m), 1157 (m), 1135 (w), 1097 (m), 1069 (w), 1054 (w), 1031 (w), 1015 (s), 982 (m), 968 (w), 958 (w), 932 (w), 918 (w), 904 (w), 862 (w), 838 (m), 799 (s), 787 (m), 769 (m), 754 (m), 730 (m), 716 (w), 706 (w), 660 (s), 637 (w), 627 (w), 596 (w), 577 (m), 549 (m), 532 (w), 522 (m), 500 (s), 481 (m), 464 (m), 444 (m), 429 (w), 416 (m), 409 (w), 405 (w).

Elemental Analysis: calc. for $C_{46}H_{64}KN_7Ni_2O_3$: C 60.08, H 7.02, N 10.66; found C 58.60, H 6.21, N 10.05.

(K[2.2.2]-cryptand)LNi$_2$O$_2$NC$_6$H$_4$CHO (14$^{\text{Bna}}$-cK)

In a 20 mL screw cap vial in a glove box **2-K** (50 mg, 63 µmol, 1.0 eq.) and [2.2.2]-cryptand were dissolved in THF (3 mL, abs.) and nitrobenzaldehyde (9.5 mg, 63 µmol, 1.0 eq.) was added. An immediate color change from bright orange to light blue was observed. To ensure completion of the reaction the mixture was stirred overnight. The reaction mixture was filtered and overlayered with hexane. After crystallization at -35 °C for one week **14$^{\text{Bna}}$-cK** was isolated as blue needles. (10.1 mg, 11.4 µmol, 46%)

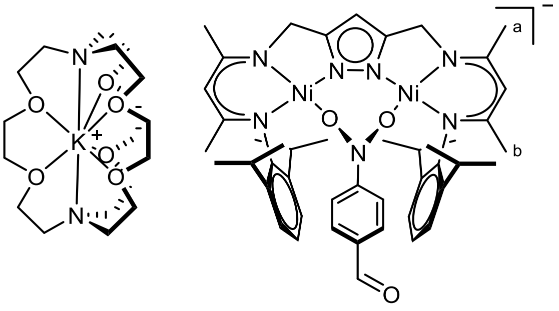

14$^{\text{Bna}}$-cK

^{1}H NMR (400.25 MHz, THF-d$_8$): δ [ppm] = 9.09 (s, 1H, CHO), 8.09 (d, $^{3}J_{\text{H-H}}$ = 9.0 Hz, 1H, CH$^{o\text{-Nitrobenzald}}$), 8.00 (d, $^{3}J_{\text{H-H}}$ = 9.0 Hz, 1H, CH$^{o\text{-Nitrobenzald}}$), 7.27 (d, $^{3}J_{\text{H-H}}$ = 8.0 Hz, 1H, CH$^{m\text{-Nitrobenzald}}$), 6.84 (m, 1H, CH$^{m\text{-Nitrobenzald}}$), 6.83 (d, $^{3}J_{\text{H-H}}$ = 4.5 Hz, 4H, H-DiPP^{p}), 6.72 (t, $^{3}J_{\text{H-H}}$ = 4.5 Hz, 2H, H-DiPP^{p}), 5.33 (s, 1H, CH$^{\text{pz}}$), 4.48 (s, 2H, CH$^{\text{NacNac}}$), 4.18 (sep, $^{3}J_{\text{H-H}}$ = 6.9 Hz, 2H, CH$^{i\text{Pr}}$), 3.91 (d, $^{2}J_{\text{H-H}}$ = 16.8 Hz, 2H, CH$_2$), 3.67 (d, $^{2}J_{\text{H-H}}$ = 16.8 Hz, 2H, CH$_2$), 3.56 (bs, 12H, crypt-H), 3.53-3.50 (m, 12H, crypt-H), 3.42 (sep, $^{3}J_{\text{H-H}}$ = 6.7 Hz, 2H, CH$^{i\text{Pr}}$), 2.52-2.54 (m, 12H, crypt-H), 1.76 (s, 6H, CH$_3^{\text{NacNac-a}}$), 1.64 (d, $^{3}J_{\text{H-H}}$ = 6.9 Hz, 6H, CH$_3^{i\text{Pr}}$), 1.27 (s, 6H, CH$_3^{\text{NacNac-b}}$), 1.18 (d, $^{3}J_{\text{H-H}}$ = 6.9 Hz, 6H, CH$_3^{i\text{Pr}}$), 1.15 (d, $^{3}J_{\text{H-H}}$ = 6.8 Hz 6H, CH$_3^{i\text{Pr}}$), 0.97 (d, $^{3}J_{\text{H-H}}$ = 6.8 Hz, 6H, CH$_3^{i\text{Pr}}$). [UHK22, 5]

^{13}C NMR (100.65 MHz, THF-d$_8$): δ [ppm] = 182.71 (CH, CHO), 158.4 (Cq, C$^{\text{NacNac-b}}$), 158.1 (Cq, C$^{\text{NacNac-a}}$), 153.7 (Cq, C$^{\text{Pz}}$), 145.7 (Cq, C-DiPP^{i}), 145.1 (Cq, C-DiPP^{o}), 143.8 (Cq, C-DiPP^{o}), 134.1 (CH, C$^{m\text{-Nitrobenzald}}$), 125.9 (CH, C$^{m\text{-Nitrobenzald}}$), 124.2 (CH, C-DiPP^{m}), 122.8 (CH, C-DiPP^{m}), 122.1 (CH, C-DiPP^{p}), 118.7 (Cq, C$^{p\text{-Nitrobenzald}}$), 112.5 (CH, C$^{o\text{-Nitrobenzald}}$), 109.7 (CH, C$^{o\text{-Nitrobenzald}}$), 97.1 (CH, CH$^{\text{NacNac}}$), 91.8 (CH, CH$^{\text{pz}}$), 71.3 (CH$_2$, C-crypt), 68.4 (CH$_2$, C-crypt), 54.8 (CH$_2$, C-crypt), 50.7 (CH$_2$, CH$_2$), 28.9 (CH, CH$^{i\text{Pr}}$), 28.7 (CH, CH$^{i\text{Pr}}$), 26.3 (CH$_3$, CH$_3^{i\text{Pr}}$), 25.8 (CH$_3$, CH$_3^{i\text{Pr}}$), 24.8 (CH$_3$, CH$_3^{i\text{Pr}}$), 24.7 (CH$_3$, CH$_3^{i\text{Pr}}$), 24.2 (CH$_3$, CH$_3^{\text{NacNac-b}}$), 21.0 (CH$_3$, CH$_3^{\text{NacNac-a}}$). [UHK22, 1]

FT-IR (ATR): $\tilde{\nu}$ [cm^{-1}] = 3052 (w), 3012 (w), 2952 (m), 2920 (w), 2896 (m), 2882 (m), 2863 (m), 2809 (m), 2722 (w), 2690 (w), 1621 (m), 1567 (s), 1525 (m), 1477 (w), 1462 (m), 1440 (m), 1435 (w), 1404 (m), 1377 (m), 1358 (m), 1354 (m), 1336 (m), 1311 (m), 1302 (m), 1289 (s), 1231 (vs), 1187 (s), 1149 (s), 1131 (s), 1113 (m), 1099 (vs), 1081 (s), 1055 (s), 1029 (m), 1013 (s), 997 (m), 982 (s), 948 (s), 932 (s), 862 (w), 831 (m), 819 (w), 797 (m), 772 (w), 761 (m), 754 (m), 745 (m), 725 (m), 713 (m), 645 (s), 624 (m), 584 (w), 568 (w), 535 (m), 523 (s), 512 (m), 480 (m), 472 (m), 465 (w), 455 (w), 449 (m), 442 (w), 429 (w), 417 m), 401 (w).

KLNi$_2$O$_2$NPh (14$^{\text{Ph}}$-K)

In a 20 mL screw cap vial in a glove box **2-K** (20 mg, 25 µmol, 1.0 eq.) was dissolved in THF (3 mL, abs.) and nitrobenzene (2.6 µL, 25 µmol, 1.0 eq.) was added. An immediate color change from bright orange to deep purple was observed. To ensure completion of the reaction the mixture was stirred overnight. The suspension was filtered and overlayered with hexane. After crystallization for one week at -35 °C **14^{Ph}-K** was isolated as purple needles. (10.1 mg, 11.4 µmol, 46 %)

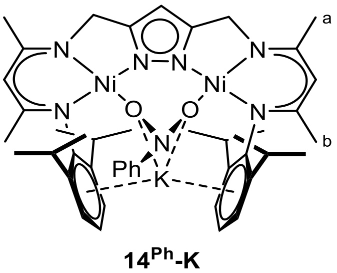

14^{Ph}-K

^{1}H NMR (400.25 MHz, THF-d$_8$): δ [ppm] = 10.20 (d, $^3J_{H\text{-}H}$ = 8.3 Hz, 2H, $\mathrm{CH}^{o\text{-Nitrobenz}}$), 7.11 (t, $^3J_{H\text{-}H}$ = 8.3 Hz, 2H, $\mathrm{CH}^{m\text{-Nitrobenz}}$), 7.11 (t, $^3J_{H\text{-}H}$ = 8.3 Hz, 2H, H-DiPP$^{m\text{-ONO}}$), 7.00 (t, $^3J_{H\text{-}H}$ = 7.6 Hz, 2H, H-DiPP^{p}), 6.79 (d, $^3J_{H\text{-}H}$ = 7.8 Hz, 2H, H-DiPP^{m}), 6.49 (t, $^3J_{H\text{-}H}$ = 7.5 Hz, 2H, $\mathrm{CH}^{p\text{-Nitrobenz}}$), 5.16 (s, 1H, CH^{pz}), 4.52 (s, 2H, CH^{NacNac}), 4.19 (sep, $^3J_{H\text{-}H}$ = 7.0 Hz, 2H, CH^{iPr}), 3.72 (d, $^2J_{H\text{-}H}$ = 17.5 Hz, 2H, CH$_2$), 3.63 (d, $^2J_{H\text{-}H}$ = 17.5 Hz, 2H, CH$_2$), 3.41 (sep, $^3J_{H\text{-}H}$ = 6.9 Hz, 2H, $\mathrm{CH}^{iPr\text{-ONO}}$), 2.31 (d, $^3J_{H\text{-}H}$ = 6.9 Hz, 6H, $\mathrm{CH_3}^{iPr}$), 1.77 (s, 6H, $\mathrm{CH_3}^{NacNac\text{-}a}$), 1.27 (d, $^3J_{H\text{-}H}$ = 6.9 Hz, 6H, $\mathrm{CH_3}^{iPr}$), 1.21 (s, 6H, $\mathrm{CH_3}^{NacNac\text{-}b}$), 0.99 (d, $^3J_{H\text{-}H}$ = 6.8 Hz 6H, $\mathrm{CH_3}^{iPr\text{-ONO}}$), 0.88 (d, $^3J_{H\text{-}H}$ = 6.8 Hz, 6H, $\mathrm{CH_3}^{iPr\text{-ONO}}$). [TK562, 59]

^{13}C NMR (100.65 MHz, THF-d$_8$): δ [ppm] = 158.7 (Cq, $\mathrm{C}^{NacNac\text{-}a}$), 156.9 (Cq, $\mathrm{C}^{NacNac\text{-}b}$), 153.7 (Cq, C^{Pz}), 151.6 (Cq, $\mathrm{C}^{i\text{-Nitrobenz}}$), 147.4 (Cq, C-DiPP^{i}), 146.4 (Cq, C-DiPP^{o}), 143.9 (Cq, C-DiPP^{o}), 126.3 (CH, $\mathrm{C}^{m\text{-Nitrobenz}}$), 122.9 (CH, C-DiPP^{p}), 121.8 (CH, C-DiPP$^{m\text{-ONO}}$), 121.6 (CH, C-DiPP^{m}), 114.2 (CH, $\mathrm{C}^{o\text{-Nitrobenz}}$), 114.1 (CH, $\mathrm{C}^{p\text{-Nitrobenz}}$), 95.9 (CH, CH^{NacNac}), 89.9 (CH, CH^{pz}), 49.5 (CH$_2$, CH$_2$), 28.2 (CH, CH^{iPr}), 27.2 (CH, $\mathrm{CH}^{iPr\text{-ONO}}$), 26.5 (CH$_3$, $\mathrm{CH_3}^{iPr}$), 23.6 (CH$_3$, $\mathrm{CH_3}^{iPrONO}$), 23.6 (CH$_3$, $\mathrm{CH_3}^{iPr\text{-ONO}}$),23.4 (CH$_3$, $\mathrm{CH_3}^{NacNac\text{-}b}$), 22.4 (CH$_3$, $\mathrm{CH_3}^{iPr}$), 20.4 (CH$_3$, $\mathrm{CH_3}^{NacNac\text{-}a}$). [TK562, 62]

UV-Vis (THF): λ [nm] (ε = L·mol^{-1}·cm^{-1}) = 270 (41320), 370 (11900), 385 (12550), 412 (sh, 7510), 517 (3890).

FT-IR (ATR): $\tilde{\nu}$ [cm^{-1}] = 3064 (w), 2982 (w), 2959 (m), 2924 (vw), 2863 (m), 1588 (m), 1557 (m), 1544 (w), 1526 (m), 1521 (m), 1479 (s), 1463 (s), 1432 (s), 1400 (vs), 1382 (vw), 1363 (m) 1359 (w), 1342 (w) 1313 (vs), 1279 (s), 1247 (s), 1229 (m), 1186 (m), 1167 (m), 1142 (w), 1099 (m), 1064 (m), 1054 (m), 1028 (m), 1015 (m), 985 (m), 970 (w), 957 (w), 933 (m), 918 (w), 911 (w), 883 (w), 871 (vw), 861 (m), 846 (w), 829 (w), 801 (s), 766 (s), 745 (m), 726 (vs), 715 (s), 686 (s), 665 (w), 654 (w), 645 (m), 638 (w), 629 (w), 622 (w), 615 (vw), 595 (w), 559 (w), 549 (w), 538 (w), 51 (m), 486 (m), 476 (w), 461 (w), 455 (w), 448 (w), 441 (m), 435 (m), 421 (s), 418 (s) 414 (vs), 407 (vs), 405 s), 401 (vs).

MS (ESI$^+$, THF) m/z:[$\mathrm{NaLNi_2O_2CH_2}$]$^+$ = 804.32.

Elemental Analysis: calc. for $\mathrm{C_{45}H_{58}KN_7Ni_2O_3}$: C 61.04, H 6.60, N 11.07; found C 60.52, H 6.62, N 10.82.

$\mathrm{NaLNi_2O_2NPh}$ (14^{Ph}-Na)

In a 20 mL screw cap vial in a glove box **2-Na** (40 mg, 51 µmol, 1.0 eq.) was dissolved in THF (3 mL, abs.) and nitrobenzene (5.2 µL, 50 µmol, 1.0 eq.) was added. An immediate color change from bright orange to purple was observed. To ensure completion of the reaction the mixture was stirred for 2 h at room temperature. The suspension was filtered and overlayered with hexane.

After crystallization for 1 week at -35 °C **14^{Ph}-Na** was isolated as purple cubes. (28.0 mg, 32 µmol, 62%)

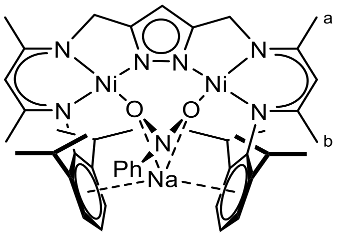

14^{Ph}-Na

^{1}H NMR (400.25 MHz, THF-d$_8$): δ [ppm] = 7.83 (bs, 2H, CH$^{o\text{-Nitrobenz}}$), 7.20-7.15 (m, 4H, H-DiPP), 6.96-6.90 (m, 2H, H-DiPP), 6.85-6.77 (m, 2H, CH$^{m\text{-Nitrobenz}}$), 6.38 (t, $^3J_{H\text{-}H}$ = 6.7 Hz, 1H, CH$^{p\text{-Nitrobenz}}$), 5.34 (s, 1H, CH^{pz}), 4.61 (s, 2H, CH^{NacNac}), 3.90 (d, $^2J_{H\text{-}H}$ = 17.3 Hz, 2H, CH$_2$), 3.73 (d, $^2J_{H\text{-}H}$ = 17.3 Hz, 2H, CH$_2$), 3.54 (m, 2H, CH^{iPr}), 3.23 (sep, $^3J_{H\text{-}H}$ = 6.7 Hz, 2H, CH^{iPr}), 1.91 (d, $^3J_{H\text{-}H}$ = 6.4 Hz, 6H, CH$_3^{iPr}$), 1.82 (s, 6H, CH$_3^{NacNac\text{-}a}$), 1.38 (s, 6H, CH$_3^{NacNac\text{-}b}$), 1.20 (d, $^3J_{H\text{-}H}$ = 6.5 Hz, 6H, CH$_3^{iPr}$), 1.04 (d, $^3J_{H\text{-}H}$ = 6.8 Hz 6H, CH$_3^{iPr}$), 0.94 (d, $^3J_{H\text{-}H}$ = 6.7 Hz, 6H, CH$_3^{iPr}$). [TK679, 150]

^{13}C NMR (100.65 MHz, THF-d$_8$): δ [ppm] = 159.9 (Cq, C$^{NacNac\text{-}a}$), 158.5 (Cq, C$^{NacNac\text{-}b}$), 153.9 (Cq, C^{Pz}), 152.5 (CH, C$^{i\text{-Nitrobenz}}$), 147.0 (Cq, C-DiPP^{i}), 146.5 (Cq, C-DiPP^{o}), 145.0 (Cq, C-DiPP^{o}), 127.2 (CH, C$^{m\text{-Nitrobenz}}$), 124.4 (CH, C-DiPP), 123.1 (CH, C-DiPP), 122.7(CH, C-DiPP), 116.8 (CH, C$^{p\text{-Nitrobenz}}$), 116.2 (CH, C$^{o\text{-Nitrobenz}}$), 97.4 (CH, CH^{NacNac}), 91.2 (CH, CH^{pz}), 51.1 (CH$_2$, CH$_2$), 28.7 (CH, CH^{iPr}), 28.6 (CH, CH^{iPr}), 26.6 (CH$_3$, CH$_3^{iPr}$), 25.0 (CH$_3$, CH$_3^{iPr}$), 24.3 (CH$_3$, CH$_3^{iPr}$), 23.9 (CH$_3$, CH$_3^{iPr}$), 23.5 (CH$_3$, CH$_3^{NacNac\text{-}b}$), 21.0 (CH$_3$, CH$_3^{NacNac\text{-}a}$). [TK679, 153]

UV-Vis (THF): λ [nm] (ε = L·mol^{-1}·cm^{-1}) = 265 (41950), 375 (12540) 387 (12670), 412 (8550), 533 (5194).

FT-IR (ATR): $\tilde{\nu}$ [cm^{-1}] = 3051 (vw), 2960 (m), 2924 (w), 2863 (w), 1587 (m), 1556 (m), 1543 (w), 1521 (s), 1482 (s), 1463 (s), 1451 (s), 1432 (s), 1404 (vs), 1365 (m), 1358 (w), 1344 (m), 1314 (vs), 1302 (w), 1281 (s), 1247 (s), 1226 (m), 1186 (m), 1226 (m), 1186 (m), 1171 (m), 1152 (w), 1142 (w), 1100 (m), 1065 (s), 1053 (s), 1027 (s), 1014 (w), 982 (m), 963 (w), 958 (w), 933 (m), 904 (m), 885 (vw), 861 (m), 836 (m), 800 (s), 767 (s), 750 (s), 719 (vs), 684 (s), 662 (wv), 649 (m), 643 (w), 622 (w), 595 (m), 570 (w), 555 (m), 548 (m), 532 (m), 519 (s), 480 (m), 459 (m), 446 (m), 416 (s), 409 (m), 405 (m).

MS (ESI$^+$, THF) *m/z*: [$KLNi_2O_2Ph$ + K]$^+$ = 922.3; [$KLNi_2O_2Ph$]$^+$ = 883.4; [$NaLNi_2O_2Ph$]$^+$ = 867.5.

Elemental Analysis: calc. for $C_{45}H_{58}NaN_7Ni_2O_3$ + C_4H_8O: C 62.51, H 7.07, N 10.41; found C 61.65, H 7.09, N 9.99.

$KLNi_2O_2NCH_3$ (14^{Me}-K)

In a 20 mL screw cap vial in a glove box **2-K** (20 mg, 25 µmol, 1.0 eq.) was dissolved in THF (3 mL, abs.) and nitromethane (1.5 mg, 1.3 µL, 25 µmol, 1.0 eq.) was added. An immediate color change from bright orange to deep red was observed. To ensure completion of the reaction the mixture was stirred for 1 h at room temperature. The reaction mixture was filtered and overlayered with hexane. After crystallization for 3 days at -35 °C **14^{Me}-K** was isolated as deep red cubes. (7 mg, 8.5 µmol, 34 %)

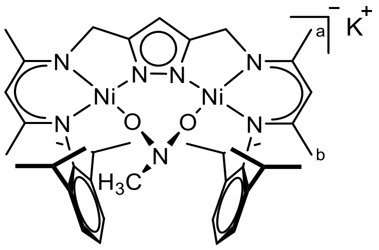

14^{Me}-K

^{1}H NMR (400.25 MHz, THF-d$_8$, -40°C): δ [ppm] = 6.81 (d, $^3J_{H\text{-}H}$ = 7.2 Hz, 2H, H-DiPP^m), 6.75 (t, $^3J_{H\text{-}H}$ = 7.4 Hz, 2H, H-DiPP^p), 6.60 (d, $^3J_{H\text{-}H}$ = 7.6 Hz, 2H, H-DiPP^m), 5.64 (s, 1H, CH^{pz}), 4.51 (s, 2H, CH^{NacNac}), 3.67 (m, 2H, CH^{iPr}), 3.92 (s, 4H, CH$_2$), 3.22 (sep, $^3J_{H\text{-}H}$ = 6.9 Hz, 2H, CH^{iPr}), 1.96 (d, $^3J_{H\text{-}H}$ = 6.9 Hz, 6H, CH$_3^{iPr}$), 1.75 (s, 6H, CH$_3^{NacNac\text{-}a}$), 1.24 (d, $^3J_{H\text{-}H}$ = 6.9 Hz, 6H, CH$_3^{iPr}$), 1.12 (s, 6H, CH$_3^{NacNac\text{-}b}$), 1.60 (d, $^3J_{H\text{-}H}$ = 6.8 Hz 6H, CH$_3^{iPr}$), 0.95 (d, $^3J_{H\text{-}H}$ = 6.8 Hz, 6H, CH$_3^{iPr}$), 0.22 (s, 3H, O$_2$NCH$_3$). [TK636, 8]

^{13}C NMR (100.65 MHz, THF-d$_8$, -40°C): δ [ppm] = 157.9 (Cq, C$^{NacNac\text{-}a}$), 157.7 (Cq, C$^{NacNac\text{-}b}$), 154.3 (Cq, C^{Pz}), 147.8 (Cq, C-DiPP^i), 143.5 (Cq, C-DiPP^o), 140.0 (Cq, C-DiPP^o), 122.8 (CH, C-DiPP^m), 121.7 (CH, C-DiPP^m), 120.9 (CH, C-DiPP^p), 96.0 (CH, CH^{NacNac}), 90.8 (CH, CH^{pz}), 50.8 (CH$_2$, CH$_2$), 47.8 (CH$_3$, O$_2$NCH$_3$) 27.6 (CH, CH^{iPr}), 27.4 (CH, CH$^{iPr\text{-}ONO}$), 25.2 (CH$_3$, CH$_3^{iPr}$), 24.5 (CH$_3$, CH$_3^{iPr}$), 24.3 (CH$_3$, CH$_3^{iPr}$),23.2 (CH$_3$, CH$_3^{NacNac\text{-}b}$), 22.4 (CH$_3$, CH$_3^{iPr}$), 20.7 (CH$_3$, CH$_3^{NacNaca}$). [TK636, 32]

UV-Vis (THF): λ [nm] (ε = L·mol^{-1}·cm^{-1}) = 267 (42460), 371 (13320), 388 (15510), 420 (7000) 512 (2500).

MS (ESI$^+$, THF) m/z:[KLNi$_2$O$_2$CH$_3$ + H]$^+$ = 821.32.

NaLNi$_2$O$_2$NCH$_3$ (14^{Me}-Na)

In a 20 mL screw cap vial in a glove box **2-Na** (40 mg, 50 µmol, 1.0 eq.) was dissolved in THF (3 mL, abs.) and nitromethane (3.0 mg, 2.6 µL, 25 µmol, 1.0 eq.) was added. An immediate color change from bright orange to deep red was observed accompanied by a vigorous gas evolution. To ensure completion of the reaction the mixture was stirred for 1 h at room temperature. The reaction mixture was filtered and overlayered with hexane. After crystallization for 3 days at -35 °C **14^{Me}-Na** was isolated as deep red cubes. (24 mg, 30 µmol, 59 %)

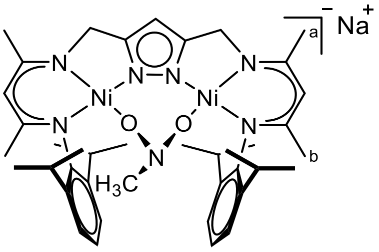

14^{Me}-Na

^{1}H NMR (400.25 MHz, THF-d$_8$, -40°C): δ [ppm] = 6.81 (dd, $^3J_{H\text{-}H}$ = 7.7 Hz, $^4J_{H\text{-}H}$ = 1.4 Hz, 2H, H-DiPP^m), 6.75 (t, $^3J_{H\text{-}H}$ = 7.5 Hz, 2H, H-DiPP^p), 6.60 (dd, $^3J_{H\text{-}H}$ = 7.4 Hz, $^4J_{H\text{-}H}$ = 1.4 Hz, 2H, H-DiPP^m), 5.67 (s, 1H, CH^{pz}), 4.53 (s, 2H, CH^{NacNac}), 3.95 (bs, 4H, CH$_2$), 3.80-3.70 (m, 2H, CH^{iPr}), 3.17 (sep, $^3J_{H\text{-}H}$ = 6.7 Hz, 2H, CH^{iPr}), 1.97 (d, $^3J_{H\text{-}H}$ = 6.9 Hz, 6H, CH$_3^{iPr}$), 1.77 (s, 6H, CH$_3^{NacNac\text{-}a}$), 1.21 (d, $^3J_{H\text{-}H}$ = 6.9 Hz, 6H, CH$_3^{iPr}$), 1.16 (d, $^3J_{H-H}$ = 6.8 Hz 6H, CH$_3^{iPr}$), 1.15 (s, 6H, CH$_3^{NacNac-b}$), 0.96 (d, $^3J_{H-H}$ = 6.8 Hz, 6H, CH$_3^{iPr}$), 0.22 (s, 3H, O_2NCH_3). [TK691, 1]

^{13}C NMR (100.65 MHz, THF-d$_8$, -40°C): δ [ppm] = 159.1 (Cq, C$^{NacNac-a}$), 158.9 (Cq, C$^{NacNac-b}$), 156.0 (Cq, C^{Pz}), 148.4 (Cq, C-DiPP^{i}), 144.7 (Cq, C-DiPP^{o}), 141.1 (Cq, C-DiPP^{o}), 124.0 (CH, C-DiPP^{m}), 122.8 (CH, C-DiPP^{m}), 122.1 (CH, C-DiPP^{p}), 97.1 (CH, CH^{NacNac}), 92.3 (CH, CH^{pz}), 51.7 (CH$_2$, CH$_2$), 48.9 (CH$_3$, O_2NCH_3) 28.8 (CH, CH^{iPr}), 28.4 (CH, CH$^{iPr-ONO}$), 25.4 (CH$_3$, CH$_3^{iPr}$), 25.2 (CH$_3$, CH$_3^{NacNac-b}$), 24.8 (CH$_3$, CH$_3^{iPr}$), 24.2 (CH$_3$, CH$_3^{iPr}$), 23.5 (CH$_3$, CH$_3^{iPr}$), 21.6 (CH$_3$, CH$_3^{NacNac-a}$). [TK691, 9]

FT-IR (ATR): $\tilde{\nu}$ [cm^{-1}] = 3050 (vw), 2955 (m), 2925 (m), 2902 (w), 2864 (m), 1581 (w), 1552 (s), 1531 (s), 1459 (s), 1438 (s), 1300 (vs), 1381 (m), 1366 (w), 1350 (w), 1314 (s), 1281 (m), 1261 (s), 1231 (m), 1185 (m), 1157 (w), 1118 (m), 1098 (m), 1052 (m), 1028 (m), 984 (w), 956 (w), 935 (w), 913 (w), 897 (m), 858 (w), 837 (w), 825 (w), 800 (s), 787 (s), 767 (vs), 760 (s), 750 (w), 725 (s), 713 (m), 662 (vw), 647 (m), 630 (m), 630 (w), 612 (w), 596 (w), 554 (vw), 545 (m), 522 (m), 468 (w), 444 (m), 421 (m), 414 (m).

MS (ESI$^+$, THF) m/z:[$NaLNi_2O_2CH_3$]$^+$ = 806.4.

LNi$_2$ONCH$_2$ (16)

In a 20 mL screw cap vial in a glove box **2-Na** (40 mg, 51.4 µmol, 1.0 eq.) is dissolved in THF (5 mL) and nitromethane (3.1 mg, 2.8 µL, 51.4 µmol, 1.0 eq.) was added. An immediate color change from bright orange to deep red was observed accompanied by a vigorous gas evolution. The reaction mixture was stirred for 10 d resulting in a green solution. The reaction mixture was filtered and overlayered with hexane. After crystallization for 1 week at -35 °C mixture of **16** and 3 was isolated as green cubes.

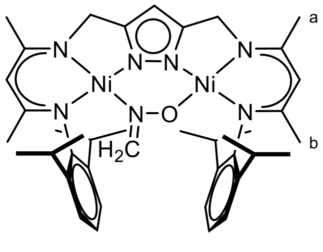

16

^{1}H NMR (500.25 MHz, THF-d$_8$, -30 °C): δ [ppm] = 7.48 (d, $^3J_{H-H}$ = 9.5 Hz, 1H, H-DiPP^{m}), 7.02-6.98 (m, 2H, H-DiPP), 6.93-6.84 (m, 3H, H-DiPP), 6.76 (d, $^1J_{H-H}$ = 5.9 Hz, 1H, ONCH$_2$), 6.68 (d, $^1J_{H-H}$ = 6.3 Hz, 1H, ONCH$_2$), 5.65 (s, 1H, CH^{pz}), 4.79 (s, 1H, CH^{NacNac}), 4.66 (s, 1H, CH^{NacNac}), 4.03 (s, 2H, CH$_2$), 3.86 (d, $^1J_{H-H}$ = 17.5 Hz, 1H, CH$_2$), 3.82-3.75 (m, 1H, CH^{iPr}), 3.70 (d, $^1J_{H-H}$ = 17.5 Hz, 1H, CH$_2$), 3.57-3.53 (m, 1H, CH^{iPr}), 3.41-3.34 (m, 1H, CH^{iPr}), 3.30-3.20 (m, 1H, CH^{iPr}), 1.98 (s, 3H, CH$_3^{NacNac-a}$), 1.95 (d, $^3J_{H-H}$ = 6.0 Hz, 3H, CH$_3^{iPr}$), 1.86 (s, 3H, CH$_3^{NacNac-a}$), 1.46 (d, $^3J_{H-H}$ = 5.7 Hz, 3H, CH$_3^{iPr}$), 1.39 (s, 3H, CH$_3^{NacNac-b}$), 1.20 (s, 3H, CH$_3^{NacNac-b}$), 1.18 (d, $^3J_{H-H}$ = 7.2 Hz, 3H, CH$_3^{iPr}$), 1.10-0.90 (m, 9H, CH$_3^{iPr}$), 0.58 (d, $^3J_{H-H}$ = 5.4 Hz, 3H, CH$_3^{iPr}$), 0.49 (d, $^3J_{H-H}$ = 5.2 Hz, 3H, CH$_3^{iPr}$). [TK709, 11]

^{13}C NMR (125.79 MHz, THF-d$_8$, -30°C): δ [ppm] = 160.9 (Cq, C$^{NacNac-a}$), 160.4 (Cq, C$^{NacNac-b}$), 160.0 (Cq, C$^{NacNac-a}$), 159.6 (Cq, C$^{NacNac-b}$), 154.6 (Cq, C^{Pz}), 154.1 (Cq, C^{Pz}), 150.9 (CH, C-DiPP^{m}), 147.3 (CH, CH^{NacNac}), 145.7 (CH, CH^{NacNac}), 144.0 (Cq, C-DiPP), 143.2 (CH, C-DiPP), 141.7 (Cq, C-DiPP), 125.9 (CH, C-DiPP), 125.6 (CH, C-DiPP), 124.6 (CH$_2$, ONCH$_2$), 123.6 (CH, C-DiPP), 123.0 (CH$_2$, ONCH$_2$), 122.7 (CH, C-DiPP), 98.2 (CH, $\mathrm{CH}^{\mathrm{NacNac}}$), 98.1 (CH, $\mathrm{CH}^{\mathrm{NacNac}}$), 92.0 (CH, $\mathrm{CH}^{\mathrm{pz}}$), 51.8 ($\mathrm{CH_2}$, $\mathrm{CH_2}$), 51.1 ($\mathrm{CH_2}$, $\mathrm{CH_2}$), 28.9 (CH, $\mathrm{CH}^{i\mathrm{Pr}}$), 28.7(CH, $\mathrm{CH}^{i\mathrm{Pr}}$), 28.6 (CH, $\mathrm{CH}^{i\mathrm{Pr}}$), 28.5 (CH, $\mathrm{CH}^{i\mathrm{Pr}}$), 26.5 ($\mathrm{CH_3}$, $\mathrm{CH_3}^{i\mathrm{Pr}}$), 25.2 ($\mathrm{CH_3}$, $\mathrm{CH_3}^{i\mathrm{Pr}}$), 25.1 ($\mathrm{CH_3}$, $\mathrm{CH_3}^{i\mathrm{Pr}}$), 24.8 ($\mathrm{CH_3}$, $\mathrm{CH_3}^{i\mathrm{Pr}}$), 25.0 ($\mathrm{CH_3}$, $\mathrm{CH_3}^{i\mathrm{Pr}}$), 24.7 ($\mathrm{CH_3}$, $\mathrm{CH_3}^{i\mathrm{Pr}}$), 24.5 ($\mathrm{CH_3}$, $\mathrm{CH_3}^{i\mathrm{Pr}}$), 24.3 ($\mathrm{CH_3}$, $\mathrm{CH_3}^{i\mathrm{Pr}}$), 24.0 ($\mathrm{CH_3}$, $\mathrm{CH_3}^{\mathrm{NacNaca}}$), 23.9 ($\mathrm{CH_3}$, $\mathrm{CH_3}^{\mathrm{NacNacb}}$), 23.6 ($\mathrm{CH_3}$, $\mathrm{CH_3}^{\mathrm{NacNac\text{-}a}}$), 21.7 ($\mathrm{CH_3}$, $\mathrm{CH_3}^{\mathrm{NacNac\text{-}a}}$), 21.3 ($\mathrm{CH_3}$, $\mathrm{CH_3}^{\mathrm{NacNac\text{-}b}}$). [TK709, 13]

FT-IR (ATR): $\tilde{\nu}$ [cm^{-1}]: = 3058 (w), 3023 (vw), 2957 (m), 2920 (m), 2868 (m), 1575 (w), 1553 (s), 1529 (vs), 1463 (s), 1436 (s), 1402 (vs), 1369 (m), 1312 (s), 1280 (s), 1251 (m), 1227 (w), 1201 (vw), 1186 (s), 1175 (w), 1105 (w), 1090 (m), 1051 (m), 1029 (m), 1010 (w), 964 (w), 936 (m), 913 (m), 867 (w), 799 (s), 762 (s), 746 (s), 726 (s), 713 (m), 660 (w), 643 (w), 615 (w), 593 (w), 549 (w), 521 (w).

8 Literature

[1] C. T. Walsh, W. H. Orme-Johnson, *Biochemistry* **1987**, *26*, 4901–4906.

[2] M. J. Maroney, S. Ciurli, *Chem. Rev.* **2014**, *114*, 4206–4228.

[3] A. L. Brauer, B. S. Learman, C. E. Armbruster, *Mol. Microbiol.* **2020**, *114*, 185–199.

[4] S. W. Ragsdale, *J. Biol. Chem.* **2009**, *284*, 18571–18575.

[5] P. Zimmermann, C. Limberg, *J. Am. Chem. Soc.* **2017**, *139*, 4233–4242.

[6] J. E. Parks, R. H. Holm, *Inorg. Chem.* **1968**, *7*, 1408–1416.

[7] M. Asay, C. Jones, M. Driess, *Chem. Rev.* **2011**, *111*, 354–396.

[8] S. P. Sarish, N. Sharanappa, S. Nagendran, R. Herbert W., *Acc. Chem. Res.* **2011**, *44*, 157–170.

[9] F. T. Edelmann, *Coord. Chem. Rev.* **2015**, *284*, 124–205.

[10] D. W. Randall, S. D. George, P. L. Holland, B. Hedman, K. O. Hodgson, W. B. Tolman, E. I. Solomon, *J. Am. Chem. Soc.* **2000**, *122*, 11632–11648.

[11] S. Pfirrmann, S. Yao, B. Ziemer, R. Stösser, M. Driess, C. Limberg, *Organometallics* **2009**, *28*, 6855–6860.

[12] S. Pfirrmann, C. Limberg, B. Ziemer, *Dalton Trans.* **2008**, *912*, 6689.

[13] S. Pfirrmann, C. Limberg, C. Herwig, R. Stößer, B. Ziemer, *Angew. Chem. Int. Ed.* **2009**, *48*, 3357–3361.

[14] D. F. J. Piesik, S. Range, S. Harder, *Organometallics* **2008**, *27*, 6178–6187.

[15] H. Gehring, R. Metzinger, C. Herwig, J. Intemann, S. Harder, C. Limberg, *Chem. Eur. J.* **2013**, *19*, 1629–1636.

[16] J. Klingele, S. Dechert, F. Meyer, *Coord. Chem. Rev.* **2009**, *253*, 2698–2741.

[17] D.-H. Manz, *Preorganized Bimetallic Nickel Complexes of Pyrazolate-Bridged Ligands for Cooperative Substrate Transformation*, Dissertation, Göttingen, **2016**.

[18] D. H. Manz, P. C. Duan, S. Dechert, S. Demeshko, R. Oswald, M. John, R. A. Mata, F. Meyer, *J. Am. Chem. Soc.* **2017**, *139*, 16720–16731.

[19] P.-C. Duan, D.-H. Manz, S. Dechert, S. Demeshko, F. Meyer, *J. Am. Chem. Soc.* **2018**, *140*, 4929–4939.

[20] E. Ferretti, S. Dechert, S. Demeshko, M. C. Holthausen, F. Meyer, *Angew. Chem. Int. Ed.* **2019**, *58*, 1705–1709.

[21] P.-C. Duan, *A Dinuclear Dihydride Complex for Bimetallic Reductive Activation and Transformation of A Range of Inert Substrates*, Dissertation, Göttingen, **2017**.

[22] K. P. Kepp, *J. Phys. Chem. A* **2017**, *121*, 9092–9098.

[23] B. M. Hoffman, D. Lukoyanov, Z. Y. Yang, D. R. Dean, L. C. Seefeldt, *Chem. Rev.* **2014**, *114*, 4041–4062.

[24] P. E. Wilson, A. C. Nyborg, G. D. Watt, *Biophys. Chem.* **2001**, *91*, 281–304.

[25] B. M. Hoffman, D. Lukoyanov, D. R. Dean, L. C. Seefeldt, *Acc. Chem. Res.* **2013**, *46*, 587–595.

[26] D. Lukoyanov, N. Khadka, D. R. Dean, S. Raugei, L. C. Seefeldt, B. M. Hoffman, *Inorg. Chem.* **2017**, *56*, 2233–2240.

[27] S. Raugei, L. C. Seefeldt, B. M. Hoffman, *Proc. Natl. Acad. Sci. U.S.A.* **2018**, *115*, E10521–E10530.

[28] D. F. Harris, D. A. Lukoyanov, S. Shaw, P. Compton, M. Tokmina-Lukaszewska, B. Bothner, N. Kelleher, D. R. Dean, B. M. Hoffman, L. C. Seefeldt, *Biochemistry* **2018**, *57*, 701–710.

[29] D. H. Manz, P. C. Duan, S. Dechert, S. Demeshko, R. Oswald, M. John, R. A. Mata, F. Meyer, *J. Am. Chem. Soc.* **2017**, *139*, 16720–16731.

[30] J. J. Curley, R. G. Bergman, T. D. Tilley, *Dalton Trans.* **2012**, *41*, 192–200.

[31] B. Horn, C. Limberg, C. Herwig, B. Braun, *Inorg. Chem.* **2014**, *53*, 6867–6874.

[32] N. G. Connelly, W. E. Geiger, *Chem. Rev.* **1996**, *96*, 877–910.

[33] C. Jones, *Nat. Rev. Chem.* **2017**, *1*, 0059.

[34] L. K. Johnson, C. M. Killian, M. Brookhart, *J. Am. Chem. Soc.* **1995**, *117*, 6414–6415.

[35] S. Z. Tasker, E. A. Standley, T. F. Jamison, *Nature* **2014**, *509*, 299–309.

[36] K. Jiao, D. Liu, H. Ma, H. Qiu, P. Fang, T. Mei, *Angew. Chem. Int. Ed.* **2020**, *59*, 6520–6524.

[37] T. J. Schmeier, N. Hazari, C. D. Incarvito, J. A. Raskatov, *Chem. Commun.* **2011**, *47*, 1824–1826.

[38] M. Abubekerov, L. Y. M. Eymann, T. L. Gianetti, J. Arnold, *Dalton Trans.* **2016**, *45*, 14581–14590.

[39] E. A. Hill, N. Zhao, A. S. Filatov, J. S. Anderson, *Chem. Commun.* **2020**, 1–4.

[40] C. A. Rettenmeier, H. Wadepohl, L. H. Gade, *Chem. Sci.* **2016**, *7*, 3533–3542.

[41] R. Kehoe, M. Mahadevan, A. Manzoor, G. McMurray, P. Wienefeld, M. C. Baird, P. H. M. Budzelaar, *Organometallics* **2018**, *37*, 2450–2467.

[42] M. D. Leatherman, S. A. Svejda, L. K. Johnson, M. Brookhart, *J. Am. Chem. Soc.* **2003**, *125*, 3068–3081.

[43] E. Kogut, A. Zeller, T. H. Warren, T. Strassner, *J. Am. Chem. Soc.* **2004**, *126*, 11984–11994.

[44] S. W. Ragsdale, M. Kumar, *Chem. Rev.* **1996**, *96*, 2515–2540.

[45] S. W. Ragsdale, H. G. Wood, W. E. Antholine, *Proc. Natl. Acad. Sci. U.S.A.* **1985**, *82*, 6811–6814.

[46] M. Can, F. A. Armstrong, S. W. Ragsdale, *Chem. Rev.* **2014**, *114*, 4149–4174.

[47] V. Svetlitchnyi, H. Dobbek, W. Meyer-Klaucke, T. Meins, B. Thiele, P. Romer, R. Huber, O.

Meyer, *Proc. Natl. Acad. Sci. U.S.A.* **2004**, *101*, 446–451.

[48] T. I. Doukov, T. M. Iverson, J. Seravalli, S. W. Ragsdale, C. L. Drennan, *Science* **2002**, *298*, 567–572.

[49] J. Seravalli, S. W. Ragsdale, *Biochemistry* **2008**, *47*, 6770–6781.

[50] P. Zimmermann, C. Limberg, *J. Am. Chem. Soc.* **2017**, *139*, 4233–4242.

[51] M. Tsuyoshi, I. Mikinao, K. Mai, T. Kazuyuki, *Dalton Trans.* **2010**, *39*, 2972–2983.

[52] M. I. Lipschutz, X. Yang, R. Chatterjee, T. D. Tilley, *J. Am. Chem. Soc.* **2013**, *135*, 15298–15301.

[53] G. R. Fulmer, A. J. M. Miller, N. H. Sherden, H. E. Gottlieb, A. Nudelman, B. M. Stoltz, J. E. Bercaw, K. I. Goldberg, *Organometallics* **2010**, *29*, 2176–2179.

[54] H. Meerwein, P. Borner, O. Fuchs, H. J. Sasse, H. Schrodt, J. Spille, *Chem. Ber.* **1956**, *89*, 2060–2079.

[55] M. Brookhart, M. L. H. Green, *J. Organomet. Chem.* **1983**, *250*, 395–408.

[56] M. E. García, S. Melón, A. Ramos, V. Riera, M. A. Ruiz, D. Belletti, C. Graiff, A. Tiripicchio, *Organometallics* **2003**, *22*, 1983–1985.

[57] M. E. García, A. Ramos, M. A. Ruiz, M. Lanfranchi, L. Marchio, *Organometallics* **2007**, *26*, 6197–6212.

[58] L. S. Jongbloed, N. Vogt, A. Sandleben, B. de Bruin, A. Klein, J. I. van der Vlugt, *Eur. J. Inorg. Chem.* **2018**, *2018*, 2408–2418.

[59] P. J. Stang, M. Hanack, L. R. Subramanian, *Synthesis* **1982**, *2*, 85–126.

[60] E. S. Lewis, S. H. Vanderpool, *J. Am. Chem. Soc.* **1978**, *100*, 6421–6424.

[61] J. P. Cheng, K. L. Handoo, V. D. Parker, *J. Am. Chem. Soc.* **1993**, *115*, 2655–2660.

[62] M. Horn, L. H. Schappele, G. Lang-Wittkowski, H. Mayr, A. R. Ofial, *Chem. Eur. J.* **2013**, *19*, 249–263.

[63] V. N. Cavaliere, D. J. Mindiola, *Chem. Sci.* **2012**, *3*, 3356–3365.

[64] D. Seyferth, A. W. Dow, H. Menzel, T. C. Flood, *J. Am. Chem. Soc.* **1968**, *90*, 1080–1082.

[65] J. A. Pople, A. A. Bothner-By, *J. Chem. Phys.* **1965**, *42*, 1339–1349.

[66] C. A. Laskowski, G. L. Hillhouse, *Chem. Sci.* **2011**, *2*, 321–325.

[67] P. Thamyongkit, A. D. Bhise, M. Taniguchi, J. S. Lindsey, *J. Org. Chem.* **2006**, *71*, 903–910.

[68] M. Marín, J. J. Moreno, C. Navarro-Gilabert, E. Álvarez, C. Maya, R. Peloso, M. C. Nicasio, E. Carmona, *Chem. Eur. J.* **2019**, *25*, 260–272.

[69] Y. Ruiz-Morales, G. Schreckenbach, T. Ziegler, *J. Phys. Chem.* **1996**, *100*, 3359–3367.

[70] A. Meltzer, S. Inoue, C. Präsang, M. Driess, *J. Am. Chem. Soc.* **2010**, *132*, 3038–3046.

[71] F. Schneck, J. Ahrens, M. Finger, A. C. Stückl, C. Würtele, D. Schwarzer, S. Schneider, *Nat.*

Commun. **2018**, *9*, 1–8.

[72] H. Hollenstein, H. H. Günthard, *Spectrochim. Acta A* **1971**, *27*, 2027–2060.

[73] P. Stavropoulos, M. Carrie, M. C. Muetterties, R. H. Holm, *J. Am. Chem. Soc.* **1990**, *112*, 5385–5387.

[74] M. S. Ram, C. G. Riordan, *J. Am. Chem. Soc.* **1995**, *117*, 2365–2366.

[75] M. S. Ram, C. G. Riordan, G. P. A. Yap, L. Liable-Sands, A. L. Rheingold, A. Marchaj, J. R. Norton, *J. Am. Chem. Soc.* **1997**, *119*, 1648–1655.

[76] F. Dalena, A. Senatore, M. Basile, S. Knani, A. Basile, A. Iulianelli, *Membranes* **2018**, *8*, 98.

[77] Y. Noriyuki, K. Satoru, Y. Makoto, P. Pujado, W. Steve, *Appl. Catal. A Gen.* **2001**, *221*, 253–265.

[78] H. H. Jaffé, M. Orchin, *Tetrahedron* **1960**, *10*, 212–214.

[79] R. Colton, M. J. McCormick, *Coord. Chem. Rev.* **1980**, *31*, 1–52.

[80] J. O. Alben, P. P. Moh, F. G. Fiamingo, R. A. Altschuld, *Proc. Natl. Acad. Sci. U.S.A.* **1981**, *78*, 234–237.

[81] R. Desiderato, G. R. Dobson, *J. Chem. Educ.* **1982**, *59*, 752–756.

[82] A. D. Cormier, J. D. Brown, K. Nakamoto, *Inorg. Chem.* **1973**, *12*, 3011–3013.

[83] U. S. D. Paul, U. Radius, *Organometallics* **2017**, *36*, 1398–1407.

[84] P. Stavropoulos, M. Carrié, M. C. Muetterties, R. H. Holm, *J. Am. Chem. Soc.* **1990**, *112*, 5385–5387.

[85] P. Stavropoulos, M. C. Muetterties, M. Carriè, R. H. Holm, *J. Am. Chem. Soc.* **1991**, *113*, 8485–8492.

[86] L. Manojlovic-Muir, K. W. Muir, W. M. Davis, H. A. Mirza, R. J. Puddephatt, *Inorg. Chem.* **1992**, *31*, 904–909.

[87] M. J. Ingleson, B. C. Fullmer, D. T. Buschhorn, H. Fan, M. Pink, J. C. Huffman, K. G. Caulton, *Inorg. Chem.* **2008**, *47*, 407–409.

[88] N. A. Eckert, A. Dinescu, T. R. Cundari, P. L. Holland, *Inorg. Chem.* **2005**, *44*, 7702–7704.

[89] B. Horn, S. Pfirrmann, C. Limberg, C. Herwig, B. Braun, S. Mebs, R. Metzinger, *Z. Anorg. Allg. Chem.* **2011**, *637*, 1169–1174.

[90] B. Horn, C. Limberg, C. Herwig, S. Mebs, *Angew. Chem. Int. Ed.* **2011**, *50*, 12621–12625.

[91] H. Yang, C. Zhang, P. Gao, H. Wang, X. Li, L. Zhong, W. Wei, Y. Sun, *Catal. Sci. Technol.* **2017**, *7*, 4580–4598.

[92] G. A. Olah, *Angew. Chem. Int. Ed.* **2013**, *52*, 104–107.

[93] B. Li, K. J. Jens, *Ind. Eng. Chem. Res.* **2014**, *53*, 1735–1740.

[94] D. S. McGuinness, J. Patel, M. H. Amin, S. K. Bhargava, *ChemCatChem* **2017**, *9*, 1837–1844.

[95] C. Bianchini, A. Meli, *Organometallics* **1985**, *4*, 1537–1542.

[96] E. L. Muetterties, J. Stein, *Chem. Rev.* **1979**, *79*, 479–490.

[97] M. D. Fryzuk, M. Mylvaganam, M. J. Zaworotko, L. R. MacGillivray, *Organometallics* **1996**, *15*, 1134–1138.

[98] L. E. Heim, H. Konnerth, M. H. G. Prechtl, *Green Chem.* **2017**, *19*, 2347–2355.

[99] A. M. Bahmanpour, A. Hoadley, A. Tanksale, *Green Chem.* **2015**, *17*, 3500–3507.

[100] A. M. Bahmanpour, A. Hoadley, S. H. Mushrif, A. Tanksale, *ACS Sustain. Chem. Eng.* **2016**, *4*, 3970–3977.

[101] L. Li, S. Zhang, J. P. Ru, J. K. Johnson, *ACS Sustain. Chem. Eng.* **2019**, *7*, 2508–2515.

[102] P. Ryabchuk, K. Stier, K. Junge, M. P. Checinski, M. Beller, *J. Am. Chem. Soc.* **2019**, *141*, 16923–16929.

[103] C. A. Huff, M. S. Sanford, *J. Am. Chem. Soc.* **2011**, *133*, 18122–18125.

[104] S. Wesselbaum, V. Moha, M. Meuresch, S. Brosinski, K. M. Thenert, J. Kothe, T. vom Stein, U. Englert, M. Hölscher, J. Klankermayer, et al., *Chem. Sci.* **2015**, *6*, 693–704.

[105] S. Bontemps, L. Vendier, S. Sabo-Etienne, *J. Am. Chem. Soc.* **2014**, *136*, 4419–4425.

[106] P. Ríos, A. Rodríguez, J. López-Serrano, *ACS Catal.* **2016**, *6*, 5715–5723.

[107] M. Glatz, B. Stöger, D. Himmelbauer, L. F. Veiros, K. Kirchner, *ACS Catal.* **2018**, *8*, 4009–4016.

[108] T. Zell, Y. Ben-David, D. Milstein, *Catal. Sci. Technol.* **2015**, *5*, 822–826.

[109] S. Fleischer, S. Zhou, K. Junge, M. Beller, *Angew. Chem. Int. Ed.* **2013**, *52*, 5120–5124.

[110] F. Panahi, M. Bahmani, N. Iranpoor, *Adv. Synth. Catal.* **2015**, *357*, 1211–1220.

[111] S. Chakraborty, Y. J. Patel, J. A. Krause, H. Guan, *Angew. Chem. Int. Ed.* **2013**, *52*, 7523–7526.

[112] S. Chakraborty, J. A. Krause, H. Guan, *Organometallics* **2009**, *28*, 582–586.

[113] H. E. Bryndza, W. Tam, *Chem. Rev.* **1988**, *88*, 1163–1188.

[114] L. M. Martínez-Prieto, E. Ávila, P. Palma, E. Álvarez, J. Cámpora, *Chem. Eur. J.* **2015**, *21*, 9833–9849.

[115] D. Walther, *J. Organomet. Chem.* **1980**, *190*, 393–401.

[116] J. Kaiser, J. Sieler, D. Walther, E. Dinjus, L. Golic, *Acta Crystallogr. B* **1982**, *38*, 1584–1586.

[117] S. Sakaki, K. Kitaura, K. Morokuma, K. Ohkubo, *Inorg. Chem.* **1983**, *22*, 104–108.

[118] S. Ogoshi, M. A. Oka, H. Kurosawa, *J. Am. Chem. Soc.* **2004**, *126*, 11802–11803.

[119] Y. Hoshimoto, M. Ohashi, S. Ogoshi, *Acc. Chem. Res.* **2015**, *48*, 1746–1755.

[120] H. Stevens, P.-C. Duan, S. Dechert, F. Meyer, *J. Am. Chem. Soc.* **2020**, *142*, 6717–6728.

[121] C. Kato, S. Konaka, T. Iijima, M. Kimura, *Bull. Chem. Soc. Jpn.* **1969**, *42*, 2148–2158.

[122] K. Gardner, J. Mayer, *Science* **1995**, *269*, 1849–1851.

[123] L. J. J. Laarhoven, P. Mulder, *J. Phys. Chem. B* **1997**, *101*, 73–77.

[124] B. Ruscic, *J. Phys. Chem. A* **2015**, *119*, 7810–7837.

[125] H. Dahn, P. Péchy, *Magn. Reson. Chem.* **1996**, *34*, 723–724.

[126] D. R. Allan, S. J. Clark, M. J. P. Brugmans, G. J. Ackland, W. L. Vos, *Phys. Rev. B* **1998**, *58*, R11809–R11812.

[127] S. Buchler, F. Meyer, E. Kaifer, H. Pritzkow, *Inorganica Chim. Acta* **2002**, *337*, 371–386.

[128] G. Casiraghi, G. Casnati, M. Cornia, G. Sartori, F. Bigi, *Makromol. Chem.* **1981**, *182*, 2973–2979.

[129] I. Noviandri, K. N. Brown, D. S. Fleming, P. T. Gulyas, P. A. Lay, A. F. Masters, L. Phillips, *J. Phys. Chem. B* **1999**, *103*, 6713–6722.

[130] M. Brookhart, M. L. H. Green, G. Parkin, *Proc. Natl. Acad. Sci. U.S.A.* **2007**, *104*, 6908–6914.

[131] G. B. Tolstorozhev, I. V. Skornyakov, M. V. Bel’kov, O. I. Shadyro, S. D. Brinkevich, S. N. Samovich, *Opt. Spectrosc.* **2012**, *113*, 179–183.

[132] R. Srinivasan, *Science* **2005**, *307*, 558–563.

[133] R. Cano, M. Yus, D. J. Ramón, *Tetrahedron* **2011**, *67*, 8079–8085.

[134] E. Ferretti, S. Dechert, S. Demeshko, M. C. Holthausen, F. Meyer, *Angew. Chem. Int. Ed.* **2019**, *58*, 1705–1709.

[135] L. P. Hammett, *J. Am. Chem. Soc.* **1937**, *59*, 96–103.

[136] M. Orlandi, D. Brenna, R. Harms, S. Jost, M. Benaglia, *Org. Process Res. Dev.* **2018**, *22*, 430–445.

[137] D. C. Caskey, D. W. Chapman, *EU Pat. 0086363 B1* **1982**.

[138] R. V. Jagadeesh, A.-E. Surkus, H. Junge, M.-M. Pohl, J. Radnik, J. Rabeah, H. Huan, V. Schunemann, A. Bruckner, M. Beller, *Science* **2013**, *342*, 1073–1076.

[139] R. Raja, V. B. Golovko, J. M. Thomas, A. Berenguer-Murcia, W. Zhou, S. Xie, B. F. G. Johnson, *Chem. Commun.* **2005**, 2026–2028.

[140] M. Studer, S. Neto, H. U. Blaser, *Top. Catal.* **2000**, *13*, 205–212.

[141] G. Wienhöfer, M. Baseda-Krüger, C. Ziebart, F. A. Westerhaus, W. Baumann, R. Jackstell, K. Junge, M. Beller, *Chem. Commun.* **2013**, *49*, 9089–9091.

[142] S. Sun, Z. Quan, X. Wang, *RSC Adv.* **2015**, *5*, 84574–84577.

[143] G. Wienhöfer, I. Sorribes, A. Boddien, F. Westerhaus, K. Junge, H. Junge, R. Llusar, M. Beller, *J. Am. Chem. Soc.* **2011**, *133*, 12875–12879.

[144] S. Letort, M. Lejeune, N. Kardos, E. Métay, F. Popowycz, M. Lemaire, M. Draye, *Green*

Chem. **2017**, *19*, 4583–4590.

[145] D. Formenti, F. Ferretti, F. K. Scharnagl, M. Beller, *Chem. Rev.* **2019**, *119*, 2611–2680.

[146] B. Barlaam, J. Boivin, S. Z. Zard, *Tetrahedron Lett.* **1993**, *34*, 1023–1026.

[147] D. Colón, E. J. Weber, J. L. Anderson, P. Winget, L. A. Suárez, *Environ. Sci. Technol.* **2006**, *40*, 4449–4454.

[148] M. G. Davlieva, J.-M. Lü, S. V. Lindeman, J. K. Kochi, *J. Am. Chem. Soc.* **2004**, *126*, 4557–4565.

[149] E. Laviron, R. Meunier-Prest, A. Vallat, L. Roullier, R. Lacasse, *J. Electroanal. Chem.* **1992**, *341*, 227–255.

[150] K. Okada, Y. Saito, M. Oda, *J. Chem. Soc. Chem. Commun.* **1992**, *53*, 1731.

[151] A. D. Dilman, A. A. Tishkov, I. M. Lyapkalo, S. L. Ioffe, Y. A. Strelenko, V. A. Tartakovsky, *Synthesis* **1998**, *1998*, 181–185.

[152] A. A. Tishkov, A. D. Dilman, V. I. Faustov, A. A. Birukov, K. S. Lysenko, P. A. Belyakov, S. L. Ioffe, Y. A. Strelenko, M. Y. Antipin, *J. Am. Chem. Soc.* **2002**, *124*, 11358–11367.

[153] N. Y. Tashkandi, F. Parsons, J. Guo, K. M. Baines, *Angew. Chem. Int. Ed.* **2015**, *54*, 1612–1615.

[154] G. Steinfeld, B. Kersting, *Z. Anorg. Allg. Chem.* **2009**, *635*, 260–264.

[155] E. Ferretti, S. Dechert, F. Meyer, *Inorg. Chem.* **2019**, *58*, 5154–5162.

[156] E. Ferretti, *Reductive Activation of Nitric Oxide and Nitrosobenzene at a Dinickel(II) Dihydride Complex and New Pyrazole-Based Diiron Compounds*, Dissertation, Göttingen, **2018**.

[157] J. A. King Jnr, G. L. Bryant Jnr, *Acta Crystallogr. C* **1996**, *52*, 1691–1693.

[158] L. Van Meervelt, *Acta Crystallogr. C* **1993**, *49*, 593–595.

[159] I. Coblentz Society, *NIST Chemistry WebBook*, National Institute Of Standards And Technology, Gaithersburg, **2020**.

[160] D. A. Shultz, A. K. Boal, N. P. Campbell, *Inorg. Chem.* **1998**, *37*, 1540–1543.

[161] S. F. Trevino, E. Prince, C. R. Hubbard, *J. Chem. Phys.* **1980**, *73*, 2996–3000.

[162] K. Shi, R. Wang, T. C. W. Mak, *J. Mol. Struct.* **1987**, *160*, 109–116.

[163] K. F. Morris, L. E. Erickson, *J. Chem. Educ.* **1996**, *73*, 471–473.

[164] S. R. Choi, M. Breugst, K. N. Houk, C. D. Poulter, *J. Org. Chem.* **2014**, *79*, 3572–3580.

[165] G. M. Sheldrick, *Acta Crystallogr. A* **2015**, *71*, 3–8.

[166] A. L. Spek, *Acta Crystallogr. C* **2015**, *71*, 9–18.

[167] STOE & CIE GmbH, Ed. , *X-RED*, Darmstadt, Germany, **2002**.

[168] BRUKER AXS GmbH, Ed. , *SADABS*, Karlsruhe, Germany, **2016**.

[169] A. D. Becke, *Phys. Rev. A* **1988**, *38*, 3098–3100.

[170] L. Goerigk, S. Grimme, *J. Chem. Phys.* **2010**, *132*, 184103.

[171] F. Weigend, R. Ahlrichs, *Phys. Chem. Chem. Phys.* **2005**, *7*, 3297.

[172] F. Weigend, *Phys. Chem. Chem. Phys.* **2006**, *8*, 1057.

9 Appendix

9.1 NMR Data

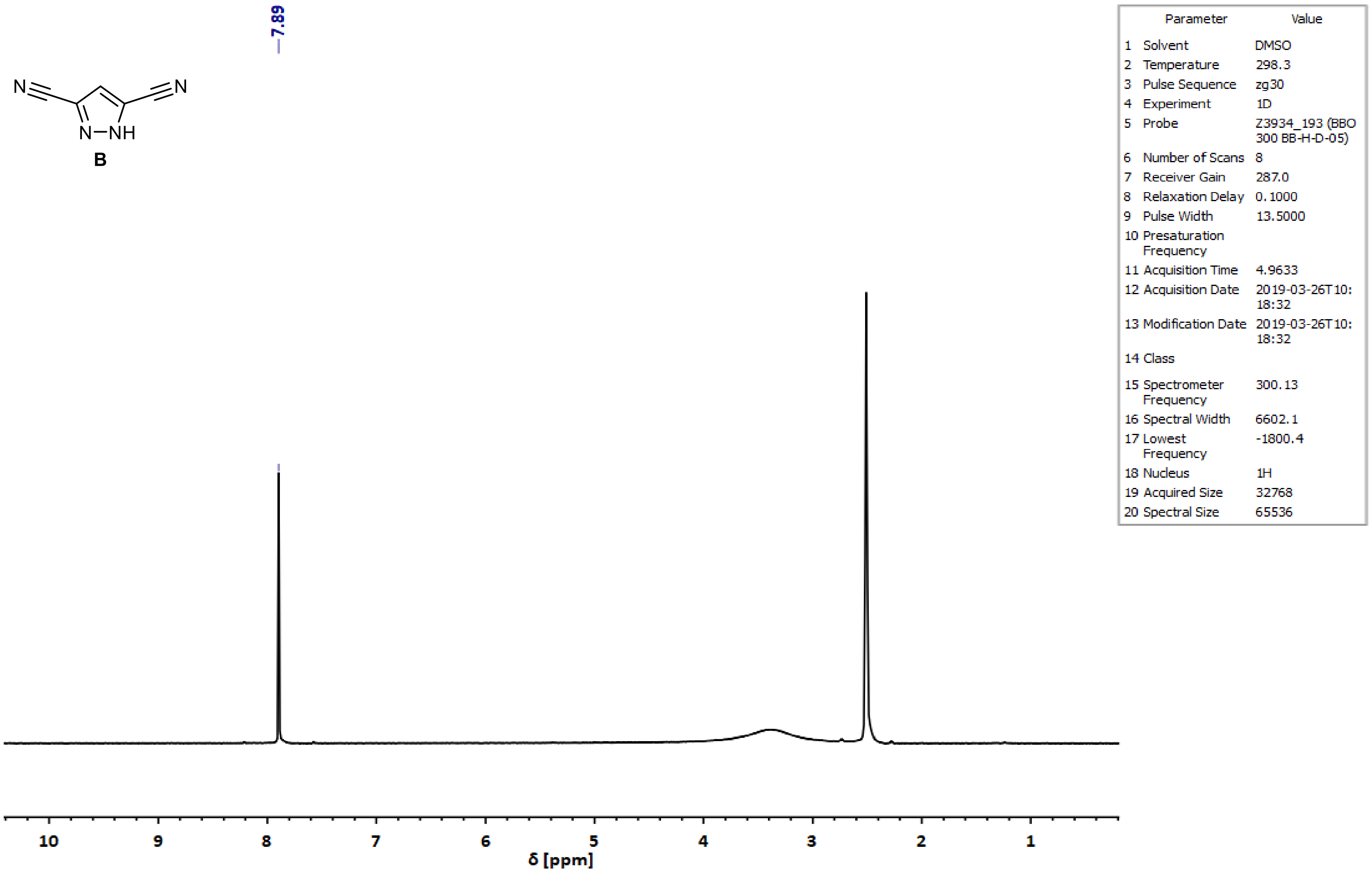

	Parameter	Value
1	Solvent	DMSO
2	Temperature	298.3
3	Pulse Sequence	zg30
4	Experiment	1D
5	Probe	Z3934_193 (BBO 300 BB-H-D-05)
6	Number of Scans	8
7	Receiver Gain	287.0
8	Relaxation Delay	0.1000
9	Pulse Width	13.5000
10	Presaturation Frequency	
11	Acquisition Time	4.9633
12	Acquisition Date	2019-03-26T10:18:32
13	Modification Date	2019-03-26T10:18:32
14	Class	
15	Spectrometer Frequency	300.13
16	Spectral Width	6602.1
17	Lowest Frequency	-1800.4
18	Nucleus	1H
19	Acquired Size	32768
20	Spectral Size	65536

Figure S 1: ^{1}H NMR of **B** in DMSO-d_6 at room temperature.

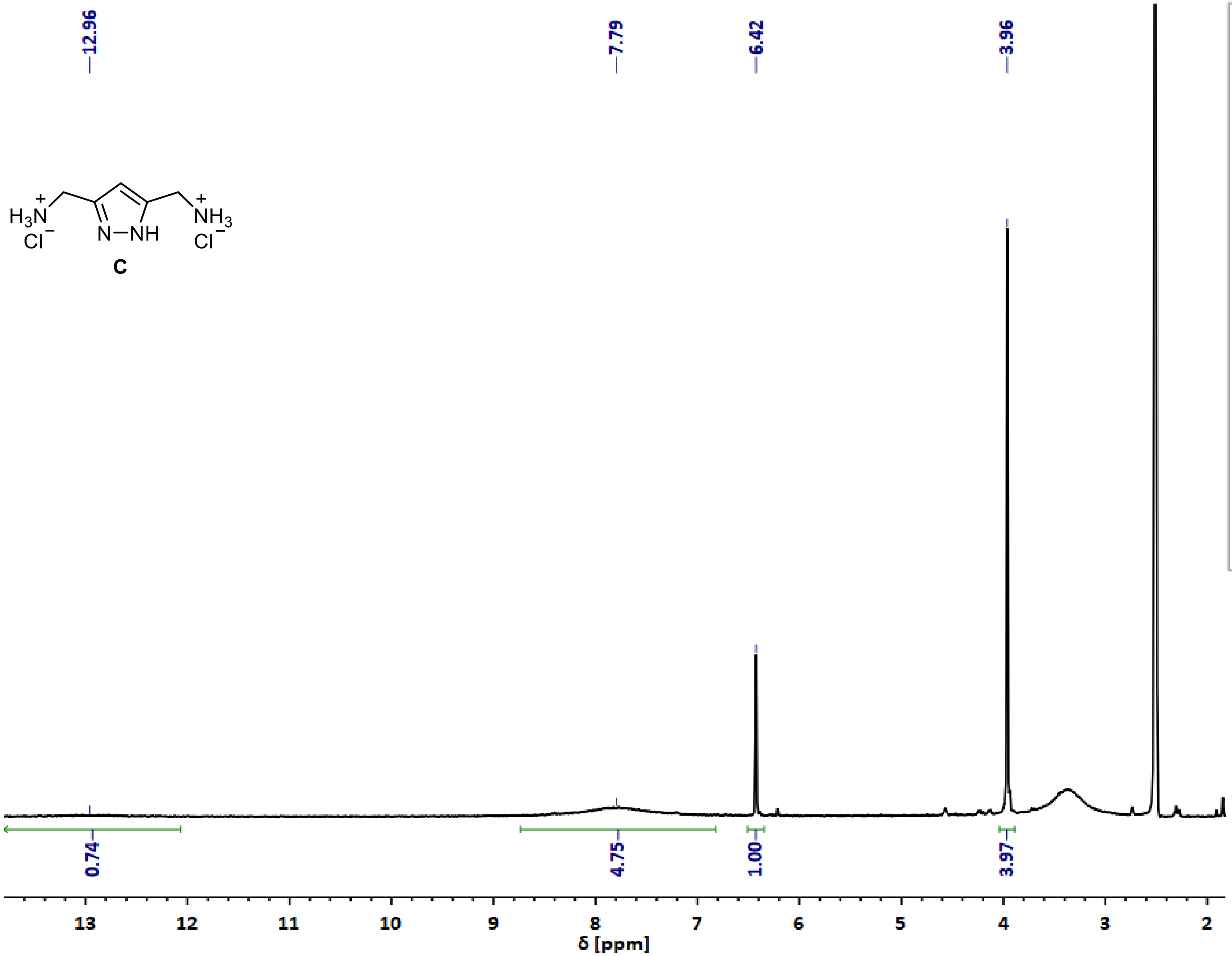

	Parameter	Value
1	Solvent	DMSO
2	Temperature	298.3
3	Pulse Sequence	zg30
4	Experiment	1D
5	Probe	Z3934_193 (BBO 300 BB-H-D-05)
6	Number of Scans	8
7	Receiver Gain	456.0
8	Relaxation Delay	0.1000
9	Pulse Width	13.5000
10	Presaturation Frequency	
11	Acquisition Time	4.9633
12	Acquisition Date	2019-03-27T09:51:17
13	Modification Date	2019-03-27T09:51:18
14	Class	
15	Spectrometer Frequency	300.13
16	Spectral Width	6602.1
17	Lowest Frequency	-1800.4
18	Nucleus	1H
19	Acquired Size	32768
20	Spectral Size	65536

Figure S 2: ^{1}H NMR of **C** in DMSO-d_6 at room temperature.

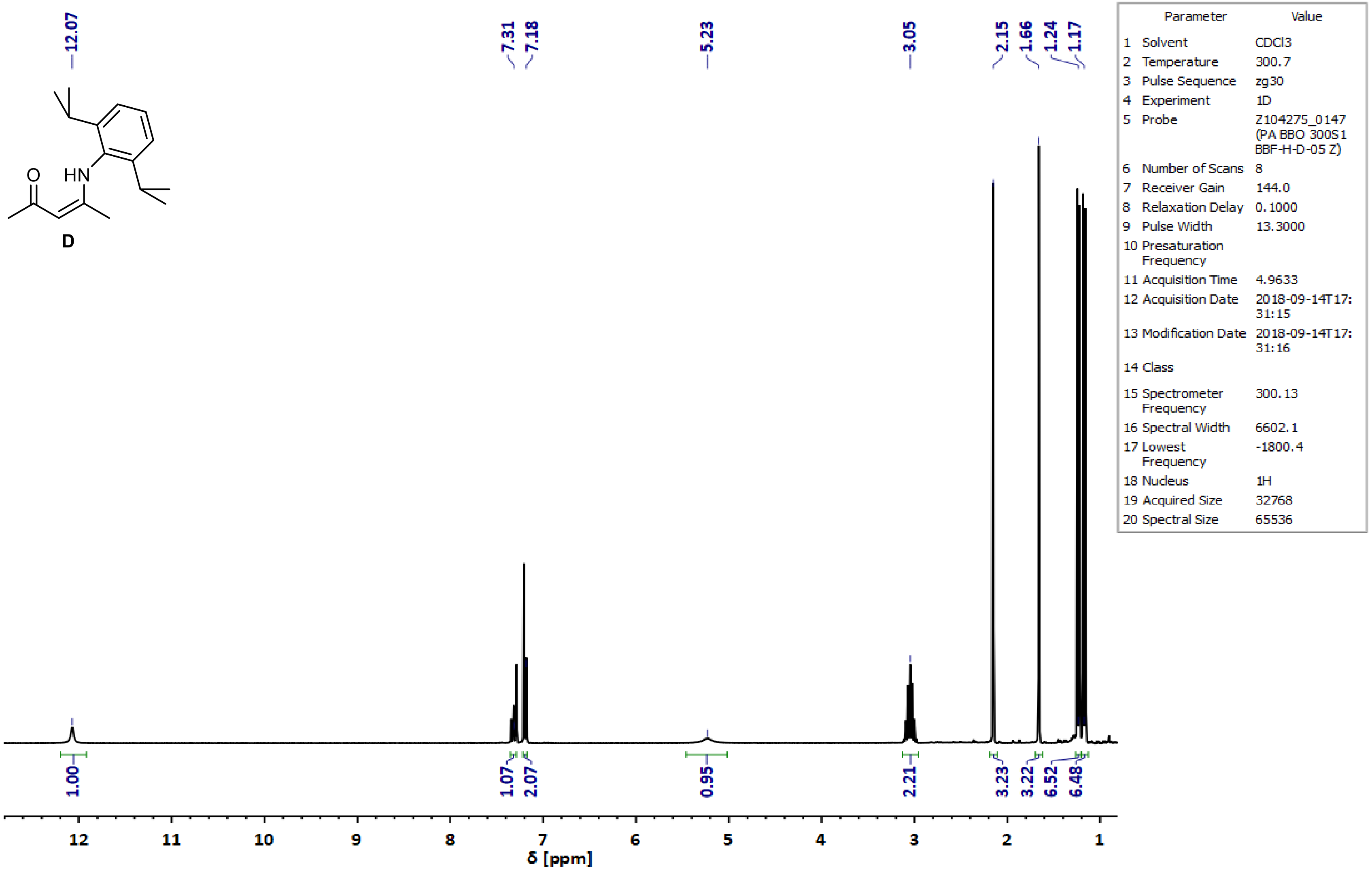

	Parameter	Value
1	Solvent	CDCl3
2	Temperature	300.7
3	Pulse Sequence	zg30
4	Experiment	1D
5	Probe	Z104275_0147 (PA BBO 300S1 BBF-H-D-05 Z)
6	Number of Scans	8
7	Receiver Gain	144.0
8	Relaxation Delay	0.1000
9	Pulse Width	13.3000
10	Presaturation Frequency	
11	Acquisition Time	4.9633
12	Acquisition Date	2018-09-14T17:31:15
13	Modification Date	2018-09-14T17:31:16
14	Class	
15	Spectrometer Frequency	300.13
16	Spectral Width	6602.1
17	Lowest Frequency	-1800.4
18	Nucleus	1H
19	Acquired Size	32768
20	Spectral Size	65536

Figure S 3: ^{1}H NMR of **D** in $CDCl_3$ at room temperature.

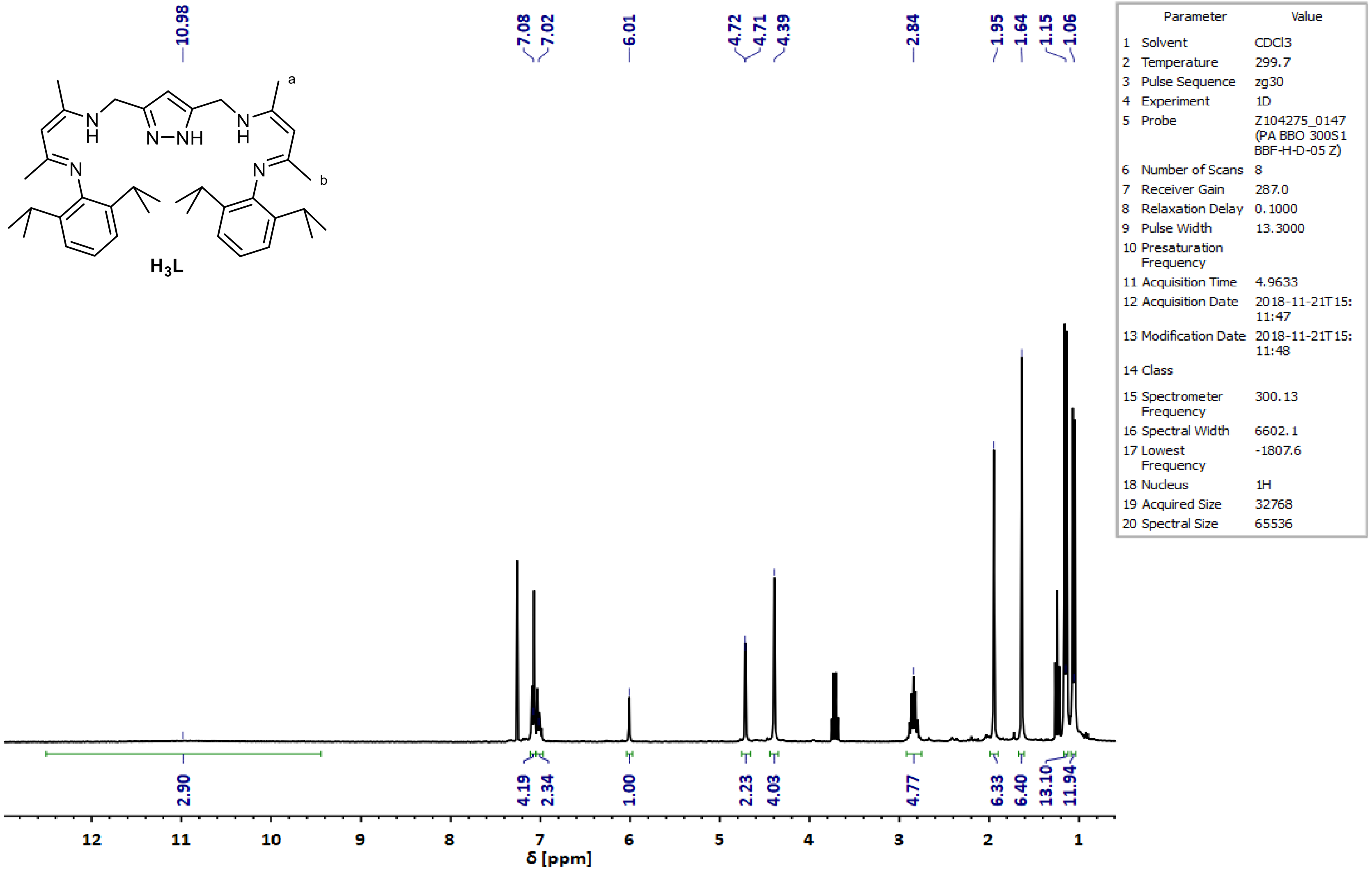

	Parameter	Value
1	Solvent	CDCl3
2	Temperature	299.7
3	Pulse Sequence	zg30
4	Experiment	1D
5	Probe	Z104275_0147 (PA BBO 300S1 BBF-H-D-05 Z)
6	Number of Scans	8
7	Receiver Gain	287.0
8	Relaxation Delay	0.1000
9	Pulse Width	13.3000
10	Presaturation Frequency	
11	Acquisition Time	4.9633
12	Acquisition Date	2018-11-21T15:11:47
13	Modification Date	2018-11-21T15:11:48
14	Class	
15	Spectrometer Frequency	300.13
16	Spectral Width	6602.1
17	Lowest Frequency	-1807.6
18	Nucleus	1H
19	Acquired Size	32768
20	Spectral Size	65536

Figure S 4: ^{1}H NMR of **H_3L** in $CDCl_3$ at room temperature.

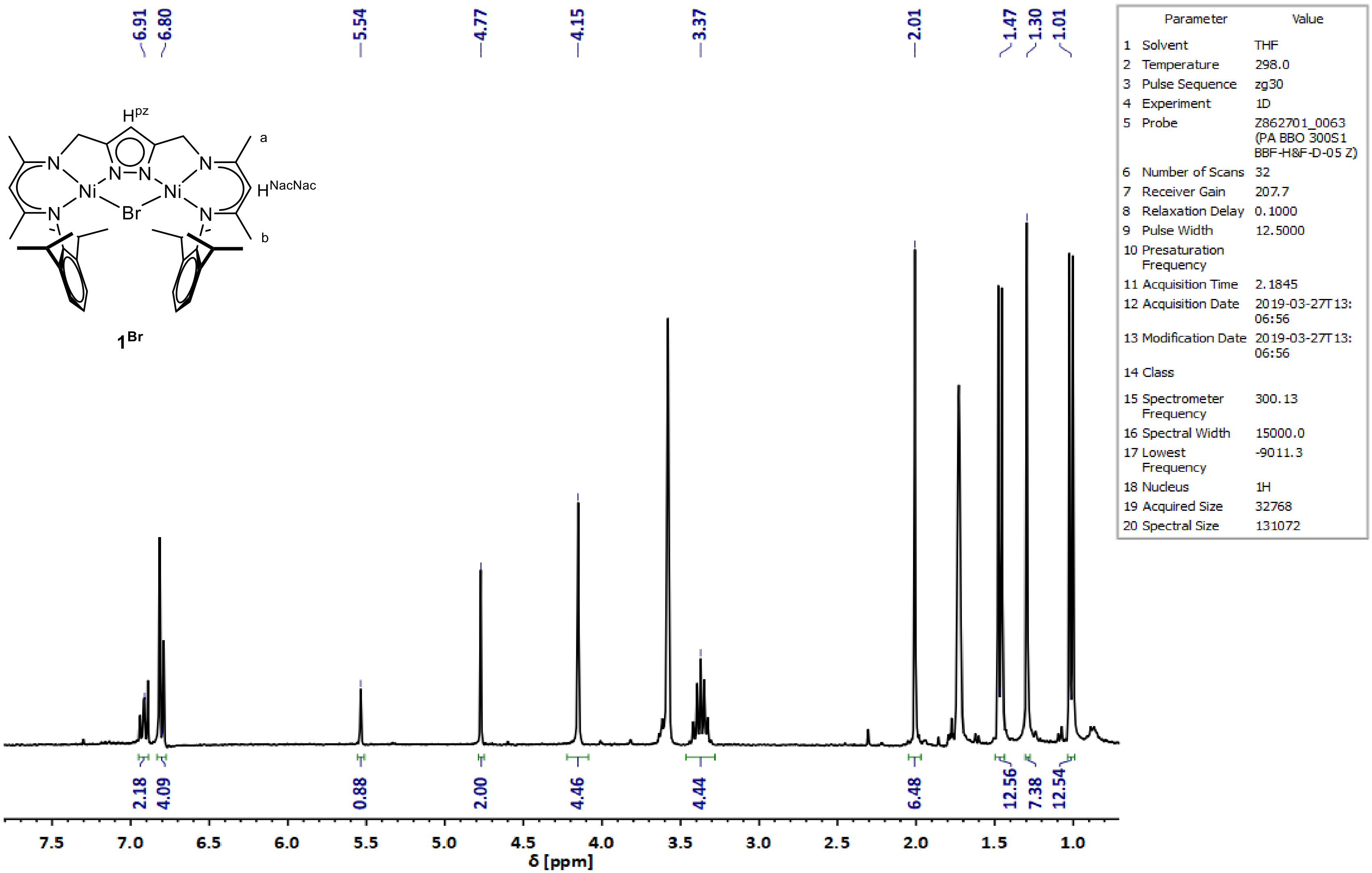

	Parameter	Value
1	Solvent	THF
2	Temperature	298.0
3	Pulse Sequence	zg30
4	Experiment	1D
5	Probe	Z862701_0063 (PA BBO 300S1 BBF-H&F-D-05 Z)
6	Number of Scans	32
7	Receiver Gain	207.7
8	Relaxation Delay	0.1000
9	Pulse Width	12.5000
10	Presaturation Frequency	
11	Acquisition Time	2.1845
12	Acquisition Date	2019-03-27T13:06:56
13	Modification Date	2019-03-27T13:06:56
14	Class	
15	Spectrometer Frequency	300.13
16	Spectral Width	15000.0
17	Lowest Frequency	-9011.3
18	Nucleus	1H
19	Acquired Size	32768
20	Spectral Size	131072

Figure S 5: ^{1}H NMR of **1**^{Br} in THF-d_8 at room temperature.

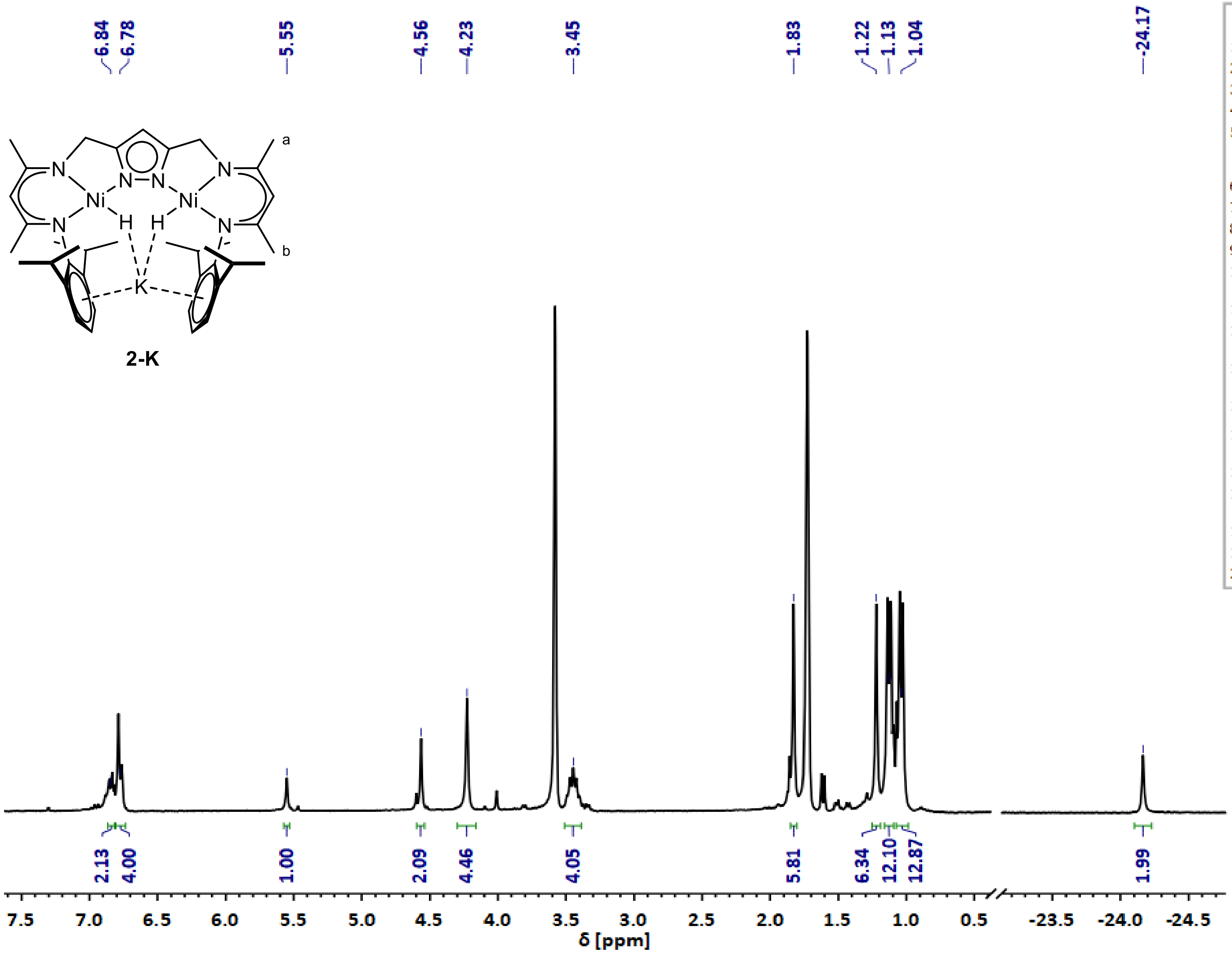

	Parameter	Value
1	Solvent	THF
2	Temperature	298.0
3	Pulse Sequence	zg30
4	Experiment	1D
5	Probe	Z862701_0063 (PA BBO 300S1 BBF-H&F-D-05 Z)
6	Number of Scans	32
7	Receiver Gain	186.8
8	Relaxation Delay	0.1000
9	Pulse Width	12.5000
10	Presaturation Frequency	
11	Acquisition Time	2.1845
12	Acquisition Date	2018-09-26T16:12:35
13	Modification Date	2018-09-26T16:12:36
14	Class	
15	Spectrometer Frequency	300.13
16	Spectral Width	15000.0
17	Lowest Frequency	-9012.0
18	Nucleus	1H
19	Acquired Size	32768
20	Spectral Size	131072

Figure S 6: ^{1}H NMR of **2-K** in THF-d_8 at room temperature.

2-K-d$_2$

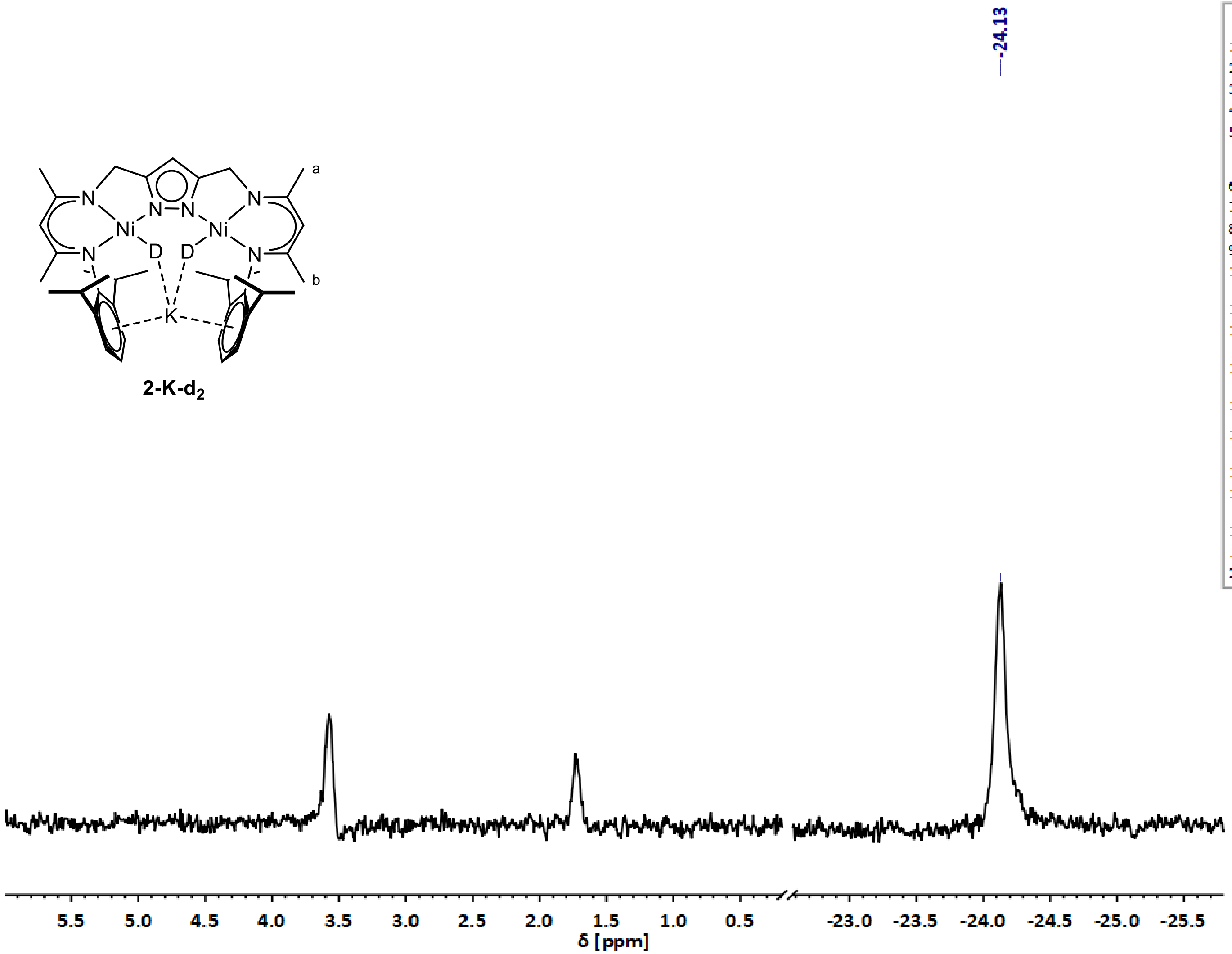

	Parameter	Value
1	Solvent	None
2	Temperature	298.0
3	Pulse Sequence	zg2h
4	Experiment	1D
5	Probe	Z104275_0147 (PA BBO 300S1 BBF-H-D-05 Z)
6	Number of Scans	4096
7	Receiver Gain	0.5
8	Relaxation Delay	0.1000
9	Pulse Width	270.0000
10	Presaturation Frequency	
11	Acquisition Time	2.2228
12	Acquisition Date	2019-10-23T22:04:18
13	Modification Date	2019-10-23T22:04:18
14	Class	
15	Spectrometer Frequency	46.07
16	Spectral Width	2303.4
17	Lowest Frequency	-1400.0
18	Nucleus	2H
19	Acquired Size	5120
20	Spectral Size	16384

Figure S 7: ^{2}H NMR of **2-K-d$_2$** in THF-d$_8$ at room temperature.

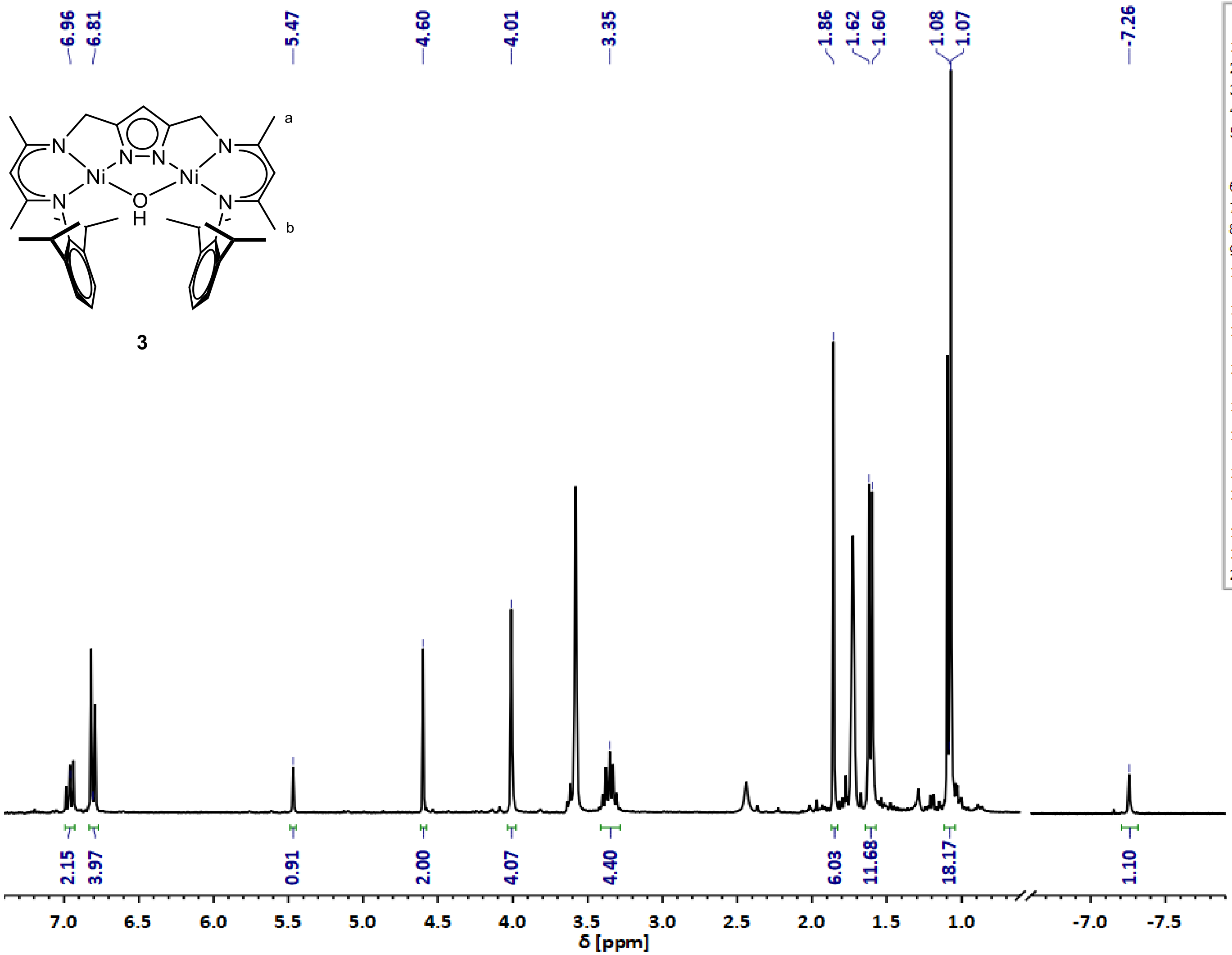

	Parameter	Value
1	Solvent	THF
2	Temperature	298.0
3	Pulse Sequence	zg30
4	Experiment	1D
5	Probe	Z862701_0063 (PA BBO 300S1 BBF-H&F-D-05 Z)
6	Number of Scans	32
7	Receiver Gain	207.7
8	Relaxation Delay	0.1000
9	Pulse Width	12.5000
10	Presaturation Frequency	
11	Acquisition Time	2.1845
12	Acquisition Date	2019-06-18T11:09:58
13	Modification Date	2019-06-18T11:09:58
14	Class	
15	Spectrometer Frequency	300.13
16	Spectral Width	15000.0
17	Lowest Frequency	-9011.4
18	Nucleus	1H
19	Acquired Size	32768
20	Spectral Size	131072

Figure S 8: ^{1}H NMR of **3** in THF-d$_8$ at room temperature.

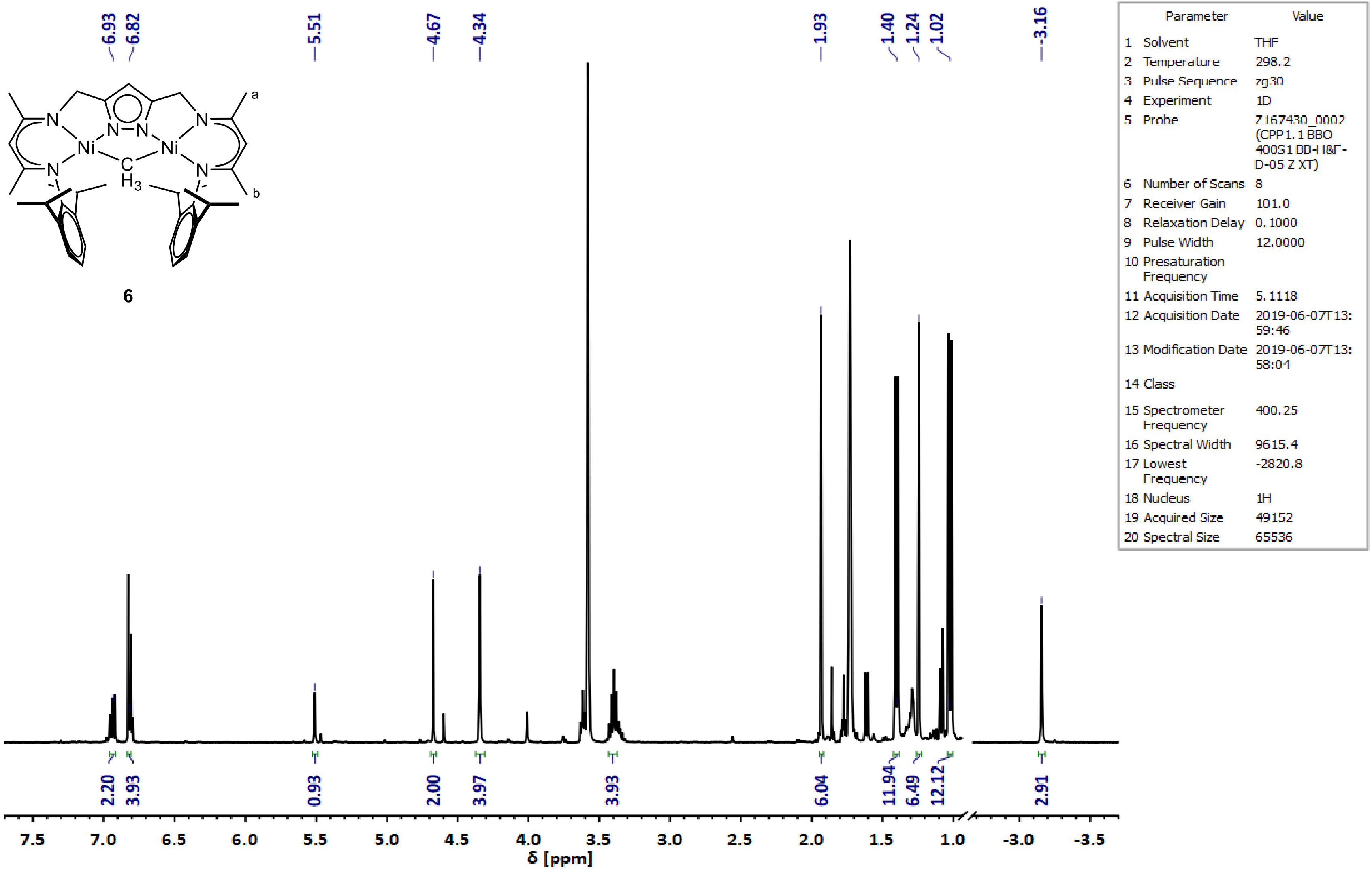

	Parameter	Value
1	Solvent	THF
2	Temperature	298.2
3	Pulse Sequence	zg30
4	Experiment	1D
5	Probe	Z167430_0002 (CPP1.1 BBO 400S1 BB-H&F-D-05 Z XT)
6	Number of Scans	8
7	Receiver Gain	101.0
8	Relaxation Delay	0.1000
9	Pulse Width	12.0000
10	Presaturation Frequency	
11	Acquisition Time	5.1118
12	Acquisition Date	2019-06-07T13:59:46
13	Modification Date	2019-06-07T13:58:04
14	Class	
15	Spectrometer Frequency	400.25
16	Spectral Width	9615.4
17	Lowest Frequency	-2820.8
18	Nucleus	1H
19	Acquired Size	49152
20	Spectral Size	65536

Figure S 9: ^{1}H NMR of **6** in THF-d_8 at room temperature.

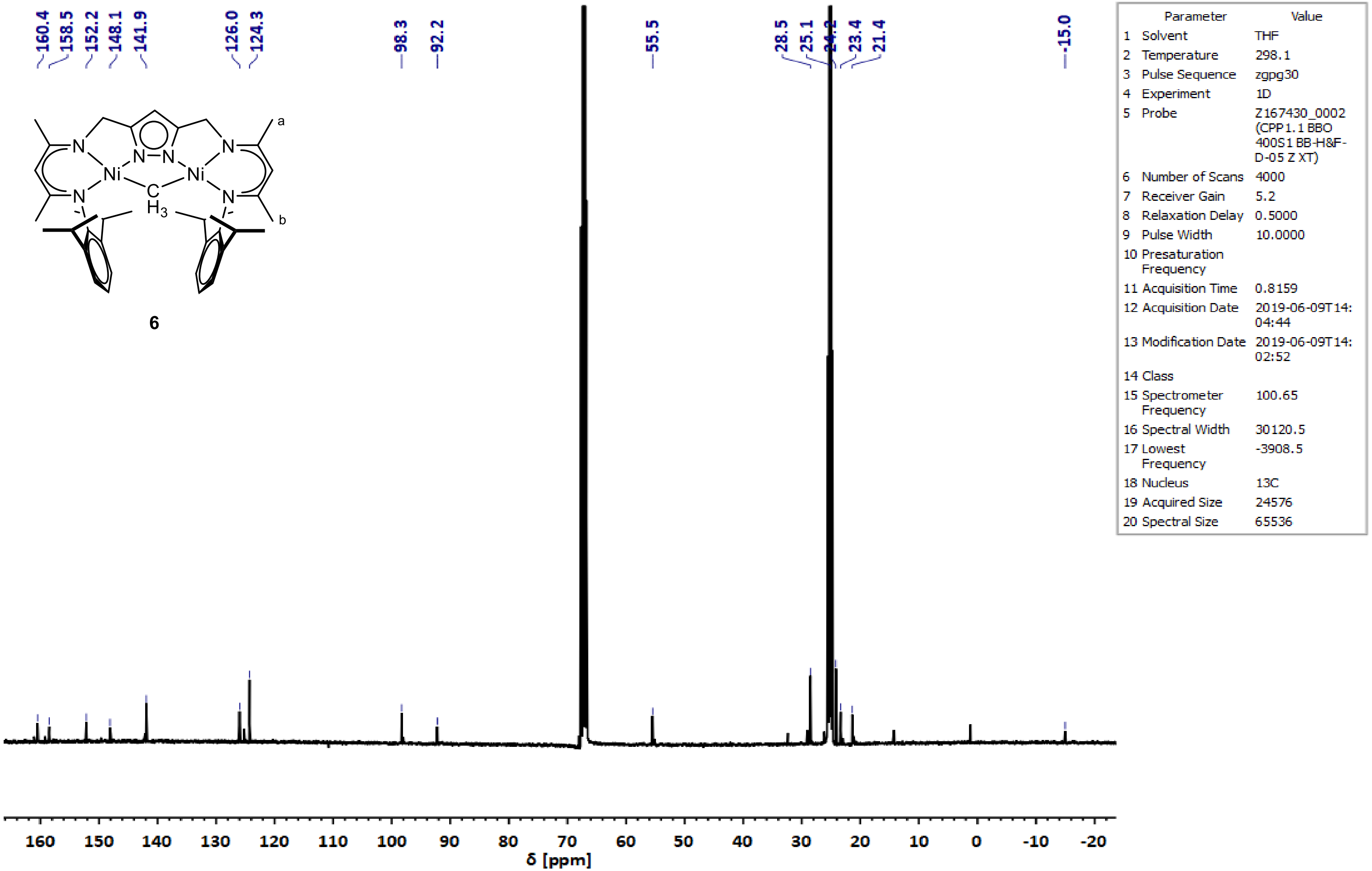

	Parameter	Value
1	Solvent	THF
2	Temperature	298.1
3	Pulse Sequence	zgpg30
4	Experiment	1D
5	Probe	Z167430_0002 (CPP1.1 BBO 400S1 BB-H&F-D-05 Z XT)
6	Number of Scans	4000
7	Receiver Gain	5.2
8	Relaxation Delay	0.5000
9	Pulse Width	10.0000
10	Presaturation Frequency	
11	Acquisition Time	0.8159
12	Acquisition Date	2019-06-09T14:04:44
13	Modification Date	2019-06-09T14:02:52
14	Class	
15	Spectrometer Frequency	100.65
16	Spectral Width	30120.5
17	Lowest Frequency	-3908.5
18	Nucleus	13C
19	Acquired Size	24576
20	Spectral Size	65536

Figure S 10: ^{13}C NMR of **6** in THF-d_8 at room temperature.

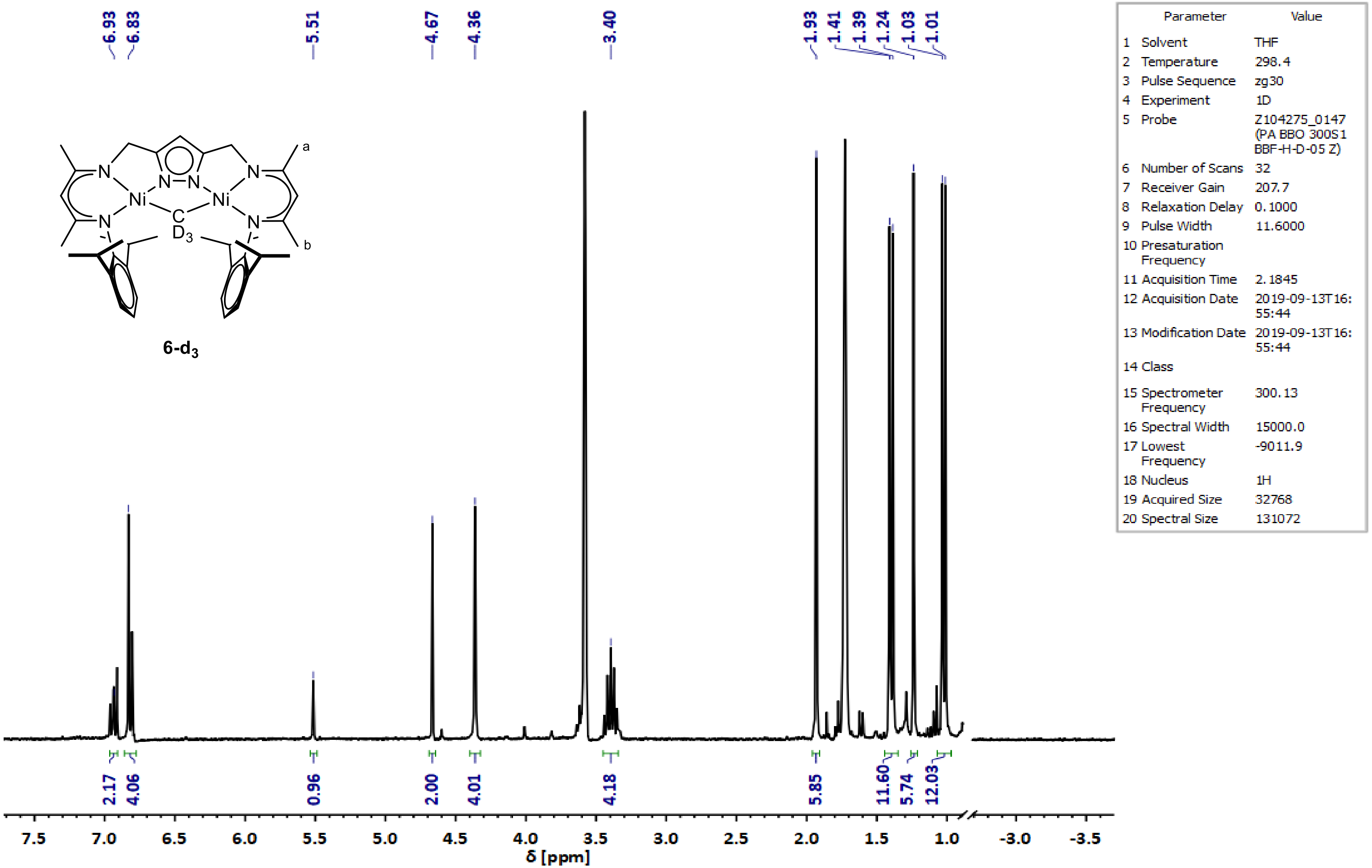

	Parameter	Value
1	Solvent	THF
2	Temperature	298.4
3	Pulse Sequence	zg30
4	Experiment	1D
5	Probe	Z104275_0147 (PA BBO 300S1 BBF-H-D-05 Z)
6	Number of Scans	32
7	Receiver Gain	207.7
8	Relaxation Delay	0.1000
9	Pulse Width	11.6000
10	Presaturation Frequency	
11	Acquisition Time	2.1845
12	Acquisition Date	2019-09-13T16:55:44
13	Modification Date	2019-09-13T16:55:44
14	Class	
15	Spectrometer Frequency	300.13
16	Spectral Width	15000.0
17	Lowest Frequency	-9011.9
18	Nucleus	1H
19	Acquired Size	32768
20	Spectral Size	131072

Figure S 11: ^{1}H NMR of **6-d$_3$** in THF-d$_8$ at room temperature.

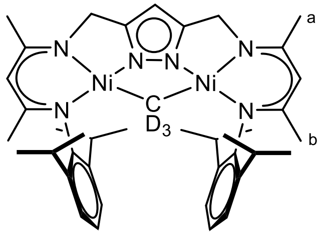

6-d$_3$

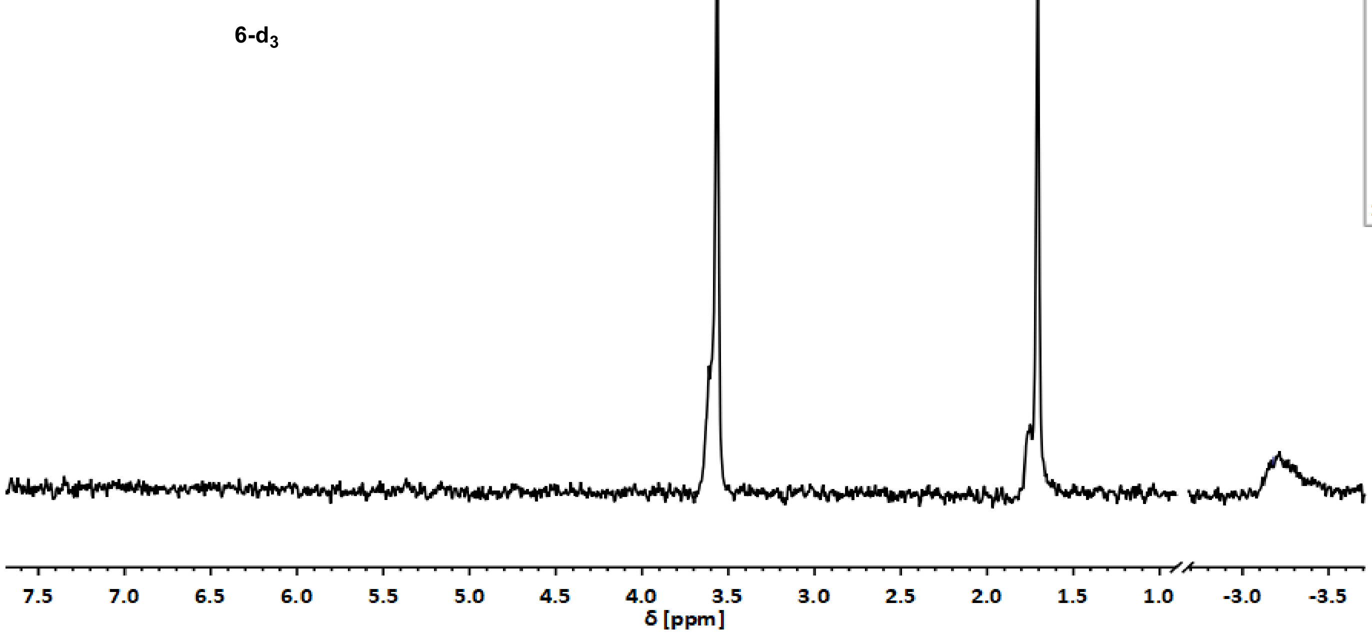

	Parameter	Value
1	Solvent	None
2	Temperature	299.7
3	Pulse Sequence	zg2h
4	Experiment	1D
5	Probe	Z862701_0063 (PA BBO 300S1 BBF-H&F-D-05 Z)
6	Number of Scans	4096
7	Receiver Gain	0.5
8	Relaxation Delay	0.1000
9	Pulse Width	282.5000
10	Presaturation Frequency	
11	Acquisition Time	3.7048
12	Acquisition Date	2019-08-24T23:57:44
13	Modification Date	2019-08-24T23:57:44
14	Class	
15	Spectrometer Frequency	46.07
16	Spectral Width	1382.0
17	Lowest Frequency	-462.0
18	Nucleus	2H
19	Acquired Size	5120
20	Spectral Size	16384

Figure S 12: ^{2}H NMR of **6-d$_3$** in THF-d$_8$ at room temperature.

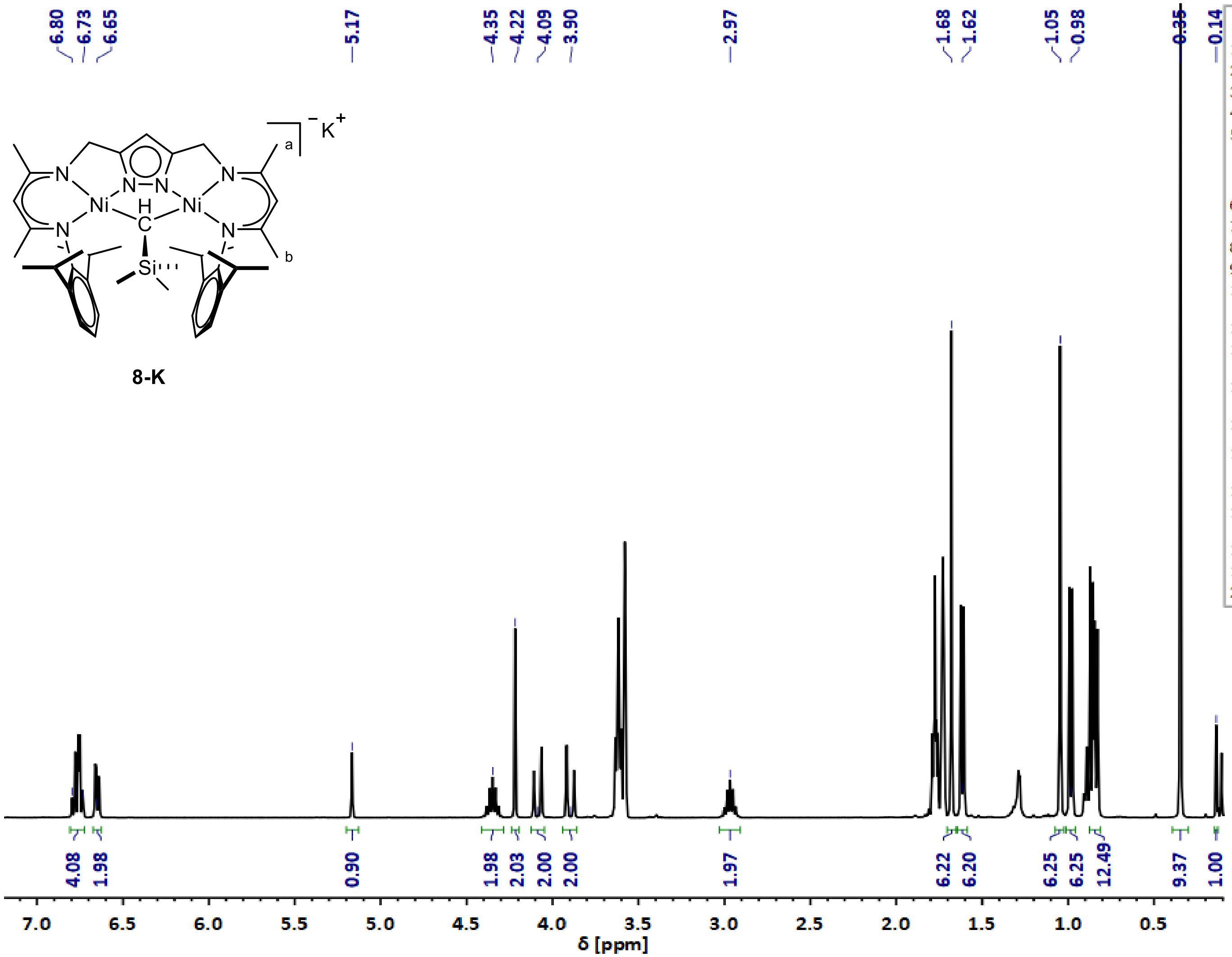

	Parameter	Value
1	Solvent	THF
2	Temperature	298.2
3	Pulse Sequence	zg30
4	Experiment	1D
5	Probe	Z167430_0002 (CPP1.1 BBO 400S1 BB-H&F-D-05 Z XT)
6	Number of Scans	32
7	Receiver Gain	101.0
8	Relaxation Delay	0.1000
9	Pulse Width	12.0000
10	Presaturation Frequency	
11	Acquisition Time	5.1118
12	Acquisition Date	2019-07-03T19:33:20
13	Modification Date	2019-07-03T19:33:14
14	Class	
15	Spectrometer Frequency	400.25
16	Spectral Width	9615.4
17	Lowest Frequency	-2820.7
18	Nucleus	1H
19	Acquired Size	49152
20	Spectral Size	65536

Figure S 13: ^{1}H NMR of **8-K** in THF-d_8 at room temperature.

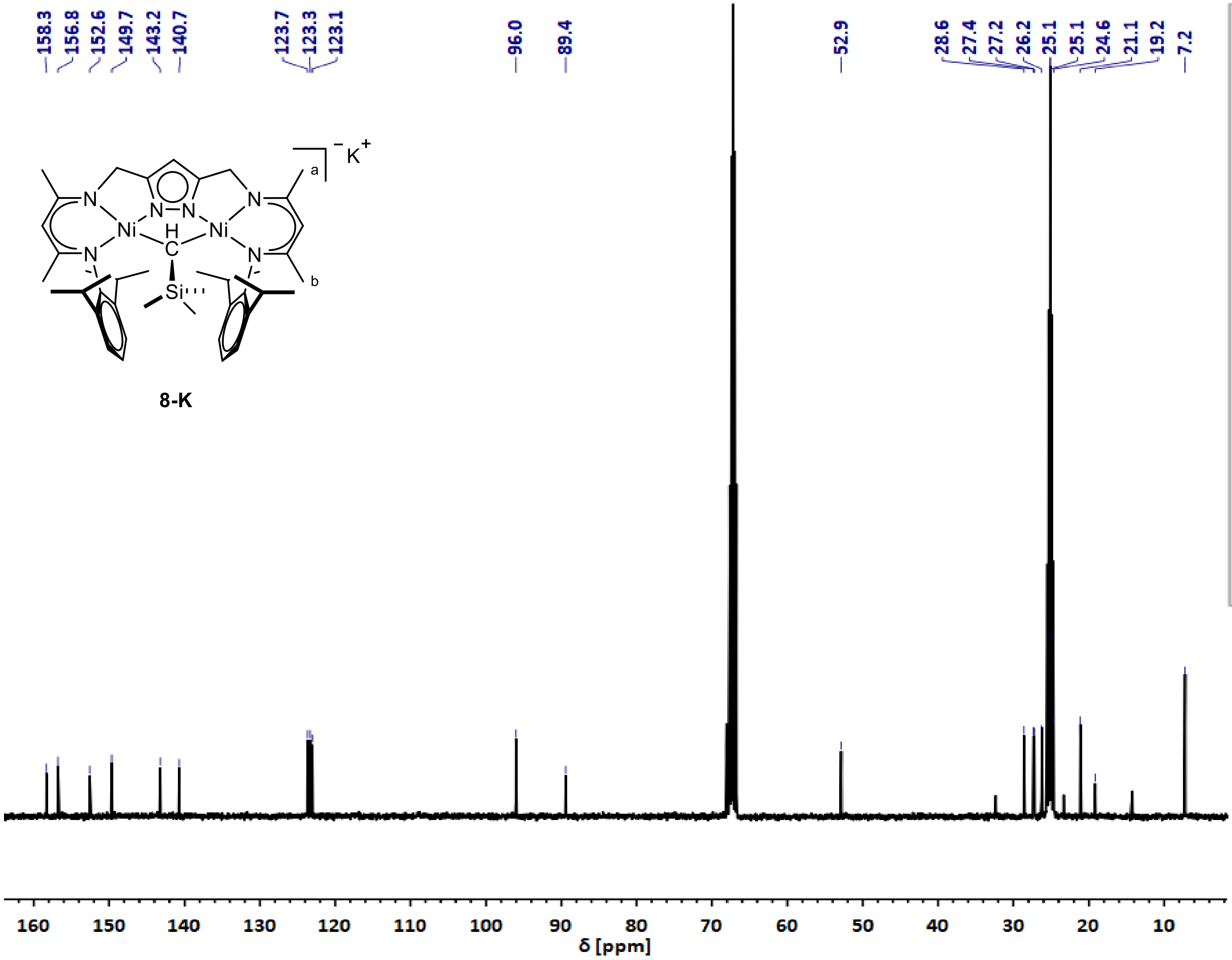

	Parameter	Value
1	Solvent	THF
2	Temperature	298.2
3	Pulse Sequence	zgpg30
4	Experiment	1D
5	Probe	Z167430_0002 (CPP1.1 BBO 400S1 BB-H&F-D-05 Z XT)
6	Number of Scans	512
7	Receiver Gain	5.2
8	Relaxation Delay	0.5000
9	Pulse Width	10.0000
10	Presaturation Frequency	
11	Acquisition Time	1.0322
12	Acquisition Date	2019-07-03T20:10:30
13	Modification Date	2019-07-03T20:10:23
14	Class	
15	Spectrometer Frequency	100.65
16	Spectral Width	23809.5
17	Lowest Frequency	-753.9
18	Nucleus	13C
19	Acquired Size	24576
20	Spectral Size	65536

Figure S 14: ^{13}C NMR of **8-K** in THF-d_8 at room temperature.

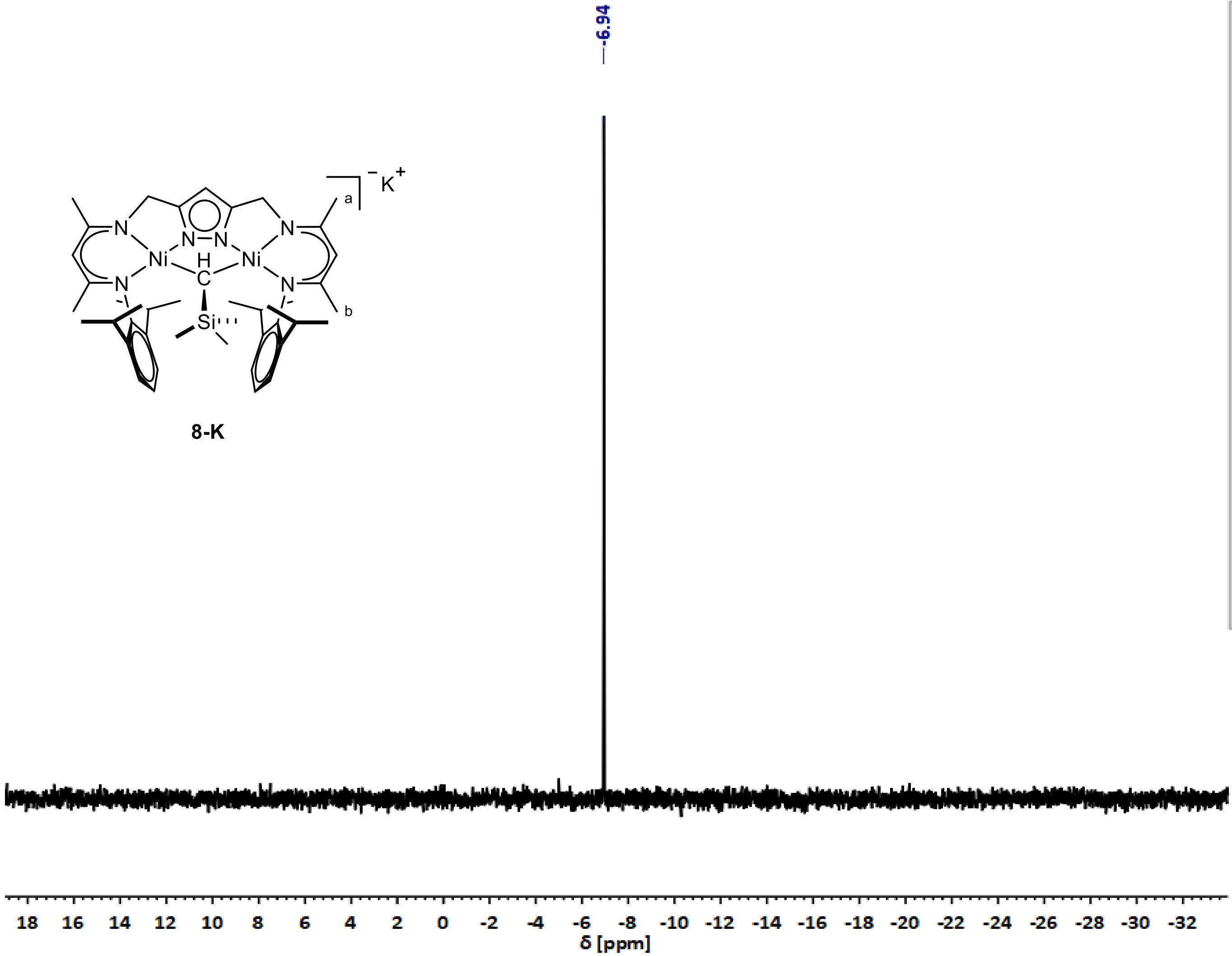

8-K

	Parameter	Value
1	Solvent	C6D6
2	Temperature	298.0
3	Pulse Sequence	ineptrdsp
4	Experiment	1D
5	Probe	5 mm CPPBBO BB-1H/ 19F/ D Z-GRD Z130036/ 0004
6	Number of Scans	143
7	Receiver Gain	184.0
8	Relaxation Delay	1.5000
9	Pulse Width	11.3000
10	Presaturation Frequency	
11	Acquisition Time	2.0622
12	Acquisition Date	2019-11-04T13:58:00
13	Modification Date	2019-11-04T14:07:14
14	Class	
15	Spectrometer Frequency	99.39
16	Spectral Width	7944.9
17	Lowest Frequency	-4469.4
18	Nucleus	29Si
19	Acquired Size	16384
20	Spectral Size	32768

Figure S 15: ^{29}Si NMR of **8-K** in C_6D_6 at room temperature.

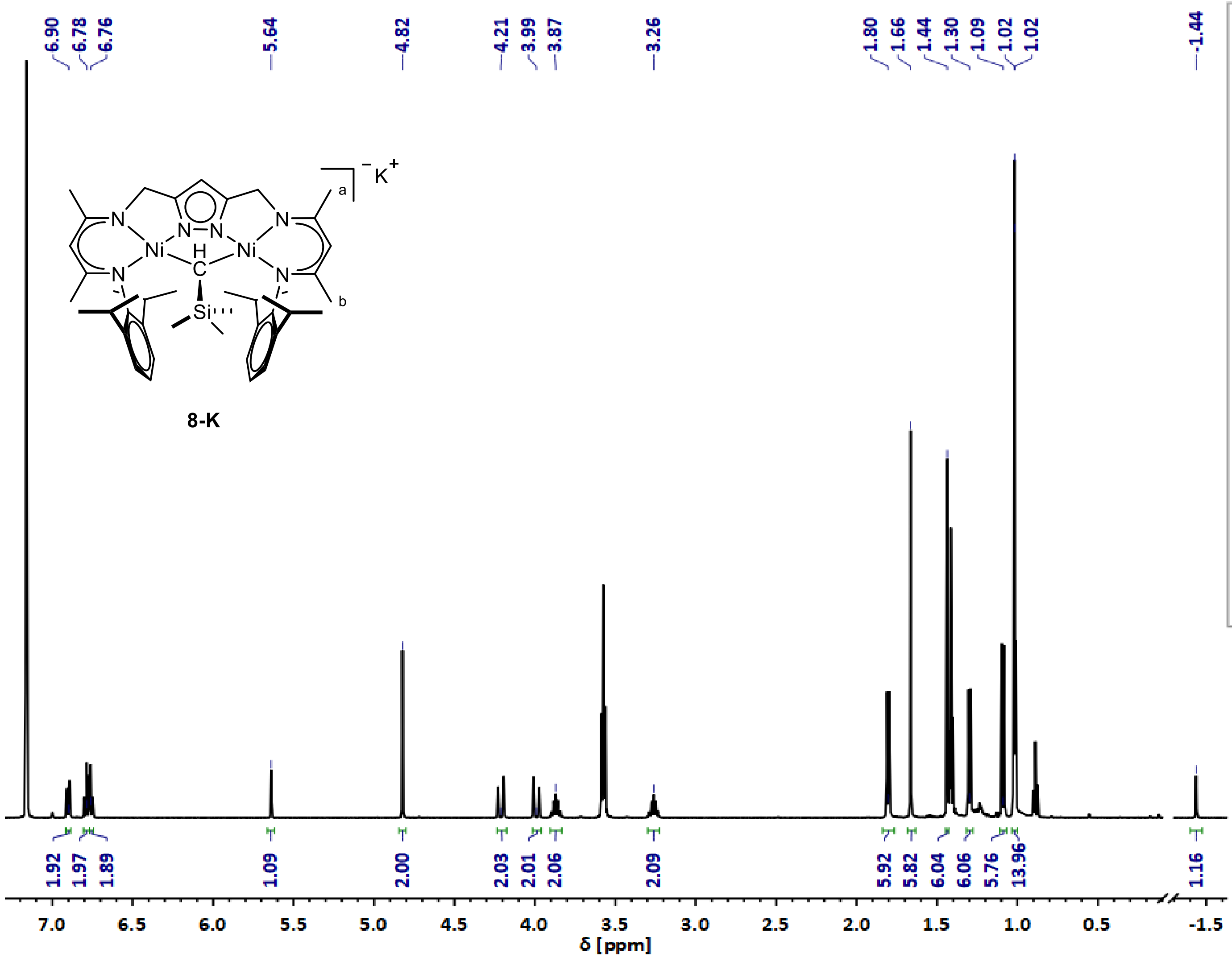

	Parameter	Value
1	Solvent	C6D6
2	Temperature	298.0
3	Pulse Sequence	zg0
4	Experiment	1D
5	Probe	5 mm CPPBBO BB-1H/ 19F/ D Z-GRD Z130036/ 0004
6	Number of Scans	32
7	Receiver Gain	92.8
8	Relaxation Delay	0.1000
9	Pulse Width	11.0000
10	Presaturation Frequency	
11	Acquisition Time	5.0332
12	Acquisition Date	2019-11-04T11:21:07
13	Modification Date	2019-11-04T11:23:47
14	Class	
15	Spectrometer Frequency	500.25
16	Spectral Width	13020.8
17	Lowest Frequency	-3500.1
18	Nucleus	1H
19	Acquired Size	65536
20	Spectral Size	131072

Figure S 16: ^{1}H NMR of **8-K** in C_6D_6 at room temperature.

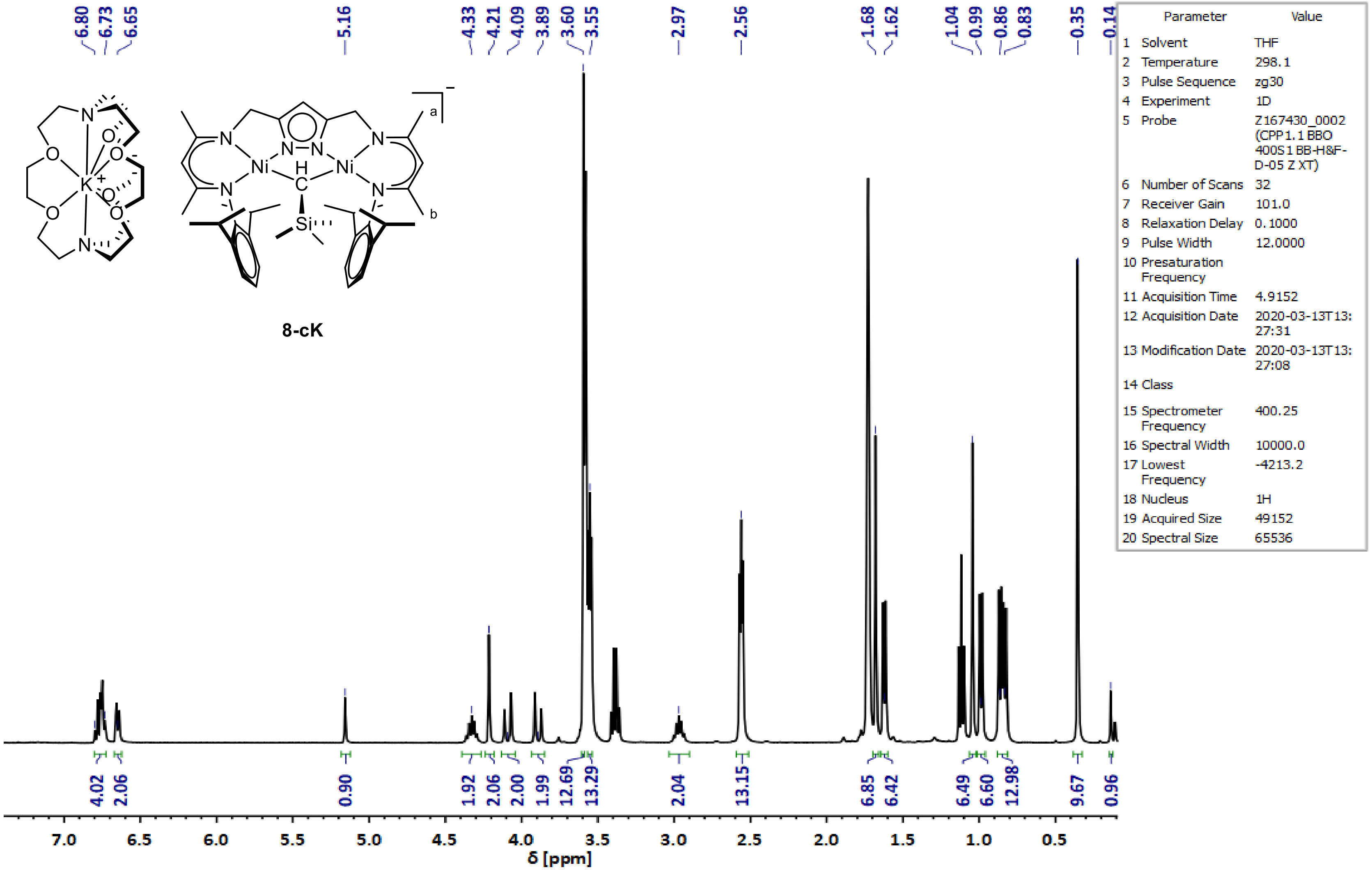

	Parameter	Value
1	Solvent	THF
2	Temperature	298.1
3	Pulse Sequence	zg30
4	Experiment	1D
5	Probe	Z167430_0002 (CPP1.1 BBO 400S1 BB-H&F-D-05 Z XT)
6	Number of Scans	32
7	Receiver Gain	101.0
8	Relaxation Delay	0.1000
9	Pulse Width	12.0000
10	Presaturation Frequency	
11	Acquisition Time	4.9152
12	Acquisition Date	2020-03-13T13:27:31
13	Modification Date	2020-03-13T13:27:08
14	Class	
15	Spectrometer Frequency	400.25
16	Spectral Width	10000.0
17	Lowest Frequency	-4213.2
18	Nucleus	1H
19	Acquired Size	49152
20	Spectral Size	65536

Figure S 17: ^{1}H NMR of **8-cK** in THF-d_8 at room temperature.

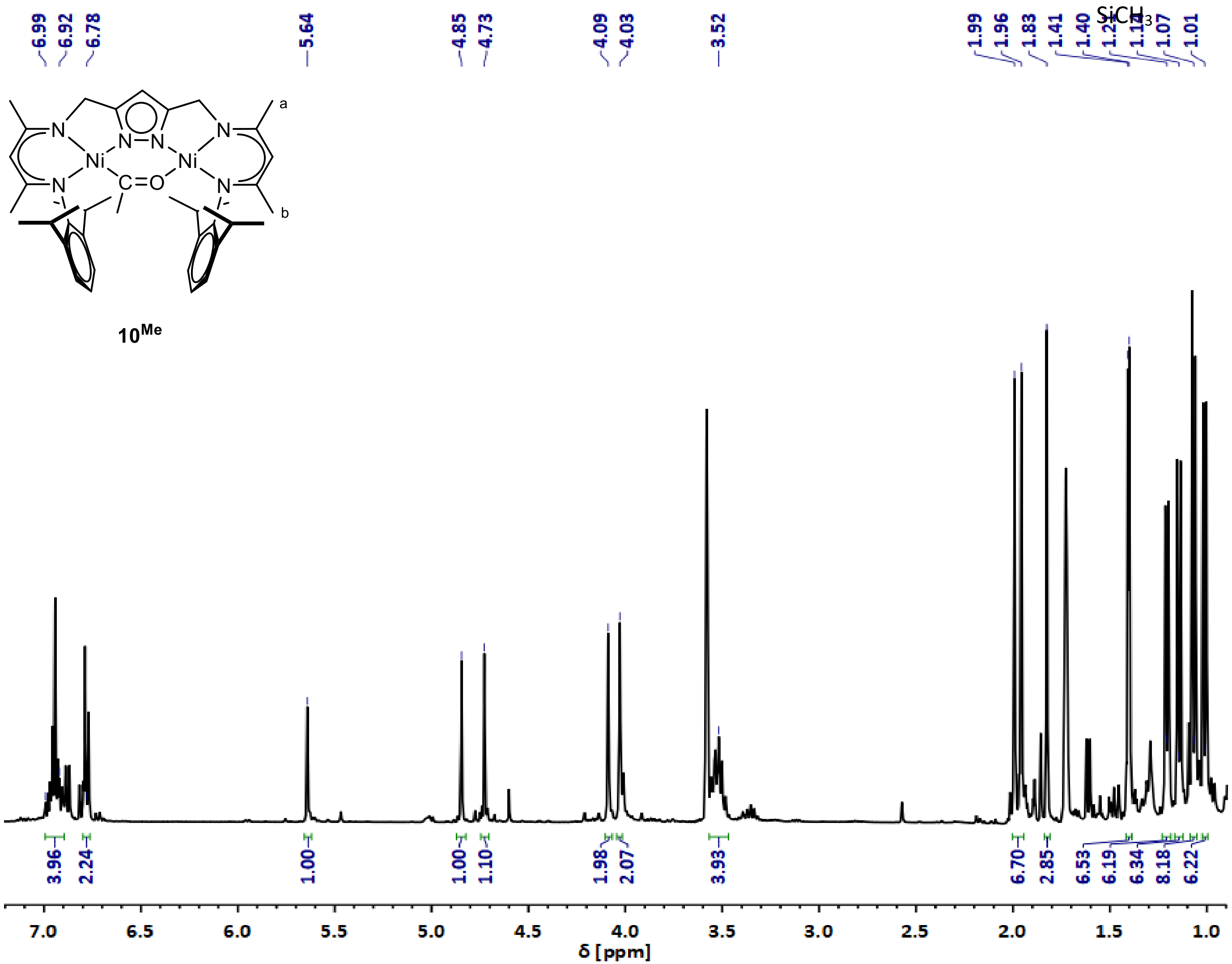

	Parameter	Value
1	Solvent	THF
2	Temperature	298.2
3	Pulse Sequence	zg30
4	Experiment	1D
5	Probe	Z167430_0002 (CPP1.1 BBO 400S1 BB-H&F-D-05 Z XT)
6	Number of Scans	64
7	Receiver Gain	101.0
8	Relaxation Delay	0.1000
9	Pulse Width	12.0000
10	Presaturation Frequency	
11	Acquisition Time	4.1288
12	Acquisition Date	2019-12-01T17:32:42
13	Modification Date	2019-12-01T17:32:28
14	Class	
15	Spectrometer Frequency	400.25
16	Spectral Width	11904.8
17	Lowest Frequency	-7969.0
18	Nucleus	1H
19	Acquired Size	49152
20	Spectral Size	131072

Figure S 18: ^{1}H NMR of **10^{Me}** in THF-d$_8$ at room temperature.

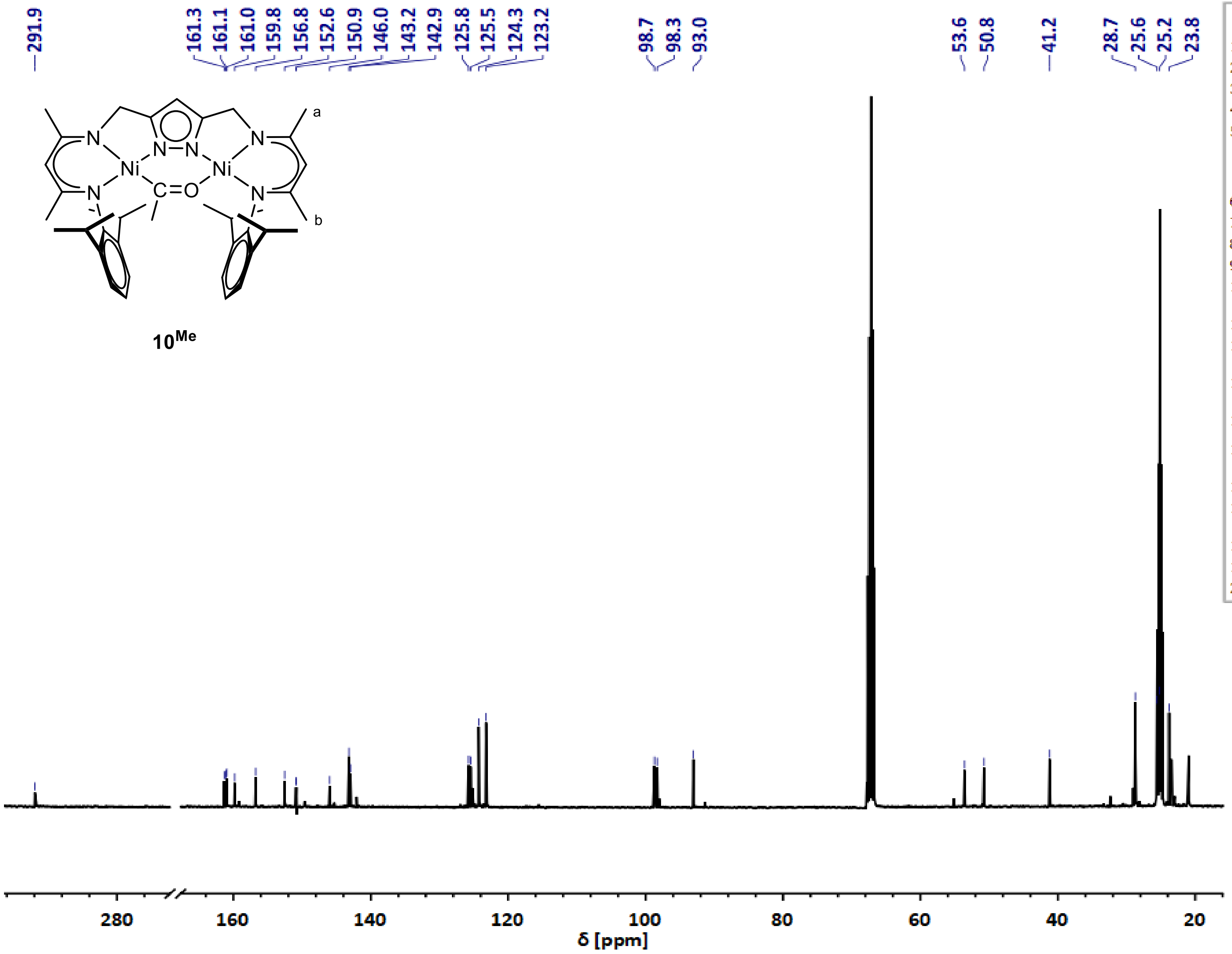

	Parameter	Value
1	Solvent	THF
2	Temperature	298.2
3	Pulse Sequence	zgpg30
4	Experiment	1D
5	Probe	Z167430_0002 (CPP1.1 BBO 400S1 BB-H&F-D-05 Z XT)
6	Number of Scans	4096
7	Receiver Gain	5.2
8	Relaxation Delay	0.5000
9	Pulse Width	10.0000
10	Presaturation Frequency	
11	Acquisition Time	0.8159
12	Acquisition Date	2019-12-01T19:35:47
13	Modification Date	2019-12-01T19:35:33
14	Class	
15	Spectrometer Frequency	100.66
16	Spectral Width	30120.5
17	Lowest Frequency	116.5
18	Nucleus	13C
19	Acquired Size	24576
20	Spectral Size	65536

Figure S 19: ^{13}C NMR of **10^{Me}** in THF-d$_8$ at room temperature.

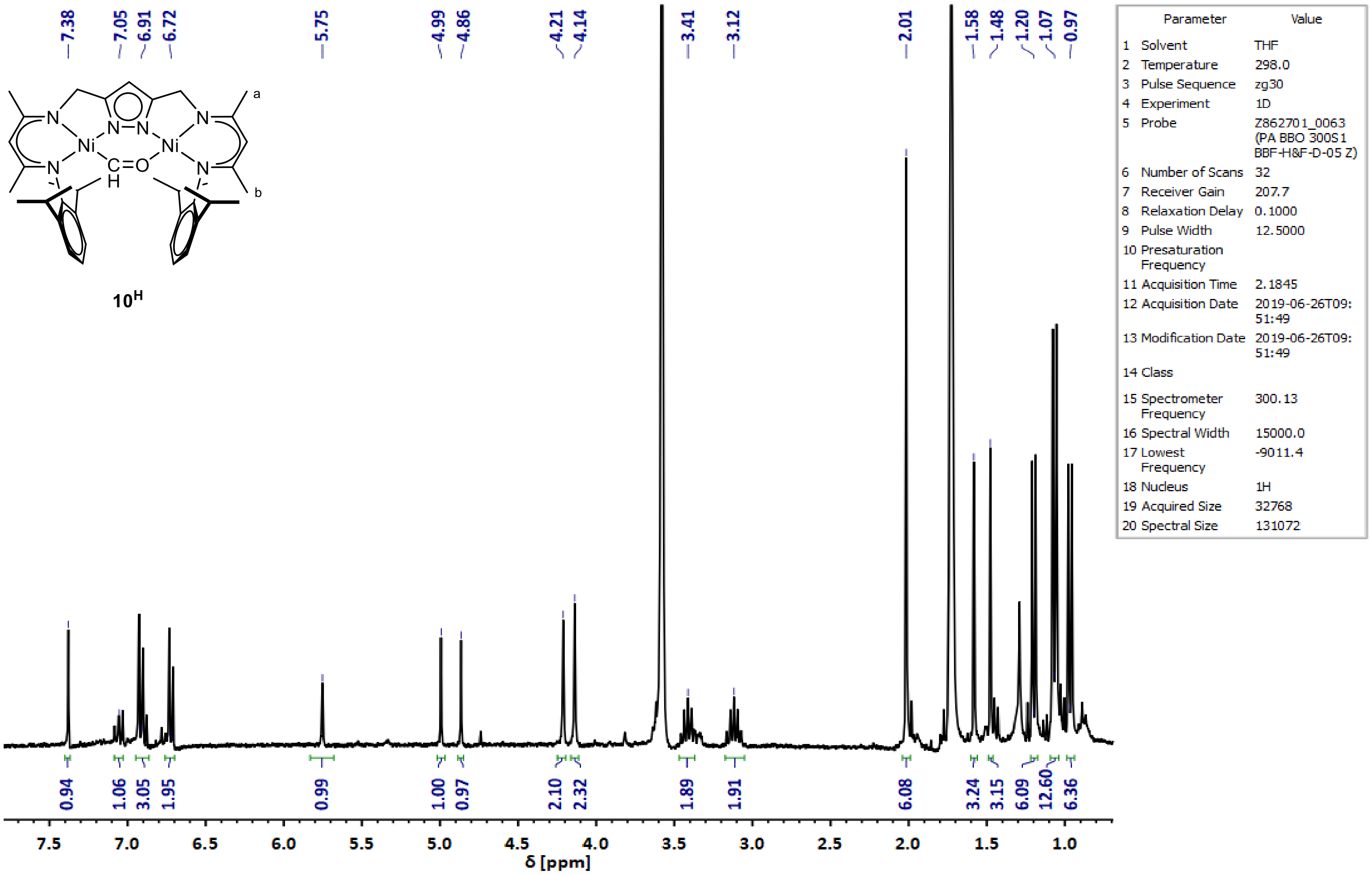

	Parameter	Value
1	Solvent	THF
2	Temperature	298.0
3	Pulse Sequence	zg30
4	Experiment	1D
5	Probe	Z862701_0063 (PA BBO 300S1 BBF-H&F-D-05 Z)
6	Number of Scans	32
7	Receiver Gain	207.7
8	Relaxation Delay	0.1000
9	Pulse Width	12.5000
10	Presaturation Frequency	
11	Acquisition Time	2.1845
12	Acquisition Date	2019-06-26T09:51:49
13	Modification Date	2019-06-26T09:51:49
14	Class	
15	Spectrometer Frequency	300.13
16	Spectral Width	15000.0
17	Lowest Frequency	-9011.4
18	Nucleus	1H
19	Acquired Size	32768
20	Spectral Size	131072

Figure S 20: ^{1}H NMR of **10^H** in THF-d_8 at room temperature.

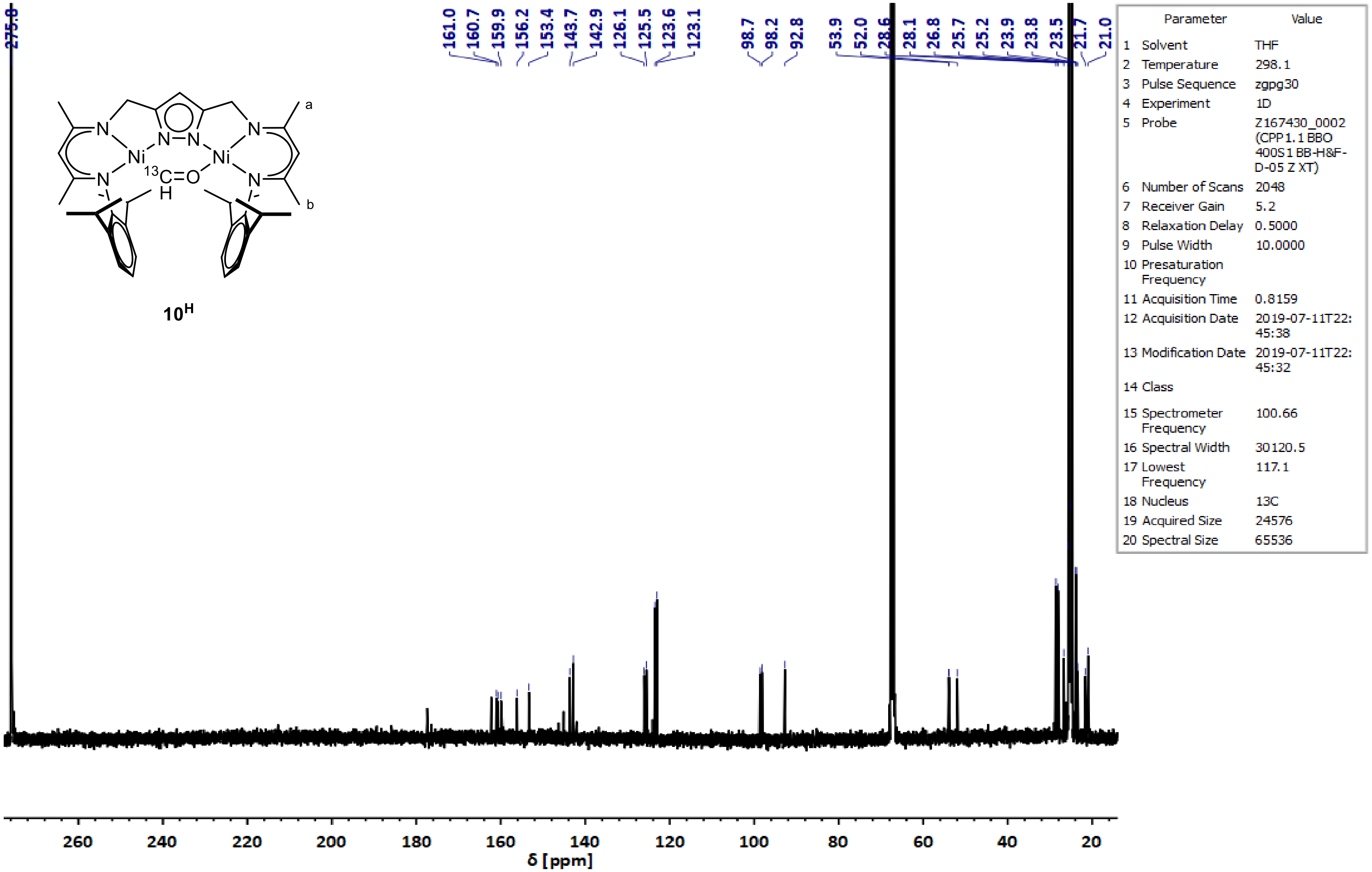

	Parameter	Value
1	Solvent	THF
2	Temperature	298.1
3	Pulse Sequence	zgpg30
4	Experiment	1D
5	Probe	Z167430_0002 (CPP1.1 BBO 400S1 BB-H&F-D-05 Z XT)
6	Number of Scans	2048
7	Receiver Gain	5.2
8	Relaxation Delay	0.5000
9	Pulse Width	10.0000
10	Presaturation Frequency	
11	Acquisition Time	0.8159
12	Acquisition Date	2019-07-11T22:45:38
13	Modification Date	2019-07-11T22:45:32
14	Class	
15	Spectrometer Frequency	100.66
16	Spectral Width	30120.5
17	Lowest Frequency	117.1
18	Nucleus	13C
19	Acquired Size	24576
20	Spectral Size	65536

Figure S 21: ^{13}C NMR of **10^{Me}** in THF-d$_8$ at room temperature.

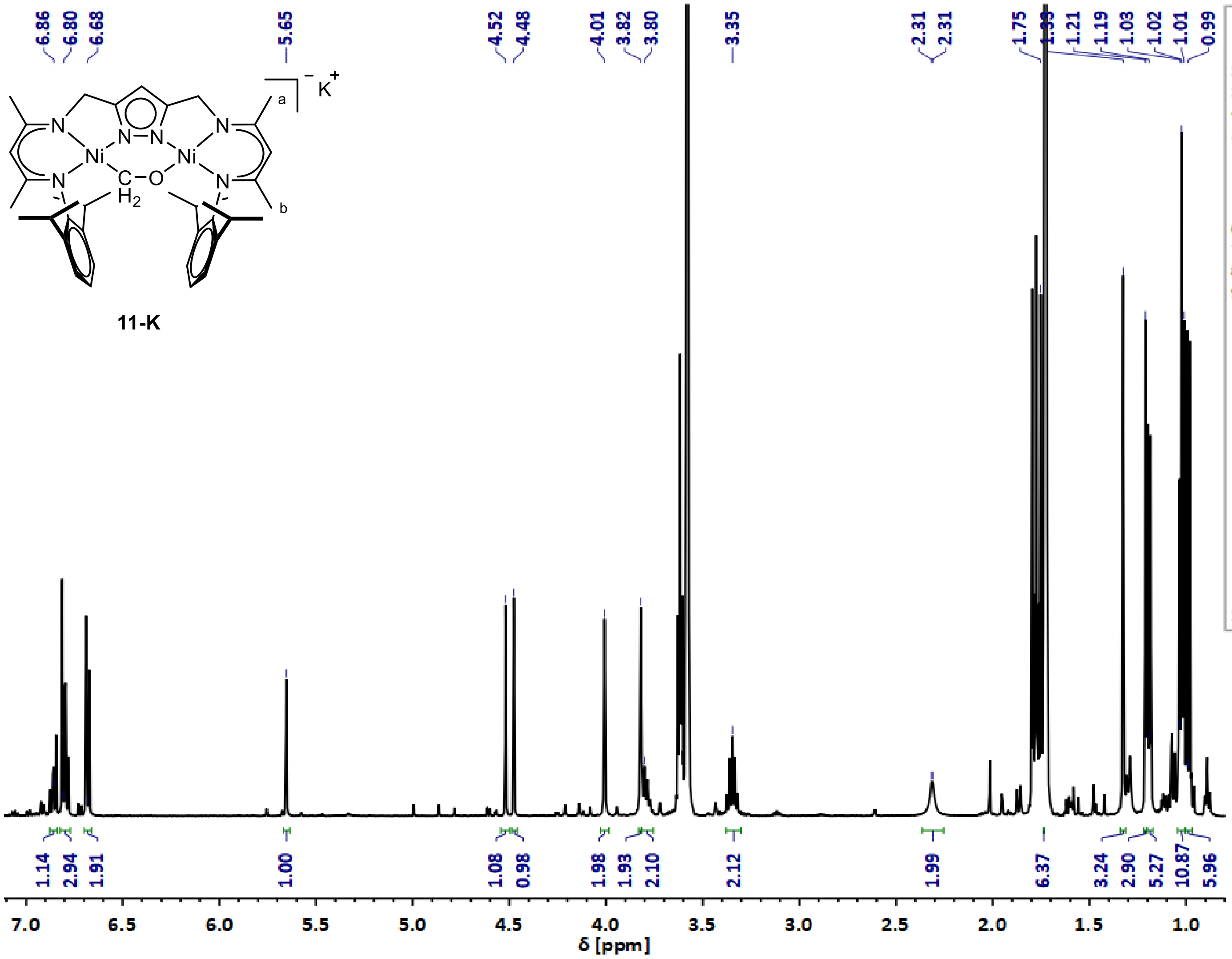

	Parameter	Value
1	Solvent	THF
2	Temperature	298.0
3	Pulse Sequence	zg0
4	Experiment	1D
5	Probe	5 mm CPPBBO BB-1H/ 19F/ D Z-GRD Z130036/ 0004
6	Number of Scans	32
7	Receiver Gain	68.3
8	Relaxation Delay	0.1000
9	Pulse Width	11.0000
10	Presaturation Frequency	
11	Acquisition Time	5.0332
12	Acquisition Date	2019-10-18T09:31:00
13	Modification Date	2019-10-18T09:34:34
14	Class	
15	Spectrometer Frequency	500.25
16	Spectral Width	13020.8
17	Lowest Frequency	-3527.1
18	Nucleus	1H
19	Acquired Size	65536
20	Spectral Size	131072

Figure S 22: ^{1}H NMR of **11-K** in THF-d_8 at room temperature.

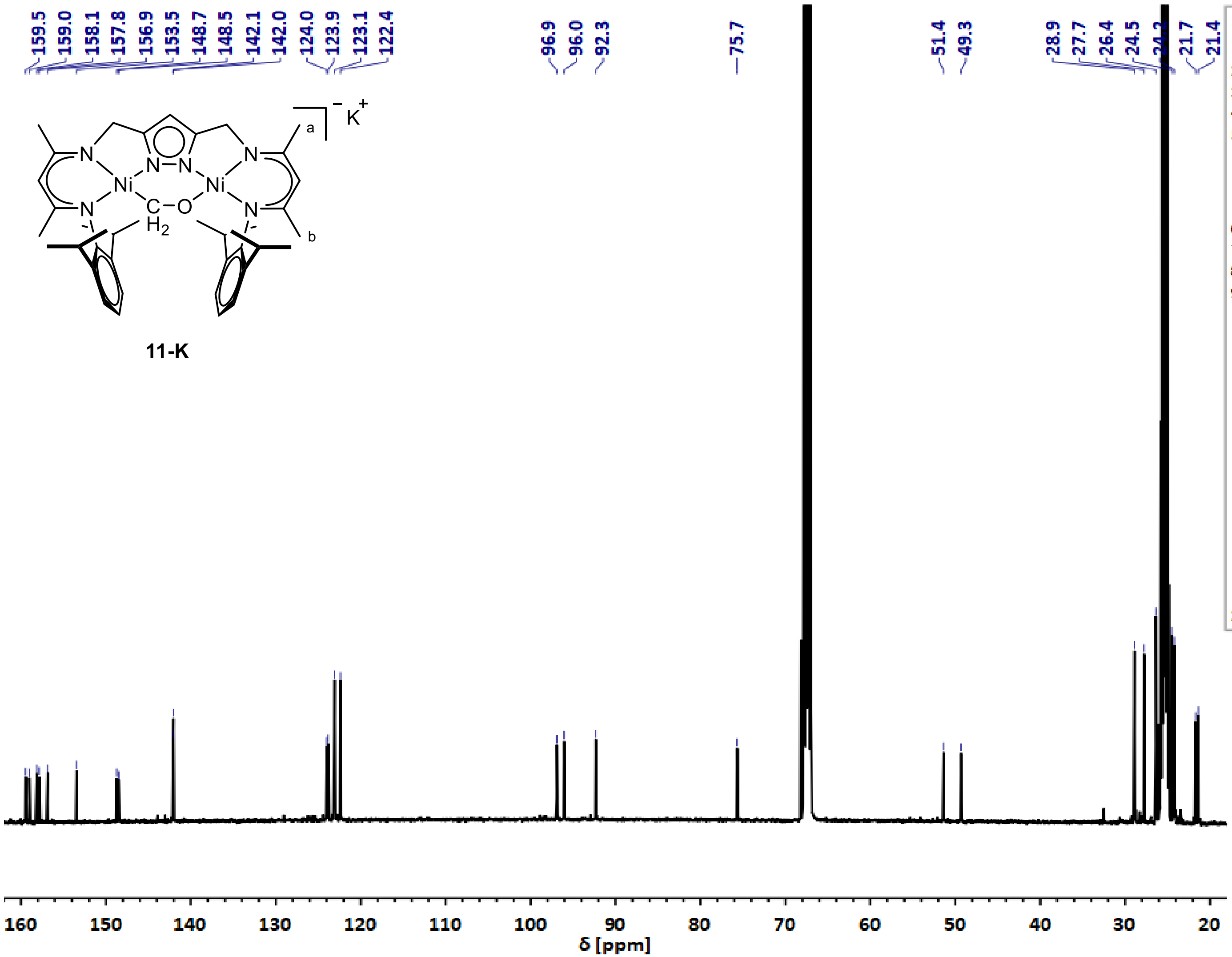

	Parameter	Value
1	Solvent	THF
2	Temperature	298.0
3	Pulse Sequence	zgpg30
4	Experiment	1D
5	Probe	5 mm CPPBBO BB-1H/ 19F/ D Z-GRD Z130036/ 0004
6	Number of Scans	24576
7	Receiver Gain	184.0
8	Relaxation Delay	0.5000
9	Pulse Width	9.8000
10	Presaturation Frequency	
11	Acquisition Time	0.9961
12	Acquisition Date	2019-10-19T03:20:00
13	Modification Date	2019-10-19T13:32:38
14	Class	
15	Spectrometer Frequency	125.80
16	Spectral Width	32894.7
17	Lowest Frequency	-3747.0
18	Nucleus	13C
19	Acquired Size	32768
20	Spectral Size	65536

Figure S 23: ^{13}C NMR of **10**$^{\mathbf{Me}}$ in THF-d_8 at room temperature.

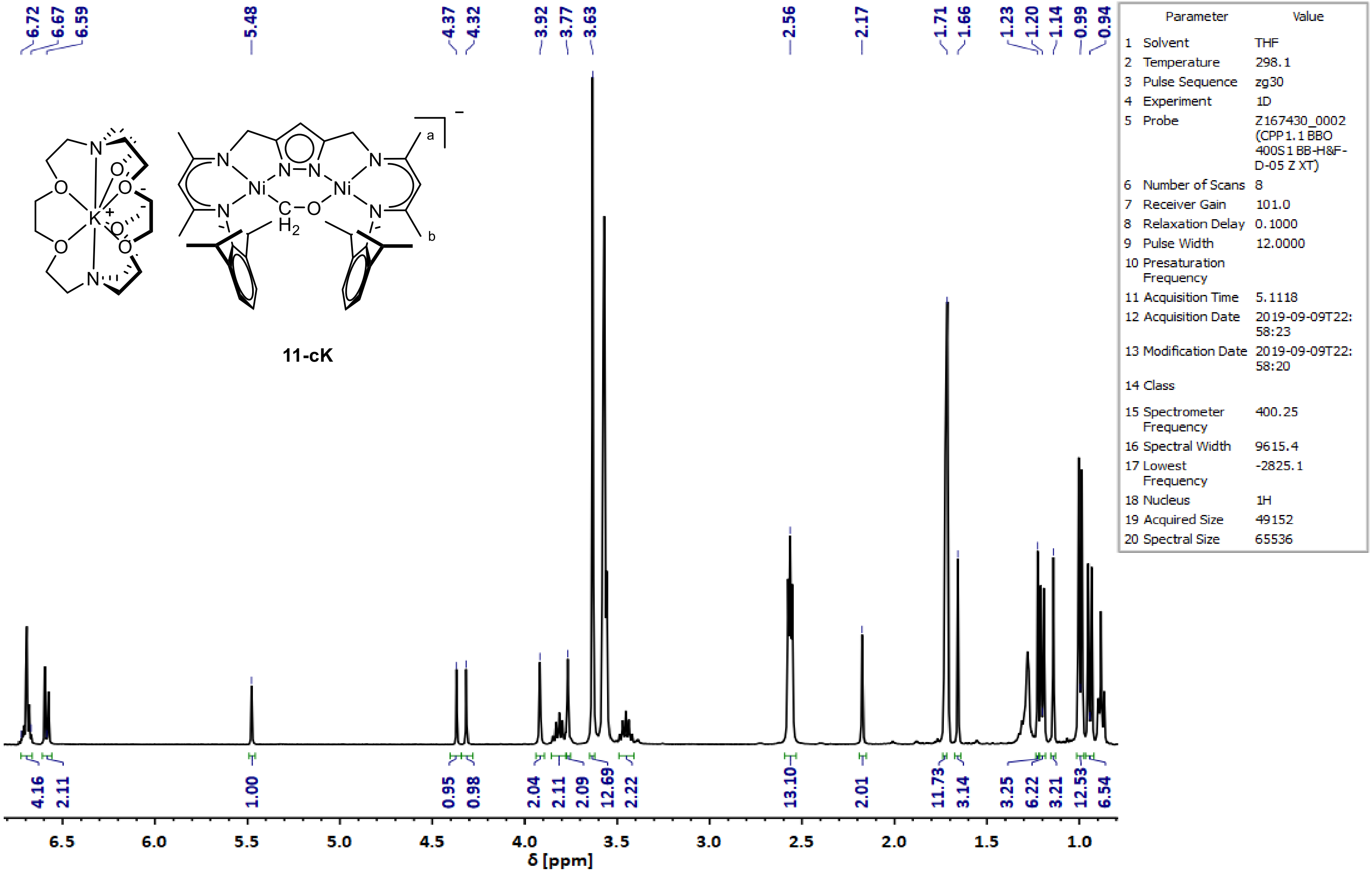

	Parameter	Value
1	Solvent	THF
2	Temperature	298.1
3	Pulse Sequence	zg30
4	Experiment	1D
5	Probe	Z167430_0002 (CPP1.1 BBO 400S1 BB-H&F-D-05 Z XT)
6	Number of Scans	8
7	Receiver Gain	101.0
8	Relaxation Delay	0.1000
9	Pulse Width	12.0000
10	Presaturation Frequency	
11	Acquisition Time	5.1118
12	Acquisition Date	2019-09-09T22:58:23
13	Modification Date	2019-09-09T22:58:20
14	Class	
15	Spectrometer Frequency	400.25
16	Spectral Width	9615.4
17	Lowest Frequency	-2825.1
18	Nucleus	1H
19	Acquired Size	49152
20	Spectral Size	65536

Figure S 24: ^{1}H NMR of **11-cK** in THF-d_8 at room temperature.

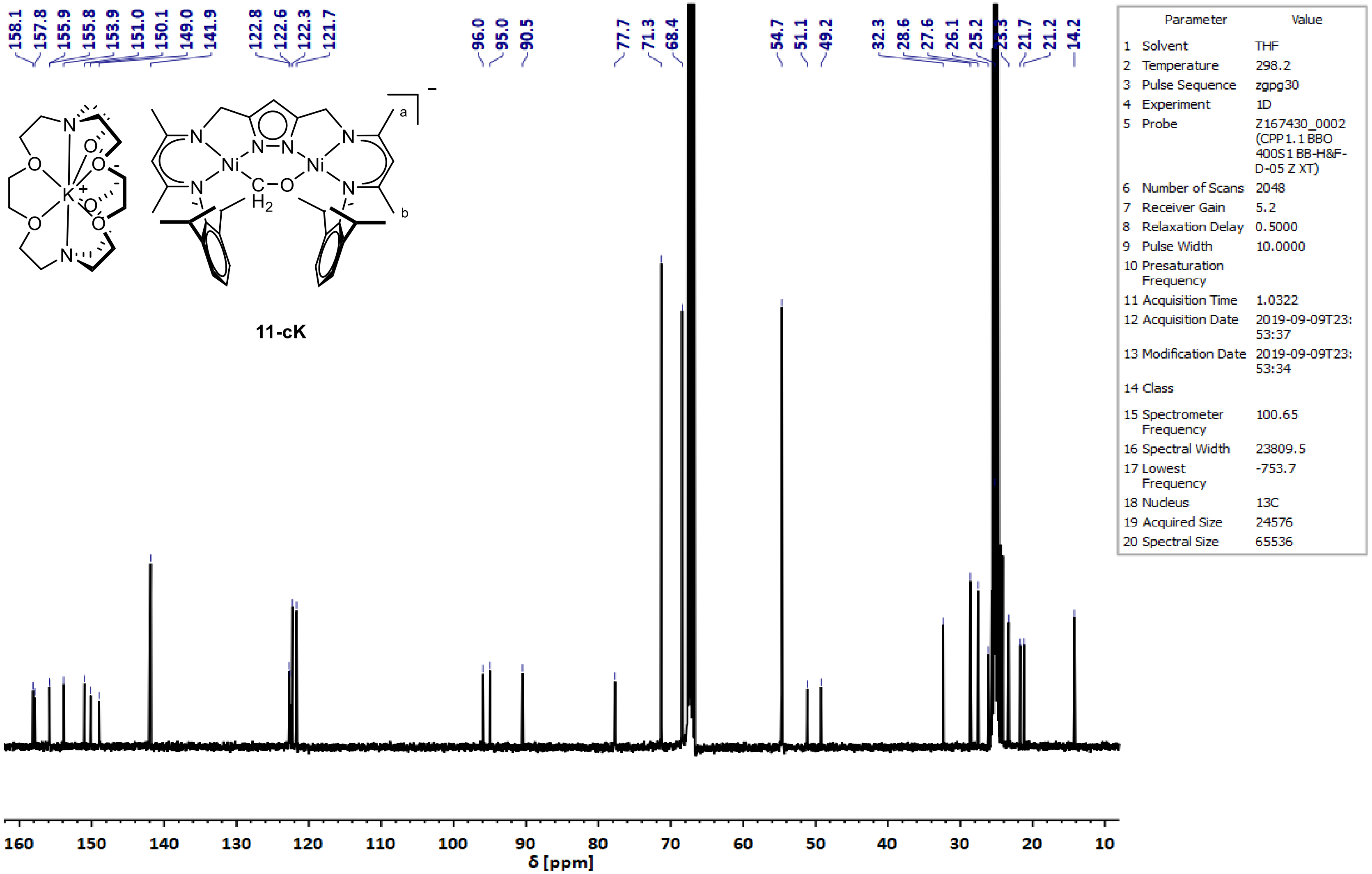

11-cK

	Parameter	Value
1	Solvent	THF
2	Temperature	298.2
3	Pulse Sequence	zgpg30
4	Experiment	1D
5	Probe	Z167430_0002 (CPP1.1 BBO 400S1 BB-H&F-D-05 Z XT)
6	Number of Scans	2048
7	Receiver Gain	5.2
8	Relaxation Delay	0.5000
9	Pulse Width	10.0000
10	Presaturation Frequency	
11	Acquisition Time	1.0322
12	Acquisition Date	2019-09-09T23:53:37
13	Modification Date	2019-09-09T23:53:34
14	Class	
15	Spectrometer Frequency	100.65
16	Spectral Width	23809.5
17	Lowest Frequency	-753.7
18	Nucleus	13C
19	Acquired Size	24576
20	Spectral Size	65536

Figure S 25: ^{13}C NMR of **11-cK** in THF-d_8 at room temperature.

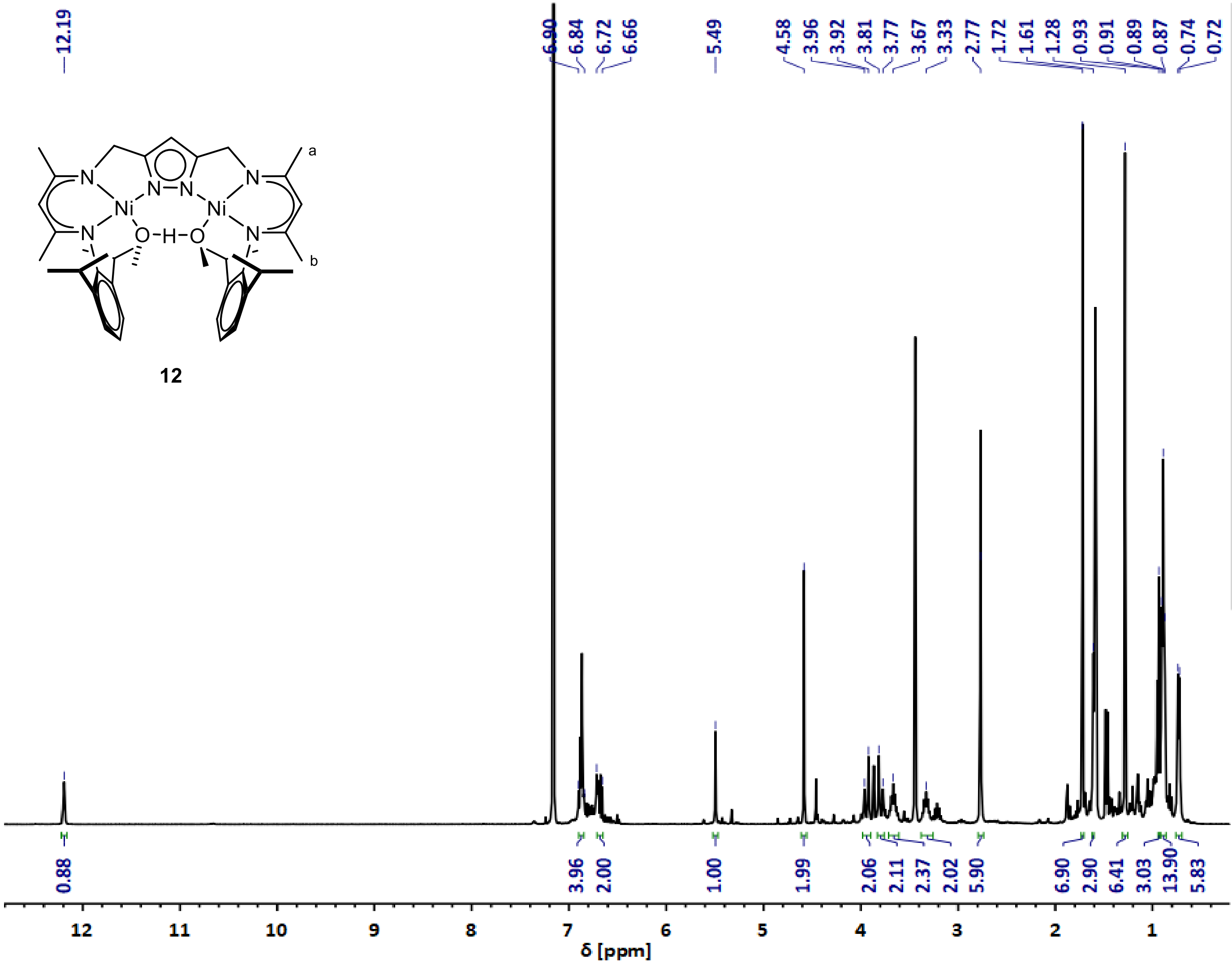

	Parameter	Value
1	Solvent	THF
2	Temperature	298.2
3	Pulse Sequence	zg30
4	Experiment	1D
5	Probe	Z167430_0002 (CPP1.1 BBO 400S1 BB-H&F-D-05 Z XT)
6	Number of Scans	8
7	Receiver Gain	101.0
8	Relaxation Delay	0.1000
9	Pulse Width	12.0000
10	Presaturation Frequency	
11	Acquisition Time	5.1118
12	Acquisition Date	2019-08-01T17:20:37
13	Modification Date	2019-08-01T17:20:32
14	Class	
15	Spectrometer Frequency	400.25
16	Spectral Width	9615.4
17	Lowest Frequency	-2877.7
18	Nucleus	1H
19	Acquired Size	49152
20	Spectral Size	65536

Figure S 26: ^{1}H NMR of **12** in THF-d_8 at room temperature.

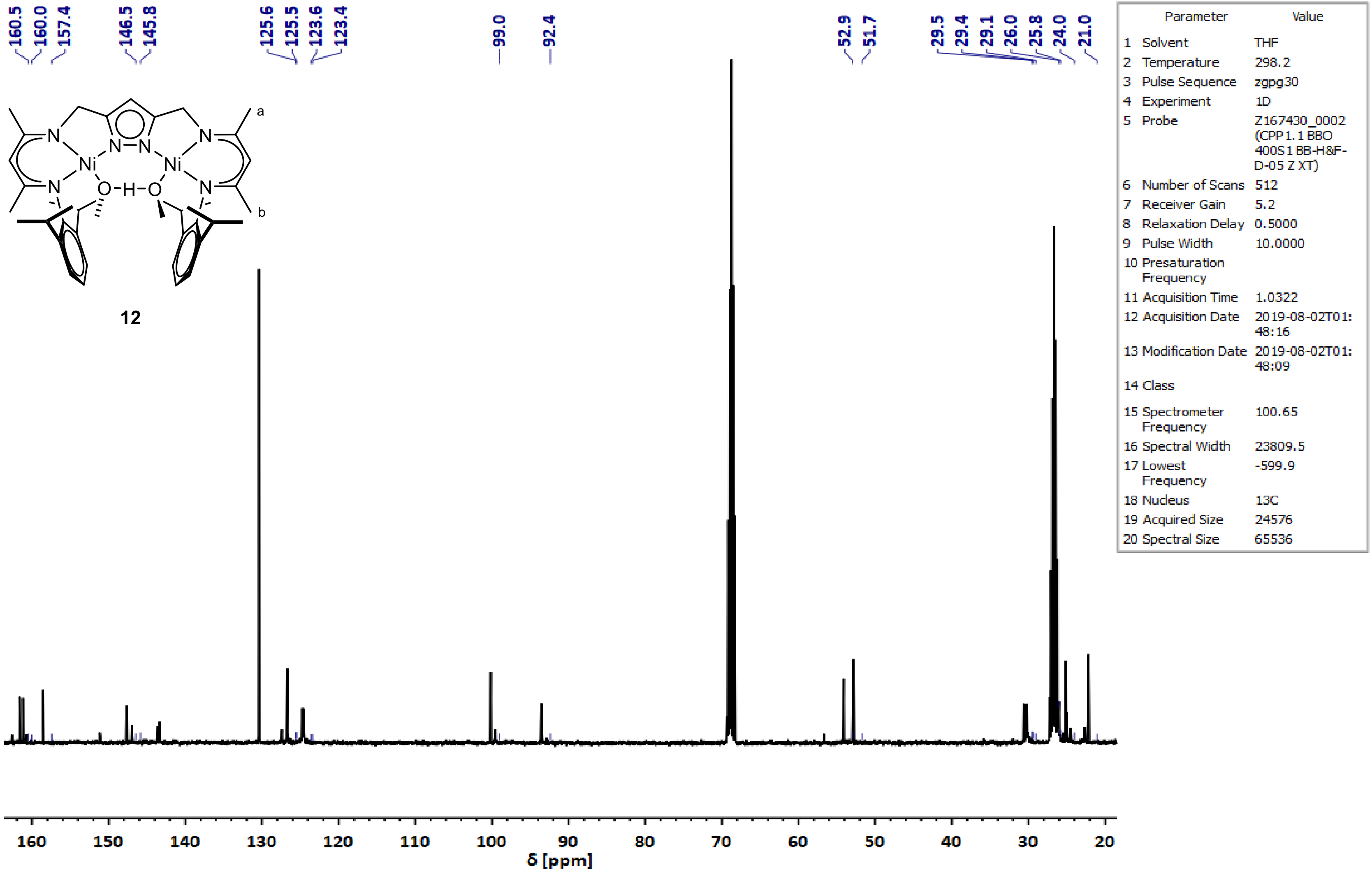

	Parameter	Value
1	Solvent	THF
2	Temperature	298.2
3	Pulse Sequence	zgpg30
4	Experiment	1D
5	Probe	Z167430_0002 (CPP1.1 BBO 400S1 BB-H&F-D-05 Z XT)
6	Number of Scans	512
7	Receiver Gain	5.2
8	Relaxation Delay	0.5000
9	Pulse Width	10.0000
10	Presaturation Frequency	
11	Acquisition Time	1.0322
12	Acquisition Date	2019-08-02T01:48:16
13	Modification Date	2019-08-02T01:48:09
14	Class	
15	Spectrometer Frequency	100.65
16	Spectral Width	23809.5
17	Lowest Frequency	-599.9
18	Nucleus	13C
19	Acquired Size	24576
20	Spectral Size	65536

Figure S 27: ^{13}C NMR of **12** in THF-d_8 at room temperature.

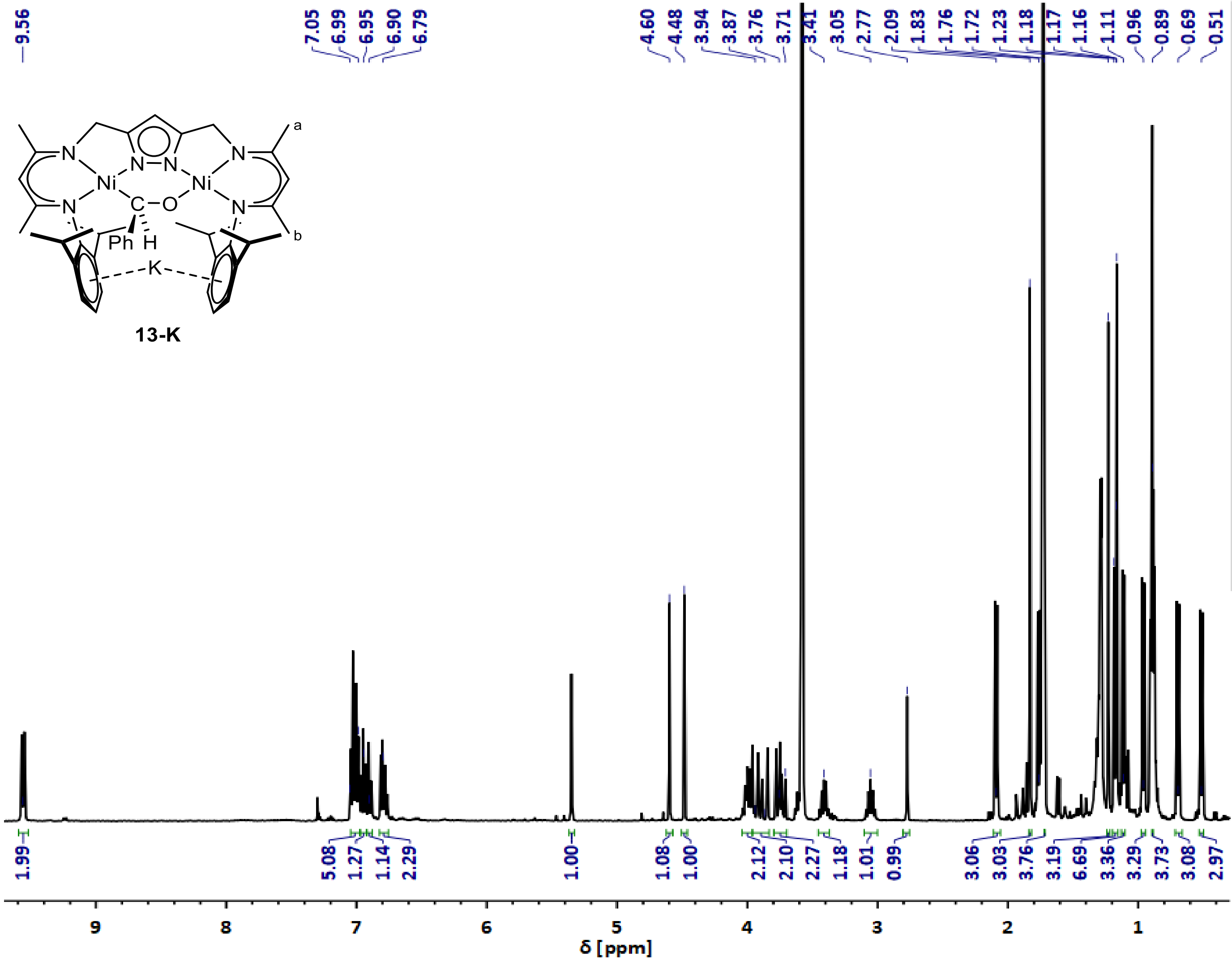

13-K

	Parameter	Value
1	Solvent	THF
2	Temperature	298.2
3	Pulse Sequence	zg30
4	Experiment	1D
5	Probe	Z167430_0002 (CPP1.1 BBO 400S1 BB-H&F-D-05 Z XT)
6	Number of Scans	8
7	Receiver Gain	101.0
8	Relaxation Delay	0.1000
9	Pulse Width	12.0000
10	Presaturation Frequency	
11	Acquisition Time	5.1118
12	Acquisition Date	2019-02-07T18:40:51
13	Modification Date	2019-02-07T18:40:50
14	Class	
15	Spectrometer Frequency	400.25
16	Spectral Width	9615.4
17	Lowest Frequency	-2820.6
18	Nucleus	1H
19	Acquired Size	49152
20	Spectral Size	65536

Figure S 28: ^{1}H NMR of **13-K** in THF-d_8 at room temperature.

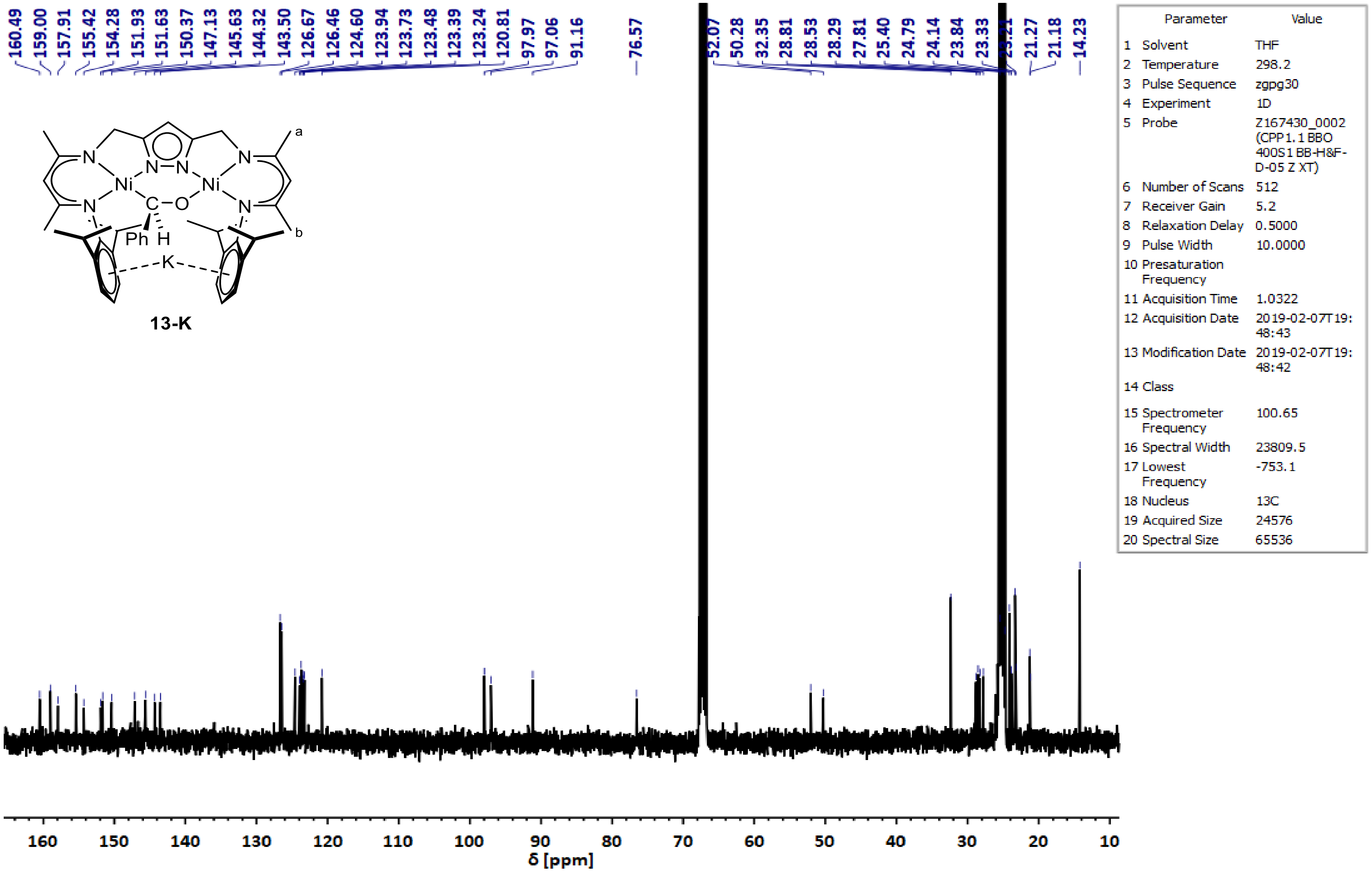

	Parameter	Value
1	Solvent	THF
2	Temperature	298.2
3	Pulse Sequence	zgpg30
4	Experiment	1D
5	Probe	Z167430_0002 (CPP1.1 BBO 400S1 BB-H&F-D-05 Z XT)
6	Number of Scans	512
7	Receiver Gain	5.2
8	Relaxation Delay	0.5000
9	Pulse Width	10.0000
10	Presaturation Frequency	
11	Acquisition Time	1.0322
12	Acquisition Date	2019-02-07T19:48:43
13	Modification Date	2019-02-07T19:48:42
14	Class	
15	Spectrometer Frequency	100.65
16	Spectral Width	23809.5
17	Lowest Frequency	-753.1
18	Nucleus	13C
19	Acquired Size	24576
20	Spectral Size	65536

Figure S 29: ^{13}C NMR of **13-K** in THF-d_8 at room temperature.

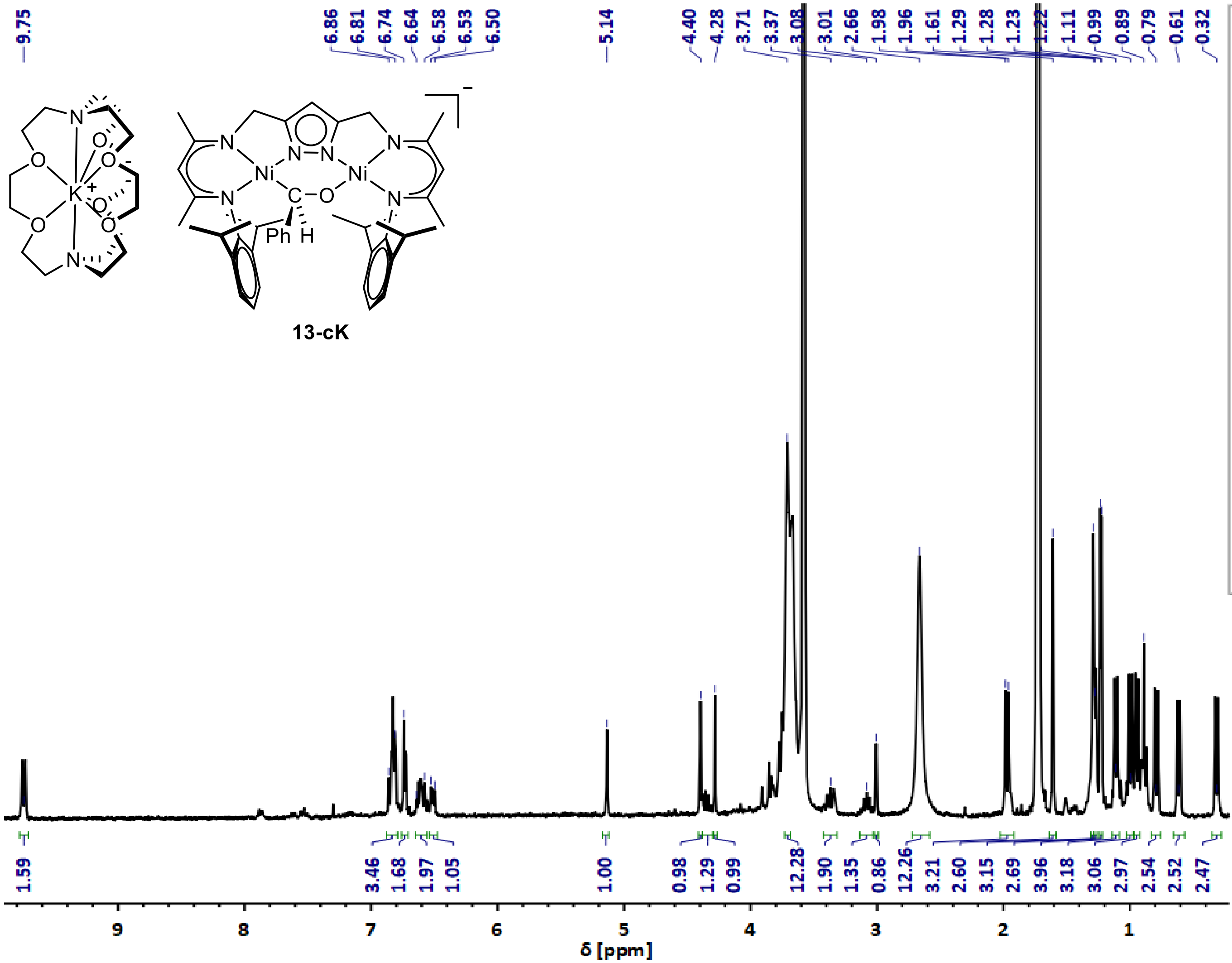

	Parameter	Value
1	Solvent	THF
2	Temperature	298.0
3	Pulse Sequence	zg30
4	Experiment	1D
5	Probe	Z862701_0063 (PA BBO 300S1 BBF-H&F-D-05 Z)
6	Number of Scans	32
7	Receiver Gain	207.7
8	Relaxation Delay	0.1000
9	Pulse Width	12.5000
10	Presaturation Frequency	
11	Acquisition Time	2.1845
12	Acquisition Date	2019-07-16T12:04:17
13	Modification Date	2019-07-16T12:04:17
14	Class	
15	Spectrometer Frequency	300.13
16	Spectral Width	15000.0
17	Lowest Frequency	-9011.2
18	Nucleus	1H
19	Acquired Size	32768
20	Spectral Size	131072

Figure S 30: ^{1}H NMR of **13-cK** in THF-d_8 at room temperature.

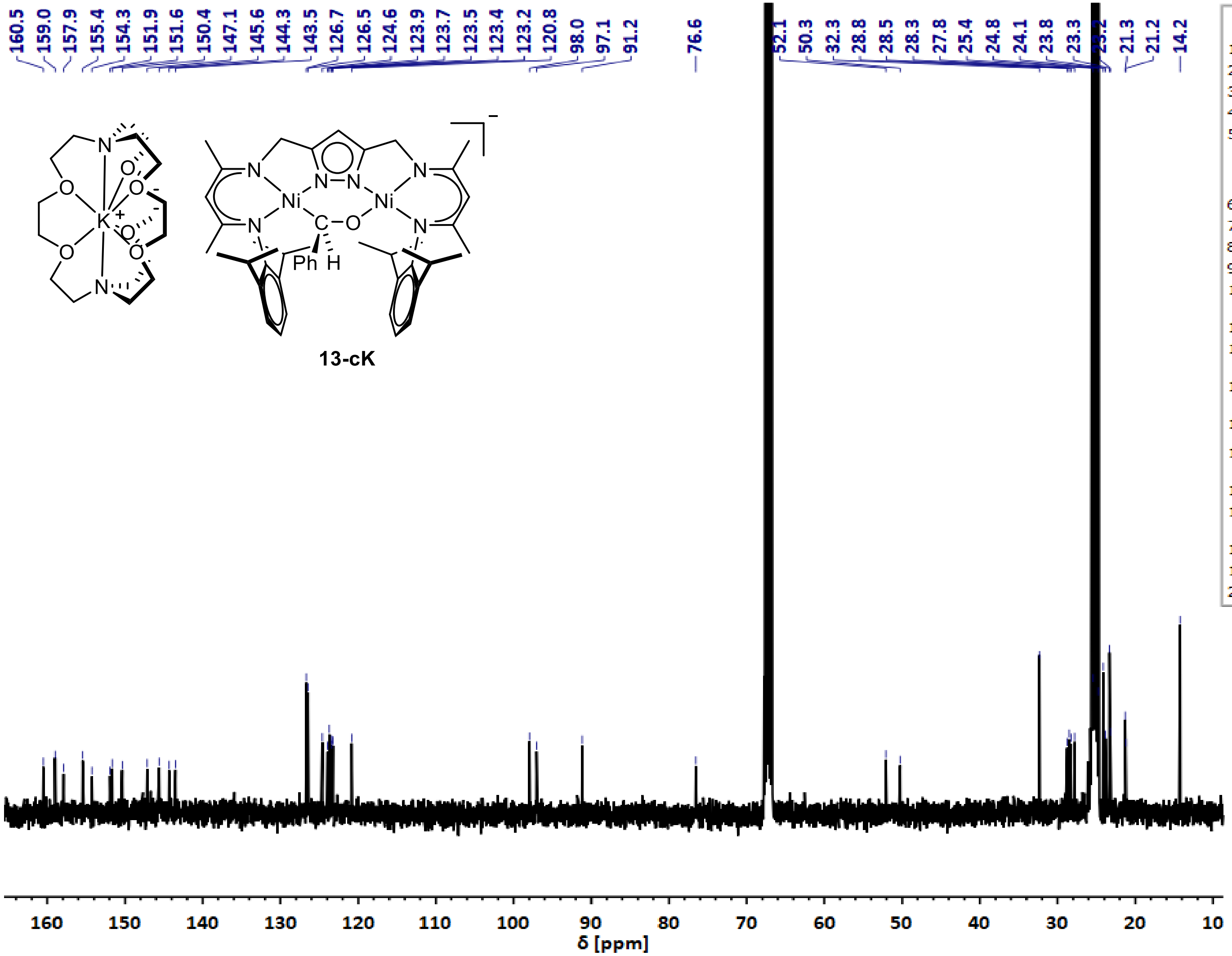

	Parameter	Value
1	Solvent	THF
2	Temperature	298.2
3	Pulse Sequence	zgpg30
4	Experiment	1D
5	Probe	Z167430_0002 (CPP1.1 BBO 400S1 BB-H&F-D-05 Z XT)
6	Number of Scans	512
7	Receiver Gain	5.2
8	Relaxation Delay	0.5000
9	Pulse Width	10.0000
10	Presaturation Frequency	
11	Acquisition Time	1.0322
12	Acquisition Date	2019-02-07T19:48:43
13	Modification Date	2019-02-07T19:48:42
14	Class	
15	Spectrometer Frequency	100.65
16	Spectral Width	23809.5
17	Lowest Frequency	-753.1
18	Nucleus	13C
19	Acquired Size	24576
20	Spectral Size	65536

Figure S 31: ^{13}C NMR of **13-cK** in THF-d_8 at room temperature.

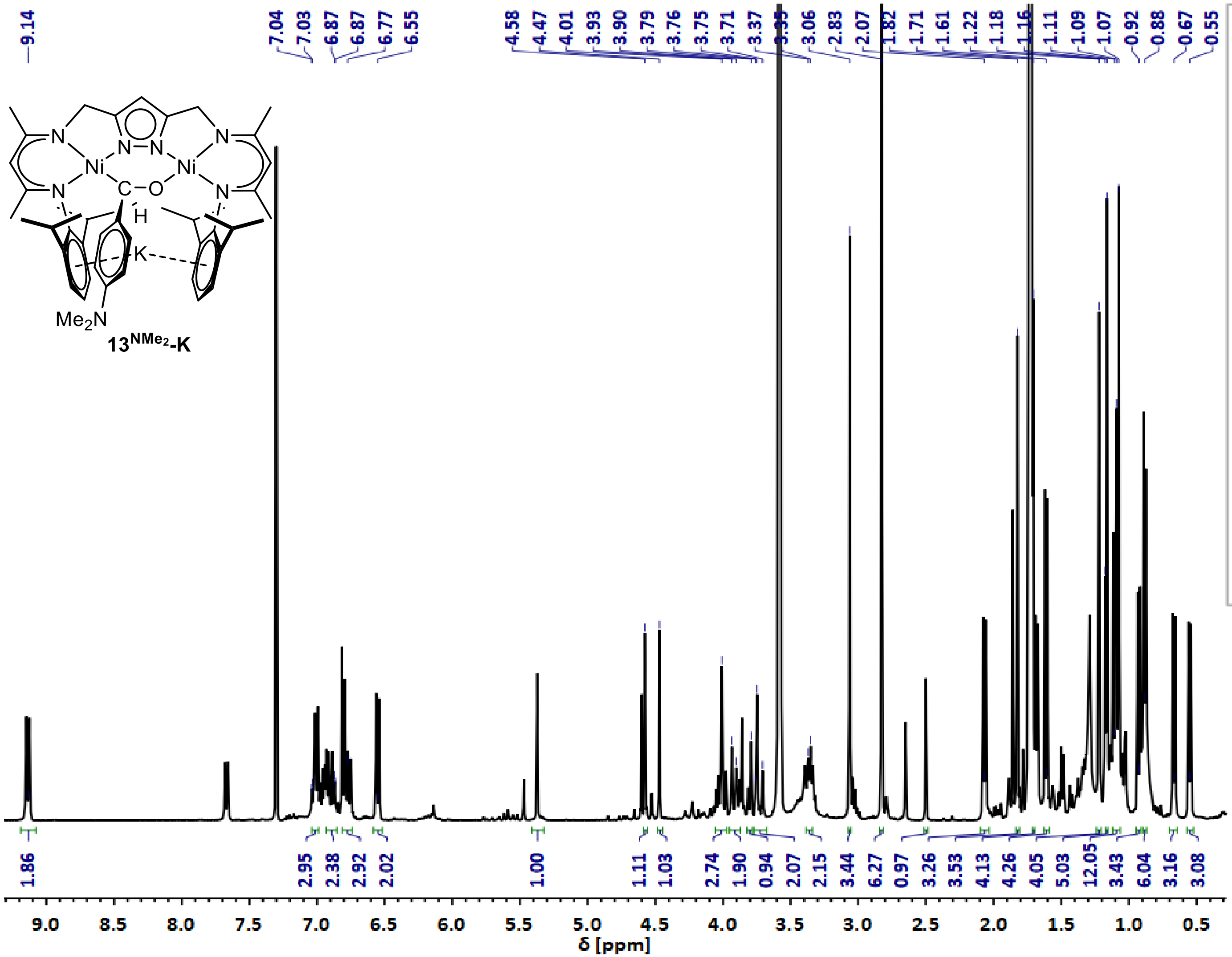

	Parameter	Value
1	Solvent	THF
2	Temperature	298.1
3	Pulse Sequence	zg30
4	Experiment	1D
5	Probe	Z167430_0002 (CPP1.1 BBO 400S1 BB-H&F-D-05 Z XT)
6	Number of Scans	64
7	Receiver Gain	101.0
8	Relaxation Delay	0.1000
9	Pulse Width	12.0000
10	Presaturation Frequency	
11	Acquisition Time	4.1288
12	Acquisition Date	2019-09-13T23:50:33
13	Modification Date	2019-09-13T23:50:30
14	Class	
15	Spectrometer Frequency	400.25
16	Spectral Width	11904.8
17	Lowest Frequency	-5966.5
18	Nucleus	1H
19	Acquired Size	49152
20	Spectral Size	131072

Figure S 32: ^{1}H NMR of **13^{NMe_2}-K** in THF-d_8 at room temperature.

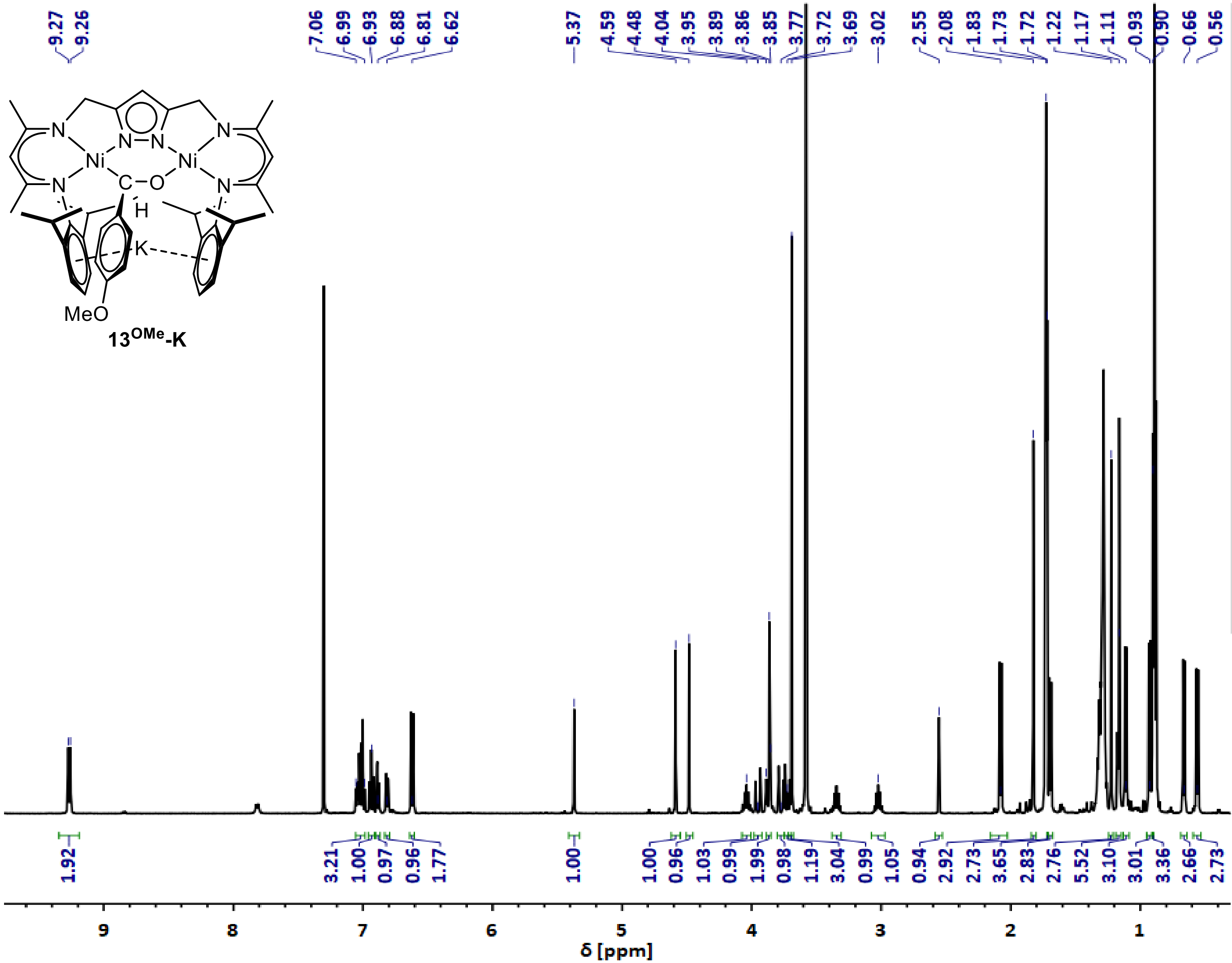

	Parameter	Value
1	Solvent	THF
2	Temperature	298.0
3	Pulse Sequence	zg0
4	Experiment	1D
5	Probe	5 mm CPPBBO BB-1H/ 19F/ D Z-GRD Z130036/ 0004
6	Number of Scans	32
7	Receiver Gain	74.8
8	Relaxation Delay	0.1000
9	Pulse Width	5.0000
10	Presaturation Frequency	
11	Acquisition Time	5.0332
12	Acquisition Date	2019-06-28T07:46:00
13	Modification Date	2019-06-28T07:49:19
14	Class	
15	Spectrometer Frequency	500.25
16	Spectral Width	13020.8
17	Lowest Frequency	-3527.5
18	Nucleus	1H
19	Acquired Size	65536
20	Spectral Size	131072

Figure S 33: ^{1}H NMR of **13^{OMe}-K** in THF-d_8 at room temperature.

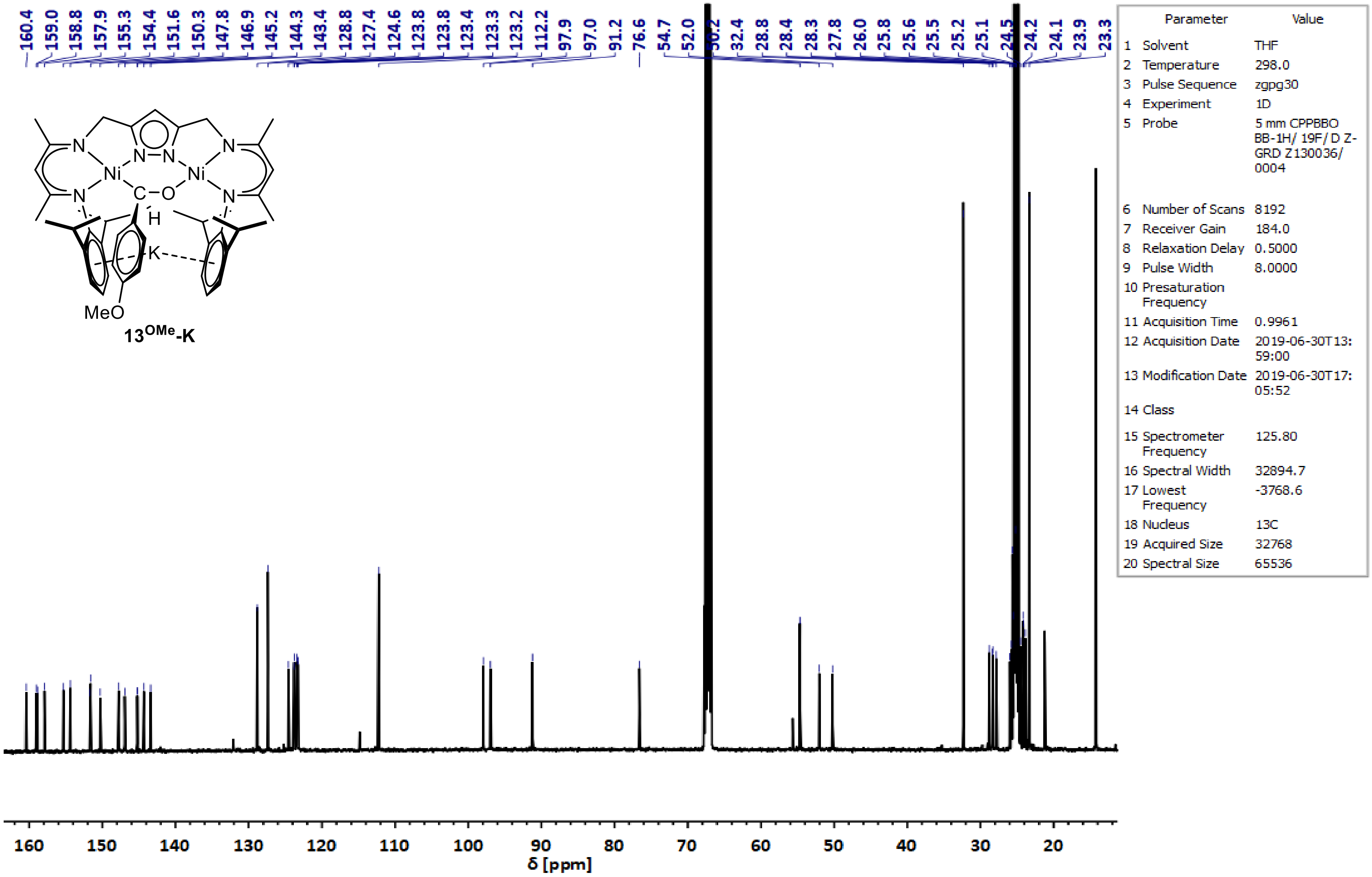

	Parameter	Value
1	Solvent	THF
2	Temperature	298.0
3	Pulse Sequence	zgpg30
4	Experiment	1D
5	Probe	5 mm CPPBBO BB-1H/ 19F/ D Z-GRD Z130036/ 0004
6	Number of Scans	8192
7	Receiver Gain	184.0
8	Relaxation Delay	0.5000
9	Pulse Width	8.0000
10	Presaturation Frequency	
11	Acquisition Time	0.9961
12	Acquisition Date	2019-06-30T13:59:00
13	Modification Date	2019-06-30T17:05:52
14	Class	
15	Spectrometer Frequency	125.80
16	Spectral Width	32894.7
17	Lowest Frequency	-3768.6
18	Nucleus	13C
19	Acquired Size	32768
20	Spectral Size	65536

Figure S 34: ^{13}C NMR of **13^{OMe}-K** in THF-d_8 at room temperature.

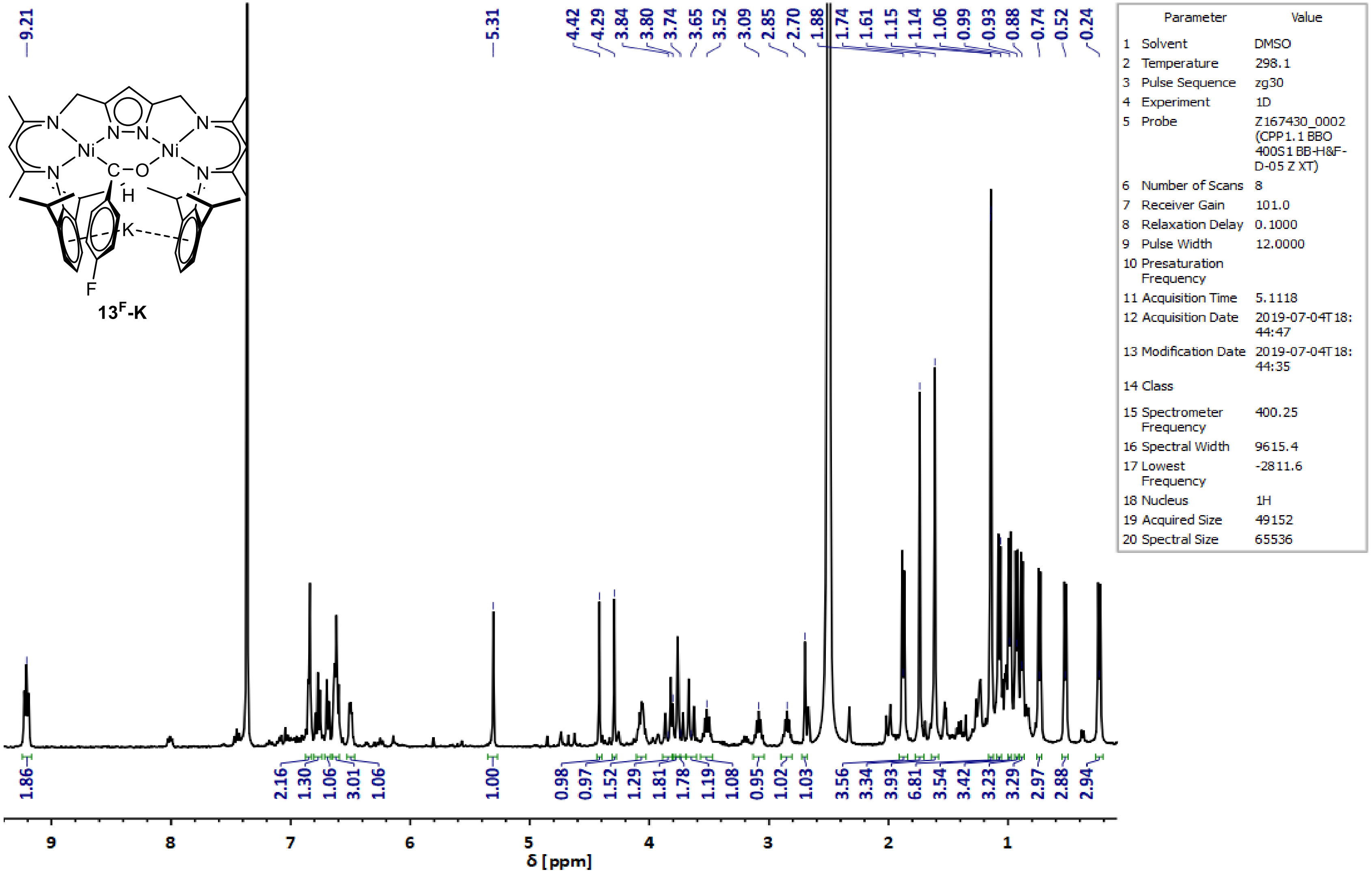

	Parameter	Value
1	Solvent	DMSO
2	Temperature	298.1
3	Pulse Sequence	zg30
4	Experiment	1D
5	Probe	Z167430_0002 (CPP1.1 BBO 400S1 BB-H&F-D-05 Z XT)
6	Number of Scans	8
7	Receiver Gain	101.0
8	Relaxation Delay	0.1000
9	Pulse Width	12.0000
10	Presaturation Frequency	
11	Acquisition Time	5.1118
12	Acquisition Date	2019-07-04T18:44:47
13	Modification Date	2019-07-04T18:44:35
14	Class	
15	Spectrometer Frequency	400.25
16	Spectral Width	9615.4
17	Lowest Frequency	-2811.6
18	Nucleus	1H
19	Acquired Size	49152
20	Spectral Size	65536

Figure S 35: ^{1}H NMR of **13^{F}-K** in DMSO-d$_6$ at room temperature.

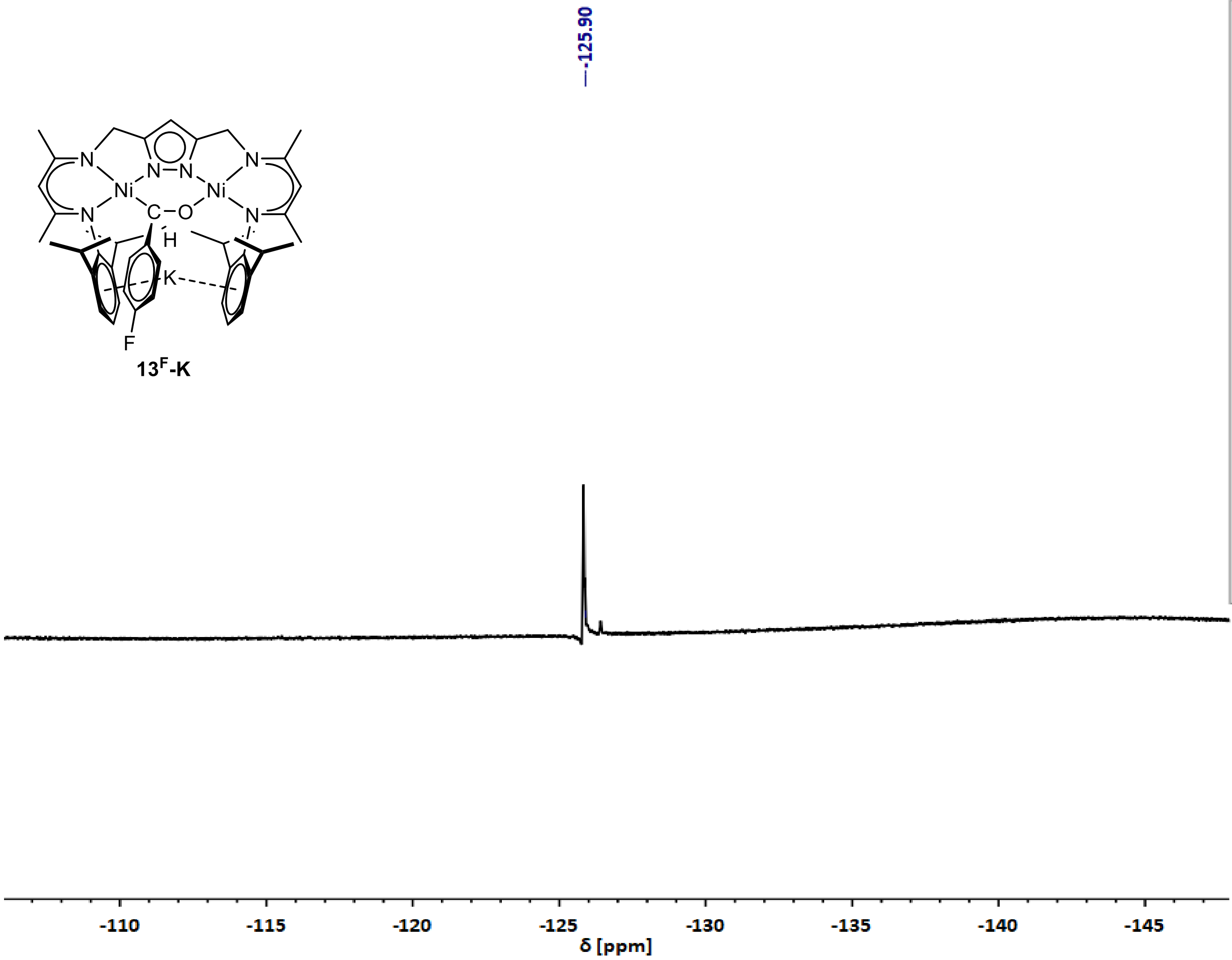

	Parameter	Value
1	Solvent	DMSO
2	Temperature	298.1
3	Pulse Sequence	zg30
4	Experiment	1D
5	Probe	Z167430_0002 (CPP1.1 BBO 400S1 BB-H&F-D-05 Z XT)
6	Number of Scans	32
7	Receiver Gain	18.3
8	Relaxation Delay	0.5000
9	Pulse Width	15.0000
10	Presaturation Frequency	
11	Acquisition Time	1.0224
12	Acquisition Date	2019-07-04T18:46:38
13	Modification Date	2019-07-04T18:46:26
14	Class	
15	Spectrometer Frequency	376.57
16	Spectral Width	96153.8
17	Lowest Frequency	-89504.2
18	Nucleus	19F
19	Acquired Size	98304
20	Spectral Size	262144

Figure S 36: ^{19}F NMR of **13^{F}-K** in DMSO-d$_6$ at room temperature.

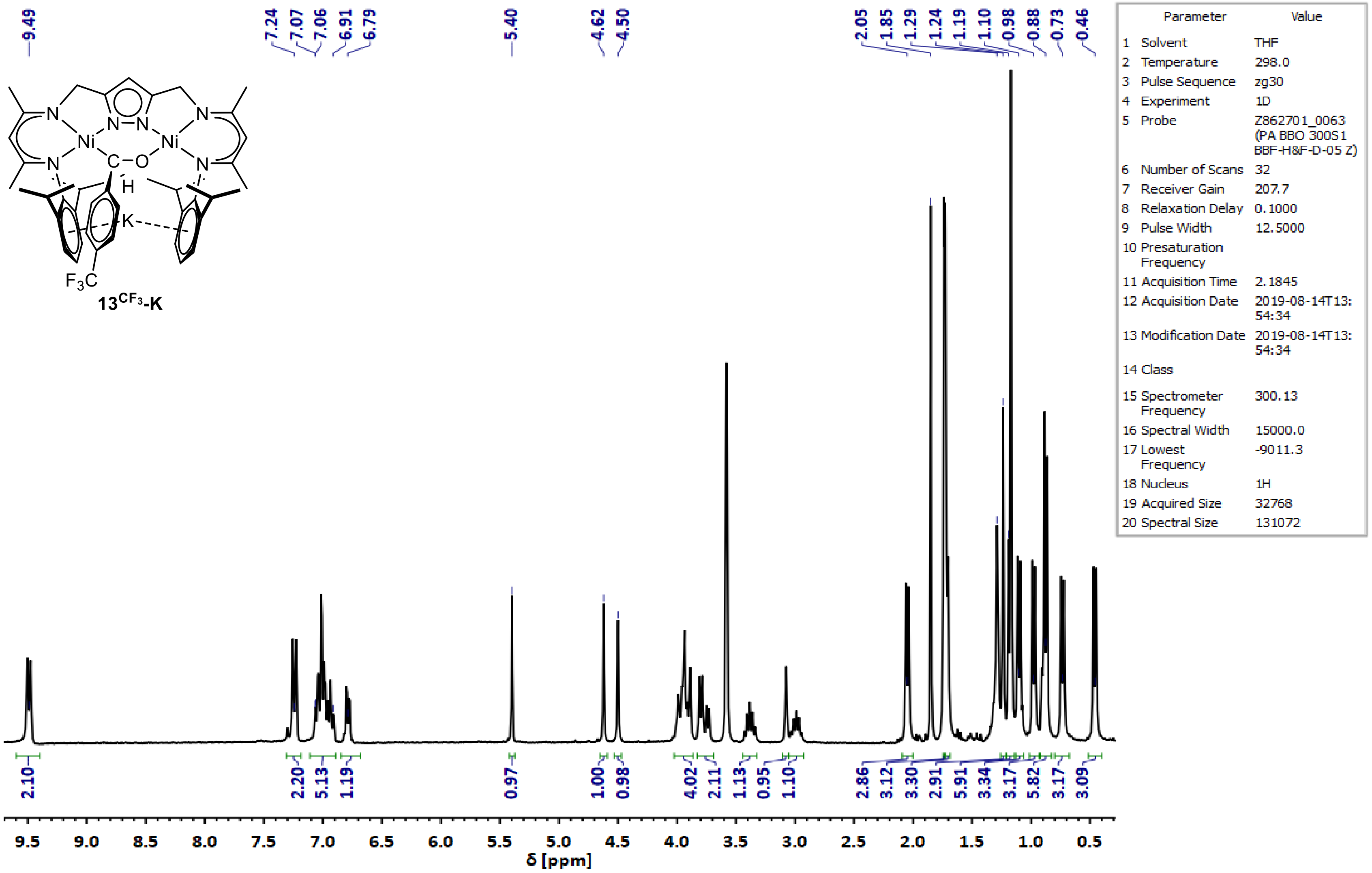

	Parameter	Value
1	Solvent	THF
2	Temperature	298.0
3	Pulse Sequence	zg30
4	Experiment	1D
5	Probe	Z862701_0063 (PA BBO 300S1 BBF-H&F-D-05 Z)
6	Number of Scans	32
7	Receiver Gain	207.7
8	Relaxation Delay	0.1000
9	Pulse Width	12.5000
10	Presaturation Frequency	
11	Acquisition Time	2.1845
12	Acquisition Date	2019-08-14T13:54:34
13	Modification Date	2019-08-14T13:54:34
14	Class	
15	Spectrometer Frequency	300.13
16	Spectral Width	15000.0
17	Lowest Frequency	-9011.3
18	Nucleus	1H
19	Acquired Size	32768
20	Spectral Size	131072

Figure S 37: ^{1}H NMR of **13^{CF_3}-K** in THF-d$_8$ at room temperature.

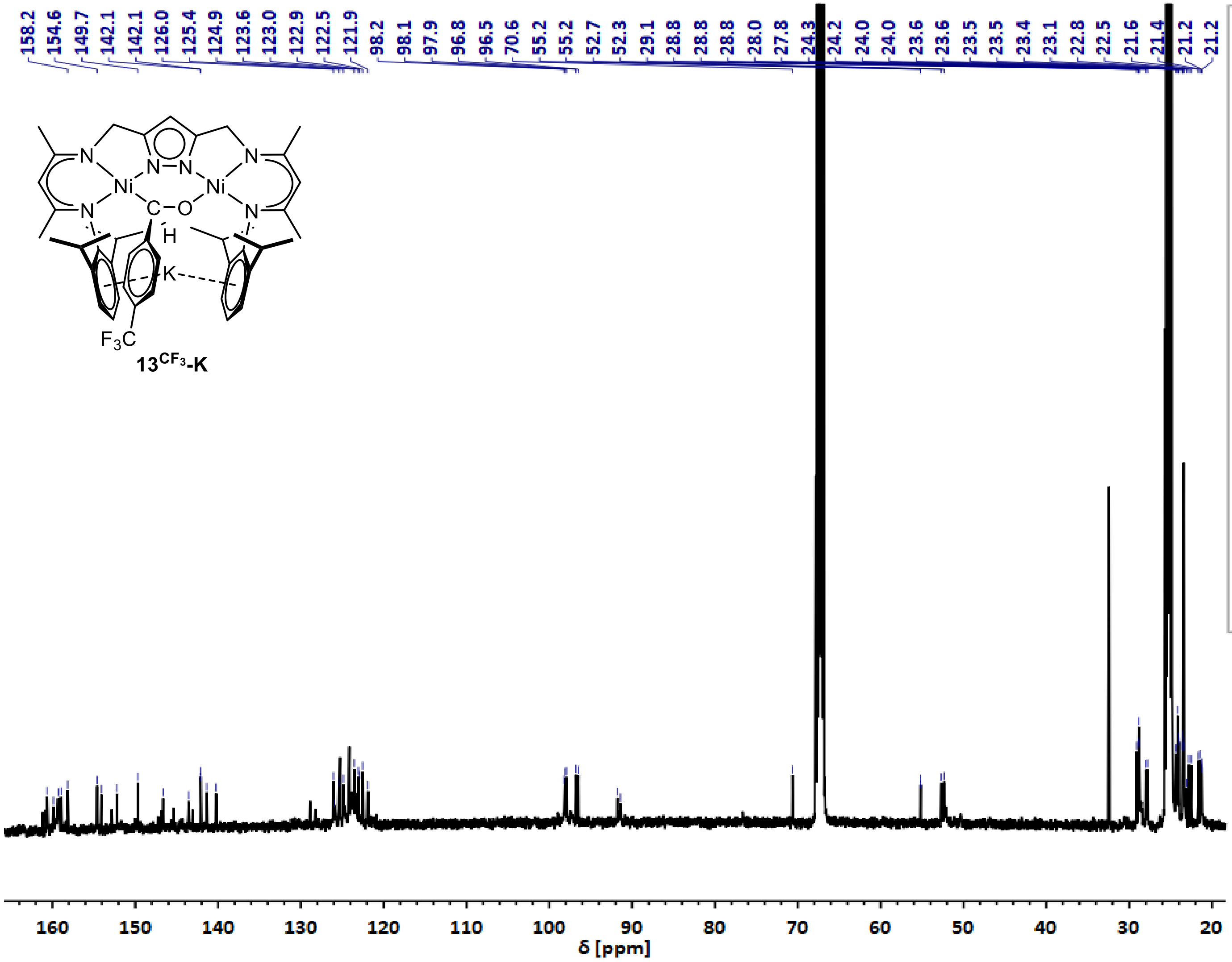

	Parameter	Value
1	Solvent	THF
2	Temperature	298.1
3	Pulse Sequence	zgpg30
4	Experiment	1D
5	Probe	5 mm CPPBBO BB-1H/ 19F/ D Z-GRD Z130036/ 0004
6	Number of Scans	7868
7	Receiver Gain	184.0
8	Relaxation Delay	0.2000
9	Pulse Width	10.0000
10	Presaturation Frequency	
11	Acquisition Time	1.3763
12	Acquisition Date	2019-08-16T06:17:34
13	Modification Date	2019-08-16T06:39:55
14	Class	
15	Spectrometer Frequency	125.80
16	Spectral Width	35714.3
17	Lowest Frequency	-5169.7
18	Nucleus	13C
19	Acquired Size	49152
20	Spectral Size	131072

Figure S 38: ^{13}C NMR of **13^{CF_3}-K** in THF-d$_8$ at room temperature.

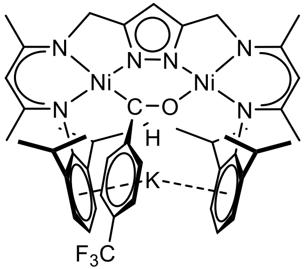

13^{CF_3}-K

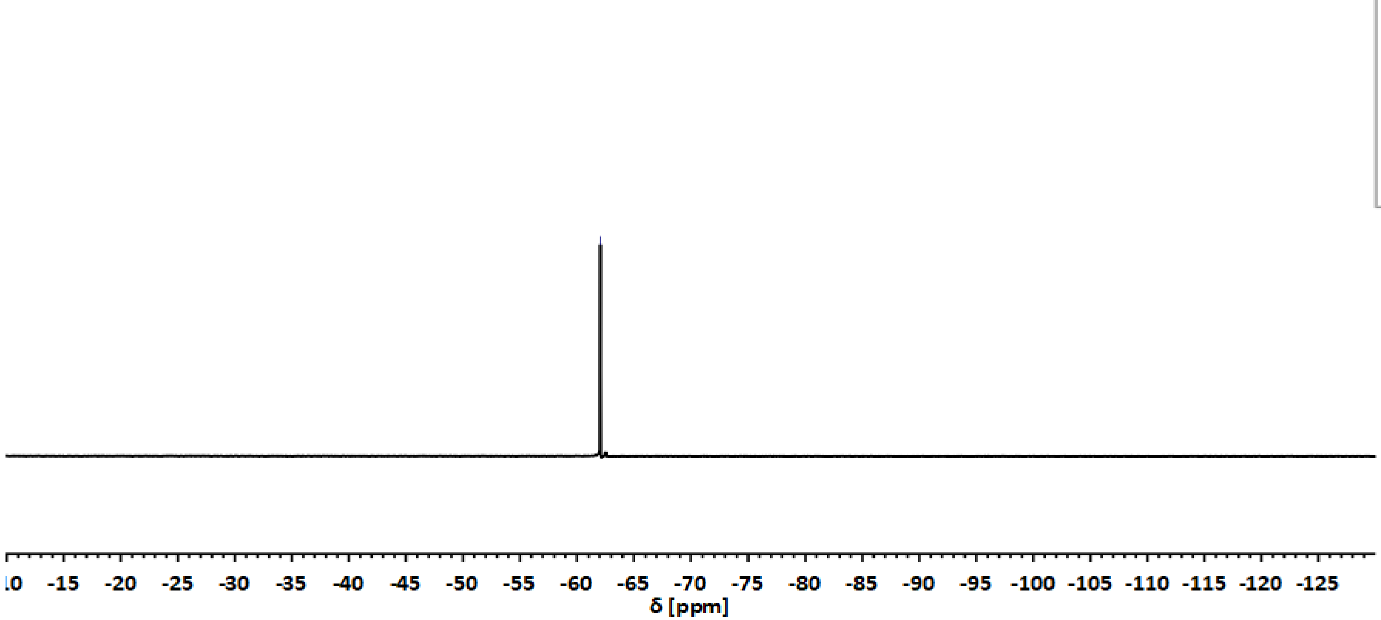

	Parameter	Value
1	Solvent	THF
2	Temperature	298.1
3	Pulse Sequence	zgdc30
4	Experiment	1D
5	Probe	Z862701_0063 (PA BBO 300S1 BBF-H&F-D-05 Z)
6	Number of Scans	32
7	Receiver Gain	207.7
8	Relaxation Delay	0.5000
9	Pulse Width	8.2000
10	Presaturation Frequency	
11	Acquisition Time	0.9961
12	Acquisition Date	2019-08-14T13:56:46
13	Modification Date	2019-08-14T13:56:46
14	Class	
15	Spectrometer Frequency	282.37
16	Spectral Width	65789.5
17	Lowest Frequency	-63959.2
18	Nucleus	19F
19	Acquired Size	65536
20	Spectral Size	131072

Figure S 39: ^{19}F NMR of **13^{CF_3}-K** in THF-d_8 at room temperature.

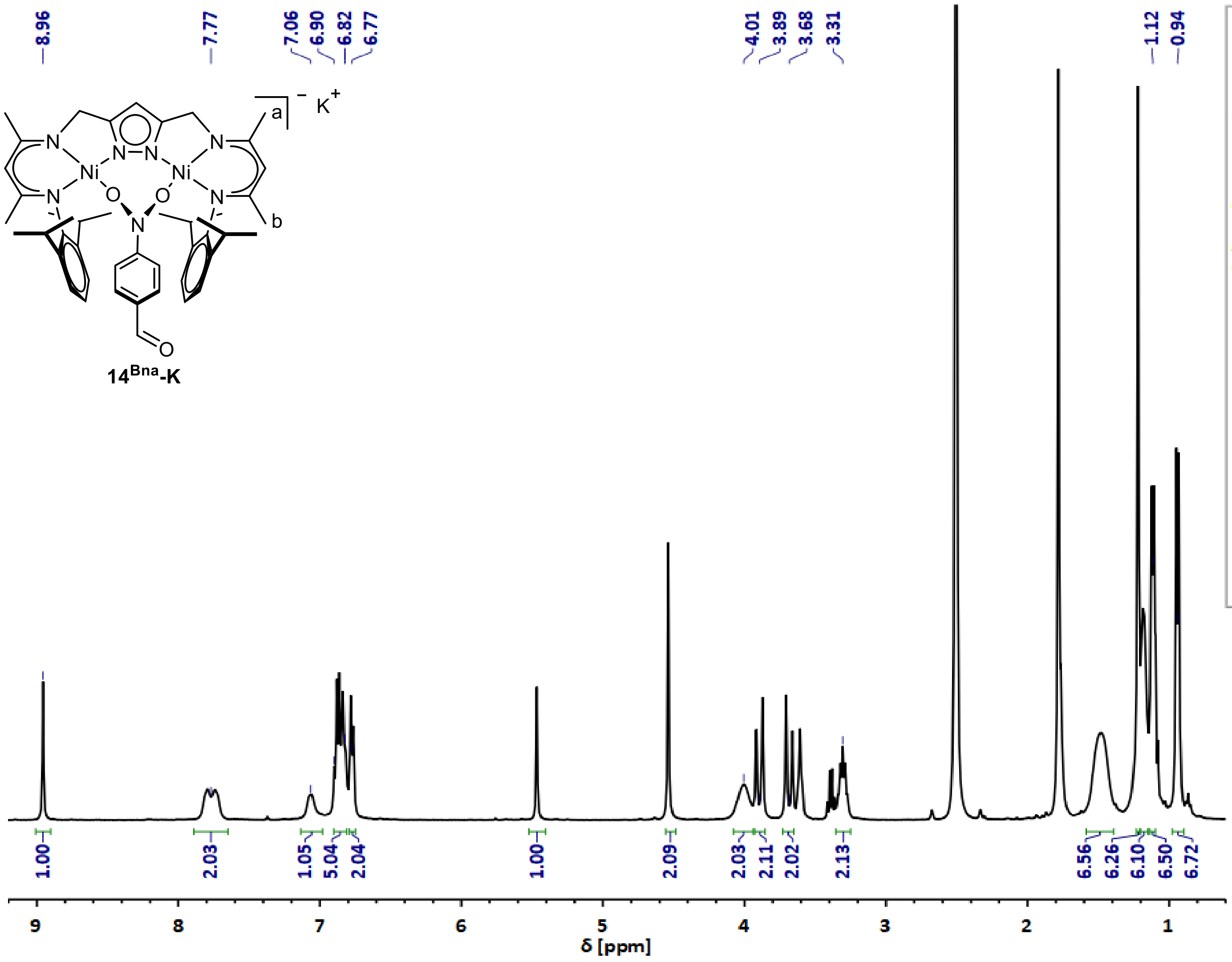

	Parameter	Value
1	Solvent	DMSO
2	Temperature	298.2
3	Pulse Sequence	zg30
4	Experiment	1D
5	Probe	Z167430_0002 (CPP1.1 BBO 400S1 BB-H&F-D-05 Z XT)
6	Number of Scans	32
7	Receiver Gain	101.0
8	Relaxation Delay	0.1000
9	Pulse Width	12.0000
10	Presaturation Frequency	
11	Acquisition Time	4.1288
12	Acquisition Date	2020-01-23T15:56:05
13	Modification Date	2020-01-23T15:56:05
14	Class	
15	Spectrometer Frequency	400.25
16	Spectral Width	11904.8
17	Lowest Frequency	-4751.6
18	Nucleus	1H
19	Acquired Size	49152
20	Spectral Size	131072

Figure S 40: ^{1}H NMR of **14^{Bna}-K** in DMSO-d$_6$ at room temperature.

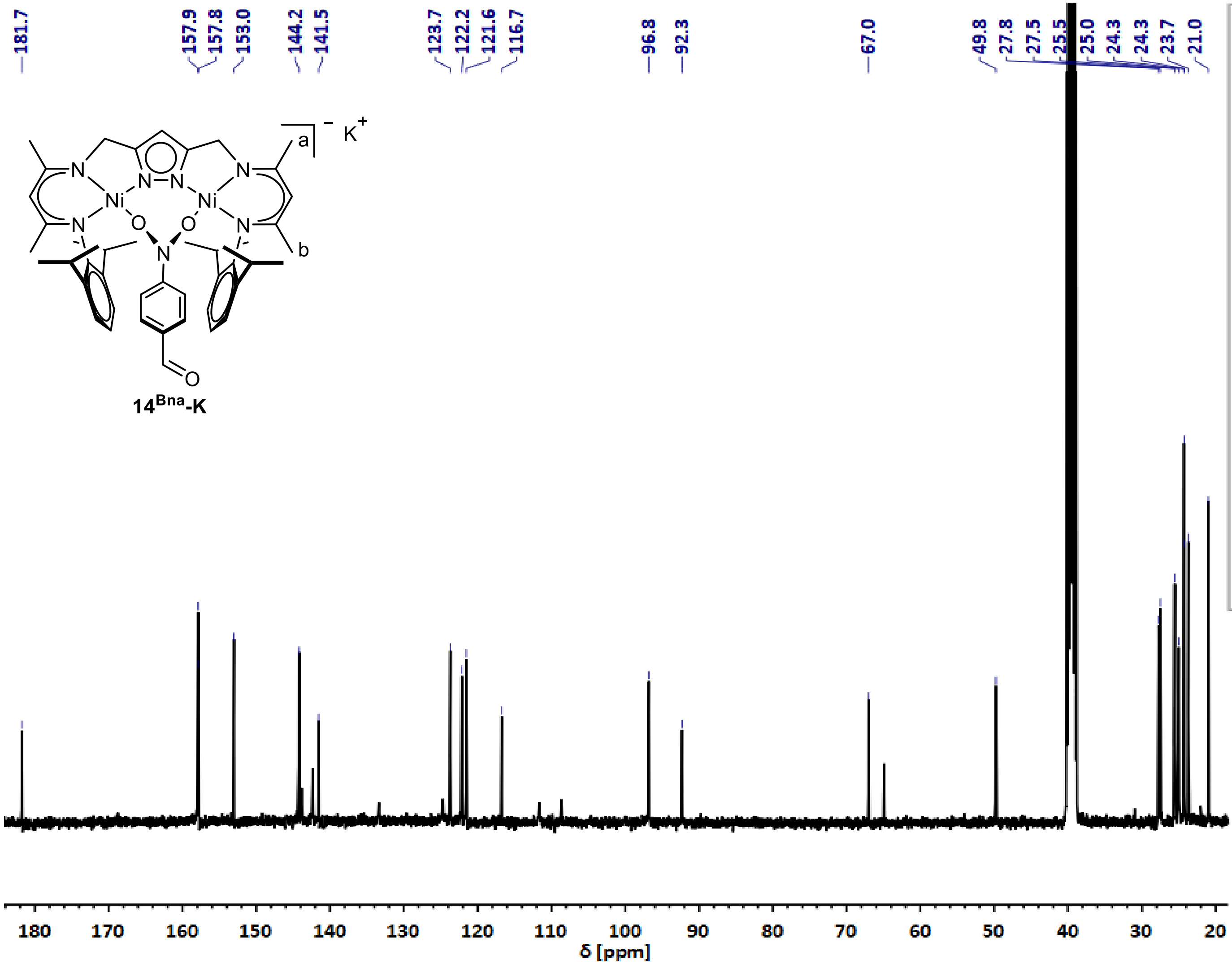

	Parameter	Value
1	Solvent	DMSO
2	Temperature	298.1
3	Pulse Sequence	zgpg30
4	Experiment	1D
5	Probe	Z167430_0002 (CPP1.1 BBO 400S1 BB-H&F-D-05 Z XT)
6	Number of Scans	4096
7	Receiver Gain	5.2
8	Relaxation Delay	0.5000
9	Pulse Width	10.0000
10	Presaturation Frequency	
11	Acquisition Time	1.0322
12	Acquisition Date	2020-01-24T04:00:09
13	Modification Date	2020-01-24T04:00:06
14	Class	
15	Spectrometer Frequency	100.65
16	Spectral Width	23809.5
17	Lowest Frequency	-881.7
18	Nucleus	13C
19	Acquired Size	24576
20	Spectral Size	65536

Figure S 41: ^{13}C NMR of **14^{Bna}-K** in DMSO-d$_6$ at room temperature.

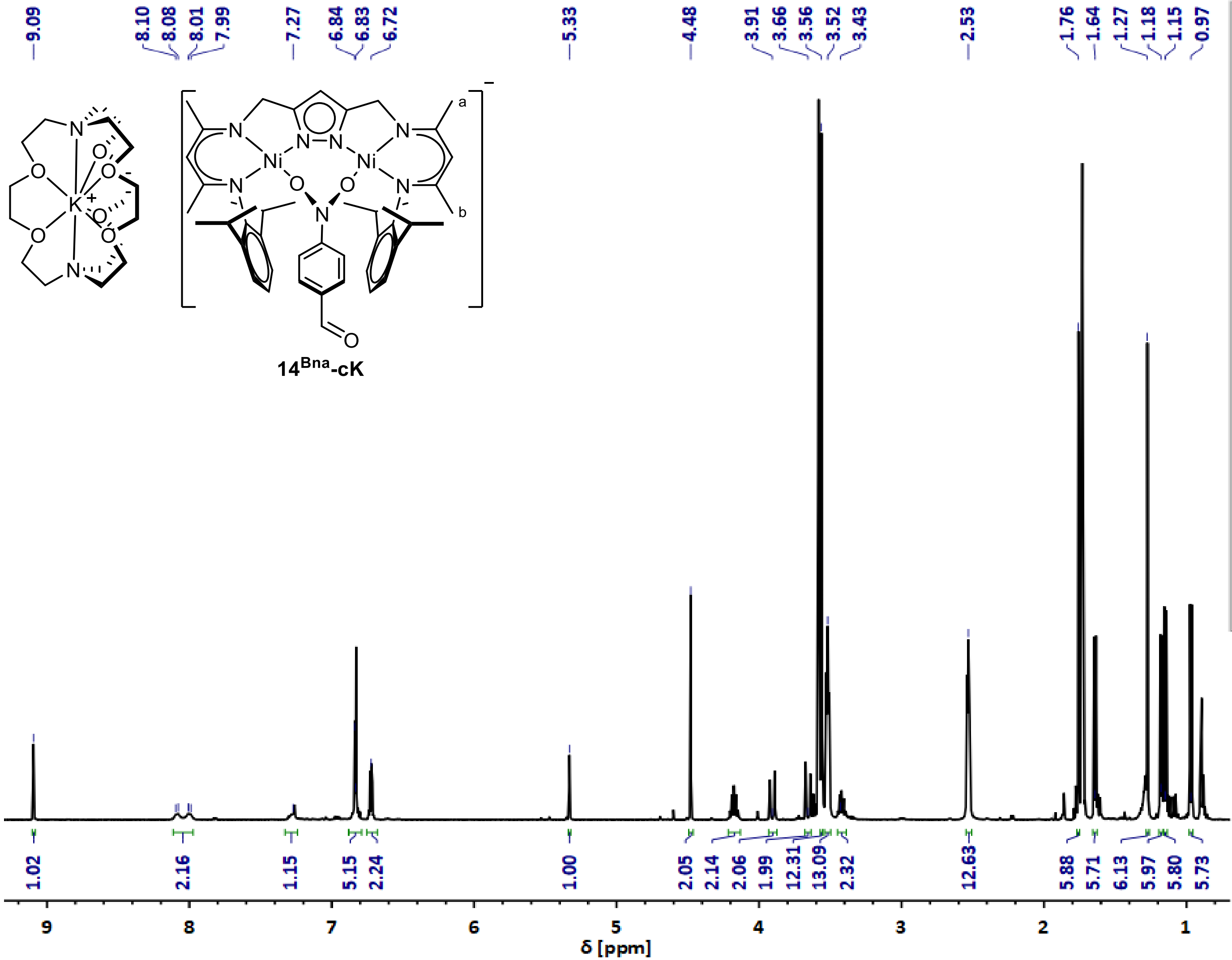

Parameter	Value
1 Solvent	THF
2 Temperature	298.0
3 Pulse Sequence	zg0
4 Experiment	1D
5 Probe	5 mm CPPBBO BB-1H/ 19F/ D Z-GRD Z130036/ 0004
6 Number of Scans	32
7 Receiver Gain	92.8
8 Relaxation Delay	0.1000
9 Pulse Width	11.0000
10 Presaturation Frequency	
11 Acquisition Time	5.0332
12 Acquisition Date	2019-08-26T10:43:00
13 Modification Date	2019-08-26T10:43:58
14 Class	
15 Spectrometer Frequency	500.25
16 Spectral Width	13020.8
17 Lowest Frequency	-3526.1
18 Nucleus	1H
19 Acquired Size	65536
20 Spectral Size	131072

Figure S 42: ^{1}H NMR of **14^{Bna}-cK** in THF-d_8 at room temperature.

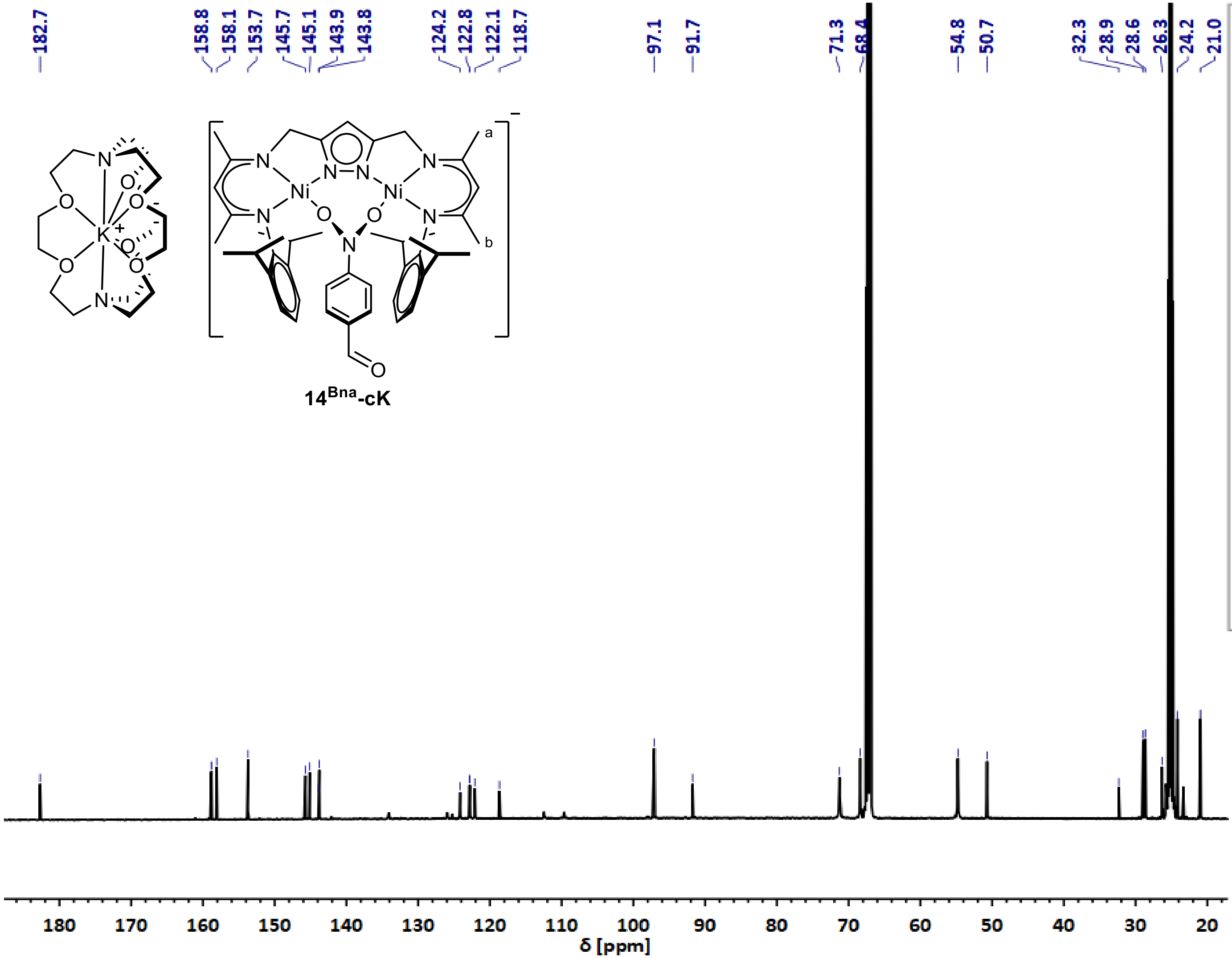

	Parameter	Value
1	Solvent	THF
2	Temperature	298.0
3	Pulse Sequence	zgpg30
4	Experiment	1D
5	Probe	5 mm CPPBBO BB-1H/ 19F/ D Z-GRD Z130036/ 0004
6	Number of Scans	16384
7	Receiver Gain	184.0
8	Relaxation Delay	0.2000
9	Pulse Width	10.0000
10	Presaturation Frequency	
11	Acquisition Time	1.3763
12	Acquisition Date	2019-08-23T12:25:00
13	Modification Date	2019-08-23T19:24:58
14	Class	
15	Spectrometer Frequency	125.80
16	Spectral Width	35714.3
17	Lowest Frequency	-5178.2
18	Nucleus	13C
19	Acquired Size	49152
20	Spectral Size	131072

Figure S 43: ^{13}C NMR of **14^{Bna}-cK** in THF-d_8 at room temperature.

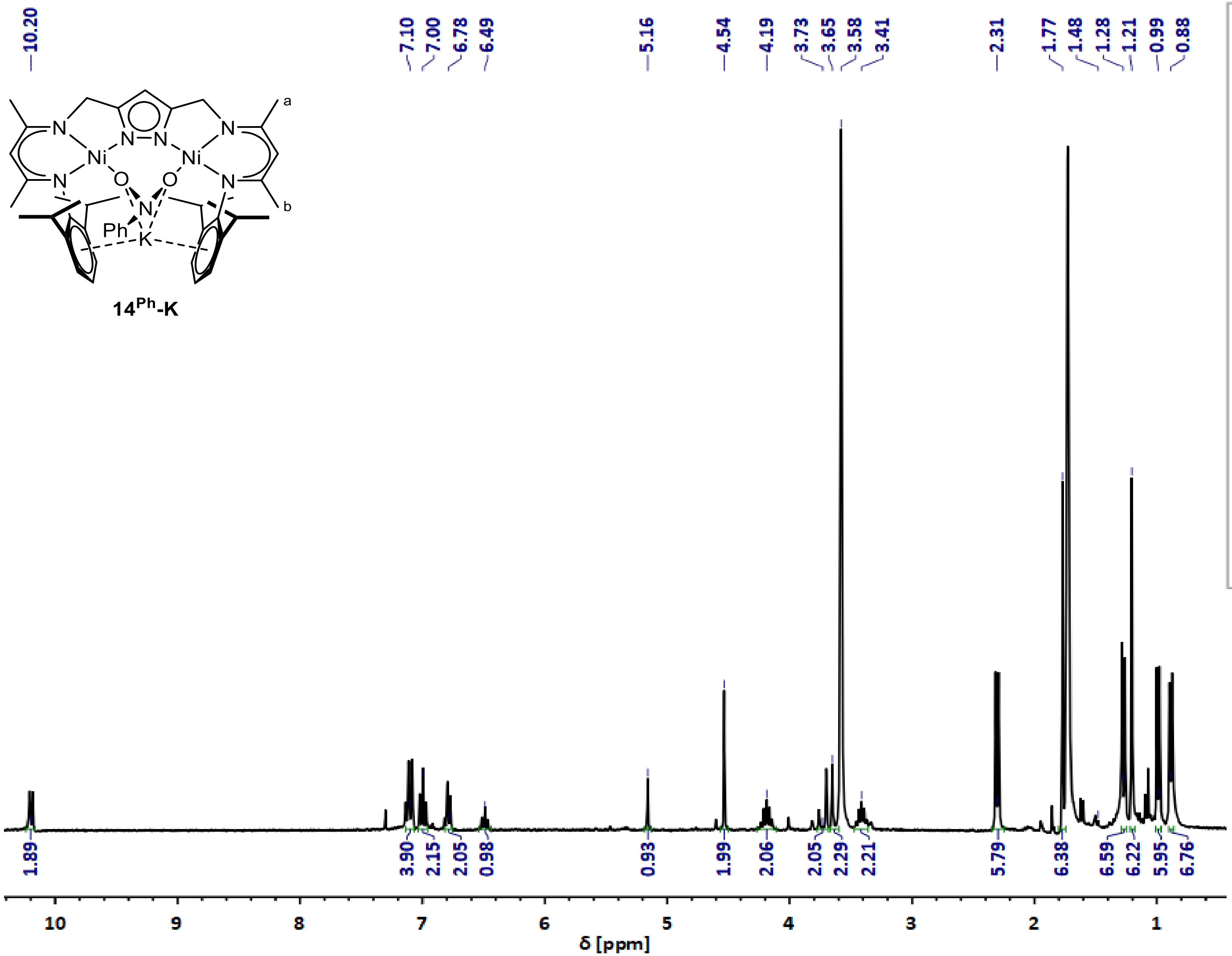

	Parameter	Value
1	Solvent	THF
2	Temperature	298.0
3	Pulse Sequence	zg30
4	Experiment	1D
5	Probe	Z862701_0063 (PA BBO 300S1 BBF-H&F-D-05 Z)
6	Number of Scans	32
7	Receiver Gain	207.7
8	Relaxation Delay	0.1000
9	Pulse Width	12.5000
10	Presaturation Frequency	
11	Acquisition Time	3.6351
12	Acquisition Date	2019-08-21T15:33:09
13	Modification Date	2019-08-21T15:33:09
14	Class	
15	Spectrometer Frequency	300.13
16	Spectral Width	9014.4
17	Lowest Frequency	-3017.2
18	Nucleus	1H
19	Acquired Size	32768
20	Spectral Size	65536

Figure S 44: ^{1}H NMR of **14^{Ph}-K** in THF-d$_8$ at room temperature.

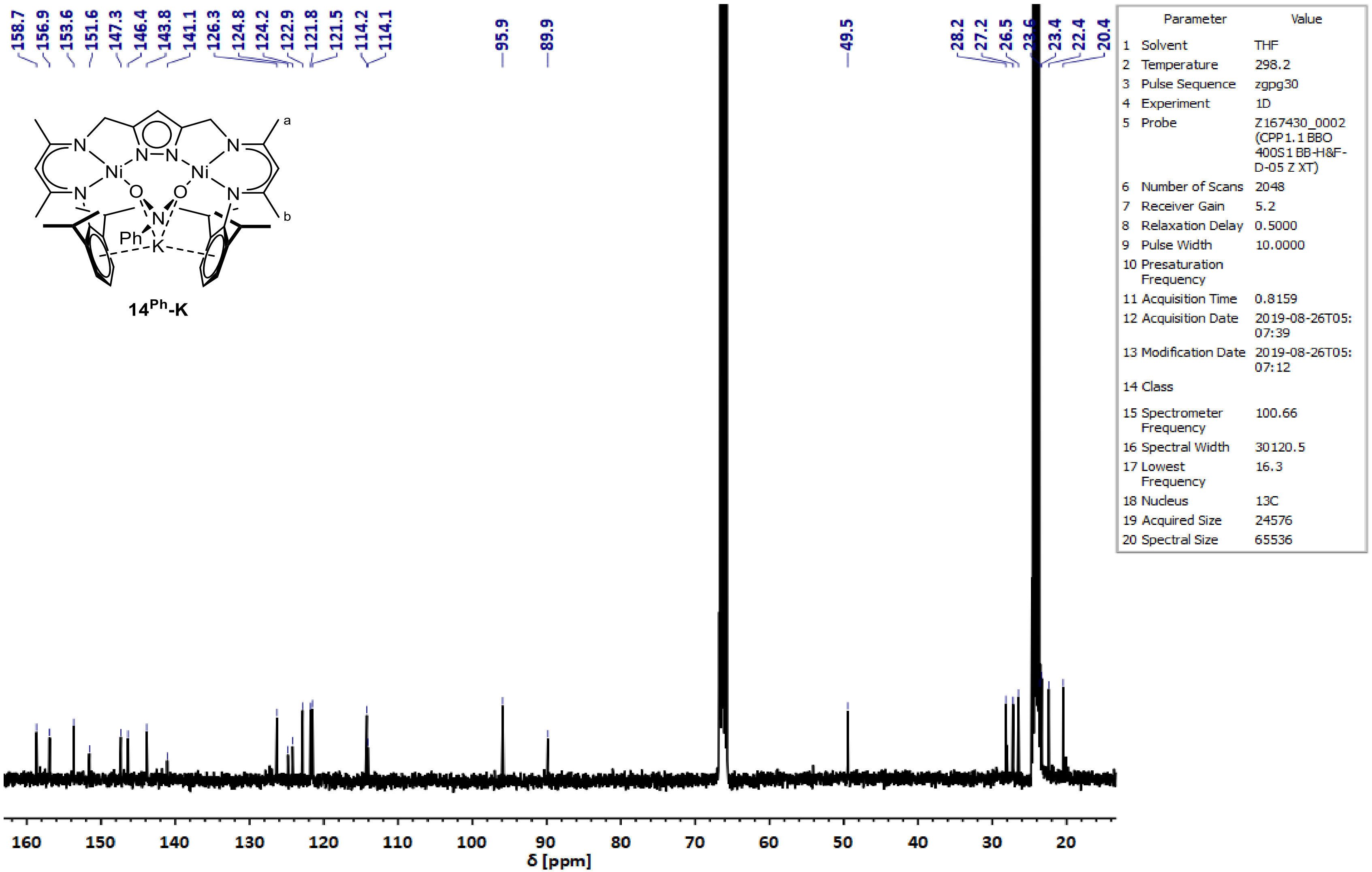

	Parameter	Value
1	Solvent	THF
2	Temperature	298.2
3	Pulse Sequence	zgpg30
4	Experiment	1D
5	Probe	Z167430_0002 (CPP1.1 BBO 400S1 BB-H&F-D-05 Z XT)
6	Number of Scans	2048
7	Receiver Gain	5.2
8	Relaxation Delay	0.5000
9	Pulse Width	10.0000
10	Presaturation Frequency	
11	Acquisition Time	0.8159
12	Acquisition Date	2019-08-26T05:07:39
13	Modification Date	2019-08-26T05:07:12
14	Class	
15	Spectrometer Frequency	100.66
16	Spectral Width	30120.5
17	Lowest Frequency	16.3
18	Nucleus	13C
19	Acquired Size	24576
20	Spectral Size	65536

Figure S 45: ^{13}C NMR of **14^{Ph}-K** in THF-d_8 at room temperature.

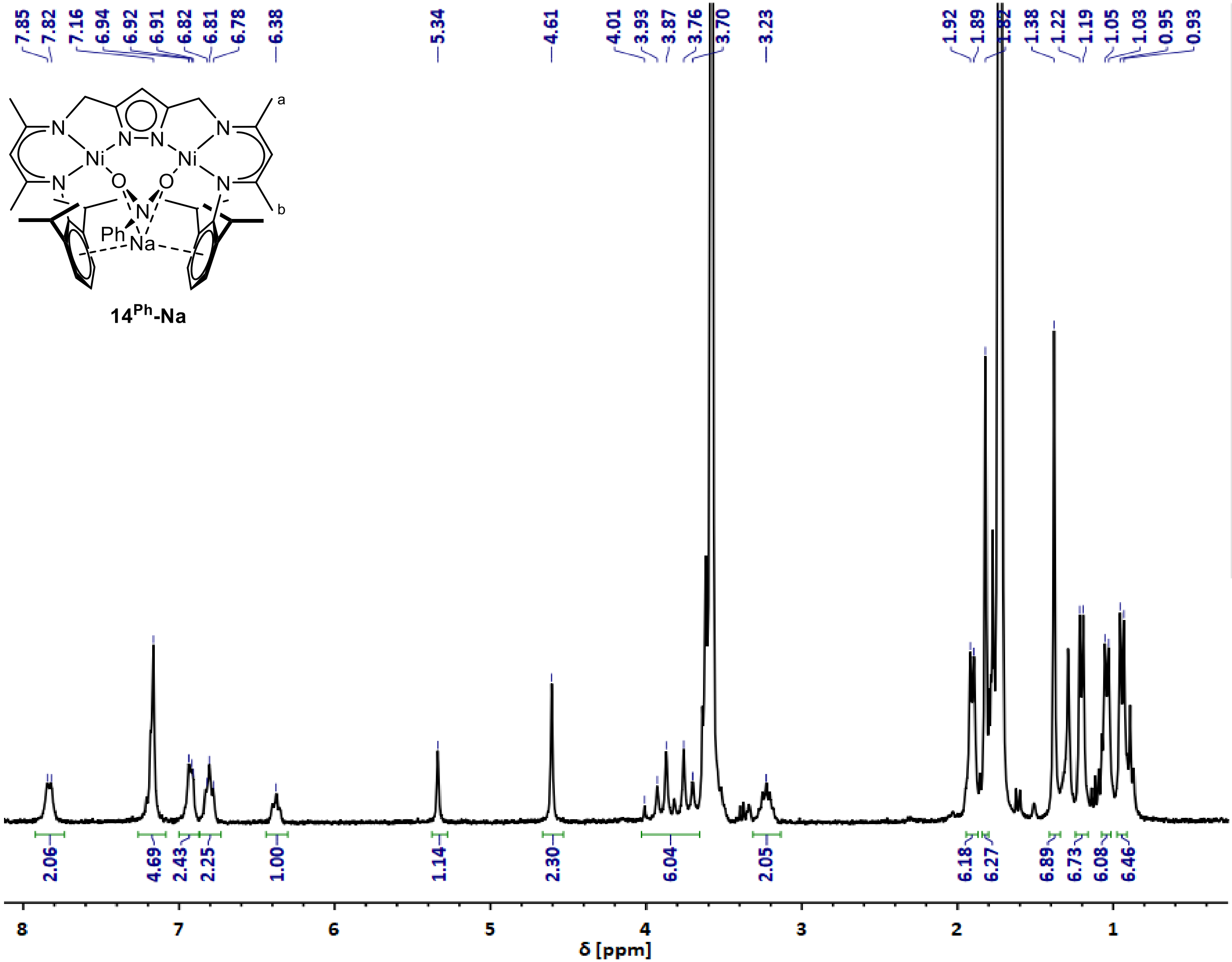

	Parameter	Value
1	Solvent	THF
2	Temperature	298.0
3	Pulse Sequence	zg30
4	Experiment	1D
5	Probe	Z104275_0147 (PA BBO 300S1 BBF-H-D-05 Z)
6	Number of Scans	16
7	Receiver Gain	207.7
8	Relaxation Delay	0.1000
9	Pulse Width	11.6000
10	Presaturation Frequency	
11	Acquisition Time	4.3691
12	Acquisition Date	2020-01-24T17:11:38
13	Modification Date	2020-01-24T17:11:38
14	Class	
15	Spectrometer Frequency	300.13
16	Spectral Width	7500.0
17	Lowest Frequency	-3160.8
18	Nucleus	1H
19	Acquired Size	32768
20	Spectral Size	65536

Figure S 46: ^{1}H NMR of **14^{Ph}-Na** in THF-d$_8$ at room temperature.

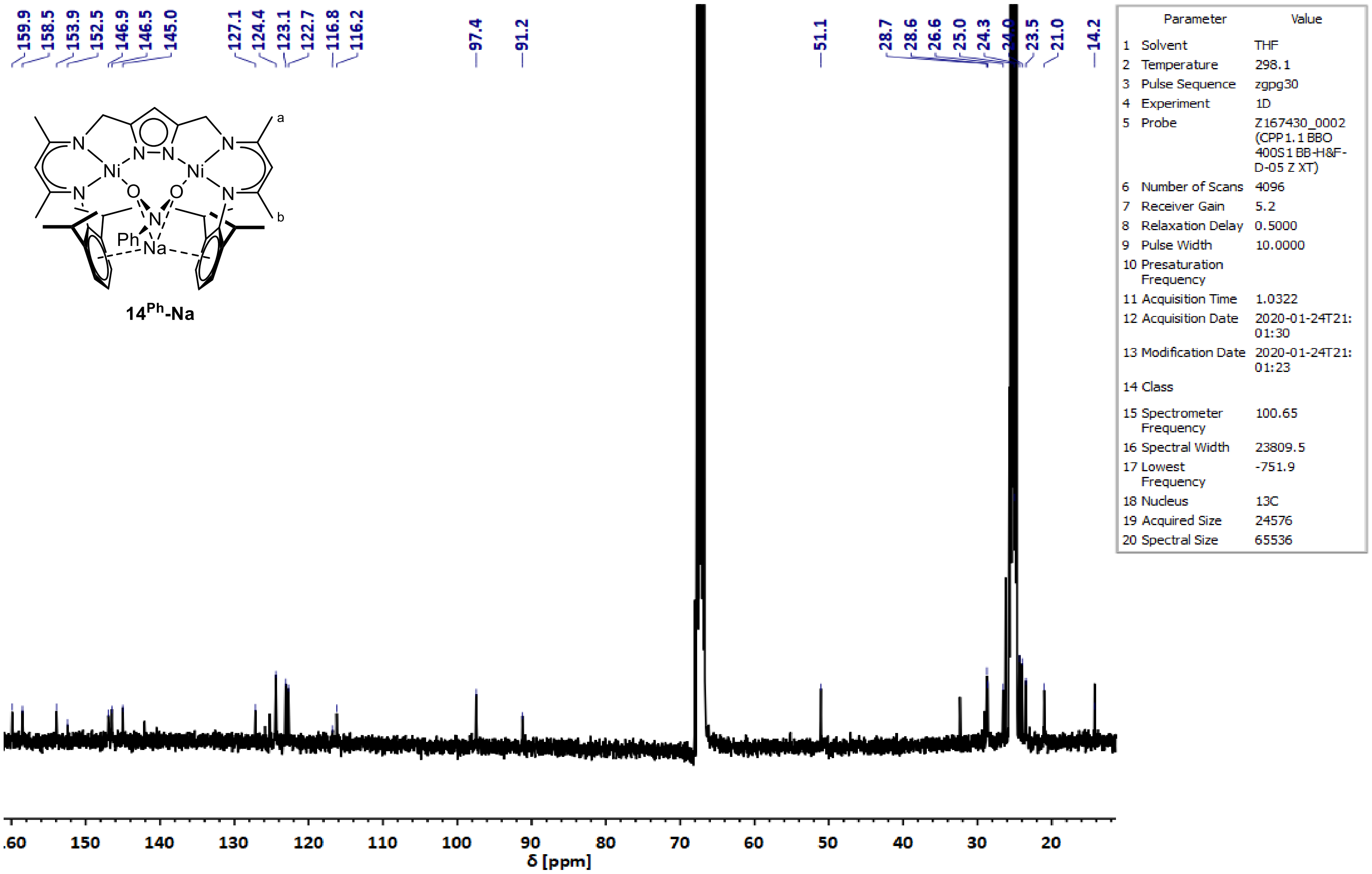

	Parameter	Value
1	Solvent	THF
2	Temperature	298.1
3	Pulse Sequence	zgpg30
4	Experiment	1D
5	Probe	Z167430_0002 (CPP1.1 BBO 400S1 BB-H&F-D-05 Z XT)
6	Number of Scans	4096
7	Receiver Gain	5.2
8	Relaxation Delay	0.5000
9	Pulse Width	10.0000
10	Presaturation Frequency	
11	Acquisition Time	1.0322
12	Acquisition Date	2020-01-24T21:01:30
13	Modification Date	2020-01-24T21:01:23
14	Class	
15	Spectrometer Frequency	100.65
16	Spectral Width	23809.5
17	Lowest Frequency	-751.9
18	Nucleus	13C
19	Acquired Size	24576
20	Spectral Size	65536

Figure S 47: ^{13}C NMR of **14^{Ph}-Na** in THF-d_8 at room temperature.

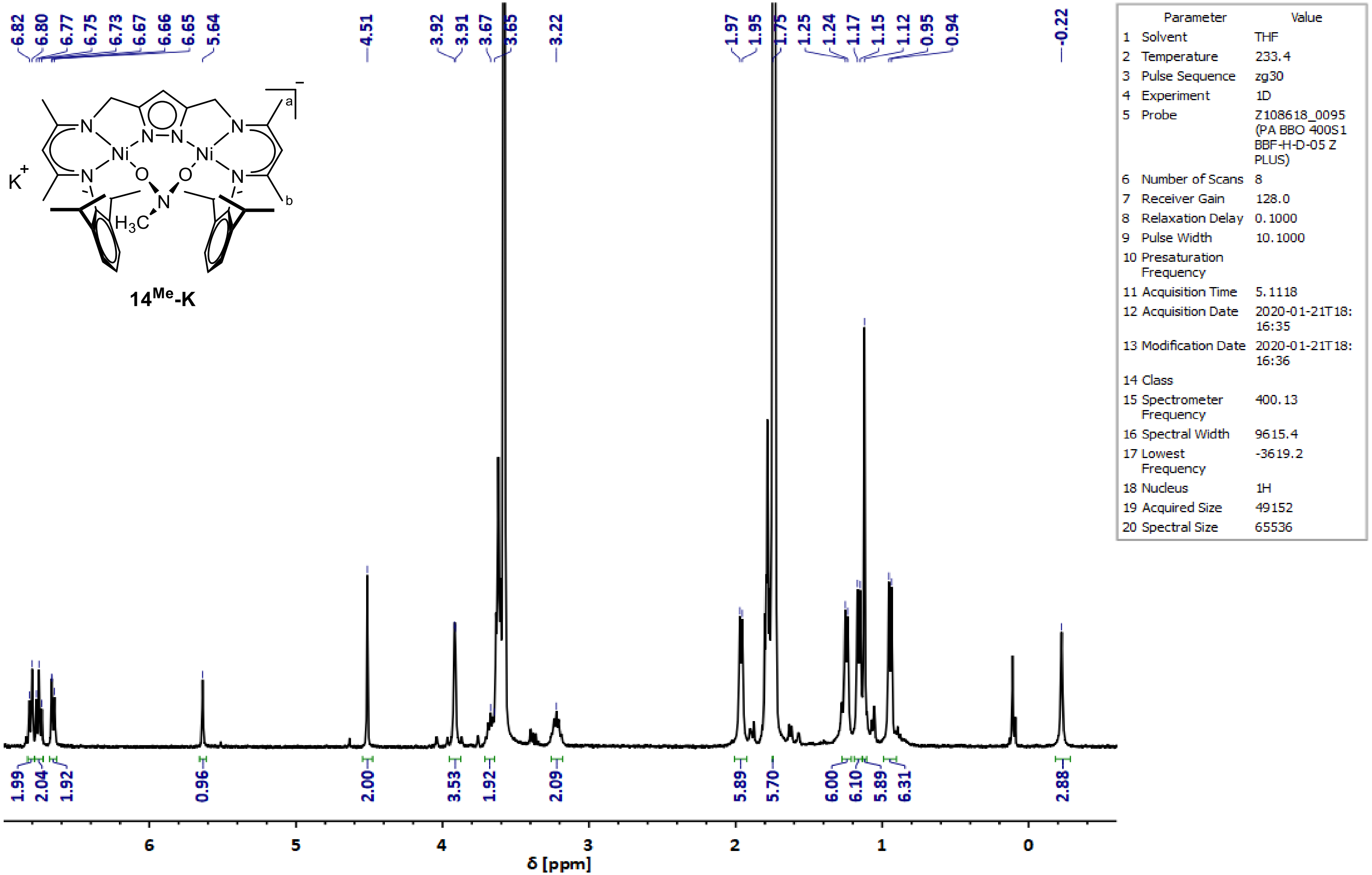

$\mathbf{14^{Me}}$**-K**

	Parameter	Value
1	Solvent	THF
2	Temperature	233.4
3	Pulse Sequence	zg30
4	Experiment	1D
5	Probe	Z108618_0095 (PA BBO 400S1 BBF-H-D-05 Z PLUS)
6	Number of Scans	8
7	Receiver Gain	128.0
8	Relaxation Delay	0.1000
9	Pulse Width	10.1000
10	Presaturation Frequency	
11	Acquisition Time	5.1118
12	Acquisition Date	2020-01-21T18:16:35
13	Modification Date	2020-01-21T18:16:36
14	Class	
15	Spectrometer Frequency	400.13
16	Spectral Width	9615.4
17	Lowest Frequency	-3619.2
18	Nucleus	1H
19	Acquired Size	49152
20	Spectral Size	65536

Figure S 48: ^{1}H NMR of $\mathbf{14^{Me}}$**-K** in THF-d_8 at -40 °C.

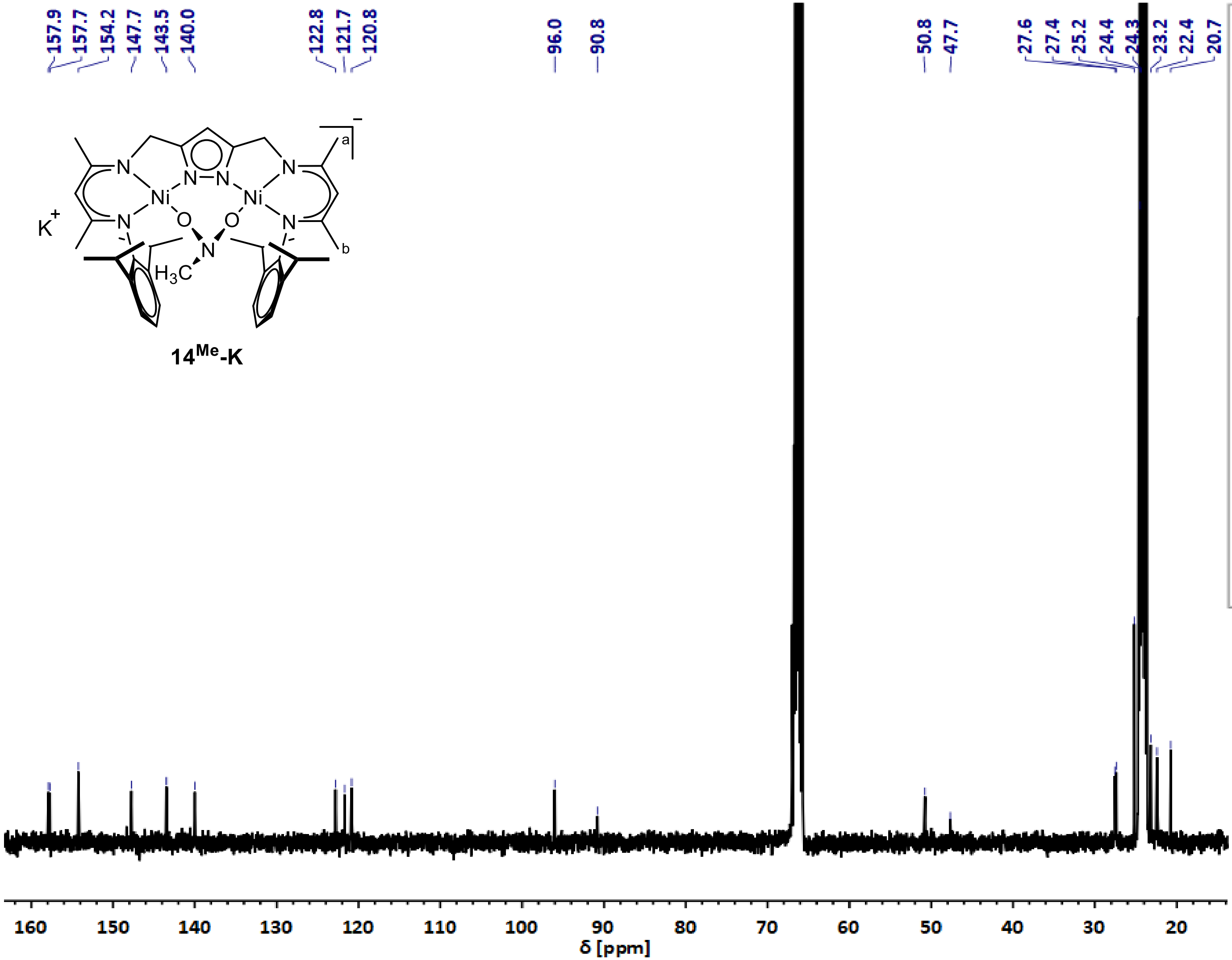

	Parameter	Value
1	Solvent	THF
2	Temperature	231.1
3	Pulse Sequence	zgdc30
4	Experiment	1D
5	Probe	Z108618_0095 (PA BBO 400S1 BBF-H-D-05 Z PLUS)
6	Number of Scans	4096
7	Receiver Gain	101.0
8	Relaxation Delay	0.5000
9	Pulse Width	9.7000
10	Presaturation Frequency	
11	Acquisition Time	0.9437
12	Acquisition Date	2020-01-21T20:28:01
13	Modification Date	2020-01-21T20:28:01
14	Class	
15	Spectrometer Frequency	100.62
16	Spectral Width	26041.7
17	Lowest Frequency	-3995.2
18	Nucleus	13C
19	Acquired Size	24576
20	Spectral Size	65536

Figure S 49: ^{13}C NMR of **14^{Me}-K** in THF-d_8 at -40 °C.

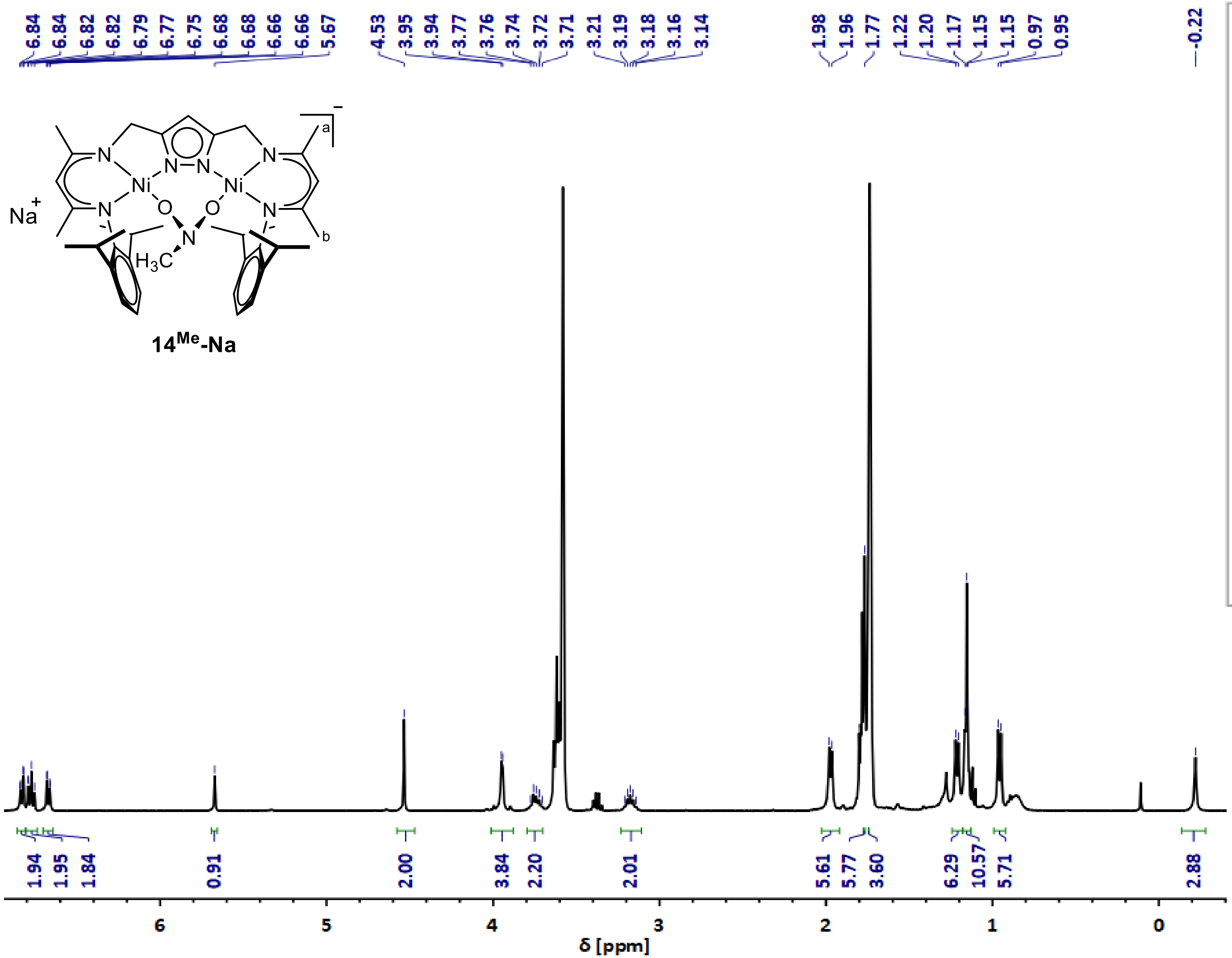

	Parameter	Value
1	Solvent	THF
2	Temperature	233.2
3	Pulse Sequence	zg30
4	Experiment	1D
5	Probe	Z108618_0095 (PA BBO 400S1 BBF-H-D-05 Z PLUS)
6	Number of Scans	32
7	Receiver Gain	128.0
8	Relaxation Delay	0.1000
9	Pulse Width	10.1000
10	Presaturation Frequency	
11	Acquisition Time	5.1118
12	Acquisition Date	2020-02-21T16:56:39
13	Modification Date	2020-02-21T16:56:39
14	Class	
15	Spectrometer Frequency	400.13
16	Spectral Width	9615.4
17	Lowest Frequency	-3620.2
18	Nucleus	1H
19	Acquired Size	49152
20	Spectral Size	65536

Figure S 50: ^{1}H NMR of **14^{Me}-Na** in THF-d$_8$ at -40 °C.

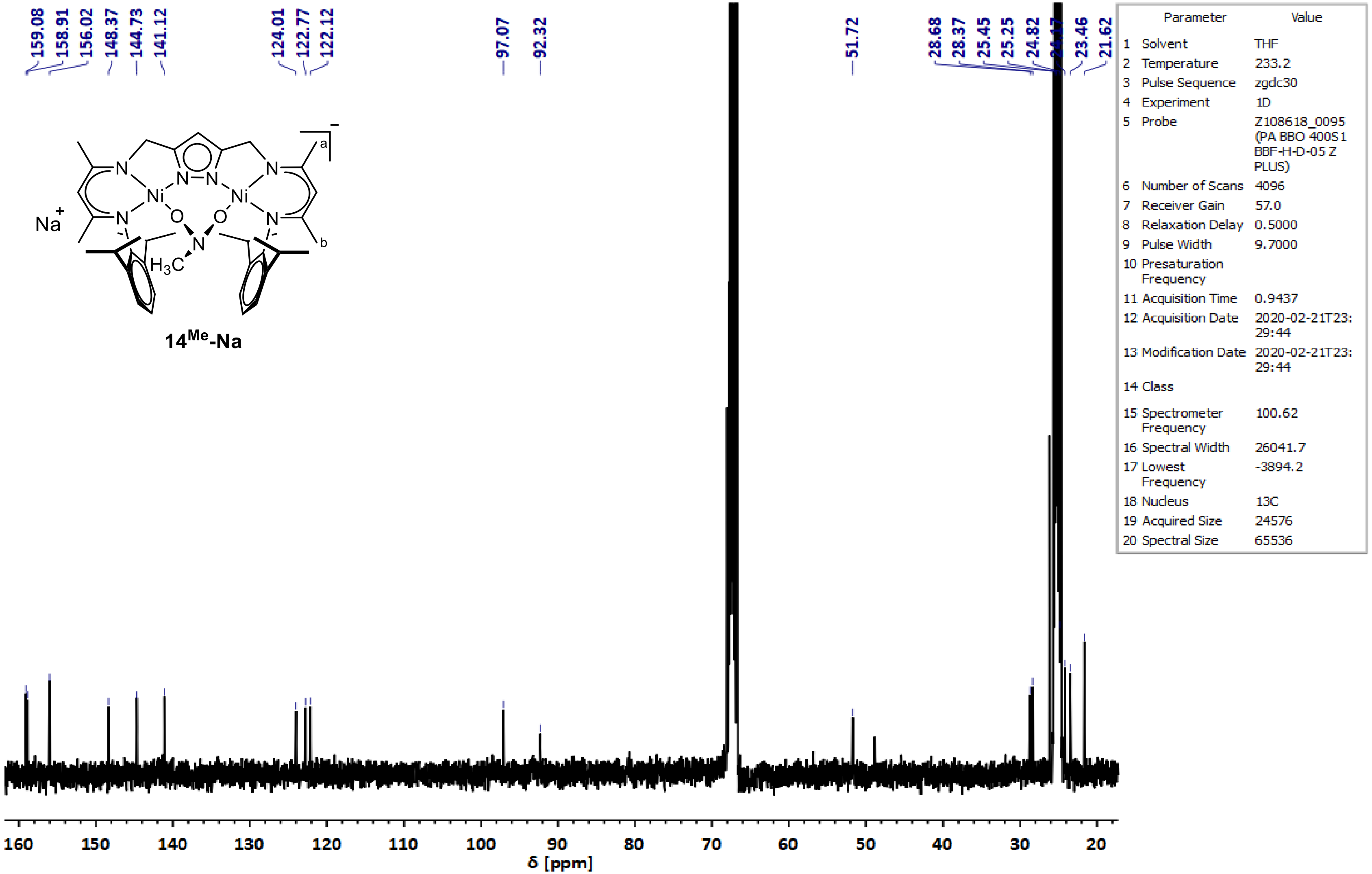

	Parameter	Value
1	Solvent	THF
2	Temperature	233.2
3	Pulse Sequence	zgdc30
4	Experiment	1D
5	Probe	Z108618_0095 (PA BBO 400S1 BBF-H-D-05 Z PLUS)
6	Number of Scans	4096
7	Receiver Gain	57.0
8	Relaxation Delay	0.5000
9	Pulse Width	9.7000
10	Presaturation Frequency	
11	Acquisition Time	0.9437
12	Acquisition Date	2020-02-21T23:29:44
13	Modification Date	2020-02-21T23:29:44
14	Class	
15	Spectrometer Frequency	100.62
16	Spectral Width	26041.7
17	Lowest Frequency	-3894.2
18	Nucleus	13C
19	Acquired Size	24576
20	Spectral Size	65536

Figure S 51: ^{13}C NMR of **14^{Me}-Na** in THF-d_8 at -40 °C.

9.2 IR Data

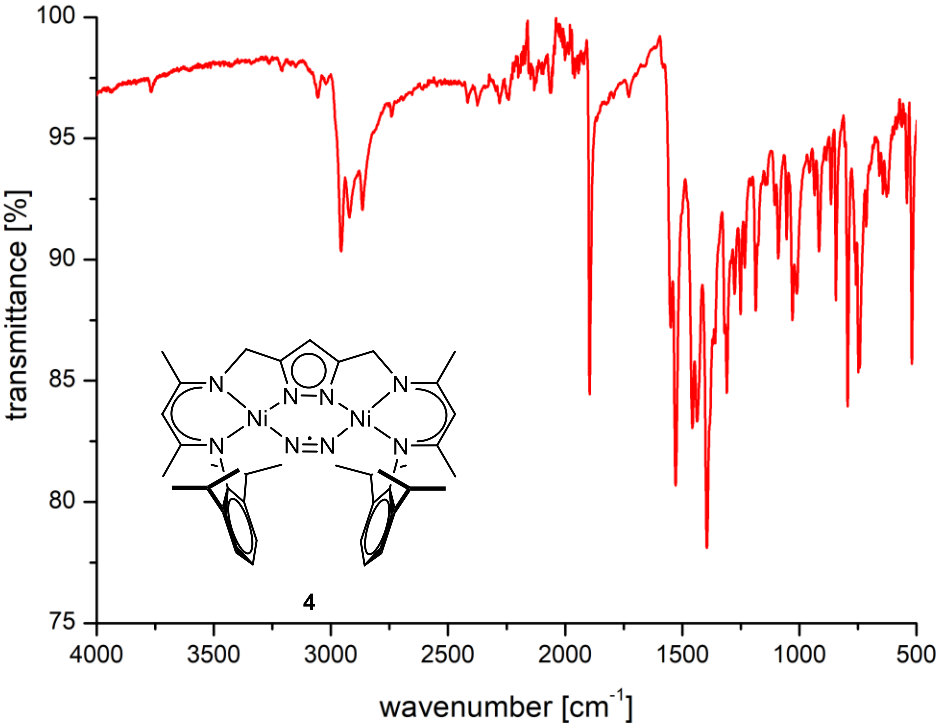

Figure S 52: ATR IR spectrum of solid material of **4.**

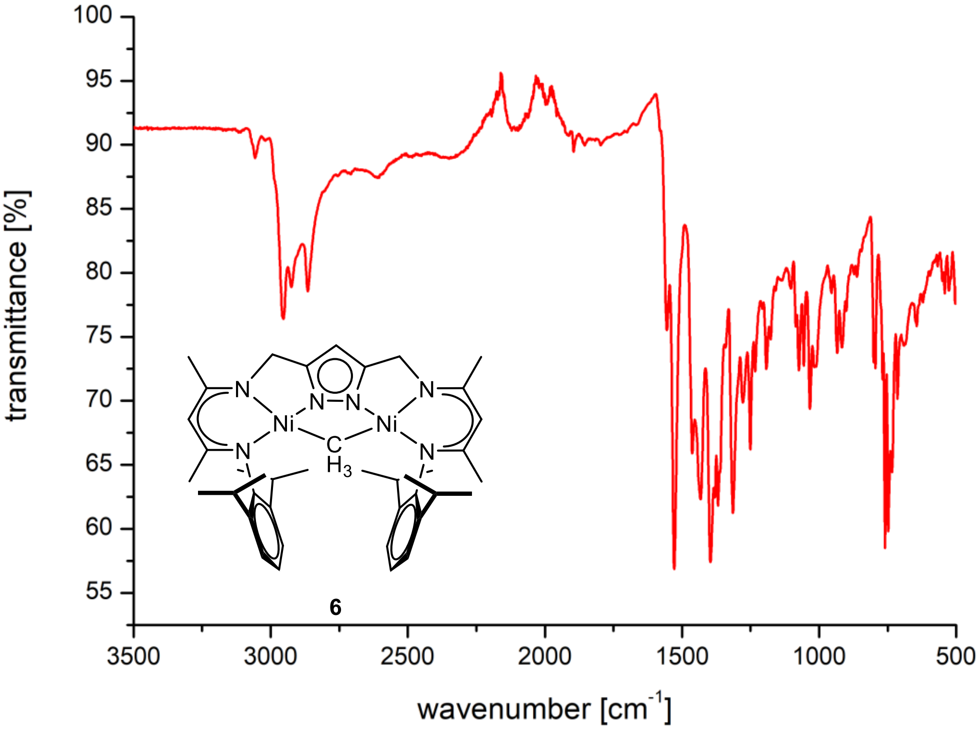

Figure S 53: ATR IR spectrum of solid material of **6.**

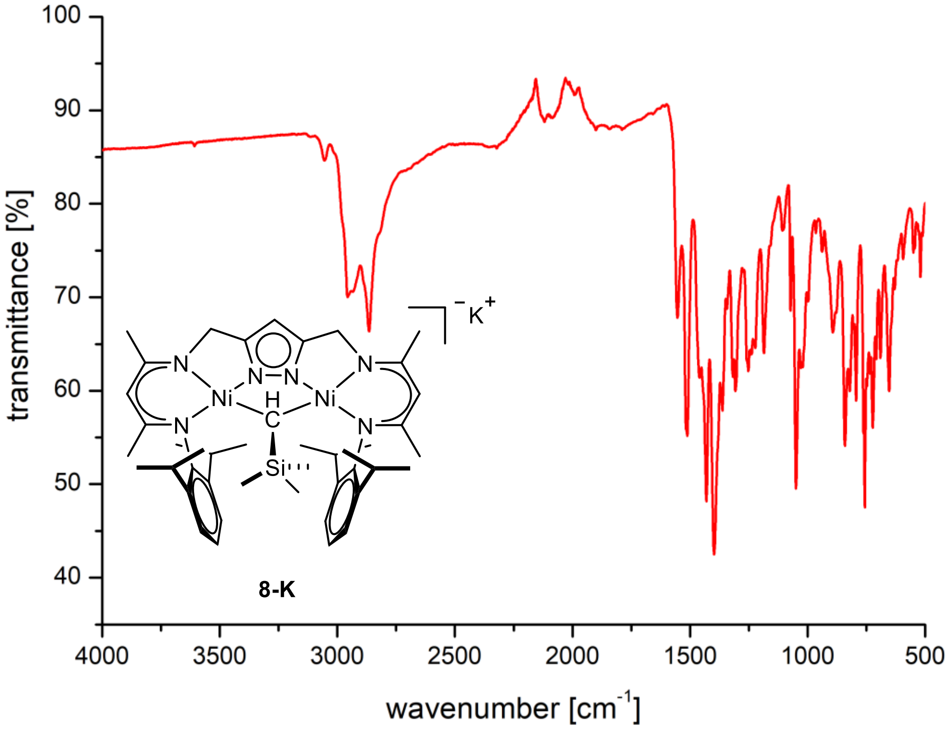

Figure S 54: ATR IR spectrum of solid material of **8-K.**

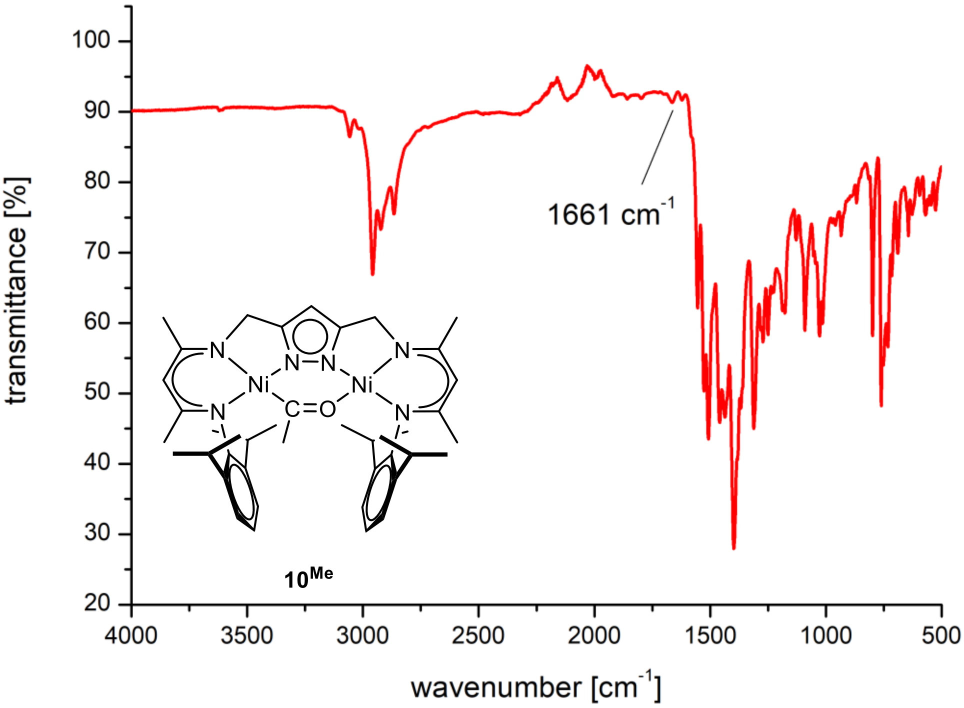

Figure S 55: ATR IR spectrum of solid material of **10^{Me}.**

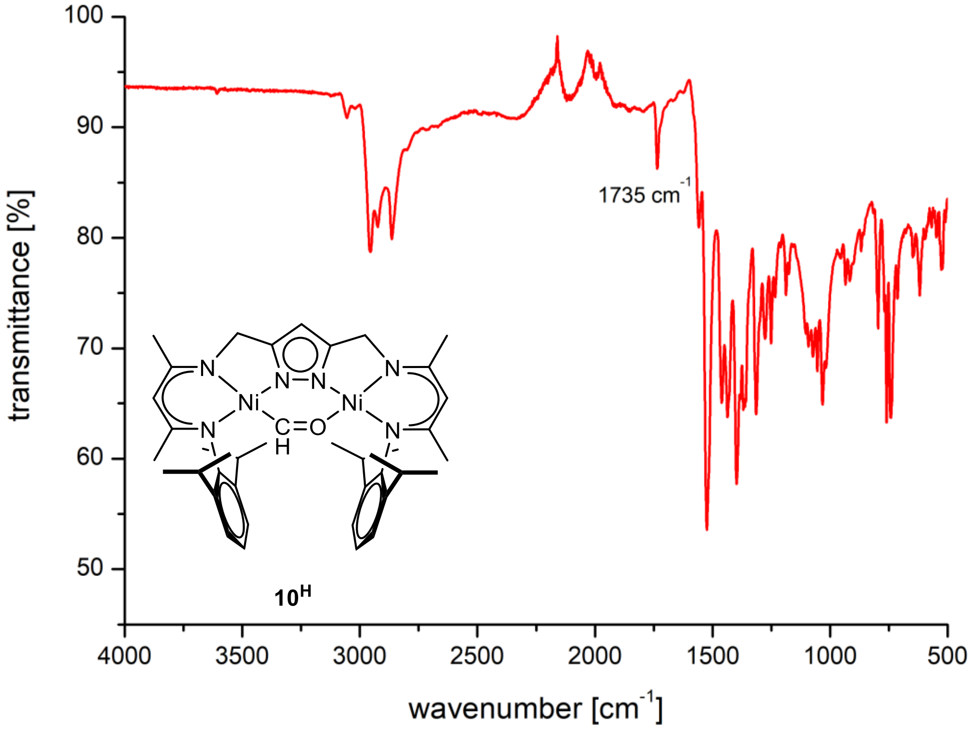

Figure S 56: ATR IR spectrum of solid material of **10^{H}.**

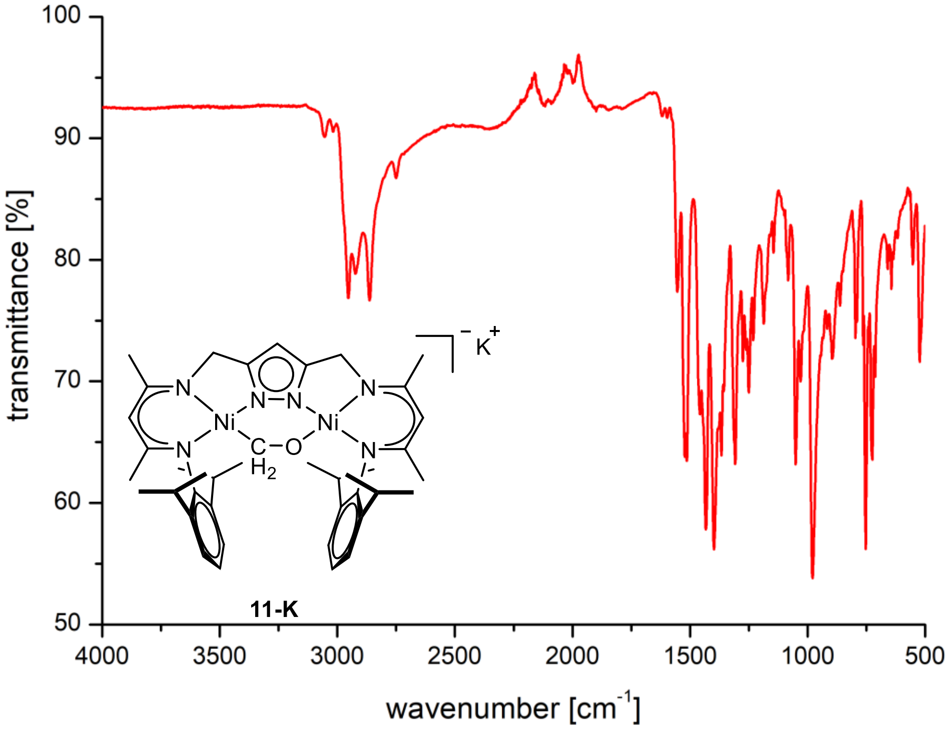

Figure S 57: ATR IR spectrum of solid material of **11-K.**

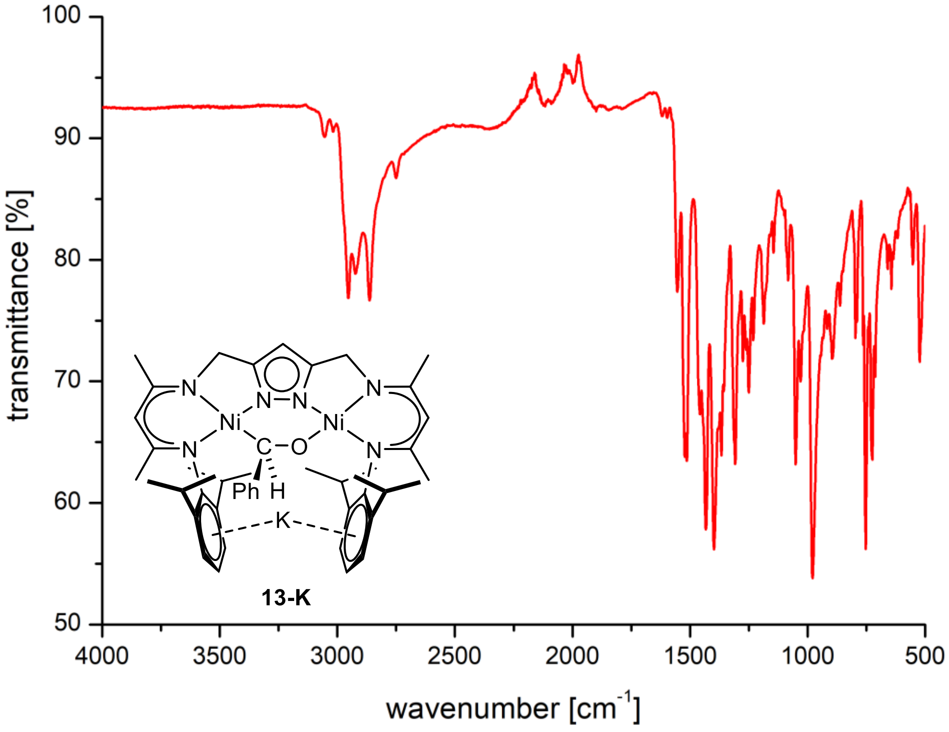

Figure S 58: ATR IR spectrum of solid material of **13-K.**

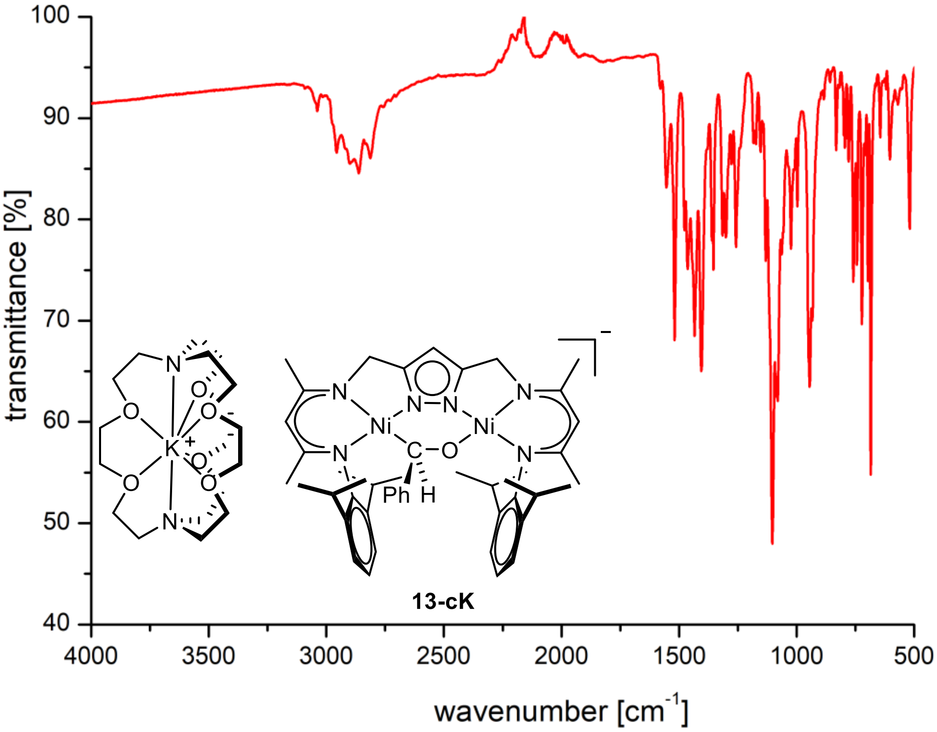

Figure S 59: ATR IR spectrum of solid material of **13-cK.**

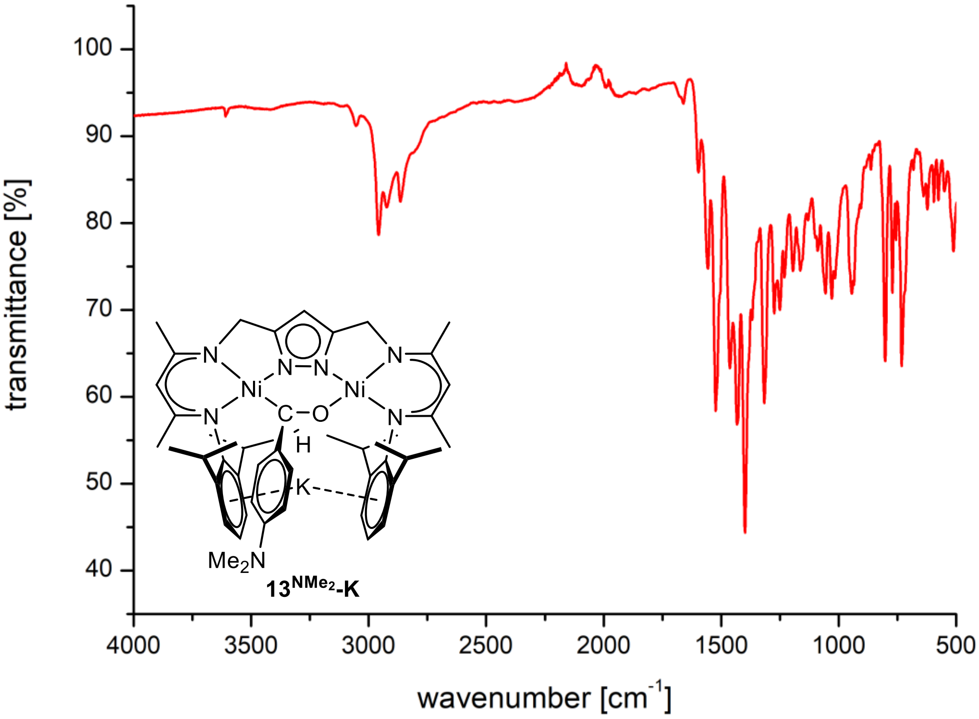

Figure S 60: ATR IR spectrum of solid material of **13^{NMe_2}-K.**

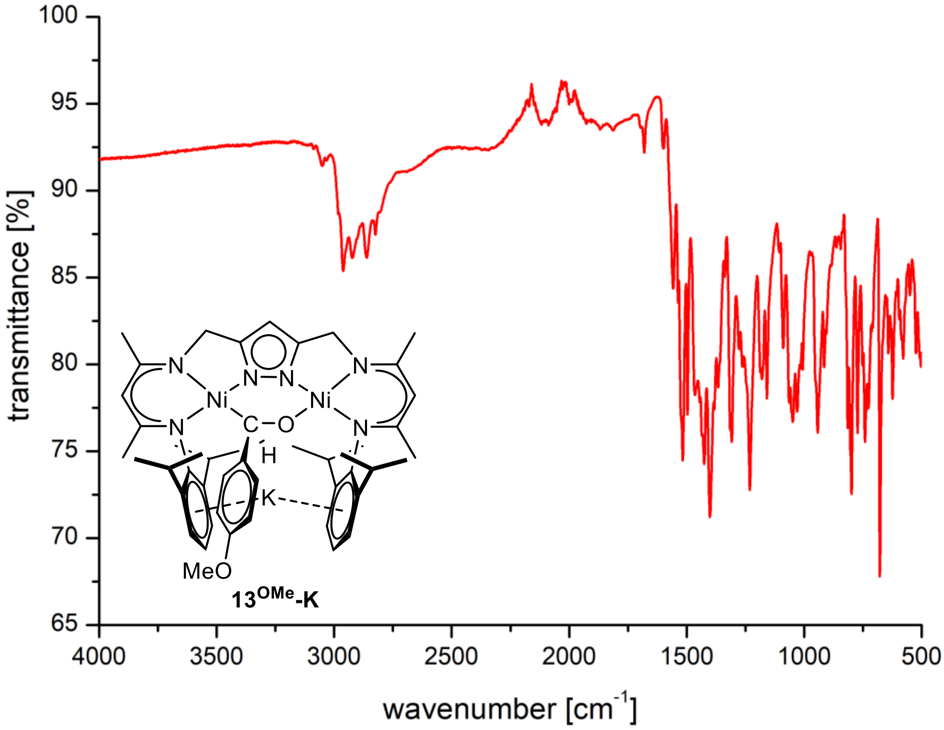

Figure S 61: ATR IR spectrum of solid material of **13^{OMe}-K.**

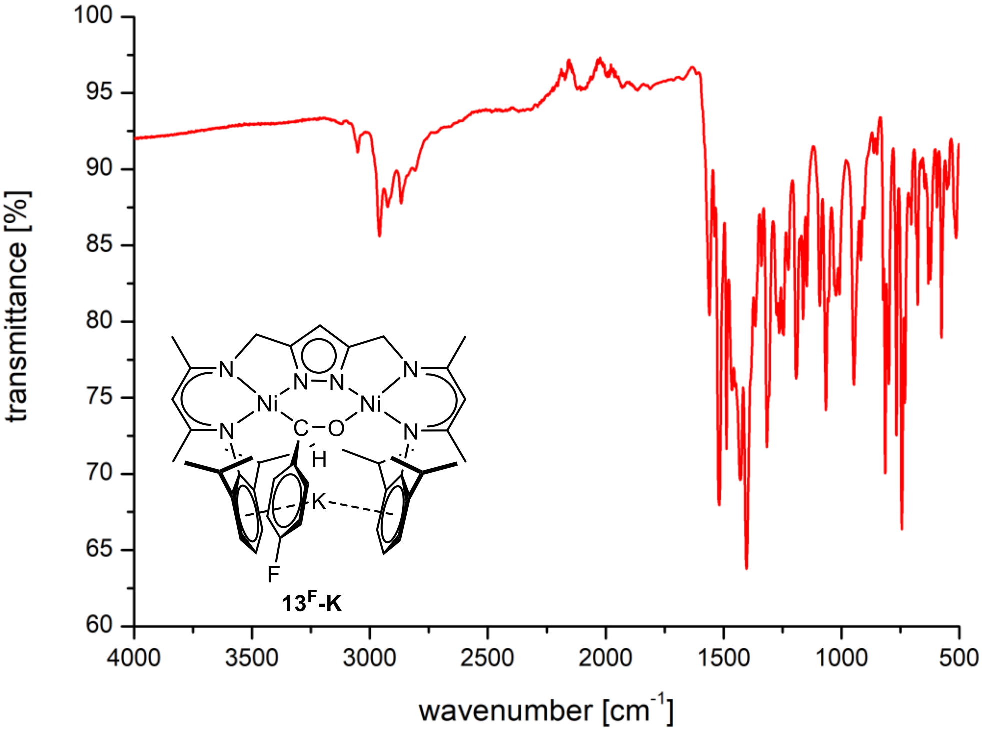

Figure S 62: ATR IR spectrum of solid material of **13^{F}-K.**

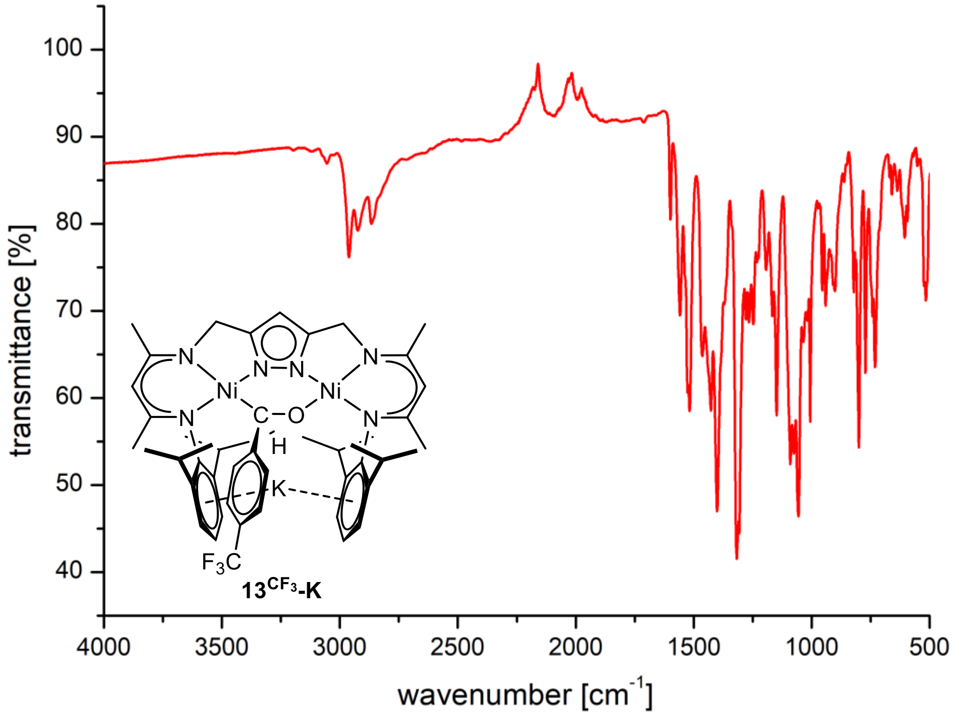

Figure S 63: ATR IR spectrum of solid material of **13^{CF_3}-K.**

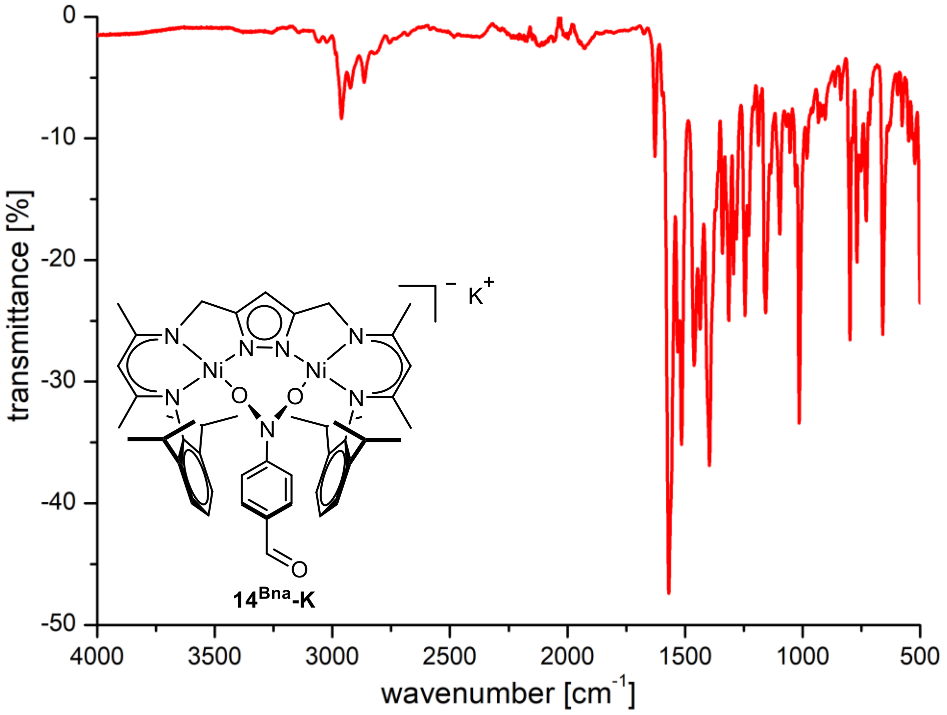

Figure S 64: ATR IR spectrum of solid material of **14^{Bna}-K.**

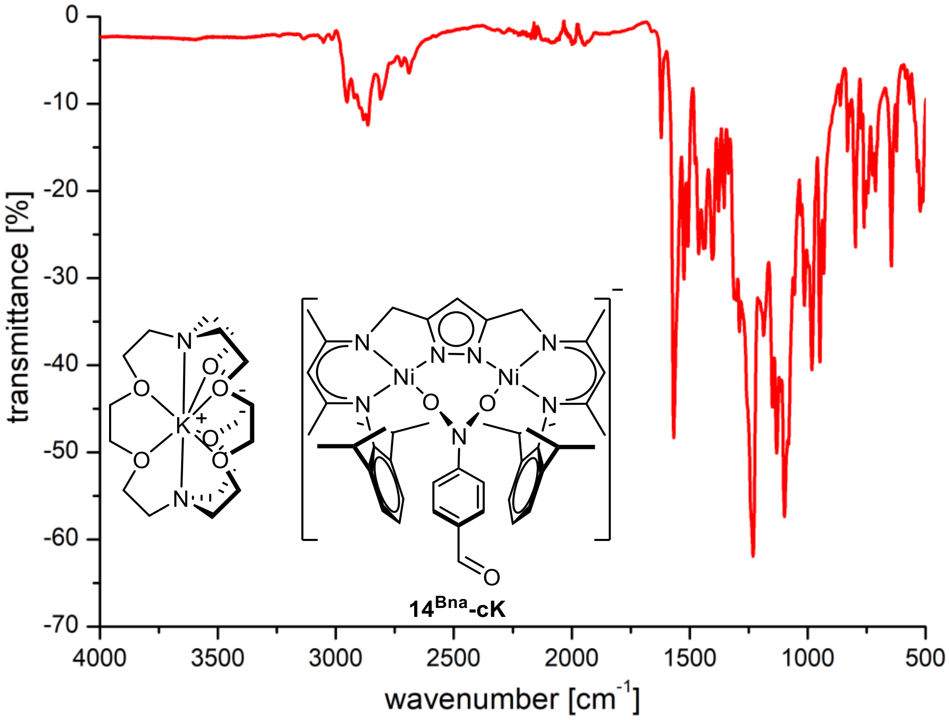

Figure S 65: ATR IR spectrum of solid material of **14^{Bna}-cK.**

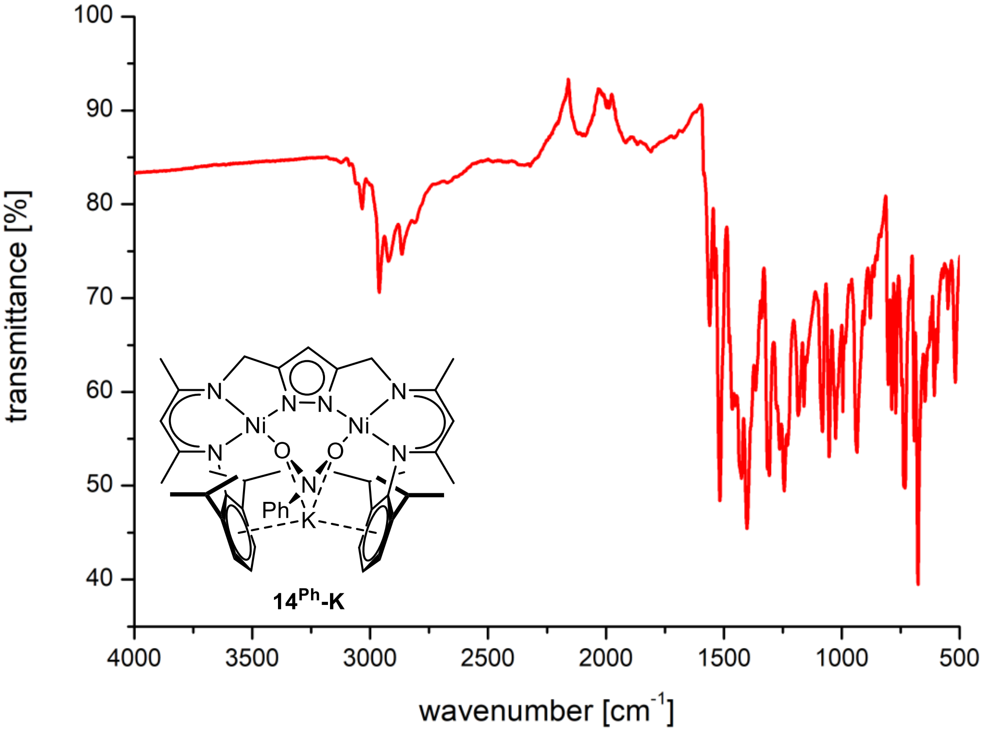

Figure S 66: ATR IR spectrum of solid material of **14^{Ph}-K.**

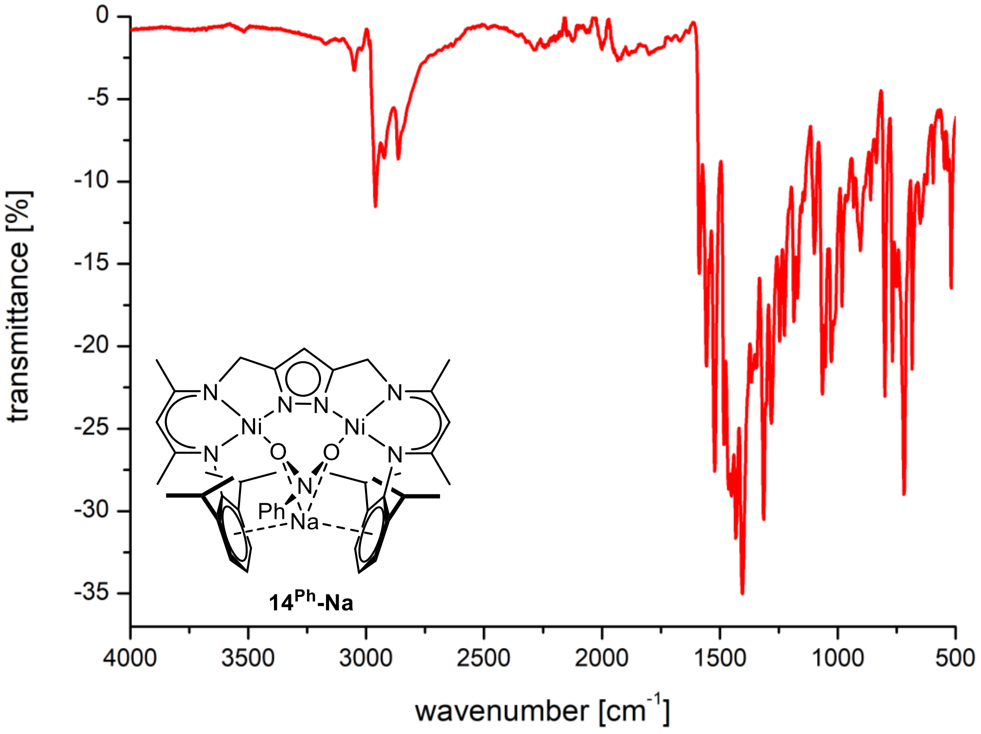

Figure S 67: ATR IR spectrum of solid material of **14^{Ph}-Na.**

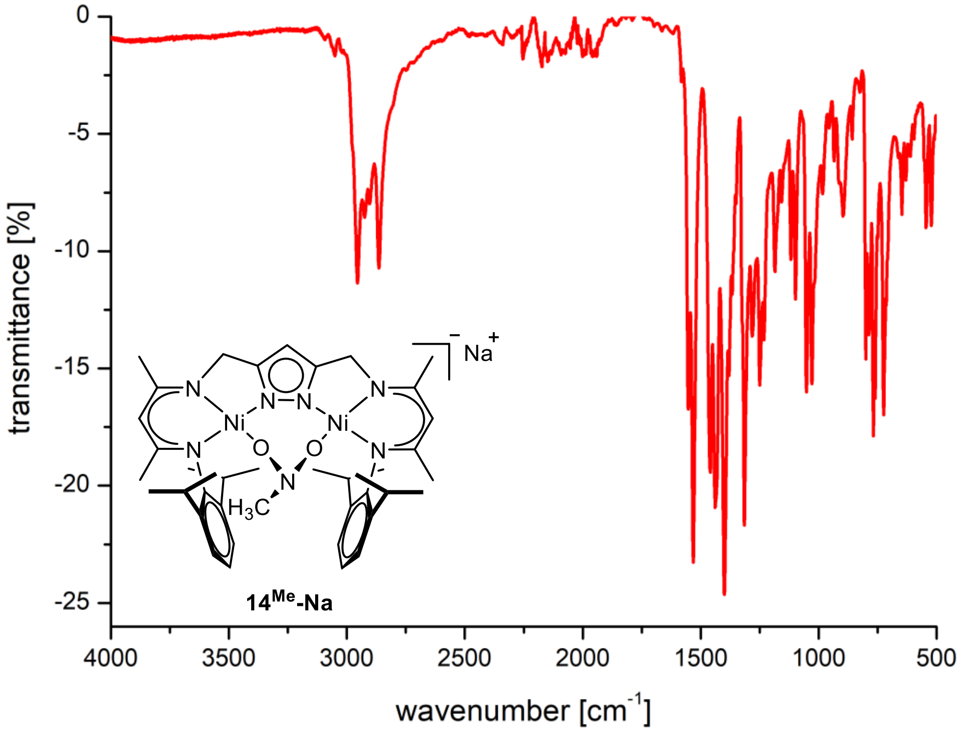

Figure S 68: ATR IR spectrum of solid material of **14^{Me}-Na.**

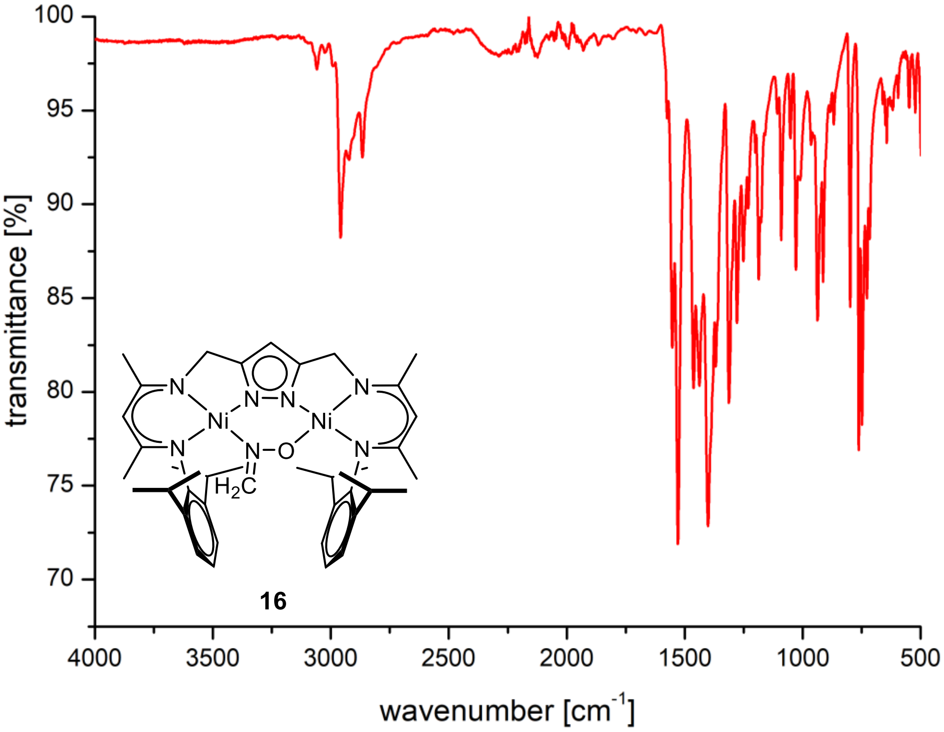

Figure S 69: ATR IR spectrum of solid material of **16.**

9.3 UV-vis Data

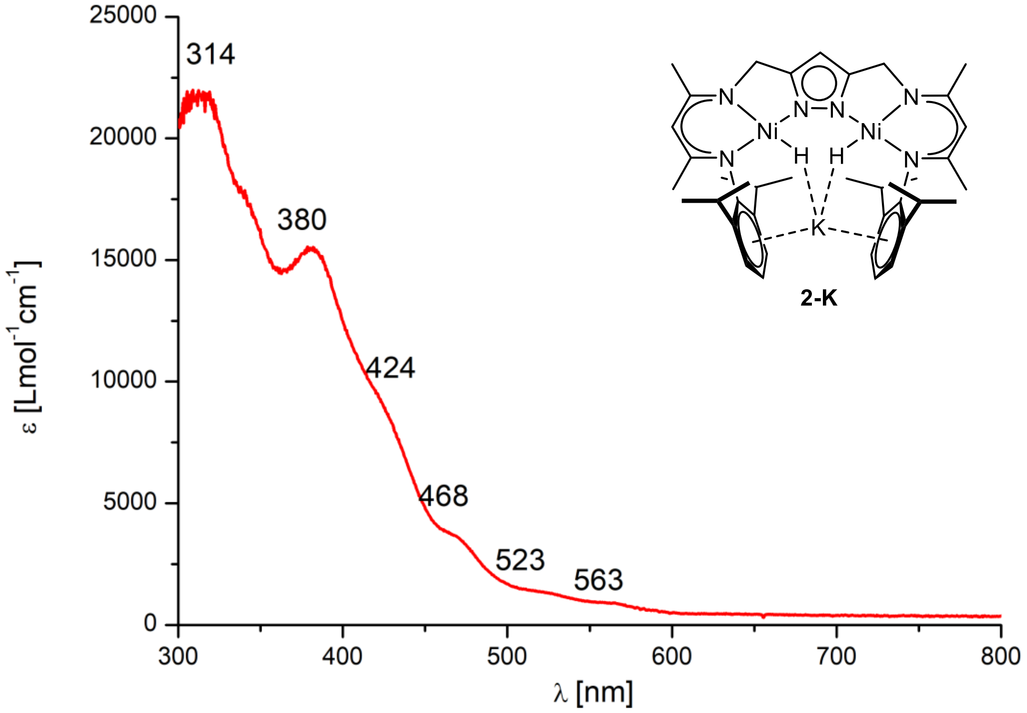

Figure S 70: UV-vis spectrum of **2-K** in THF at room temperature.

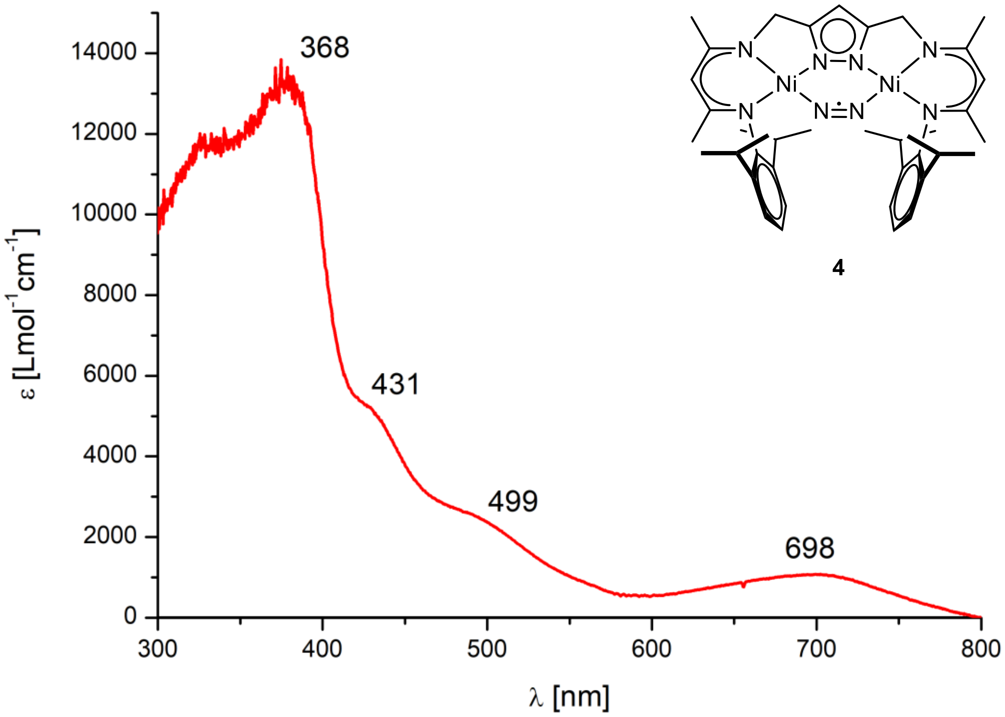

Figure S 71: UV-vis spectrum of **4** in THF at room temperature.

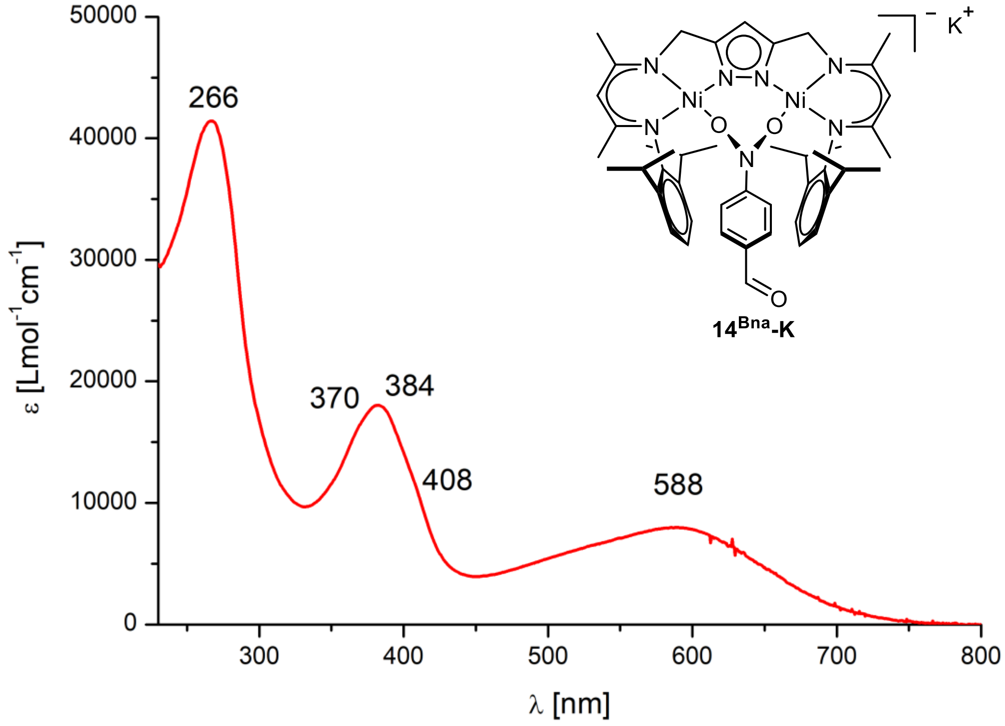

Figure S 72: UV-vis spectrum of **14^{Bna}-K** in THF at room temperature.

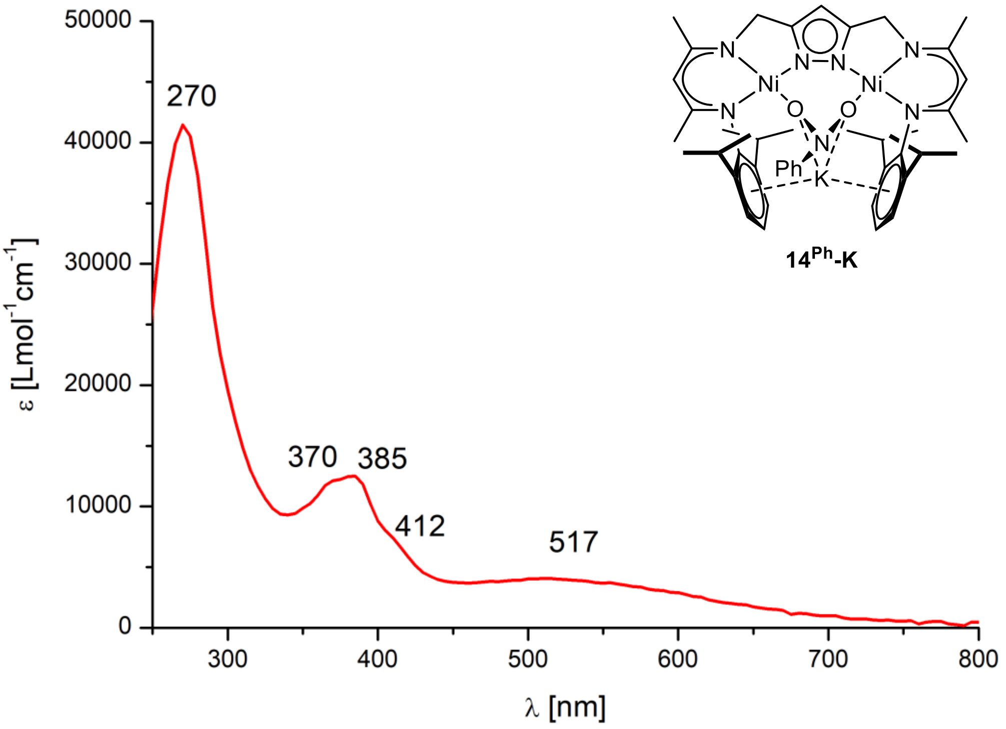

Figure S 73: UV-vis spectrum of **14^{Ph}-K** in THF at room temperature.

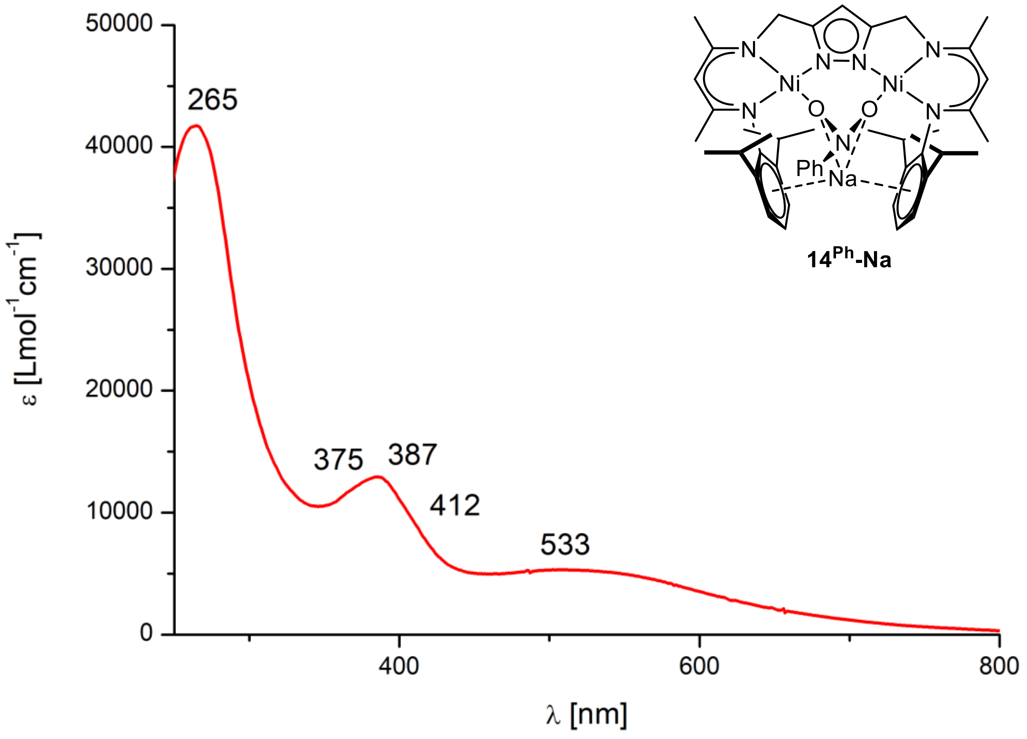

Figure S 74: UV-vis spectrum of **14^{Ph}-Na** in THF at room temperature.

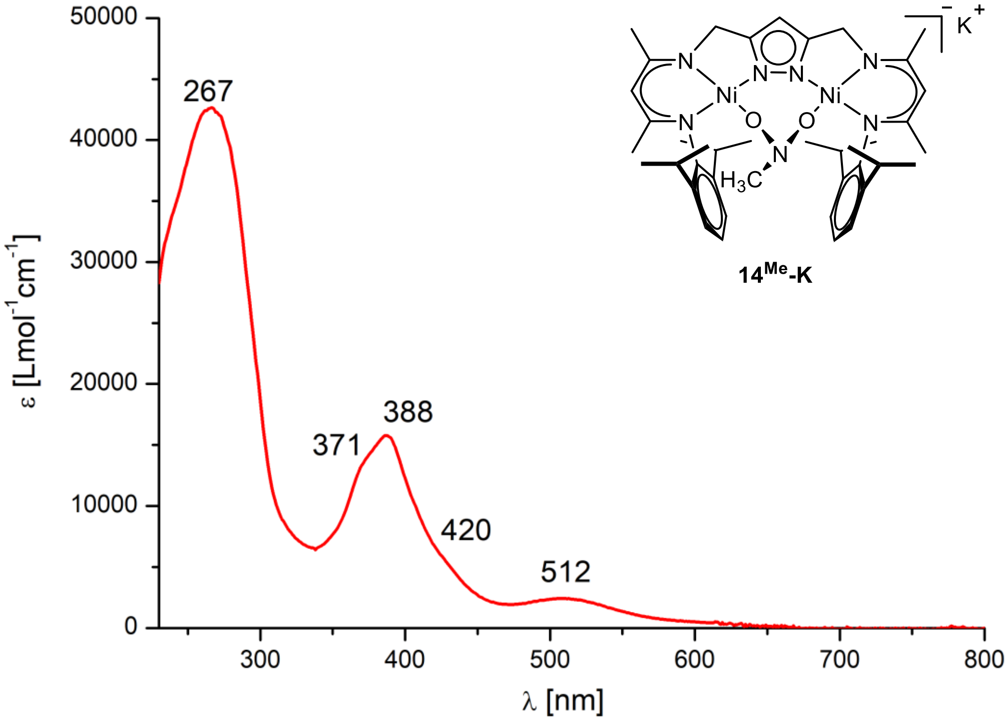

Figure S 75: UV-vis spectrum of **14^{Me}-K** in THF at room temperature.

9.4 Mass Spectrometry Data

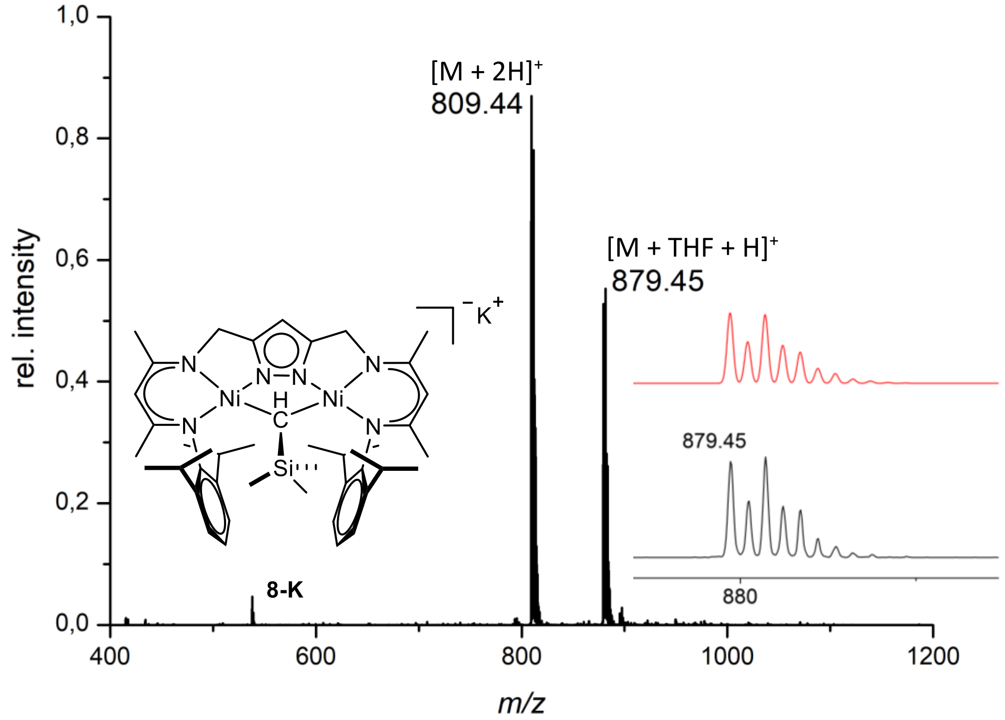

Figure S 76: ESI(+) MS of **8-K**.

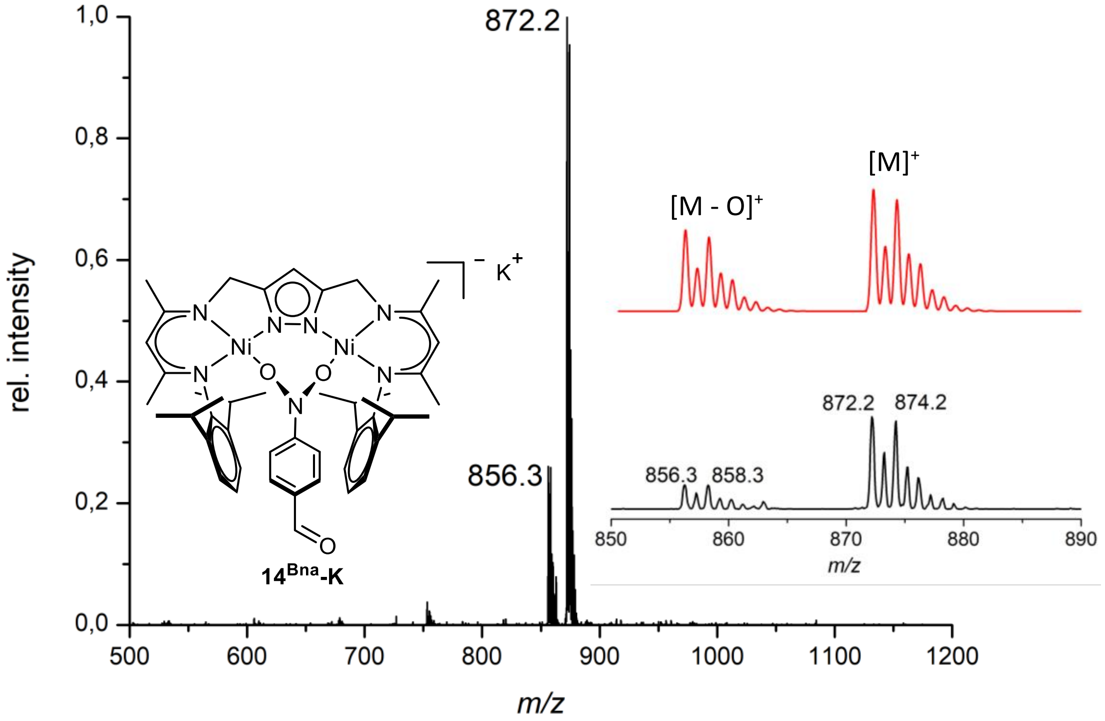

Figure S 77: ESI(+) MS of **14^{Bna}-K**.

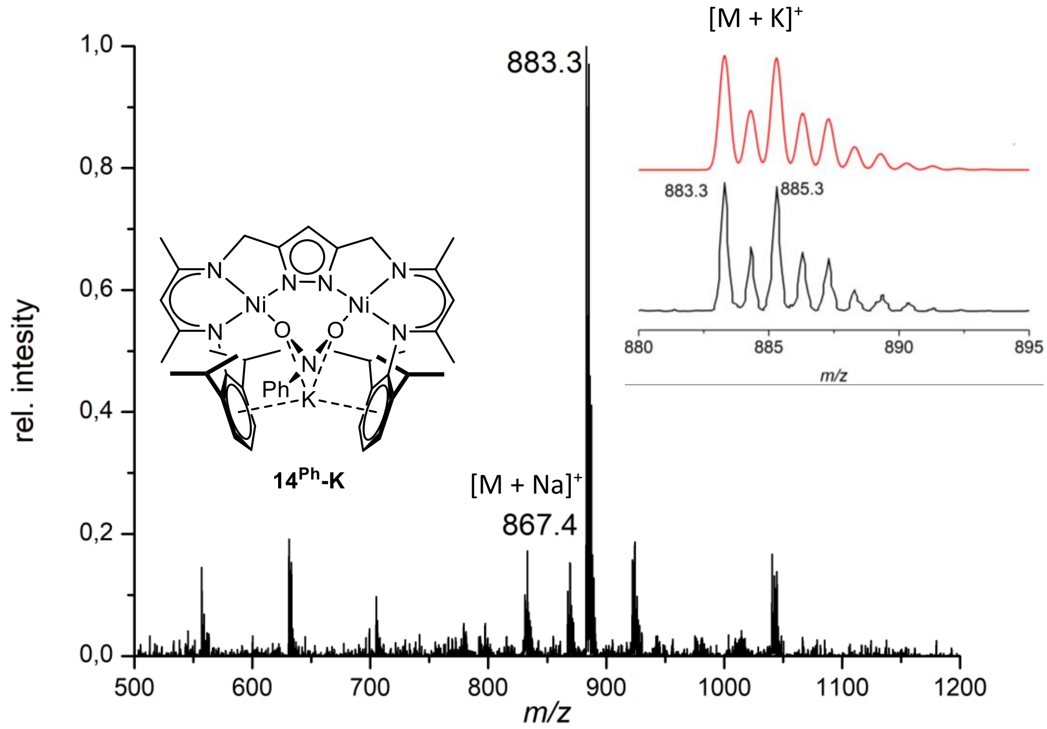

Figure S 78: ESI(+) MS of **14^{Ph}-K**.

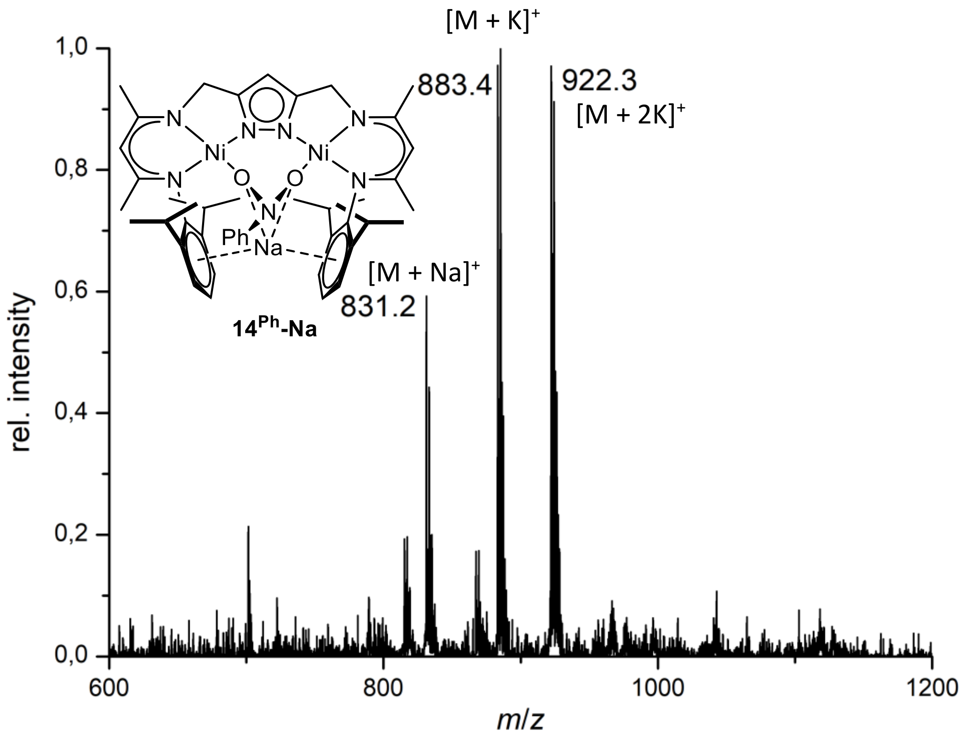

Figure S 79: ESI(+) MS of **14^{Ph}-Na**.

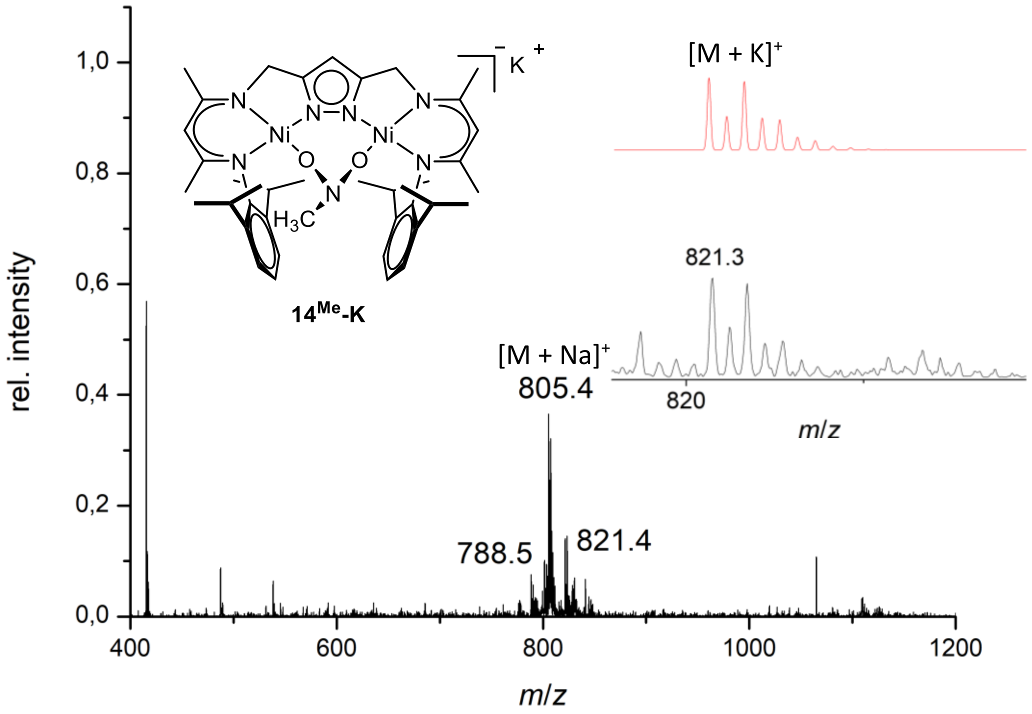

Figure S 80: ESI(+) MS of **14^{Me}-K**.

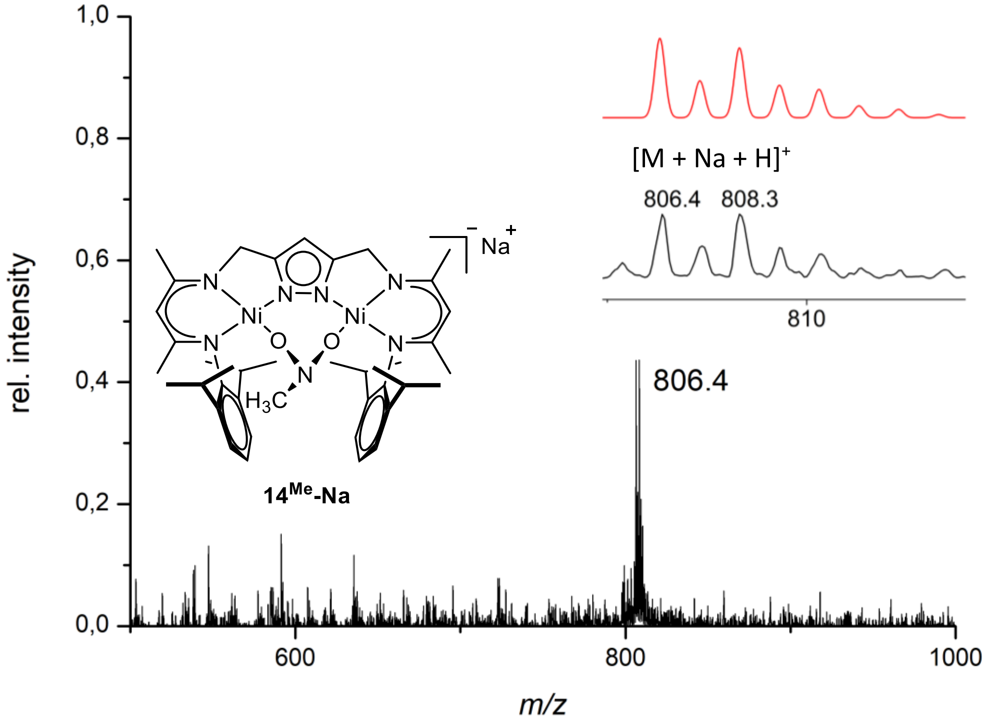

Figure S 81: ESI(+) MS of **14^{Me}-Na.**

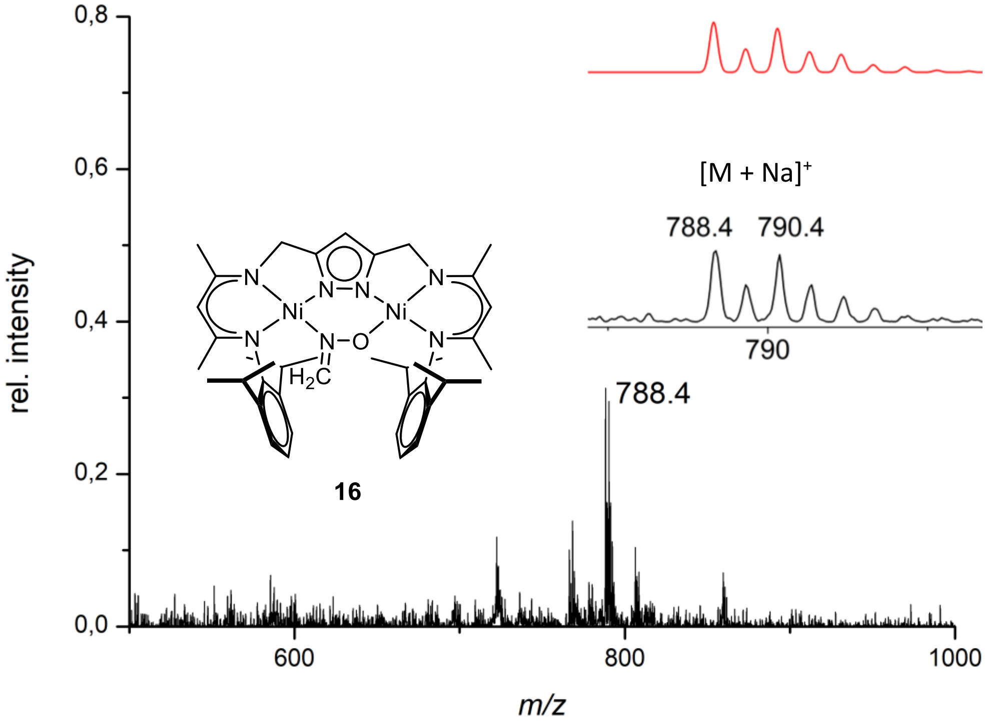

Figure S 82: ESI(+) MS of **16**.

9.5 Experimental X-ray Data

X-ray diffraction experiments have been performed by Dr. Sebastian Dechert. Crystal data and details of the data collections are given in Table 1-9, 11-12 and molecular structures are shown in Figure 19, Figure 23, Figure 28, Figure 49, Figure 56,Figure 61, Figure 68, Figure 73, Figure 77, Figure 85, Figure 93, Figure 101 and Figure 106. X-ray data were collected on a STOE IPDS II or a BRUKER D8-QUEST diffractometer (monochromated Mo-Kα radiation, λ = 0.71073 Å) by use of ω or ω and ϕ scans at low temperature. The structures were solved with SHELXT and refined on F^2 using all reflections with SHELXL.[165] Non-hydrogen atoms were refined anisotropically. In most cases hydrogen atoms were placed in calculated positions and assigned to an isotropic displacement parameter of 1.5/1.2 U_{eq}(C). In case of disorder numerous restraints and constraints have been applied to model the disordered parts (see Table S 1 for details). Face-indexed absorption corrections were performed numerically with the program X-RED[167] or by the multi-scan method with SADABS.[168] PLATON SQUEEZE[166] for strongly disordered lattice solvent molecules has been used in case of **13-cK**, **8-K**, and **16**. The contribution to the structure factors was calculated with PLATON SQUEEZE and the resulting .fab file was processed with SHELXL using the ABIN instruction. The empirical formula and derived values are in accordance with the calculated cell content.

Table S 1: Summary of disordered parts occupancy factors, and applied restraints and constraints.

compound	disordered part	occupancy factors	restraints & constraints	remark
13^{NMe_2}-K	OCH-$C_6H_4NMe_2$	0.490(9) / 0.510(9)	-	-
$6/1^{I}$	I / CH_3	0.4825(15) / 0.5175(15)	-	-
	THF	0.5 for C & H, 0.25 for O	-	fixed occupancy factors
$6/1^{N_2}$	N_2 / CH_3	0.568(7) / 0.432(7)	EADP	-
	THF	0.5 for C & H, 0.25 for O	DFIX (d(C–C)=1.51 Å, d(C–O)=1.43 Å))	fixed occupancy factors

10^{H}	THF	0.5	DFIX (d(C–C)=1.51 Å, d(C–O)=1.43 Å)); DELU; RIGU; BUMP	fixed occupancy factor
13-K	OCH-Ph	0.538(7) / 0.462(7)	DELU, RIGU	-
	THF	0.628(11) / 0.372(11)	DFIX (d(C–C)=1.54 Å, d(C–O)=1.44 Å)); RIGU; SAME	-
	THF	0.5	DFIX (d(C–C)=1.54 Å, d(C–O)=1.44 Å)); SIMU; DELU; RIGU; SAME	fixed occupancy factor
14^{Bna}-cK	THF / C_5H_{12}	0.654(7) / 0.346(7)	DFIX (d(C–C)^{THF}=1.54 Å, d(C–O)=1.44 Å), d(CH_2–CH_2)^{Pentane}=1.52 Å, d(CH_2–CH_3)^{Pentane}=1.51 Å)); SADI (d(C···C)^{Pentane}); SIMU; DELU; RIGU	-
12	-^{i}Pr	0.54(2) / 0.46(2)	SADI (d(C^{Ph}–C^{iPr})); SAME, RIGU	-
	-^{i}Pr	0.61(5) / 0.39(5)	SADI (d(C^{Ph}–C^{iPr})); SAME; RIGU	-
	THF	0.5	DFIX (d(C–C)=1.54 Å, d(C–O)=1.44 Å), d(C···C)=2.0)); SADI (d(C···O)); SIMU; DELU; RIGU	fixed occupancy factor
14^{Me}-K	(K-)THF (2C)	0.490(17) / 0.510(17)	-	-
	(K-)THF (4C)	0.311(14) / 0.689(14)	SAME; SIMU; DELU; EADP	-
	THF	0.404(16) / 0.596(16)	SAME; SIMU; DELU	-
11-K	-^{i}Pr	0.774(7) / 0.226(7)	SADI (d(C^{Ph}–C^{iPr})); SAME; RIGU; EADP	-
	(K-)THF	0.614(8) / 0.386(8)	SAME; RIGU; SIMU; DELU	-

	(K-)THF	0.800(7) / 0.200(7)	SAME; RIGU; SIMU; DELU	-
6	THF	0.5 for C & H, 0.25 for O	DFIX (d(C–C)=1.54 Å, d(C–O)=1.44 Å))	fixed occupancy factors
8-cK	[2.2.2]-Cryptand	0.570(10) / 0.430(10)	-	-
	Et$_2$O	0.52(2) / 0.48(2)	DFIX (d(C–C)=1.51 Å, d(C–O)=1.43 Å)); RIGU	-
14^{Ph}-Na	-^{i}Pr	0.64(4) / 0.36(4)	SAME; SADI (d(C^{Ph}–C^{iPr})); EADP	-
	THF	0.503(13) / 0.497(13)	DFIX (d(C–C)=1.54 Å, d(C–O)=1.44 Å)); SADI (d(O···C)); DELU; RIGU	-
	THF	0.5 for C & H, 0.25 for O	DFIX (d(C–C)=1.54 Å, d(C–O)=1.44 Å)); SADI (d(O···C)); SIMU; DELU; RIGU; EADP	fixed occupancy factors
14^{Me}-Na	THF	0.726(13) / 0.274(13)	SADI (d(O-Na)), SAME, SIMU, DELU	-
	THF	0.730(12) / 0.270(12)	SAME, SIMU, DELU	-

Table S 2: Crystal data and refinement details for **6**, **8-K**, **8-cK**, **10**$^{\mathbf{H}}$, and **11-K**.

compound	**6**	**8-K**	**8-cK**	**10**$^{\mathbf{H}}$	**11-K**
empirical formula	$C_{42}H_{60}N_6Ni_2O_{0.50}$	$C_{109}H_{173}K_2N_{12}Ni_4O_5Si_2$	$C_{65}H_{109}KN_8Ni_2O_7Si$	$C_{42}H_{58}N_6Ni_2O_{1.50}$	$C_{52}H_{79}KN_6Ni_2O_4$
formula weight	774.38	2100.80	1299.21	788.36	1008.73
T [K]	100(2)	100(2)	100(2)	133(2)	133(2)
crystal size [mm³]	0.463 x 0.171 x 0.158	0.394 x 0.349 x 0.220	0.539 x 0.449 x 0.370	0.500 x 0.480 x 0.450	0.200 x 0.190 x 0.170
crystal system	monoclinic	triclinic	monoclinic	monoclinic	monoclinic
space group	$P2_1/c$ (No. 14)	P-1 (No. 2)	$P2_1/c$ (No. 14)	$P2_1/c$ (No. 14)	$P2_1/n$ (No. 14)
a [Å]	17.2297(6)	13.6148(5)	11.8916(3)	17.2519(4)	13.9866(6)
b [Å]	14.0251(6)	21.3435(8)	36.7854(9)	14.1561(3)	16.9590(5)
c [Å]	17.1186(7)	21.5988(8)	16.6879(5)	17.3971(4)	22.5078(9)
α [°]	90	115.041(2)	90	90	90
β [°]	112.3070(10)	90.799(2)	108.0560(10)	112.708(2)	103.041(3)
γ [°]	90	97.871(2)	90	90	90
V [Å³]	3827.1(3)	5614.7(4)	6940.4(3)	3919.37(16)	5201.1(3)
Z	4	2	4	4	4
ρ [g·cm^{-3}]	1.344	1.243	1.243	1.336	1.288
F(000)	1656	2258	2800	1680	2160
μ [mm^{-1}]	1.024	0.811	0.674	1.003	0.852
T_{min} / T_{max}	0.75 / 0.85	0.75 / 0.84	0.71 / 0.79	0.7730 / 0.8663	0.6413 / 0.8930
θ-range [°]	2.036 - 27.485	1.907 - 28.322	2.165 - 27.907	1.918 - 26.925	1.518 - 26.868
hkl-range	-22 to 18, ±18, ±22	±18, ±28, ±28	±15, ±48, ±21	-20 to 21, ±17, ±21	±17, ±21, ±28
measured refl.	104356	274876	183927	55966	69075
unique refl. [R_{int}]	8771 [0.0673]	27891 [0.0685]	16569 [0.0251]	8314 [0.0298]	11083 [0.1108]
observed refl. ($I > 2\sigma(I)$)	7116	22811	15679	7003	7508
data / restr. / param.	8771 / 8 / 508	27891 / 0 / 1238	16569 / 50 / 974	8314 / 50 / 500	11083 / 373 / 702
goodness-of-fit (F^2)	1.121	1.074	1.087	1.033	1.008
$R1$, $wR2$ ($I > 2\sigma(I)$)	0.0339 / 0.0783	0.0412 / 0.0820	0.0269 / 0.0654	0.0365 / 0.0989	0.0504 / 0.1198
$R1$, $wR2$ (all data)	0.0509 / 0.0907	0.0577 / 0.0909	0.0288 / 0.0664	0.0454 / 0.1036	0.0855 / 0.1402
res. el. dens. [e·Å^{-3}]	-0.420 / 0.801	-0.697 / 0.917	-0.290 / 0.596	-0.669 / 0.752	-0.678 / 0.442

Table S 3: Crystal data and refinement details for **12**, **13-K**, **13-cK**, **13$^{\mathbf{NMe2}}$**, and **14$^{\mathbf{Bna}}$-cK**.

compound	**12**	**13-K**	**13-cK**	**13$^{\mathbf{NMe_2}}$**	**14$^{\mathbf{Bna}}$-cK**
empirical formula	$C_{43}H_{64}N_6Ni_2O_{2.50}$	$C_{52}H_{71}KN_6Ni_2O_{2.50}$	$C_{68}H_{103}KN_8Ni_2O_8$	$C_{60}H_{84}KN_7Ni_2O$	$C_{68.35}H_{103.38}KN_9Ni_2O_{9.65}$
formula weight	822.42	976.66	1317.10	1075.86	1362.11
T [K]	133(2)	133(2)	133(2)	133(2)	133(2)
crystal size [mm³]	0.420 x 0.180 x 0.150	0.500 x 0.480 x 0.460	0.360 x 0.240 x 0.140	0.500 x 0.250 x 0.160	0.500 x 0.410 x 0.400
crystal system	triclinic	triclinic	monoclinic	monoclinic	triclinic
space group	P-1 (No. 2)	P-1 (No. 2)	$P2_1/c$ (No. 14)	$P2_1/n$ (No. 14)	P-1 (No. 2)
a [Å]	9.2649(3)	11.6779(4)	13.5924(3)	12.8146(3)	11.9074(4)
b [Å]	14.8310(6)	14.3140(5)	23.6725(4)	16.1193(2)	14.4475(4)
c [Å]	16.8819(6)	16.5164(5)	23.6461(5)	27.2061(7)	22.0586(6)
α [°]	108.478(3)	105.778(2)	90	90	87.186(2)
β [°]	96.806(3)	96.526(3)	95.263(2)	95.191(2)	75.135(2)
γ [°]	104.467(3)	111.211(2)	90	90	76.021(2)
V [Å³]	2080.41(14)	2406.66(14)	7576.4(3)	5596.7(2)	3558.83(19)
Z	2	2	4	4	2
ρ [g·cm^{-3}]	1.313	1.348	1.155	1.277	1.271
F(000)	880	1040	2824	2304	1457
μ [mm^{-1}]	0.949	0.917	0.605	0.793	0.648
T_{min} / T_{max}	0.6515 / 0.8500	0.6153 / 0.7644	0.5688 / 0.8505	0.7791 / 0.9310	0.6430 / 0.9140
θ-range [°]	1.302 - 26.879	1.621 - 26.877	1.220 - 26.177	1.470 - 26.858	1.453 - 26.875
hkl-range	±11, ±18, ±21	-13 to 14, ±18, ±20	±16, -29 to 28, ±29	-15 to 16, ±20, ±34	±15, ±18, ±27
measured refl.	29689	34788	163334	67187	49927
unique refl. [R_{int}]	8838 [0.0433]	10196 [0.0251]	163334 [?]	11898 [0.0459]	15076 [0.0391]
observed refl. ($I > 2\sigma(I)$)	6324	8592	70598	9261	13194
data / restr. / param.	8838 / 145 / 583	10196 / 311 / 726	163334 / 0 / 798	11898 / 0 / 758	15076 / 134 / 871
goodness-of-fit (F^2)	1.028	1.031	1.023	1.054	1.029
$R1$, $wR2$ ($I > 2\sigma(I)$)	0.0467 / 0.1157	0.0357 / 0.0955	0.0807 / 0.1858	0.0358 / 0.0850	0.0335 / 0.0895
$R1$, $wR2$ (all data)	0.0729 / 0.1316	0.0444 / 0.0996	0.2033 / 0.2401	0.0548 / 0.0929	0.0397 / 0.0939
res. el. dens. [e·Å^{-3}]	-0.483 / 0.662	-0.522 / 0.662	-0.557 / 0.879	-0.332 / 0.306	-0.316 / 0.716

Table S 4: Crystal data and refinement details for **14^{Ph}-Na**, **14^{Me}-K**, **14^{Me}-Na**, and **16**.

compound	**14^{Ph}-Na**	**14^{Me}-K**	**14^{Me}-Na**	**16**
empirical formula	$C_{51}H_{70}N_7NaNi_2O_{3.50}$	$C_{56}H_{88}KN_7Ni_2O_6$	$C_{52}H_{80}N_7NaNi_2O_5$	$C_{43}H_{62}N_7Ni_2O$
formula weight	977.55	1111.85	1023.64	810.41
T [K]	100(2)	133(2)	133(2)	100(2)
crystal size [mm^3]	0.268 x 0.231 x 0.186	0.500 x 0.240 x 0.190	0.190 x 0.150 x 0.130	0.402 x 0.367 x 0.325
crystal system	triclinic	triclinic	monoclinic	triclinic
space group	P-1 (No. 2)	P-1 (No. 2)	$P2_1/n$ (No. 14)	P-1 (No. 2)
a [Å]	11.8771(8)	12.1570(4)	17.8048(6)	11.354(3)
b [Å]	14.0664(9)	13.9573(4)	13.7005(6)	14.651(4)
c [Å]	16.1644(10)	18.8940(5)	21.6707(9)	15.927(3)
α [°]	105.801(2)	70.117(2)	90	100.815(6)
β [°]	95.870(2)	80.522(2)	101.581(3)	98.732(6)
γ [°]	111.201(2)	69.874(2)	90	104.412(5)
V [Å^3]	2361.2(3)	2826.59(15)	5178.6(4)	2465.0(10)
Z	2	2	4	2
ρ [g·cm^{-3}]	1.375	1.306	1.313	1.092
$F(000)$	1040	1192	2192	866
μ [mm^{-1}]	0.859	0.794	0.788	0.799
T_{min} / T_{max}	0.72 / 0.86	0.7571 / 0.8358	0.8722 / 0.9849	0.64 / 0.78
θ-range [°]	1.935 - 27.928	1.632 - 26.840	1.354 - 26.890	2.042 - 27.966
hkl-range	±15, ±18, ±21	-14 to 15, ±17, ±23	±22, ±17, -27 to 23	±14, ±19, -18 to 21
measured refl.	112909	40728	42498	61129
unique refl. [R_{int}]	11310 [0.0982]	11991 [0.0372]	11024 [0.1731]	11747 [0.0918]
observed refl. ($I > 2\sigma(I)$)	8736	9850	5063	8198
data / restr. / param.	11310 / 178 / 685	11991 / 198 / 752	11024 / 261 / 709	11747 / 0 / 491
goodness-of-fit (F^2)	1.071	1.030	1.046	1.016
$R1$, $wR2$ ($I > 2\sigma(I)$)	0.0432 / 0.0969	0.0330 / 0.0817	0.0816 / 0.1292	0.0587 / 0.1310
$R1$, $wR2$ (all data)	0.0676 / 0.1117	0.0450 / 0.0876	0.2084 / 0.1749	0.0949 / 0.1536
res. el. dens. [e·Å^{-3}]	-0.821 / 0.983	-0.243 / 0.508	-0.417 / 0.481	-0.905 / 1.121

9.6 DFT Calculation

DFT calculations were performed by Dr. Sebastian Dechert. Calculation for the geometrical optimizations of the reported complexes were performed using the ORCA software package 4.2.0 with BP86 functional,[169] D3BJ dispersion correction,[170] def2-tzvp[171] and def2-txvp/j[172] basis sets.

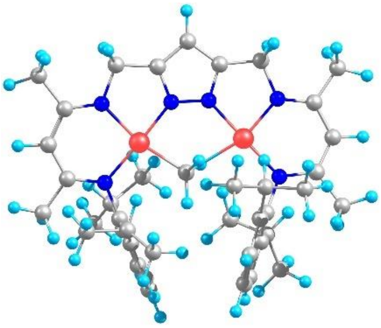

Figure S 83: DFT calculated molecular structure of **6**.

Table S 5: Geometry optimized coordinates of the structure of **6**.

Atom	Cartesian coordinates [Å]		
Ni	1.975.781	-1.107.869	0.254464
Ni	-1.860.082	-1.239.999	-0.108187
N	0.788312	-2.515.030	0.109528
N	3.252.973	-2.482.146	0.393657
N	3.233.929	0.295022	0.268466
N	-0.561969	-2.564.219	-0.054201
N	-3.016.005	-2.742.573	-0.361195
N	-3.246.158	0.059674	-0.188326
C	0.657716	0.156813	0.654693
H	-0.319001	-0.146475	0.260805
H	0.549720	0.291772	1.736.927
H	0.898685	1.134.716	0.222549
C	1.255.073	-3.772.798	0.093978
C	2.727.453	-3.857.982	0.304135
C	4.553.379	-2.327.497	0.599229
C	4.553.060	0.152196	0.437239
C	2.748.924	1.608.793	-0.092833
C	-0.919488	-3.851.747	-0.158429
C	0.209511	-4.662.629	-0.081034
C	5.166.747	-1.079.317	0.660866
C	5.442.620	-3.546.109	0.747872
C	5.475.303	1.345.997	0.336735
C	2.200.552	2.430.753	0.902370
C	2.813.463	2.005.553	-1.438.044
C	-2.380.085	-4.073.445	-0.320802
C	-4.330.027	-2.705.895	-0.548427
C	-4.531.677	-0.216882	-0.454781
C	-2.933.431	1.443.537	0.047796
C	1.728.075	3.683.820	0.509731
C	2.109.642	1.961.500	2.352.966
C	2.322.006	3.267.657	-1.760.479
C	3.384.152	1.109.324	-2.521.741

C	-5.035.800	-1.500.966	-0.610768
C	-5.114.367	-3.987.280	-0.665304
C	-5.539.327	0.905282	-0.602596
C	-3.007.892	1.947.043	1.355.194
C	-2.537.719	2.259.260	-1.023.527
C	1.792.948	4.092.443	-0.804114
C	0.945687	2.578.560	3.104.688
C	3.391.152	2.198.185	3.129.893
C	2.278.531	0.402813	-3.306.938
C	4.292.681	1.848.670	-3.495.839
C	-2.688.147	3.286.884	1.571.217
C	-3.451.103	1.079.897	2.519.578
C	-2.225.690	3.591.470	-0.753007
C	-2.430.040	1.730.517	-2.447.216
C	-2.299.457	4.105.309	0.527964
C	-4.826.218	1.464.446	3.036.649
C	-2.463.265	1.097.922	3.659.618
C	-0.990895	1.786.914	-2.938.331
C	-3.348.908	2.468.869	-3.421.145
H	0.252487	-5.610.155	-0.135863
H	2.924.417	-4.352.705	1.138.691
H	3.151.910	-4.336.290	-0.450981
H	6.091.946	-1.065.468	0.875805
H	5.112.168	-4.103.936	1.482.619
H	6.359.663	-3.259.837	0.941813
H	5.430.936	-4.062.365	-0.085038
H	5.732.360	1.482.227	-0.599056
H	6.277.792	1.185.029	0.876297
H	5.013.198	2.144.187	0.668188
H	1.354.687	4.266.084	1.160.986
H	1.468.745	4.951.460	-1.048.065
H	2.354.297	3.562.816	-2.662.884
H	1.955.930	0.973690	2.333.133
H	1.098.054	3.540.966	3.209.893
H	0.869292	2.161.094	3.988.229
H	0.117186	2.431.843	2.601.361
H	4.121.626	1.691.963	2.716.435
H	3.271.552	1.900.260	4.055.775
H	3.608.781	3.153.655	3.119.747
H	3.932.894	0.404397	-2.072.466
H	1.736.048	-0.136264	-2.694.090
H	2.680.889	-0.178537	-3.985.311
H	1.710.494	1.071.050	-3.744.996
H	4.698.711	1.206.412	-4.115.023
H	4.998.358	2.310.963	-2.996.906
H	3.767.263	2.502.751	-4.001.031
H	-2.561.780	-4.567.008	-1.159.519
H	-2.734.049	-4.600.713	0.438303
H	-5.968.207	-1.568.456	-0.779384
H	-4.832.582	-4.470.643	-1.469.894
H	-6.070.800	-3.781.451	-0.725998
H	-4.950.118	-4.544.152	0.124454
H	-5.374.272	1.584.951	0.083904
H	-6.445.135	0.547158	-0.496890

H	-5.449.313	1.310.735	-1.490.758
H	-2.738.459	3.643.149	2.450.504
H	-2.084.090	5.016.230	0.690159
H	-1.956.364	4.158.747	-1.465.780
H	-3.508.319	0.138389	2.187.355
H	-5.086.594	0.853471	3.757.310
H	-5.477.580	1.405.572	2.306.814
H	-4.800.876	2.382.115	3.379.240
H	-1.582.709	0.816451	3.332.852
H	-2.762.138	0.483181	4.361.079
H	-2.400.449	2.005.096	4.023.856
H	-2.709.089	0.770340	-2.435.812
H	-0.681025	2.716.566	-2.935.645
H	-0.942955	1.428.360	-3.849.600
H	-0.422792	1.250.626	-2.346.758
H	-4.275.990	2.401.348	-3.110.578
H	-3.272.564	2.066.897	-4.311.074
H	-3.086.700	3.413.379	-3.465.596
Ni	1.975.781	-1.107.869	0.254464
Ni	-1.860.082	-1.239.999	-0.108187
N	0.788312	-2.515.030	0.109528
N	3.252.973	-2.482.146	0.393657
N	3.233.929	0.295022	0.268466
N	-0.561969	-2.564.219	-0.054201
N	-3.016.005	-2.742.573	-0.361195
N	-3.246.158	0.059674	-0.188326
C	0.657716	0.156813	0.654693
H	-0.319001	-0.146475	0.260805

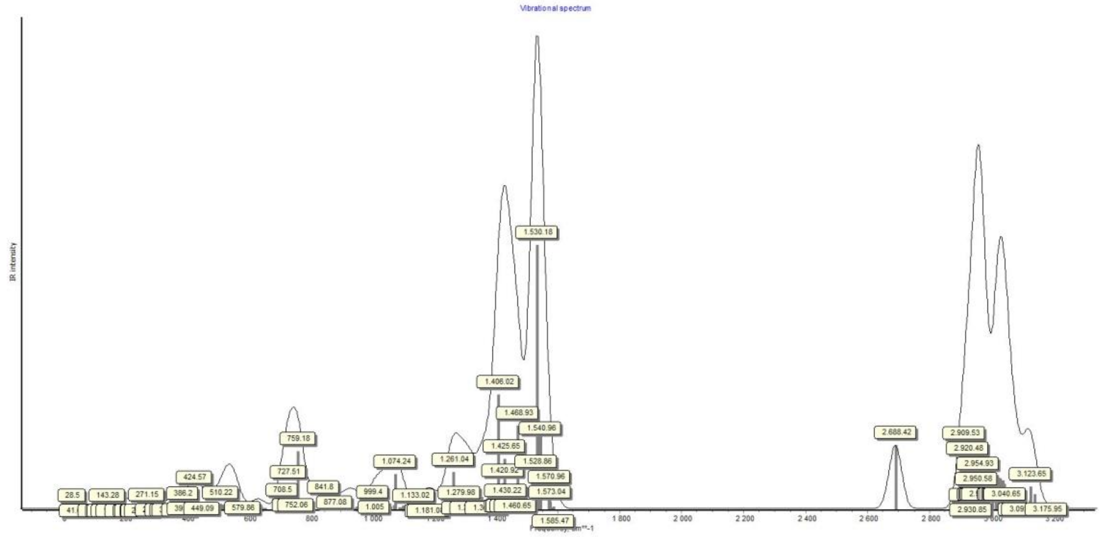

Figure S 84: Calculated IR spectrum for **6**.

9.7 Table of Compound Structures

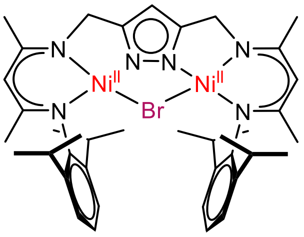
N
N–N
Ni^{II}
Ni^{II}
Br

1$^{\mathbf{Br}}$

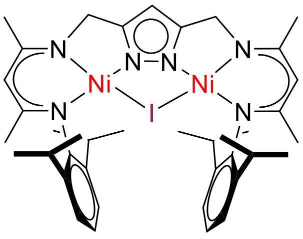

1$^{\mathbf{I}}$

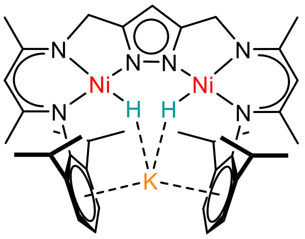
N
N–N
Ni
Ni
H
H
K

2-K

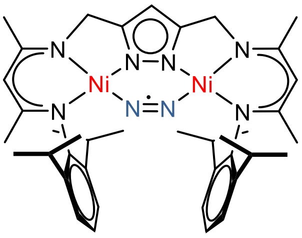

4$^{\mathbf{N_2}}$

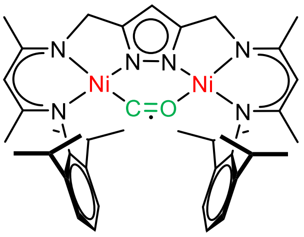

4$^{\mathbf{CO}}$

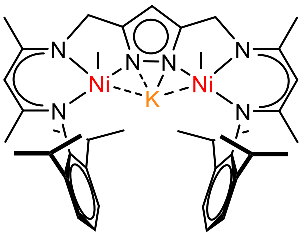

5

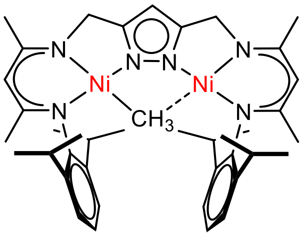
N
N–N
Ni
Ni
CH3

6

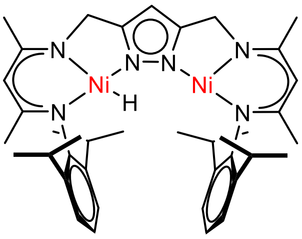

7

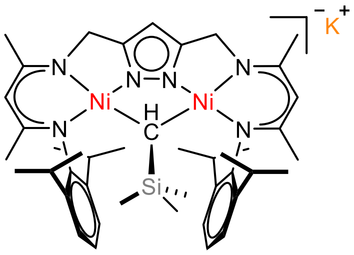
N
N–N
Ni
Ni
H
C
Si
− K+

8-K

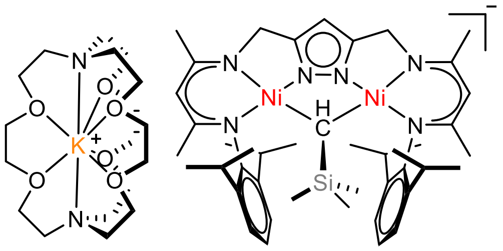
N
O
K+
N
N–N
Ni
Ni
H
C
Si
−

8-cK

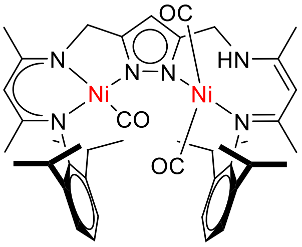
OC
N
N–N
HN
Ni
Ni
CO
N
OC

9

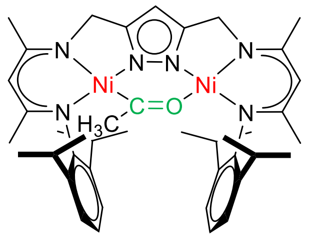
N
N–N
N
Ni
Ni
N
N
H3C
C=O

10^{Me}

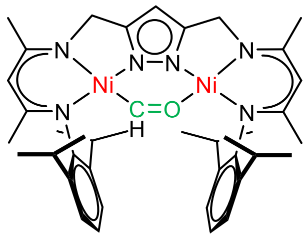
N
N–N
N
Ni
Ni
N
N
C=O
H

10^{H}

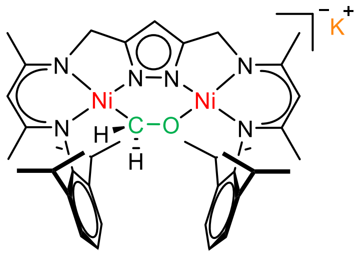
–
K+
N
N–N
N
Ni
Ni
N
N
H
C–O
H

11-K

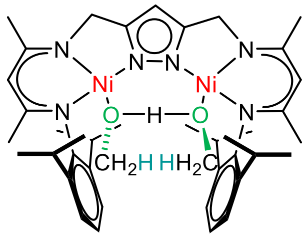
N
N–N
N
Ni
Ni
N
N
O–H–O
CH2H HH2C

12

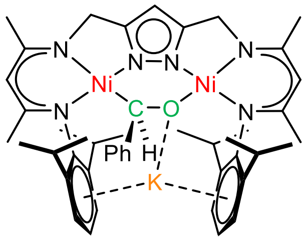
N
N–N
N
Ni
Ni
N
N
C–O
Ph
H
K

13-K

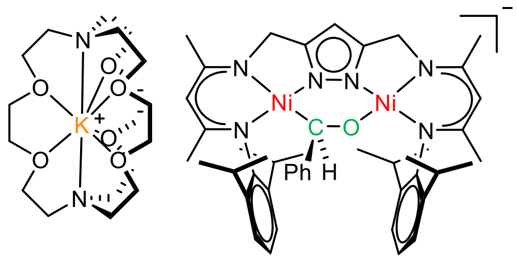
N
O
O
O
O
K+
O
O
N
–
N
N–N
N
Ni
Ni
N
N
C–O
Ph
H

13-cK

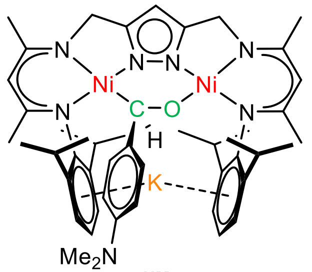
N
N–N
N
Ni
Ni
N
N
C–O
H
K
Me2N

13^{NMe_2}-K

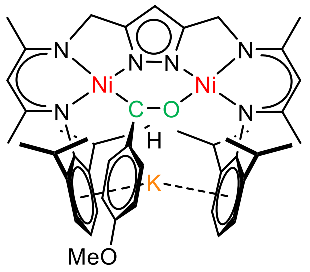
N
N–N
N
Ni
Ni
N
N
C–O
H
K
MeO

13^{OMe}-K

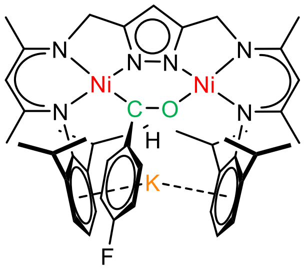
N
N–N
N
Ni
Ni
N
N
C–O
H
K
F

13^{F}-K

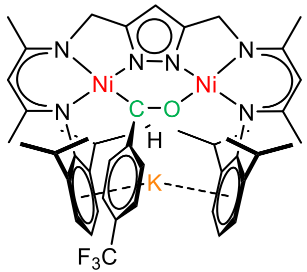
N
N–N
N
Ni
Ni
N
N
C–O
H
K
F3C

13^{CF_3}-K

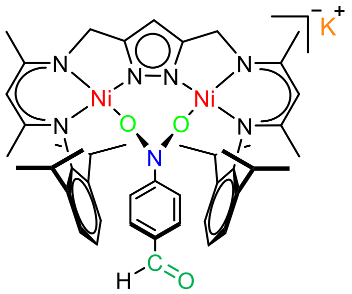

14$^{\mathrm{Bna}}$-K

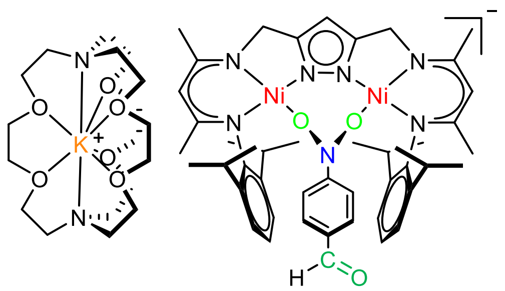

14$^{\mathrm{Bna}}$-cK

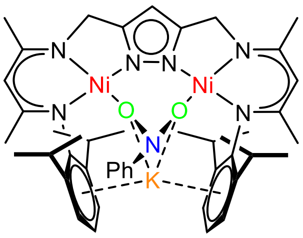

14$^{\mathrm{Ph}}$-K

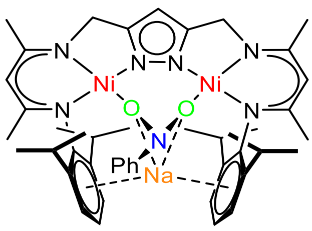

14$^{\mathrm{Ph}}$-Na

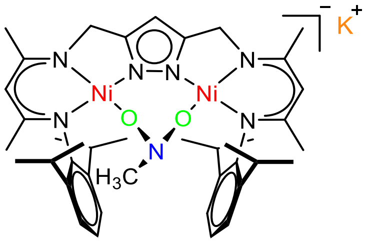

14$^{\mathrm{Me}}$-K

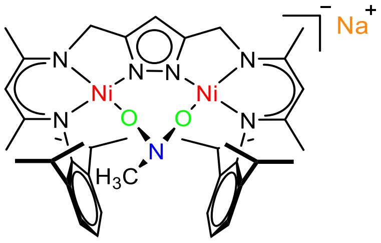

14$^{\mathrm{Me}}$-Na

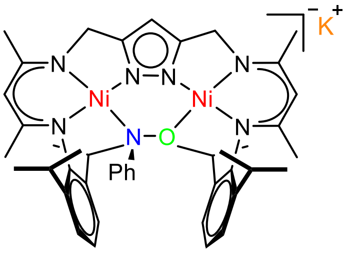

15$^{\mathrm{Ph}}$-K

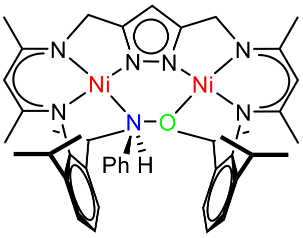

15$^{\mathrm{Ph}}$-H

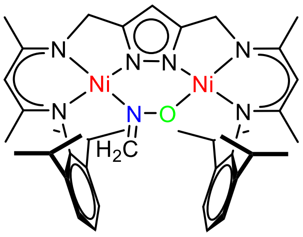

16

Acknowledgements

At first, I want to acknowledge Prof. Dr. Franc Meyer for giving me the opportunity to work on this research project. I am very grateful for his guidance and the scientific freedom I had working in his group. I thank him for his optimism, enthusiasm and trust in managing scientific problems as well as administrator tasks as coordinator for the CaSuS program. Furthermore, I want to acknowledge my co-supervisors Prof. Dr. Sven Schneider and Prof. Dr. Marc Walter for their constructive comments regarding my research.

I thank the state of Lower-Saxony for funding my PhD with the Georg-Christoph-Lichtenberg scholarship of the International Ph.D. program "Catalysis for Sustainable Synthesis (CaSuS)".and the Georg-August-Universität Göttingen for supporting this work.

I also want to thank Dr. Sebastian Dechert for performing all X-ray diffraction experiments and DFT calculations presented in this work, the NMR department of the University of Göttingen for performing NMR experiments and for making the NMR machines available for me, the analytic department of the University of Göttingen for performing elemental analyses, Andreas Schwarz for providing the starting material (3,5-dicarbamidopyrazole) for the presented ligand synthesis and Dr. Claudia Stückl for performing EPR measurements. I want to thank Britta Müller and Dr. Claudia Stückl for taking care of administrative tasks.

I thank Marvin Lange and Sarah Bete for their experimental work during their research internships under my supervision, and U-Hyun Kim for her hard work and enthusiasm during her very successful Bachelor thesis, which I was glad to supervise.

I deeply thank Dr. Josh Abbenseth, Dr. Christopher Inman, Dr. Allyssa Massie, Dr. Hendrik Stevens and Dr. Joanne Wong for their linguistic and scientific comments regarding the correction of this work.

I also want to thank my lab mates Giuseppe Lococciolo and Dr. Allyssa Massie of Lab T032 and my past lab mates Claudia Schremmer and Dr. Mike Schütze of Lab P129 for the fun times and the good atmosphere during work. I especially want to thank Dr. Hendrik Stevens who accompanied me the entire PhD as a colleague and friend. I thank him for the sometimes heated scientific discussions, the fruitful collaboration regarding our research projects and for being there as a friend during my time in Göttingen.

Furthermore, I want to thank the people who I met during my studies in Heidelberg. I thank Dr. Marcel Brill and Dr. Joachim Ballmann, who taught me the practical laboratory skills that are essential for being a chemist during my master studies. I thank Jan Wenz, Florian Mulks, Roxana Lorenz and Steffanie Auras for their friendship and support during my Bachelor and Master studies. I thank Jan Wenz in particular for the late nights we spend learning for exams or writing protocols and the good times we had together on the rare evenings we did not have to study.

Finally, I thank my family. My sister Laura Kothe for her love and affection, my mother Irene Kothe for raising me with all her love and for fueling my pursuit for knowledge in all areas and my father Reinhard Kothe for his endless support and for sparking my passion for science.

Curriculum Vitae

Thomas Kothe
Zimmermannstraße 13
37075 Göttingen
E-Mail: thomas.kothe@chemie.uni-goettingen.de
Tel.: +49 151 28720625

Date of birth: 01.03.1988
Place of birth: Gelnhausen (Hessen)
Nationality: Deutsch

Academic Career

Since 10/2015	PhD candidate: “Catalysis for Sustainable Synthesis (CaSuS)” Georg-August Universität Göttingen (Workgroup: Meyer) Christoph-Lichtenberg Fellow of the state of Lower-Saxony
09/2011 – 02/2015	Master of Science (Chemistry) Ruprecht-Karls Universität Heidelberg Master thesis: „Ein neuer tripodaler Bisamidophosphinligand und dessen Gruppe IV Metallkomplexe“ (Workgroup: Ballmann)
09/2008 – 07/2011	Bachelor of Science (Chemistry) Ruprecht-Karls Universität Heidelberg Master thesis: „Synthese spirocyclischer Pyrrolidine“ (Workgroup: Helmchen)
08/2007 – 08/2008	Apprenticeship: Chemisch-technischer Assistenten Ludwig-Geißler-Schule Hanau
Bis 06/2007	Allgemeines Abitur Ludwig-Geißler-Schule Hanau Leistungskurse: Chemie-Technik/Physik

27.09.20 Göttingen